Karlsruhe Institute of Technology

Tritium ions in KATRIN: blocking, removal and detection

Zur Erlangung des akademischen Grades eines
Doktors der Naturwissenschaften
von der Fakultät für Physik
des Karlsruher Instituts für Technologie
genehmigte
Dissertation
von

M. Sc. Manuel Klein

aus Kandel

Referent:	Prof. Dr. G. Drexlin Institut für Experimentelle Teilchenphysik, KIT
Korreferent:	Prof. Dr. G. Quast Institut für Experimentelle Teilchenphysik, KIT
Korreferent:	Dr. Kathrin Valerius Institut für Kernphysik, KIT

Tag der mündlichen Prüfung: 14. Dezember 2018

Erklärung der Selbstständigkeit

Hiermit versichere ich, dass ich die vorliegende Arbeit eigenständig angefertigt habe. Ich habe nur die angegebenen Quellen und Hilfsmittel benutzt und mich keiner unzulässigen Hilfe Dritter bedient. Insbesondere habe ich wörtlich oder dem Sinn nach aus anderen Werken übernommene Inhalte als solche kenntlich gemacht.

Karlsruhe, Oktober 2018 Manuel Klein

Introduction

Neutrinos are the lightest massive particle species in the universe and the second most abundant at an average density of 340 per cm^3 [Per09]. The finite mass of neutrinos follows from the observed neutrino oscillations due to the mixing of the three neutrino mass eigenstates in vacuum [Ams07, Per09, Pov09]. A non-zero neutrino mass already implies physics beyond the standard model, which considers only left-handed neutrinos [Ams07]. But the neutrino mass might provide even further keys to "new physics", given that it is at $\lesssim 1$ eV/c^2 considerably smaller than the mass of the other fundamental fermions [Per09]. But until today, the absolute values of the neutrino masses remain unknown.

The KArlsruhe TRItium Neutrino (KATRIN) experiment aims at the model-independent determination of the absolute neutrino mass scale with a sensitivity of 0.2 eV/c^2 (90% CL) for the effective electron neutrino mass after three full years of measurement time [CDR04]. For this purpose, KATRIN investigates the imprint of the neutrino mass on the tritium beta spectrum near its kinematic end point. KATRIN employs a high-luminosity Windowless Gaseous Tritium Source (WGTS), which creates 10^{11} beta electrons per second. The beta electrons are guided by a strong magnetic field up to 6 T to the Main spectrometer, which acts as a high-pass MAC-E filter in order to scan the end point region of the beta spectrum.

Tritium ions are the inadvertent by-products of tritium beta decay and inelastic scattering of beta electrons in the WGTS. Under nominal conditions, $2 \cdot 10^{11}$ positive ions/s leave the WGTS along the magnetic guiding field towards the spectrometers. There, they could create background due to the radioactivity of the tritium and via the ionisation of residual gas. For this reason, the ion flux into the Pre-spectrometer (PS) has to be restricted to $1 \cdot 10^4$ ions/s.

Ring and dipole electrodes were therefore installed in the KATRIN beamline in order to block the positive tritium ions with electrostatic potentials and to remove the stored ions via $E \times B$-drift in negative dipole potentials. A proof-of-principle for the ion blocking and removal was achieved in the First Light measurement campaign in 2016 with a pencil beam of non-radioactive deuterium ions. Nevertheless, the ring electrode potentials could be neutralised during tritium operation due to the trapping of secondary electrons and negative ions in the positive potential wells. For this reason, a constant monitoring of the ion flux into the PS is required.

Monitoring of the ion flux in the KATRIN beamline is based on several ion detection methods. The most sensitive method exploits the background from secondary electrons due to ionisation of residual gas by the positive ions, which are accelerated to keV-energies by the high voltage of the Pre- or Main spectrometer; the produced secondary electrons provide the signal for this detection method. Inside the PS, about 20% of the ions will be accelerated onto the one solid inner electrode; the neutralisation of the ions can be measured as current in the connected voltage sup-

ply and allows a continuous monitoring of the ion flux into the PS. If the ion flux surpasses the limit of $2 \cdot 10^8$ ions/s into the PS, which is imposed by the regulations of radiation protection, the valve to the PS will be closed automatically. Further ion detection methods include the ion neutralisation current on the dipole electrodes, which is monitored continuously.

The First Tritium measurements in May and June 2018 at about 0.5% of the nominal tritium concentration marked the first tritium operation with KATRIN. With regard to ion safety, the ionisation method applied to the PS allowed to derive an upper limit on the ion flux into the PS at the aspired level of $1 \cdot 10^4$ ions/s. During the first scans of the tritium beta spectrum with KATRIN, the PS current measurement monitored the ion flux into the PS continuously. In the meantime, only about 50% of the expected ion flux was measured with the current measurement at the dipole electrode closest to the source, while the other dipole electrodes observed no ions at all. Such inadvertent ion blocking had already been observed during First Light and is attributed to work function differences of different beam tube materials. Whether the inadvertent ion blocking also occurs during measurements with 100% tritium and how the trapped ions might affect the neutrino mass measurements needs to be subject to future investigations.

This thesis reports the first safe tritium operation of KATRIN with regard to ion safety. First, the motivation for the measurement of the neutrino mass will be underlined (chapter I) and an overview of the KATRIN experiment for the neutrino mass search will be given (chapter II). With regard to ions, chapter III will explain the creation of tritium ions inside KATRIN, and chapter IV discusses the potential background by tritium ions in the spectrometers. The impact of tritium ions on the neutrino mass measurement will be summarised in chapter V along with consequent limits on the ion flux into the PS and on the concentration of ions in the WGTS. In order to maintain and monitor these limits, specific hardware is required: the ring and dipole electrodes for ion blocking and removal, which will be described in chapter VI, and various setups for ion detection, as described in chapter VII. A test of the ion blocking and removal was possible during the First Light campaign, the results of which will be presented in chapter VIII. Then the even more prolific ion measurements during the First Tritium campaign will be summarised in chapter IX. Finally, several conclusions from this thesis will be given in chapter X along with an outlook on future work with regard to tritium ion safety in KATRIN.

Contents

Introduction v

I Neutrinos and their masses 1
- I.1 Neutrinos in the standard model . . . 2
- I.2 Neutrinos in cosmology . . . 3
- I.3 Oscillation of massive neutrinos . . . 4
  - I.3.1 Oscillation mechanism . . . 4
  - I.3.2 Discovery of the oscillation of atmospheric neutrinos . . . 5
  - I.3.3 The solar neutrino problem and MSW effect . . . 7
  - I.3.4 Measurement of neutrino mass splittings . . . 10
- I.4 Determination of the absolute neutrino mass scale . . . 11
  - I.4.1 Spectroscopy of beta decay and electron capture . . . 11
  - I.4.2 Neutrinoless double beta decay . . . 14
  - I.4.3 Neutrino mass impact on cosmological models . . . 16
- I.5 What we know and don't know about the neutrino mass . . . 17

II The KATRIN experiment 19
- II.1 Measurement principle . . . 21
- II.2 Overview of the KATRIN beamline . . . 24
- II.3 Software for data acquisition and analysis . . . 29
- II.4 Experimental conditions during the neutrino mass measurements . . . 30
  - II.4.1 Temperature regimes . . . 30
  - II.4.2 Pressure regimes and gas species . . . 30
  - II.4.3 Magnetic fields . . . 33
  - II.4.4 Electric fields . . . 33
  - II.4.5 Source plasma . . . 35
- II.5 Effect of background on the neutrino mass sensitivity . . . 38

III Ion creation and transport 39
- III.1 Beta electrons and secondary electrons . . . 40
  - III.1.1 Tritium activity . . . 40
  - III.1.2 Charged particles in a static electric and magnetic field . . . 41
  - III.1.3 Beta electron flux into the PS . . . 44
  - III.1.4 Flux of secondary electrons into the DPS . . . 45
- III.2 Positive and negative thermal ions . . . 46
  - III.2.1 Positive ion creation and transformation . . . 46
  - III.2.2 Negative ion creation . . . 47
  - III.2.3 Thermalisation . . . 48

III.2.4 Recombination 50
III.2.5 Expected flux of positive ions into the DPS 51
III.2.6 Expected flux of negative ions into the DPS 54
III.3 Ions from molecular dissociation 56
III.3.1 Theory of molecular excitation and dissociation 56
III.3.2 Dissociative ionisation by electron scattering 59
III.3.3 Dissociation of daughter ions from tritium decay 62
III.3.4 Expected flux of dissociation ions into the PS 68
III.3.5 Proposal for future simulations and measurements 73
III.4 Ions from Penning discharges in ring electrodes 75
III.4.1 Penning discharge mechanism 75
III.4.2 Expected Penning ion rate from ring electrodes 75
III.5 Ion creation in the DPS and CPS 78
III.6 Ions and electrons in the transport section 79
III.6.1 Ion trapping by magnetic mirror effect 79
III.6.2 Inadvertent blocking potentials 80
III.6.3 Neutralisation of blocking potentials by space charges 81

IV Ions in the spectrometers **83**
IV.1 Ion transport through the Pre-spectrometer 84
IV.2 Ionisation of residual gas by tritium ions: the ionisation efficiency $\mathcal{E}$. 87
IV.3 Background from tritium activity
after ion implantation 93
IV.3.1 Background due to neutral tritium in the Main spectrometer . 94
IV.3.2 Diffusion of neutral tritium in the Pre- and Main spectrometer 96
IV.3.3 Reemission of neutral tritium after ion implantation 98
IV.3.4 Expected background by a constant tritium ion flux into the PS 104
IV.3.5 Expected background after a short tritium ion flux into the PS 106
IV.4 Conclusion 108

V Impact of tritium ions on the neutrino mass measurement **109**
V.1 Tritium retention for radiation protection 109
V.2 Main spectrometer background 110
V.2.1 Tritium activity 110
V.2.2 Ionisation of residual gas 111
V.3 First countermeasure: ion blocking and limit on ion flux into the PS . 111
V.4 Distortion of the measured tritium beta spectrum 112
V.4.1 Smearing of the beta spectrum by plasma instabilities 112
V.4.2 Distortion of the source potential by negative ion space charges 113
V.4.3 End point energies of tritium ions 114
V.5 Second countermeasure: ion removal in the DPS 115

VI Ion blocking and removal **117**
VI.1 Ring electrodes block ions 118
VI.2 Dipole electrodes remove ions 121
VI.2.1 Ion removal with $E \times B$-drift 122
VI.2.2 Effect on the beta electrons 124

VI.2.3 Optimisation of the dipole electrode voltages . . . 126
VI.2.4 Stable voltage supply to prevent change of beta electron energy 129
VI.3 Ion flux reduction in the PS . . . 133
VI.4 Monitoring of the ion blocking in the DPS . . . 135

VII Ion detection **137**
VII.1 Ionisation in the spectrometers . . . 139
VII.2 Current measurements . . . 142
VII.2.1 Detection principle: ion neutralisation current . . . 142
VII.2.2 DPS dipole electrodes . . . 143
VII.2.3 Faraday Cup at the Forward Beam Monitor . . . 145
VII.2.4 PS downstream cone electrode . . . 148
VII.2.5 PULCINELLA . . . 151
VII.2.6 Statistical analysis . . . 152
VII.2.7 Systematic effects . . . 154
VII.3 Fourier Transform Ion Cyclotron Resonance (FT-ICR) . . . 157
VII.4 Monitoring of the residual ion flux into the PS . . . 161
VII.5 Monitoring of the plasma parameters . . . 164

VIII The First Light campaign **165**
VIII.1 Creation of deuterium ions with the ELIOTT ion source . . . 166
VIII.1.1 Ion creation principle of the ELIOTT ion source . . . 168
VIII.1.2 The ELIOTT setup at the rear section . . . 168
VIII.1.3 Deuterium pressure in ELIOTT . . . 171
VIII.1.4 Energy spectra of the ELIOTT ions . . . 173
VIII.1.5 Transformation of D_2^+ to D_3^+ ions in ELIOTT . . . 175
VIII.2 Ion detection via ionisation of residual gas in the MS . . . 178
VIII.2.1 Measurement principle, systematic effects and analysis . . . 178
VIII.2.2 High voltage dependence of the ionisation efficiency . . . 180
VIII.2.3 Absolute ionisation efficiency . . . 182
VIII.2.4 Measurement scheme of the following sections . . . 184
VIII.3 Ion blocking with the ring electrodes in DPS and PS . . . 185
VIII.4 Ion removal with the DPS dipole electrodes . . . 187
VIII.5 Ion transport through the Pre-spectrometer . . . 192
VIII.5.1 Dependence on the magnetic field strength . . . 192
VIII.5.2 Dependence on the high voltage . . . 193
VIII.6 Inadvertent blocking of thermal ions in the beamline . . . 196
VIII.7 Summary and consequences . . . 199

IX The (Very) First Tritium campaign **201**
IX.1 Performance of the ion detectors . . . 202
IX.1.1 Current measurement at the DPS dipole electrodes . . . 202
IX.1.1.1 Proof-of-principle of ion detection . . . 203
IX.1.1.2 Systematic effects . . . 204
IX.1.1.3 Measurement procedure: minimal detectable ion flux 206
IX.1.2 Faraday cup . . . 210
IX.1.3 Current measurement on the PS downstream cone electrode . 213

IX.1.3.1 Automatic closing of the valve between CPS and PS 214
IX.1.3.2 Systematic effects . . . 214
IX.1.3.3 Minimal detectable ion flux . . . 217
IX.1.4 Argon ionisation in the PS . . . 220
IX.1.4.1 Systematic effects related to the argon pressure . . . 220
IX.1.4.2 Systematic effects of the Pre-spectrometer . . . 224
IX.1.4.3 Minimal detectable ion flux . . . 227
IX.1.5 Comparison of PS cone current and ionisation method . . . 228
IX.1.6 Current measurement of the beta electron flux . . . 232
IX.2 Three energy regimes of tritiated ions . . . 237
IX.2.1 Positive thermal ions . . . 237
IX.2.1.1 Ion flux dependence on the tritium purity ϵ_{T} . . . 237
IX.2.1.2 Ion flux dependence on the column density $\mathcal{N}$ . . . 239
IX.2.1.3 Conclusion . . . 242
IX.2.2 Penning discharge ions . . . 243
IX.2.3 Ions from molecular dissociation . . . 247
IX.2.3.1 Expected energy range and rate of dissociation ions . 247
IX.2.3.2 Measurement conditions . . . 247
IX.2.3.3 Dipole electrode in BT1 at nominal negative voltage 248
IX.2.3.4 Dipole electrode in BT1 at +15 V . . . 249
IX.2.3.5 Dipole electrode in BT2 at +15 V . . . 250
IX.2.3.6 Summary and outlook . . . 251
IX.3 Inadvertent ion blocking and neutralisation of the blocking potentials 255
IX.3.1 Ion flux from the WGTS during Very First Tritium . . . 255
IX.3.2 Inadvertent blocking and possible neutralisation effects . . . 256
IX.3.3 Consequences of inadvertent ion blocking . . . 259
IX.4 Upper limit on the ion flux into the PS . . . 260
IX.4.1 MS background over the course of the tritium campaigns . . . 261
IX.4.2 Faraday cup measurements during Very First Tritium . . . 262
IX.4.3 Continuous monitoring with the PS cone electrode . . . 263
IX.4.4 PS argon ionisation measurement . . . 265
IX.4.5 Conclusion . . . 268
IX.5 Optimisation of the ring electrode voltages . . . 269
IX.6 Summary and conclusions . . . 272

X Conclusion and Outlook 275

A Calculations 279
A.1 Downstream escape probability of electrons in the spectrometers . . . 279
A.2 Magnetic self-shielding in the spectrometers . . . 280
A.3 Diffusion of gaseous tritium in the spectrometers . . . 282
A.4 Expected background after a short tritium ion flux into the PS . . . 285
A.5 Diffusion constant of tritium in stainless steel . . . 293
A.6 Drift distance in the dipole electrodes . . . 295
A.7 Ion detection probability of the dipole electrodes . . . 297
A.8 Background due to dipole electrode potentials . . . 300

A.9 Stability requirements for the voltage of ring and dipole electrodes . 302
A.10 Statistical analysis of current measurements 304
A.11 Probability for closing the valve V4 due to ions 308
A.12 Absolute pressure in ELIOTT during First Light 310

B Hardware **313**
B.1 Data sheet of the voltage supply for ring and dipole electrodes 313
B.2 Data sheets of the amperemeters for ion detection 315
B.3 Operating instructions for the Faraday cup 322

C Residual rate during First Tritium PS ionisation measurements **325**

References **329**

Acknowledgements **339**

I. Neutrinos and their masses

Neutrinos are the uncharged leptonic partners of electrons, muons, and taus. Relic neutrinos from the early phases of the universe are ubiquitous at an average density of 340 neutrinos per cm^3 [Per09]. Today's natural neutrino sources include supernovae, fusion processes in our sun, cosmic rays in the atmosphere and radioactive decays in the crust of the earth [Ams07, Per09, Pov09, Fuk98, SNO09]. Human-made neutrino sources are for example nuclear reactors and particle accelerators for scientific purposes [Ams07, Day12].

Among the most striking features about neutrinos are their very weak interactions and their extremely small mass. Because neutrinos interact only via the weak interaction [Ams07, Pov09], it is particularly difficult to detect them although they might be the key to several urgent questions of particle physics and cosmology. For example, "new physics" beyond the Standard Model (SM) of particle physics are already implied by the finite neutrino mass, which in turn follows from the observation of neutrino oscillations [Per09]. Further, the observed matter-antimatter asymmetry in the universe could be tied to the absolute mass of neutrinos and their possible Majorana nature [Per09]. The determination of the neutrino mass is therefore of paramount importance for particle physics and cosmology.

This chapter will first illustrate the importance of the neutrino mass for particle physics (section I.1) and cosmology (section I.2). Then the mechanism of neutrino oscillation will be detailed, which implies not only the existence of a non-vanishing neutrino mass but also allows to determine the neutrino mass squared splittings (see section I.3). However, the absolute neutrino mass cannot be determined by oscillation experiments; this requires a direct measurement, and three different neutrino mass observables for this purpose will be discussed in section I.4. Finally, section I.5 will summarise what we know and don't know about the neutrino mass.

I.1. Neutrinos in the standard model

The neutrino was first postulated in 1930 by Wolfgang Pauli in order to preserve the principle of energy conservation in beta decay [Pau30]. A continuous energy spectrum was observed for the emitted beta electrons (see for example figure I.5; but originally, monoenergetic electrons had been expected in the presumed two-body decay with one resulting beta electron and one heavy daughter molecule. Pauli resolved the problem by the introduction of a neutrino as electrically neutral and very light third decay product.

It took until 1956 for the existence of neutrinos to be confirmed in the Savannah River reactor experiment by Cowan and Reines: the capture of electron anti-neutrinos on protons was observed via the decay products, creating a prompt positron signal and a delayed neutron signal [Ams07].

As of today, three neutrino generations corresponding to the charged leptons electron, muon and taus have been observed. The existence of further generations of light neutrinos was excluded via the precise measurement of the Z^0 decay width at the LEP [Ams07]: in comparison with the predictions of the Standard Model of particle physics (SM), the measurement yields 2.994 ± 0.012 neutrino generations with a mass below $m_{Z^0}/2 \approx 45$ GeV.

Neutrinos do not participate in the electro-magnetic or the strong interaction; they take only part in the weak interaction via charged and neutral currents ($W^{\pm}$ and Z^0 bosons) [Pov09]. Because the violation of P parity by the weak interaction is maximal, only left-handed neutrinos can be created as confirmed by the Goldhaber experiment[Pov09, Ams07]. The Standard Model (SM) of particle physics considers therefore only left-handed neutrinos via the electro-weak interaction [Pov09, Ams07].

The observation of neutrino oscillation proves however the finite mass of at least two of the neutrino mass eigenstates [Pov09, Ams07, Per09] (see section I.3). This implies that neutrinos can also have a right-handed helicity component [Pov09], which in turn corresponds to "new physics" beyond the Standard Model [Per09]. The right-handed neutrinos, which cannot be observed in weak interactions, are called sterile and serve as candidates for dark matter (see following section) [Per09].

Among all fundamental fermions of the SM, neutrinos could be the only ones to be their own anti-particles, so called Majorana particles [Ams07, Pov09, Per09]. The reason is that neutrinos have no electric charge, which would otherwise change under charge conjugation by the operator of C parity.

If neutrinos are in fact Majorana particles, their masses could result from a mixture of Dirac and Majorana mass terms [Per09]. This assumption leads to the see-saw model, with two different neutrino mass scales: a heavy neutrino with mass M and a light second neutrino mass $(m_D)^2/M$, which is suppressed by the heavy neutrino. The see-saw mechanism would explain why the masses $\lesssim$ eV/c^2 of the three known neutrino flavours (see section I.4) are so much smaller than the mass scale $m_D \sim$ GeV/c^2 of the other Dirac fermions in the SM.

Massive Majorana neutrinos from the see-saw mechanism would point to "new physics" on the scale of the heavy neutrino mass $M \sim 10^{12}$ GeV/c^2, for example by Great Unification Theories (GUT). The decay of these massive neutrinos could create a lepton asymmetry and result in the matter-antimatter asymmetry, as specified

by the Sakharov criteria which will be discussed in the following section. All of this shows that the nature and absolute scale of the neutrino mass are of utmost importance for particle physics and cosmology.

I.2. Neutrinos in cosmology

Neutrinos are the most abundant massive particles in the universe with a number density of 340 neutrinos per cm^3 [Per09]. Only the massless photons are more numerous at a density of 411 photons per cm^3, observable as the Cosmic Microwave Background (CMB).

This abundance of relic neutrinos was created in the early universe, before the thermal decoupling of neutrinos from protons and neutrons allowed nucleosynthesis [Per09]. The relic neutrinos played a crucial role in the creation of large scale structures of matter in the universe: due to their very weak interaction, the neutrino free streaming damped any density fluctuations within a certain horizon which depended on the neutrino mass. In this way, the neutrino mass left an imprint on the power spectrum of the CMB (see section I.4).

The SM neutrinos were formerly candidates for dark matter; they are meanwhile ruled out, however, due to their light masses and because the observed large scale structures of the universe are incompatible with such hot dark matter [Aba12]. Nevertheless, the dark matter candidates still include sterile neutrinos (see previous section). The parameter space of keV-sterile neutrinos for example could be explored with the TRISTAN experiment, a follow-up of the KATRIN experiment which will be explained in chapter II [Adh17].

Neutrinos might even be the key to the baryon-antibaryon asymmetry in the universe [Per09]. According to Sakharov, one out of three criteria for the observed asymmetry is the violation of C and CP symmetry. It is possible that the asymmetry of baryons was initially caused via CP violation by leptons, namely the decay of heavy Majorana neutrinos according to the see-saw mechanism as discussed in the previous section.

Type II supernovae are an example for cosmic events in our era of the universe which are still strongly affected by neutrinos and their mass [Per09]: according to computer simulations, the outward moving shock wave from the collapse of the stellar core would actually be stalled by the infalling matter from outside the core; it is the energy transfer from the outward moving neutrinos which keeps the shockwave moving.

In fact, 99% of the energy from a type II supernova is radiated in form of neutrinos [Per09]. For example, the supernova 1987A created a neutrino flux of 10^{10} neutrinos per cm^2. This led to the detection of 20 supernova neutrinos with energies on the order of 10 MeV in three water Cherenkov detectors about 7 h before the observation of the optical signal. The time of flight of these supernova neutrinos can be used to derive an upper limit on the neutrino mass of 5.8 eV/c^2 at 95% confidence level [Pag10]. Stricter limits on the neutrino mass will be derived below; their discussion requires however first the introduction of the neutrino mass eigenstates at the example of neutrino oscillations.

I.3. Oscillation of massive neutrinos

The three flavour neutrinos which take place in the weak interaction are linear combinations of three neutrinos with distinct masses [PDG18, Ams07]. This leads to neutrino flavour mixing in vacuum and to so called neutrino oscillations: the probability to detect a neutrino in flavour β after its creation with flavour α depends periodically on the neutrino's energy E, its distance of propagation L and on the two flavours α and β. Further, the oscillation is influenced by the relative mass difference squared Δm^2_{ij} between the neutrino mass eigenstates i and j. This allows to determine the neutrino mass splittings.

The observation of neutrino oscillations implies that at least two out of three neutrino mass eigenstates are massive. This is in contradiction to the Standard Model of particle physics and implies the existence of "new physics", as explained in section I.1. The significance of neutrino oscillations for particle physics is underlined by the Nobel Prize in Physics 2015, which was awarded to Takaaki Kajita and Arthur B. McDonald "for the discovery of neutrino oscillations, which shows that neutrinos have mass" [Nob15]. Their achievement was the experimental prove of the oscillation of atmospheric neutrinos (by T. Kajita in section I.3.2) and solar neutrinos (A. B. McDonald in section I.3.3).

This section will first explain the mechanism of neutrino oscillation in section I.3.1 and recall its experimental discovery in section I.3.2. With regard to the ordering of the neutrino masses, the MSW effect shows the ordering of two out of three masses of neutrino mass eigenstates; this effect will therefore be explained in the section I.3.3 in the context of the solar neutrino problem which it allowed to resolve. The final section I.3.4 will state the current status of the measurement of neutrino oscillation parameters and especially of the neutrino mass splittings.

I.3.1. Oscillation mechanism

The neutrino flavours ν_e, ν_μ and ν_τ are assumed to mix in vacuum and to oscillate between their flavour states [PDG18]. A consequence of this neutrino mixing is the violation of single lepton number conservation, whereas the total lepton number is still conserved [Zub06, PDG18].

The experimental data on neutrino oscillations can be described with a model of three-flavour neutrino mixing in vacuum [PDG18]. This model assumes that the (left-handed) fields of the flavour neutrinos, which participate in the weak interaction via charged currents, are linear combinations of the (left-handed) components of three massive neutrinos ν_i ($i = 1,2,3$) with a mass m_i [PDG18, Ams07]:

$$|\nu_\alpha\rangle = \sum_{i=1}^{3} U_{\alpha i} |\nu_i\rangle, \tag{I.1}$$

where α denotes the three neutrino flavours e, ν or τ. The unitary mixing matrix U is called Pontecorvo-Maki-Nakagawa-Sato (PMNS)-matrix [Zub06, PDG18]. Because each flavour eigenstate is a superposition of the three mass eigenstates, only an effective mass $m_{\alpha,\mathrm{eff}}$ can be observed for each flavour eigenstate.

The mixing matrix U can be parametrised with three rotation matrices if neutrinos are Dirac particles [Zub06]. If neutrinos should be Majorana particles, a diagonal matrix with two additional CP-violating phases has to be added [Ams07, PDG18, Zub06]:

$$U = \begin{pmatrix} 1 & 0 & 0 \\ 0 & c_{23} & s_{23} \\ 0 & -s_{23} & c_{23} \end{pmatrix} \begin{pmatrix} c_{13} & 0 & s_{13} \cdot e^{-i\delta} \\ 0 & 1 & 0 \\ -s_{13} \cdot e^{i\delta} & 0 & c_{13} \end{pmatrix} \begin{pmatrix} c_{12} & s_{12} & 0 \\ -s_{12} & c_{12} & 0 \\ 0 & 0 & 1 \end{pmatrix} \begin{pmatrix} 1 & 0 & 0 \\ 0 & e^{i\alpha_2} & 0 \\ 0 & 0 & e^{i\alpha_3} \end{pmatrix}.$$

This nomenclature uses the abbreviations $s_{ij} \equiv \sin(\theta_{ij})$ and $c_{ij} \equiv \cos(\theta_{ij})$. The matrix depends on the following four or six free parameters [Ams07, PDG18]:

- 3 neutrino mixing angles θ_{12}, θ_{13} and θ_{23} which can take values [0,π/2),
- 1 Dirac CP-violating phase[1] δ = [0,2π],
- and 2 Majorana CP-violating phases $\alpha_{2,3}$.

In the illustrative case of two-neutrino mixing, the rotation can be expressed with a 2×2 matrix and a single mixing angle θ. Then the relation between the flavour eigenstates[2] $|\nu_{\alpha,\beta}\rangle$ and the mass eigenstates $|\nu_{1,2}\rangle$ becomes [PDG18]:

$$|\nu_\alpha\rangle = \quad \cos(\theta) \cdot |\nu_1\rangle + \sin(\theta) \cdot |\nu_2\rangle, \tag{I.2}$$

$$|\nu_\beta\rangle = -\sin(\theta) \cdot |\nu_1\rangle + \cos(\theta) \cdot |\nu_2\rangle. \tag{I.3}$$

The probability for observing a neutrino in the flavour eigenstate β after its creation in the flavour eigenstate α is then [PDG18, Ams07]:

$$P^{2\nu}(\nu_\alpha \to \nu_\beta) = \sin^2(2\theta) \cdot \sin^2\left(\frac{\Delta m_{ij}^2 \cdot L}{E}\right), \tag{I.4}$$

where L is the distance between creation and observation, E is the energy of the neutrino and the corresponding mass squared splitting is $\Delta m_{ij}^2 = m_i^2 - m_j^2$. This two neutrino model was for example applied for the analysis of neutrino oscillation in the Superkamiokande experiment [PDG18], which will be discussed next.

I.3.2. Discovery of the oscillation of atmospheric neutrinos

The occurrence of neutrino oscillation as described in the previous section requires at least two massive neutrino mass eigenstates. Therefore, the observation of neutrino oscillations implies physics beyond the standard model of particle physics, which only knows massless neutrinos.

The first evidence for neutrino oscillations was found in 1998 in the Superkamiokande experiment, which observed cosmic ray-induced neutrinos from the atmosphere [Per09].

[1] CP violation means $P(\nu_\alpha \to \nu_\beta) \neq P(\bar{\nu}_\alpha \to \bar{\nu}_\beta)$ and occurs if δ is not an even multiple of π [Ams07].

[2] The two-neutrino description is also valid for the oscillation from an active flavour eigenstate into a sterile (anti-) neutrino eigenstate [PDG18].

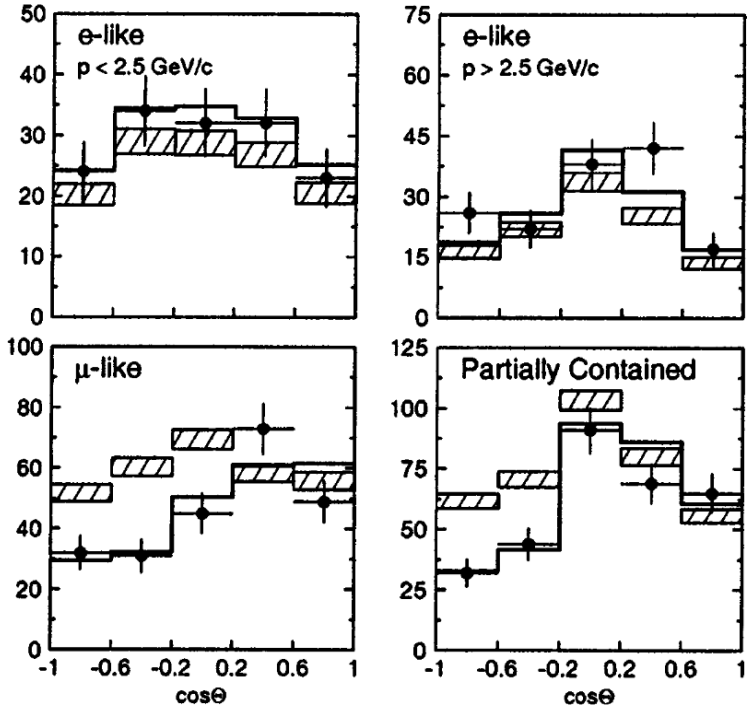

Figure I.1.: **Oscillation of multi-GeV atmospheric neutrinos in Superkamiokande.** Displayed is the neutrino rate depending on the zenith angle θ. The measured rate of muon neutrinos (points with error bars) from the opposite side of the earth ($\cos(\theta) \approx -1$) is only about 50% of the expected rate (hatched boxes; muon tracks in lower left graph were fully contained in inner detector, while muon tracks for lower right graph were only partially contained). The missing rate can be explained with neutrino oscillations from muon flavour to tau flavour, as indicated by the corresponding fit (solid line). No oscillation of electron neutrinos is observed. Figure from [Fuk98].

These neutrinos scattered elastically in a 50,000 ton water target and created electrons or muons, respectively. The Cherenkov light from the charged particles was measured with 11,000 photomultiplier tubes in order to derive the energy and direction of the incident neutrinos.

Figure I.1 shows the observed asymmetry of the neutrino rate for muons with multi-GeV momenta [Fuk98]. The rate of neutrinos coming from the atmosphere above the detector ($\cos(\theta) \approx 1$) fits well to the expectations without neutrino oscillation; but the rate of neutrinos from below ($\cos(\theta) \approx -1$) is only about 50% of the predicted value. This discrepancy can be explained with neutrino oscillations from muon to tau flavour; the factor 1/2 corresponds to the mean of the sinus from eq. I.4, because the neutrino energies and path lengths are distributed over a broad range [Per09]. No oscillation is observed for the electron neutrinos at these energies and oscillation lengths.

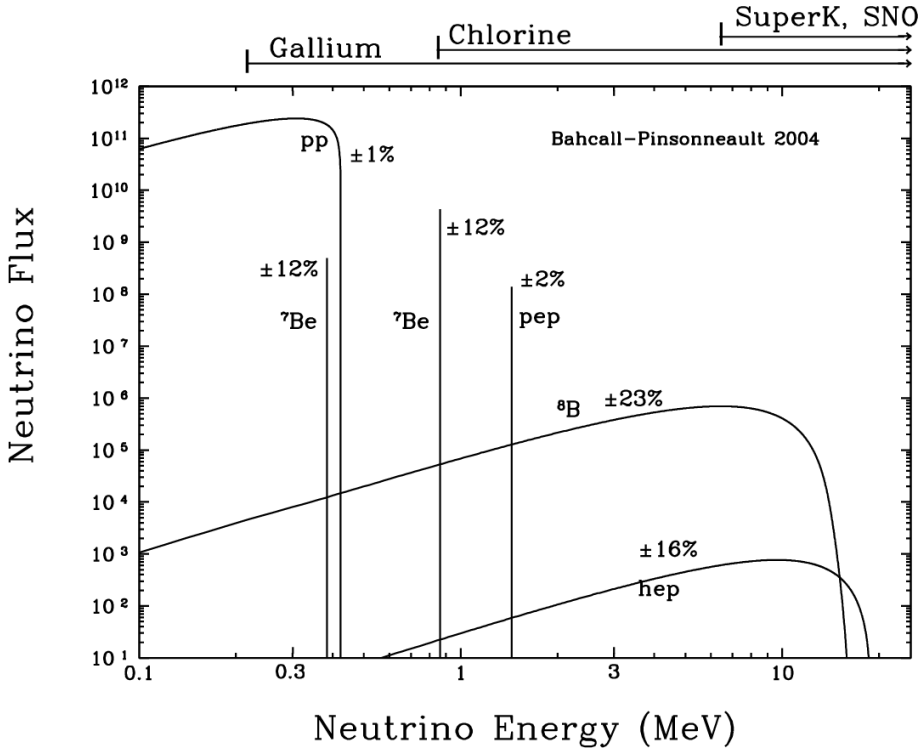

Figure I.2.: **Energy spectrum of solar neutrinos.** According to the Standard Solar Model, neutrinos are created with discrete energies and in continuous spectra during the various steps of the *pp* fusion cycle in the sun. The arrows above indicate which of these neutrinos were accessible for the gallium, chlorine and water Cherenkov detectors, depending on the energy threshold of each method. From [BPG04].

I.3.3. The solar neutrino problem and MSW effect

Matter can affect the neutrino oscillation, as in the case of the MSW (Wolfenstein-Mikhaev-Smirnov) effect [Per09]: it reduces the flux of electron neutrinos leaving the sun as compared to their creation rate via fusion reactions. This discrepancy between theory and experiment was known as the solar neutrino problem.

The solar neutrino problem The Standard Solar Model (SSM) allows to calculate the neutrino energy spectrum from various reactions in the *pp* fusion chain in the sun, as shown in figure I.2 [BPG04]. But the predicted neutrino flux rates were not found in radiochemical and in water Cherenkov experiments like Superkamiokande. First measurements were carried out since the 1960s with a 615 ton tank of dry-cleaning fluid (C_2Cl_4) in the Homestake gold mine by Ray Davis [Per09, SNO09] [Per09, SNO09]. The Homestake experiment observed only a factor 0.34 ± 0.03 of the predicted neutrino flux [Per09]. Figure I.3 shows that also Superkamiokande and the gallium experiments GALLEX and SAGE measured a clear deficit of electron neutrinos.

The solution to the neutrino problem was given by the SNO experiment. Previous experiments had only measured the electron neutrino flux from the sun via charged

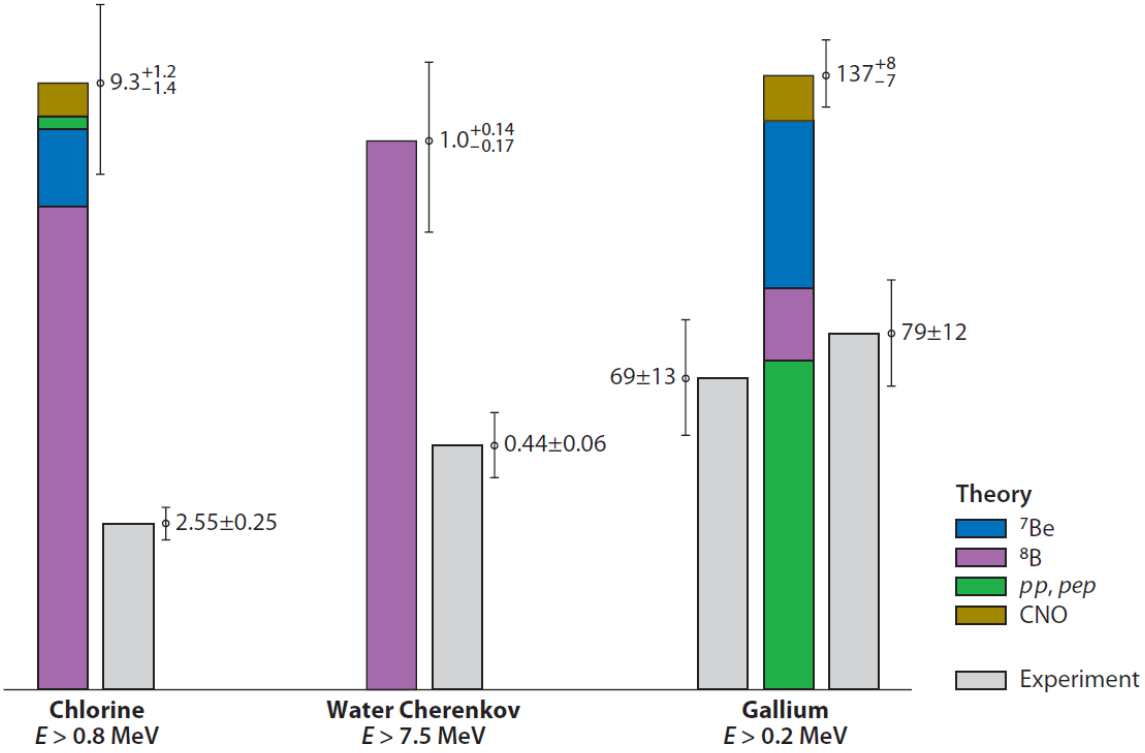

Figure I.3.: **The solar neutrino problem.** The gray bars show the neutrino rates which were measured with three different detection methods. Much higher are the predictions of the Standard Solar Model with contributions from the *pp* chain (see figure I.2). From [SNO09], adapted from [Bah96].

current or elastic scattering [Per09]; SNO instead was capable of measuring the complete neutrino flux irrespective of the flavour via neutral current reactions[3] [SNO09]. The observed neutrino flux via neutral currents agreed to a factor 0.98 ± 0.09 with the prediction of the Standard Solar Model, while the electron neutrino flux from charged current reactions was in fact only a factor 0.30 ± 0.05 of the prediction [Per09].

The MSW effect The energy dependence of the observed electron neutrino rates is due to neutrino oscillation in matter according to the MSW (Wolfenstein-Mikhaev-Smirnov) effect [Per09, Smi03]. All neutrinos interact via neutral currents (Z^0) inside the sun, but only electron neutrinos ν_e can also interact via charged currents ($W^{\pm}$) because the neutrino energies below 20 MeV are not sufficient to create the corresponding charged lepton of ν_μ and ν_τ. Consequently, the electron neutrinos experience an extra potential $V_e = \sqrt{2} G_F N_e$ in dependence of the electron density N_e and the Fermi constant G_F. This potential increases the effective mass squared of the electron neutrino linearly with the electron density N_e or the density of the sun, respectively (see figure I.4). The effective masses of the electron and muon neutrino are not affected, instead.

[3]The neutrinos scattered on deuterium and produced free neutrons in the 1 kton heavy water target.

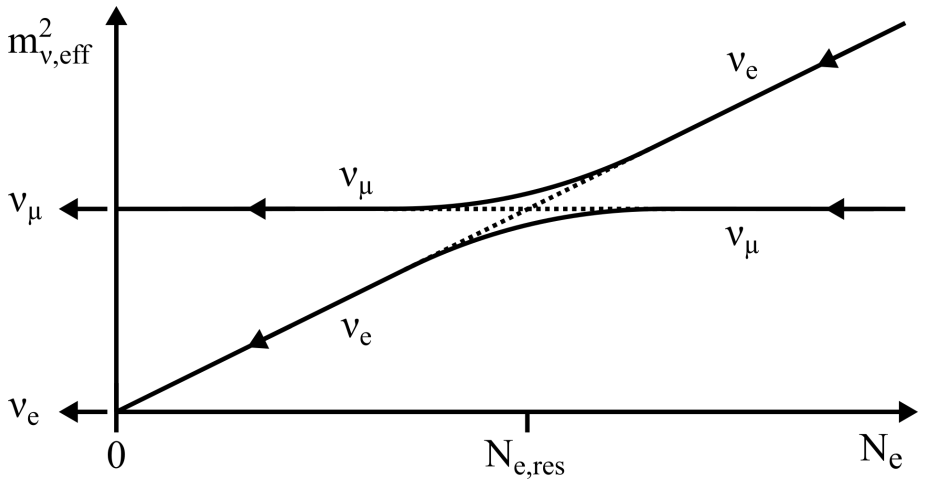

Figure I.4.: **Level crossing in the MSW effect.** Electron neutrinos experience an extra weak potential in the sun via charged current interactions with electrons, while muon neutrinos remain unaffected. This potential increases the effective mass squared m_ν^2 of the electron neutrino linearly with the electron density N_e. At the critical density $N_{e,\mathrm{res}}$, a resonant conversion between neutrino flavours occurs according to eq. I.5 in dependence of the neutrino energy E (compare figures I.2 and I.3). If N_e changes sufficiently slow, the conversion is permanent and increases the probability to measure the initial electron neutrino as a muon neutrino on earth. Figure according to [Per09].

When electron neutrinos are created in the center of the sun, they move outside through the ever smaller electron density N_e [Per09, Smi03]. If they traverse a certain electron density $N_{e,\mathrm{res}}$ and the electron density changes slowly enough, a resonant conversion of the mass eigenstates occurs. As a result, the initial electron neutrinos will be measured with an increased probability as muon neutrinos in vacuum. More neutrinos with a large energy E than low-energetic neutrinos pass through the resonance density, due to the resonance condition [Per09]:

$$\tan(2\theta_m) = \frac{\sin(2\theta)}{\cos(2\theta) - 2\sqrt{2}G_\mathrm{F}N_eE/\Delta m_{21}^2}, \tag{I.5}$$

Here θ is the mixing angle between electron and muon neutrino in vacuum and θ_m is the mixing angle in presence of the matter of the sun. A resonance will only appear if $\Delta m_{21}^2 > 0$. The observation of neutrino oscillation in the sun therefore also implies the mass ordering $m_2 > m_1$.

I.3.4. Measurement of neutrino mass splittings

Neutrino oscillation experiments allow to investigate the neutrino mass squared splittings Δm^2_{ij}, the mixing angles θ_{ij} and the CP violating phase δ which were introduced in section I.3.1. For example, solar neutrinos give the dominant contribution to the determination of the mass squared splitting Δm^2_{21} and the mixing angle θ_{12} [Nuf17] (see section I.3.3).

Atmospheric neutrinos are particularly suited to determine the mass squared splitting Δm^2_{3l} ($l = 1,2$) as well as the mixing angle θ_{23} due to the involved oscillation lengths (see section I.3.2). But the most precise measurement of the mass squared splitting Δm^2_{3l} is possible with reactor neutrino experiments and in long baseline (LBL) experiments with accelerator neutrinos [Nuf17].

Another important result of oscillation experiments since the discovery of neutrino oscillation is the non-zero mixing angle θ_{13}; this was first reported by the Daya Bay experiment (and later bei RENO and Double Chooz) using the disappearance of reactor electron anti-neutrinos $P(\bar{\nu}_e \to \bar{\nu}_e)$ [Day12]. The investigation of leptonic CP violation is currently driven by the LBL experiments T2K and NoνA, but yielded no significant result for the value of the phase δ so far [Nuf17].

Updated values for all mentioned parameters can be found on www.nu-fit.org. As of October 2018, the neutrino mass squared splittings were [Nuf17]:

$$\Delta m^2_{21} = 7.40^{+0.21}_{-0.20} \cdot 10^{-5}\ \mathrm{eV/c^2}, \tag{I.6}$$

$$\Delta m^2_{3l} = 2.494^{+0.033}_{-0.031} \cdot 10^{-3}\ \mathrm{eV/c^2}\ \text{(NO)}, \tag{I.7}$$

$$\Delta m^2_{3l} = 2.465^{+0.032}_{-0.031} \cdot 10^{-3}\ \mathrm{eV/c^2}\ \text{(IO)}, \tag{I.8}$$

where Normal Ordering (NO) denotes the case $\Delta m^2_{31} > 0$ and the Inverted Ordering (IO) corresponds to $\Delta m^2_{32} < 0$.

I.4. Determination of the absolute neutrino mass scale

While neutrino oscillations allow the precise investigation of neutrino mass splittings, the ordering of neutrino masses and their absolute scale require a direct measurement of the neutrino mass. But as explained in the previous section, the neutrino fields which take part in the weak interactions are superpositions of the neutrino mass eigenstates [PDG18, Ams07]. Therefore, three complementary neutrino mass observables have to be distinguished and will be detailed in this section.

Tritium beta decay and electron capture in holmium are used to search for an effective neutrino mass, which is the non-coherent sum of all three masses of neutrino mass eigenstates (see section I.4.1). On the other hand, the observation of neutrinoless double beta decay would involve the effective mass of a coherent sum of the neutrino masses; at the same time, the observation of neutrinoless double beta decay would prove that neutrinos are Majorana particles (see section I.4.2). The strictest upper limits on the neutrino mass as of today were set by the Planck satellite, which determines the sum of all three neutrino masses via a model-dependent analysis of the power spectrum of the Cosmic Microwave Background (see section I.4.3).

I.4.1. Spectroscopy of beta decay and electron capture

A direct and model-independent measurement of the effective neutrino mass is possible via precision spectroscopy of tritium beta decay electrons [CDR04, Asn15] and of electron capture in holmium [Gas17, Alp15]:

$$\mathrm{T}_2 \rightarrow {}^3\mathrm{HeT} + \mathrm{e}^-_\beta + \bar{\nu}_\mathrm{e}, \tag{I.9}$$

$${}^{163}\mathrm{Ho} + \mathrm{e}^- \rightarrow {}^{163}\mathrm{Dy} + \nu_\mathrm{e}. \tag{I.10}$$

This kinematic approach measures the electron-flavour weighted effective (anti-)electron neutrino mass [Ott08, Asn15, Gas17]:

$$m^2_\beta = \sum_{i=1}^{3} |U_{ei}|^2 \cdot m_i^2. \tag{I.11}$$

The strictest limits on the effective anti-electron neutrino mass in the past and near future arise from tritium beta spectroscopy with MAC-E filters. Currently, the Troitsk experiment states the strictest upper limit with $m_\beta < 2.05$ eV/c^2 at 95% confidence level [Lob03]. A slightly larger upper limit of $m_\beta < 2.3$ eV/c^2 at 95% confidence level was derived by the Mainz experiment [KBB05]. However, next-generation experiments are being developed[4] based on cyclotron radiation loss of tritium beta electrons and calorimetric investigation of electron capture in ^{163}Ho. All three types of experiments will be detailed in the following.

[4] A measurement of the neutrino mass is also aspired by the PTOLEMY experiment, although its primary goal is the detection of relic neutrinos from early stages of the universe [PTO13].

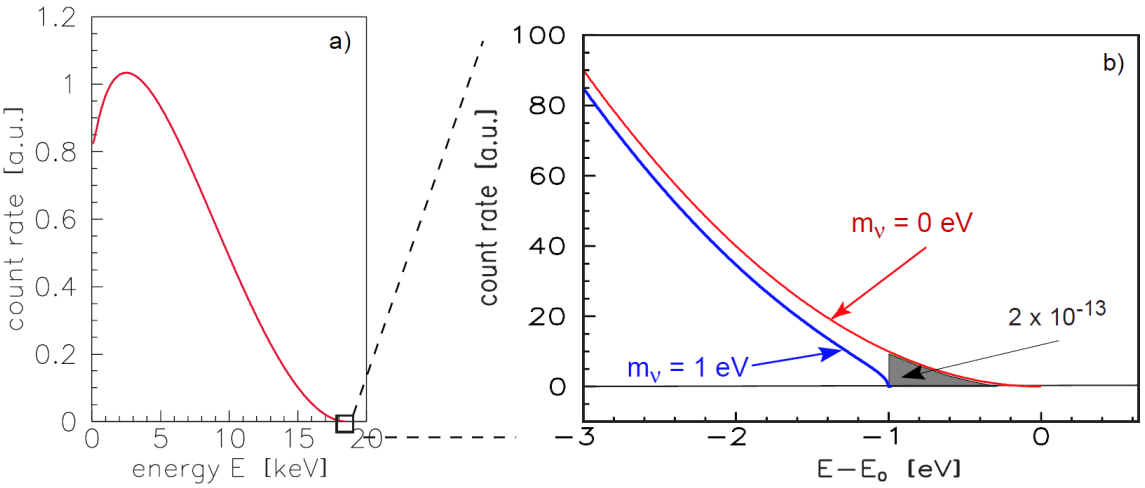

Figure I.5.: **Tritium beta spectrum.** The tritium decay via the weak interaction is a three-body decay, which produces a daughter ion, a beta electron and a neutrino. Consequently, the energy of the beta electron is no monoelectronic line but rather a statistically distributed spectrum. The neutrino mass can be measured due to its imprint on the beta spectrum via precision spectroscopy. For this purpose, the end point region offers the best signal to noise ratio. If the energy resolution were large enough, a shift of the end point energy corresponding to the neutrino mass could be observed. From [CDR04].

MAC-E filter The Troitsk and the Mainz experiment were developed independently during the 1980s in order to measure the neutrino mass via spectroscopy of beta electrons from tritium decay [KBB05, Lob03] (see figure I.5). Both experiments employed a MAC-E filter for this purpose, which will be explained in detail in section II.1; but while the Mainz experiment used a source of quench-condensed tritium, the beta electrons for the Troitsk experiment were created in gaseous tritium [Ott08]. Eventually, an upper limit on the neutrino mass of about 2 eV/c^2 at 95% confidence level could be derived with both experiments.

In order to further reduce the statistic and systematic uncertainty by a factor of 10, the KATRIN (KArlsruhe TRItium Neutrino) experiment was launched under significant contributions of the Mainz and Troitsk collaborations [CDR04]. KATRIN was designed in order to measure a neutrino mass down to $m_\beta = 0.3$ eV/c^2 at 3σ significance; alternatively, it should set an upper limit of $m_\beta < 0.2$ eV/c^2 at 90% confidence level. For this purpose, KATRIN combines a MAC-E filter with a gaseous tritium source (see chapter II). KATRIN started its first tritium operation in 2018 and was officially inaugurated on June 11 of this same year.

Cyclotron Radiation Emission Spectroscopy (CRES) The experiment Project 8 intends to measure the end point region of the tritium energy spectrum via Cyclotron Radiation Emission Spectroscopy (CRES). Radio frequency antennae pick up the cyclotron radiation from tritium beta electrons due to their cyclotron motion (see section III.1.2) in the magnetic field $\sim$ 1 T of a superconducting magnet [Esf17].

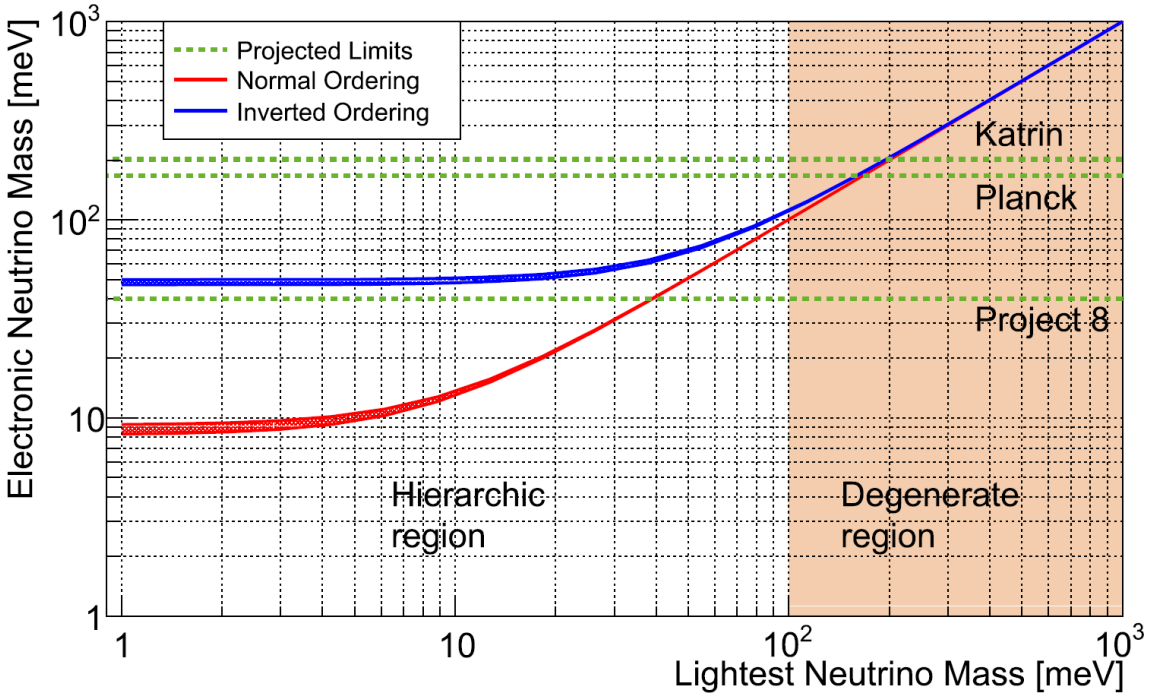

Figure I.6.: **Neutrino mass sensitivity of KATRIN, Project 8 and the Planck satellite.** KATRIN and Project 8 are sensitive to the non-coherent sum of neutrino mass eigenstates as stated in eq. I.11; conversely, Planck measures the sum of all three neutrino masses from eq. I.14 based on models for the evolution of the universe. Figure from [Esf17].

This allows to detect the beta electrons right inside the tritium source, which has several advantages [Asn15]: the source can be smaller at larger tritium density and beta electrons over a broad energy region of interest can be measured event-by-event instead of stepped integration.

So far, cyclotron radiation of single electrons from a ^{83m}Kr source was successfully detected with CRES [Esf17]. Based on this technique, a neutrino mass sensitivity $m_\beta \lesssim 2$ eV/c^2 is envisaged. As a long-term goal, Project 8 intends to create a monoatomic tritium source in order to remove systematic effects from final states distributions of the daughter ions of tritium decay (compare section III.3.1). Only then, the ultimately aspired neutrino mass sensitivity of $m_\beta \lesssim 0.04$ eV/c^2 can be reached (compare figure I.6).

Calorimetry The ECHo and HOLMES experiments [Gas17, Alp15] attempt to measure m_β via the weak interaction process of electron capture in ^{163}Ho according to eq. I.10. With a beta source implanted into a calorimetric detector, the complete decay energy is measured as a short pulse regardless whether it is liberated via X-rays, Auger electrons or recoil[5] [Alp15]. The calorimetric method prevents systematic effects from energy loss in the source and also from the final states of

[5]This assumes that there are no metastable states in the calorimeter material [Alp15].

the daughter molecule; however, radioactivity in the detector material can create background and spectral distortions.

While ECHo uses Metallic Magnetic Calorimeters (MMCs), the HOLMES experiment employs Transition Edge Sensors (TES). Both experiments are in the phase of design and of the first test measurements, with an aspired neutrino mass sensitivity in the sub-eV range – HOLMES states a target sensitivity of $m_\beta \sim 0.4\,\mathrm{eV/c^2}$ [Alp15].

I.4.2. Neutrinoless double beta decay

Neutrinos could be Majorana particles, which means that neutrinos and anti-neutrinos are identical (see section I.1). In this case, a neutrinoless double beta decay can occur [Zub06]. This simultaneous decay of two neutrons in a nucleus involves only one virtual neutrino, which acts as neutrino in one vertex and as anti-neutrino in the other. The occurrence of double beta decay requires massive neutrinos, in order to allow the helicity flip of the virtual neutrino between the vertices. Neutrinoless double beta decay is thus forbidden in the Standard Model; furthermore, this decay would violate lepton number conservation by two units.

In general, double beta decay ($2\nu\beta\beta$) is a nuclear process of higher order between isobaric isotopes [Zub06]: the decay changes the nuclear charge Z by two units while the atomic mass A is left unchanged; this can only happen between even-even nuclei. If the double beta decay is furthermore neutrinoless ($0\nu\beta\beta$):

$$(Z,A) \rightarrow (Z+2,A) + 2\mathrm{e}^- . \tag{I.12}$$

Neutrinoless double beta decay yields the effective Majorana mass of the electron neutrino [Zub06]:

$$m_{\beta\beta} = \left| \sum_{i=1}^{3} U_{\mathrm{e}i}^2 \cdot m_i \right| = \left| \sum_{i=1}^{3} |U_{\mathrm{e}i}|^2 \cdot e^{2i\alpha_i} \cdot m_i \right| . \tag{I.13}$$

This effective neutrino mass is a coherent sum of all neutrino mass eigenstates, whereas electron spectroscopy yields a non-coherent sum (see eq. I.11) [CDR04]. The difference is that the CP-violating phases α_i from section I.3.1 appear in the effective Majorana mass and allow destructive interference between the neutrino masses m_i. This can decrease the observable effective neutrino mass $m_{\beta\beta}$: given the values for the neutrino mass splittings, $m_{\beta\beta}$ can completely vanish for a resonance mass of the lightest mass eigenstate as illustrated in figure I.7.

The signal of neutrinoless double beta decay are two simultaneously emitted electrons with a combined energy corresponding to the Q-value of the nuclear transition [Zub06]. From the observed number of $0\nu\beta\beta$ decays, the half-life $T_{1/2}^{0\nu}$ can be determined. The half-life increases proportionally to the measurement time and used target mass in case of a background free experiment, but only with their square root in the presence of background; for this reason, background mitigation is essential for $0\nu\beta\beta$ experiments. Finally, the half-life leads to the effective Majorana mass via the exactly calculable phase space integral $G^{0\nu\beta\beta}$ and the nuclear matrix element $|M^{0\nu\beta\beta}|^2$, which has an uncertainty of a factor 2 or 3.

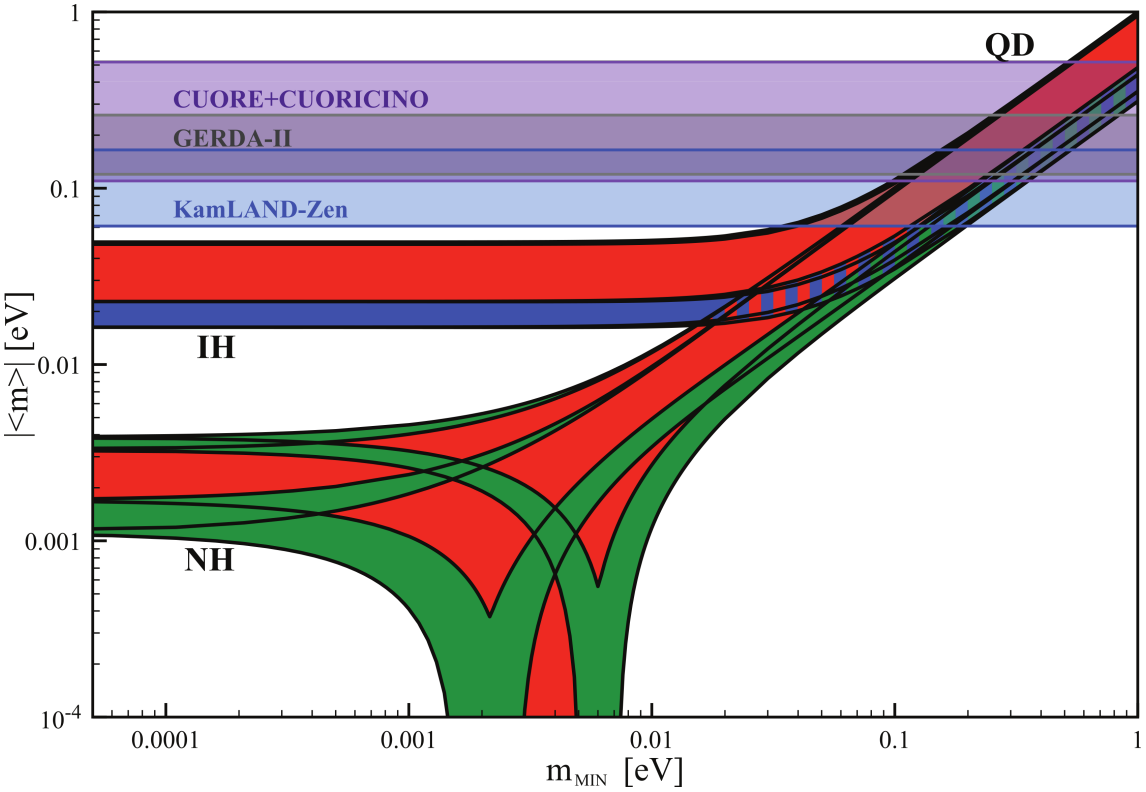

Figure I.7.: **Effective Majorana mass as function of the lightest neutrino mass eigenstate.** The neutrino masses can interfere destructively due to the CP-violating Majorana phases in eq. I.14. For the given neutrino mass splittings (see section I.3.4), the observable effective neutrino mass could vanish if the neutrino mass eigenstate m_1 has a value of a few meV. The figure was derived from the best fit values and 1σ ranges for the neutrino mass splittings and mixing angles, and then taking a 2σ uncertainty. From [PDG18].

The first background-free $0\nu\beta\beta$ experiment was GERDA Phase II, which reported a background rate of $(0.7^{+1.1}_{-0.5}) \cdot 10^{-3}$ cts/(keV·kg·yr) using ^{76}Ge in BEGe detectors [Ago17]. Currently, GERDA places a lower limit on the $0\nu\beta\beta$ half-life in ^{76}Ge of $T^{0\nu}_{1/2} > 8.0{\cdot}10^{25}$ yr at 90% confidence level [Ago18]; this corresponds to an upper limit on the effective Majorana mass of the electron neutrino of $m_{\beta\beta} = 0.12 \ldots 0.26$ eV/c^2.

Still, an even stricter limit is set by the KamLAND-Zen experiment [Gan16]: two electrons from $\beta\beta$ decay in ^{136}Xe would produce scintillation light inside 13 tons of Xe-loaded liquid scintillator, which are viewed by 1,879 photomultiplier tubes (PMTs). KamLAND-Zen places a lower limit on the half-life in ^{136}Xe of $T^{0\nu}_{1/2} > 1.07 \cdot 10^{26}$ yr at 90% confidence level, corresponding to an effective Majorana mass of $m_{\beta\beta} = 61 \ldots 165$ meV/c^2. As of today, no neutrinoless double beta decay has been observed and it remains unclear whether the neutrino is a Majorana particle.

I.4.3. Neutrino mass impact on cosmological models

A direct access to the neutrino masses without weak interactions is possible through the power spectrum of the cosmic microwave background (CMB). The anisotropy of the CMB was affected by the neutrino mass in the early universe before recombination via neutrino free streaming (see section I.2) and later via gravitational lensing. These mechanisms allow to observe the sum of all three neutrino mass eigenstates [Agh18, Cou17]:

$$m_\Sigma = \sum_{i=1}^{3} m_i. \tag{I.14}$$

The first measurements of the CMB were carried out with the COBE and WMAP satellites [Per09]. As of today, the most precise investigation of the CMB and its angular anisotropies were performed by the Planck satellite [Agh18].

Analysis of the CMB power spectrum with regard to the sum of neutrino masses requires however model assumptions on the structure of the universe. An upper limit on the sum of neutrino masses of $m_\Sigma < 0.54$ eV/c^2 at 95% confidence level can be derived from the Planck data, using the ΛCDM model together with data on the temperature power spectrum of the CMB and its polarisation [Agh18]. The limit can be tightened even further to $m_\Sigma < 0.12$ eV/c^2 at 95% confidence level if additional data on polarisation, lensing and the Baryon Acoustic Oscillation (BAO) is used.

I.5. What we know and don't know about the neutrino mass

The observation of neutrino oscillations implies the existence of a non-zero neutrino mass and allows at the same time the investigation of the neutrino mass splittings (see section I.3); even the mass ordering $m_1 < m_2$ can be deduced (section I.3.3). On the other hand, the absolute mass scale of neutrinos is being probed via beta decay and electron capture, neutrinoless double beta decay and the effect of neutrino masses on the power spectrum of the universe (see section I.4).

This section will give an overview of what we know about the neutrino mass and of the remaining unknowns. Finally, the necessity for a direct neutrino mass search with the KATRIN experiment will be detailed.

What we know:

- The observation of neutrino oscillations implies the existence of neutrino mass eigenstates with different masses [Ams07, Per09, Pov09]. Due to the non-vanishing mass squared splittings, at least two neutrino mass eigenstates must have a non-zero mass m_i ($i = 1,2,3$).

- The observation of the MSW effect implies an ordering for the mass eigenstates $m_1 < m_2$ [Per09]:
$$\Delta m^2_{21} = m^2_2 - m^2_1 > 0. \tag{I.15}$$

- Neutrino oscillation experiments allow to determine the neutrino mass splittings $\Delta m^2_{ij} = m^2_i - m^2_j$ [Nuf17]:
$$|\Delta m^2_{21}| = 7.4 \cdot 10^{-5}\ \text{eV}^2, \tag{I.16}$$
$$|\Delta m^2_{31}| \approx |\Delta m^2_{32}| = 2.5 \cdot 10^{-3}\ \text{eV}^2. \tag{I.17}$$

What we don't know:

- The absolute scale of the neutrino mass is unknown, but upper and lower limits can be given: from the neutrino mass splitting $|\Delta m^2_{3i}|$ follows the existence of at least one neutrino mass eigenstate of at least 50 meV; and with regard to the effective electron neutrino mass follows an absolute lower bound of $m_\beta \gtrsim 9 \pm 0.1$ meV [Esf17]. An upper limit on the neutrino mass of $m_\beta < 2.05\ \text{eV/c}^2$ was derived via tritium beta spectroscopy (see section I.4.1) [Lob03]. An even stricter, but model-dependent upper limit on the sum of neutrino masses of $m_\Sigma < 0.12\ \text{eV/c}^2$ can be derived from the power spectrum of the CMB, based on the ΛCDM model and data on the Baryon Acoustic Oscillations (BAO) (see section I.4.3) [Agh18].

- The mass ordering of the neutrino mass eigenstates are either quasi-degenerate ($m_1 \approx m_2 \approx m_3$) or hierarchical [PDG18]: in the latter case, the mass splittings would be on the same order as the individual masses. It is unclear whether m_3 is the heaviest or lightest neutrino mass. If m_3 is the heaviest neutrino mass, the ordering is called normal (NO, $\Delta m^2_{3i} > 0$); otherwise it is called inverted ordering (IO, $\Delta m^2_{3i} < 0$).

- The current neutrino mass limits on the scale of eV/c^2 or below show that neutrinos are at least six orders of magnitude lighter than the other fundamental fermions, which have masses on the scale of MeV/c^2 or GeV/c^2 [Per09]. This smallness could be explained with a see-saw mechanism, which implies the existence of heavy right-handed neutrinos on the scale of 10^{12} GeV/c^2 (see section I.1). Such a see-saw mechanism could be rooted in the possible Majorana nature of neutrinos, meaning that they are their own anti-particles. However, whether neutrinos are Majorana particles remains unclear as of today.

Neutrino mass measurement with KATRIN The previous sections showed that the knowledge about the neutrino mass is of utmost importance for particle physics (due to "new physics", see section I.1) and cosmology (with regard to the baryon asymmetry in the universe, see section I.2). Out of the three methods for neutrino mass measurements from section I.4.1, only the spectroscopy of beta decay and electron capture offer a model-independent access to the absolute neutrino mass, without dependence on the possible Majorana nature of neutrinos.

Among the presented spectroscopic experiments, only the KATRIN experiment will be able to start data taking in 2019 at its ultimate design sensitivity. The aspired sensitivity of 0.2 eV/c^2 would be sufficient to probe almost the complete quasi-degenerate scale of possible neutrino masses. A detailed overview of the KATRIN experiment will be given in the following chapter.

II. The KATRIN experiment

The KArlsruhe TRItium Neutrino (KATRIN) experiment aims at the model-independent determination of the effective electron anti-neutrino mass $m_{\bar{\nu}_e}$. For this purpose, KATRIN investigates the neutrino mass imprint on the tritium beta spectrum close to its kinematic end point. KATRIN has a 5σ discovery potential for a neutrino mass of 350 meV/c^2 and a 90% C.L. sensitivity of 200 meV/c^2. This is an improvement by one order of magnitude with regard to previous direct neutrino mass searches [Lob03, KBB05, Ase11].

Reaching the design sensitivity will require three years of measurement time over the course of about five calendar years. Since the fall of 2016, the following measurement campaigns have been carried out with the fully integrated beamline:

- **First Light campaign (Oct. & Nov. 2016)** The first transmission of electrons through the complete beamline allowed to investigate the alignment of the individual beam tube components with respect to the magnetic guiding field. At the same time, the ion blocking and removal instruments were tested in situ with deuterium ions from the ELIOTT ion source (see chapter VIII).

- **^{83m}Kr campaign (July 2017)** An admixture of gaseous krypton to the source gas can be used in order to investigate properties of the source plasma and the effects of ion blocking and removal (see section VI.2.3). The krypton campaign served as a first reference run of krypton operation, in a first step without carrier gas. Further, high voltage operation and temperature dependent source properties were investigated with gaseous krypton. Besides, a condensed krypton source for the calibration of high voltage properties was tested [KFL18].

- **First Tritium campaign (May & June 2018)** This campaign marked the first operation of the beamline with tritium and the first measurement of a tritium beta spectrum with KATRIN. A major purpose of the measurements was the confirmation of tritium ion safety, using multiple new ion detectors in the beamline (see chapter IX). For safety reasons, only about 0.5% tritium were added to the circulation of deuterium source gas.

- **Commissioning and calibration campaign ("STS IIIa", Sept. & Oct. 2018)** Before the operation of the KATRIN beamline with the design concentration of almost 100% tritium, several commissioning measurements were carried out with deuterium source gas or with empty source. Using inactive ions, the pressure dependence of the ionisation efficiency was investigated (see section IV.2), as well as the emission of secondary electrons upon ion impact on the PS downstream cone electrode (see section VII.2.4).

This chapter will give an overview of the KATRIN experiment and its experimental setup. First, the measurement principle of KATRIN will be explained in the

following section II.1. Then, an overview of the KATRIN beamline will be given in section II.2, followed by the related software for data acquisition and analysis in section II.3. The detailed experimental conditions inside the beamline will be discussed in section II.4. Finally, section II.5 explains the effect of background on the neutrino mass sensitivity of KATRIN, especially with regard to background by tritium activity in the Main spectrometer.

II.1. Measurement principle

In the KATRIN experiment, 10^{11} beta electrons will be created each second via radioactive decay in a high-luminosity tritium source. A strong magnetic field up to 6 T guides the electrons to the spectrometers, which act as a high-pass energy filter for the electron-counting detector. This setup allows to measure an integrated energy spectrum around the end point region of the tritium beta spectrum of 18.6 keV.

In this section, first the measurement principle of the MAC-E filter will be explained. Afterwards, an overview of the analysis procedure and the consideration of systematic effects will be presented.

MAC-E filter The high-pass energy filter in the Main spectrometer works according to the MAC-E principle, which is short for Magnetic Adiabatic Collimation combined with an Electrostatic filter [Lob85, Pic92]. Basically, a retarding potential is applied in order to reject all electrons below a certain energy threshold. The electric field in the analysis plane is parallel to the magnetic guiding field and affects therefore only the electron energy component $E_{\parallel}$ parallel to the magnetic field. On the other hand, the beta electrons are created in the source isotropically with an arbitrary pitch angle θ between the electron momentum $\vec{p}$ and the magnetic field $\vec{B}$ (see section III.1.2). In order to investigate the total electron energy $E_{\mathrm{tot}} = E_{\parallel} + E_{\perp}$, the conservation of the magnetic moment $\vec{m}$ in the non-relativistic approximation is used [Bit04]:

$$\vec{m} = E_{\perp}/B = \mathrm{const.} \tag{II.1}$$

Because the magnetic field inside the Main spectrometer decreases by about four orders of magnitude with regard to the maximum magnetic field, the transversal energy component $E_{\perp}$ is decreased likewise. Under adiabatic conditions[1], the electron momenta will thus be collimated parallel to the magnetic field by virtue of the magnetic gradient force. The remaining transversal energy $E_{\perp,\mathrm{A}}$ of an electron is limited by the finite magnetic field B_{A} in the analysing plane and a second condition: at the location of the maximum magnetic field B_{max} in the beamline, the transversal energy of a detected electron might have been as large as its total kinetic energy $E_{\perp,\mathrm{max}} < E$. Due to the conservation of the magnetic moment, the energy resolution of the MAC-E filter reads as follows for $E_{\perp,\mathrm{A}} = \Delta E$:

$$\frac{\Delta E}{E} = \frac{B_{\mathrm{A}}}{B_{\mathrm{max}}}. \tag{II.2}$$

According to the KATRIN design report [CDR04], the magnetic field in the analysing plane will be $B_{\mathrm{A}} = 0.3$ mT and the maximum magnetic field is 6 T at the pinch magnet (compare figure II.7). For electron energies around the end point of the tritium beta spectrum $E_0 \approx 18.6$ keV, the filter width of the Main spectrometer is:

$$\Delta E = \frac{E_0 \cdot B_{\mathrm{A}}}{B_{\mathrm{max}}} \approx 0.93 \text{ eV}. \tag{II.3}$$

[1] The spatial variation of B inside the particle orbit has to be small compared to the magnitude of B [Bit04].

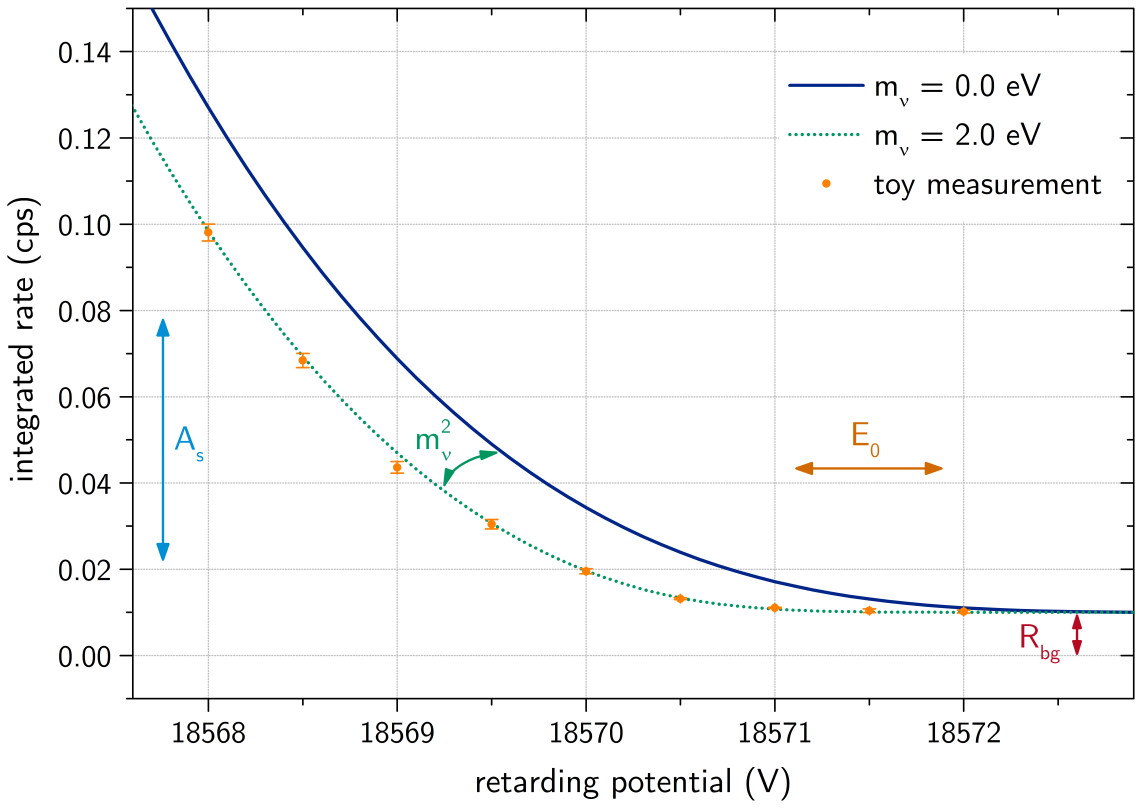

Figure II.1.: **End point region of the energy spectrum of tritium beta decay.** In order to determine the neutrino mass squared, a fit is applied to the data of a toy measurement corresponding to the statistics of 3 years. The four parameters used are the signal amplitude A_s, the nominal background rate R_{bg} = 10 mcps, the end point energy E_0 and the neutrino mass squared m_ν^2 = 2.0 eV for better visualisation. Figure taken from the PhD thesis of Marco Kleesiek [Kle14].

The inverse effect of the magnetic collimation is a magnetic mirror: as the magnetic field increases, the longitudinal energy $E_{\parallel}$ is decreased until the particle may advance no further. The magnetic mirror is used in KATRIN in order to reject electrons which were created in the source magnetic field $B_{\mathrm{S}} = 3.6$ T with a large pitch angle $\theta > \theta_{\mathrm{max}}$. This allows to reduce systematic effects, as will be discussed in the following. The acceptance angle for the detection of beta electrons from the source is:

$$\theta_{\mathrm{max}} = \arcsin \sqrt{\frac{B_{\mathrm{S}}}{B_{\mathrm{max}}}} = 50.8°. \tag{II.4}$$

Neutrino mass analysis In order to derive the neutrino mass from the observed electron count rates at various retardation potentials, a model for the well understood tritium beta spectrum is fitted to the measured data. This fit employs four parameters, as illustrated in figure II.1:

- the signal amplitude A_{s} of the beta electron rate,
- the overall background rate R_{bg} (see section II.5),
- the effective end point energy $E_0 \approx 18.6$ keV,
- and the neutrino mass squared m_{ν}^2.

The observed integrated energy spectrum differs due to several systematic effects from the theoretical integrated energy spectrum of a bare tritium nucleus decaying at rest: for example, the final states distribution of the daughter molecule from tritium decay is considered in the calculation of the tritium beta spectrum [Kle18]. After the beta decay, the electron energy may be changed for example by voltage fluctuations on dipole electrodes, which will be discussed in section VI.2.4. These effects during the electron transport are taken into account by the transmission function, along with the finite energy resolution of the MAC-E filter according to eq. II.3.

The energy loss of beta electrons by inelastic scattering on tritium source gas has to be taken into account separately; for this purpose, the transmission function is convolved with the energy loss function, yielding the "response function". The effect of inelastic scattering can be controlled to a certain extent at the expense of statistics via the rejection of beta electrons with a pitch angle $\theta > 50.8°$ according to eq. II.4 – these electrons have a comparatively large path length inside the source gas because of their gyrating motion. Due to the energy threshold for electronic T_2 excitation of about 12 eV, a plateau from unscattered beta electrons is observed in the end point region of the integrated spectrum at about 41% of the total transmission probability.

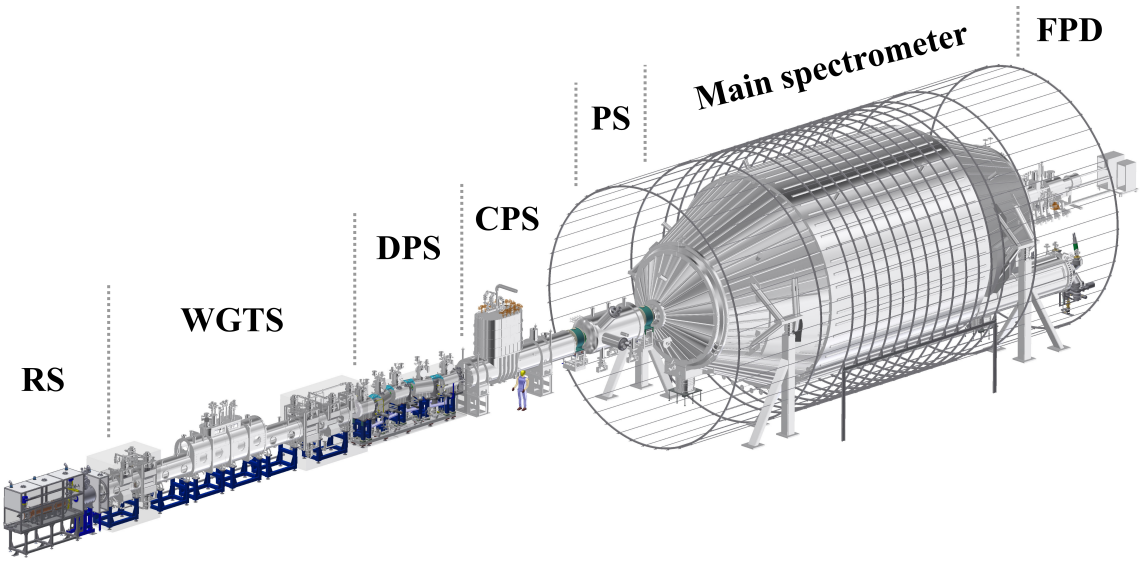

Figure II.2.: **Overview of the KATRIN beamline.** The rear section (RS) houses the rear wall, which defines the plasma potential inside the Windowless Gaseous Tritium Source (WGTS). Neutral tritium gas, which is injected in the WGTS, is removed by the Differential Pumping Section (DPS) and Cryogenic Pumping Section (CPS). Beta electrons, which are created by tritium decay in the WGTS, follow the magnetic guiding field to the spectrometers. Most of the beta electrons are rejected already by the Pre-spectrometer (PS), which is nominally at a filter potential of -18.3 kV during the neutrino mass measurements. The end point region of the tritium beta spectrum is then closely investigated with the MAC-E filter of the Main spectrometer (MS) by variation of a retarding potential of about -18.6 kV. Those beta electrons which overcome the retading potential of the MS are counted by the Focal Plane Detector (FPD), which measures thus an integrated tritium beta spectrum.

II.2. Overview of the KATRIN beamline

The 70 m long KATRIN setup is shown in figure II.2. It consists of a Windowless Gaseous Tritium Source (WGTS), a transport section for beta electrons, consisting of an active Differential Pumping Section (DPS) and a passive Cryogenic Pumping Section (CPS), the Pre-spectrometer (PS) and Main spectrometer (MS) and the Focal Plane Detector (FPD); the opposite end of the beamline is formed by the Rear Section (RS). In the following, all of these beamline components will be detailed.

Rear section (RS): The rear end of the KATRIN setup houses a calibration and monitoring system; this includes a precision electron source for the investigation of the response function and two BIXS detectors for a continuous monitoring of the tritium source activity. The magnetic field lines which connect source and detector are terminated on the gold coated surface of the rear wall, defining the potential of the source plasma.

A UV irradiation of the rear wall creates photoelectrons, which continuously re-

plenish the electron source plasma and prevent the creation of positive space charges. Photoelectrons were also used for alignment measurements during the First Tritium campaign (see figure VIII.3) and for creating non-active ions via inelastic scattering during the STS IIIa campaign.

Windowless Gaseous Tritium Source (WGTS): Tritium gas is injected in the center of the WGTS through a set of capillaries and pumped off at both ends with turbomolecular pumps. This creates a non-linear pressure profile in which 10^{11} beta electrons per second are created. The corresponding column density $\mathcal{N}$ of tritium in the source therefore has to be known with a relative precision of 0.1%. In order to increase the density of the tritium gas at a reasonable pressure, the gas is cooled by the WGTS cryostat to 30 K. Inside the source, a weak plasma is created via self-ionisation due to the beta decay (see section II.4.5).

In order to reach the design level of 95% T_2 concentration, the source gas is circulated through the tritium loops and purified in the process. A Laser Raman (LARA) setup monitors the actual tritium purity of the source gas. The inlet pressure to the WGTS is stabilised within a band of $\pm 0.1\%$ around the mean value using a buffer vessel [PSB15]. In order to handle the yearly throughput of 10 kg tritium [Bab12], the WGTS is located inside the Tritium Laboratory Karlsruhe (TLK) along with the tritium retention systems of the DPS and CPS, the calibration and monitoring systems of the rear section and the tritium analytics.

Besides the gas inlet, the central part of the WGTS is a 10 m long monolithic stainless steel tube of 90 mm diameter. This central part is termed in this thesis WGTS-C, whereas the region between the first two differential pump ports at the front side towards the detector is called WGTS-F; the corresponding region between the pump port on the rear side is the WGTS-R (see figure II.5). Further, the tritium gas flow from the WGTS constitutes a reference frame which is especially useful for the consideration of tritium ions: downstream refers to parts of the beam tube closer to the detector, whereas upstream refers to parts closer to the WGTS center; the terminology is usually not applied to the rear end between the WGTS and the rear section.

Differential Pumping Section (DPS): The DPS consists of five beam tube elements (BT) which are interconnected by six pump ports (PP) and linked to the WGTS and CPS [Hac17]. In five of these pump ports, the beam tube is evacuated via differential pumping with turbo molecular pumps; only PP5 between the DPS and CPS contains no pumps. While tritium is the most abundant gas species at the upstream end of the DPS, the pressure at the downstream end is dominated by leak gas[2].

The five beam tube elements of the DPS are each located inside the warm bore of superconducting magnets [Hac17]. The four upstream beam tubes 1 to 4 contain dipole electrodes for ion removal via $E \times B$-drift (see section III.1.2 and figure III.1). Two ring electrodes in BT5 and PP5 stop ions with electrostatic blocking potentials (see section VI.1). In between the ring electrodes, an FT-ICR unit was imple-

[2]Private communication with Carsten Röttele.

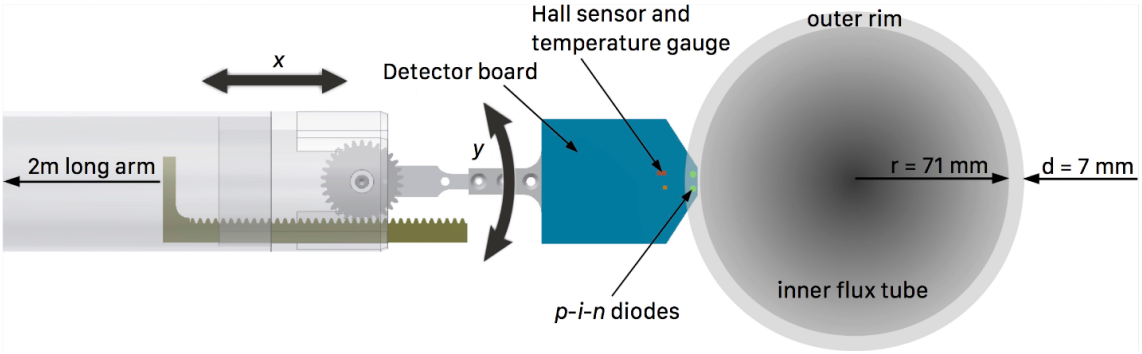

Figure II.3.: **Front end of the Forward Beam Monitor (FBM).** The FBM board with its p-i-n diodes, Hall sensor and temperature gauge can be moved with the lever arm along the x and y coordinates in order to scan the entire flux tube area; during the neutrino mass measurements, the p-i-n diodes monitor the source activity in the outer rim of the flux tube without shadowing the inner flux tube, which is transmitted to the FPD. For commissioning measurements during First Tritium with regard to tritium ion safety, the FBM board was exchanged for a Faraday cup board (see section VII.2.3). Figure from [KFL18].

mented in order to detect various ion species and distinguish their e/m-ratios (see section VII.3).

Cryogenic Pumping Section (CPS): The residual tritium flow from the DPS is removed in the CPS via cryogenic pumping. For this purpose, an argon frost layer is created inside the central beam tube of the CPS, which is cooled to 3 K [CDR04, Roe17].

Two monitoring and calibration systems are located at the downstream end of the CPS, right upstream from the spectrometers but still inside the TLK: the Forward Beam Monitor (FBM) monitors the source activity in the outer rim of the flux tube with two p-i-n diodes [Ell17] (see figure II.3); but also alternative boards like a Faraday cup can be mounted to the lever arm (see section VII.2.3). Towards the spectrometers, a Condensed Crypton Source (CKrS) emits krypton decay electrons for calibration purposes [KFL18].

Pre-spectrometer (PS): The Pre-spectrometer serves for the pre-filtering of the beta electron flux from the WGTS [CDR04]. For this purpose, a high voltage of -18.3 kV will be applied in nominal operations. The PS vessel is 3.4 m long and has a diameter of 1.7 m [KAV16]. An extensive discussion of the applications of the PS with regard to background by beta electrons, Penning traps and tritium ions can be found in section VI.3.

Main spectrometer (MS): The Main spectrometer acts as a high pass filter for the tritium beta electrons according to the MAC-E principle (see previous section). To this end, a retarding potential close to the tritium end point energy is created in the analysing plane.

In order to decrease the magnetic field by more than four orders of magnitude with regard to the 6 T in the pinch magnet, the magnetic flux tube is expanded adiabatically to a field strength of 0.3 mT. Since the transmitted magnetic flux tube expands to a diameter of 9 m [CDR04], the Main spectrometer has an even larger diameter of 9.8 m, a length of 23.3 m and a weight of 200 t [CDR04, KAV16]. For the fine tuning of the magnetic field in the analysing plane, the Main spectrometer is surrounded by an air coil system with 12.6 m diameter [Erh18].

The inside walls of the Main spectrometer vessel are covered with wire electrodes which allow the fine-shaping of the electrostatic potential and serve along with the self-shielding of the magnetic flux tube for the mitigation of cosmic-ray-induced background [Val10]. A pressure in the range of 10^{-11} mbar can be achieved by pumping with turbo molecular pumps (TMPs) and non-evaporable getter pumps (NEGs), which are located in three tubular pump ports with 1.7 m diameter [KAV16] (see figure II.4). In order to mitigate background by radon which emanates from the NEGs, LN_2-cooled baffles are installed in front of the pump ports. Since the pressure gauges are likewise located inside the pump ports, the actual pressure inside the MS vessel can only be inferred from simulations while the baffles are cooled.

The stability of the high voltage of the Main spectrometer is monitored with the spectrometer of the former Mainz Neutrino Mass Experiment [CDR04]: this monitor spectrometer measures continuously the electron rate of a krypton source in a parallel beamline, using the retarding voltage of the MS.

Focal Plane Detector (FPD): The FPD consists of a monolithic 148-pixel p-i-n diode array on a single silicon wafer [FPD15]. It is placed inside a post acceleration electrode, which allows to boost the beta electron energy to a range with a more favourable intrinsic background rate (see figure VII.7). The calibration system of the FPD includes the PULCINELLA disc, which can also be used for current measurements as described in section VII.2.5. A first readout stage consists of pre-amplifiers within the vacuum before the second stage located outside vacuum.

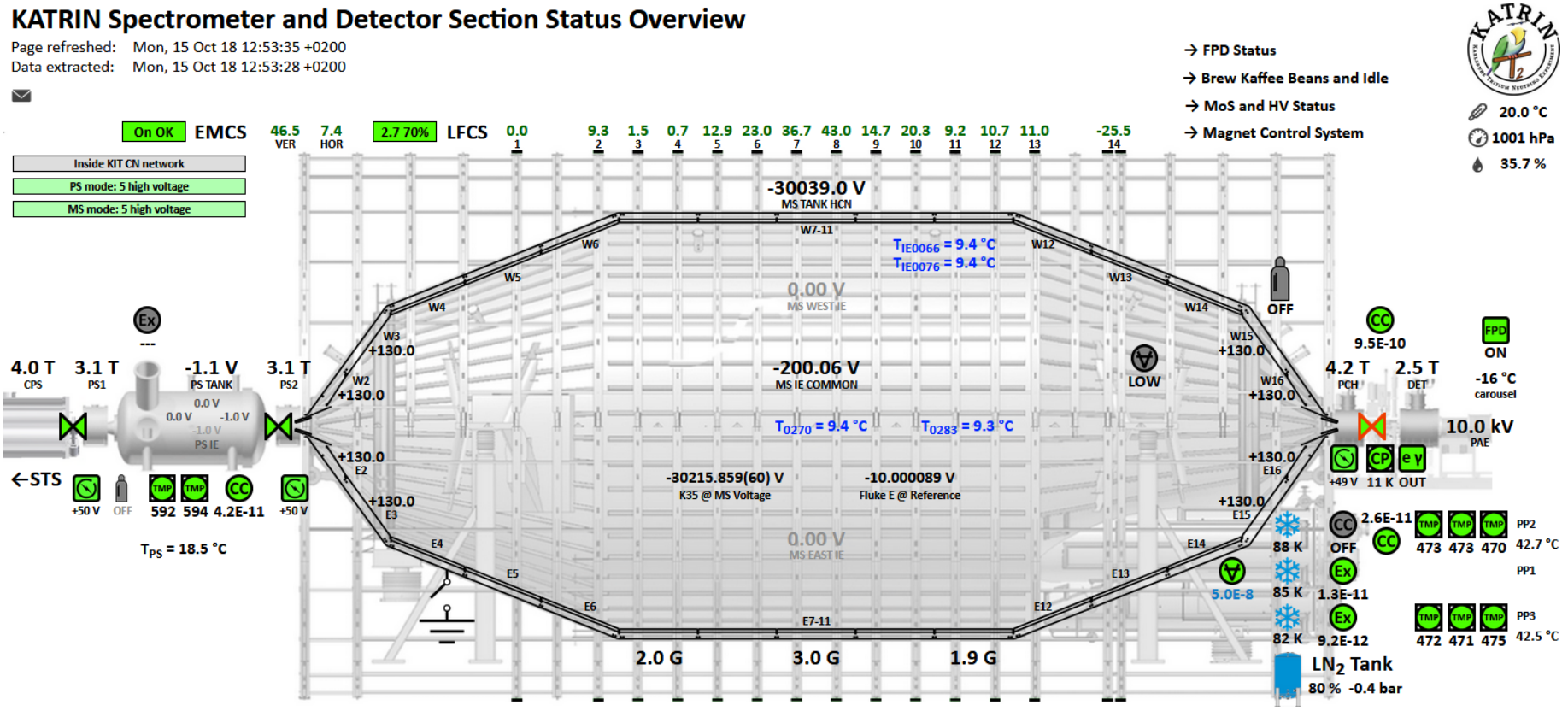

Figure II.4.: **Status overview for the spectrometer and detection section.** The picture illustrates the position of the superconducting magnets, the 14 air coils around the Main spectrometer and the 15 wire electrode rings, which are arranged in two steep cones at both ends and two flat cones towards one central part. Pressure gauges are located in the tubular pump ports at the detector side end of the Main spectrometer. This screenshot of the browser interface was taken during the STS IIIa campaign on October 15, 2018 at 12:53 h.

II.3. Software for data acquisition and analysis

The acquisition of measurement data in KATRIN is divided into two classes: detector data acquisition (DAQ) and slow control.

Event based data is read out with the detector DAQ. It primarily serves the acquisition of data from the FPD and related systems [FPD15], but is also used for the data acquisition of the FBM. The software of the detector DAQ is based on the ORCA package (Object-oriented Real-time Control and Acquisition) [FPD15].

All other devices are read out via slow control: this concerns time series data such as from pressure and temperature sensors, but also the current measurements at the DPS dipole electrodes (see section VII.2.2) and the PS cone electrode (section VII.2.4). The devices usually communicate via a compact Field Point (cFP) with the data management system ZEUS (ZEntrale datenerfassung Und Steuerung) [FPD15].

The measurement data from slow control and detector DAQ are first recorded in a local database, then copied to the central KATRIN database and permanently archived with the Advanced Data Extraction Infrastructure (ADEI) [FPD15]. Besides its function as database, ADEI acts as data manager which can cache and preprocess the raw data, as well as display them via a web interface. Also, ADEI allows communication between ORCA and the slow controls.

Essential tools developed within the KATRIN collaboration for data analysis and simulation are collected in a common C++ software framework called KASPER [Kle14]. Most relevant for the analysis of FPD data from the First Light and First Tritium campaigns were the following two modules: the KaLi package retrieves data from the ADEI database via the KATRIN database (KDB); these measurement data were then analysed with the BEANS analysis software.

Another important module of KASPER with regard to ions is KASSIOPEIA: it allows to track charged particles in electro-magnetic fields, partially by the use of numeric Monte Carlo simulations [Kle14]. This was used extensively in order to investigate the trajectories of ions in the spectrometers (see section IV.1) and evaluate the data from the First Light and First Tritium campaigns (see chapters VIII and IX).

During the measurements, a quick access to the current status of the beamline is given via status monitors. Figure II.4 shows an example for the status monitor of the spectrometer and detector section as recorded during the STS IIIa commissioning campaign in October 2018.

II.4. Experimental conditions during the neutrino mass measurements

In order to measure the neutrino mass, the KATRIN experiment employs extreme experimental conditions along the beamline; this concerns temperature, pressure, magnetic and electric fields. All of these will be detailed in the following sections. As a special case, the electric potential inside the source is determined by a plasma which will be described in section II.4.5.

II.4.1. Temperature regimes

Most of the overall 70 m long beamline is at room temperature during the neutrino mass measurements, except for the cryostats of the WGTS and the CPS: the WGTS is cooled to 30 K in order to increase the tritium density at a reasonably low pressure and to reduce the Doppler broadening and space charge potential [CDR04, Kuc18, Hoe12]; in case of the CPS, the central beam tubes are at a temperature of 3 K, which allows to pump the neutral tritium via adsorption on an argon frost layer [Roe17]. The rear wall lies outside the WGTS cryostat and will be close to room temperature during the neutrino mass measurements.

II.4.2. Pressure regimes and gas species

The source gas is injected through a gas inlet in the center of the 10 m long WGTS-C stainless steel tube and pumped off with turbo molecular pumps at both ends. This creates a gas density profile as shown in figure II.5 with a stabilised pressure of $3{\cdot}10^{-3}$ mbar in the center and about 1% of this pressure at both ends [Kuk16, Kuc18]. During the neutrino mass measurements, the source gas has a tritium purity of at least 95% – for test measurements, there might however be added traces of gaseous krypton-83m [CDR04].

At the entrance to the DPS, the tritium pressure is already reduced to[3] to about $4 \cdot 10^{-7}$ mbar due to the differential pumping in the WGTS-F (see figure II.6). Further differential pumping with turbo molecular pumps in the DPS reduces the tritium partial pressure below 10^{-10} mbar. Measurements of the total pressure in the DPS during the First Tritium campaign indicate that from PP3 on downstream, the pressure is dominated by leak gas (presumably H_2) and the outgassing of the FT-ICR unit in DPS PP5 (presumably methanes; see section VII.3)[4].

The CPS is the last stage of neutral tritium retention. It employs a cryotrap in form of an argon frost layer at 3 K. During First Tritium, total gas pressures on the order of $1{\cdot}10^{-9}$ mbar were measured. However, the actual pressure in the beam tubes is assumed to be several orders of magnitude smaller, because the pressure gauges are located in some distance to the beam tube and at liquid nitrogen temperature. According to simulations, the tritium flow is reduced by at least a factor 10^{11} in the

[3] The tritium pressure in the DPS was simulated by Susmita Mondal using Molflow+ [Mol16] during an internship at KIT-IKP in spring 2017.

[4] Private communication with Carsten Röttele (KIT-ETP).

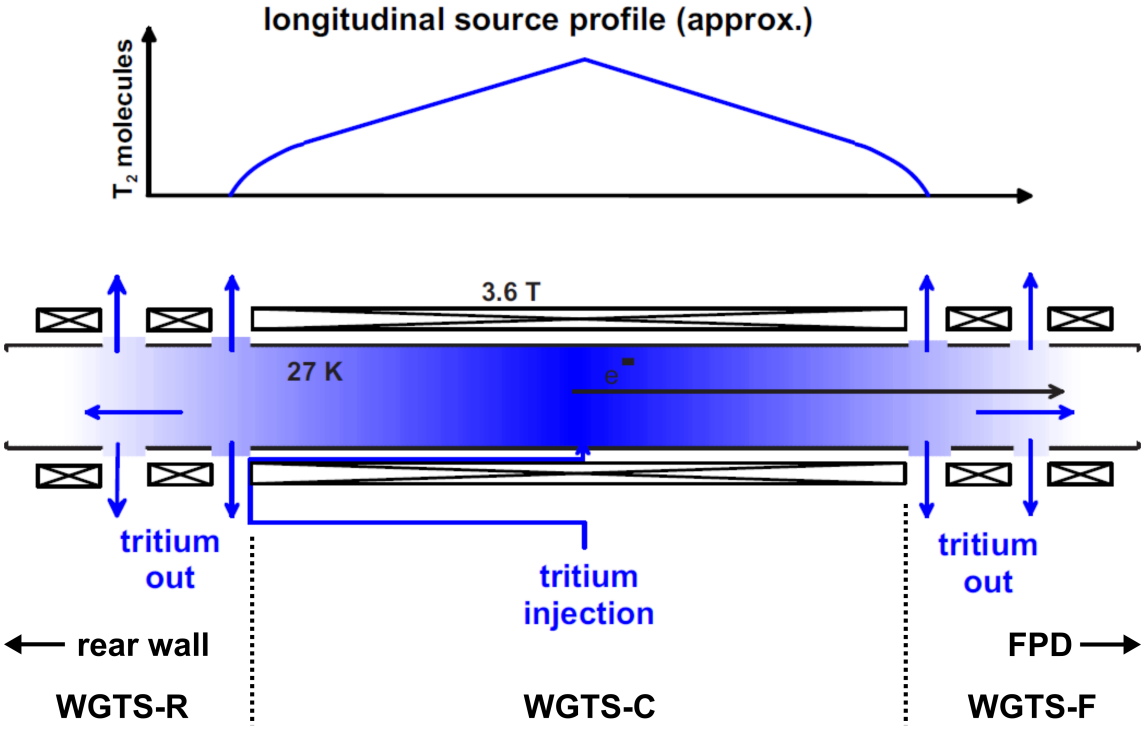

Figure II.5.: **Gas density profile in the WGTS.** The longitudinal profile is determined by the tritium injection in the center of the WGTS-C and the differential pumping in the WGTS-F and WGTS-R. Due to the pumping, the pressure is reduced from $3 \cdot 10^{-3}$ mbar at the gas inlet to a few 10^{-5} mbar at the exit of the 10 m long stainless steel tube. In order to increase the tritium density at a reasonable pressure, the source beamtube is cooled to about 30 K. Figure adopted from [CDR04].

CPS [FRS18]; this was confirmed by dedicated measurements, as will be reported by Carsten Röttele in his Ph.D. thesis [Roe19].

In total, the neutral tritium flow from the WGTS to the end of the CPS is expected to be reduced by at least a factor $2 \cdot 10^{19}$ [FRS18]. This is more than five orders of magnitude above the initial design value of 10^{14} [CDR04]. However, tritium ions from the source cannot be pumped off neither differentially nor cryogenically; for this reason, methods of ion blocking and removal with electric fields will be discussed in the following chapters of this thesis.

Inside the spectrometers, the residual gas pressure is dominated by hydrogen outgassing [KAV16]. During First Tritium, the design pressure of $1 \cdot 10^{-11}$ mbar in the MS was reached in the baked setup. Nevertheless, it should be kept in mind that the pressure gauges in the MS are located behind cooled baffles and might therefore slightly underestimate the actual pressure in the MS volume (see figure II.4). The pressure in the adjacent vacuum vessel of the PS was also on the level of a few 10^{-11} mbar.

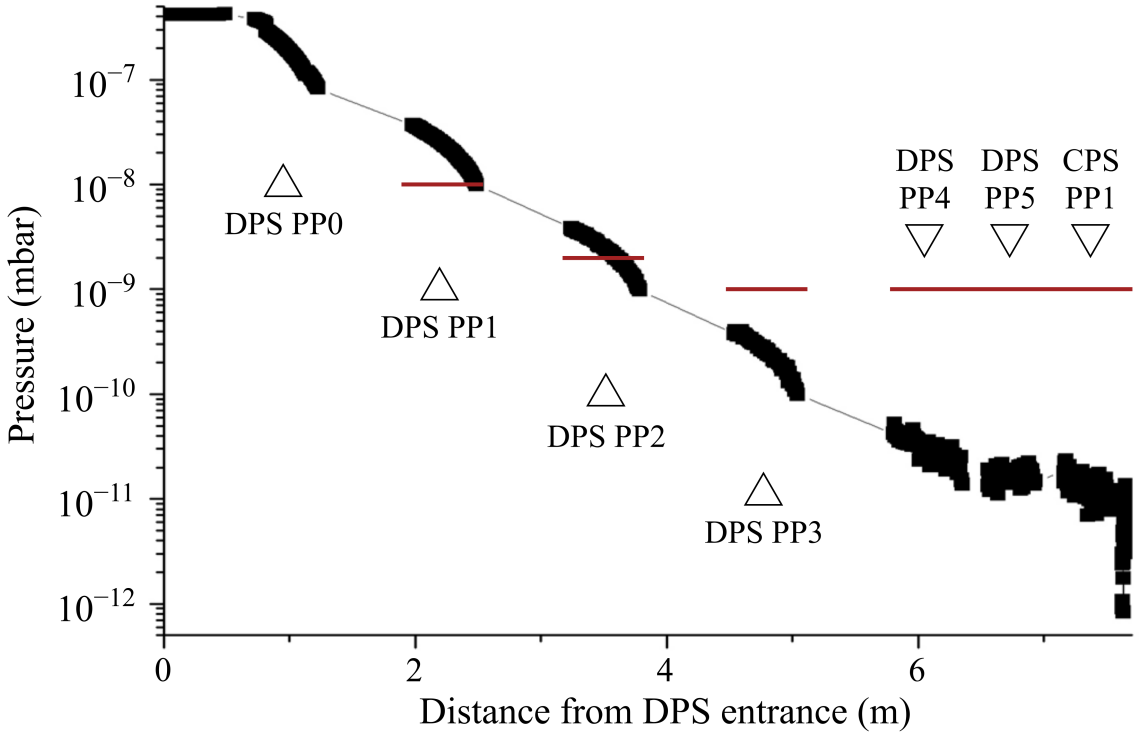

Figure II.6.: **Pressure along the DPS.** The black squares indicate the tritium partial pressure during nominal tritium circulation as simulated by Susmita Mondal with Molflow+ [Mol16]. The red lines show the measured total pressures in the individual pump ports after several days of continuous deuterium circulation on June 11 during the First Tritium campaign. From PP3 on downstream, the expected tritium partial pressure is much smaller than the measured total pressure, which is attributed to leak gas and outgassing of the FT-ICR unit in DPS BT5 (see section VII.3). Inside the CPS beam tubes at 3 K, the actual pressure presumably several orders below the measured pressure of about 10^{-9} mbar, because the pressure gauges are located in some distance to the beam tube at liquid nitrogen temperature.

II.4.3. Magnetic fields

The beta electrons are guided by a strong magnetic field of up to several Tesla from the tritium source to the spectrometers. As explained in section II.1, the adiabatic expansion of the magnetic field lines in the Main spectrometer is the basis for the MAC-E filter principle.

The magnetic guiding field along the beamline is created by superconducting solenoids: 10 of these magnets are single modules with warm bores and 14 more are part of the cryostats of the WGTS and CPS [Gil18]. Inside of the superconductors, the magnetic field reaches between 3.6 T and 6.0 T for the design settings. These maxima of the magnetic field alternate with dips in the pump ports between the solenoids. For technical reasons, the magnetic field was overall reduced previously to 20% during the First Light campaign [Gil18] (see chapter VIII) or 70% during the Krypton campaign [Gil18] and the First Tritium campaign (see chapter IX).

The minimal magnetic field of $B_{\mathrm{A}} = 0.3$ mT in the center of the Main spectrometer is tuned by the Low Field Correction System (LFCS) and the Earth Magnetic field Compensation System (EMCS) [Erh18]. With 14 air coils of the LFCS, the shape and strength of the magnetic field in the analysing plane can be corrected and scaled up to $B_{\mathrm{A}} = 1.8$ mT. The EMCS allows to compensate the earth magnetic field with two cosine coil systems in vertical and horizontal direction around the spectrometer. While the magnetic field inside the MS cannot be measured directly, it can be calculated from measurements of the magnetic field outside the MS with a relative accuracy of better than 1% [Erh18].

Due to geometric obstructions and collisions, only a part of the total magnetic flux tube in the WGTS is transmitted to the FPD. Its area depends on the alignment of the superconducting magnet coils, which was checked during the First Light campaign [Hac17]. According to [Gil18], the flux tube of 191 Tcm^2 was found to be unobstructed apart from shadows on a few pixels on the right side of the FPD.

II.4.4. Electric fields

While measuring the end point region of the tritium beta spectrum, a high voltage of -18.6 kV will be applied in the MS and -18.3 kV in the PS [CDR04]. Both spectrometers can in principle[5] be operated up to -35 kV.

The inner electrodes of the spectrometers allow to fine tune the electric field due to the vessel voltages. In the PS, two cone electrodes are located on the upstream and downstream side and one wire electrode sits in the center[6]. In the MS, 15 rings of wire electrodes serve at the same time for the mitigation of background from muon induced electrons and from Penning traps [Val09, Val10] (see figure II.4).

The electrons which are observed with the FPD are accelerated by two further voltages: a Post Acceleration Electrode (PAE) in front of the FPD increases the

[5] Internal communication with Oliver Rest (WWU Münster) from the *KATRIN operator training High Voltage* for the Krypton campaign in 2017.

[6] For the inner electrode setup of the PS see also the Diploma thesis of Florian Fränkle, *Erste Messungen der elektromagnetischen Eigenschaften des KATRIN Vorspektrometers*, Karlsruhe University (2006).

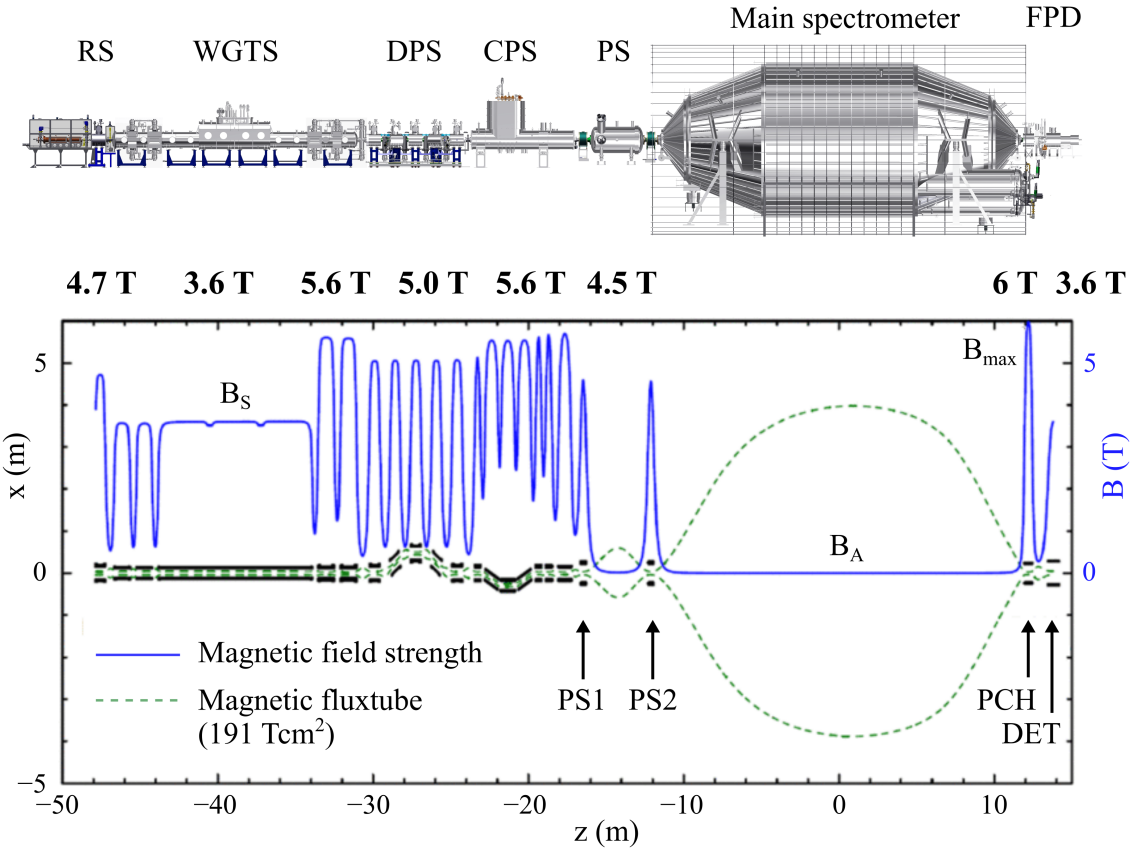

Figure II.7.: **Magnetic fields in the KATRIN beamline.** The graph indicates the magnetic field strength in the center of the beamline and in bird's eye view a contour of the 191 Tcm^2 flux tube which is transmitted from the WGTS to the FPD. Above, the bold numbers state the design values for the magnetic field strength inside the superconductors. The magnetic fields in the source (B_s), in the analysis plane ($B_\mathrm{A} = 0.3$ mT) and the maximum field B_max affect the energy resolution of the MAC-E filter (see section II.1). Marked in the plot are the four superconductors in the spectrometer section: the PS1 and PS2 magnet on both sides of the Pre-spectrometer, the pinch magnet (PCH) on the downstream end of the Main spectrometer and the detector magnet (DET), in which the FPD is located. Based on a graph and values from [Gil18].

energy of all negativly charged particles with a high voltage of usually +10 kV and a bias voltage of 120 V is applied to the FPD itself [FPD15].

Inside the source, the electric potential is assumed to be determined by a plasma which in turn can be controlled via the rear wall potential [CDR04, Kuk16]. As will be explained in section II.4.5, the homogeneity of the source potential depends on the voltage difference between rear wall and the beam tube of the WGTS. The source beam tube is electrically connected with the beam tubes of the rear section, the DPS and CPS and defines the electric ground potential in the source and transport section.

In general, it has to be kept in mind that any electrode within the solenoidal magnetic field of the beamline acts as a Penning trap for charges of the opposite polarity [CDR04], for example the PS and MS. Further, a Penning trap for charged particles of the same polarity as the spectrometers is created in between them. Another Penning trap is assumed to create ions inside several of the ring electrodes for ion blocking (see section IX.2.2). In order to prevent discharges between the ring and dipole electrodes and the beam tube walls, the maximum applied voltage was limited during commissioning measurements like the First Light campaign (see chapter VIII) or the First Tritium campaign (see chapter IX).

Besides, several other electrodes can be moved into the beamline for commissioning measurements. The ion measurements during the First Light and First Tritium campaign used for example the Faraday cup board for the Forward Beam Monitor (see section VII.2.3) and the Pulcinella disc between the MS and the FPD (see section VII.2.5).

II.4.5. Source plasma

The decay of tritium molecules creates daughter ions [CDR04]. Further, each beta electrons creates on average 15 more ions and secondary electrons via ionisation of the tritium gas in the WGTS (see section III.1.4). These ions and secondary electrons create a plasma, which defines the electric start potential of the beta electrons from tritium decay in the source.

To first order, the plasma potential is determined by the rear wall due to the strong magnetic field which restricts the transversal motion of ions and electrons [CDR04]. Due to the collective behaviour of the plasma which attempts to restore quasi-neutrality, a homogeneous plasma potential might be assumed at first glance [Bit04].

Detailed plasma simulations by Laura Kuckert [Kuk16] indicate, however, that the homogeneity of the plasma potential depends in fact on the potential difference between the rear wall and the walls of the WGTS beam tube. This potential difference would need to be kept on the technologically challenging level of ≤ 10 mV in order to meet the KATRIN design homogeneity of $\Delta U \leq 10$ meV along the WGTS. But experimentally observable is only a longitudinal inhomogeneity of the plasma potential of at least 22 meV using an admixture of ^{83m}Kr to the source gas at 110 K. During standard operation of the WGTS around 30 K, the work function of the WGTS beam tube walls might be changed via tritium adsorption. The resulting inhomogeneity of the plasma potential would be 29 meV, and the resulting shift of the neutrino mass squared $\Delta m_\nu^2 = (-1.5 \pm 0.25) \cdot 10^{-3}$ eV^2 according to the same plasma

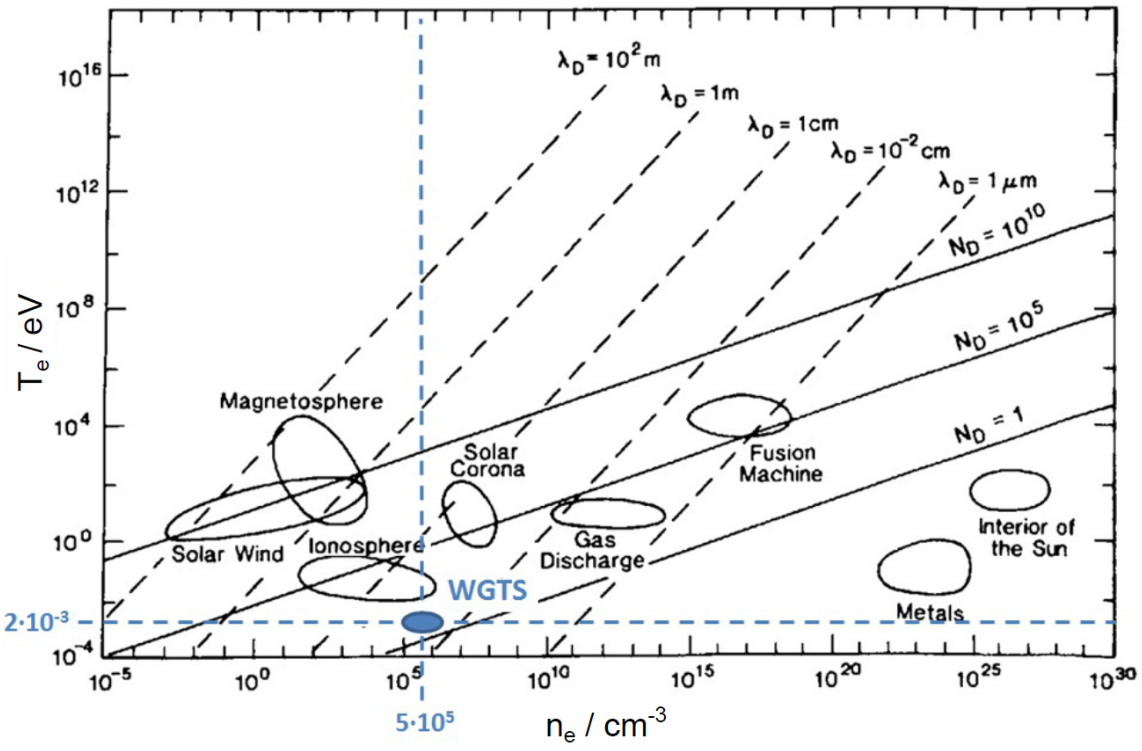

Figure II.8.: **Plasma in the WGTS in comparison.** Knowledge about conventional plasmas cannot be transferred to the WGTS easily due to the special experimental conditions. This includes mainly the extremely small electron temperature T_e and the comparatively small electron density n_e. Also indicated are the Debye length λ_D and the plasma parameter N_D. From [Kuk16] based on a figure from [Gal12].

simulation [Kuk16]. For comparison: the KATRIN design report [CDR04] assumed a shift of only $\Delta m_\nu^2 = 0.2 \cdot 10^{-3}$ eV^2. One remedy for longitudinal plasma inhomogeneities could be the injection of electrons into the plasma via the UV irradiation of the rear wall, which will need to be optimised for this purpose experimentally.

Further influence on the neutrino mass measurements could arise from instabilities of the plasma. These instabilities might create time-dependent electric fields which could change the energy of traversing beta electrons (see section V.4.1). The occurrence of instabilities is favoured by the non-monotone shape of the energy spectrum of secondary electrons in the source[7].

The investigation of the WGTS plasma is particularly difficult due to the special experimental conditions which are not comparable to most other applications of plasma physics (see figure II.8) [Kuk16]:

- **Temperature:** the secondary electrons are mostly thermalised around 30 K. This is extremely cold, even compared to classical low-temperature plasmas which are usually orders of magnitudes hotter.

- **Density:** the number density of charged particles of $10^{11\ldots12}$ m^{-3} is rather low.

[7]Internal communication with Felix Spanier.

- **Self-ionisation:** the plasma is created from tritium gas via beta decay of the tritium molecules. Usually, the plasma is created by discharges due to large external electric fields or by high temperatures.
- **Dimensions:** the length of the WGTS of more than 10 m is particularly large compared to the diameter of 9 cm.

Obviously, the plasma investigations are closely related to tritium ions. The removal of positive ions with dipole electrodes in the DPS (section VI.2) is an important boundary condition for simulations of the source plasma. Another important boundary condition is the inadvertent blocking of tritium ions which was observed during the First Light and First Tritium campaigns (see sections VIII.6 and IX.3). Also, the negative potential of the dipole electrodes may lead to the formation of a negative ion space charge potential in the WGTS-F (see section V.4.2). Nevertheless, the dipole electrodes are indispensable for the KATRIN experiment, because tritium ions may otherwise leave the plasma and cause background if they reached the spectrometers (see section IV.2 and IV.3). The effect of an increased background on the neutrino mass measurements will be discussed in the following section.

II.5. Effect of background on the neutrino mass sensitivity

The neutrino mass measurements are subject to various types of background: for example, cosmic rays may induce background inside the FPD [FPD15]; radioactive decays in the spectrometers give rise to trapped particles which create secondary electrons which in turn follow the magnetic field lines to the FPD [Mer13]; and an energy-dependent background can be created by tritium decay in a negative offset potential from space charges (see section V.4.2) or the dipole electrodes in the DPS (see section VI.2.2).

The largest background contribution arises from the Main spectrometer. Estimates in the design report [CDR04] are based on a reference background of 10 mcps. However, long-term measurements of the spectrometer background from 2014 to 2015 revealed a background of about 400 mcps, which is attributed to excited Rydberg atoms of neutral hydrogen [Har15]. The background was observed to depend on the volume of the magnetic flux tube imaged onto the detector; it could thus be reduced with an increased magnetic field in the analysing plane, but only at the expense of a reduced energy resolution of the MAC-E filter (see section II.1).

A larger background rate decreases the sensitivity of the KATRIN experiment for the neutrino mass, but investigating the actual relationship requires extensive spectrum simulations [CDR04]. The KATRIN design report suggests in a rough estimate that the statistical sensitivity for the neutrino mass squared increases with $\sqrt[6]{b}$ of the background rate b. Another consequence of a larger background is that it changes the optimal measurement time distribution at various retarding potentials of the MS; that's because the best sensitivity for the neutrino mass squared is reached for a signal rate $s \approx 2b$.

In order to account for the increased background, the statistical uncertainty could be reduced in a trade-off for a slightly larger systematical uncertainty. Statistics could be improved by measuring larger electron rates in an extended measurement interval of for example 45 eV below the tritium end point energy instead of the 30 eV interval as proposed in the design report[8]. On the other hand, the larger measurement interval would increase systematic uncertainties due to the final states distribution of the daughter molecules from tritium decay and due to inelastic scattering of beta electrons in the source.

With regard to tritium activity in the MS, a background limit of 1 mcps is stated by the design report [CDR04]. The retention of neutral tritium surpasses the design requirements by more than five order of magnitude [FRS18] (see section II.4.2). Tritium ions, by contrast, cannot be pumped off and might follow the magnetic field to the spectrometers. In order to prevent this, tritium ions in the beamline are blocked, removed and the residual ion flux detected, as will be explained in the following chapters of this thesis.

[8] The effect of the measurement time distribution on the neutrino mass sensitivity was investigated by Marco Kleesiek [Kle14].

III. Ion creation and transport

10^{12} ions/s will be created in the tritium source during nominal operation: either by tritium beta decay or by scattering of the tritium beta electrons on the tritium gas. Most of these ions will be thermalised immediately due to collisions with the neutral source gas, but there is also a small fraction of ions with eV energies from molecular dissociation.Furthermore, ions may be created during First Tritium by Penning discharges in the ring electrodes which are actually intended to block ions. An additional inadvertent ion blocking was observed during the First Light and First Tritium campaigns up to ion energies of about 1 eV.

This chapter will provide theoretical descriptions for all of these ion creation mechanisms and discuss aspects of the ion transport through the beamline. Since most of the ions are created due to tritium decay, the rates of beta electrons and secondary electrons from beta electron scattering will be calculated in the first section III.1. Then, section III.2 details the creation and thermalisation of positive and negative tritium ions in the WGTS. A special case are daughter ions from molecular dissociation, because they have kinetic energies up to several eV as detailed in section III.3. The third ion creation process are Penning discharges in those ring electrodes (see section III.4), which are actually intended to block the ions inside the beamline. A small rate of ions can further be created within the CPS due to inelastic scattering of beta electrons on non-tritium residual gas (see section III.5). At the end of this chapter, section III.6 will discuss several phenomena which affect the ion transport through the beam tube, namely the magnetic mirror effect, inadvertent ion blocking and the neutralisation of blocking potentials.

III.1. Beta electrons and secondary electrons

The ion fluxes from the WGTS are inevitably linked to the fluxes of beta electrons and secondary electrons: whenever ions are created, electrons are created, too; and the recombination between ions and slow secondary electrons can reduce the ion flux out of the WGTS. It is therefore useful to first derive the rates of beta electrons and secondary electrons, before the ion fluxes will be calculated in the upcoming sections.

This section will first discuss the tritium activity (section III.1.1) and the motion of charged particles in static electric and magnetic fields (see section III.1.2). Based on this, the beta electron flux into the PS will be calculated in section III.1.3. Finally, also the flux of secondary electrons into the DPS will be assessed in section III.1.4.

III.1.1. Tritium activity

Tritium beta decay is the origin of most charged particles in the KATRIN experiment during nominal operation: the decay creates beta electrons which in turn ionise the tritium gas in the source and the residual gas in other parts of the beamline; this includes Penning discharges in the ring electrodes, which were observed during First Tritium to be neither self-igniting nor self-sustainable. For all of these applications, it is crucial to know the tritium activity inside the full beam tube or inside a certain section of the beam tube.

In order to calculate the activity inside the full beam tube, a reasonable starting point is the number of tritium atoms n_T in the beam tube:

$$n_\mathrm{T}(\epsilon_\mathrm{T},\mathcal{N}) = 2 \cdot \sigma_\mathrm{WGTS} \cdot \epsilon_\mathrm{T} \cdot \mathcal{N}, \tag{III.1}$$

which relies on the following quantities:

- The column density $\mathcal{N} = \rho d$ is the number of gas molecules within a unit area integrated along the whole beam tube.

- Multiplication with the tube area leads to the absolute number of molecules in the gas column. Because almost all of the gas is concentrated in the WGTS, the area of the WGTS of $\sigma_\mathrm{WGTS} = \pi r_\mathrm{WGTS}^2 = 63.6$ cm^2 can be used. The radius $r_\mathrm{WGTS} = 4.5$ cm corresponds to a flux tube of $\Phi_\mathrm{WGTS} = 229$ Tcm^2 at nominal magnetic field strength.

- A factor 2 accounts for the average number of atoms per molecule, because most of the molecules are assumed to be hydrogen dimers.

- The tritium purity ϵ_T considers the fraction of tritium atoms relative to the total number of atoms in the gas column.

Knowing the number of tritium atoms, the tritium activity can be calculated with

the decay constant λ_T of tritium[1] [Pov09]:

$$\begin{aligned} A(\epsilon_\mathrm{T},\mathcal{N}) &= \lambda_\mathrm{T} \cdot n_T(\epsilon_\mathrm{T},\mathcal{N}) \\ &= 2\lambda_\mathrm{T} \cdot \sigma_\mathrm{WGTS} \cdot \epsilon_\mathrm{T} \cdot \mathcal{N}. \end{aligned} \tag{III.2}$$

According to this calculation, $1.1 \cdot 10^{11}$ tritium atoms will decay per second in the KATRIN source during nominal operation with a tritium purity of 100% and a column density of $5 \cdot 10^{21}$ m^{-2}. During the First Tritium measurements, the tritium purity was about 200 times smaller and the column density only $4.46 \cdot 10^{21}$ m^{-2}; the corresponding activity was $5.1 \cdot 10^{8}$ decays per second.

III.1.2. Charged particles in a static electric and magnetic field

The motion of beta electrons, secondary electrons and ions will be confined by a strong magnetic guiding field inside the KATRIN beamline. Along their way, the charged particles encounter electric fields, for example from the ring and dipole electrodes and from the spectrometers.

As will be discussed in the following, the particles are accelerated and decelerated by the electric fields, undergo an $E \times B$-drift by the combination of electric and magnetic field and move in cyclotron spirals along the magnetic field. It is due to this cyclotron motion that the charged particles carry an energy component perpendicular to the magnetic field, a consequence of the conserved magnetic moment of a charged particle in a magnetic field. The conservation of the magnetic moment allows charged particles to be stopped and reflected by a static magnetic field. All of these topics will be discussed in the following section based on [Bit04] unless otherwise noted.

Cyclotron motion and $E\times B$-drift The electric and magnetic fields in the KATRIN beamline are in good approximation constant in time and spatially uniform. Under these conditions, the velocity $\vec{v}(t)$ of an electron or ion with charge q and mass m depends on the electric field $\vec{E}$ and the magnetic field $\vec{B}$ via:

$$\vec{v}(t) = \vec{v}_\parallel(0) + \frac{q\,\vec{E}_\parallel}{m} \cdot t + \frac{\vec{E}_\perp \times \vec{B}}{B^2} + \vec{\omega}_c \times \vec{r}_c. \tag{III.3}$$

The first two terms describe the particle's velocity parallel to the magnetic field: the particle can have an initial velocity $\vec{v}_\parallel(0)$ and may be further accelerated due to the Coulomb force from the component of the electric field $\vec{E}_\parallel$ parallel to the magnetic field. For example, the dipole electrodes will accelerate (decelerate) the ions when they enter (leave) the negative potential (see appendix A.6); the electrons experience the opposite effect.

The third term corresponds to a constant drift in the direction which is perpendicular to both the magnetic and electric field. Such a magnetron drift or $E \times B$-drift is employed by dedicated electric dipole electrodes in the DPS in order to remove and measure the ion flux from the WGTS (see section VI.2.1 and VII.2.2). The

[1] The decay constant $\lambda_\mathrm{T} = \ln(2)/T_{1/2} = 1.78 \cdot 10^{-9}$ s^{-1} can be calculated from the tritium half-life $T_{1/2} = 4500 \pm 8$ d [Pov09, Luc00].

magnitude of the drift velocity depends only on the electric and magnetic fields. Also, the magnetron drift does not change the energy of the affected particles and can be transformed away by the choice of a corresponding reference frame.

Within the reference frame of the $E \times B$-drift, the charged particles perform a circular motion with cyclotron frequency ω_c and cyclotron radius r_c. In contrast to the $E \times B$-drift, the cyclotron motion does not depend on the electric field, but on the particle's mass m and charge q:

$$\omega_c = \frac{|q|\,B}{m}. \tag{III.4}$$

The cyclotron frequency is associated with an energy component of the charged particle perpendicular to the magnetic field. As will be discussed in the following, the conservation of the ratio between this energy $E_\perp$ and the magnetic field is the basis for the magnetic mirror effect.

Conservation of the magnetic moment The orbital magnetic moment $|\vec{m}|$ of a charged particle in a magnetic field is conserved if the spatial variation of the field $\vec{B}$ is small compared to its magnitude B. Thus, the magnetic moment is called an adiabatic invariant:

$$|\vec{m}| = \frac{E_\perp}{B} = \text{const.} \tag{III.5}$$

When the particle moves into a stronger magnetic field, its perpendicular kinetic energy $E_\perp = \frac{1}{2}mv_\perp^2$ must increase. This can ultimately lead to the magnetic mirror effect, which will be discussed below.

On the other side, the pitch angle will be reduced when the particle moves into a smaller magnetic field. This enables the KATRIN measurements in the first place, because it allows the magnetic adiabatic collimation of the beta electron energies in the analysis plane of the main spectrometer (see section II.1). From eq. III.5 follows the relative sharpness $\Delta E/E$ of the MAC-E-filter [CDR04]:

$$\frac{\Delta E}{E} = \frac{E_{\perp,\text{ap}}}{E_{\perp,\text{max}}} = \frac{B_\text{ap}}{B_\text{max}}. \tag{III.6}$$

Magnetic mirror and acceptance angle The conservation of the magnetic moment can lead to the reflection of charged particles by a static magnetic field. In order to understand the so called magnetic mirror effect, it is useful to consider the pitch angle θ between the total momentum $\vec{p}$ of the particle and the magnetic field $\vec{B}$ (see figure III.1).

As the particle moves into a stronger magnetic field, its perpendicular energy must increase and the pitch angle likewise becomes larger. There is nothing that prevents the particle from reaching a pitch angle $\theta = \pi/2$; but in this case, the longitudinal energy of the particle vanishes and it cannot be transported further. This mirror effect is particularly relevant for electrons, whereas ions change their pitch angle in most cases by repeated scattering on the source gas until they can escape.

The maximum angle which an electron may be created with in the WGTS in order to overcome the magnetic mirror is called the acceptance angle. If the pitch angle is

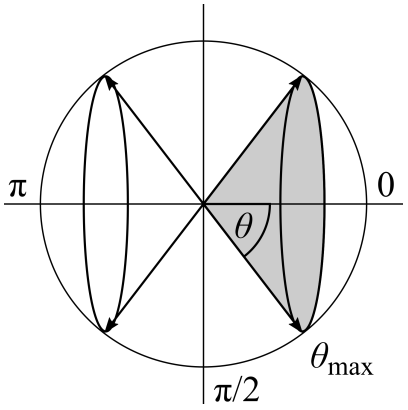

Figure III.1.: **Acceptance cone (grey) of a magnetic mirror.** The orientation of a charged particle's momentum in a magnetic guiding field is described by the pitch angle θ. When the particle moves into a stronger magnetic field, its pitch angle will increase due to the conservation of the magnetic moment from eq. III.5. Ultimately, the particle can be stopped completely. In order to overcome this magnetic mirror, the particle's pitch angle at the location of its creation must fall into the acceptance cone which is defined by the acceptance angle θ_{max}.

smaller than this θ_{max}, the electron falls into the loss cone (gray area in figure III.1) and can escape the magnetic mirror:

$$\theta_{\mathrm{max}} = \arcsin\sqrt{\frac{B_{\mathrm{WGTS}}}{B_{\mathrm{max}}}}. \tag{III.7}$$

B_{max} is the maximum nominal magnetic field between the source at $B_{\mathrm{WGTS}} = 3.6$ T nominal and wherever the electrons are supposed to be detected. For FPD measurements, the maximum magnetic field is given by the pinch magnet of 6 T, which leads to an acceptance angle of $\theta_{\mathrm{max}} = 50.8°$ (compare eq. II.4). If the maximum field is reached in the CPS with $\theta_{\mathrm{max}} = 5.72$ T, the acceptance angle becomes only $\theta_{\mathrm{max}} = 52.5°$.

The fraction p_{acc} of electrons which can leave the WGTS follows from integration over the solid angle of the loss cone $\theta = (0,\theta_{\mathrm{max}})$. Because the electrons are emitted isotropically, the fraction can be normalised with the integral over the full range of the polar pitch angle $\theta = (0,\pi)$:

$$p_{\mathrm{acc}} = \frac{\int_0^{\theta_{\mathrm{max}}} \sin(\theta)\ \mathrm{d}\theta}{\int_0^{\pi} \sin(\theta)\ \mathrm{d}\theta} = \frac{1-\cos(\theta_{\mathrm{max}})}{2}. \tag{III.8}$$

With the acceptance angles from above, the probability for the detection of beta electrons from the WGTS becomes $p_{\mathrm{acc}}^{\mathrm{DPS}} = 0.18$ at the FPD and $p_{\mathrm{acc}}^{\mathrm{PS}} = 0.20$ for measurements between the CPS and the pinch magnet. The integration already accounts for the fact that only 50% of the electrons are emitted towards the spectrometers, because the loss cone $(\pi/2 - \theta_{\mathrm{max}},\pi/2)$ was not considered (see figure III.1).

Conservation of the magnetic flux Directly from the conservation of the magnetic moment follows the conservation of the magnetic flux Φ_m, which can be thought of

as the flux enclosed by one orbit of the charged particle. As the particle moves into a stronger magnetic field B, its cyclotron radius r will decrease so that the magnetic flux which is enclosed by its orbit remains constant:

$$\Phi_m = \int_S \vec{B}\,\mathrm{d}\vec{S} = \pi r^2 \cdot B. \tag{III.9}$$

The conservation of the magnetic flux can be used to calculate the area of the electron and ion flux tube at any position along the beamline, as long as the magnetic field strength B is known. For example, the detection efficiency of the Faraday cup at the FBM can be determined by comparing the magnetic fields of the WGTS and the end of the CPS (see section IX.1.6); and the drift distance inside the dipole electrodes can be projected onto the FPD in order to assess the effect on the beta electrons (see appendix A.6). Also, the conservation of the magnetic flux allows to quantify the effect of geometric obstructions on the magnetic flux tube, for example between the CPS and PS in the next section.

III.1.3. Beta electron flux into the PS

The creation rate of beta electrons is given by the tritium activity A_T from equation III.1. But only 20% of these electrons arrive at the spectrometers due to the magnetic mirror effect, which was discussed in the previous section. This factor already includes the 50% probability of the electrons to be emitted into the direction of the detector.

The magnetic flux tube is filled homogeneously with beta electrons from the WGTS, where the magnetic flux is $\Phi_\mathrm{WGTS} = 229$ T cm^2. An increase of the magnetic field strength reduces the flux tube area, but the magnetic flux and thus the number of transported electrons are conserved (see previous section). However, there are geometric obstructions which cut away the outer rim of the flux tube between the WGTS and spectrometers: a flux tube of 210 T cm^2 is transported through the connection of CPS and PS[2], but due to further collisions in the transport section, the actually transmitted flux tube[3] into the PS is $\Phi_\mathrm{PS} \approx 190$ T cm^2. This reduction can be accounted for with a factor $p^\mathrm{PS}_\mathrm{trans} = \Phi_\mathrm{PS}/\Phi_\mathrm{WGTS} = 0.83$.

In summary, the beta electron flux into the PS becomes:

$$\Phi^\mathrm{dec}_\mathrm{\beta el} = p^\mathrm{PS}_\mathrm{acc} \cdot p^\mathrm{PS}_\mathrm{trans} \cdot A(\epsilon_\mathrm{T},\mathcal{N}) \tag{III.10}$$

$$= 2\lambda_\mathrm{T} \cdot \sigma_\mathrm{WGTS} \cdot p^\mathrm{PS}_\mathrm{acc} \cdot p^\mathrm{PS}_\mathrm{trans} \cdot \epsilon_\mathrm{T} \cdot \mathcal{N}. \tag{III.11}$$

A flux of $1.7 \cdot 10^{10}$ beta electrons per second is expected to flow into the PS for a nominal column density of $\mathcal{N} = 5.0 \cdot 10^{21}$ m^{-2} and a tritium concentration of 100%. During First Tritium, the column density was usually about $\mathcal{N} = 4.5 \cdot 10^{21}$ m^{-2} and the tritium concentration about 0.5%; this leads to an expected flux of $7.7 \cdot 10^7$ beta electrons per second.

[2]Transmission of the complete 210 T cm^2 requires a magnetic field in the WGTS slightly above the nominal value. This setting was used during First Tritium.

[3]Analysis by Ferenc Glück based on First Tritium data.

III.1.4. Flux of secondary electrons into the DPS

Each beta electron creates on average 15 secondary electrons by ionisation of tritium gas via inelastic scattering. In principle, this scattering probability $\mathcal{P}$ can be calculated from the cross section $\sigma(E)$ for inelastic scattering of electrons on hydrogen molecules:

$$\mathcal{P} = \sigma(E) \cdot \rho \cdot l, \tag{III.12}$$

but the energy dependent cross section requires to take into account the energy spectrum of the beta electrons. Even more difficult, the effective path length l of the electrons depends on the pitch angle θ: larger pitch angles increase the path length due to additional cyclotron motion (see section III.1.2). For an analytic treatment of these effects, see section III.3.4.

Using the result of a simulation[4], the scattering probability can be estimated with the electron multiplicity of $p_{\mathrm{sc},0} = 15$ ions per β electron. Because the scattering probability is $\mathcal{P} \propto \rho \propto \mathcal{N}$, the electron multiplicity can be written for arbitrary column densities as $p_{\mathrm{sc}}(\mathcal{N}) = p_{\mathrm{sc},0} \cdot \frac{\mathcal{N}}{\mathcal{N}_0}$.

The magnetic mirror effect does not need to be considered for any detection of secondary electrons from the source in the scope of this thesis. That's because the secondary electrons were only measured with the dipole electrode in DPS BT1 (see section IX.3.2); there, the magnetic field is slightly smaller than in the WGTS-F, where the pitch angle of the secondary electrons is frequently changed by scattering on neutral molecules.

Also, no geometric obstructions need to be considered when the secondary electrons are calculated in the DPS: $p_{\mathrm{trans}}^{\mathrm{DPS}} = 95.47\%$ of the field lines[5] which start in the center of the WGTS will lead without collision into the dipole electrode in DPS BT1. An additional factor 1/2 accounts for the probability that the secondary electrons leave the WGTS towards the DPS.

In summary and with the tritium activity A_{T} from eq. III.2, the flux of secondary electrons into the DPS becomes:

$$\begin{aligned}\Phi_{\mathrm{sel}}^{\mathrm{sc}} &= \frac{1}{2} \cdot p_{\mathrm{trans}}^{\mathrm{DPS}} \cdot p_{\mathrm{sc}}(\mathcal{N}) \cdot A(\epsilon_{\mathrm{T}},\mathcal{N}) \\ &= \lambda_{\mathrm{T}} \cdot \sigma_{\mathrm{WGTS}} \cdot p_{\mathrm{trans}}^{\mathrm{DPS}} \cdot p_{\mathrm{sc},0} \cdot \epsilon_{\mathrm{T}} \cdot \frac{\mathcal{N}^2}{\mathcal{N}_0}.\end{aligned} \tag{III.13}$$

A flux of $8.1 \cdot 10^{11}$ secondary electrons per second is expected to flow into the DPS at a nominal column density of $\mathcal{N} = 5.0 \cdot 10^{21}$ m^{-2} and a tritium concentration of 100%. During First Tritium, the column density was $\mathcal{N} = 4.5 \cdot 10^{21}$ m^{-2} and the tritium concentration 0.5%; this leads to an expected flux of $3.2 \cdot 10^{9}$ secondary electrons per second.

[4]Simulation by Ferenc Glück

[5]A simulation of 10^4 magnetic field lines was carried out by Marco Deffert with KASSIOPEIA.

III.2. Positive and negative thermal ions

Beta decay and inelastic scattering of the fast beta electrons on tritium gas in the WGTS lead to the creation of ions. In collisions with the neutral gas, these ions and the corresponding secondary electrons transform into a variety of positive and negative ions. The large density of neutral gas in the center of the WGTS leads to the thermalisation of ions; and at nominal tritium concentration, the plasma density of ions and secondary electrons is large enough for the recombination of most of the ions before they can leave the source. Nevertheless, a flux of $2 \cdot 10^{11}$ positive ions per second and $1 \cdot 10^{10}$ negative ions per second is expected from the WGTS into the DPS at nominal source conditions.

III.2.1. Positive ion creation and transformation

A tritium activity of $1 \cdot 10^{11}$ beta decays per second is expected under nominal conditions in the WGTS according to section III.1.1. These decays in T_2 molecules leave behind an equal number of positive $({}^3\mathrm{HeT})^+$ ions, part of which dissociates into monoatomic T^+ [CDR04]:

$$T_2 \rightarrow ({}^3\mathrm{HeT})^+ + e^-_\beta + \bar{\nu}_e \rightarrow {}^3\mathrm{He} + T^+ + e^-_\beta + \bar{\nu}_e. \tag{III.14}$$

As discussed in section III.1.4, each beta electron e^-_β will create on average 15 more ions by inelastic scattering. These ions are mostly T_2^+, but also T^+ ions are created at a small rate [CDR04]:

$$e^-_\beta + T_2 \rightarrow e^-_\beta + e^-_s + T_2^+ \qquad (\approx 96\%), \tag{III.15}$$

$$e^-_\beta + T_2 \rightarrow e^-_\beta + e^-_s + T^+ + T \quad (\approx 4\%). \tag{III.16}$$

These ions from beta decay ($({}^3\mathrm{HeT})^+$) and inelastic scattering (T_2^+ and T^+) undergo transformation by collision with neutral T_2 molecules [CDR04]:

$$({}^3\mathrm{HeT})^+ + T_2 \rightarrow T_3^+ + {}^3\mathrm{He}, \tag{III.17}$$

$$T_2^+ + T_2 \rightarrow T_3^+ + T, \tag{III.18}$$

$$T^+ + 2\,T_2 \rightarrow T_3^+ + T_2. \tag{III.19}$$

The T_3^+ ions can be further transformed into cluster ions like T_5^+ [Joh76], and even larger cluster ions like T_7^+ are expected from ternary collisions:

$$T_3^+ + 2\,T_2 \rightarrow T_5^+ + T_2. \tag{III.20}$$

The relative densities of the various ion species are a function of the gas pressure and therefore of the distance to the gas inlet in the center of the tritium source. Figure III.2 shows the results of a simulation[6]: near the center of the WGTS, the gas density is large and the frequent collisions lead to a majority of T_5^+ ions. As the ions follow the neutral gas flow along the WGTS, their mean free path increases and the T_3^+ becomes dominant. The total ion density depends on the density and the flow speed of the neutral tritium gas. Figure III.2 also shows the resulting electron density based on the assumption of quasi-neutrality.

[6]Simulation by Ferenc Glück.

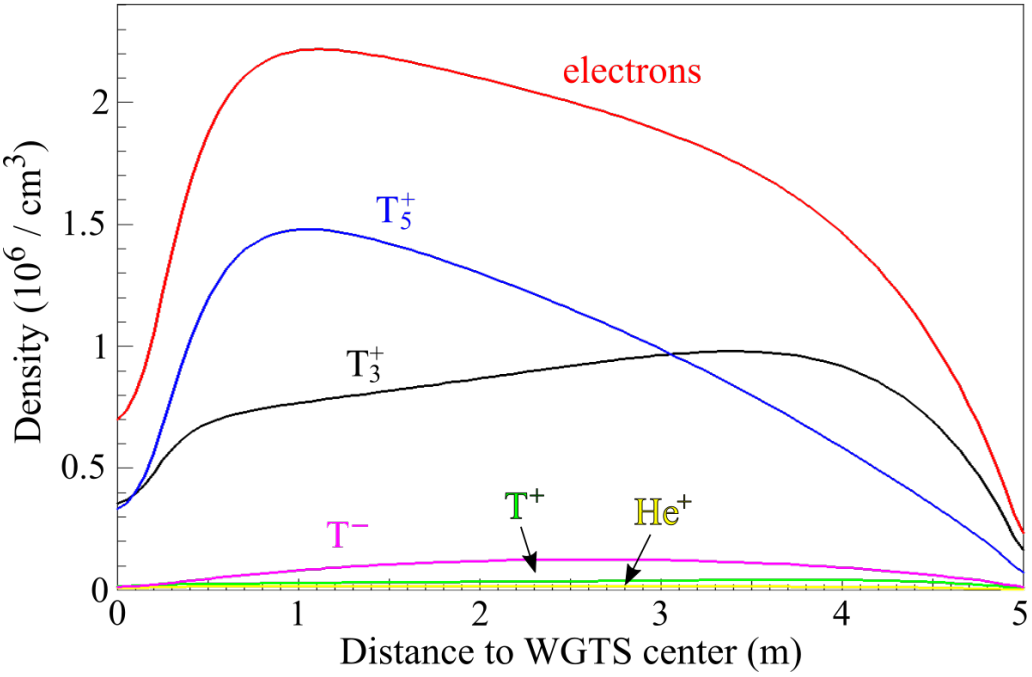

Figure III.2.: **Ion densities in the WGTS.** Close to the center, the neutral gas density is large (compare figure III.4). There, the frequent scattering allows the creation of large cluster ions like T_5^+. As the pressure decreases, the T_3^+ ions become dominant. Because the plasma attempts to restore quasi-neutrality, the electron density corresponds to the total positive ion density. Compare figure III.5 for the relative radial densities of the ion species 5 m away from the gas inlet. Figure and simulation by Ferenc Glück.

III.2.2. Negative ion creation

Besides positive ions, also negative tritium ions are expected to be created. The underlying process is dissociative attachment of electrons with a few eV to the ground state T_2 [CDR04]:

$$e^- + T_2 \rightarrow T^- + T. \tag{III.21}$$

However, the cross section for dissociative attachment upon electron scattering is small compared to the vibrational excitation of the T_2 [CDR04].

Under nominal source conditions, the negative ions are trapped between the negative potentials of the DPS dipole electrodes (see section VI.2) and the gas flow from the WGTS. The only way for negative ions to leave the beam tube is via recombination with positive ions (see section III.2.4); but this recombination probability is small even at nominal tritium concentration. Hence, almost all of the negative ions which are created in the tritium source are expected to flow into the DPS[7]. For the same reason, negative ions require special attention with regard to systematic effects (see section V.4).

[7]Simulation by Ferenc Glück

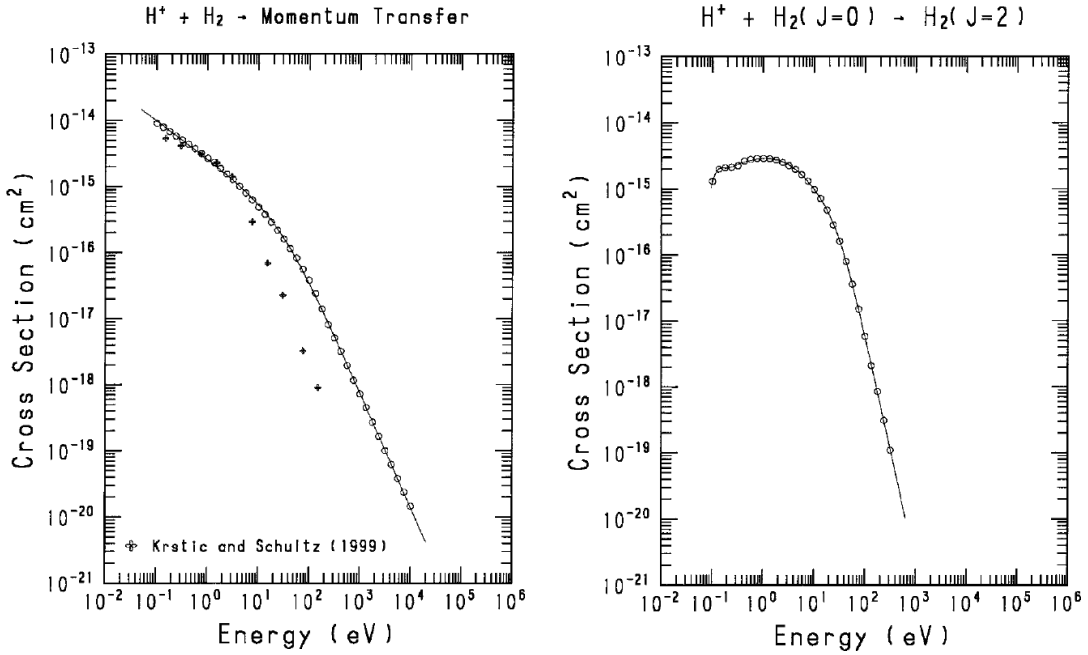

Figure III.3.: **Cross sections for elastic scattering of H^+ ions on neutral H_2.** Both momentum transfer (left) and rotational excitation $J = 0 \rightarrow 2$ (right) have cross sections of a few 10^{-15} cm^2 at ion energies around 1 eV. From [Tab00].

III.2.3. Thermalisation

Upon beta decay, the debris molecule or atom will receive a recoil energy of up to 3.41 eV. If the daughter molecule subsequently dissociates, several more eV will be transferred to the debris (see section III.3.3). However, the ions are assumed to thermalise quickly in the tritium source due to frequent scattering with neutral gas.

This section will first discuss the scattering probability by means of the scattering cross sections and mean free path; it will then detail that the ions lose on average half of their energy in each collision.

Scattering probability Frequent scattering on neutral gas leads to the thermalisation of ions in the tritium source. Figure III.3 shows the dominant cross sections $\sigma(E)$ for elastic scattering and rotational excitation of the T_2 molecule in case of an incoming H^+ ion. The cross sections for elastic scattering of ions from two or three hydrogen atoms are very similar.

The ion scattering probability in the WGTS can best be expressed with the mean free path λ, which is calculated from the number density $n(x)$ of source gas molecules according to [Per09]:

$$\lambda = \frac{1}{\sigma(E) \cdot n(x)}. \tag{III.22}$$

Because the gas density decreases from the gas inlet in the center of the WGTS towards the pumping sections, the mean free path increases the further the ions get away from the gas inlet. Figure III.4 shows the mean free path for the gas density

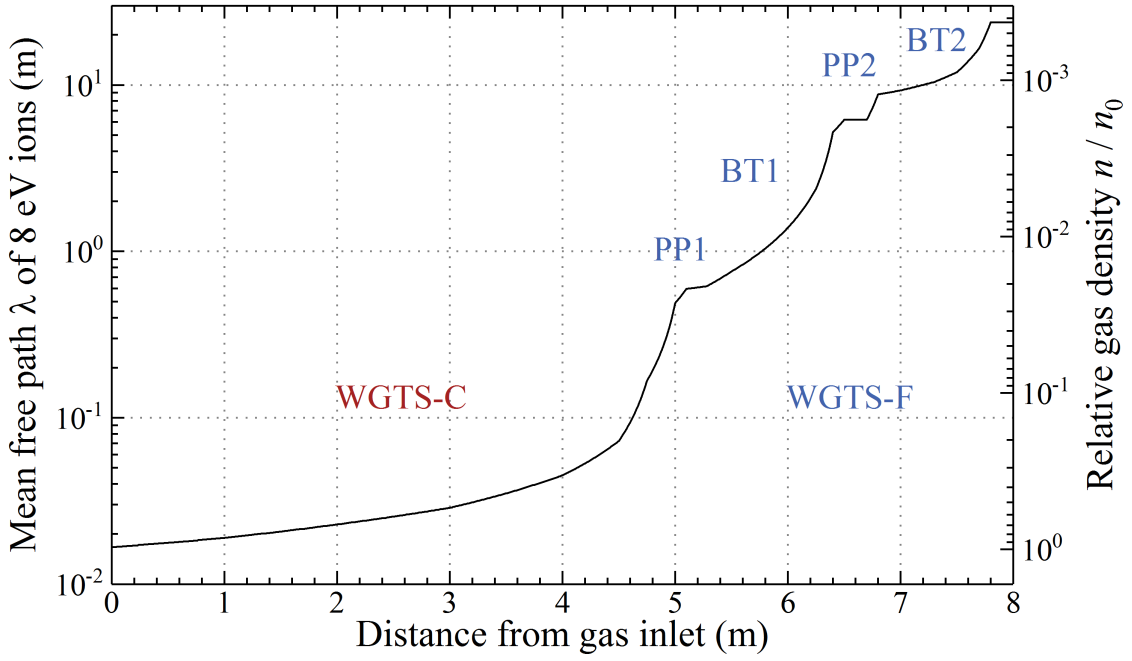

Figure III.4.: **Mean free path of hydrogen ions in the WGTS and relative gas density.** Marked by the dashed line is the original region of the eV ions. The gas density values were taken from the PhD thesis of Laura Kuckert [Kuk16]. The mean path was calculated from the gas density with the cross section $\sigma = 6 \cdot 10^{-16}$ cm^2 for momentum transfer of ions with 8 eV according to [Tab00].

$\rho(x)$ according to simulations from the PhD thesis of L. Kuckert [Kuk16], using a cross section of $\sigma(8\text{ eV}) = 6 \cdot 10^{-16}$ cm^2 [Tab00].

According to figure III.4, the ions in the center of the WGTS will scatter about one hundred times before they leave the WGTS. With each collision they lose on average half of their kinetic energy, as will be discussed below. Ultimately, the ion energy reaches a thermal Boltzmann spectrum according to the WGTS temperature of 30 K or 2.5 meV.

Close to the ends of the tritium source, the scattering probability becomes small. Ions from these regions are not fully thermalised and can retain a significant part of their original kinetic energy. Due to the small gas density, the flux of these ions becomes likewise small. But within a narrow region in the WGTS-F, the mean free path of the ions is already on the order of 1 m and the tritium density is still significant. This is the presumed origin of ions with several eV energy which were observed during First Tritium (see calculations in section III.3.4 and measurements in section IX.2.3.3).

Energy loss at scattering For a quantitative treatment of the thermalisation process, consider an ion of mass m_1 scattering on a source gas molecules with mass m_2. Before the scattering, the ion has a velocity v_1 and energy $E_1 = \frac{1}{2} m_1 v_1^2$, while the velocity $v_2 \approx 0$ of the thermal gas can be neglected. After the scattering, the two particles will fly apart with angles θ_1 and θ_2 relative to the initial ion mo-

mentum. According to [Lan60], the velocity of the target molecule will then be $v_2' = \frac{2m_1m_2}{m_1+m_2}\cos(\theta_2)$. The energy transfer between the two particles in this elastic collision is just $\Delta E = \frac{1}{2}m_2(v_2')^2$. Therefore, the relative energy loss of the incoming ion is:

$$\frac{\Delta E}{E} = \frac{4m_1m_2}{(m_1+m_2)^2}\cdot\cos^2(\theta_2). \tag{III.23}$$

Depending on the split angle $\theta_2 = (0,\frac{\pi}{2})$, the ion can lose almost all to none of its kinetic energy in the collision. Because the number of ions and their collisions in the center of the tritium source is large, the angular contribution can be averaged: $\langle\cos^2(\theta_2)\rangle = \frac{1}{\pi/2}\int_0^{\pi/2}\cos^2(\theta_2)\,\mathrm{d}\theta_2 = \frac{1}{2}$.

In summary, the average energy loss depends only on the masses of the ion and its scattering partner, which is usually neutral gas. The maximum average energy transfer of 50% is reached for the short-lived $(^3\mathrm{HeT})^+$ debris of tritium decay, which has the same mass as the T_2 molecule. Nevertheless, a T^+ ion will also lose 44% of its energy and the most abundant T_3^+ ions even lose 48% of their energy on average.

III.2.4. Recombination

Positive ions can recombine with secondary electrons as well as with negative ions. Recombination is negligible for small tritium concentrations like 0.5% during First Tritium; but under nominal source conditions, only about 20% of the positive ions will actually leave the tritium source towards the DPS. As will be discussed in the following, the recombination rate for arbitrary tritium concentrations can only be simulated numerically and not be calculated analytically.

Recombination of positive ions with thermal electrons Positive ions and thermal electrons can recombine under radiation of a photon:

$$\mathrm{A}^+ + \mathrm{e}^- \rightarrow \mathrm{A}^* + \gamma. \tag{III.24}$$

Also, dissociative recombination is possible:

$$\mathrm{T}_3^+ + e^- \rightarrow \mathrm{T}_2 + \mathrm{T}, \tag{III.25}$$

The recombination rate $R_{\mathrm{sel}}^{\mathrm{rec}}$ depends on the densities ρ of the positive ions and thermal electrons, which are mostly secondary electrons:

$$R_{\mathrm{sel}}^{\mathrm{rec}} = \alpha\rho_+\rho_{\mathrm{sel}}. \tag{III.26}$$

In fact, the dissociative recombination dominates with coefficients between 10^{-8} cm^3/s and 10^{-5} cm^3/s.

Recombination between positive and negative ions Positive and negative ions can recombine to neutral tritium molecules [Ols70]:

$$\mathrm{T}^- + \mathrm{T}^+ \rightarrow \mathrm{T}_2, \tag{III.27}$$

$$\mathrm{T}^- + \mathrm{T}_3^+ \rightarrow 2\,\mathrm{T}_2. \tag{III.28}$$

The recombination coefficient is for example $\alpha(\mathrm{T}^-\mathrm{T}^+) \approx 5\cdot10^{-7}$ cm^3/s.

Recombination rate 80% of the created ions will recombine still within the WGTS at nominal column density and tritium concentration. This is the result of the same simulation which lead up to figure III.2. During First Tritium, in contrast, recombination was negligible because the 200 times smaller tritium concentration created a smaller plasma density.

For an ansatz of the recombination rate, several simple assumptions can be made. First of all, the recombination of positive ions with secondary electrons dominates, while the recombination between positive and negative ions can be neglected. Also, the density of secondary electrons equals the density of positive ions ($\rho_{\mathrm{sel}} = \rho_+^{\mathrm{tot}}$), because the plasma attempts to maintain quasi-neutrality. Taking into account the various recombination coefficients α_i for different ion species leads to a recombination rate of:

$$R_+^{\mathrm{rec}} = \sum_i \alpha^i \rho_+^i \rho_{\mathrm{sel}} \tag{III.29}$$

$$= \sum_i \alpha^i \frac{\rho_+^i}{\rho_+^{\mathrm{tot}}} \cdot \left(\rho_+^{\mathrm{tot}}\right)^2 . \tag{III.30}$$

Nevertheless, an analytic solution of this ansatz is not possible: that's because the relative ion densities $\rho_+^i/\rho_+^{\mathrm{tot}}$ are a function of the distance from the gas inlet in the center of the tritium source. According to figure III.2, the dominating ion species at nominal source conditions are T_5^+ ions near the center of the WGTS while T_3^+ ions dominate further downstream[8].

III.2.5. Expected flux of positive ions into the DPS

A flux of $2 \cdot 10^{11}$ positive ions per second is expected to flow from the WGTS into the DPS at nominal source conditions. This is the result of a numeric simulation, which will be summarised in the following. Afterwards, the influence of the tritium concentration and column density will be estimated analytically.

Numeric simulation According to simulation[9], $2 \cdot 10^{11}$ positive ions per second are expected to flow from the WGTS into the DPS at nominal tritium concentration and column density. This flux is five times smaller than the ion creation rate (see section III.2.1) due to the recombination of positive ions with secondary electrons (see previous section).

The expected abundances of the different ion species can be found in table III.1. Further, figure III.5 shows the various ion fluxes as a function of the beam tube radius: related to the neutral gas flux, the ion flux is larger in the center of the beam tube and decreases towards the outside.

[8] In a very rough approximation, the sum over different ion species could be replaced with a single effective $< \alpha\rho_+ >$. This would lead to a non-linear differential equation for the ion flux out of the tritium source.

[9] Simulation by Frenc Glück.

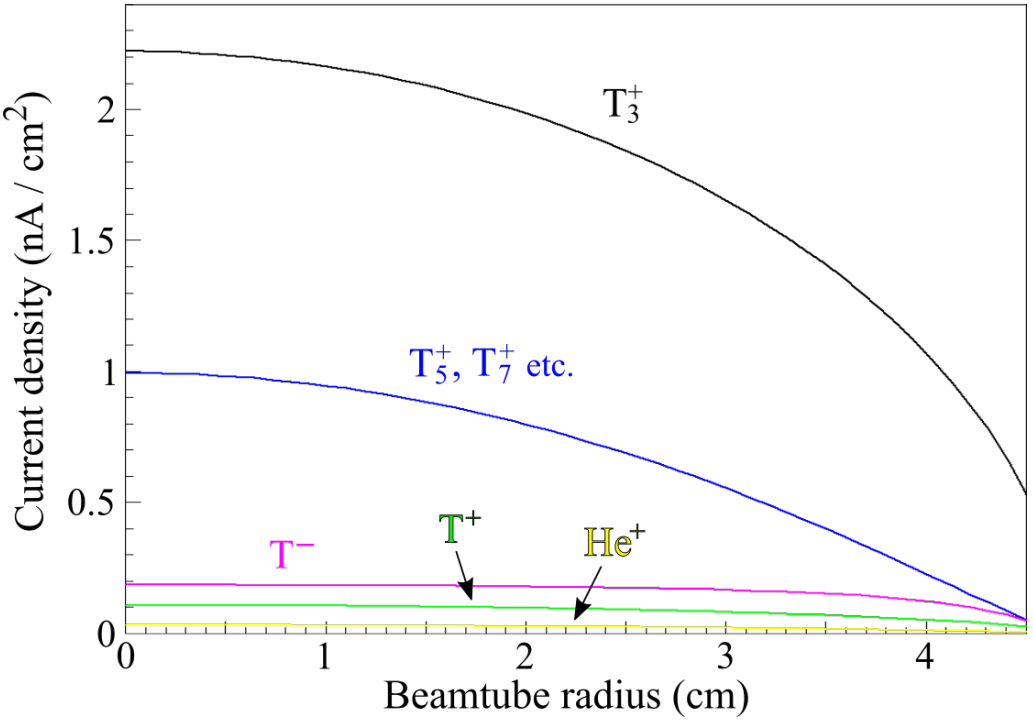

Figure III.5.: **Ion densities as a function of the beam tube radius** in the first pump port of the WGTS. The T_3^+ ions are more abundant than larger cluster ions like T_5^+ and T_7^+ (compare figure III.2). In the center of the beam tube, the ion flux is larger as a result of the larger neutral gas flux. Figure and simulation by Ferenc Glück.

Analytic calculation During the commissioning phase of the KATRIN experiment, various tritium concentrations ϵ_T and column densities $\mathcal{N}$ were created inside the tritium source. In order to quantify the effect of these parameters on the ion flux, an analytic model will be derived in the following. This model cannot include recombination (see previous section), but applies to small tritium concentrations like 0.5% during First Tritium when recombination becomes negligible.

According to section III.2.1, ions can be created via tritium decay and via scattering of beta electrons. In the first case, the ion rate is equal to the rate of beta electrons (see section III.1.3): besides the tritium activity $A(\epsilon_T,\mathcal{N})$, a factor 1/2 accounts for the probability that the ions leave the WGTS towards the DPS. Another factor $p_{\mathrm{DPS}}^{\mathrm{mag}}$ accounts for the geometric transmission of the magnetic flux tube from the WGTS to the DPS BT1.

$$\Phi_{\mathrm{ion}}^{\mathrm{dec}} = \frac{1}{2} \cdot p_{\mathrm{trans}}^{\mathrm{DPS}} \cdot A(\epsilon_T,\mathcal{N}). \tag{III.31}$$

In the case of beta electron scattering, the ion flux is identical to the flux of secondary electrons. There is no magnetic mirror effect, because the ions change their pitch angle frequently in collisions with neutral gas. With the secondary electron rate from section III.1.4 follows:

$$\Phi_{\mathrm{ion}}^{\mathrm{sc}} = \Phi_{\mathrm{sel}}^{\mathrm{sc}} = \lambda_T \cdot \sigma_{\mathrm{WGTS}} \cdot p_{\mathrm{trans}}^{\mathrm{DPS}} \cdot p_{\mathrm{sc},0} \cdot \epsilon_T \cdot \frac{\mathcal{N}^2}{\mathcal{N}_0}. \tag{III.32}$$

The total ion flux into the DPS is:

$$\begin{aligned}\Phi_{\text{ion}}^{+} &= \Phi_{\text{ion}}^{\text{dec}} + \Phi_{\text{ion}}^{\text{sc}} \\ &= \lambda_{\text{T}} \cdot \sigma_{\text{WGTS}} \cdot p_{\text{trans}}^{\text{DPS}} \cdot \epsilon_{\text{T}} \cdot \left(\mathcal{N} + \frac{p_{\text{sc},0}}{\mathcal{N}_0} \cdot \mathcal{N}^2 \right). \end{aligned} \tag{III.33}$$

At nominal column density and almost 100% tritium concentration, the analytic calculation predicts the creation of $8.7 \cdot 10^{11}$ positive ions/s. As discussed in the previous section, only 20% of those ions will flow into the WGTS due to recombination with secondary electrons. The resulting flux of $1.7 \cdot 10^{11}$ ions/s agrees completely with the simulation result of $2 \cdot 10^{11}$ ions/s.

The model predicts a linear relationship between the ion flux and the tritium purity ϵ_{T}. As for the column density $\mathcal{N}$, there is a linear component from tritium decay and a quadratic component from beta electron scattering. Both predictions agree with the observations during the First Tritium measurements (see section IX.2.1). That the observed ion flux was a factor 2 smaller than expected is not attributed to a flaw of the model but to inadvertent ion blocking between WGTS and DPS (see section III.6.2).

A summary of the expected ion and electron fluxes is given in tables III.2 and III.3: for nominal source conditions as well as for First Tritium.

Table III.1.: **Flux of different ion species from the WGTS into the DPS:** besides the dominant T_3^+, larger cluster ions like T_5^+, T_7^+ and monoatomic ions will be created. A total flux of $2 \cdot 10^{11}$ ions/s into the DPS is expected for nominal source conditions. The simulation results by Ferenc Glück are stated as current densities in nA. These can be converted into ion fluxes with the Coulomb number 1 C $= 6.24 \cdot 10^{18}$ elementary charges. The corresponding flux of activity can be calculated with the decay constant for tritium $\lambda_{\text{T}} = 1.79 \cdot 10^{-9}$ Bq; five atoms per cluster ion were assumed for the T_5^+, T_7^+ etc.

Ion species	Activity flux (Bq/s)	Ion flux (ions/s)	Current (nA)
T_3^+	637	$1.2 \cdot 10^{11}$	19
T_5^+, T_7^+ etc.	363	$4.1 \cdot 10^{10}$	6.5
T^+	11	$6.2 \cdot 10^{9}$	1
He^+	0	$1.6 \cdot 10^{9}$	0.25
T^-	22	$1.2 \cdot 10^{10}$	2

III.2.6. Expected flux of negative ions into the DPS

A rate of $1.2 \cdot 10^{10}$ T^- ions per second is expected to flow from the WGTS into the DPS according to the same numeric calculation which was presented in the previous section. The recombination between negative and positive ions can be neglected due to the small cross section, considering that the ions leave the WGTS after a few seconds. Therefore, the expected flux into the DPS almost corresponds to the creation rate. In order to obtain the flux of negative ions into the DPS at arbitrary tritium concentrations ϵ_T, the result for 100% tritium can be scaled linearly:

$$\Phi_{ion}^{-} \approx \epsilon_T \cdot 1.2 \cdot 10^{10}\ T^-/s. \tag{III.34}$$

After leaving the WGTS, the negative ions will be blocked by the negative potential of the DPS dipole electrodes (see section VI.2). Due to the gas flow from the WGTS, the T^- ions are trapped until they recombine with positive ions. This can lead to a negative ion space charge in the WGTS-F and possibly even inside the WGTS-C, which would affect the neutrino mass measurements (see section V.4.2).

Table III.2.: **Expected fluxes of electrons and thermal ions.** The values were calculated according to sections III.1 and III.2 using the parameters from the table below. Nominal measurement conditions are assumed as a column density of $\mathcal{N} = 5 \cdot 10^{21}$ m^{-2} and $\epsilon_\mathrm{T} = 100\%$ tritium concentration; during First Tritium, the column density was usually $\mathcal{N} = 4.46 \cdot 10^{21}$ m^{-2} and the tritium concentration was about $\epsilon_\mathrm{T} = 0.5\%$.

	Symbol	Nominal (1/s)	First Tritium (1/s)
Total tritium activity	A_T	$1.1 \cdot 10^{11}$	$5.1 \cdot 10^{8}$
Beta electron flux into PS	$\Phi_{\beta\mathrm{el}}^{\mathrm{dec}}$	$1.7 \cdot 10^{10}$	$7.7 \cdot 10^{7}$
Secondary electron flux into DPS	$\Phi_{\mathrm{sel}}^{\mathrm{sc}}$	$8.1 \cdot 10^{11}$	$3.2 \cdot 10^{9}$
Ion flux due to tritium decay	$\Phi_{\mathrm{ion}}^{\mathrm{dec}}$	$5.4 \cdot 10^{10}$	$2.4 \cdot 10^{8}$
Ion flux due to scattering	$\Phi_{\mathrm{ion}}^{\mathrm{sc}}$	$8.1 \cdot 10^{11}$	$3.2 \cdot 10^{9}$
Total ion flux into DPS	$\Phi_{\mathrm{ion}}^{\mathrm{tot}}$	$8.7 \cdot 10^{11}$	$3.5 \cdot 10^{9}$

Table III.3.: **Parameters for the calculation of the expected ion and electron fluxes.** All parameters were derived in sections III.1 and III.2. In particular, the decay constant [Pov09] $\lambda_\mathrm{T} = \ln(2)/T_{1/2} = 1.78 \cdot 10^{-9}$ s^{-1} can be calculated from the tritium half-life $T_{1/2} = 4500 \pm 8$ d [Luc00].

Parameter	Symbol	Value
Decay constant of tritium	λ_T	$1.78 \cdot 10^{-9}$ s^{-1}
WGTS flux tube area	σ_WGTS	$6.36 \cdot 10^{-3}$ m^2
Acceptance probability to PS	$p_{\mathrm{acc}}^{\mathrm{PS}}$	0.20
Transport probability to PS	$p_{\mathrm{trans}}^{\mathrm{PS}}$	0.83
Transport probability to DPS BT1	$p_{\mathrm{trans}}^{\mathrm{DPS}}$	0.95
Ionisation probability per β electron	$p_{\mathrm{sc},0}$	15
Nominal column density	$\mathcal{N}_0$	$5 \cdot 10^{21}$ m^{-2}

III.3. Ions from molecular dissociation

Tritium ions can be produced by beta decay and inelastic scattering of beta electrons – these mechanisms and the resulting ion fluxes have been discussed already in the previous section. But so far, all ions have been assumed to be thermalised inside the tritium source.

In fact, a significant flux of ions with energies up to 15 eV has been observed during the First Tritium measurements (see section IX.2.3). These ions received kinetic energy due to molecular dissociation: both tritium decay and beta electron scattering can leave the daughter ion in an excited molecular state. The ion may subsequently dissociate and transfers a fraction of its excitation energy to the ion.

The goal of this section[10] is to calculate the flux of ions with eV energies. To this end, first the theory of molecular excitation and dissociation will be summarised in section III.3.1. Then the branching ratios for molecular dissociation and the energy spectra of the debris ions will be discussed: first for the case of beta electron scattering (section III.3.2) and then for the case of tritium beta decay (section III.3.3). Based on these results, the expected ion flux with eV energies will be calculated in section III.3.4 for the measurement conditions during First Tritium. Finally, section III.3.5 proposes some ways of refining the theoretical description with the help of future simulations and experiments.

III.3.1. Theory of molecular excitation and dissociation

Inside the electric potential of a molecule, each electron exists in a discrete state with a specific energy. For the discussion of dissociation, only the electronic states and their vibrational excitations are important; rotational excitations do not matter. In the following, first the basics of molecular state transitions will be discussed and then the specifics of molecular dissociation.

State transitions Figure III.6 shows the molecular potential curves for different electronic states (energy E) with vibrational excitations (frequency ν) as a function of the internuclear distance R, which varies due to the vibration. The transition probability between a lower state with energy E'' and a higher state with E' can be calculated with the Franck-Condon principle. It makes use of the fact that the motion of an electron and its change of state are fast compared to the motion of the nuclei. Because the internuclear distance R does not change during the electronic transition, these transitions correspond to vertical lines in figure III.6.

While the distance R between the nuclei is conserved at the time of the transition, the equilibrium distance R_e of the old and new electronic state can differ. Usually R_e increases with the excitation of the electron, because the molecular bond becomes weaker. In figure III.6, the change in R_e corresponds to a shift of the potential curve. Depending on this shift, different excited states come in reach of the vertical transitions.

[10] This section is based on paper research and discussion by Ferenc Glück, Guido Drexlin, Hamish Robertson and Alejandro Saenz.

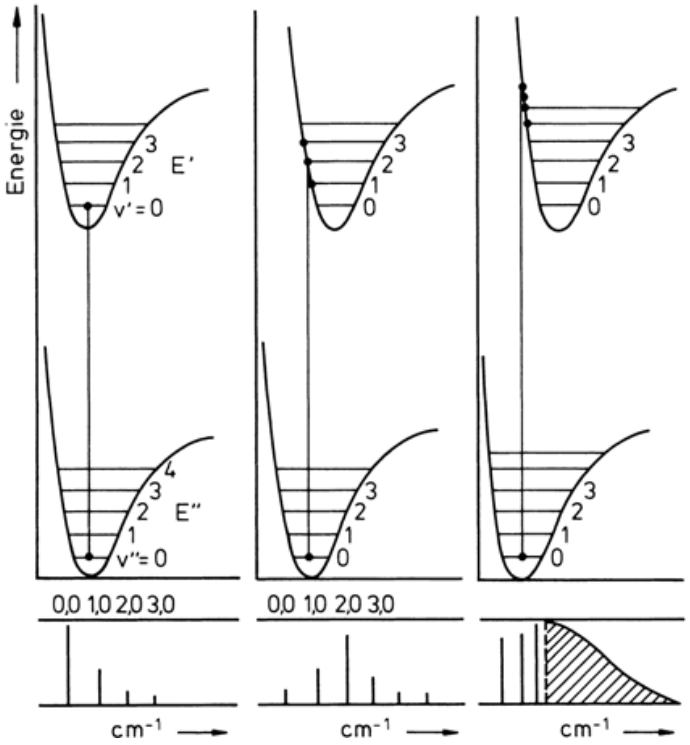

Figure III.6.: **Franck-Condon principle.** The graphs show the electron energy as a function of the internuclear distance. Electronic transitions between vibrational states are shown by vertical lines. The probability for the final state depends on the residence probability of the nuclei. If the minima of the electronic states are at different internuclear radii, the number of vibrational states which can be reached increases with the steepness of the potential curve of the final electronic state. From [Hak06].

The transition probability is high if there is a high probability to find the nuclei at a given distance R in the initial and the final state. Usually, the residence probability of the nuclei is maximal at their turning points in classical view, which is the intersection of vibrational states and potential curves. Only in the ground states $\nu = 0$, the probability to find a nucleus becomes maximal in the center of the potential.

The effect of the can be illustrated with the following two extremes:

- If the internuclear distance is the same for both electronic states ($R''_e = R'_e$), the maximal transition probability will be between identical vibrational states: $\nu'' \to \nu' = 0 \to 0, 1 \to 1$, etc.

- If the equilibrium distance in the excited state is much larger ($R''_e < R'_e$), the electron can reach discrete vibrational states as well as states in the dissociation continuum (see figure III.7). The relative intensities of the transitions depend on the overlap of the residence probabilities of the nuclei in the initial and final vibrational states. With the steepness of the potential curve of the final electronic state increases the number of possible vibrational states.

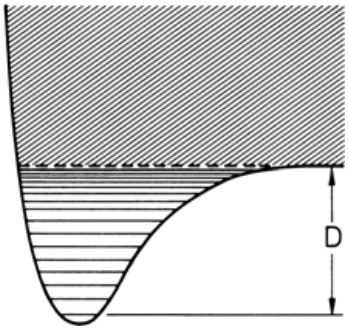

Figure III.7.: **Dissociation continuum.** Whon is the potential energy (vertical) versus the internuclear distance. The higher the vibrational excitations, the smaller the potential difference to the neighbouring states. Above the dissociation energy D, the vibrational states form a continuum. Because the internuclear radius can become infinitely large without additional energy input, the molecule is no longer bound. From: Wolf, Haken, and H. Haken. "Molekülphysik und Quantenchemie." (2006).

Dissociation The discussion so far only involved discrete, bound states below the dissociation energy D of the molecular potential curve (see figure III.7). If the electron is excited to a state above the dissociation threshold, the internuclear distance can become infinitely large without need for additional kinetic energy of the electron. Because the electron is no longer bound either, its state are no longer discrete but form a continuum instead.

Dissociation can occur with a time delay after the excitation: in the special case of predissociation, the molecule makes a (radiationless) transition to an unbound vibrational state in the dissociation continuum of another electronic state.

So far, only bonding electronic states were considered. But there is also the possibility of transitions to anti-bonding electronic states, which have no potential minimum. Molecules that are excited to anti-bonding states will always dissociate. This case applies for example to the T_2, HT and DT molecules in KATRIN.

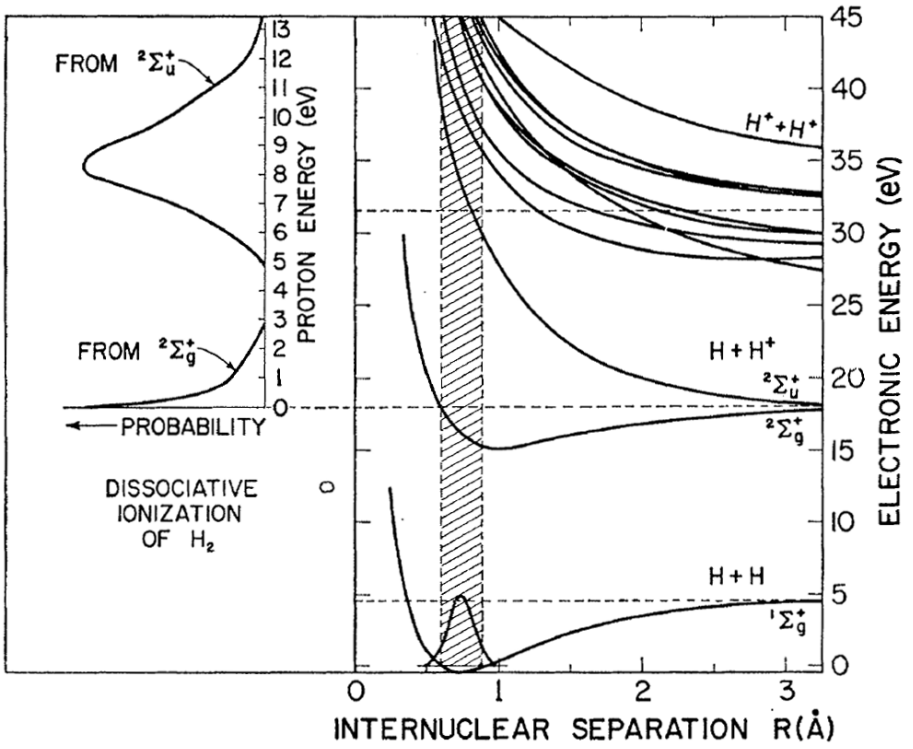

Figure III.8.: **Electronic states after inelastic electron scattering on H_2 molecules.** Except for the electronic ground state of H_2^+, the daughter ion can reach only anti-bonding states according to the Franck-Condon principle, including H_2^{++}. The energy spectrum of protons from the most probable excited states $^2\Sigma_g^+$ (bound) and $^2\Sigma_u^+$ (unbound) are indicated on the left: the relative heights of the two peaks are not to scale and no angular effects are assumed. From [Dun63].

III.3.2. Dissociative ionisation by electron scattering

Inside the KATRIN beam tube and especially inside the tritium source, beta electrons will ionise gas molecules which are mostly composed of hydrogen-isotopes. Due to the energy transfer from inelastic scattering, the ion can be left in an excited state. As will be discussed below, about 5% of these ions will dissociate. One of the dissociation fragments will of course also be an ion which receives kinetic energies between 0 eV and 15 eV [Dun63].

Electronic final states Figure III.8 shows the potential energy of the electronic ground state of H_2 and of some of the states of H_2^+ and H^{++} [Dun63]. Electrons can ionise the H_2 molecule by inelastic scattering and leave the H_2^+ ion either in a bound or dissociative state. Transitions to higher dissociative states of H_2^+ are also possible but rather unlikely because both shell electrons need to be excited. Most protons from dissociative ionisation of H_2 therefore arise from excitation to slightly above the dissociation limit of the bound state and from excitation to the unbound state. The expected energy distribution of these protons is indicated on the left of figure III.8, although the relative heights are not to be compared.

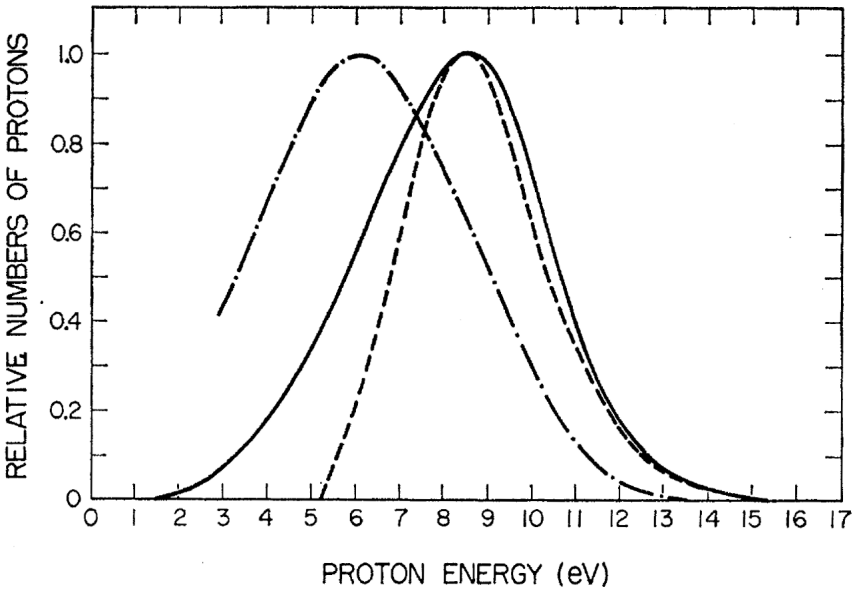

Figure III.9.: **Energy spectrum of protons from dissociative ionisation of H_2 by inelastic electron scattering.** The solid and dashed-dotted lines show two different experiments using incoming electrons with 75 eV. The dashed line shows a theoretical calculation of the transition probability from the ground state of H_2 to the anti-bonding state $^2\Sigma_u^+$ of H_2^+. This theoretical estimate corresponds to the left side of figure III.8. Due to an energy cut-off of the detector at 1.5 eV, no low-energetic protons from the $^2\Sigma_g^+$ state were observed. From [Dun63].

Energy spectrum The energy spectrum of protons from dissociative H_2 ionisation shows a peak at about 8 eV [Dun63, Bot74]. Figure III.9 shows a spectrum that extends up to 15 eV and has a maximum at 8.5 eV (solid line). This fits extremely well to the theoretical expectation (dashed line) which can be derived with the Franck-Condon principle. A discrepancy between theory and experiment below 8 eV can be attributed to failing approximations in the theoretical calculation. Previous publications had reported deviating results (for example the dash-dotted line).

Low energetic ions as expected from figure III.8 are not shown in figure III.9 because the detector excluded ions below 1.5 eV. The existence of these low-energetic ions has however been confirmed qualitatively [Dun63].

As for high-energetic ions, there are several more dissociative states of H_2^+ at higher excitation energies according to figure III.8. Their branching ratios are assumed to be small by [Dun63] and so the possible kinetic energies of the dissociation fragments were however not reported.

The energy of the incoming electron has considerable effect on the peak position of the energy spectrum below 100 eV [Dun63]. Especially between the ionisation energy of around 15 eV and up to 40 eV, the peak position moves rather linearly from 0 eV to about 8 eV. Also below 100 eV, [Bot74] reports the appearance of two low-energetic peaks at 2 eV and 4 eV due to excited vibrational and electronic states.

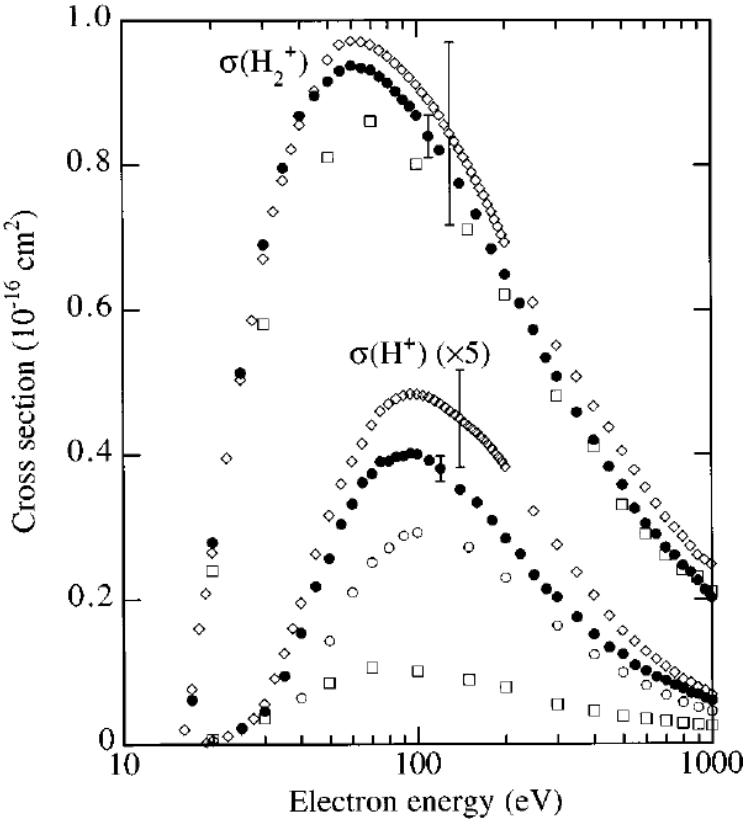

Figure III.10.: **Relative cross sections for dissociative (H^+) and non-dissociative (H_2^+) ionisation of H_2 by inelastic electron scattering.** The branching ratio for dissociation is roughly 5%. Squares, diamonds, full and empty circles correspond to various measurements. Representative error bars are shown for the full circles and diamonds; the empty circles consider only protons with kinetic energies above 2.5 eV. From [Str96].

Branching ratio The cross section for dissociative ionisation of H_2 is shown in figure III.10 as a function of the energy of the incoming electron. Around 100 eV, the distribution shows a considerable peak at $8 \cdot 10^{-18}$ cm^2 [Str96]. A calculation of the proton creation rates inside the KATRIN beam tube will have to consider the energy spectrum of the beta electrons by calculating an effective cross section.

The branching ratio of proton production by inelastic electron scattering on H_2 can be calculated from the relative magnitudes of the cross sections for dissociative and non-dissociative ionisation given by [Str96]. Around the peak at 100 eV, proton creation is the effect of 8.5% of the scattering processes. Towards the depletion of the cross section at 1 keV electron energy, the fraction is only 5.6%. Given that the majority of beta electrons have energies above 1 keV and the fact that no isotopic effects can be considered, the branching ratio for dissociative ionisation after inelastic electron scattering is roughly estimated to be $p_{\mathrm{diss}}^{\mathrm{inel}} = 0.05$.

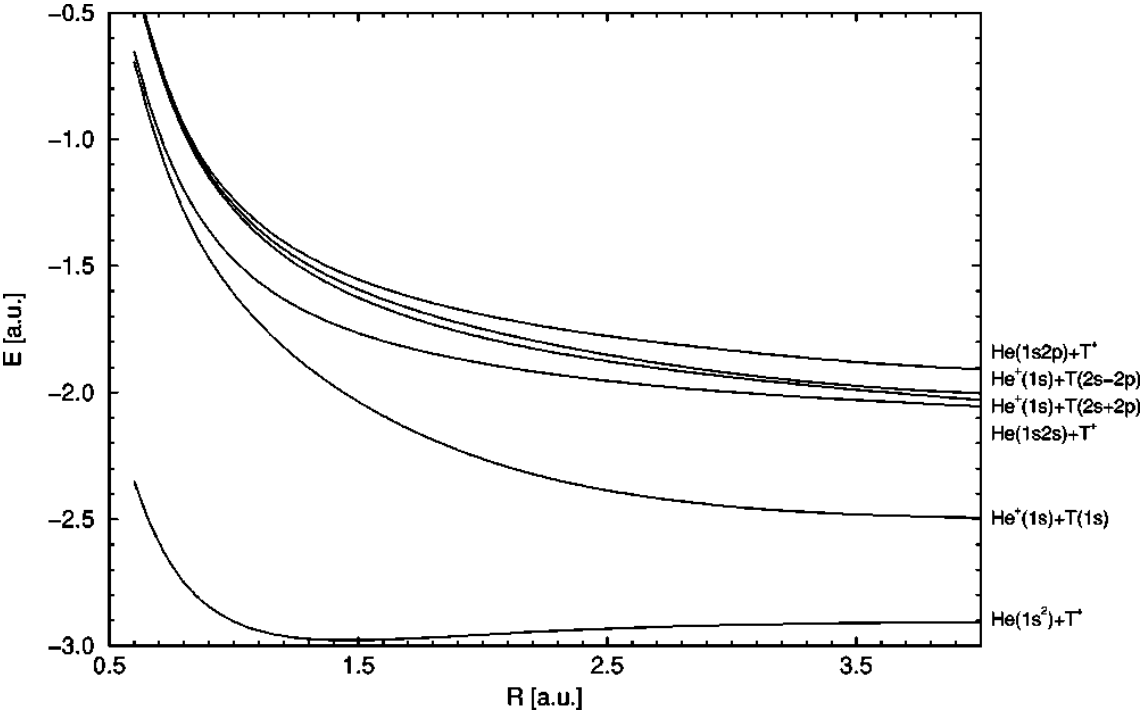

Figure III.11.: **Electronic states of the daughter molecule from tritium decay.** All of the excited states are anti-bonding inside the Franck-Condon region. The abscissa shows the internuclear distance R in atomic units (1 a.u. $= \hbar/m_e\alpha$) and the ordinate the binding energy E in atomic units relative to the total break-up threshold. Figure from [Jon99].

III.3.3. Dissociation of daughter ions from tritium decay

Not only the scattering of beta electrons, also tritium decay itself can create excited ions inside the KATRIN beamtube. Ionisation is the consequence of the beta electron leaving the mother molecule and a part of the decay energy will be transferred to the electronic shell and leave the daughter ion in an excited final state.

About half of the decays will lead to dissociation and the creation of atomic ions with energies up to 15 eV; to a minor fraction, the kinetic energies might even reach up to 100 eV. There are however substantial discrepancies between theoretical prediction and experiment, which make it hard to quantify an uncertainty for these values.

Final states At tritium decay, some of the decay energy can be transferred to the electron shell of the molecule and leave the daughter ion $^3HeQ^+$ in an excited state [Jon99]. The corresponding potential energy curves are shown in figure III.11.

In contrast to the excitation of H_2 by electron scattering, all excited states of the $^3HeQ^+$ are anti-bonding [Bod15]. The daughter ion will dissociate into a ^3He and an atomic hydrogen isotope with one of the two being ionised.

Also in contrast to inelastic scattering, there is a non-negligible probability that the daughter ion ends up in the electronic continuum [Bod15]. One or even two

shell electrons would be emitted as shake-off electrons and the $^3HeQ^{++}$ might subsequently dissociate.

Finally, there is an appreciable probability that the daughter ion remains in the electronic ground state but is excited into the vibrational dissociative continuum [Bod15]. Such an ion is quasi-bound and would eventually dissociate under emission of a T^+ or H^+ depending on the mother molecule.

Branching ratios Concerning the branching ratio to the bound $^3HeQ^+$ after tritium decay, there is substantial contradiction between theory and experiment [Bod15]. While theory predicts that only up to 57% of the decays lead to the bound state, a probability around 90% has been stated by two independent experiments (see table III.5).

The theoretical framework which lead to this prediction of 57% has however found experimental confirmation by a wide variety of other experiments [Bod15]. At the same time, there are several reasons to doubt the reliability of the experimental result: for example an insufficient account for the ionisation of neutral tritiated gas by beta electron scattering or the long dissociation times of the quasi-bound states. Unpublished results of the TRIMS experiment now seem to support the theoretical predictions.

Given these considerations, the theoretical predictions will be used for the following estimations. One of the possible reasons for the discrepancy between theory and experiment should however be kept in mind: the theory employs the sudden approximation which is valid for beta electron energies much larger than the atomic binding energies of several eV [Bod15].

In order to consider the probabilities for dissociation into $^3HeT^+$ and T^+, the theoretical predictions from [Bod15] will be discussed in more detail (see also tables III.5 and III.5):

- With 57% probability, the daughter ion remains in its electronic ground state. From there it can dissociate if the excitation energy is larger than the dissociation energy of 1.897 eV. In case of the $^3HeT^+$, this leads to the formation

Table III.4.: **Branching ratio for the beta decay of HT and T_2 to a bound molecular ion.** The measurements by Snell et al. [Sne57] (1957) and Wexler [Wex59] (1958) observed the large majority of debris ions from tritium decay in bound states. Theory (1999) in contrast predicts only about 50% of the debris ions to stay bound. While several explanations can be given to reconcile theory and observation, the motivation for new experimental tests is clearly given. From [Bod15].

Molecule	Theory [Jon99]	Snell et al. [Sne57]	Wexler [Wex59]
HT	$0.55 - 0.57$	0.932(19)	0.895(11)
T_2	$0.39 - 0.57$	–	0.945(6)

Table III.5.: **Dissociation fragments of T_2 after beta decay**. The table states discrete kinetic energies $E(^3\mathrm{He})$ and $E(\mathrm{T})$ for the decay fragments, calculated for an internuclear distance of $R = 1.4$ a.u.; actually, the energies will be smeared because the decay can occur at various internuclear distances. The branching ratios are valid for the sudden approximation (beta electron energies much larger than the binding energies) and $J_i = 0$, but values for $J_i = 1,2,3$ are similar. Table from [Bod15].

	State	Asymptotic structure	$E(^3\mathrm{He})$ (eV)	$E(\mathrm{T})$ (eV)	Branch (%)
Ground state	1	$^3\mathrm{He}(1s^2) + \mathrm{T}^+$	0	0	39.0
Quasi-bound		$^3\mathrm{He}(1s^2) + \mathrm{T}^+$			18.4
Excited state	2	$^3\mathrm{He}^+(1s) + \mathrm{T}(1s)$	$6.8 + 3.4\eta$	6.8	17.4
Excited state	3	$^3\mathrm{He}(1s2s) + \mathrm{T}^+$	$5.4 + 3.4\eta$	5.4	7.8
Excited state	4	$^3\mathrm{He}^+(1s) + \mathrm{T}(2s + 2p)$	$7.5 + 3.4\eta$	7.5	0.8
Excited state	5	$^3\mathrm{He}^+(1s) + \mathrm{T}(2s - 2p)$	$7.8 + 3.4\eta$	7.8	0.01
Excited state	6	$^3\mathrm{He}(1s2p) + \mathrm{T}^+$	$8.3 + 3.4\eta$	8.3	0.9
Continuum		double ionised			15.8

Table III.6.: **Dissociation fragments of HT after beta decay**. See table III.5 for explanations. From [Bod15].

	State	Asymptotic structure	$E(^3\mathrm{He})$ (eV)	$E(\mathrm{H})$ (eV)	Branch (%)
Ground state	1	$^3\mathrm{He}(1s^2) + \mathrm{H}^+$	0	0	55.4
Quasi-bound		$^3\mathrm{He}(1s^2) + \mathrm{H}^+$			1.5
Excited state	2	$^3\mathrm{He}^+(1s) + \mathrm{H}(1s)$	$3.4 + 3.4\eta$	10.2	17.4
Excited state	3	$^3\mathrm{He}(1s2s) + \mathrm{H}^+$	$2.7 + 3.4\eta$	8.2	7.8
Excited state	4	$^3\mathrm{He}^+(1s) + \mathrm{H}(2s + 2p)$	$3.7 + 3.4\eta$	11.2	0.8
Excited state	5	$^3\mathrm{He}^+(1s) + \mathrm{H}(2s - 2p)$	$3.9 + 3.4\eta$	11.7	0.01
Excited state	6	$^3\mathrm{He}(1s2p) + \mathrm{H}^+$	$4.1 + 3.4\eta$	12.4	0.9
Continuum		double ionised			16.2

of T^+ ions with eV-energies in about 18% of all tritium decays; in case of the $^3HeH^+$, only 1.5% of all decays lead to H^+ due to dissociation in the ground state.

- 27% of the decays will excite the daughter molecule to an anti-bonding state. The subsequent dissociation creates $^3He^+$ ions in about 18% of all decays and T^+ or respectively H^+ in about 9% of all decays.

- At 16% probability, the excitation energy is sufficient to remove one or even both of the shell electrons in so called shake-off. According to unpublished results of the TRIMS experiment, charge-3 branch with two shake-off electrons can be limited to less than about 10^{-4}; the charge-2 branch appears to be in fact on the order of a few percent. It is reasonable to assume that these ions dissociate as well due to the weakened electronic bond, but the branching ratio is unknown.

Summarising the theoretical expectations, the $^3HeT^+$ daughter ion will dissociate into a $^3He^+$ ion after 18% of all tritium decays and into T^+ after 27% of all decays. In case of the $^3HeH^+$ daughter ion, the branching ratio to $^3He^+$ remains the same, but T^+ are created after only 11% of all decays. For the decays of both T_2 and HT, there is an additional but unknown probability of up to 16% of all decays for dissociation after electron shake-off.

For the calculation of the dissociation probability of DT daughters after tritium decay, a value of $p_{\mathrm{diss}}^{\mathrm{dec}} = 0.5$ will be used. About half of the ions from dissociation might be $^3HeH^+$.

Energy spectrum Already the daughter ion $^3HeQ^+$ receives some kinetic energy $E_{\mathrm{rec}}^{\mathrm{kin}} = (0 \ldots 1.8)$ eV due to the recoil of the beta electron. In case of dissociation, this energy will be split among the fragments and depending on the orientation of their emission will either increase or diminish the energy of the atomic ion. The original energy spectrum thus becomes smeared additionally.

As a consequence of tritium decay, the molecular shell of the daughter ion will be excited over a broad energy spectrum which is shown in figure III.12 [Bod15]. The ground state is visible as a large peak around 0 eV. Around 20 eV begins a continuum from anti-bonding excited states and double ionised states, reaching up to a few hundred eV. Based on this molecular excitation spectrum, the kinetic energies of the dissociation fragments can be calculated, although three cases have to be considered again:

- Tritium decay can leave the daughter ion in an excited vibrational state of the electronic ground state. If the excitation energy E_{exc} is equal to or larger than the binding energy E_{B} of the daughter ion, it is quasibound and can eventually dissociate. Dissociation of the quasibound daughter ions from the electronic ground state with vibrational excitations leads to atomic ions with a continuum of kinetic energies in the eV range [Bod15]. The laboratory energies

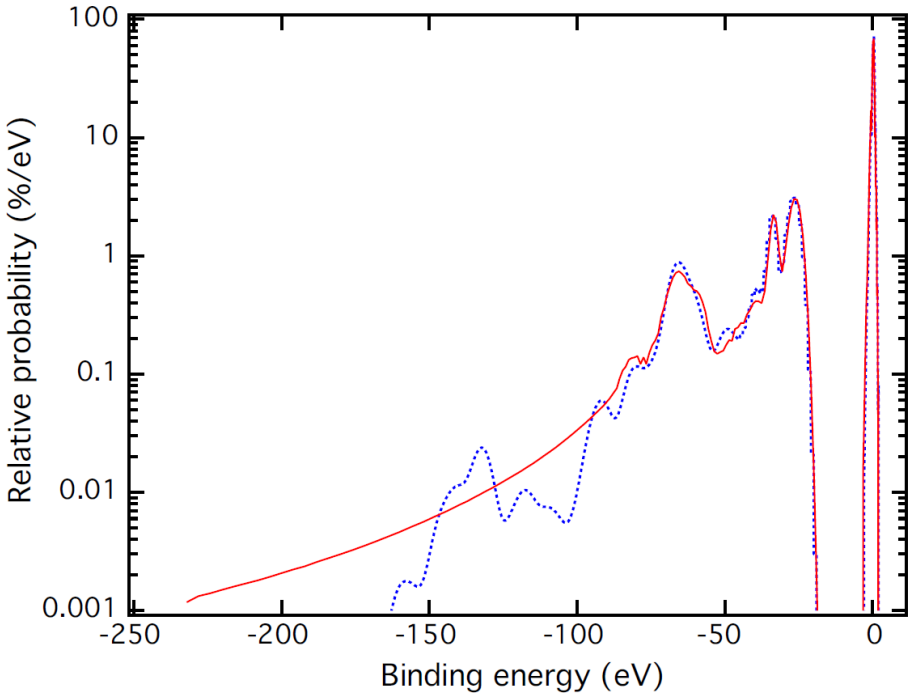

Figure III.12.: **Final state energy spectrum of the ^{3}HeT$^+$ daughter ion.** After beta decay, the ^{3}HeT$^+$ electron shell can be excited up to 200 eV. Because part of this energy goes to shake-off electrons during dissociation, ions with kinetic energies up to 100 eV are assumed to be very unlikely. The red and blue curves show two different theoretical calculations for the vibrational ground states ($J = 0$). Between 20 eV and 45 eV lie the excited states below the ionisation threshold (see also figure III.13 for a close-up). From [Bod15].

$E_{i(\mathrm{lab})}$ for fragments of mass m_i are uniformly distributed in the interval:

$$E_{i(\mathrm{lab})} = \frac{1}{m_i + m_j} \cdot \left\{ \left[\sqrt{m_i E_{\mathrm{rec}}^{\mathrm{kin}}} - \sqrt{m_j (E_{\mathrm{exc}} - E_{\mathrm{B}})} \right]^2 , \left[\sqrt{m_i E_{\mathrm{rec}}^{\mathrm{kin}}} + \sqrt{m_j (E_{\mathrm{exc}} - E_{\mathrm{B}})} \right]^2 \right\} . \tag{III.35}$$

Here, m_j is the mass of the other dissociation fragment and $E_{\mathrm{rec}}^{\mathrm{kin}}$ the kinetic energy of the ^{3}HeQ$^+$ ion. Because the lower bound of the interval requires $m_i E_{\mathrm{rec}}^{\mathrm{kin}} \geq m_j (E_{\mathrm{exc}} - E_{\mathrm{B}})$, the energy of these fragments cannot be significantly larger than $E_{\mathrm{rec}}^{\mathrm{kin}} = (0 \ldots 1.8)$ eV.

- Figure III.13 shows the energy spectrum of some of the excited anti-bonding states of the ^{3}HeT$^+$ and ^{3}HeH$^+$ daughter ions. Obviously, the species of the nuclei makes an impact because the spectrum from HT decay is shifted by about 1.5 eV to smaller energies compared to the spectrum from T_2 decay. The peaks are broadened due to the random internuclear distance at the time of the decay, which affects the binding energy of the daughter ion.
  In order to calculate the kinetic energies of the dissociation fragments, the

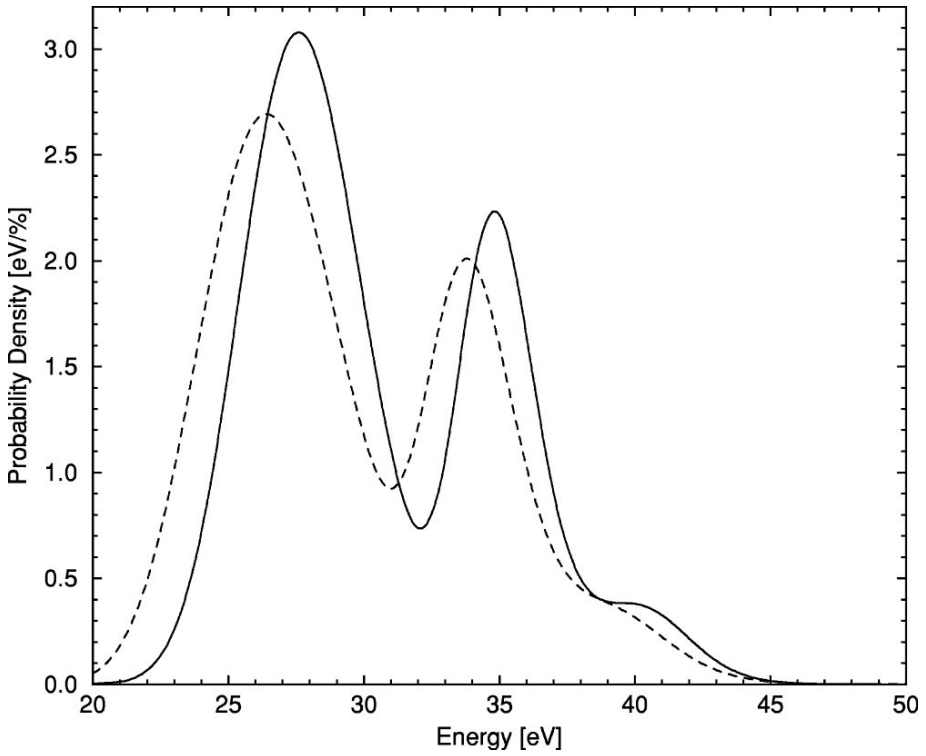

Figure III.13.: **Energy spectrum of the excited states below the ionisation threshold of $^3HeT^+$ (solid line) and $^3HeH^+$ (dashed line).** The peaks correspond to the states 2, 3, 4 and 6 from tables III.5 and III.6. Figure from [Jon99].

binding energy at infinite nuclear separation $R = \infty$ has to be subtracted. The total available energy is distributed among the fragments according to their masses and can be calculated with kinematic arguments. Calculation results are shown in table III.6 for the T_2 decay and in table III.5 for the HT decay for a specific internuclear separation of 1.4 a.u. at the time of the decay. Additionally, the ^{3}He receives up to 3.4 eV energy as the daughter nucleus of the decay from the recoil of the beta electron. In summary, the dissociation fragments receive kinetic energies of up to 15 eV.

- The energies of the dissociation fragments after electron shake-off are not stated in the literature. At least the excitation energies can be seen however from the molecular spectrum in figure III.12.
  In order to derive the maximum kinetic energy of these fragments, binding energies on the order of $\sim$ 20 eV just as for the excited electronic states of the $^3HeQ^+$ will be assumed. The shake-off electron(s) will take away a certain fraction of the excitation energy as well, but for an estimate of the maximum ion energy this fraction will be assumed as zero. Splitting the remaining kinetic energies between the two dissociation fragments shows that they can still reach kinetic energies up to 100 eV. Just as for the excited states of $^3HeQ^+$, the H^+ fragments are assumed to receive higher energies then the T^+.

III.3.4. Expected flux of dissociation ions into the PS

The previously discussed branching ratios of ion creation after molecular dissociation can be applied to the First Tritium measurements conditions, in order to predict the total rate of eV ions. Comparing the ion energy spectrum would be much more difficult, because the eV ions can lose energy in many scatterings with the neutral source gas.

The total ion rate was measured two times during First Tritium: one time with no positive blocking potential larger than 4 eV, so that dissociation ions from the WGTS could be observed; and a second time when the dipole electrode in DPS BT1 was set to +15 V in monopole mode – all ions from the WGTS were then blocked and instead all ions from the DPS BT1 were accelerated by the offset potential to about 15 eV. In these two measurements, the observed ions originated dominantly from rather short sections of the beam tube which will be called original regions.

As it turns out, the largest uncertainty to the calculation of the eV ion rates comes from the relative column densities inside the original regions. The estimation of these relative column densities will therefore be discussed at the beginning of this section. Afterwards, the expected fluxes of eV ions due to tritium decay and beta electron scattering will be calculated in analogy to the ion and electron rates from the previous sections. Then, the total expected eV ion flux will be stated and finally compared to the First Tritium measurement results.

Original region of ions with eV energies In the center of the WGTS, all ions will be thermalised by scattering on neutral gas (see section III.2.3). Ions with energies of a few eV due to molecular dissociation can only be observed if they originate from the WGTS-F and further downstream, where their mean free path becomes larger than 1 m according to figure III.4. However, with the gas density decreases also the ion creation rate. Due to this trade-off, only ions from the WGTS-F are assumed to make a sizeable contribution to the observable rate of dissociation ions with eV energies. A very rough estimate leads to an original region OR= $(5.8 \ldots 6.4)$ m from the position of the gas inlet.

For the upcoming calculations, it is helpful to express the gas density inside the original region in terms of the column density $\mathcal{N}$. According to the PhD thesis of Laura Kuckert, the column density inside the complete first beam tube of WGTS-F is $\mathcal{N}_{\mathrm{BT1}} = 2.7 \cdot 10^{-3}\, \mathcal{N}$ (table 4.1 of her thesis). According to figure III.4, the relative column density inside the original region is roughly a quarter of BT1:

$$\mathcal{N}_{\mathrm{OR}} \approx 6.8 \cdot 10^{-4}\, \mathcal{N}. \tag{III.36}$$

Inside the DPS BT1, the mean free path of the ions is already large enough in order to let them pass unscattered. Because the relative column density of this beam tube was not stated in in [Kuk16], it has to be estimated very roughly, too. The relative column density decreased by about one order of magnitude from BT1 of the WGTS-F to BT2, where it reached $\mathcal{N}_{\mathrm{BT2}} = 3.1 \cdot 10^{-4}\, \mathcal{N}$. Therefore, the following column density is expected inside the dipole electrode in DPS BT1:

$$\mathcal{N}_{\mathrm{DE1}} \approx 5 \cdot 10^{-5}\, \mathcal{N}. \tag{III.37}$$

Expected flux of eV-ions from tritium decay The beta activity inside the original region can be calculated from the total tritium activity A_T in analogy to the total beta electron rate in section III.1.3. As discussed above, the ions originate however only from a region with the relative column density $\mathcal{N}_\mathrm{OR}/\mathcal{N} \approx 6.8 \cdot 10^{-4}\,\mathcal{N}$. Just like the beta electrons, the dissociation ions were observed in the spectrometer section and the transported flux tube of 191 Tcm^2 in contrast to the full flux tube in the WGTS of 229 Tcm^2 has to be considered by a factor $p_\mathrm{trans}^\mathrm{PS} = 0.83$.

Also, a factor 1/2 has to account for the 50% probability that the ions are emitted towards the spectrometers – otherwise the ions will also leave the WGTS, but only after they changed their direction due to scattering. As was explained in section III.2.3, the ions lose on average half of their energy at every scattering. At start energies around 8 eV, they can fall after only one scattering below the experimental energy threshold of 4 eV.

Eventually, only a fraction of the daughter molecules from tritium decay will dissociate. The dissociation probability was estimated in section III.3.3 to be $p_\mathrm{diss}^\mathrm{dec} \approx 0.5$.

Putting all of these considerations together yields the rate of dissociation ions due to tritium decay:

$$\Phi_\mathrm{eVion}^\mathrm{dec} = \frac{1}{2} \cdot p_\mathrm{diss}^\mathrm{dec} \cdot p_\mathrm{trans}^\mathrm{PS} \cdot \frac{\mathcal{N}_\mathrm{OR}}{\mathcal{N}} \cdot A_\mathrm{T}(\epsilon_\mathrm{T},\mathcal{N}) \tag{III.38}$$

$$= p_\mathrm{diss}^\mathrm{dec} \cdot p_\mathrm{trans}^\mathrm{PS} \cdot \lambda_\mathrm{T} \cdot \sigma_\mathrm{WGTS} \cdot \epsilon_\mathrm{T} \cdot \mathcal{N}_\mathrm{OR}. \tag{III.39}$$

Expected flux of eV-ions from electron scattering The rate of secondary electrons from inelastic scattering of beta electrons was extrapolated from a numeric simulation in section III.1.4, because an analytic estimate would not have been able to consider the various magnetic field settings along the beamline. An analytic estimate for the rate of dissociation ions from beta electron scattering must therefore be specially developed in the following. Fortunately, the focus on the original region simplifies the magnetic field settings significantly.

The rate of dissociation ions from electron scattering depends on the beta electron flux $\Phi_\mathrm{\beta el}^\mathrm{OR}$ through the original region and the electron's probability $\mathcal{P}_\mathrm{inel}^\mathrm{OR}$ to scatter there. As discussed in section III.3.2, the dissociation probability of ions from electron scattering is $p_\mathrm{diss}^\mathrm{inel} = 0.05$. Just like for the dissociation ions from beta decay, a factor 1/2 has to account for the 50% probability that ions leave the original region unscattered and with all their energy. Inserting the expressions for the beta electron flux and the scattering probability leads to:

$$\begin{aligned}\Phi_\mathrm{eVion}^\mathrm{inel} &= \frac{1}{2} \cdot \Phi_\mathrm{\beta el}^\mathrm{OR} \cdot \mathcal{P}_\mathrm{inel}^\mathrm{OR} \cdot p_\mathrm{diss}^\mathrm{inel} \\ &= 2 \cdot p_\mathrm{diss}^\mathrm{inel} \cdot p_\mathrm{trans}^\mathrm{PS} \cdot p_\mathrm{acc}^\mathrm{WGTS\text{-}F} \cdot \langle\sigma_\mathrm{inel}\rangle \cdot \langle\cos^{-1}(\theta)\rangle \cdot \lambda_\mathrm{T} \cdot \sigma_\mathrm{WGTS} \cdot \epsilon_\mathrm{T} \cdot \mathcal{N}_\mathrm{OR} \cdot \mathcal{N}.\end{aligned} \tag{III.40}$$

The beta electron flux is two times the total beta electron flux from tritium decay, which was calculated in section III.1.3:

$$\Phi_\mathrm{\beta el}^\mathrm{OR} = 2 \cdot p_\mathrm{PS}^\mathrm{mag} \cdot p_\mathrm{WGTS\text{-}F}^\mathrm{mag} \cdot A_\mathrm{T}(\epsilon_\mathrm{T},\mathcal{N}). \tag{III.41}$$

The factor two arises because almost all electrons which leave the WGTS towards the spectrometers will be reflected at the PS potential and cross the original region a second time. Just like for the total beta electron flux, the transported flux tube of 191 Tcm^2 into to the PS is accounted for by the factor $p_{\text{trans}}^{\text{PS}} = 0.83$. Even the acceptance probability by the magnetic mirror between WGTS-C and WGTS-F is with $p_{\text{acc}}^{\text{WGTS-F}} = 0.20$ the same: the magnetic field in the WGTS-F is already 5.6 T, which comes close to the 5.72 T in the CPS.

The probability for inelastic electron scattering in the original region can be calculated from the molecular number density n_{OR}, the effective cross section $\langle\sigma_{\text{inel}}\rangle$ and the path length $l \cdot \langle\cos^{-1}(\theta)\rangle$ of the beta electrons:

$$\mathcal{P}_{\text{inel}}^{\text{OR}} = n_{\text{OR}} \cdot \langle\sigma_{\text{inel}}\rangle \cdot l \cdot \langle\cos^{-1}(\theta)\rangle \tag{III.42}$$

$$= \langle\sigma_{\text{inel}}\rangle \cdot \langle\cos^{-1}(\theta)\rangle \cdot \mathcal{N}_{\text{OR}}, \tag{III.43}$$

where the parameters are defined as follows:

- **Molecular number density n_{OR}** As was discussed before, the molecular column density of the original region of the eV-ions is $\mathcal{N}_{\text{OR}} = 6.8{\cdot}10^{-4}\,\mathcal{N}$. From this, the molecular number density can be calculated with the longitudinal length l of the original region to be:

$$n_{\text{OR}} = \frac{\mathcal{N}_{\text{OR}}}{l}. \tag{III.44}$$

  Due to the dependence on the inverse of l, the length of the original region will not be explicitly considered in the final expression for the scattering probability. The length of the original region is however implicitly considered by its column density, which is shorter and therefore smaller than the total column density.

- **Effective cross section $\langle\sigma_{\text{inel}}\rangle$** The cross section for H_2 ionisation by electron impact depends on the electron energy; the electrons however have various kinetic energies according to the tritium beta spectrum $w_\beta(E)$. One can calculate the effective scattering cross section via (calculation of F. Glück):

$$\langle\sigma_{\text{inel}}\rangle = \frac{1}{N} \int_0^{E_0} \mathrm{d}E \cdot \sigma_{\text{inel}}(E) \cdot w_\beta(E) \approx 10^{-21}\ \text{m}^2. \tag{III.45}$$

- **Transversal electron path length $\langle\cos^{-1}(\theta)\rangle$** The total path length of the electrons inside the original region depends on their pitch angle θ[11]. Evidently, the longitudinal velocity of the electrons is $v_l = v_{\text{tot}} \cdot \cos(\theta)$, where v_{tot} is the total velocity of the electron. At the same time holds $v_l = l/t$, with l being the length of the original region and t the electron's total time of stay in it. With these two formulas, the total path length s becomes:

$$s = v_{\text{tot}} \cdot t = v_{\text{tot}} \cdot \frac{l}{v_l} = l \cdot \cos^{-1}(\theta). \tag{III.46}$$

[11] It can be assumed for the following considerations that the pitch angles are distributed isotropically. Even though some of the original pitch angle distribution from the WGTS-C was cut away, the remaining pitch angles are still isotropic.

When calculating the ion creation rate, the electron scattering probability has to be averaged over all acceptance angles between 0 and $\theta_{\max} = \pi/2$. This leads to a singular integral $\cos^{-1}(\theta)$, which can be solved for example by numeric integration (calculation by F. Glück):

$$\langle \cos^{-1}(\theta) \rangle = \int_0^{\pi/2} \mathrm{d}\theta \cdot \cos^{-1}(\theta) = 2.2. \tag{III.47}$$

Total expected flux of eV-ions The total rate of ion with eV energies from the WGTS is the sum of dissociation ions from tritium decay and beta electron scattering:

$$\Phi_{\mathrm{eVion}}^{\mathrm{tot}} = \frac{\mathcal{N}_{\mathrm{OR}}}{\mathcal{N}} \cdot \lambda_{\mathrm{T}} \cdot p_{\mathrm{trans}}^{\mathrm{PS}} \cdot \sigma_{\mathrm{WGTS}} \cdot \epsilon_{\mathrm{T}} \cdot \left(p_{\mathrm{diss}}^{\mathrm{dec}} \cdot \mathcal{N} + 2 \cdot p_{\mathrm{diss}}^{\mathrm{inel}} \cdot p_{\mathrm{acc}}^{\mathrm{WGTS\text{-}F}} \cdot \langle \sigma_{\mathrm{inel}} \rangle \cdot \langle \cos^{-1}(\theta) \rangle \cdot \mathcal{N}^2 \right). \tag{III.48}$$

Just like for thermal ions, the contribution by beta decay scales only linearly with the column density, while the contribution from beta electron scattering scales with the square of the column density. This can be used for test measurements, in order to observe dominantly the spectrum of ions from molecular dissociation after tritium decay.

Comparison with First Tritium measurements Equation III.48 can be used to calculate the expected flux of ions with eV energies during the First Tritium measurements, using the parameters from table III.8. The results for 0.5% tritium concentration and a column density of $\mathcal{N} = 89\%$ are shown in table III.7.

The first observation were ions which came presumable from the original region in the WGTS-F. Using the relative column density $\mathcal{N}_{\mathrm{OR}}/\mathcal{N} \approx 6.8 \cdot 10^{-4}\ \mathcal{N}$ leads to a total expected ion rate of $1 \cdot 10^5$ ions/s. But experimentally, an ion rate of $2.5 \cdot 10^5$ ions/s was already observed when the peak of the ion energy spectrum remained still blocked. This calculation assumes a pressure-dependent ionisation efficiency in the PS according to section IX.1.4.1; instead, preliminary results of the STS IIIa commissioning measurements indicate a pressure-independent ionisation efficiency, which would imply a roughly ten times smaller rate of dissociation ions. The disagreement between calculation and experiment is attributed to the definition of the original region, which could only be estimated roughly. In order to improve the estimate, dedicated Monte Carlo simulations should be carried out as will be discussed in the next section.

The second measurement concerned only ions from the DPS BT1, because the dipole in this beam tube section was set to +15 V in order to block the ions from the WGTS. Accordingly, the relative column density $\mathcal{N}_{\mathrm{DE1}}/\mathcal{N} \approx\sim 5 \cdot 10^{-5}\ \mathcal{N}$ has to be used for this calculation while the other parameters remain unaffected. However, the offset potential accelerated all ions over the inadvertent blocking potentials, including those which were not created from dissociation. The dissociation coefficients therefore have to be set to 1 and the calculated rate of $5.2 \cdot 10^4$ ions/s becomes the

Table III.7.: **Expected fluxes of eV ions from the original region and from DPS BT1.** The values were calculated according to the formulas III.39 and III.40 using the parameters from the table below. A tritium density of $\epsilon_T \approx 0.5\%$ and a column density of $\mathcal{N} = 4.46 \cdot 10^{21}$ m^{-2} were assumed, which were the usual conditions during the First Tritium campaign; this column density value corresponds to 89% of the nominal column density.

Flux	Symbol	OR (1/s)	DPS BT1 (1/s)
Flux of eV ions from tritium decay	$\Phi_{\text{eVion}}^{\text{dec}}$	$7.1 \cdot 10^4$	$1.0 \cdot 10^4$
Flux of eV ions from electron scattering	$\Phi_{\text{eVion}}^{\text{inel}}$	$2.8 \cdot 10^4$	$4.1 \cdot 10^4$
Total flux of eV ions	$\Phi_{\text{eVion}}^{\text{tot}}$	$9.9 \cdot 10^4$	$5.2 \cdot 10^4$

Table III.8.: **Parameters for the calculation of the expected eV ion fluxes.** All parameters were derived in section III.3.4. In particular, the decay constant [Pov09] $\lambda_T = \ln(2)/T_{1/2} = 1.78 \cdot 10^{-9}$ s^{-1} can be calculated from the tritium half-life $T_{1/2} = 4500 \pm 8$ d [Luc00].

Parameter	Symbol	Value
Decay constant of tritium	λ_T	$1.78 \cdot 10^{-9}$ s^{-1}
WGTS flux tube area	σ_{WGTS}	$6.36 \cdot 10^{-3}$ m^2
Transport probability to PS	$p_{\text{trans}}^{\text{PS}}$	0.83
Dissociation probability after decay	$p_{\text{diss}}^{\text{dec}}$	0.5
Dissociation probability after scattering	$p_{\text{diss}}^{\text{inel}}$	0.05
Acceptance probability to WGTS-F	$p_{\text{acc}}^{\text{WGTS-F}}$	0.20
Average transversal path length	$\langle \cos^{-1}(\theta) \rangle$	2.2
Average inel. scattering cross section	$\langle \sigma_{\text{inel}} \rangle$	$1 \cdot 10^{-21}$ m^2
Relative column density in WGTS-F	$\mathcal{N}_{\text{OR}}/\mathcal{N}$	$6.8 \cdot 10^{-4}$
Relative column density in DPS BT1	$\mathcal{N}_{\text{DE1}}/\mathcal{N}$	$5 \cdot 10^{-5}$

total ion creation rate in DPS BT1. When comparing this prediction with the experimental result of $3 \cdot 10^4$ ions/s, a rather good agreement is found. This confirms the validity of the theory, although the uncertainty on the relative column density in DPS BT1 should not be forgotten.

III.3.5. Proposal for future simulations and measurements

Future ion safety work will need to show credibly that the flux of tritium ions from the WGTS is reduced below the limit of 10^4 ions/s into the PS. During the First Tritium measurements, a PS ionisation rate corresponding to slightly more than 10^4 ions/s was observed and ions with energies of a few hundred 100 eV from molecular dissociation after tritium decay need to be excluded as explanation. The direct experimental proof of the blocking of these high energetic ions was not possible due to the creation of Penning ions in the ring electrodes at energies above $\sim$ 30 eV. Instead, the theoretical predictions for the maximum energy of the ions from molecular dissociation need to be confirmed in order to set the ring electrode potentials safely above it.

In the following, experimental and simulation approaches to confirm the theory of high energetic ions from dissociation will be discussed. Additionally, there is also possible use of the ion energy spectroscopy for the understanding of the tritium Final States Spectrum (FSD).

Measurement of the ion dissociation probability after tritium decay with TRIMS After tritium decay, theory predicts molecular excitation up to a few hundred eV. This same theory is however in strong contradiction with the available experimental results on the branching ratio of subsequent ion dissociation. The TRIMS experiment can help to resolve the contradiction between theory and experiment by measuring accurately the branching ratios of the various ion species after dissociation. First tritium measurements with TRIMS have already been carried out and will be published soon.

Monte Carlo simulation and refined measurement of the ion energy spectrum in KATRIN There is only a small probability for ions with energies of a few hundred eV due to tritium decay, but their rate can still exceed the background constraint of $1 \cdot 10^4$ ions/s (see section V.3) if the total creation rate for ions from dissociation is large enough. The above model predicts a by orders of magnitude smaller total ion rate than observed during First Tritium. In order to gain confidence in the predicted rate of high energetic ions, the contradiction between prediction and measurement has to be resolved. By reconciling estimates and observation, one can also exclude that relevant mechanism for creation or acceleration of ions in the KATRIN beam tube have gone unnoticed.

On theoretical side, the approximation of a limited original region OR has to be refined by a dedicated Monte Carlo simulation. The simulation could consider the creation of dissociation ions throughout the WGTS and the subsequent scattering between ions and neutral gas including the energy loss; further, the simulation would need to take into account that the ring electrodes measure only the longitudinal ion

energy. In the end, this would allow to estimate much more accurately the ion energy spectrum and the rate of ions with energies above the thermal limit.

Experimentally, the measurement of the ion energy spectrum could be repeated with more measurement points using the PS ionisation method. At higher tritium concentrations than the 1% of First Light, this implies however a larger tritium flux into the PS.

Investigation of the tritium Final State Distribution with KATRIN On top of that, the Final States Distribution (FSD) could be investigated with KATRIN itself by measuring the energy spectrum of the ions which are created by dissociation of the daughter ion from tritium decay. In order to reduce the contribution of ions from dissociation after electron scattering, the column density would be reduced: this reduces the rate of ions from electron scattering quadratically but the rate of ions from tritium decay only linearly; also, the energy loss by inelastic ion scattering would be reduced. Also this measurement would profit from the simulation of the total ion rate in order to estimate if a measurement would be worthwhile.

III.4. Ions from Penning discharges in ring electrodes

During the First Tritium measurements, the ion rate was observed to increase linearly with the voltage at some of the ring electrodes. This is attributed to Penning discharges inside the positive potential of the ring electrodes.

In an attempt to explain the observations, this section will first explain the mechanism of Penning discharges and then try to model the rate of Penning ions from the ring electrodes. However, the predicted exponential increase of the ion rate does not correspond to the observed linear dependence; also the total observed ion rate was much larger than expected. The consequences for the modeling of the Penning ion rate are discussed at the end of this section.

III.4.1. Penning discharge mechanism

A Penning trap consists of two limiting electrostatic potentials between which the charged particles are reflected along a magnetic guiding field. Small pressures are necessary in order to reduce the scattering probability of the stored particles. If the charged particles have enough kinetic energy to ionise the residual gas, an ionisation cascade increases the amount of stored particles exponentially – a Penning discharge is ignited.

Penning discharges can be distinguished depending on whether an external flux of charged particles is required to fuel the discharge: if the discharge persists without an external flux of charged particles, it is called self-sustaining; and if the discharge even starts without an external flux, it is called self-igniting.

The strong magnetic guiding field of the KATRIN experiment favours the creation of Penning traps in multiple places. During First Tritium, ions were presumably created by Penning discharges in the ring electrodes.

The positive potential of the ring electrode traps the electrons, while accelerating all created ions away from the trap. Depending on whether the ion was created in the center or at the edge of the ring electrode, its energy can be larger or smaller. The electrons lose energy at each ionisation process and drop ever further down into the potential well, which also narrows their motions ever closer around the center of the ring electrode longitudinal to the magnetic field (see figure III.14). Eventually, all electrons will have not enough energy for ionisation of residual gas anymore; these electrons accumulate and create a space charge, which can lead to the neutralisation of the ring electrode (see section III.6.3).

III.4.2. Expected Penning ion rate from ring electrodes

During First Tritium, the Penning discharges inside the ring electrodes were observed to be not self-sustaining: when the beta electron flux was interrupted, the ion flux stopped at once. For the calculation of the Penning ion rate it will therefore be assumed that all electron cascades are created by primary electrons from inelastic scattering of beta electrons inside the ring electrode potential.

Under this assumption, the number of primary electrons depends on the flux $\Phi_{\beta\mathrm{el}}$ of beta electrons and their inelastic scattering probability $\mathcal{P}_{\mathrm{inel}}$. Each primary

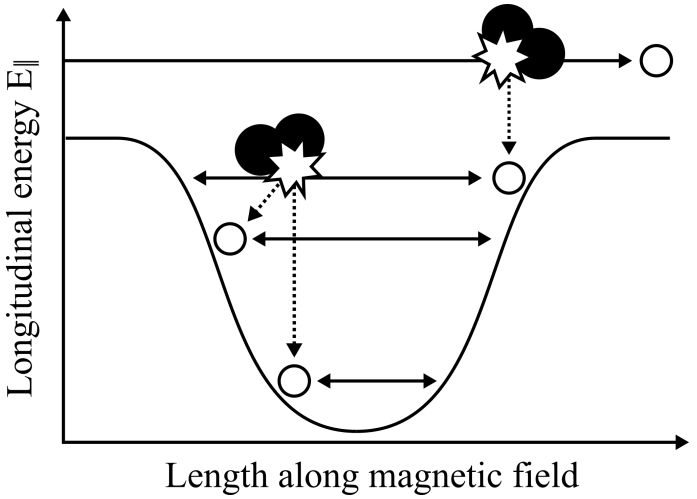

Figure III.14.: **Illustration of a Penning discharge in the ring electrodes.** Beta electrons scatter on residual gas inside the ring electrode potential. A secondary electron is created with negligible kinetic energy. This electron is trapped inside the positive potential and oscillates around the center of the potential well, where it gains enough kinetic energy to ionise the residual gas itself. The positive H_2^+ ions from the ionisation cascade are accelerated away from the potential; their kinetic energy corresponds to the depth of the electric potential at the location of their creation.

electron will produce an average number of $p_{\mathrm{cas}}^{\beta\mathrm{el}}$ secondary electrons and associated ions. With that follows:

$$\Phi_{\mathrm{ion}} = \Phi_{\beta\mathrm{el}} \cdot \mathcal{P}_{\mathrm{inel}} \cdot p_{\mathrm{cas}}^{\beta\mathrm{el}} \tag{III.49}$$

$$= \Phi_{\beta\mathrm{el}} \cdot l \cdot \langle \cos^{-1}(\theta) \rangle \cdot \langle \sigma_{\mathrm{inel}} \rangle \cdot \rho \cdot 2^{eU_{\mathrm{RE}}/(2E_{\mathrm{ion}})}. \tag{III.50}$$

In the second line, expressions for the inelastic scattering probability $\mathcal{P}_{\mathrm{inel}} = l \cdot \langle \cos^{-1}(\theta) \rangle \cdot \langle \sigma_{\mathrm{inel}} \rangle \cdot n$ and for $p_{\mathrm{cas}}^{\beta\mathrm{el}}$ were inserted:

- The beta electron flux in the transport section was estimated in section III.1.3 to be $\Phi_{\beta\mathrm{el}} = 7.7 \cdot 10^7$ beta electrons per second.
- The electron path length inside the ring electrodes depends on the electrode length $l = 60$ mm. According to section III.3.2, the cyclotron motion might increase the effective path length by about $\langle \cos^{-1}(\theta) \rangle \approx 2$.
- The average cross section for inelastic scattering was taken from section III.3.2 to be about $\langle \sigma_{\mathrm{inel}} \rangle = 10^{-21}$ m^2. This calculation used the total beta electron spectrum, although the beta electrons with the largest cross sections around 100 eV cannot reach the ring electrodes due to the blocking potentials in the dipole electrodes. Considering this cut-off would severely decrease the effective scattering cross section.
- The number density of particles in the ring electrodes is estimated to be $\rho = 2 \cdot 10^{11}$ m^{-3} from the ideal gas law, based on a temperature of 300 K and a

pressure of about 10^{-11} mbar at the DPS ring electrodes. This pressure is however known only very roughly from simulations and might easily be several orders of magnitude larger, especially if there should be outgassing of the FT-ICR between the two DPS ring electrodes.

- With each ionisation process, the number of stored electrons is doubled. Therefore, the average number of ionisation which follow each trapped primary electron is estimated with $p_{\mathrm{cas}}^{\beta\mathrm{el}} = 2^n \approx 10$ at 100 eV. The shower depth $n = E_0/E_{\mathrm{ion}}(H_2)$ corresponds to the number of scatterings that the primary electron will undergo before it has deposited all its energy into the ionisation of residual H_2. $E_{\mathrm{ion}}(H_2) = 15.4$ eV is the ionisation energy of H_2 [Shi93]. Because each secondary electron can be created everywhere inside the potential, its initial energy $E_0 = eU_{\mathrm{RE}}/2$ is estimated with half of the applied voltage U_{RE} at the ring electrode. A more precise estimate of the average number of ionisations should be obtained in the future with a Monte Carlo simulation of the scattering processes inside the ring electrode; this would allow to take into account the longitudinal and radial potential distribution, as well as the energy spectra of scattering and secondary electron after the collision according to differential cross sections from literature.

According to this model, the Penning ion rate should increase exponentially with the voltage U_{RE} at the ring electrode. Also, the ion rate is expected to increase linearly with the pressure at the ring electrode due to the larger number of target molecules for the inelastic scattering of the beta electrons. The average number of ionisations $p_{\mathrm{cas}}^{\beta\mathrm{el}}$ is however not affected by the pressure: the pressure increases the scattering frequency, but the deposited amount of energy remains the same.

Comparison between the model and First Tritium measurements The above model predicts a Penning ion flux of about 10^{-2} ions/s during First Tritium for a voltage of 100 V at the ring electrodes. However, the observed rate for 100 V at the PP5 ring electrode corresponded to about 10^5 ions/s. Also, the rate of the Penning ions scales rather linearly with the ring electrode voltage – the predicted exponential increase was not observed.

Nevertheless, a Penning discharge in the ring electrode potentials remains the most reasonable explanation for the observations. In order to describe the observed Penning ion rates correctly, this simple model needs to be improved in the future. The average number of ions of each primary electron could be determined more accurately with Monte Carlo simulations; such simulations would be able to consider the actual start energy of the electrons which are created in the cascade, as well as the energies of the incoming and the secondary electrons after the scattering process based on literature values. As for the pressure inside the ring electrodes, it seems however experimentally not possible to determine its magnitude to at least one order accurately. Simulations could also consider a possible effect of the potential depth on the trapping probability, because the ion loses about half of its current kinetic energy in the scattering (compare section III.2.3).

III.5. Ion creation in the DPS and CPS

The previous sections discussed only ions from the WGTS, which are created by beta decay and beta electron scattering including the dissociation of the excited daughter molecules, as well as Penning ions from the ring electrodes. Aside from the WGTS and the ring electrodes, ions can however also be created in the DPS and CPS.

In the DPS, both beta decay and ionisation by beta electrons can create ions from the residual gas, which is still mostly tritium. The creation rates are however much smaller than in the WGTS, because the differential pumping reduces the pressure significantly: according to simulations (see section II.4.2), the pressure decreases from the the order of 10^{-6} mbar in DPS PP0 to a level of about 10^{-11} mbar or higher in DPS PP5. These DPS ions are therefore negligible when measuring the total ion rates with the dipole electrodes. Lastly, the DPS ions are also completely blocked by the ring electrodes in BT5 and PP5 of the DPS and are therefore not relevant for the ion safety in KATRIN either.

Even in the CPS, ions can still be created by ionisation of the residual gas. Beta decay is almost impossible because the residual gas contains almost no tritium anymore and is mostly made up by leaked hydrogen. Because of their small tritium concentration and due to the ring electrode in the PS1 magnet, these ions play no role for tritium ion safety. Without the ring electrode in PS1 however, a considerable background flux of roughly 10^6 ions/s into the PS would blind the ion flux detectors: the analytic model from section III.2.5 predicts for these conditions an ion creation rate due to beta electron scattering in the WGTS of almost 10^{12} ions/s. Given that the pressure in the WGTS is between $(5 \cdot 10^{-5} \ldots 10^{-3})$ mbar and about 10^{-10} mbar in the CPS, the creation rate would be roughly six order of magnitude smaller; the lengths of both sections are comparable. However, this estimate is necessarily rough because the actual pressure inside the CPS cannot be measured.

III.6. Ions and electrons in the transport section

In contrast to the neutral tritium, ions cannot be pumped off the beam tube but will follow the strong magnetic guiding field through the beam tube. At the rear side of the WGTS, they can be neutralised on the rear wall and the neutral tritium can then be pumped off. But on the opposite side of the WGTS, the ions would reach the spectrometers and create background during the neutrino mass measurements if they were not blocked and removed with ring and dipole electrodes (see section VI.1 and VI.2).

Ions and electrons can however also interact with the electric and magnetic fields along the beamline: they may be trapped by the magnetic mirror effect and can be blocked inadvertently, presumably due to different work functions of the materials along the beam tube; on the other side, accumulations of ions and electrons might neutralise the inadvertent blocking potentials as well as the safety relevant blocking potentials of the ring electrodes. This section will discuss the magnetic mirror effect, inadvertent blocking and neutralisation in this order.

III.6.1. Ion trapping by magnetic mirror effect

Ions are subject to the magnetic mirror effect, which occurs according to section III.1.2 when the ion enters a stronger magnetic field. If the magnetic field becomes stronger in both of its directions, the ion can be trapped in a so called magnetic bottle. Such magnetic traps exist in the KATRIN experiment everywhere between the superconducting magnets, most notably in the pump ports.

The ion can only be trapped if its pitch angle is close enough to 90°; according to eq. III.5, the longitudinal energy of the ion parallel to the magnetic field can vanish when the magnetic field increases sufficiently. The pitch angle can however be changed by scattering between the ion and the residual gas, so that the ion may escape through the loss cone of the magnetic bottle. As shown in figure III.4, the mean free path of ions from molecular dissociation is below 1 m throughout most of the WGTS; for thermal ions, it is even smaller. But outside the WGTS, the scattering probability becomes smaller; ions could accumulate in the magnetic trap after having been created inside it.

An ion space charge could affect the neutrino mass measurements, because the different molecular structure of the ions leads to different end point energies of the beta electrons from tritium decay inside the ions. According to section V.4.3, the relative concentration of positive ions has to remain below 10^{-4} of the neutral tritium density and the negative ion concentration below 10^{-6}. Whether the ion densities in magnetic traps along the beamline can actually become so large has to be investigated with simulations of the magnetic field and the ion kinematics inside the traps. Also, the space charge potential of the ions needs to be considered, because it increases the longitudinal energy and can accelerate the ions out of the trap. Experimentally, the ion density in the magnetic traps can not be investigated.

III.6.2. Inadvertent blocking potentials

During the First Light measurements, thermalised positive ions from the ELIOTT ion source were only observed to be transported to the spectrometers when equipped with a small offset energy at the rear wall; ions with less than about 1 eV did not reach the DPS. This observation was confirmed during First Tritium, when only about half of the expected positive ion flux was measured in the DPS.

The inadvertent blocking of positive ions with energies below about 1 eV is attributed to work function differences along the beamline. Inside the beam tube, the electric potential is defined by the surrounding materials. A common measure for the electric field above a certain material is the work function, which describes how much energy is required to remove a test electron from the surface. Naturally, the work function of different materials will not be the same and work function differences on the order of several 100 eV are expected. This effective potential variation will affect the charged particles and might block them.

According to the observations of First Tritium, only one half of the positive ion flux can leave the WGTS. The other half of the flux feeds a positive space charge of ions which are trapped between the gas flux and the inadvertent blocking potentials. These trapped ions can only leave the beam tube by recombination with secondary electrons or negative ions. In order to determine the equilibrium concentration of positive ions, dedicated plasma simulations will have to be carried out in the future. It is not possible to measure the ion density inside the WGTS directly.

The accumulated ions could create an energy dependent background due to their different final states (see section III.6.1 and V.4.3). Also, an ion space charge would of course influence the plasma potential and thereby the start energy of the beta electrons in the WGTS (see section V.4.2). Finally, the increased plasma density can lead to unpredictable plasma instabilities which might distort the beta electron spectrum, as will be discussed in section V.4.1.

Even though inadvertent blocking of positive ions was observed during First Tritium, there were also hints for neutralisation of the positive inadvertent blocking potentials by negative space charges; this effect will be discussed in the next section. At measurements with higher tritium concentration, the neutralisation is expected to be even more efficient and the inadvertent blocking to be even stronger suppressed.

III.6.3. Neutralisation of blocking potentials by space charges

Space charges can neutralise blocking potentials in the beamline: those which lead to inadvertent ion blocking as described in the previous section, as well as the deliberate blocking potentials of the ring electrodes which will be introduced in section VI.1.

Because positive ions are the most abundant ion species, the neutralisation is usually discussed for negative space charges from electrons which got trapped inside positive potential wells[12]: secondary electrons can be created inside the potential by beta electron scattering or come from outside and lose sufficient longitudinal energy to leave the potential as consequence of inelastic or even elastic scattering. Close to the WGTS, also negative ions can contribute to the negative space charge.

Neutralisation of the inadvertent ion blocking between WGTS and DPS is favourable for the KATRIN experiment, because it allows the positive ions to leave the source and prevents the plasma effects which were discussed in the previous section. Such a neutralisation was the presumed reason for observations during the Very First Tritium campaign (see section IX.3.1): the ion flux from the WGTS varied on the first measurement day and remained stable from the second measurement day on.

In case of the ring electrodes, neutralisation of the positive potential could suddenly interrupt the ion blocking and would allow a flux of tritiated ions into the PS. For that reason, a continuous ion monitoring was installed in form of the PS cone current measurement (see section VII.2.4). A neutralisation of the ring electrode potential is assumed to create a slow, continuous increase of the PS cone current – in that case, the system would close the valve between the CPS and PS automatically.

As countermeasure to slow neutralisation, the ring electrode potentials could be inverted to a negative voltage regularly after a certain time. This would drive out negative space charge and restore the original depth of the potential well. In order to actually remove all negative electrons and ions from the two DPS electrodes, the valve V2 between them could be closed; as soon as the charged particles hit the valve surface, they would be neutralised. However, there is no way of measuring the actual effect of such a space charge expulsion. Also, it is unknown how often the procedure is necessary.

The estimation of the time scale of neutralisation will require dedicated Monte Carlo simulations in the future, which can consider the kinematics of inelastic and elastic electron scattering. Special care has to be paid to the modeling of shallow or nearly neutralised potentials, because most of the ions have thermal energies around 2.5 meV in the WGTS or 25 meV in the DPS. In general, the simulation is however similar to the simulation of Penning discharges in the ring electrode potentials and could be carried out together.

[12]Ferenc Glück, Plasma effects in the transport system, talk at the 32. KATRIN Collaboration Meeting in spring 2017.

IV. Ions in the spectrometers

The flux of $2 \cdot 10^{11}$ positive ions/s from the WGTS would follow the magnetic guiding field into the spectrometers, if there were not the ion blocking potentials of the ring electrodes (see section VI.1) or the inadvertent ion blocking which was mentioned in section III.6.2. Such ion blocking is crucial for the KATRIN experiment, because the tritium ions might otherwise create background in the spectrometers by tritium decay. As a second source of background, the ions can in turn ionise the residual gas when they are accelerated by the high voltage of the spectrometers.

The acceleration of positive ions in the negative spectrometer potentials allows however also to detect the ions in two ways: secondary electrons from the ionisation processes can be measured with the FPD, which allows to detect the smallest ion fluxes of all ion detectors in the beamline; also, about 20% of the ions are accelerated in the PS onto the downstream cone electrode, where they are neutralised and create a current in the voltage supply. This current allows the continuous monitoring of the tritium ion flux into the PS during the neutrino mass measurements.

This chapter will discuss the transport of tritium ions in the spectrometers, as well as the diffusion of neutral tritium after a possible tritium ion implantation into the stainless steel walls of the spectrometers. In the first section IV.1, an overview will be given on the transport of tritium ions in the PS. The second section IV.2 investigates the background and ion detection method via ionisation of residual gas in both the PS and MS. A much more extensive discussion in section IV.3 will investigate the background by tritium decay in the case that tritium ions would actually flow into the PS and be implanted beneath the stainless steel surfaces. Finally, the conclusions of this chapter with regard to tritium ion safety and ion detection will be drawn in section IV.4.

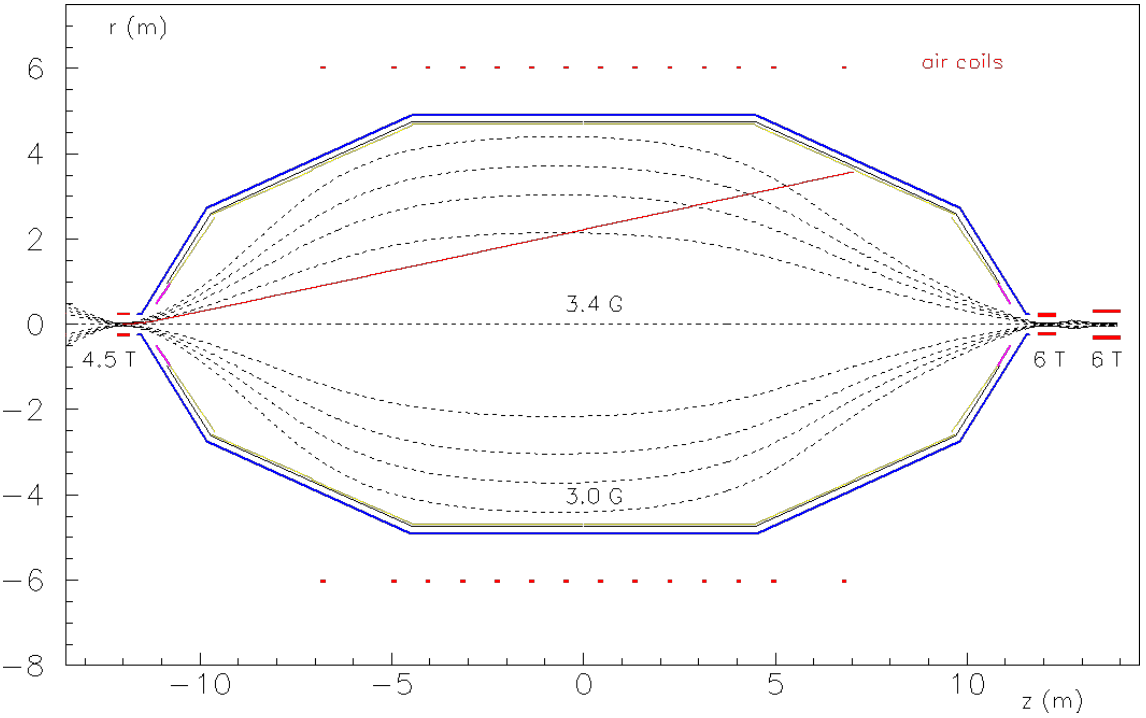

Figure IV.1.: **Trajectory of a T_3^+ ion in the MS at −18.6 kV.** Simulation by Ferenc Glück.

IV.1. Ion transport through the Pre-spectrometer

If the positive[1] tritium ions reached the entrance of the Pre- or Main spectrometer, they would be almost instantaneously accelerated by the negative potential to 18.3 keV in the PS and about 18.6 keV in the MS[2] [CDR04]. Due to these large kinetic energies, most of the ions would leave the magnetic flux tube non-adiabatically (see figures IV.1 and IV.2). These ions would bombard the inner surfaces of the PS and be implanted into the stainless steel[3]. Since the ion transmission probability through the PS is very small, any residual tritium ion flux into the MS becomes further reduced (see section VI.3); nevertheless, many of the implanted tritium atoms would reemerge from the stainless steel, diffuse from the PS into the MS and create background by tritium decay, as will be discussed in section IV.3.

The ions, which leave the magnetic flux tube in the PS, reach the PS downstream cone electrode with a certain probability; these ions create a neutralisation current, which can be measured in order to detect the ion flux into the PS (see section VII.2.4) and for a continuous ion monitoring during the neutrino mass measurements (see section VII.4). A successful demonstration of this ion detection method was given during the First Tritium measurements (see section IX.1.3). The ion signal is fur-

[1]Negative ions would be reflected by the negative potential of the spectrometers.

[2]During the neutrino mass measurements, the high voltage of the MS will be varied to scan the energy interval $[E_0 - 30\text{ eV}, E_0 + 5\text{ eV}]$ around the endpoint $E_0 \approx 18.6$ keV of the tritium beta spectrum [CDR04].

[3]About 5% of the tritium ions are reflected from the stainless steel surfaces during the bombardment and presumably enter the gas phase as neutral molecules (see section IV.3.3) [Wil81].

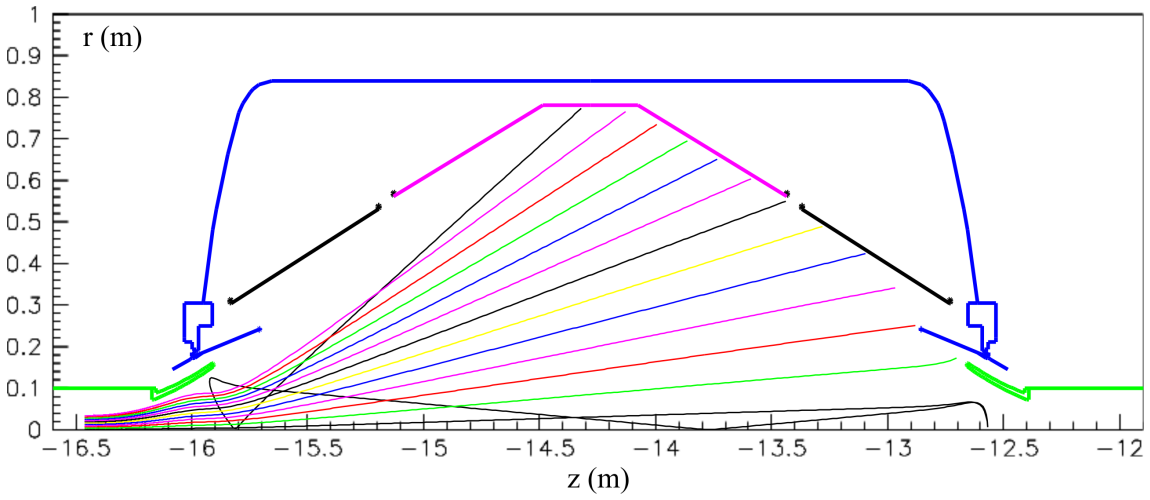

Figure IV.2.: **Trajectories of T_3^+ ions in the PS.** The PS vessel is at −18.6 kV and the inner electrodes are at (upstream cone / wire electrode / downstream cone) = (−500/−450/−400) V relative to the vessel. Ions from the center and periphery of the flux tube go through the wire electrode to the vessel. The downstream cone electrode detects about 23% of the ions with 10 meV start energy. Simulation by Ferenc Glück.

ther increased by charge multiplication due to the emission of secondary electrons from the stainless steel during the ion bombardment, as will be discussed in section VII.2.7.

Numerical values for the ion detection efficiency of the downstream cone electrode and for the ion transmission through the PS can be derived from simulations; however, there are conflicting results. The first simulations[4] with KASSIOPEIA indicated an ion detection efficiency with the cone electrode of almost 100% during nominal operation of the PS at −18.3 kV (see table IV.1). In October 2018, simulations by Ferenc Glück indicated an ion detection efficiency of only $23 \pm 0.16\%$, instead (see table IV.2). Until finishing this thesis at the end of October 2018, a similar ion detection efficiency of $23 \pm 1.6\%$ could be reproduced[5] with KASSIOPEIA. Therefore, an ion detection efficiency of about 20% will be assumed for the evaluation of the PS current measurement throughout this thesis. Nevertheless, it will require further investigation to identify the cause of the previous discrepancy.

The ion transmission probability through the PS was simulated with KASSIOPEIA and by Ferenc Glück. In both cases, the transmission probability $< 1 \cdot 10^{-4}$ at nominal PS high voltage settings[6].

On their way across the spectrometer, the positive ions with keV energies can in turn ionise the residual gas. The resulting secondary electrons create a background rate at the FPD, which can also be used to measure the ion flux into the PS or MS. An extensive discussion of the ionisation effect will follow in the next section.

[4]The KASSIOPEIA simulations were carried out by Woo-Jeong Baek.
[5]Simulation by Ana Paula Vizcaya Hernandez.
[6]According to the KASSIOPEIA simulations, the ions are reflected back to the CPS with a similar probability of $1 \cdot 10^{-4}$.

Table IV.1.: **Interactions of positive hydrogen ions in the PS.** The probability for ionisation of residual gas, neutralisation on the cone electrode or transmission into the MS depends on the voltage settings of the PS vessel and its inner electrodes: the upstream cone electrode (UC), the wire electrode (WE) and the downstream cone electrode (DC). For the KASSIOPEIA simulations, a number # of particles were started inside the PS1 magnet homogeneously distributed across a disc with radius r_{start} around the center of the beam tube. The magnetic field was always set to 70% of the nominal values. Usually, the ions with an initial kinetic energy of 10 meV were T_3^+; only for the simulation of the ionisation probability H^+ ions were simulated which scattered on residual H_2 at $3 \cdot 10^{-6}$ mbar. Simulations by Woo-Jeong Baek.

Vessel (kV)	UC (V)	WE (V)	DC (V)	r_{start} (mm)	#	Ionisation (counts/ion)	Cone electrode	Transmission
0.0	0	0	−400	5	10^5	-	83%	$6 \cdot 10^{-5}$
0.0	0	0	−500	5	10^5	-	86%	$2 \cdot 10^{-5}$
−17.9	−300	−300	−400	5	10^5	-	97%	$1 \cdot 10^{-5}$
−17.9	−400	−400	−400	37	10^4	$7.8 \cdot 10^{-3}$	99%	$< 1 \cdot 10^{-4}$
−16.0	−400	−400	−400	37	10^4	-	99.73%	-
−18.6	−400	−400	−400	37	10^4	-	99.72%	-
−18.6	−500	−450	−400	37	10^4	-	99.73%	-

Table IV.2.: **Detection efficiency of the PS cone electrode for positive hydrogen ions.** 10 meV ions were simulated for the same conditions as in table IV.1 by Ferenc Glück.

Vessel (kV)	UC (V)	WE (V)	DC (V)	r_{start} (mm)	#	Ion species	Cone electrode	Transmission
0.0	0	0	−400	5	$2 \cdot 10^4$	T_3^+	98.4%	$1 \cdot 10^{-3}$
−16.0	−400	−400	−400	37	$2 \cdot 10^4$	T_3^+	19.7%	$< 5 \cdot 10^{-5}$
−17.9	−400	−400	−400	37	$2 \cdot 10^4$	H^+	23%	$< 5 \cdot 10^{-5}$

IV.2. Ionisation of residual gas by tritium ions

The positive ions will be accelerated by the negative potential inside the Pre- or Main spectrometer, become non-adiabatic and bombard the spectrometer walls. Due to their keV energies, the ions can in turn ionise the residual gas molecules while they move across the spectrometers. The secondary electrons from the ionisation process can basically follow the magnetic guiding field up to the FPD, but the detection efficiency depends on the high voltage settings of the spectrometers.

During the neutrino mass measurements, such a rate of secondary electrons from the MS volume would constitute a background which will be discussed in detail in section V.2.2. On the other hand, the ionisation can be used in order to detect ions by using either the PS or MS as gas ionisation chamber; this allows in fact to detect the smallest ion fluxes of all ion detectors inside the beamline, as will be detailed in section VII.1.

This section will first discuss the ionisation efficiency $\mathcal{E}$, which is the central parameter in order to quantify the effects of both background and ion detection via ionisation. These considerations will then be compared with the measurement result for the ionisation efficiency in the MS from the First Light campaign; finally, this allows to derive the ionisation efficiency in the PS for the evaluation of the First Tritium campaign.

Ionisation efficiency The central parameter to quantify both background and ion detection via ionisation is the ionisation efficiency $\mathcal{E}$. It describes the measured FPD rate R_{FPD} for a given ion flux Φ_{ion} into either the PS or MS:

$$\mathcal{E} = \frac{R_{\mathrm{FPD}}}{\Phi_{\mathrm{ion}}}. \tag{IV.1}$$

The ionisation efficiency in the MS was measured during First Light (see section VIII.2.3). As will be discussed below, the result can be estimated within a factor 2 by the ion scattering probability $\mathcal{P}$: it depends on the ion's mean free path $\lambda = 1/(n\sigma_{\mathrm{i}})$ [Per09] with regard to ionisation, multiplied with the ion's average path length $\langle s \rangle$ inside the spectrometer:

$$\mathcal{E} \approx \mathcal{P} = \langle s \rangle \cdot n \cdot \sigma_{\mathrm{i}}, \tag{IV.2}$$

where the following parameters enter the calculation:

- **Average path length $\langle s \rangle$:** The path length of the ions can be roughly estimated from the dimensions[7] of the spectrometers to be about 3 m for the PS and about 20 m in the MS. The ionisation efficiency inside the MS is therefore assumed to be ten times higher at the same pressure and high voltage settings (see next two list items). The path length can however increase drastically if the ions are stored by the electric and magnetic fields. This needs to be investigated with simulations, for example in KASSIOPEIA (see below). Although the ions are accelerated almost instantaneously by the high voltage once they enter the spectrometer, the initial ion energy influences the adiabaticity and thereby the ion's path length.

[7] The MS has a diameter of 10 m and is 23.3 m long.

- **Gas density n:** The gas density can be calculated from the pressure p inside the spectrometer with the ideal gas law. Inserting p in the unit mbar, the density is $n = p \cdot \frac{1}{4} \cdot 10^{23}$ mbar$^{-1}\cdot$ m^{-3} at 300 K.

- **Ionisation cross section σ_i:** The cross section depends on the species of the projectile ion and the target molecule, as well as on the energy of the incoming ion. These incoming ions consist mostly of hydrogen isotopes in the form of single atoms or tertiary clusters. As for the target gas, three different species have to be considered in this thesis:
  - During First Light, the residual gas in the spectrometers was mostly water.
  - During First Tritium, the PS was filled with argon in order to increase the ionisation efficiency.
  - During the neutrino mass measurements, ions might create background by ionisation of residual H_2 in the MS.

  Some cross sections for a fixed projectile ion energy of 20 keV are listed in table IV.3. Energy dependent cross sections for these three target species are shown in figures IV.5, IV.3 and IV.4.

A more precise estimate of the ionisation efficiency can be obtained via KASSIOPEIA simulations[8]. The path length of the ions in the spectrometer can be determined more accurately via ion tracking simulations. After each simulation step, a secondary electron might be created according to the current ionisation probability[9]; this allows to consider also the effect of the ion energy, although the ions are accelerated almost instantaneously once they enter the spectrometer. Finally, the created secondary electrons can be tracked, too: this allows to consider the effect of their initial spatial distribution and their probability to reach the FPD due to magnetic and electrostatic mirrors.

Both the scattering probability $\mathcal{P}$ and the KASSIOPEIA simulations can reproduce within a factor 2 the ionisation efficiency in the MS, as will be discsussed in the following. But in contrast to the above expectations, the PS ionisation efficiency was found to be pressure-independent and several orders of magnitudes larger than expected according to preliminary results of the STS IIIa commissioning measurements with non-active ions in October 2018. The cause of this observation is unkown; therefore, the results of the KASSIOPEIA simulations for the PS ionisation efficiency will be used in the analysis of the First Tritium data as a conservative estimate, as detailed at the end of this section.

[8] All tracking simulations with KASSIOPEIA which are presented in this thesis were carried out by Woo-Jeong Baek, for example in her Master's thesis: *Investigation of background processes of ions and Rydberg atoms in the KATRIN spectrometers*, Karlsruhe Institute of Technology (KIT), 2017.

[9] A systematic error arises because the ion tracking is stopped once a secondary electron is created. The creation of secondary electrons in the upstream part of the spectrometer is therefore larger than in the part closer to the detector, where the secondary electrons might be detected with a larger probability. In order to estimate this effect, the systematic uncertainty was estimated with the probability for double ionisation by a single ion; then the statistical uncertainty was only reduced only to the same level.

Ionisation efficiency in the Main spectrometer During the First Light campaign, an ionisation efficiency in the MS of $\mathcal{E} = (1.18 \pm 0.05) \cdot 10^{-4}$ counts/ion was determined with an ion pencil beam in the center of the beam tube (see section VIII.2.3). The D_3^+ ions scattered mostly on the residual H_2O with a pressure of $3 \cdot 10^{-9}$ mbar inside the MS, which was at -18.6 kV; a magnetic field strength of 40% nominal was created by the PS1 and PS2 magnets, but the Pinch magnet was only at 20% nominal field. The measurement suffered however from large systematic uncertainties: most notably, the pressure in the flux tube cannot be determined exactly, and it is unsure how many of the ions also reached the downstream end of the MS in order to be measured with the PULCINELLA disc.

Under the same conditions, the ionisation efficiency can be estimated theoretically with the ionisation probability $\mathcal{P}$ according to eq. IV.2. This yields $\mathcal{E} \approx 5.8 \cdot 10^{-5}$ counts/ion. Obviously, the theory underestimates the measurement by about a factor 2. This might be due to the experimental uncertainties, which lead to an overestimation of the true ionisation efficiency. From theoretical side, the largest uncertainty is the estimate of the ion path length; additionally, the ionisation cross section was approximated with H^+ scattering on water, which has a 20% systematic uncertainty according to table IV.3 and another systematic uncertainty due to the different species of the projectile ion.

The KASSIOPEIA simulations yield only a slightly larger result than the theoretical estimate: with the beamline settings of the First Light measurement, an ionisation efficiency of $\mathcal{E} = (7.7 \pm 0.18) \cdot 10^{-5}$ counts/ion is obtained[10]. While the uncertainty on the ion path length is negligible here, the same ionisation cross section was used for the simulation as for the previous calculation, although in differential form.

It is not possible to resolve whether the theoretical estimated underestimate the true ionisation efficiency or whether the experiment overestimates it due to systematic effects. A conservative limit for the ionisation efficiency would depend on the intended use:

- If the background $R_{\mathrm{FPD}} = \Phi_{\mathrm{ion}} \cdot \mathcal{E}$ of a certain ion flux Φ_{ion} has to be predicted, the larger result from the First Light measurements should be used.
- If however a measured FPD rate R_{FPD} is used to derive an upper limit on the ion flux $\Phi_{\mathrm{ion}} = R_{\mathrm{FPD}}/\mathcal{E}$, it is conservative to use for example the smaller value from the ionisation probability $\mathcal{P}$.

After all, the First Light measurement is only about 50% larger than the KASSIOPEIA simulation. Based on this benchmarking, the simulations can be used in order to predict the ionisation efficiency in the PS. However, a larger-than-expected and pressure-independent ionisation efficiency was observed in the PS experimentally, as will be described below.

[10] According to the Master's thesis of Woo-Jeong Baek, the ionisation efficiency is $\mathcal{E} = (7.66 \pm 0.18) \cdot 10^{-2}$ counts/ion at -18.6 kV and $3 \cdot 10^{-6}$ mbar residual water in the MS. The secondary electrons were however not tracked from their creation place to the FPD. In order to consider the position of the ion pencil beam in the center of the flux tube, additional simulations for the ion transport through the PS were carried out; eventually, a start radius of 7 mm around the flux tube center was assumed.

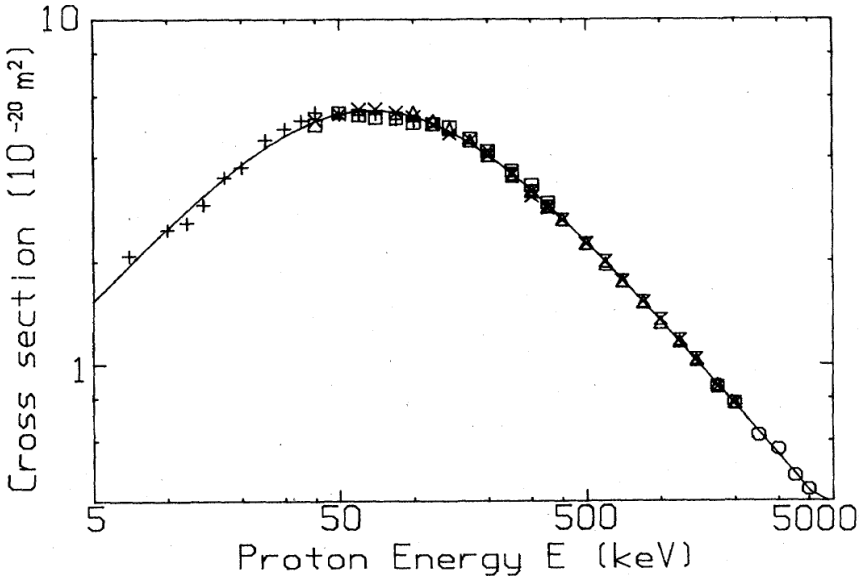

Figure IV.3.: **Ionisation cross section for H^+ ion scattering on neutral H_2O.** The various symbols depict experimental measurement results, to which the solid line is fitted. From [Rud01].

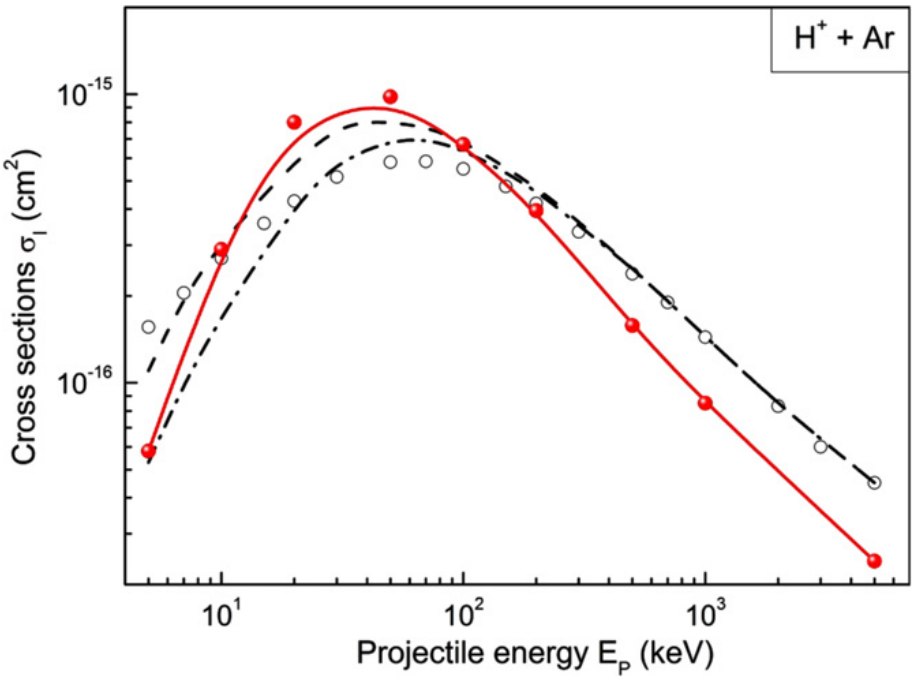

Figure IV.4.: **Ionisation cross section for H^+ ion scattering on neutral Ar.** The black open circles are experimental values, whereas the red full circles and all curves depict theoretical calculation results. From [Fre16].

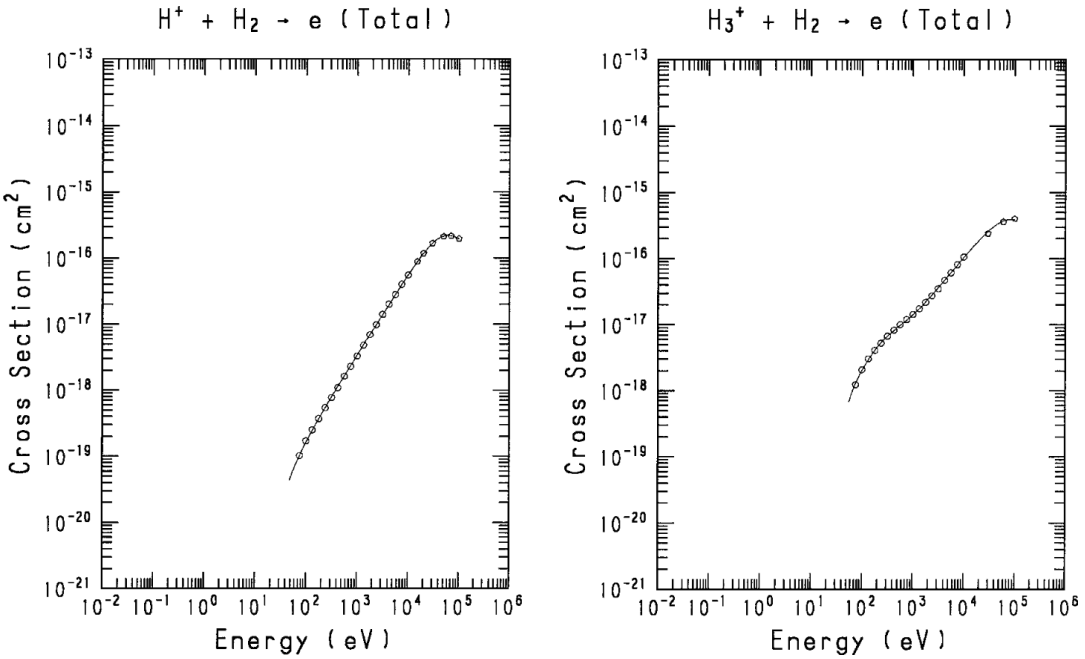

Figure IV.5.: **Ionisation cross sections for H^+ and H_3^+ ion scattering on neutral H_2.** Ionisation of residual H_2 in the MS would create a background rate at the FPD during the neutrino mass measurements. From [Tab00].

Table IV.3.: **Ionisation cross sections for 20 keV hydrogen ions.** The energy dependence of the cross section for H^+ impact is shown in the figures IV.5 (H_2), IV.3 (H_2O) and IV.4 (Ar).

Ion	Residual gas	σ_i (cm^2)	Uncertainty	Source
H^+	H_2	$1 \cdot 10^{-16}$	unknown	[Tab00]
H_2^+	H_2	$2 \cdot 10^{-16}$	unknown	[Tab00]
H_3^+	H_2	$2 \cdot 10^{-16}$	unknown	[Tab00]
H^+	H_2O	$3.79 \cdot 10^{-16}$	±20%	[Rud01, Din00]
H^+	Ar	$4.22 \cdot 10^{-16}$	unknown	[Rud02, Fre16]
H_2^+	He	$1.0 \cdot 10^{-16}$	±20%	[Tok85]
H_3^+	He	$1.2 \cdot 10^{-16}$	unknown	[Tok85]

Ionisation efficiency in the Pre-spectrometer During the First Tritium campaign, the ion flux into the PS was measured with the ionisation method in the PS. In order to derive an upper limit on the ion flux, the ionisation efficiency is required to know. The benchmarked KASSIOPEIA simulations predict a value for the ionisation efficiency of H^+ ions in the PS of $7.8 \cdot 10^{-3}$ counts/ion at $3 \cdot 10^{-6}$ mbar residual H_2 and the nominal high voltage settings, as stated in table IV.1. However, this value is contradicted by the experimental observations with non-tritium ions during First Light and the commissioning campaign STS IIIa.

During the First Light campaign, the rate of secondary electrons due to ionisation in the PS was found to be 1,500 times larger than the rate of secondary electrons from the MS. This was partially attributed to the higher pressure in the PS, which was not being pumped during these measurements and was not baked out; under these conditions, the pressure in the PS might be about 300 times larger than in the MS, due to the conductance between the spectrometers and the pumping speed of the MS (see appendix A.3). The remaining discrepancy was attributed to the different experimental conditions in the PS and MS, as discussed in section VIII.2.2. Actually, a roughly 10 times smaller ionisation efficiency is expected in the PS, due to the shorter ion path length.

Preliminary results of the STS IIIa commissioning campaign indicate a pressure-independent PS ionisation efficiency for D_2^+ ions of about $2 \cdot 10^{-3}$ counts/ion, in stark contrast to theoretical predictions. The pressure-independence suggests stored ions, which deposit a fix kinetic energy in the ionisation of the residual gas; but so far, no indication for storage of the accelerated positive ions was found by simulations with -18 kV in the PS. Thus, the cause of this observation remains unclear.

Since the reason for the experimental observations cannot be explained, the smaller estimate for the ionisation efficiency from the KASSIOPEIA simulations will be used in the analysis of the First Tritium data; the derived upper limit on the tritium ion flux into the PS can thus be considered as a conservative upper limit. Moreover, the measurement procedures during First Tritium still mirror the assumption of a pressure-dependent ionisation efficiency. Whether the pressure-dependence also applies to the MS is also unclear, but not relevant for the upcoming evaluation of measurement data in this thesis.

IV.3. Background from tritium activity after ion implantation

Tritium ions cannot only create background via ionisation as discussed in the previous section, but also due to the radioactivity of the tritium. A background from ionisation could be stopped by suppressing any residual ion flux into the spectrometers; the background from tritium activity would however subside only extremely slowly after a possible tritium ion implantation due to the slow reemission of neutral tritium atoms from the stainless steel surfaces in the spectrometers. The calculation of the tritium reemission rate and the corresponding background is not trivial and afflicted with large uncertainties due to the involved surface physics.

In order to estimate the background from tritium activity, this section will start with calculating the FPD background for a certain number of neutral tritium atoms in the gas phase of the two spectrometers (section IV.3.1). It shows that a much smaller number of tritium atoms is allowed in the MS than in the PS; but according to the previous sections, almost the entire tritium ion flux would be implanted in the PS and from there the neutral tritium would reemerge. For this reason, section IV.3.2 will relate the number of tritium atoms in either spectrometer to a neutral tritium flow into the PS.

The tritium implantation and reemission will be discussed qualitatively in section IV.3.3 as a basis for the quantitative analysis, which needs to consider two different scenarios: a continuous ion flux up to $2 \cdot 10^8$ ions/s into the PS (section IV.3.4) and the total ion flux from the WGTS of $2 \cdot 10^{11}$ ions/s flowing into the PS for 60 s (section IV.3.5). These scenarios are derived from the continuous ion monitoring with the PS downstream cone electrode (see section VII.2.4): it will automatically close the valve to the PS within about 1 min after the detection of an ion flux on the order of the radiation safety limit of $2 \cdot 10^8$ ions/s or above.

IV.3.1. Background due to neutral tritium in the Main spectrometer

A tritium activity A_T inside either the MS or PS would lead to an electron rate to the FPD and a consequent background R_T:

$$R_\mathrm{T} = \epsilon \cdot A_\mathrm{T} \tag{IV.3}$$
$$= \epsilon \cdot \lambda_\mathrm{T} \cdot N_\mathrm{T}. \tag{IV.4}$$

The decay constant of tritium $\lambda_\mathrm{T} = 1.78 \cdot 10^{-9}$ s^{-1} [Luc00] was already introduced in section III.1.1. N_T denotes the number of tritium atoms in gaseous form inside either spectrometer – this parameter will be calculated in the next section from an arbitrary tritium flow into the PS.

Only tritium in the gas phase is assumed to contribute to the background due to the magnetic shielding inside the spectrometers, as explained in appendix A.2. The relation between the tritium activity in the gas phase and the electron rate at the FPD is given by the parameter ϵ, which was introduced by [Mer13] and consists of the following systematic effects:

- **Flux tube volume $\epsilon_\mathbf{V}$:** The magnetic flux tube fills only a fraction of the spectrometer vessel.
- **Magnetic trapping $\epsilon_\mathbf{trap}$:** Electrons can be trapped for hours inside the spectrometer due to the magnetic mirror effect [Mer13] (see section III.1.2). While the are trapped, beta electrons can ionise the residual gas.
- **Ionisation of residual gas by beta electrons $\epsilon_\mathbf{ion}$:** Trapped beta electrons can deposit their kinetic energy into the ionisation of the residual gas and the creation of secondary electrons [Mer13].
- **Escape towards the detector $\epsilon_\mathbf{down}$:** Only about 40% of the trapped electrons reach the FPD at the downstream side of the spectrometers: as calculated in appendix A.1, the larger magnetic field of the pinch magnet leads to a smaller escape probability on the downstream than on the upstream side.

Except for the escape probability towards the detector, which can calculated as in appendix A.1, all of the above probabilities were obtained from simulations for [Mer13][11]. The results are shown in table IV.4 and need to be combined as follows for the total ϵ factor of the PS and MS:

$$\epsilon^\mathrm{PS} = \epsilon^\mathrm{PS}_\beta = \epsilon_\mathrm{V} \cdot \epsilon_\mathrm{trap} \approx 0.25, \tag{IV.5}$$
$$\epsilon^\mathrm{MS} \approx \epsilon^\mathrm{MS}_\mathrm{sec} = \epsilon_\mathrm{V} \cdot \epsilon_\mathrm{trap} \cdot \epsilon_\mathrm{ion} \cdot \epsilon_\mathrm{down} = 20. \tag{IV.6}$$
$$\tag{IV.7}$$

In these definitions, it was considered that secondary electrons from the PS cannot overcome the about 300 V more negative retarding potential of the MS. As for the

[11] The simulation results for [Mer13] were received via internal communication from Joachim Wolf.

MS, the contribution from secondary electrons is however much larger than the one from beta electrons, which was therefore neglected. Not taken into account is the energy cut due to the region of interest (ROI) of the FPD: most of the beta electrons have a kinetic energy of more than 5 keV and will be cut away from the analysis, because the ROI width is only a few keV. Without consideration of the ROI, the background due to beta electrons from the PS can be seen as a conservative upper limit.

Based on these results, the critical number of tritium atoms inside the spectrometers can be calculated in order to create 1 mcps of background at the FPD:

$$N_{1\text{mcps}}^{\text{PS}} = 2 \cdot 10^6 \text{ T atoms}, \tag{IV.8}$$

$$N_{1\text{mcps}}^{\text{MS}} = 3 \cdot 10^4 \text{ T atoms}. \tag{IV.9}$$

In order to derive a limit on the tritium ion flux into the PS, these total numbers of tritium atoms are however not very useful; the diffusion and pumping of neutral tritium in both spectrometers needs to be considered, too. This will be done in the following section.

Table IV.4.: **Conversion probability of tritium activity in the spectrometers to a background electron rate at the FPD.** All values were simulated for [Mer13] and obtained via internal communication fro J. Wolf; the simulations are however from 2011 and require update, especially the values for the PS. An analytic calculation for the downstream escape probability ϵ_{down} can be found in appendix A.1.

Value		PS	MS
Flux tube volume	ϵ_{V}		0.7
Magnetic trapping	ϵ_{trap}		0.58
Ionisation processes	ϵ_{ion}		111
Downstream escape	ϵ_{down}		0.4
Detection of beta electrons	ϵ_{β}	0.25	0.30
Detection of secondary electrons	ϵ_{sec}	100	20

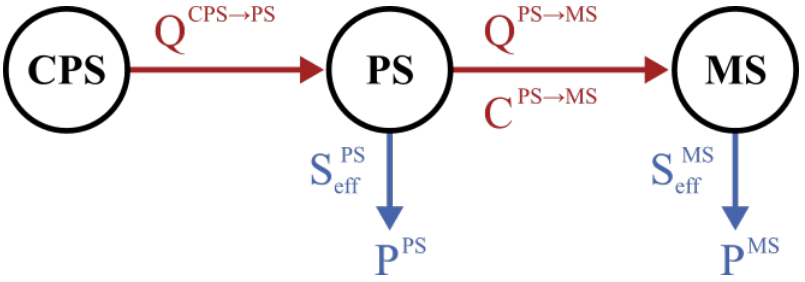

Figure IV.6.: **HT flux from the CPS into the spectrometers.** In the PS and MS, the incoming flow rate $Q^{\mathrm{CPS}\to\mathrm{PS}}$ will be pumped with the effective pumping speed S_{eff} at a pump rate P. This leads in equilibrium to a HT flow rate $Q^{\mathrm{PS}\to\mathrm{MS}}$ from the PS into the MS through the conductance $C^{\mathrm{PS}\to\mathrm{MS}}$.

IV.3.2. Diffusion of neutral tritium in the Pre- and Main spectrometer

In the previous section, the background rate at the FPD due to tritium decay in the spectrometers was stated relative to the number of tritium atoms in the gas phase of either the PS or MS. But the number of tritium atoms is hard to determine; instead, the ion flux into the PS can be measured constantly during the neutrino mass measurements (see section VII.4). This section will therefore relate the number of tritium atoms to a neutral tritium flow into the PS. The relation between the neutral tritium and a tritium ion flux will then be discussed in the next section.

The required vacuum calculations are based on the model[12] from figure IV.6. both the PS and the MS are pumped by turbo molecular pumps with a pumping speed S_{eff} and a throughput P. Gas flows between them and from the CPS into the PS with a flow rate Q, which depends on the pumping speed and the conductance C.

According to the detailed calculations from appendix A.3, the number of tritium atoms N_{T} in the PS and MS depends as follows on the flux $\Phi_{\mathrm{T}}^{\to\mathrm{PS}}$ of tritium atoms per second into the PS:

$$N_{\mathrm{T}}^{\mathrm{PS}} = 0.4\ \mathrm{s}\ \cdot \Phi_{\mathrm{T}}^{\to\mathrm{PS}}, \tag{IV.10}$$

$$N_{\mathrm{T}}^{\mathrm{MS}} = 0.2\ \mathrm{s}\ \cdot \Phi_{\mathrm{T}}^{\to\mathrm{PS}}. \tag{IV.11}$$

For a given tritium flux into the PS, the tritium partial pressure in the PS will be about 300 times larger than the tritium partial pressure in the MS. However, the MS volume is more than 100 times larger than the PS volume. Therefore, almost the same number of tritium atoms in both spectrometers will be reached in equilibrium if there should be a tritium flux into the PS.

For the calculation, it was assumed that all tritium which arrives in the PS from the CPS is bound in HT molecules due to numerous adsorption and desorption processes on the way from the WGTS [Mer13]. The results can however also be

[12] The simplified scheme does not take into account beaming effects for neutral tritium from the CPS through the PS into the MS. This is however not necessary with regard to tritium ions: the neutral tritium, which ought to be described, will reemerge isotropically from the inner surfaces of the PS, predominantly from its downstream side.

interpreted with regard to reemission of tritium atoms in neutral HT molecules from the surfaces of the PS after tritium ion bombardment.

These results can be used to calculate the critical tritium flow into the PS which would create 1 mcps of background by tritium activity during the neutrino mass measurements. Combination with the critical numbers of tritium atoms in the PS and MS from eq. IV.8 and eq. IV.9 yields:

$$\Phi^{\rightarrow \mathrm{PS}}_{1\mathrm{mcps}}(1 \text{ mcps from PS}) = 6 \cdot 10^6 \text{ tritium atoms/s}, \tag{IV.12}$$

$$\Phi^{\rightarrow \mathrm{PS}}_{1\mathrm{mcps}}(1 \text{ mcps from MS}) = 2 \cdot 10^5 \text{ tritium atoms/s}. \tag{IV.13}$$

In order to restrict the background by tritium decay in the spectrometers to 1 mcps, the tritium flow into the PS should consequently not exceed $2 \cdot 10^5$ ions/s. This limit is due to the tritium activity inside the MS; the activity inside the PS has less effect anyway, because the more negative MS blocks the secondary electrons from the PS. A very good agreement exists between this calculation and the requirement from the KATRIN collaboration report, that not more than $2.5 \cdot 10^5$ tritium atoms per second should flow into the PS [CDR04, Mer13]. This requirement will be applied in section V.2.1 also on the flux of tritium ions into the PS.

However, about 2.7% of any tritium flow into the PS will also reach the MS: this result of the calculations from appendix A.3 depends only on hardware parameters, namely the conductance $C^{\mathrm{PS}\rightarrow\mathrm{MS}}$ between the PS and MS and on the pumping speed $S^{\mathrm{PS}}_{\mathrm{eff}}$ in the PS. For this reason, roughly 1% of any tritium ion flow into the PS will also reach the MS: if the tritium ions are not transmitted, they will be implanted according to section IV.1. In case of a long, continuous ion flux, about 50% of the tritium is assumed to reemerge and flow into the PS volume bound in neutral molecules (see section IV.3.4).

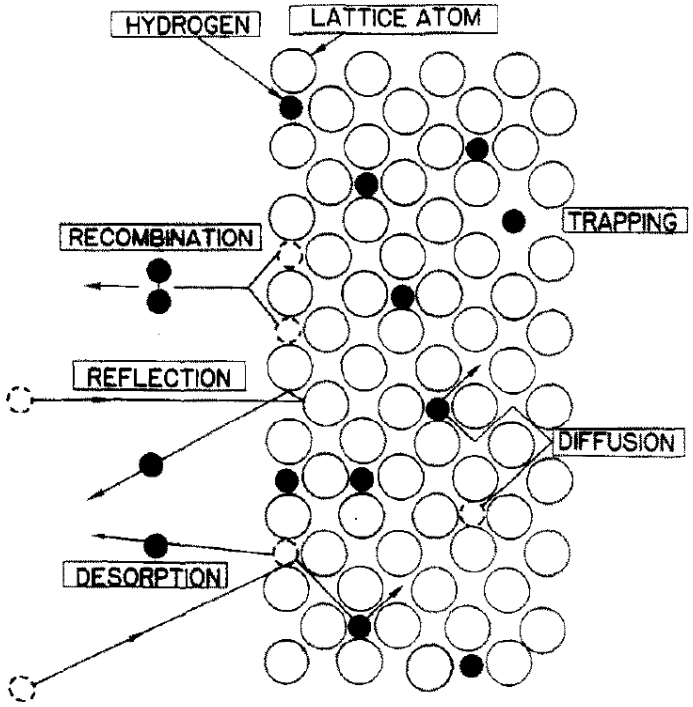

Figure IV.7.: **Interactions of hydrogen ions with a solid during ion bombardment.** While some of the ions are reflected from the surface, the rest is implanted into the bulk. In the solid, the ions can diffuse and undergo trapping, but may eventually reach the surface from which they can desorb via recombination: either with another adsorbed atom (Langmuir-Hinshelwood desorption) or with an impinging atom from the gas phase (Eley-Rideal desorption) [Zan88]. Figure from [Wil81].

IV.3.3. Reemission of neutral tritium after ion implantation

When tritium ions enter either one of the spectrometers, they are accelerated by the negative high voltage. According to section IV.1, almost all of the ions will bombard the stainless steel surfaces of the vessel and the electrodes. However, the implanted tritium atoms can reemerge from the stainless steel by diffusion through the bulk and desorption from the surface into the gas phase. A tritium ion flux into the PS will therefore reach the MS eventually, mostly bound in neutral HT molecules.

The previous sections allow to calculate the background by tritium activity in the spectrometers for a given neutral tritium flux into the PS. In order to determine this neutral tritium flux, this section will give an overview of the physical processes of tritium implantation and reemission at stainless steel surfaces. The actual calculations will then be carried out in the next two sections, for a constant and a short tritium ion flux into the PS.

Not all of the tritium ions will be implanted into the surface: a certain fraction of the ions will be reflected and enters directly the gas phase as neutral tritium. This effect will be treated at the beginning of this section. Then the physical processes of the ions during their implantation with the solid and with the previously implanted tritium atoms will be discussed. The reemission rate of the tritium atoms from

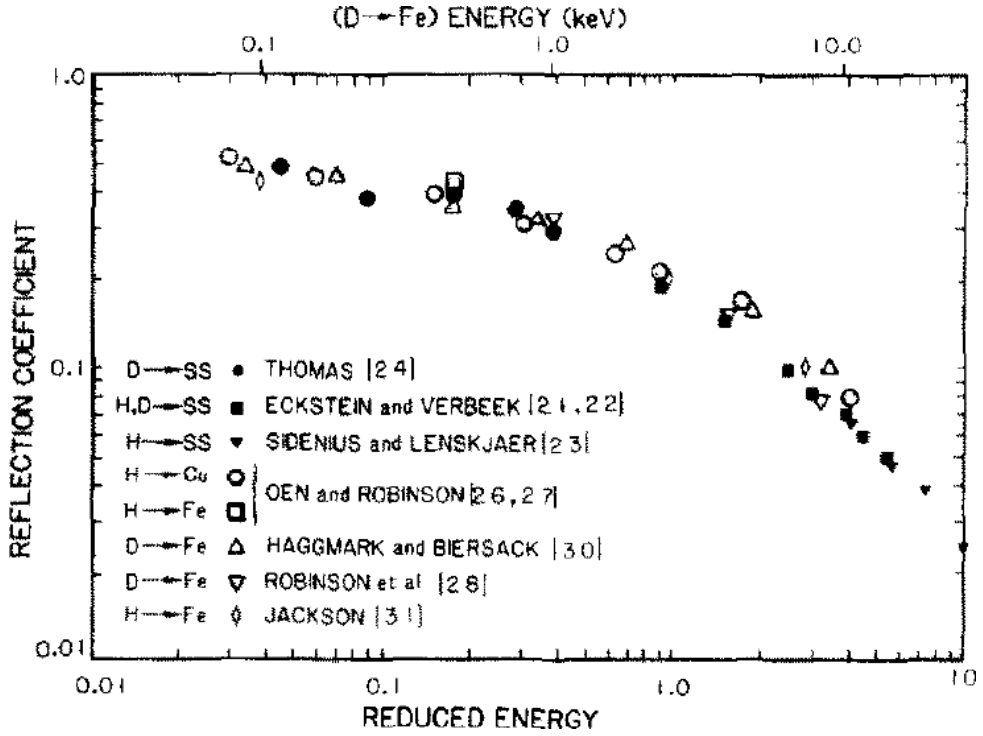

Figure IV.8.: **Reflection of hydrogen ions from a solid surface.** The reflection probability for D^+ ions at iron surfaces decreases when the ion energy increases (upper axis). Filled symbols show experimental results while empty symbols are based on calculations. From [Wil81].

the solid is finally limited by one of the three processes which will be discussed at last (see figure IV.10): diffusion through the solid, trapping at lattice defects and desorption from the solid surface. The complete discussion is based on the review of interactions between hydrogen ions and solids in [Wil81], unless otherwise noted.

Reflection of keV ions at the surface Ions will be reflected with a certain probability from a stainless steel surface, even if they have keV energies like in the spectrometers at their typical high voltages. Figure IV.8 shows however that the reflection probability decreases with the ion energy [Wil81, Oen76, Ble78]; around 20 keV, only about 5% of the ions will still be reflected.

Ion implantation If not reflected, 20 keV hydrogen ions which impinge a stainless steel surface will be implanted into the bulk. It is commonly assumed that during the bombardment, cluster ions with keV energies are broken down into their atomic components with equal shares of the total energy [Tho80, Beh75]; that's because the ion impact energy of about 20 keV is much higher than the ion cluster binding energies on the order of several eV [Pop11]. The implantation depth of hydrogen cluster ions with several keV energy is on the order of 0.1 µm at room temperature [Wil81]. For a detailed simulation of the implantation profile can be obtained with the SRIM package [SRI10].

The stainless steel can be damaged by the bombardment with keV hydrogen ions.

Radiation damage sites may trap hydrogen atoms with binding energies of for example 0.1 eV or 0.3 eV [Wil81]. When the ion flux densities were large enough, even blisters have been observed on the surface [Als78].

Previously implanted hydrogen atoms can be pushed deeper into the bulk by scattering of impinging ions [Ble78]. This so called recoil implantation can create a tail of the ion concentration profile towards larger distance from the surface, but its extent is ambiguous in the literature [Als78, Ble78].

Additionally, impinging ions can cause the reemission of previously implanted hydrogen atoms: this was observed in isotope exchange measurements by [Ble78]. Explanations are generally based on radiation enhanced diffusion or trap filling mechanisms [Wil81].

The time-integrated ion flux onto the surface is commonly referred to as the fluence. If the fluence is large enough, no more hydrogen atoms can be accommodated by interstitial sites and the complete impinging hydrogen flux will be released immediately. Such total reemission was observed for example at a saturation fluence of about 10^{17} deuterium atoms per cm^2 when using 1 keV D^+ ions on 304 stainless steel at 300 K [Tho80]. The saturation fluence depends however on the energy of the ions: when they have larger kinetic energies, the ions can be implanted deeper into the bulk and spread over a larger volume. Saturation is however not relevant for the stainless steel walls of the Pre- and Main spectrometer: the total tritium ion flux of 10^{11} T_3^+ ions would need to flow unhindered into the spectrometers for 10^6 s, so about 10 days.

Thermal diffusion Implanted hydrogen atoms will move through the solid due to diffusion processes [Wil81]. The diffusion speed depends on the solid temperature, its material as well as the species of the diluted atoms; all of these effects together can be considered with the diffusion coefficient D.

According to [Cra79], each atom can move independently of the others in a random walk – sometimes towards a region of higher, sometimes to lower concentration. For a large number of diluted atoms, there is however a net transfer along the concentration gradient. It is possible to calculate the diffusion flux and the concentration of the diluted substance as a function of space and time using Fick's first and second law, as will be done in the next two sections.

Trapping at lattice defects During their random walk through the solid, the diluted hydrogen atoms can be trapped at lattice defects, for example vacancies or interstitial loops [Wil81]. According to figure IV.10, trapping seems to be at room temperature the rate limiting step for tritium reemission after ion implantation in stainless steel.

Significant hydrogen retention can occur due to trapping at radiation damage sites which are a consequence of the ion beam [Wil81]; for example, the implantation of 6 keV D_3^+ ions led to two dominant radiation damage traps with binding energies of about 0.1 eV and 0.3 eV at 295 K. Also in a second experiment with 10 keV D_3^+ ions, the reemission rate was limited at 323 K due to radiation damage traps with 0.1 eV binding energy (see figure IV.10). These literature values could be applied very well to tritium ion implantation in the spectrometers, but the corresponding

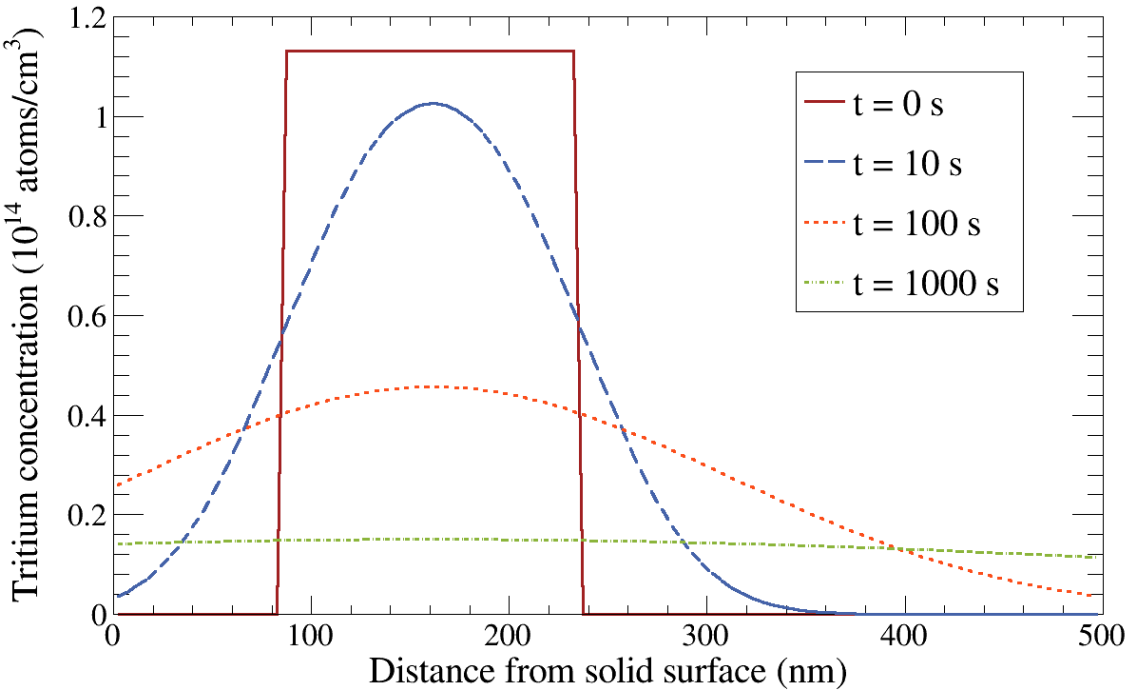

Figure IV.9.: **Thermal diffusion of tritium in stainless steel.** The concentration package is initially confined, but dissolves over the time t. Because no boundary condition at the surface is applied, the diffusion corresponds to the case of an infinite solid. For the borders of the initial concentration package, see the SRIM simulations [SRI10] in figure IV.11 and appendix A.4.

differential equations could not be solved analytically. For this reason, it is not possible to consider trapping effects in the following sections for the calculation of tritium reemission rates from stainless steel.

Desorption from the solid surface If the implanted ions diffuse to the solid surface, they can enter the gas phase via desorption. Just like diffusion and trapping, desorption can limit the hydrogen reemission rate. This is however only expected for temperatures > 323 K in the case of hydrogen atoms in stainless steel, according to figure IV.10.

The following desorption processes are possible:

- **Langmuir-Hinshelwood desorption [Zan88]**, also called molecular recombination [Wil81], denotes the associative recombination of chemisorbed atoms on the solid surface. Alternatively, this thermally activated desorption process might also occur via recombination from bulk sites just below the surface without equilibration at chemisorption sites [Wil81]. This is assumed to be the most relevant desorption process for hydrogen in the spectrometers during the neutrino mass measurements. The tritium atoms will leave the surface bound in HT molecules, because the residual gas is dominated by H_2.

- **Eley-Rideal desorption [Zan88]** occurs between a chemisorbed atom and

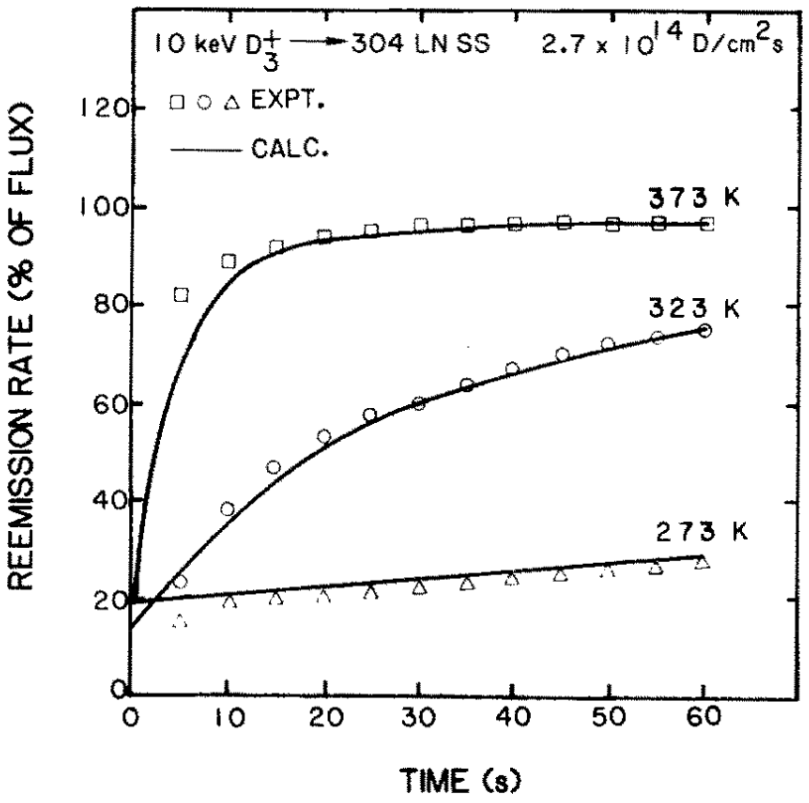

Figure IV.10.: **Rate limits for deuterium reemission from stainless steel.** The deuterium reemission rate from a 304 LN stainless steel sample increases during bombardment with 10 keV D_3^+ ions. Solid lines indicate numerical simulations results for the corresponding temperatures. At 273 K, reemission is small because diffusivity is low. At 323 K, the reemission is rate limited primarily by radiation damage traps with 0.1 eV binding energy, which are filled during the bombardment. At 373 K finally, the deuterium atoms have enough thermal energy to leave the traps and the reemission is limited by molecular recombination. The oxide layer on the individual surface was decreased by prebombardment with a fluence of $\geq 5 \cdot 10^{18}$ D/cm^2. From [Wil81].

an impinging atom from the gas phase; as the two atoms recombine to a molecule, they gain sufficient kinetic energy to leave the surface. Most of the residual gas in the spectrometers will however be H_2, so that the recombination probability with unbound hydrogen atoms is assumed negligible.

- **Stimulated desorption processes** is also cause by a flux of particles onto the solid surface, but in contrast to the Eley-Rideal desorption not by neutral atoms. Instead, desorption may be induced by the following three particle species:
  - **Photodesorption** is caused by photon irradiation. During the neutrino mass measurements, photodesorption in the spectrometers can be neglected. However, a Lighthammer UV lamp is installed inside the MS which could be used to increase the speed of hydrogen desorption in the MS if required.
  - **Electron Stimulated Desorption (ESD)** requires an impinging electron flux on the surface. The electrons are however guided inside the magnetic flux tube and therefore do not reach the stainless steel surfaces.
  - **Ion impact Desorption (IID)** is induced by an impinging ion flux, which will naturally occur during the ion implantation. The magnitude of this effect might be significant, but has not been calculated so far.

All of these desorption mechanisms depend on the surface conditions: for example, the surface roughness determines the number of available adsorption sites and the number of nearest neighbour atoms from the solid phase, which bind the adsorbed atom with their electric fields [Zan88]. The influence of the surface finish on the desorption is however discussed controversially in literature [Sug85, Gra88]. A significant influence is expected by oxide layers or water on the solid surface.

IV.3.4. Expected background by a constant tritium ion flux into the PS

A constant flux of tritium ions into the spectrometers cannot be larger than the radiation protection limit of $2 \cdot 10^8$ ions/s; that's because the detection of such a large flux by the PS current measurement will automatically trigger the closing of the valve between the CPS and PS (see section VII.2.4). Should a residual ion flux up to this threshold enter the spectrometers, would the tritium ions almost entirely be implanted into the stainless steel walls of the PS (see section IV.1). The background by ionisation due to the residual ion flux into the MS is negligible compared to the activity of tritium atoms which reemerge from the stainless steel after their implantation (see previous section) and diffuse into the MS (see section IV.3.2). In the following, this background via tritium activity will be estimated.

Most of the tritium ions during tritium operation will be T_3^+ ions, according to section III.2.1. If these ions should bombard the PS vessel walls and electrodes, they would be split into three single tritium atoms as explained in the previous section. After their implantation into the stainless steel (see section IV.1), the tritium atoms can be released again via diffusion (see section IV.3.3). Assuming a semi-infinite solid and no desorption barrier in a conservative barrier[13], about half of the tritium atoms would enter the gas phase again (compare figure IV.11).

As a result of these considerations, the maximum neutral tritium flux $\Phi_T^{\rightarrow PS}$ into the PS will be about 3/2 of the maximum tritium ion flux $\Phi_{ion} = 2 \cdot 10^8$ ions/s into the PS[14]:

$$\Phi_T^{\rightarrow PS} \approx 3/2 \cdot \Phi_{ion} = 2 \cdot 10^8 \text{ atoms/s}. \tag{IV.14}$$

This equation can be combined with the vacuum calculations from section IV.3.2 (eq. IV.10 and IV.11) and the relation between tritium activity and background as described in section IV.3.1 (eq. IV.4). Then, the total background R_T by tritium activity in the PS and MS becomes:

$$R_T^{PS} = 2.5 \cdot 10^{-10} \text{ cps} \cdot \Phi_{ion} \leq 0.05 \text{ cps}, \tag{IV.15}$$

$$R_T^{MS} = 8.8 \cdot 10^{-9} \text{ cps} \cdot \Phi_{ion} \leq 1.8 \text{ cps}. \tag{IV.16}$$

While the requirements of radiation protection are fulfilled by the trigger threshold, the resulting background by tritium activity of 1.8 cps would be far too large: only 1 mcps background by tritium activity is allowed according to the KATRIN design report [CDR04] (see section V.2.1), and the actual MS background is about 400 mcps (see section II.5). However, this calculation probably overestimates the actual reemission rate: if the desorption is much slower than the diffusion, most of the tritium will be driven by the diffusion gradient deeper into the bulk[15].

[13] If the desorption is much larger than the diffusion speed, the reemission probability might actually be slightly larger than 50%. Also, about 5% of the ions is not implanted but reflected as neutral tritium during the ion bombardment. Finally, this argument assumes that the tritium concentration in the bulk is far below the saturation. However, all three effects are assumed to be negligible given the roughness of this estimate.

[14] The trigger threshold of the PS cone electrode is actually about $1.5 \cdot 10^8$ ions/s and therefore slightly smaller than the radiation protection limit.

[15] No sizeable effect is expected due to trapping at radiation damage sites, because the traps should be filled at some point.

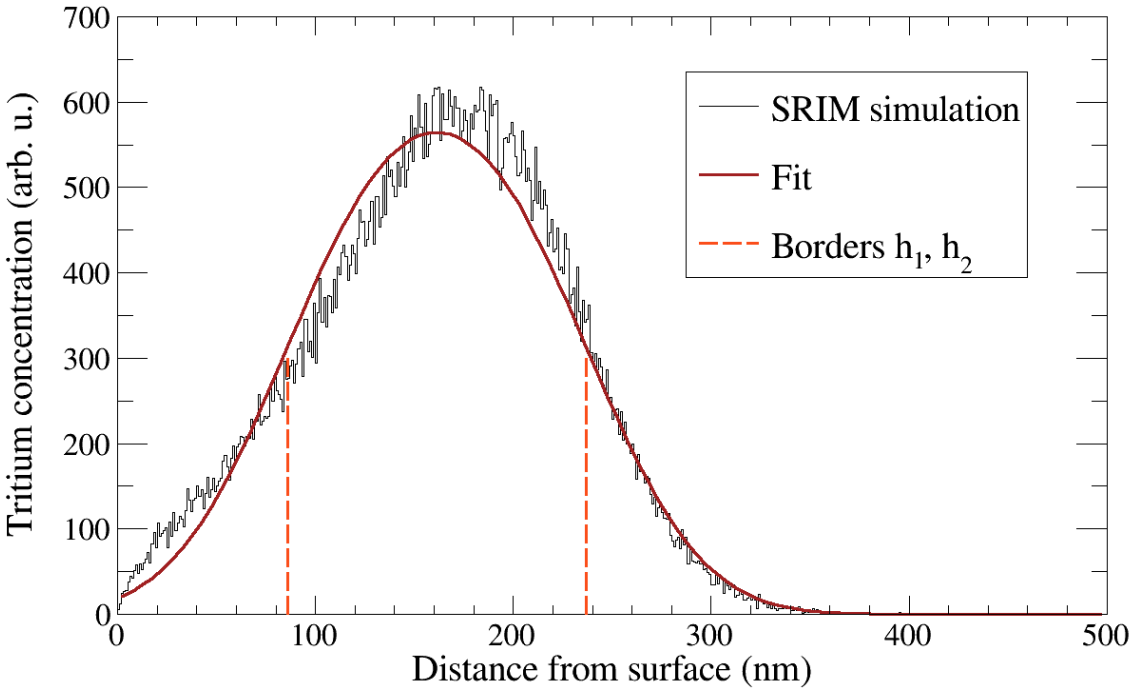

Figure IV.11.: **Tritium concentration in stainless steel after implantation of T_3^+ ions with about 18.3 keV.** The result of the SRIM simulation [SRI10] (black histogram) agrees rather well with a fit of the solution to Fick's second law from app. A.4 (red solid line). Indicated by the yellow dashed lines are the borders h_1 and h_2 of a thought rectangular concentration profile with amplitude C_0, which would have needed 10.3 s to reach this shape via diffusion. It was assumed that the T_3^+ ions brake down to 3 T atoms when they impinge on the surface.

The expected background from a constant tritium flux could be reduced to an acceptable level of about 4 mcps: a long-time evaluation of the PS current over 2 hours would allow the detection of down to $4 \cdot 10^5$ ions/s at 3σ significance, according to section IX.1.3.3. Such an automatic analysis in order to trigger the closing of the valve between CPS and PS has, however, not been implemented yet.

IV.3.5. Expected background after a short tritium ion flux into the PS

The previous section discussed the background from tritium activity due to a constant tritium ion flux into the PS. Such a continuous flux is limited by the continuous ion monitoring with the PS current measurement: if the ion flux exceeds $2{\cdot}10^8$ ions/s, the valve between the CPS and PS will be closed automatically (see section VII.2.4). This leaves however the possibility of a short, but large ion flux into the PS. The question is: how long will it take afterwards until a background level of 1 mcps from tritium activity is reached again?

The time evolution of the background from tritium activity in the spectrometers depends on the diffusion, trapping and desorption processes, which have been introduced qualitatively in section IV.3.3. They govern the tritium reemission in neutral HT molecules form the stainless steel surfaces of the PS, in which the tritium ions would be implanted almost entirely (see section IV.1). Appendix A.4 estimates the time scale of reemission based on Fick's second law of diffusion [Cra79]. In order to apply this law to tritium ion implantation in the stainless steel of the PS, the initial tritium concentration was simulated with SRIM [SRI10] as shown in figure IV.11.

The implanted tritium concentration diffuses through the solid until it reaches the surface and desorbs. Two rate limiting steps can however be distinguished: if diffusion is the rate limiting step, there will be basically no tritium at the surface; but if the reemission is limited by desorption, then the tritium atoms are approximately reflected by the surface and diffuse deeper into the bulk. Actually, the reemission rate is however expected to be limited by trapping of tritium atoms in radiation damage sites, as suggested by figure IV.10. Because trapping can however not be considered analytically, the calculations rather indicate a lower limit until only 1 mcps background is reached again.

Figure IV.12 shows the tritium reemission rate for the purely diffusion and purely desorption limited case. Two lines for the desorption limited case account for the uncertainty on the recombination rate constant k of ± 2 orders of magnitude. During the first hour after the tritium implantation, the desorption rate is clearly smaller than the diffusion rate. Desorption is therefore the rate limiting step.

Diffusion becomes rate limiting around the time that the two curves intersect. This is a rather rough approximation, because the desorption limited case will leave a slightly larger tritium concentration below the surface; however, much of it has diffused deep into the bulk up to this time.

The time to reach a reemission rate which produces only 1 mcps background via tritium decay will therefore lie somewhere between the times for the desorption and the diffusion limited case. If the recombination rate constant k is close to its minimal presumed value, this time can be narrowed down to between 2 weeks and 4 months after the tritium implantation. However, if the actual value of k should be larger, it would easily require several years until the background goes down to 1 mcps again.

This calculation demonstrates that the tritium ion flux from the WGTS must under no circumstances flow into the PS unblocked – not even for a single minute.

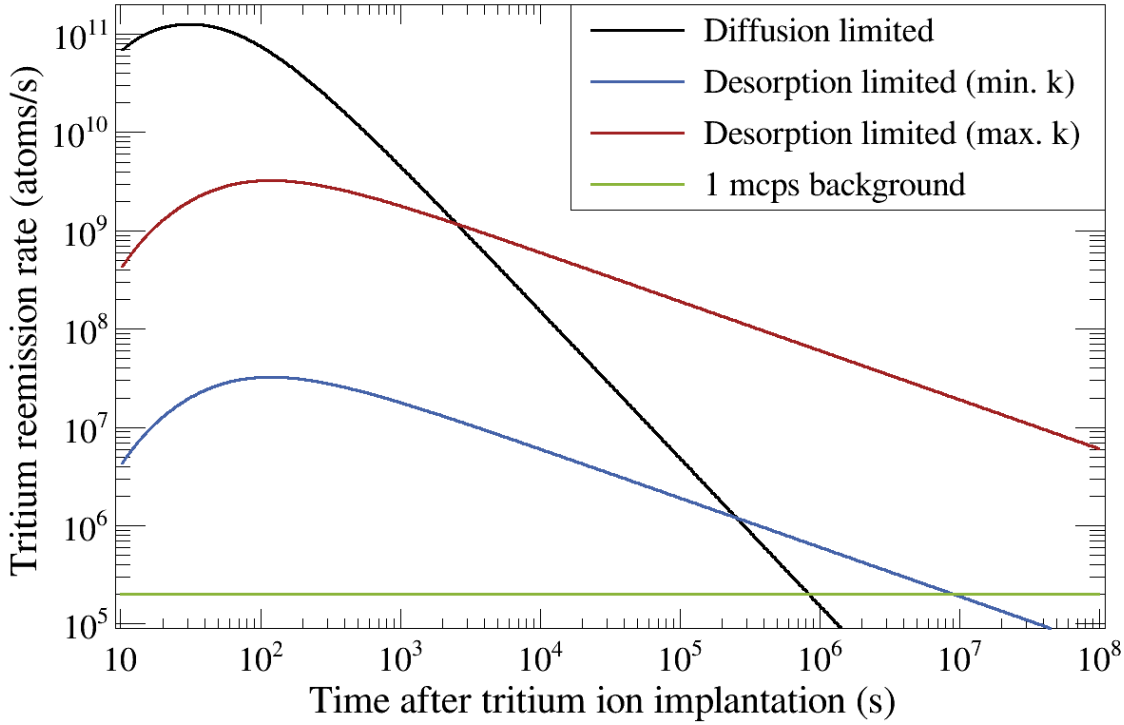

Figure IV.12.: **Tritium reemission after 1 min unblocked tritium ion flux into the PS.** The rate limiting during the first hours after the implantation is desorption. Around the time where the curves for desorption and diffusion intersect, diffusion becomes the rate limiting step. The intersection depends however on the absolute value of the recombination rate constant, which has an uncertainty of about two order of magnitude. Eventually, the tritium reemission would reach again the level of 1 mcps background by tritium decay in the spectrometers. This takes however at least two weeks up to several years. The calculation demonstrates that the tritium ion flux from the WGTS must under no circumstances flow into the PS unblocked – not even for a single minute.

IV.4. Conclusion

Inside the spectrometers, positive ions from the CPS would be accelerated to more than 18 keV due to the negative potential during nominal operation. At keV energies, the ions can ionise the residual gas and thus create background to the neutrino mass measurements if they enter the MS (see section IV.2). On the other hand, the ionisation can be used for the detection of the smallest ion flux among all ion detectors in the beamline (see section VII.1). The central parameter in order to quantify both the background and the detection method is the ionisation efficiency $\mathcal{E} = R_{\mathrm{FPD}}/\Phi_{\mathrm{ion}}$, which depends on the count rate R_{FPD} at the FPD for a given ion flux Φ_{ion}. Conservative estimates for the ionisation efficiency in the PS and MS have been derived in section IV.2.

Due to the high voltage of the spectrometer, the accelerated ions would become non-adiabatic and leave the magnetic flux tube. About 20% of the ions which enter the PS hit the PS downstream cone electrode at nominal high voltage settings (see section IV.1). The resulting neutralisation current in the voltage supply of the cone electrode allows to measure the ion flux into the PS (see section VII.2.4).

According to KASSIOPEIA simulations, less than 10^{-4} of the ion flux into the PS would reach the MS (see section IV.1). Instead, more than 99% of the ions are implanted into the stainless steel walls and electrodes of the PS after leaving the flux tube non-adiabatically. Still, about 1% of the implanted tritium ions could create background via tritium activity: the implanted tritium reemerges bound in neutral HT molecules from the stainless steel in the PS and diffuses into the MS (see section IV.3). Due to the ion monitoring with the PS downstream cone electrode, the ion flux into the PS will be limited but could still create up to 1.8 cps background via tritium activity. Nevertheless, further advances in the automation software could restrict the maximum background to 4 mcps using only the available hardware for long-term measurements of about 2 hours (see section IV.3.4). Section IV.3.5 showed that the unblocked flux of 10^{11} tritium ions/s from the WGTS must not enter the PS even for 1 min; otherwise, the background from tritium activity would decrease to 1 mcps only after a couple of weeks, if not years.

So far, the findings about the background from tritium activity and ionisation were not yet used to constrain on the observable tritium ion flux into the spectrometers. This will be discussed in the next chapter.

V. Impact of tritium ions on the neutrino mass measurement

A large flux of about $2 \cdot 10^{11}$ positive ions per second is expected from the WGTS (see section III.2.5). These tritium ions would follow the magnetic guiding field to the spectrometers, where they would be implanted into the walls due to the negative potential in the PS and MS (see section IV.1). As will be explained in this chapter, this has to be prevented for several reasons: due to radiation protection (see section V.1) and because of the background from the tritium activity (see section V.2.1) and the ionisation of residual gas inside the MS (section V.2.2). The first countermeasure described in this chapter will therefore be the ion blocking with ring electrodes, which will be introduced in section VI.1 of the next chapter. The goal of this ion blocking is to reduce the ion flux into the PS by more than seven orders of magnitude to $1 \cdot 10^4$ ions/s, as will be explained in section V.3.

Besides the MS background, ions can also affect the neutrino mass measurement via systematic effects in the tritium source, which will be discussed in section V.4. One major problem is that the ion blocking itself leads to an increased plasma density in the DPS and WGTS-F, which can cause systematic effects from plasma instabilities. For this reason, a second countermeasure is presented in this chapter: ions need to be removed with dipole electrodes, which will be introduced in section VI.2 of the next chapter. Because even the negative potential of the dipole electrodes causes systematic effects, it needs to be optimised as explained in section V.5.

V.1. Tritium retention for radiation protection

Not more than $2 \cdot 10^8$ T_3^+ ions/s may flow into the PS during the three years net measurement time of the KATRIN experiment. This value is based on the exemption limit of the Federal German Radiation Protection Order, which states that radioactivity below 10^9 Bq in total is not subject to regulation[1]. Since the spectrometers are not located inside the TLK (Tritium Laboratory Karlsruhe) and therefore not subject to regulation, the exemption limit is considered the maximum amount of tritium which may accumulate inside the spectrometers.

The above ion flux limit can be derived from the exemption limit in the following way: over the course of the three years net measurement time for the neutrino mass, the exemption limit corresponds to a continuous flux of about 10 Bq/s into the PS. But besides the tritium ions, tritium may also flow into the spectrometers as neutral molecules. Considering this and adding some safety margin, the ion flux limit into

[1] Internal communication with Michael Sturm. See also the internal KATRIN report: *Tritium ion safety in KATRIN: Conceptual Design Report*, (2018)

the PS due to radiation protection has been defined by the responsible persons of the TLK as 1 Bq/s. Assuming that all ions are T_3^+ ions (see section III.2.1), this radiation protection limit corresponds[2] to a flux of $2 \cdot 10^8$ ions/s into the PS.

V.2. Main spectrometer background

Tritium ions could create background in the MS via two mechanisms: by tritium decay (see section IV.2) and by the ionisation of residual gas (see section IV.3). In order to restrict the background, a limit needs to be imposed on the tritium ion flux into the spectrometers.

The limit will be specified for the ion flux into the PS, although background can only be created inside the MS volume. But if tritium ions were implanted into the walls of the PS, the neutral tritium could reemerge and diffuse into the MS as well; thus, both spectrometers need to be considered as a connected system. Fortunately, the ion flux into the PS can be monitored quite well during the neutrino mass measurements and allows to continuously monitor the ion flux limit (see section VII.4).

According to the KATRIN design report [CDR04], the background from tritium activity in the spectrometers should be restricted to 1 mcps. This limit was defined with regard to neutral tritium only; therefore, in analogy to the previous section, 10% of the total background will be allowed for the contributions from neutral tritium and tritium ions each. In the following, the corresponding ion flux limits will be derived first for the background from tritium activity (see section V.2.1) and then for the background from ionisation (see section V.2.2).

V.2.1. Tritium activity

The effect of tritium activity on the MS background has been discussed in detail in section IV.3. If positive tritium ions entered the negative high voltage of the PS, they would be mostly implanted into the PS walls and electrodes (see section IV.1). The neutral tritium could reemerge from the stainless steel surfaces (see section IV.3.3), diffuse into the MS volume (see section IV.3.2) and decay there. The decay electrons can create background if they either reach the FPD directly or if they create secondary electrons via ionisation of residual gas (see section IV.3.1).

The results of section IV.3 allow to calculate the relationship between the tritium ion flow into the PS and the background from tritium activity in the MS. However, the systematic uncertainties on these results are deemed too large in order to derive a reliable ion flux limit. Instead, the original tritium flow limit from the KATRIN design report [CDR04] will be used, which was also found to agree well with the calculations from section IV.3.

According to the KATRIN design report[3], the background by tritium activity in

[2]The number of tritium atoms was calculated from the activity via the decay constant, see section III.1.3.

[3]The KATRIN design report states in section 4.2: 'The tritium flow (T_2 and HT molecules) into the pre-spectrometer should be smaller than 10^{-14} mbar l/s to limit the increase of background caused by the decay of tritium molecules in the pre-spectrometer as well as in the main spectrometer to 10^{-3} counts/s.' In [Mer13], this gas flow is converted to a number of $2.5 \cdot 10^5$ HT

the spectrometers should be limited to 1 mcps by keeping the neutral tritium flow into the PS below $2.5 \cdot 10^5$ HT molecules per second. But in contrast to neutral HT molecules, the dominant T_3^+ ion species will contain three times more tritium atoms. Also, the background limit from tritium activity was reduced in the introduction above to 0.1 mcps. This leads to an ion flux limit of about:

$$\Phi_{\text{limit}}^{\text{decay}} \text{ (CPS} \rightarrow \text{PS)} < 1 \cdot 10^4 \text{ ions/s}, \tag{V.1}$$

V.2.2. Ionisation of residual gas

When positive ions enter the spectrometers, they are accelerated by the negative high voltage and ionise the residual gas (section IV.2). If his happens inside the MS, the produced secondary electrons can be detected as background by the FPD.

The ionisation efficiency of hydrogen ions in the MS was measured during the First Light campaign (see section IV.2). Conservatively, it will be assumed for the following calculation to be $\mathcal{E} = 10^{-5}$ counts per ion in the MS at -18.6 kV and 10^{-10} mbar H_2. Due to the relationship $\Phi_{\text{ion}} = R_{\text{FPD}}/\mathcal{E}$, the background limit of $R_{\text{FPD}} = 0.1$ mcps can be achieved with an ion flux of:

$$\Phi_{\text{limit}}^{\text{ionisation}} \text{ (PS} \rightarrow \text{MS)} < 10 \text{ ions/s}. \tag{V.2}$$

This limit on the ion flux into the MS cannot easily be transferred to the PS, because the ion transmission through the PS depends on its high voltage settings. But even for moderate high voltage settings like -400 V at the upstream cone electrode, the ion transmission probability through the PS is $< 10^{-3}$ ions/s (see table IV.2). The corresponding ion flux limit into the PS is $\Phi_{\text{limit}}^{\text{ionisation}}$ (CPS $\rightarrow$ PS) $< 10^4$ ions/s, similar to the limit from tritium activity in the previous section.

V.3. First countermeasure: ion blocking and limit on the ion flux into the PS

Not more than $1 \cdot 10^4$ T_3^+ ions/s should flow into the PS in order to limit the ion induced background in the MS[4]. This ion flux would create only about 0.1 mcps MS background due to tritium activity (see section V.2.1) and probably the same amount due to ionisation of residual gas (see section V.2.2). With that, the 1 mcps background requirement of the KATRIN design report is clearly met. At the same time, this flux would be four orders of magnitude more stringent than the limit from

molecules per second. With regard to neutral tritium, the flow limit will be more than achieved by pumping in the WGTS-F, the DPS and the CPS.

[4] During the First Tritium measurements, the tritium concentration was only 0.5%. This allowed for an ion flux limit of $1 \cdot 10^6$ ions/s in order to observe the background requirements from tritium activity. The background from ionisation in the MS was probably still below 1 mcps given the presumed ion transmission probability through the PS at the used -16 kV in the PS (see table IV.2). Because the larger flux limit was only maxed out during ion test measurements, the temporary background from ionisation in the MS was not relevant. The larger limit was also still two orders of magnitude below the legal limit from radiation protection.

radiation protection, which requests less than $2 \cdot 10^8$ T_3^+ ions/s to flow into the PS (see section V.1).

In order to reach this ion flux limit of $1 \cdot 10^4$ ions/s into the PS, the expected flux of $2 \cdot 10^{11}$ T_3^+ ions/s from the WGTS has to be reduced by more than seven orders of magnitude. For this purpose, ring electrodes in the beamline create positive electrostatic potentials which block the positive ions – this ion blocking will be detailed in section VI.1. However, the blocked ions will be stored between the ring electrode potentials and the gas flow from the WGTS. There, the ions could affect the neutrino mass measurements in various ways, as will be discussed in the following parts of this chapter.

V.4. Distortion of the measured tritium beta spectrum

The ion blocking, which was motivated in the previous section, would lead to an accumulation of positive ions: between the positive potentials of the ring electrodes and the gas flow from the WGTS, the positive ions are trapped by the strong magnetic guiding field. The increased plasma density would likewise increase the effect of plasma instabilities, which might in the end smear the observable beta spectrum. This will be discussed in the following section V.4.1.

In order to prevent plasma instabilities, the positive ions have to be removed with negative dipole potentials from dipole electrodes (see section VI.2). Howver, now the negative ions are stored between the dipole electrodes and the gas flow. The only way for the negative ions to leave the flux tube is by recombination with positive ions. If the positive ion density were decreased too efficiently with the dipole electrodes, the resulting negative space charge potential would distort the plasma potential in the source; this would also affect neutrino mass measurements, as will be discussed in section V.4.2.

Finally, both positive and negative ions can lead to a distortion of the measured tritium beta spectrum, because their final state spectra are different from the neutral tritium molecules. In order to prevent a systematic effect on the neutrino mass measurements, the relative ion densities as compared to neutral tritium may not exceed the limits which will be derived in section V.4.3.

V.4.1. Smearing of the beta spectrum by plasma instabilities

If positive ions are trapped in the WGTS, they will accumulate and create a space charge, which in turn draws the secondary electrons to accumulate in the same region in order to restore the quasi-neutrality of the plasma [Bit04]. Depending on the recombination probability of the positive ions, the plasma density might increase and so would the effect of plasma instabilities.

Plasma instabilities can create time-dependent electric fields [Bit04, CDR04], which are not conservative and therefore will change the energy of the beta electron flying through. The effect is similar to ripples on the voltage supply of the ring and dipole electrodes: for this case, the relation between the amplitude of the

electric field change and the change of the beta electron energy has been calculated in appendix A.9.

The exact effect of the plasma instabilities on the neutrino mass measurements cannot be quantified easily: there is a variety of possible instabilities [Bit04] which might occur depending on the conditions of the plasma in the front system of the tritium source; these plasma conditions are however not known in detail and will therefore be approached with dedicated particle-in-cell simulations in the future.

Even if the influence of the plasma instabilities might be quantified, it might be so large that it could seriously affect the neutrino mass measurements. For this reason, the plasma instabilities have to be prevented in the first place by removing the positive ions with the dipole electrodes.

V.4.2. Distortion of the source potential by negative ion space charges

When ions are trapped in the WGTS-F or DPS, they create a space charge with a corresponding electric potential. For positive ions, this space charge will most probably be neutralised by secondary electrons. A space charge formed by negative ions, however, cannot be compensated if the positive ions are removed too efficiently. This would distort the plasma potential in the source, which provides the starting potential for the beta electrons: any inhomogeneity of the plasma potential will smear the measured beta spectrum and therefore affect the neutrino mass measurements.

The magnitude of a negative space charge potential might be on the order[5] of -100 mV. For comparison: detailed simulations of the WGTS plasma potential without negative ions predict an inhomogeneity along the source of only about 22 mV [Kuk16][6].

The effect on the neutrino mass measurements by a negative space charge in the WGTS is similar to the energy shift which the beta electrons receive when they are created inside the negative potential of the DPS dipole electrodes (see section VI.2.2 and the calculations in appendix A.8). But due to the much larger tritium density in the WGTS, a negative space charge there will affect the neutrino mass measurements much stronger than the same potential at the dipole electrodes in the DPS.

More detailed plasma simulations will be necessary in order to estimate the magnitude of the negative space charge precisely. Experimentally, the effect could be investigated with a small krypton concentration in the source gas or via observation of the count rate at a given MS retarding potential, as will be discussed in section VI.2.3.

In order to prevent the accumulation of negative ions, the dipole electrodes could be pulsed between negative and positive dipole voltages in order to remove the positive and negative ions alternately. Currently, this is not possible because changing the polarity of the voltage supply takes several seconds. Also, the application of positive voltages to the dipole electrodes is prohibited for radiation protection reasons (see section VI.4).

[5] Estimate by Ferenc Glück.

[6] The corresponding shift of the neutrino mass squared is $\Delta m_\nu^2 = (-1.14 \pm 0.26) \cdot 10^{-3}$ eV^2 [Kuk16].

Decoupling of the plasma potential from the rear wall Another space charge of negative ions could possibly arise on the other side of the source, between the WGTS and the rear wall. It has not been investigated so far whether the negative ions will be able to reach the rear wall just like the lighter and faster secondary electrons. If the negative ions accumulate in front of the rear wall, the electron flux might be hampered and the plasma potential could decouple from the rear wall. This would not necessarily lead to a charging of the source and to a distortion of the source potential, but controlling the plasma potential would no longer be possible, either. Eventually, whether this effect occurs will have to be tested with 100% tritium source strength by changing the rear wall potential and observing the effect on the measured tritium endpoint.

V.4.3. End point energies of tritium ions

The debris of a tritium ion after beta decay has other molecular final states than the daughter ions of neutral T_2 molecules. For this reason, the beta electrons will have slightly different energy spectra, too. In order to prevent a distortion of the measured beta spectrum during the neutrino mass measurements, the densities of positive and negative ions have to remain below certain limits relative to the density of neutral tritium.

Constraints on the relative densities of positive and negative ions have already been calculated in the KATRIN design report and will be summarised below. According to calculations, these constraints are fulfilled with the nominal dipole electrode settings according to section VI.2.3. Eventually, the ion densities will need to be measured experimentally with a tritium plasma, using the techniques which are also described in section VI.2.3.

Negative T^- ions The negative T^- ions have to remain especially rare: of all tritium ions which are assumed to occur in the WGTS, they are the only ones which create beta electrons with a larger end point of the energy spectrum than the neutral T_2 molecules. In fact, the shift is about 16 eV, which is qualitatively on the scale of the allowed negative offset potentials from the DPS dipole electrodes (see the discussion in section VI.2.2 and calculation in appendix A.8). The different end point energy of electrons from the T^-, however, might also distort the shape of the measured tritium spectrum (compare section VI.2.2).

The negative ion density in the WGTS has to remain below a few 10^{-6} relative to the neutral T_2 density[7]; this would then lead to a shift of the measured neutrino mass squared by $\Delta m_\nu^2 = 0.01\ \mathrm{eV}^2$ according to the KATRIN design report [CDR04]. As a conservative estimate, the expected T^- density is $\leq 2 \cdot 10^{-8}$ of the neutral T_2 density; the estimate considered only the recombination of T^- with T^+ ions, but neglected the even more efficient recombination with T_3^+.

The T^- density also remains below the bound of $2 \cdot 10^{-8}$ if the negative ions are blocked by by the negative potentials of the dipole electrodes[8]. For this case,

[7] The average T_2 density in the WGTS is $5 \cdot 10^{14}\ T_2/\mathrm{cm}^3$ [CDR04]. The relative limit on the T^- density was calculated by Nikita Titov.

[8] Calculations by Ferenc Glück yield a T^- density in the WGTS-F of $10^7\ \mathrm{cm}^{-3}$ when using the

the KATRIN design report originally proposed a pulsed operation of the dipole electrodes in order to remove the negative ions with a 100 V more positive dipole potential every 100 s between two measuring intervals [CDR04]. However, this is not possible with the exmployed voltage supply (see section VI.2.4), because changing the polarity of the voltage supply takes several seconds.

Positive ions Likewise, positive ions can affect the measured tritium beta spectrum. The end point energies of all expected positive ions is however smaller than the end point energy of neutral tritium molecules [CDR04], such that their contribution to the beta spectrum is suppressed according to figure VI.6 in section VI.2.2.

In order to restrict the effect of positive ions also to a neutrino mass squared shift of $\Delta m_\nu^2 = 0.01$ eV^2, their relative density should not exceed 10^{-4} of the neutral tritium density[9]. This requirement seems to be easily fulfilled: the expected T^+ density is about $2 \cdot 10^{-8}$ relative to the neutral tritium density [CDR04], and the total positive ion density will be less than two orders of magnitude above this value (see section III.2.1).

However, these assumptions do not take into account the ion blocking with the ring electrodes, which increases the positive ion density in the DPS and WGTS-F. If the ions are reflected at the ring electrode in DPS BT5, about one half of the ions will return to the WGTS-F without being drifted out by the dipole potentials (see section VI.2.1). Nevertheless, this increase of the expected positive ion density by 50% is still small compared to the limit on the positive ion density.

V.5. Second countermeasure: ion removal in the DPS

According to the previous section, the density of positive ions in the WGTS and DPS relative to the neutral T_2 density has to be restricted to 10^{-4} or less. Likewise, the relative density of negative T^- ions must not be more than 10^{-6}. Thats's because a large positive ion density could lead to plasma instabilities (see section V.4.1), the space charge potential from negative ions would distort the plasma potential in the source (see section V.4.2) and both positive and negative ions create beta electrons with different end point energies than neutral tritium molecules (see section V.4.3).

All of these effects (plasma instabilities, space charge potential and end point energy) would distort the measured tritium beta spectrum. The positive and negative ion densities are currently assumed to remain below the constraints which were placed with regard to the different end point energies. But the negative space charge from T^- ions is expected to become 5 times larger than the potential inhomogeneity in the WGTS, which was determined by [Kuk16].

In order to assess the effect of the negative space charge potential on the beta spectrum, it will be necessary to investigate with dedicated particle-in-cell simulations whether the negative space charge is limited to the WGTS-F or whether it also

dipole electrodes at nominal voltages (see section VI.2.3). In contrast, the average T_2 density is 10^{15} cm^{-3} in the WGTS-C.

[9] Estimate by N. Titov according to an internal document of the KATRIN collaboration: *Tritium ion concentrations in WGTS and transport system* by F. Glück

extends to the WGTS-C; there, the tritium density and the beta electron creation rate are much larger, which would increase the energy dependent background. Further, the effect of various dipole electrode settings on the tritium beta spectrum can be observed experimentally (see section VI.2.3): smaller negative dipole voltages would lead to a larger positive ion density and consequently to a smaller density of negative ions, which can leave the flux tube only via recombination due to the negative dipole potential.

The effect of plasma instabilities cannot be estimated so far, but their creation would be favoured by the observed inadvertent blocking of positive ions (see section III.6.2, VIII.6 and IX.3). which leads to an increased plasma density. This, too, will require investigations with particle-in-cell simulations and possibly with e-gun measurements (see also section VI.2.3).

The First Tritium measurements showed that the ion blocking and removal is essential to reduce the ion flux as demanded in section V.1 to V.3 and to remove positive ions for the previously discussed reasons. However, even the corresponding ring and dipole electrodes can cause systematic effects to the neutrino mass measurements: if beta electrons are created inside a too negative dipole potential, they would distort the measured beta spectrum just like a space charge potential from negative ions (see section VI.2.2); and ripples on the voltage supply will smear the beta electron energy similar to plasma instabilities (see section VI.2.4). These effects will be discussed in the following chapter along with the hardware of the ring and dipole electrodes in the broader context of ion blocking and removal in KATRIN.

VI. Ion blocking and removal

In order to not exceed the ion flux limit of $1 \cdot 10^4$ ions/s into the PS, the expected flux of $2 \cdot 10^{11}$ positive ions/s from the WGTS has to be reduced by more than seven orders of magnitude. For this purpose, five ring electrodes are installed in the beamline of the KATRIN experiment: they block all positive ions with likewise positive electrostatic potentials. In this way, the background requirements with regard to tritium activity and ionisation of residual gas in the MS can be achieved (see sections V.2). Most crucial are the two redundant ring electrodes in the DPS, because they prevent the tritium ions from leaving the tritium laboratory as required by radiation safety (see sections V.1).

However, the blocked ions would be trapped between the blocking potentials and the gas flow from the WGTS due to the strong magnetic guiding field. Over time, the stored ions would accumulate and lead to distortions of the measured tritium beta spectrum via several systematic effects which have been discussed in section V.4. In order to prevent such an influence on the neutrino mass measurements, the positive ions are removed with dipole electrodes via $E \times B$-drift (see section VI.5). The negative potential of the dipole electrodes prevents at the same time all negative ions from leaving the tritium laboratory; further, both negative ions and secondary electrons are blocked and cannot neutralise the ring electrodes (compare section III.6.3). The dipole electrodes themselves cannot be neutralised: while negative particles can be trapped and stored in the positive potential of the ring electrodes, any positive particles inside the negative potential of the dipole electrodes is constantly drifted out.

In the first section of this chapter, the ring electrodes will be discussed. Then the dipole electrodes and the $E \times B$-drift will be detailed in section VI.2; this includes the effect of ripples on the voltage supply of the ring and dipole electrodes, which leads to special stability requirements as explained in section VI.2.4. Besides the dipole electrodes, also the Pre-spectrometer high voltage can remove positive ions from the flux tube; section VI.3 will discuss the consequences for the choice of the Pre-spectrometer high voltage in order to reduce the residual ion flux into the Main spectrometer during the neutrino mass measurements. Finally, section VI.4 will explain how the ion blocking is monitored in the DPS.

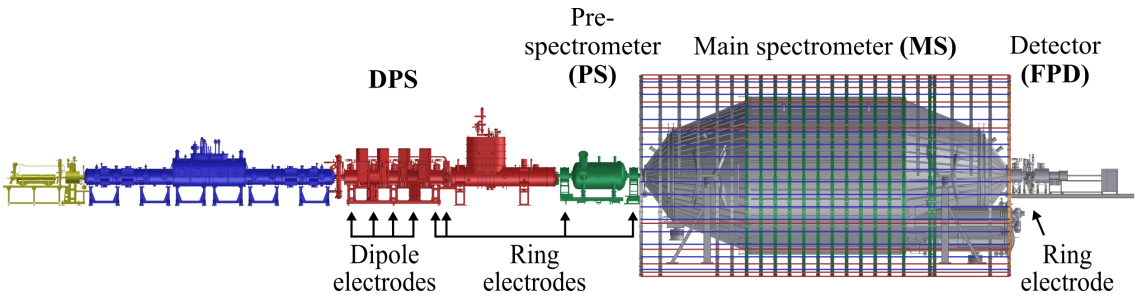

Figure VI.1.: **Position of the ring and dipole electrodes in the beamline.**

VI.1. Ring electrodes block ions

The positive ion flux from the WGTS of $2 \cdot 10^{11}$ ions/s has to be reduced by about seven orders of magnitude in order to observe the ion flux limit into the PS of $1 \cdot 10^4$ ions/s (see section V.3). For this purpose, several ring electrodes in the beam tube create positive electrostatic blocking potentials which reject positive ions.

Location The location of all five ring electrodes is shown in figure VI.1. Reduction of the ion flux into the PS is only possible with the three ring electrodes in in DPS BT5, DPS PP5 and the PS1 magnet; for radiation protection, only the two DPS electrodes are even relevant (compare section V.1). The two ring electrodes on both sides of the MS can be used for various test measurements and reduce the flux of non-tritium ions into the MS, which might also create background by ionisation (see section V.2.2).

Geometry The geometry of the ring electrodes is shown in figure VI.2. Each electrode consists of a metal ring, which is split at one point in order to prevent the induction of a current in case of the quench of a superconducting magnet. Because the width of the metal rings is much smaller than their radius, there is a potential grip of the surrounding ground potential of the beam tube: in the center, the potential drops to 80% or even 40% of the applied voltage[1] (see table VI.1).

Voltage settings The voltage settings of the ring electrodes are based on the results of the First Tritium measurements: wihle most ions from the WGTS are thermal, an ion energy spectrum up to at least 15 eV has been observed, presumably due to molecular dissociation. These dissociation ions are expected to receive kinetic energies up to about 100 eV. However, raising the ring electrode potentials to the maximum is not possible due to the creation of ions in Penning discharges. As discussed in section IX.5, the ring electrode potentials were therefore chosen to be +20 V at the two DPS dipole electrodes, +200 V for the PS1 electrode and +50 V for the two ring electrodes on either side of the MS (see also table VI.1).

[1]Simulations with KASSIOPEIA by Rudolf Sack for his Master's thesis: *Aufbau einer Ionenquelle und Simulation der Transporteigenschaften der DPS und CPS am KATRIN Experiment*, (2015)

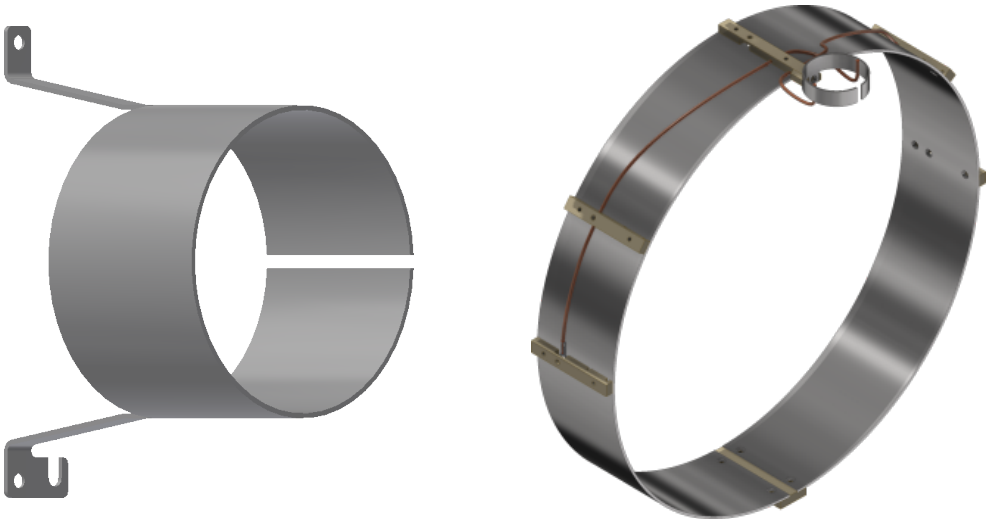

Figure VI.2.: **Technical drawings of the DPS ring electrodes.** The BT5 electrode (left) is similar to the ring electrodes in the spectrometer section. Because it is installed inside a pump port, the PP5 electrode (right) has a larger diameter and is mounted differently. Due to the larger radius of the PP5 electrode, the potential in its center will drop to about 40% of the applied voltage; in contrast, the potential in the BT5 electrode will remain at least 84% of the applied voltage (see table VI.1).

Table VI.1.: **Ring electrode voltages.** The voltage from the voltage supply is only about 81% in case of the DPS ring electrodes due to the voltage monitoring. All ring electrodes suffer potential grip from the surrounding beam tube, which is on ground potential; this grip was simulated for the electrodes in DPS BT5, PP5 and the PS1 magnet in the Master's thesis of Rudolf Sack (2015).

Electrode	DPS BT5	DPS PP5	PS1	PS2	Detector
Voltage supply	+20 V	+20 V	+200 V	+50 V	+50 V
Due to monitoring	81.13%	81.13%	100%	100%	100%
Voltage at electrode	+16.2 V	+16.2 V	+200 V	+50 V	+50 V
Due to potential grip	84.2%	40.0%	46.5%		
Potential in center	+13.7 eV	+6.5 eV	+93.0 eV		

Effect on beta electrons: low pass filters Beta electrons are effectively not affected by the positive voltage of the ring electrodes: the potential well accelerates the electrons only temporarily while they fly through the electrostatic potential. But if the potential should fluctuate due to voltage ripples, the electron energy would no longer be conserved – this will be discussed in detail for the dipole electrodes in section VI.2.4. In order to minimise any voltage ripple, low pass filters were installed[2] close to the beam tube, right outside the glove box of the DPS (see figure VI.7).

Voltage supply and voltage monitoring The voltage supply for all five ring electrodes[3] provides up to 500 V with a maximum ripple of 7 mVpp. However, only 350 V can be applied to the ring electrodes: the control program limits the voltage in order to prevent discharges between the electrodes and the grounded beam tube[4]. In order to change the polarity of the ring electrodes, the output voltage needs to be about 0 V.

Due to radiation protection concerns (see section V.1), the voltage of the two DPS ring electrodes is monitored: if the voltage at the ring electrodes drops below 120 V, the radiation protection measures take effect and the measurements are interrupted (see section VI.4). For the voltage monitoring, a redundant cable to each ring electrode is used, as shown in figure VI.7; this allows to detect if a cable in the voltage supply is broken.

Monitoring the voltage at the DPS ring electrodes draws a small current from the voltage supply. The RC elements of the low pass filters act as a voltage divider, so that the actual voltage at the ring electrodes is reduced to $(81.13 \pm 3.87)\%$ of the output voltage at the voltage supply[5]. Even with the maximum 350 V from the voltage supply, the DPS ring electrodes will therefore reach at the most 283.5 V and an even smaller potential in the center due to the potential grip.

Ion blocking requires ion removal with dipole electrodes If the positive ion flux would only be blocked, the ions would accumulate and create a positive space charge. According to section V.4.1, this increased plasma density could undergo instabilities which might change the beta electron energy and affect the neutrino mass measurements; also, positive ions have a larger end point energy and could distort the tritium beta spectrum if they accumulate at sufficient density. For this reason, the blocked ions need to be removed with the dipole electrodes, which will be discussed in the next section.

[2] During First Tritium, low pass filters were only installed at the DPS electrodes.

[3] iseg DPr 05 106 24 5_SHV-THQ-EPU

[4] Another limit of 450 V arises from the voltage limitations of the plugs and feedthroughs.

[5] The voltage is measured with a Knick VariTrans P29000P2/00 isolating amplifier, which has an input resistance of 2 MΩ in the range of ±450 V. This resistance is in series with the low pass filters, which are double Π elements based on three capacitors with 10 nF and two resistances; these resistances have 1 MΩ in the filter between voltage supply and electrode, and 3.3 MΩ in the other filter between electrode and isolating amplifier. The resistance of the cables (0.3 Ω each) and the resistance between the electrodes and the beam tube (> 20 GOhm) are all negligible.

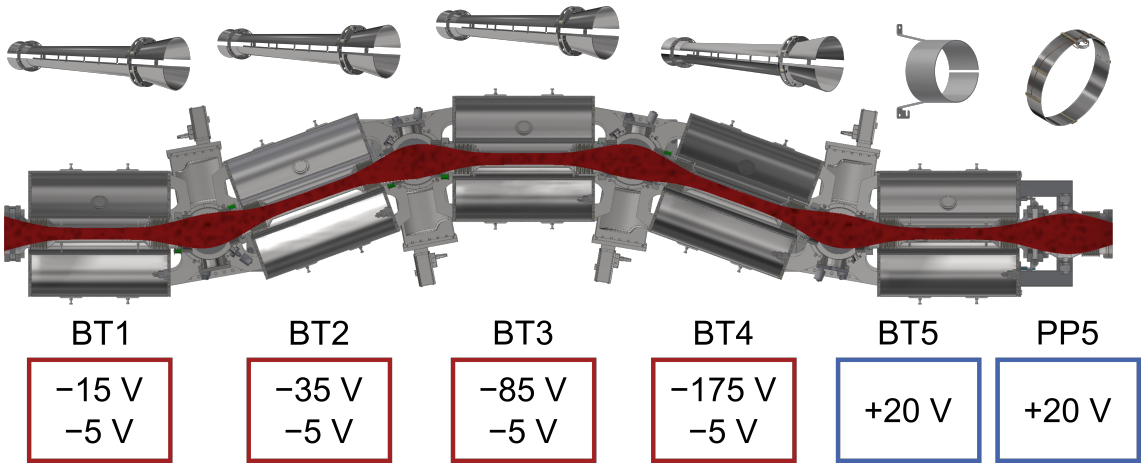

Figure VI.3.: **Ring and dipole electrodes in the DPS.** Two ring electrodes in beam tube 5 and pump port 5 block the ions with a positive potential of up to 20 eV. The positive ions would be stored, accumulate and distort the tritium beta spectrum. Therefore, they are removed via $E \times B$-drift with four dipole electrodes in the beam tubes 1 to 4: the upper electrodes are set to $(-15 \ldots -175)$ V, while the lower electrodes are all at -5 V.

VI.2. Dipole electrodes remove ions

In order to reduce the tritium ion flux into the PS, positive blocking potentials are created with the ring electrodes which were discussed in the previous section. But secondary electrons and negative ions from the source could neutralise the blocking potentials if they accumulate in the positive potential well of the ring electrodes (see section III.6.3). Also, the negative ions have to be stopped within the tritium laboratory in the first place. Finally, the ring electrodes trap the positive ions due to the magnetic field and the gas flow from the WGTS; the plasma density would increase and possibly undergo plasma instabilities, which might affect the neutrino mass measurements (see section V.4.1).

For these reasons, four dipole electrodes were installed in the DPS[6] (see figure VI.3). They create a negative electric dipole field, which removes the positive ions via $E \times B$-drift. Since the positively charged ions are drifted out, the dipole potentials cannot be neutralised like the ring electrodes.

This section will first discuss the ion removal with the $E \times B$-drift. Then the effect of the negative dipole potentials on the beta electrons will be discussed in section VI.2.2, which leads to requirements for the dipole voltages as detailed in section VI.2.3. The final section VI.2.4 will explain the voltage supply, which has to be extremely stable in order to prevent changes of the beta electron energy due to voltage fluctuations.

[6]The dipole electrode in DPS beam tube 1 was only installed after the First Light campaign, as explained in section VIII.7.

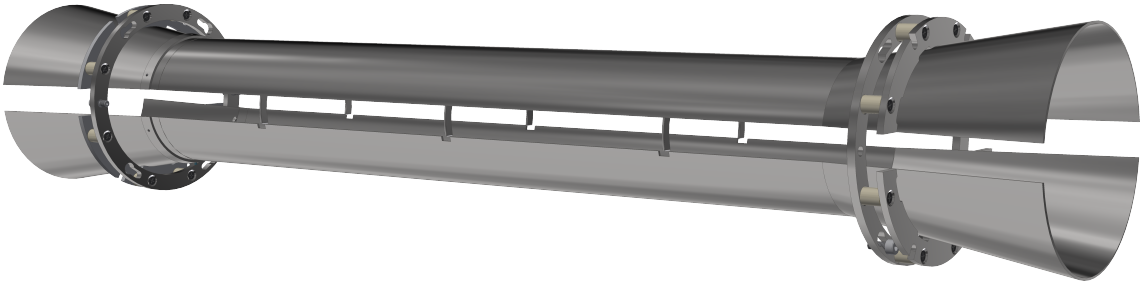

Figure VI.4.: **Technical drawing of a dipole electrode in the DPS.** The upper and lower electrode create a dipole potential which drifts the ions together with the magnetic field onto the vertical lobes in the gap between the electrodes (see $\vec{E} \times \vec{B}$-drift in figure VI.5). The ions are neutralised when they hit the lobes and can be pumped off as neutral molecules; at the same time, the neutralisation current can be measured with an amperemeter in the voltage supply (see section VII.2.2). The lobes are usually welded to the upper electrode; only in the DPS BT4 they are at the lower electrode.

VI.2.1. Ion removal with $E \times B$-drift

Any charged particle moving through a magnetic field and an electric dipole field will undergo the $E \times B$-drift which was introduced in section III.1.2, eq. III.3:

$$|\vec{v}_{\mathrm{DE}}| = \left| \frac{\vec{E} \times \vec{B}}{B^2} \right| = \frac{E}{B}. \tag{VI.1}$$

The drift velocity $\vec{v}_{\mathrm{DE}}$ depends only on the strength of the electric field $\vec{E}$ and of the magnetic field $\vec{B}$. Consequently, the slower particles will be drifted further than faster particles, because they are exposed longer to the drift. Further, the drift is independent of the particle charge and direction of motion.

The $E \times B$-drift does not change the kinetic energy of the ions. For this reason, the ions will move on equipotential surfaces between the electrodes, as shown in figure VI.5.

In order to prevent the ions from circling endlessly around the electrodes, perpendicular lobes are welded to one electrode of each dipole[7]: as the positive ions move longitudinally through the dipole due to their acceleration in the negative potential, they will mostly hit one of the lobes and be neutralised, thus being removed. However, the probability for an ion to slip through the lobes to the outside of the dipole is about 63% in BT4, according to appendix A.7. Only in BT1 will all ions neutralise on the lobes of the dipole electrode, due to the considerably smaller dipole voltage.

Starting from the drift velocity, the drift distance s_{DE} of a charged particle inside

[7]The lobes are welded to the upper electrode in BT1, BT2 and BT3, but at the lower electrode in BT4.

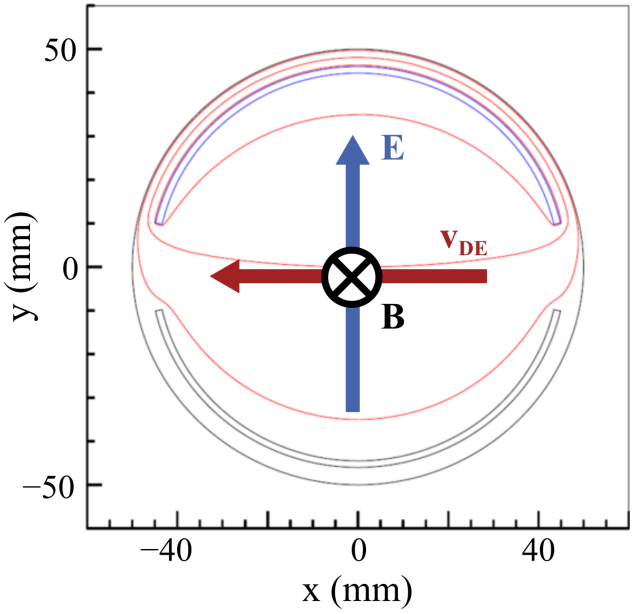

Figure VI.5.: $\vec{E} \times \vec{B}$**-drift in the dipole electrodes.** The upper electrode is on a negative potential, so that the electric field points upwards. The magnetic field goes into the plane, which is the perspective of the FPD. Due to the $\vec{E} \times \vec{B}$-drift, the ions move to the left along the electric field lines. Eventually, they hit one of the lobes in the gap between the electrodes due to their longitudinal motion; if they are drifted fast enough, the ions will neutralise on cables or electrode mounts outside the dipole.

the dipole electrodes can be approximated as done in appendix A.6:

$$s_{\mathrm{DE}} = v_{\mathrm{DE}} \cdot t_{\mathrm{DE}} \approx \frac{\sqrt{m}}{B} \cdot \frac{l_{\mathrm{DE}}}{h_{\mathrm{DE}}} \cdot \frac{|eU_{\mathrm{up}} - eU_{\mathrm{low}}|}{\sqrt{|eU_{\mathrm{up}} + eU_{\mathrm{low}}| + 2E_0}}. \tag{VI.2}$$

The calculation involves the following parameters:

- The mass m of the particle – this is the only parameter which depends on the particle species.
- The absolute value B of the rather homogeneous magnetic field inside the dipole electrode. At nominal magnetic field strength, $B = 5$ T in all DPS beam tubes; during the neutrino mass measurements, however, the magnetic field will be at 70% nominal which corresponds to $B = 3.5$ T.
- The length $l_{\mathrm{DE}} = 844$ mm of the dipole electrode and the distance h_{DE} between the two electrodes. The diameter of the dipole is $h_{\mathrm{DE}} = 89$ mm, but at the side of the dipole the two electrodes are only $h_{\mathrm{DE}} = 20$ mm apart (compare figure VI.4).
- The initial kinetic energy E_0 of the charged particle. As will be discussed below, beta electrons are hardly affected, and most of the remaining particles are thermalised with $E_0 \approx 0$.

- The voltages U_{up} and U_{low} of the upper and lower electrode. If one of the electrodes is grounded and the initial energy of the particle is negligible, the drift distance becomes proportional to the square root of the voltage on the other electrode; this prediction was experimentally validated during First Light for ions with about 2 eV energy (see section VIII.4).

Expression VI.2 for the drift distance can be used to estimate how often an ion has to traverse the DPS in order to be removed. During the neutrino mass measurements, the dipoles electrodes will be set to the voltages from table VI.2 due to the reasons which will be discussed in section VI.2.4. After passing once through all four dipole electrodes, a T_3^+ ion with negligible initial energy in the center of the beam tube will be shifted by about 24 mm; because the inner radius of the lobes is 40 mm, the ion will be removed after moving one time back and forth through the DPS. This average removal time will increase (decrease) if the ion starts further from (closer to) the lobe, relative to the drift direction. If the ion starts above or below the center of the beam tube, the removal time will always be longer due to the curvature of the electric field. As the ion approaches the electrodes, the drift velocity increases due to the increasing electric field.

The relative ion removal probability in each dipole electrode can be obtained by comparing the calculated ion drifts as shown in table VI.2: about half of the ions will be removed in the BT4 dipole at nominal voltage settings; but less than 10% are removed in BT1. This result is valid for all species of charged ions and independent of their start position or the strength of the magnetic field in the DPS.

VI.2.2. Effect on the beta electrons

The electrostatic potential of the dipole electrodes changes the energy of the beta electron only temporarily as it passes the dipole electrode. Nevertheless, the dipole electrodes can affect the neutrino mass measurements, as will be discussed in this section: the $E \times B$-drift changes also the position of the beta electrons slightly, which can be considered in the neutrino mass analysis. Further, ripples on the voltage supply of the dipole electrodes change the beta electron energy and therefore have to be prevented with an extremely stable voltage supply (details in section VI.2.4). And finally, the measurement of beta electrons from the DPS constitutes an energy-dependent background because they gain energy from the negative potential of the dipole electrodes; this requires an experimental optimisation of the dipole electrode voltages in the future, as will be discussed in section VI.2.3.

$E \times B$-drift of the beta electrons The $E \times B$-drift in the four dipole electrodes will shift the position of the beta electrons with 18.6 keV by not more[8] than 43 µm. Whether this effect can affect the neutrino mass analysis is not yet investigated; this could be done in principle with KASSIOPEIA since the electric and magnetic fields are well known. On the other hand, the small shift from the dipole electrodes is negligible to similar drifts in the Main spectrometer.

[8] The estimate assumes that the beta electrons are close to the gap between the electrodes where electric field is maximal; this is however outside the flux tube which will be transmitted onto the FPD.

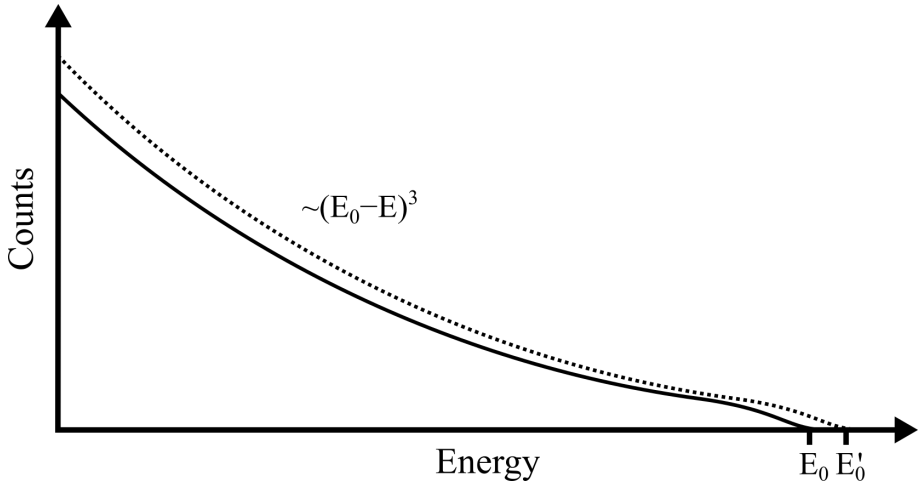

Figure VI.6.: **Sketch of the background from a shifted electron start potential.** Primary beta spectrum around the end point energy E_0 (continuous line) and a secondary spectrum with the same amplitude but larger end point energy E_0' (dashed line): the shifted spectrum grows faster with $(E_0 - E)^3$, where E is the electron energy. Therefore, even a small tritium activity can create a large background if it occurs in a large negative offset potential. This background is energy dependent, because it changes with the retarding potential of the MS.

Distortion of the beta spectrum by ripples on the dipole voltages The kinetic energy of the beta electrons will be changed only temporarily when they traverse the negative electrostatic potentials. But if the potential varies over time, it is not conservative [Lan60] and the energy of the beta electron will be changed: the electron is decelerated by a different negative electric field upon entering the dipole, than the field by which the electron is accelerated as it leaves the dipole again. This time-of-flight effect would smear the measured beta spectrum and the imprint of the neutrino mass.

As a countermeasure, an extremely stable voltage supply with a typical voltage ripple of < 2 mVpp and a maximum ripple of 7 mVpp was chosen for the dipole electrodes; in addition, low pass filters were installed as close as possible to the beamline (see section VI.2.4). The effect can also occur in the ring electrodes, which have therefore been equipped with the same stable voltage supplies. Eventually, the magnitude of this effect will need to be investigated experimentally with the e-gun.

Background due to the negative dipole potential When the beta electrons are created inside the negative potential of the dipole electrodes, they gain extra kinetic energy with regard to the beta electrons from the source. The spectrum of these beta electrons can be thought of as a second spectrum which is shifted to larger energies compared to the primary spectrum from the source (see figure VI.6).

Although the tritium activity decreases with the tritium density by about a factor 5 between each beam tube of the DPS[9], the shifted beta electrons can distort

[9]The tritium density in the DPS beam tubes can be measured by application of a monopole

the measured beta spectrum significantly: that's because the tritium beta spectrum decreases with $(E_0 - E)^3$ towards the end point energy E_0 for increasing electron energies E. This is an energy dependent background which changes with the MS retarding potential[10].

In order to restrict the background to the arbitrary limit of 10 mcps, limits on the dipole voltages were derived[11] for each of the four DPS beam tubes in appendix A.8. According to table VI.2, the dipole voltage in DPS BT1 must not exceed −10.3 V while a dipole voltage of −174.7 V is allowed in BT4, due to the about 125 times smaller tritium density.

The set voltages of the dipole electrodes (see also table VI.2) were chosen mainly based on these voltage limits. Further optimisation of the dipole voltages will be necessary in the future, as will be discussed in the next section. Moreover, this background needs to be investigated more closely with simulations: the approximation of the beta spectrum with $(E_0 - E)^3$ leads to a maximum background at the maximum retarding potential of 30 eV; but as illustrated by figure VI.6, there might also be an impact on the beta spectrum just around the imprint of the neutrino mass.

VI.2.3. Optimisation of the dipole electrode voltages

The set voltages of the dipole electrodes are shown in table VI.2. In order to remove positive ions with the highest available efficiency, these voltages were chosen as large as possible under consideration of the effect on the neutrino mass measurements: direct effects by the dipole electrode voltages have been discussed in the previous sections and the consequences of the negative dipole potential for the source plasma were treated in section V.4. Along with these physics constraints, there are several technical conditions:

- **Maximum voltage** The voltage supply output is limited to 350 V absolute in order to prevent electrical discharges between the electrode and the grounded beam tube.

potential to the dipole electrodes. With a negative potential, the increase of the beta electron rate above the end point of the tritium spectrum can be observed. A positive potential would accelerate the positive ions from within the dipole electrode towards the PS where even a small rate could be measured via ionisation; although this method involves a tritium ion flux into the PS, it would allow to investigate even the tritium density in the DPS BT3 and BT4 because the ion creation rate is larger than the creation rate of beta electrons. In the end, both methods can be compared to each other and to simulations.

[10] The tritium pressure in the DPS beam tubes could be determined by measuring the ion flux: when applying a voltage of about +30 V in monopole mode to each dipole individually, all ion from this beam tube would receive an offset energy and could be detected further downstream. Using the PS ionisation measurement would allow to keep the tritium ion flux into the PS as small as possible. The larger part of the tritium ion flux could be blocked with the ring electrodes, along with the dissociation ions which were observed at significant rates at up to 15 eV. Comparison of the measurement with simulations would yield an estimate of the tritium density. A similar measurement could be carried out with beta electrons by applying negative offset potentials in monopole mode.

[11] The calculation assumes that the voltage is completely applied to one electrode while the other is on beam tube potential, which defines ground.

- **Minimum voltage** The minimum voltage at either electrode must be 5 V absolute: below this value, the specific voltage supply in use undergoes drifts because it is only stable to 1% at a full scale voltage of 500 V.

- **Blocking negative ions** One upper and one lower electrode in the whole DPS must be on a negative potential of at least −5 V in order to block the negative ions; this is mandatory for radiation protection reasons in order to ensure tritium retention inside the tritium laboratory. While the positive ions are removed with negative dipole potentials, the negative ions can only be blocked and not be removed.

- **No acceleration of positive ions** For radiation protection reasons, the maximum voltage of any upper or lower dipole electrode must be 120 V smaller than the minimal voltage of the two DPS ring electrodes. This is required to prevent the acceleration of positive ions over the ring electrode potentials.

- **Same drift direction** All dipole electrodes should drift the ions to the same direction in order to maximise the combined drift distance. Therefore either the upper or lower electrode should always be the more negative one.

- **Electrode with lobes at more negative potential** The electrode with the lobes should be on a more negative potential than the electrode without lobes. Otherwise, ions might be trapped in the dipole electrode after losing energy by scattering with neutral gas: as they approach the lobes, they see effectively a positive potential. Whether they can leave the dipole electrodes sideways via $E \times B$-drift has to be investigated with simulations, for example in KASSIOPEIA. However, the lobes are on the lower electrode in DPS BT4 while they are at the upper electrode in all other beam tubes; due to the requirement that all dipoles drift the ions into the same direction, the electrode without lobes will be on the more negative potential in BT4. One alternative would be to ground this dipole electrode in the future.

The dipole voltage settings in table VI.2 result in a background of slightly more than 10 mcps due to beta electrons which are created with an offset energy (see section VI.2.2). That is mainly because the lower electrodes have to be set to −5 V in order to prevent voltage drifts by the voltage supply, while at the same time the upper electrodes were set to the proposed maximum dipole voltages. In the BT1 dipole, the voltage of the upper electrode was even increased over this limit in order to increase the ion removal efficiency.

For the neutrino mass measurements, the set voltages of the dipole electrodes will need to be optimised in order to consider correctly the background by beta electrons with extra energy from the negative offset potential. Also, the effect of negative ion space charges due to too efficient removal of the positive ions could not yet be considered (see previous section). Both backgrounds could be remedied by a reduction of the dipole voltages; but a smaller dipole voltage could in turn increase the density of positive ions so much that plasma instabilities might occur and smear the beta electron energy.

The dipole voltages could be optimised during test measurements by searching the minimum change of the electron energy at various dipole electrode settings. Most notably, krypton measurements with a tritium plasma in the WGTS would allow to investigate all three effects at the same time: plasma instabilities would change the width of the Krypton line while the two other backgrounds would shift the central energy of the Krypton line. The Krypton measurements have the additional advantage that they allow access to the potential inhomogeneity along the z-axis by comparison with simulations, although only at 100 K source temperature.

At arbitrary temperatures, the smearing of the electron energy by plasma instabilities can be monitored with the e-gun and a shift of the end point energy can be detected by measuring the beta electron rate at a fixed MS retarding potential[12]. Such count rate measurements indicate only the average source potential along the z-axis, but they are always available and can be used to monitor a possible shift of the source potential by a growing space charge of negative ions. All of these measurements require supplemental simulations for the analysis.

[12]The measurement of the beta electron rate at a fixed retarding potential also allows to measure the tritium density inside the dipole electrodes in all four DPS beamtubes. For this measurement, it is however favourable to use the dipole electrodes in monopole mode.

Table VI.2.: **Set voltages of the DPS dipole electrodes.** The voltages of the upper electrodes were chosen based on the background limits which were derived in appendix A.8 and all lower electrodes were set to −5 V in order to prevent drifts of the voltage supply; further optimisation of these voltage settings with theoretical and experimental investigations in the future (see section VI.2.3) will most likely lead to smaller dipole voltages in order to reduce the T^- density (see section V.4.2). At each dipole voltage, the drift distance can be calculated for thermal T_3^+ ions in the center of the dipole electrode at 70% nominal magnetic field strength (see section VI.2.1). The removal probability of each dipole follows from the relative drift distance, independent of the particle species, its radial position inside the dipole electrode or the magnetic field strength.

Dipole electrode	BT1	BT2	BT3	BT4
Max. dipole voltage (V)	−10.3	−33.8	−83.9	−174.7
Upper electrode (V)	−15	−35	−85	−175
Lower electrode (V)	−5	−5	−5	−5
Drift distance (mm)	1.9	4.1	7.2	10.9
Removal probability	8%	17%	30%	45%

VI.2.4. Stable voltage supply to prevent change of beta electron energy

Ripples on the voltage supply will change the energy of the beta electrons, because a time-dependent electric field is not conservative (compare the plasma instabilities mentioned in section VI.2.4) [Lan60]. Changes of the beta electron energy must be avoided, because they would smear the measured beta spectrum and the imprint of the neutrino mass. In order to ensure a stable voltage supply, an iseg high voltage source is used in combination with passive stabilisation by low pass filters.

This section will first discuss the stability conditions which have to be observed in the first place by the high voltage source, which will be discussed subsequently. The field cabling can pick up additional high-frequency noise which is removed with low pass filters right outside the DPS glove box. Between the voltage supply and the low pass filters, amperemeters are installed in order to measure the current from ion neutralisation (see figure VI.8 for the position of the amperemeter and section VII.2.2 for the ion detection method). In order to not spoil the current measurement, the voltage at the dipole electrodes is not being monitored.

Stability requirements The stability conditions for the voltage ripple are derived in detail in appendix A.9. In order to constrain the energy shift of the beta electrons to 5 meV, the peak-to-peak amplitude U_{pp} of a discrete ripple frequency f has to obey:

$$f > 15\ \mathrm{MHz} : U_{\mathrm{pp}} < 5\ \mathrm{mVpp}, \tag{VI.3}$$

$$f < 15\ \mathrm{MHz} : U_{\mathrm{pp}} < \frac{5\ \mathrm{mVpp}}{\sin(2\pi f \Delta t)}. \tag{VI.4}$$

This criterion is based on the time-of-flight of the beta electrons. Eq. VI.4 considers the case that the electron has a short time-of-stay $\Delta t \leq 16$ ns inside the dipole electrode compared to the rise time of the voltage fluctuation: then the electron energy is changed only by a fraction of the amplitude of the voltage fluctuation. The constraints can be relaxed for frequencies below $f \approx 15$ MHz, because the dipole electrodes have a length of 844 mm and the relevant electrons have an energy of about 18.6 keV.

The same stability requirements also apply to the ring electrodes. Because they are considerably shorter than the dipole electrode, the threshold frequency decreases however so that the same stable voltage supply and similar low pass filters could be used.

Voltage supply In order to fulfill the strict stability requirements for the voltage supply, a high voltage source from iseg[13] was chosen for the DPS dipole electrodes (and for all five ring electrodes): this voltage supply provides up to 500 V with a typical voltage ripple < 2 mVpp and a maximum ripple of 7 mVpp, according to data sheet (see appendix B.1). This would not necessarily fulfill the stability requirements from eq. VI.3 and VI.4 if the voltage ripples occur above $f = 15$ MHz.

[13] iseg DPr 05 106 24 5_SHV-THQ-EPU

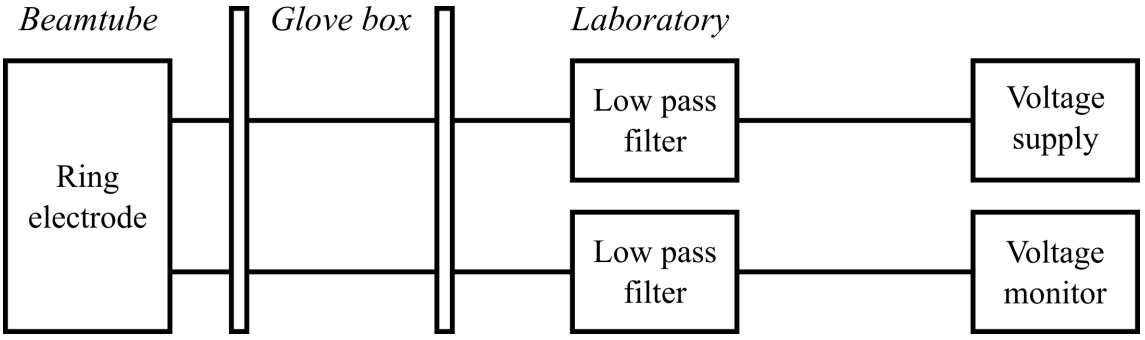

Figure VI.7.: **Voltage supply and voltage monitoring of the ring electrodes.** Two redundant cables run from the ring electrode to the outside of the glove box: one is used for the voltage supply while the other allows to monitor the actual voltage at the electrode. Voltage ripples on the electrodes have to be prevented, because they could affect the beta electron energy. For this reason, extremely stable voltage supplies are used. Additionally, low pass filters just outside the DPS glove box remove any high-frequent noise which might have been picked up by the field cabling. For more on the ring electrodes, see section VI.1.

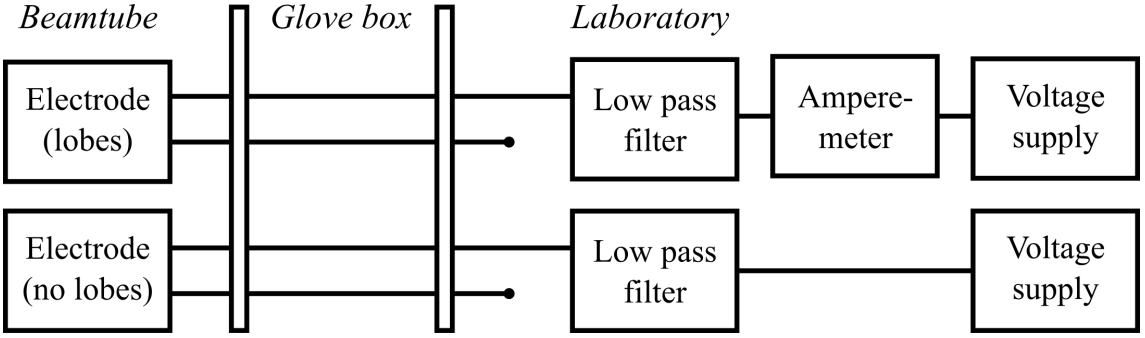

Figure VI.8.: **Voltage supply of the dipole electrodes.** The same stable voltage supply and low pass filter as for the ring electrodes are used, in order to reduce high-frequent noise. An amperemeter inside the voltage supply allows to measure the neutralisation current from ions which are removed with the dipole electrodes (see section VII.2.2). The voltage at the dipole electrodes is not monitored in order to not spoil the current measurement; therefore, the redundant cables are not connected, but accessible from outside the glove box.

However, a direct measurement of the integral voltage ripple showed that the stability requirements are met[14]:

$$f > 100 \text{ kHz} : U_0 < 2 \text{ mVpp}, \tag{VI.5}$$

$$10 \text{ Hz} < f < 100 \text{ MHz} : U_0 < 5 \text{ mVpp}. \tag{VI.6}$$

The measurement of the integrated voltage ripples in the two frequency bands is more meaningful than a measurement of the differential noise with a spectrum analyser for two reasons: first, the superposition of the voltage ripples from several ripple frequencies might exceed the limit of 5 meV on the energy shift, even if the ripple amplitudes of the discrete frequencies wouldn't; and second, the observation of the maximum voltage amplitude considers also noise with a rise time corresponding to the frequency f, whereas the spectrum analyser searches for periodic frequencies.

Field cabling All cables between the voltage supply and the beamtubes[15] are coaxial cables in order to minimise the induction of high-frequent electro-magnetic noise[16]. However, these cables had to be installed in common cable trays where they can pick up noise over a distance of about 10 m; the large frequencies of this noise will be removed by the low pass filters outside the glove box of the DPS.

Even inside the beam tube, the cables between the electrodes and the vacuum feedthroughs are coaxial cables with the shield on the ground potential of the beam tube. It has to be prevented, however, that the insulated cable mantles are charged by ions or electrons, which would create inadvertent blocking potentials. For this reason, the cables are wrapped transversally by another wire shield. This shield was replaced after First Light with a broader wire in order to narrow the gaps between the wire at the cable bends and in order to connect the cables to the beam tube potential. During First Light, some of these cables also still protruded into the flux tube, which could only be remedied after the campaign.

Low pass filters Although the voltage supply itself fulfills the stability requirements, high-frequency noise can be picked up by the roughly 15 m long field cabling between the voltage supply and the dipole electrode. In order to remove this noise, low pass filters are installed in the field cabling as close as possible to the beam tube, but outside the glove box around the DPS. The low pass filters for the dipole electrodes consist of two RC filters, chained to a double Π element with three capacitors of 10 nF and two resistances of 4.7 MΩ.

Amperemeters Amperemeters are included in the voltage supplies of the electrodes with lobes in order to measure the neutralisation current of the ions (see section VII.2.2). Because the amperemeters may produce high-frequency noise which

[14] These measurements were carried out by Sascha Wüstling (KIT-IPE). The results are valid both for a load of 1 MΩ and for full load when 500 V and 10 mA are drawn from the device. Also, the control input for $(0 \dots 5)$ V was observed to be not sensitive to noise on the control voltage.

[15] Coaxial cables of ~ 10 m run from the highly stable voltage supplies to the top of the glove box around the DPS. There, an amperemeter might be included with a short cable right in front of the low pass filters. The cables between the low pass filters and the glove boxes are on the order of 30 cm; those from the glove box feedthroughs to the beam tube are about 3 m long.

[16] The field cabling was installed by Alexander Jansen, Heike Bolz and Moritz Hackenjos.

may influence the neutrino mass measurements, low pass filters are installed in the voltage supply as shown in figure VI.8. A USB connection serves for read out and voltage supply; in case this connection is interrupted, the amperemeters have a resistance of 1.2 MΩ.

No voltage monitoring The voltage at the dipole electrodes will not be monitored via a redundant cable like in case of the ring electrodes (see figure VI.7). This is due to the current measurement at the dipole electrodes: a background current would be created from the voltage supply over the electrode to the voltage monitor. Also, some of the current from ion neutralisation would flow through the voltage monitor instead of the amperemeter, which increases the minimal detectable ion flux. All in all, the measurement uncertainty on the absolute ion flux would be increased. A monitoring of the voltage between the amperemeter and the voltage supply was discarded, too, because it hardly yields any additional information compared to the internal monitoring of the voltage supply.

VI.3. Ion flux reduction in the PS

Blocking and removing the large tritium ion flux from the WGTS has to be accomplished entirely by the ring and dipole electrodes in the DPS: only there will the neutralised tritium be pumped off without risk of residual tritium activity in the MS. However, non-tritium ions can also be generated downstream from the DPS by ionisation of residual gas (see section III.5). Even these ions would create background to the neutrino mass measurements if they would in turn ionise the residual gas in the MS. Only about 10 ions/s are allowed for this reason to flow into the MS (see section V.2.2).

The flux of non-tritium ions into the PS can be blocked with positive potentials at the three ring electrodes upstream, between and downstream from the PS and MS. However, at least the ring electrode upstream from the PS is assumed to also create ions in a Penning discharge, based on observations during First Tritium (see section IX.2.2).

An alternative way of preventing the ions from entering the MS is the high voltage of the PS: negative ions will be blocked, while positive ions are accelerated into the walls of the PS vessel (see section IV.1). According to table IV.1, a reduction of the ion flux by more than four orders of magnitude can be achieved when at least the downstream cone electrode is set to -400 V. During First Light, only a reduction factor of 700 could be verified for 1 kV at the PS vessel and an ion pencil beam in the center of the flux tube (see section VIII.5.2).

The transmission probability for positive ions through the PS during the neutrino mass measurements will depend on the high voltage settings of the PS. These settings are however still being discussed with regard to the reduction of the MS background by beta electrons and Penning discharges. The following comprehensive list will detail these issues along with the implications of the PS high voltage for tritium ion safety:

- **Reduction of the beta electron flux into the MS** According to the KATRIN design report [CDR04], the PS should reduce the beta electron flux into the MS by six orders of magnitude in order to minimise the background component arising from ionisation of residual gas. For this purpose, the PS high voltage should be set to ≈ 300 eV below the endpoint energy of the tritium beta spectrum, i.e. about -18.3 kV. The setting of the inner electrodes has to be chosen such as to achieve an energy resolution of $\Delta E \approx 100$ eV; then the beta spectrum remains undistorted down to 200 eV below the end point energy, which is much larger than the 30 eV nominal scanning interval during the neutrino mass measurements.

- **Penning discharge between the spectrometers** Strong Penning discharges have been observed between the two spectrometers when the PS was operated at high potential at an elevated pressure of $\sim 10^{-9}$ mbar in the unbaked vacuum-setup [KFL18, Val09, Fra10, Hil11, Pra11]. The electrons from the discharge can reach the FPD and do not only create a large background but could even damage the detector – in order to prevent this, the PS high voltage would need to be reduced. However, no Penning discharges have been observed

so far at nominal spectrometer pressures of $< 10^{-10}$ mbar. The final setting of the PS high voltage during the neutrino mass measurements is therefore still in discussion.

- **Reduction of the ion flux into the MS** The flux of tritium ions into the PS has to be reduced to about $1 \cdot 10^4$ ions/s in order to prevent background by tritium decay (see section V.2.1). An even stricter limit of only about 10 ions/s into the MS applies even to non-tritium ions, because they could create background in the MS via the ionisation of residual gas (see section V.2.2).

  The negative high voltage of the PS will block all residual negative ions and accelerate the positive ions into the vessel walls, as described in section IV.1. According to table IV.1, the positive ion flux into the MS could be reduced by at least four orders of magnitude if at least the downstream cone electrode is set to -400 V. This voltage setting should therefore at least be applied whenever the valve V4 between the CPS and PS is open while tritium is being circulated in the source.
  As for the tritium flow into the MS however, no larger reduction than two orders of magnitude can be achieved due to the diffusion of neutral tritium (see section IV.3): about half of the implanted tritium atoms will reemerge from the vessel walls eventually; about 1% of the tritium ion flux into the PS will therefore eventually reach the MS as neutral tritium. In order to match this tritium flux reduction by about two orders of magnitude, already -400 V at the downstream cone electrode are sufficient according to table IV.1 in section IV.1.

- **Ion detection via PS cone current** The positive ion flux is almost entirely accelerated onto the downstream cone electrode of the PS, where the ion neutralisation creates a detectable current: this allows the constant monitoring of the ion flux into the PS during the neutrino mass measurements (see section VII.2.4). The probability of the ions to reach the downstream cone electrode is about 20% at the nominal voltage of -18.3 kV (see table IV.2 in section IV.1). Due to technical constraints of the amperemeter, which floats on the electric potential of the PS vessel, the voltage of the downstream cone electrode is limited to ± 500 V relative to the PS vessel voltage.

- **Ion detection via ionisation in the PS** The most sensitive ion detection method in the KATRIN experiment is via ionisation of the residual gas in the PS: when the ions are accelerated in the negative high voltage of the spectrometers, their cross section for inelastic scattering on the residual gas increases strongly (see section IV.2). The large ionisation efficiency can be used in order to detect the ions via the secondary electrons which are produced (see section VII.1).

  In fact, this ion detection method proved suitable to measure the smallest ion fluxes among all ion detectors during the First Tritium campaign (see section IX.4.4). Blocking the most energetic beta electrons requires a high voltage above the tritium endpoint of about -18.6 kV, and the detection of the secondary electrons requires a more negative potential in the PS than in

the MS. Obviously, these high voltage settings will not be used during the neutrino mass measurements.

With regard to ion safety, a PS high voltage of −18.3 kV as specified in the KATRIN design report seems best suited. Yet, a minimal PS voltage of −400 V at the inner electrodes would agree with the same requirements as well.

VI.4. Monitoring of the ion blocking in the DPS

Not more than $1 \cdot 10^4$ ions/s are allowed to enter the PS due to the MS background and radiation protection (see section V.3). This requires the ion blocking with the DPS ring electrodes, which were discussed in section VI.1, and the ion removal with the dipole electrodes, which were detailed in section VI.2.

In order to monitor the actual voltage of the ring electrodes in the DPS, a redundant cable to the electrode can be used as shown in figure VI.8. The voltage of the dipole electrodes is not monitored, because this would affect the measurement of the ion neutralisation current (see section VII.2.2); nevertheless, the voltage supply monitors its own output voltage as opposed to its set voltage.

In case the ion blocking is no longer guaranteed, radiation protection measures will be triggered and the valve between the CPS and the PS will be closed. This implies that the KATRIN measurements will be interrupted. The trigger for radiation safety measures with regard to ions has been defined based on two conditions:

- One of the two ring electrodes in DPS BT5 and PP5 must always have a voltage larger than +120 V.
- The minimum voltage of any of the two ring electrodes must be 120 V more positive than the voltage of any single electrode at the four dipole electrodes – otherwise, ions which are created inside the dipole electrode potentials would see effectively a smaller blocking potential than 120 V.

However, monitoring the voltage of the ring electrodes cannot detect the neutralisation of the electric potential by a negative space charge of secondary electrons (see section III.6.3). These secondary electrons might be created inside the positive potential by inelastic scattering of beta electrons on residual gas; the creation rate would be additionally increased by a Penning discharge inside the ring electrode, as presumably observed in the PP5 electrode during First Tritium (see section IX.2.2).

While the neutralisation of the blocking potentials cannot be observed directly, it is possible to monitor the most relevant observable for ion safety: the residual ion flux into the PS can be measured with several of the ion detectors which will be presented in the following chapter. Most notably, the current measurement at the PS downstream cone electrode allows a constant monitoring of the ion flux into the PS (see section VII.2.4); this detector will trigger the closing of the valve between the CPS and PS in case the ion flux rises above the radiation safety limit of $2 \cdot 10^8$ ions/s.

VII. Ion detection

An ion flux limit of $1 \cdot 10^4$ ions/s into the PS was imposed in section V.3 to restrict the MS background from tritium ions to about 1 mcps. The required reduction of the tritium ion flux from the WGTS can be achieved with the positive blocking potentials of the ring electrodes from the previous chapter; but if secondary electrons accumulate inside the positive potential wells, they might neutralise the blocking potentials (see section III.6.3). For this reason, the residual ion flux has to be measured directly.

Seven different detection methods can be used in order to measure ions in the beamline. Figure VII.1 shows these detectors starting at the source and going towards the FPD:

- **DPS dipole current:** The removal of positive ions via $E \times B$-drift (see section VI.2.1) creates a neutralisation current on the DPS dipole electrodes.
- **FT-ICR:** Fourier Transform Ion Cyclotron Resonance can be applied with a dedicated unit in the DPS BT5. This allows to distinguish ion species with different charge-to-mass ratios.
- **Faraday cup:** A Faraday cup board can be inserted into the flux tube with the Forward Beam Monitor (FBM).
- **PS cone current:** 20% of the positive ions which enter the PS are accelerated by the negative potential onto the PS downstream cone electrode; their neutralisation current can be measured.
- **Ionisation in the PS:** The accelerated ions in the PS ionise in turn the residual gas and create secondary electrons, which can be measured with the FPD.
- **Ionisation in the MS:** The ionisation measurement with the MS works just like in the PS. However, only a fraction of the ions which enter the PS will be transported also to the MS.
- **PULCINELLA:** The PULCINELLA disc was designed for the determination of the absolute detection efficiency of the FPD; it can however also be used to measure the neutralisation current of charged particles from the MS or even upstream of it.

This chapter will present all of these seven ion detection methods. In the first section, the ionisation method in the PS and MS is treated. Section VII.2 covers all current measurements together, including the statistical evaluation of their results and systematic effects. Then the FT-ICR is discussed in section VII.3.

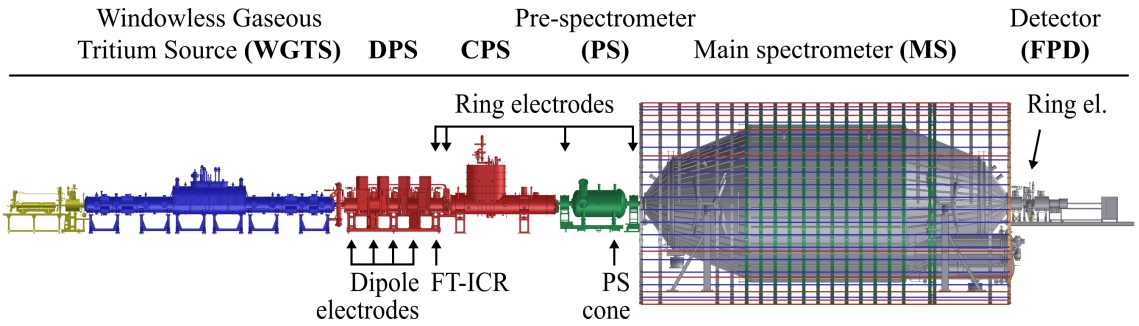

Figure VII.1.: **Position of the ion detectors in the beamline.** All charted detectors measure a current from ion neutralisation, except for the FT-ICR unit in the DPS. Additionally, the ionisation method can be used with the Pre- and Main spectrometer.

During the neutrino mass measurements, the ion flux into the PS needs to be monitored to the level of $1 \cdot 10^4$ ions/s (see section V.3). Several of the presented ion detectors can be used for that purpose, with different advantages regarding the minimum detectable ion flux, the continuity of the monitoring and their location in the beamline (see section VII.4). As will be explained in section VII.5, it is in contrast not possible to monitor the plasma parameters which can cause systematic effects (compare discussion in section V.5).

VII.1. Ionisation in the spectrometers

When the positive ions enter the negative potential of either the Pre- or the Main spectrometer, they will be accelerated by the negative potential into the stainless steel walls and electrodes. On their way across the spectrometer, the ions in turn ionise the residual gas (see section IV.2). The secondary electrons will follow the magnetic guiding field and are partially detected by the FPD. From the measured FPD rate R_{FPD}, the incoming ion flux Φ_{ion} can be derived with the ionisation efficiency $\mathcal{E}$ from section IV.2:

$$\mathcal{E} = \frac{R_{\mathrm{FPD}}}{\Phi_{\mathrm{ion}}} \approx s \cdot n \cdot \sigma \tag{VII.1}$$

A qualitative understanding for the ionisation probability and the systematic effects of the ion detection via ionisation can be obtained from the probability $\mathcal{P}$ for inelastic scattering of the ions (see section IV.2). This model predicted also quantitatively the ionisation efficiency in the MS within a factor 2 of the result from the First Light measurements (see section VIII.2.3). In contrast to the predicted linear pressure dependence, however, preliminary results of the STS IIIa commissioning measurements in October 2018 indicated a pressure-independent and larger-than-expected ionisation efficiency in the PS; the cause for these observations is so far unknown. In the following, the current understanding of the ionisation method will therefore be summarised based on the inelastic scattering probability $\mathcal{P}$:

- **Ion path length s:** The longer the path of the ions through the spectrometer, the larger their probability to scatter inelastically. Therefore, the ionisation probability inside the MS is about ten times larger than in the PS at the same pressure and high voltage settings. A more refined estimate of the ion path length given their deflection by the negative potential requires dedicated simulations with KASSIOPEIA.

- **Gas density n:** The scattering probability depends on the gas density $n = p/(kT)$ inside the spectrometer, which follows from the pressure p, the Boltzmann constant k and the temperature $T \approx 300$ K. Consequently, a linear increase of the ionisation efficiency with the spectrometer pressure is expected so that the PS pressure was increased with argon during the First Tritium measurements (see section IX.1.4). Instead, preliminary results of the STS IIIa measurements from October 2018 indicate a pressure-independent ionisation efficiency in the PS.

  Pressure-independence of the ionisation method have several advantages: this would removethe practical challenge to create stable and reproducible argon pressure, as it was the case during the First Tritium campaign (see section IX.1.4.1); instead, ionisation measurements could be performed quickly between neutrino mass runs. Further, the determination of the measurement pressure includes some of the largest uncertainties for the ionisation efficiency; especially in the MS, the pressure can only be measured with a pressure gauge in a pump port behind a cold baffle, which might however differ significantly

from the pressure in the flux tube. Whether the pressure-independence applies also to the MS is, however, unknown.

- **Inelastic scattering cross section σ:** The cross section for inelastic scattering depends on the species of the impinging ions and the target molecules. In general, the cross section increases with the energy of the impinging ions (see figures in section IV.2). In order to maximise the ionisation efficiency, a large high voltage should be applied during the measurement to the spectrometer which is supposed to be used for the detection; a high voltage of -18.6 kV is necessary in order to prevent background by beta electrons during tritium measurements.

- **Detected secondary electron rate $R_{\mathbf{FPD}}$:** Not all of the secondary electrons from the ionisation processes will reach the FPD; instead, they will leave the spectrometer towards the source. In order to detect as many secondary electrons as possible, the inner electrodes on the upstream side of the spectrometer are set more negative than the downstream electrodes; the resulting slide potential drives the secondary electrons to the FPD. This electrode settings was used during most of the First Light and First Tritium measurements. The corresponding detection efficiency for the secondary electrons can be simulated with KASSIOPEIA.

The minimum detectable ion flux depends on the background rate from the respective spectrometer and – as always – on the desired significance as compared to a background fluctuation. Some of the background can be cut away with an energy region of interest (ROI) around the expected energy of the secondary electrons from the spectrometer potential at the FPD. A dedicated myon veto can cut away a small contribution of 5 mcps from the intrinsic background of the FPD – this is however negligible compared to the observed backgrounds in the PS and MS, as discussed below.

Both the PS and the MS can be used in order to measure the ion flux via ionisation. The PS method is however strongly preferred in order to prevent the tritium ions from entering the MS. Also, the ion flux into the MS might be smaller than the ion flux into the PS because not all ions are be transported through the weak magnetic field of the PS (see section VIII.5). And ultimately, the ion flux into the PS is the actually relevant observable in order to limit the background by tritium activity in the MS (see section IV.3).

Ionisation in the PS For ionisation measurements in the PS, the MS has to be at a smaller high voltage than the PS so that the secondary electrons reach the FPD; a slightly negative MS potential may be chosen, though, in order to improve the adiabaticity of the electron transport through the MS.

During the First Tritium measurements, the ionisation method was used with the PS. Although the method was dominated by background Ar^+ ions, a conservative upper limit on the ion flux into the PS of $1 \cdot 10^4$ ions/s could be derived (see section IX.4.4). To this end, the pressure-dependent ionisation efficiency $\mathcal{E}$ had been

derived from the KASSIOPEIA simulation result[1], which was stated in table IV.2:

$$\mathcal{E} = 1.0 \cdot 10^{-6} \text{ counts/H}^+ \text{ ion at } -18.3 \text{ kV and } 1 \cdot 10^{-10} \text{ mbar Ar.} \quad \text{(VII.2)}$$

During the STS IIIa commissioning measurements, however, a pressure-independent ionisation efficiency was observed in the PS with deuterium ions. According to the preliminary results, the absolute value of the ionisation efficiency was also much larger than expected at $\mathcal{E} = 2 \cdot 10^{-3}$ counts/ion. While the reason is unknown, this would allow to detect an ion flux of about 1000 ions/s almost instantaneously[2]. This ultra-precise measurement could be applied regularly within about 10 min between neutrino measurement runs.

There is also a maximum ion flux which can be detected via ionisation, because the secondary electron rate should be limited to $< 10^6$ cps in order to not damage the FPD. For the pressure-independent ionisation efficiency of $\mathcal{E} = 2 \cdot 10^{-3}$ counts/ion follows a maximum detectable ion flux of $5 \cdot 10^8$ ions/s.

Ionisation in the MS: For ion detection via ionisation in the MS, the PS high voltage has to be ramped down in order to let the ions enter the MS. During First Light, the PS was usually grounded (see section VIII.2); a slightly negative potential of about -1 V at the PS is preferred in order to prevent inadvertent ion blocking by work function differences (see section III.6.2).

The ionisation efficiency in the MS was measured during the First Light campaign, but with large systematic uncertainties as explained in section VIII.2.3. A conservative estimate of the ionisation efficiency is according to section IV.2:

$$\mathcal{E} \approx 2 \cdot 10^{-6} \text{ counts/ion at } -18.6 \text{ kV and } 1 \cdot 10^{-10} \text{ mbar } H_2. \quad \text{(VII.3)}$$

Using this ionisation efficiency, the minimum detectable ion flux can be calculated. After 15 min, an ion flux of about $3 \cdot 10^4$ ions/s could be distinguished[3] with 3 sigma significance from the intrinsic MS background of about 400 mcps. The maximum ion flux should be limited to $5 \cdot 10^{11}$ ions/s at $1 \cdot 10^{-10}$ mbar H_2 in order to not exceed 10^6 cps at the FPD – such a large ion flux could however only be reached during commissioning measurements, because the expected tritium ion flux from the WGTS is only $2 \cdot 10^{11}$ ions/s (see section III.2.1).

During the STS IIIa commissioning measurements, a pressure-independent ionisation efficiency was observed in the PS according to preliminary results. Because the reason is unknown so far, it is not clear whether the ionisation efficiency in the MS might be pressure independent as well. Investigation this requires additional information.

[1] Simulations by Woo-Jeong Baek.

[2] The measurement would be limited by a background of about 10^3 H_2^+ ions/s, which would be created by beta electrons from the about $5 \cdot 10^{-10}$ mbar residual H_2. This large residual pressure is the result of the removal of the getter pumps from the PS, which was decided end of October 2018. The intention is to mitigate background in the MS from radon which emanates from the getter pumps in the PS.

[3] The calculation via $\Phi_{\text{ion}} = R_{\text{FPD}}/\mathcal{E}$ assumes that a one sigma deviation of 20 mcps can be distinguished from the background of 400 mcps after 15 min.

VII.2. Current measurements

Several electrodes in the beamline allow to measure ions via the neutralisation current which the ions induce as they impinge on the surface. One way for the ions to reach the electrode is to insert the electrode into the flux tube: this is the case for the Faraday cup at the FBM and the PULCINELLA disc in front of the FPD. It is however also possible to drift the ions onto the electrode, as do the DPS dipole electrodes, or to accelerate the ions sufficiently so that they leave the magnetic flux tube non-adiabatically – this is the case in the negative potential of the Pre-spectrometer, where 20% of the ions hit the downstream cone electrode.

This section will first discuss the basic detection principle of the current measurements via ion neutralisation on an electrode. Then the four ion detectors are discussed according to their order in the beamline: first the DPS dipole electrodes (section VII.2.2), then the Faraday cup at the FBM (section VII.2.3), the PS cone current measurement (section VII.2.4 and finally the PULCINELLA disc near the FPD (section VII.2.5). All of these detectors can be analysed with the same statistical methods, which will be presented in section VII.2.6, and are subject to the same systematic effects, as discussed in section VII.2.7.

VII.2.1. Detection principle: ion neutralisation current

When the ions reach the surface of a conducting material, they will be neutralised. If the corresponding surface is an electrode, the charge compensation draws a current from the voltage supply. This current can be measured with an amperemeter between the voltage supply and the electrode.

The measurement of the neutralisation current I in Ampere (Coulomb per second) allows to calculate the ion flux Φ_{ion} onto the electrode:

$$\Phi_{\text{ion}} = I \cdot C, \tag{VII.4}$$

where $C = 6.2415 \cdot 10^{18}$ elementary charges per Coulomb [FeP09]. This assumes reasonably that all ions are singly ionised (compare section III.2.1). Whether the ions are positive or negative depends on the sign of the electrode or in more complex cases on the electrode setup.

Systematic effects like secondary electron emission might however affect the trueness of this ion flux measurement, as will be discussed in section VII.2.7. Apart from that, the above conversion is the basis for the statistical analysis which will be presented in section VII.2.6.

There are however various ways how the ions reach the electrode surface: the electrode can be inserted into the flux tube, like for example the Faraday cup board at the FBM (section VII.2.3) or the Pulcinella disc (section VII.2.5); in the negative potential of the PS, the positive ions will be accelerated until they leave the flux tube non-adiabatically and bombard the downstream cone electrode (section VII.2.4); or the ions are drifted perpendicular to the magnetic field in a dedicated dipole potential via $E \times B$-drift, as will be discussed in the following section.

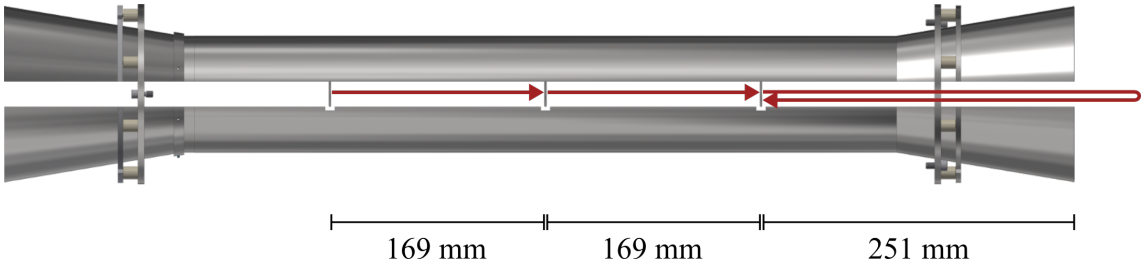

Figure VII.2.: **Ion detection efficiency of the dipole electrodes.** The calculation assumes that the ions are trapped inside one single dipole. Two times, the ion can hit a lobe while passing through the center of the dipole. For the third time, the ion has to be reflected which leads to a total path of 502 mm inside the dipole field.

VII.2.2. DPS dipole electrodes

Inside the electric dipole field of the dipole electrodes, the ions are drifted perpendicular to the flux tube via the $E \times B$-drift which was introduced in section VI.2.1. Eventually, the ions hit the electrode surface and create a neutralisation current, which can be measured with an amperemeter in the voltage supply of the dipole electrodes. The electronic layout of the voltage supply was shown in section VI.2.4 in figure VI.8.

The measurement of the neutralisation current at the dipole electrodes allows to monitor the ion flux from the WGTS during the neutrino mass measurements. Also, the ion transport through the DPS can be observed: during First Tritium, only the dipole electrode in DPS BT1 detected an ion flux from the WGTS[4] due to inadvertent ion blocking in the DPS (see section IX.3). This even allowed to monitor the residual ion flux downstream from the inadvertent blocking potentials, as will be discussed in section VII.4.

During the First Tritium measurements (see section IX.1.1), the measurements of 5 min signal and 5 min background were mostly limited by the electronic noise. This allowed to detect currents down to 2 pA at 1σ significance, corresponding to a 3σ minimal detectable flux of $3 \cdot 10^7$ ions/s (see section IX.1.1.3). Measuring such small currents is possible because the four rbd 9103 picoampemeters have a minimum measurement range[5] of 2 nA with an accuracy of 0.5% on the measurement value or at least 0.5 pA. During the neutrino mass measurements with $> 95\%$ tritium concentration, the expected ion flux is however larger; then the measurement range of 20 nA may be used, which offers also 0.5% relative uncertainty or at least 3 pA.

The data acquisition by a LabView program via USB allows down to 400 ms measurement intervals for all four amperemeters at the same time. The integration time of the RC elements was not observed to affect the current measurement so far: during the First Tritium measurements, the ion induced current rose instantaneously when the valve V1 between the WGTS and DPS was opened (see figure IX.2).

[4]The cable to the BT2 dipole was damaged, but no ions were observed in the BT3 or BT4 either.
[5]The maximum detectable current of the rbd 9103 is 2 mA or $1 \cdot 10^{16}$ ions per second.

Detection efficiency Actually, the ions would follow the equipotential lines of the electric field, which lead in circles around the dipole electrodes (compare figure VI.5). In order to neutralise the ions, perpendicular lobes are attached to one of the electrodes as shown in figure VII.2: the ions hit these lobes due to their longitudinal motion through the dipole electrode along the magnetic field.

The detection efficiency of the dipole electrodes at their nominal voltage setting can be calculated via the probability that the ions miss the lobes: if the drift is too strong, the ions might leave the dipole before they hit a lobe on their motion along the magnetic field. The calculation is carried out in appendix A.7 for each dipole electrode individually; this corresponds to the case that the ions are trapped inside the dipole, for example because of inadvertent blocking potentials or because the ion lost energy by scattering on neutral gas inside the dipole.

Table VII.1 shows the results: the small dipole potential in BT1 allows to detect all of the removed ions, but only 37% of the removed ions are also neutralised on the lobes in BT4. Of practical relevance is the case that the ions are trapped in the whole DPS and can be removed by either of the four dipoles: multiplication of the individual detection efficiency with the ion removal probability of each dipole (compare section VI.2.3) leads to the total detection probability. According to table VII.1, the BT1 dipole electrode should measure 8% of the total ion flux from the DPS, whereas both dipoles in BT3 and BT4 would measure 17%. In total, at least 54% of the ions from the WGTS would be detected.

The lobes are usually welded to the upper electrode of the dipole, but attached to the lower electrode in BT4. In order to drift the ions with all dipole to the same direction, the lower electrode with the lobes has to be the more positive one. Therefore, ions might be rejected by an effectively positive potential if they lost kinetic energy by scattering with neutral gas inside the dipole potential. Whether the ions could leave the dipole by circling around the upper electrode needs to be investigated with simulations, for example in KASSIOPEIA.

Table VII.1.: **Ion detection probabilities.** For each individual dipole electrode, the detection efficiency was calculated in appendix A.7. Multiplied with the ion removal probability from section VI.2 follows the total detection probability for the case that the ions can reach all four dipole electrodes. At nominal dipole voltage settings, only 54% of the ion flux from the WGTS will be detected.

Dipole electrode	BT1	BT2	BT3	BT4
Upper electrode	−15 V	−35 V	−85 V	−175 V
Lower electrode	−5 V	−5 V	−5 V	−5 V
Individual detection efficiency	100%	74%	56%	37%
Removal probability	8%	17%	30%	45%
Total detection probability	8%	12%	17%	17%

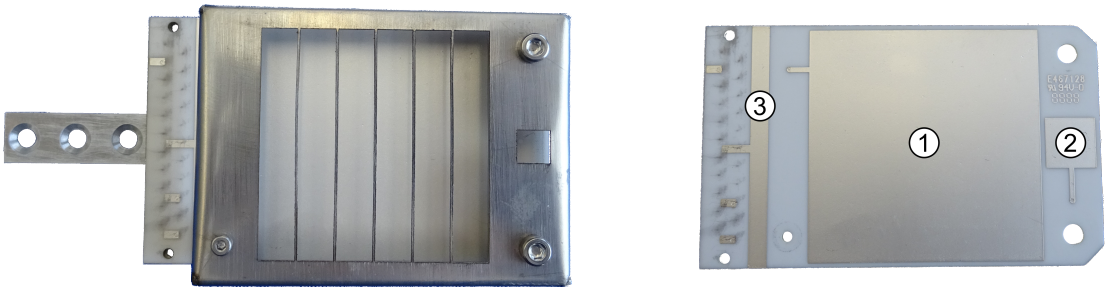

Figure VII.3.: **Faraday cup board for the FBM.** Left: Circuit board with shield on top and backplate below. Right: Silver printed conductor paths on the circuit board form a large (1) and small (2) Faraday cup. Four pads on the left side of the board provide electrical connection to the pogo pins of a custom-made D-Sub plug, which is not shown. Between the pads and the shield, a grounded strip (3) prevents charging of the ceramics board by beta electrons. Due to this strip, the conducting paths run partially on the backside of the board.

VII.2.3. Faraday Cup at the Forward Beam Monitor (FBM)

A Faraday cup board at the Forward Beam Monitor (FBM) was designed to measure the residual ion flux and the beta electron flux downstream from the ring electrodes, but with still closed valve V4 between the CPS and PS. The lever arm of the FBM allows to move the Faraday cup board through the flux tube.

During the First Tritium campaign, the measured beta electron flux was however found to be 50 times smaller than expected (see section IX.1.2). An overview of the measurement setup will be given in the following nevertheless.

The Faraday cup at the FBM consists of the following four components:

- **The circuit board** contains the silver printed conductor paths (see figure VII.3). Two areas serve as Faraday cups: a large cup (1) for a small minimal detectable ion flux and a ten times smaller cup (2) optimised for spatial resolution.

  The strip (3) is kept at ground potential in order to prevent charging of the board by beta electrons between the shield and the D-Sub plug, which will be discussed below. Charging could lead to electrical discharges which might damage the Faraday cup, or to electric potentials which could reject beta electrons; all other parts of the board will be covered by the metal shield and the D-Sub plug.

  At the side of the board, four pads allow the electric connection with the pogo pins of the D-Sub plug. Due to the grounded strip, the conductor paths run on the backside of the board.

- **The shield and its grid** retain the secondary electrons which are ejected by the keV-beta electrons from the Faraday cup surface. Electrical contact to the voltage supply is maintained via a metal stand-off, which is screwed to a conducting path on the backside of the board.

- **The backplate** provides mechanical stability to the circuit board and mounts it to the FBM front end. Due to the conducting paths on the back of the board, the backplate actually consists of several branches; this prevents also current induction in case a superconductor quenches. The backplate is on ground potential due to its connection to the lever arm.

- **The D-Sub plug** is attached to the FBM cabling. It is pressed with two small screws onto the board. Four of the 22 pogo pins inside the custom made plug contact the pads on the circuit board and provide the electrical contact between the two Faraday cups, the shield and the grounded strip to the voltage supply outside the vacuum. An own metal shield on top of the plug prevents it from being charged by the keV-beta electrons.

Three different types of particles can be measured with different voltages on the grid and the Faraday cup areas on the board surface, as summarised in table B.1:

- **Beta electrons** cannot be blocked from reaching the board surface and neutralising on it, because the FBM cabling is not laid out for high voltages; instead, the background from beta electrons needs to be measured first and then to be subtracted from the measurement with low energetic particles. In order to measure only beta electrons, the positive ions can be rejected with a retarding voltage of +2 V on the board surface. Secondary electrons from the board are retained with −20 V at the grid, in order to increase the trueness of the measurement.

- **Positive ions** with thermal energies can be measured with −2 V on the board surface, which prevents any blocking by work function differences. The grid remains at −20 V.

- **Secondary electrons and negative ions** from the WGTS with thermal energies can be measured if the shield is at +2 V, in order to prevent blocking by work function differences. The board surface is set to +20 V, so that secondary electrons are still rejected by an effectively negative potential at the grid.

Table VII.2.: **Measurement modes of the Faraday Cup.** Positive potentials at the board reject positive ions, negative potentials reject negative ions and secondary electrons. The potential of the shield is always more negative than the board in order to retain secondary electrons.

Investigated particles	Shield	Board
Beta electrons	−20 V	+2 V
Positive ions	−20 V	−2 V
Secondary electrons and negative ions	+2 V	−20 V

The Faraday Cup will cover only 8.2% of the flux tube. A precise assessment of the detection efficiency needs however to take into account the radial concentration profiles of the respective particles in the flux tube. The small Faraday cup was designed in order to measure the relative radial concentration profile. Positioning the Faraday cup in the center of the flux tube allows however a conservative upper limit on the total flux.

During First Tritium, the current of the large Faraday cup was read out with a Keithly 6514 picoamperemeter; the identical device was used with the Faraday cup ring in ELIOTT during First Light (see section VIII.1) and the same type of picoamperemeter is also used for the current measurement at the PS cone electrode (see next section). For details on the electric cabling, see appendix B.3.

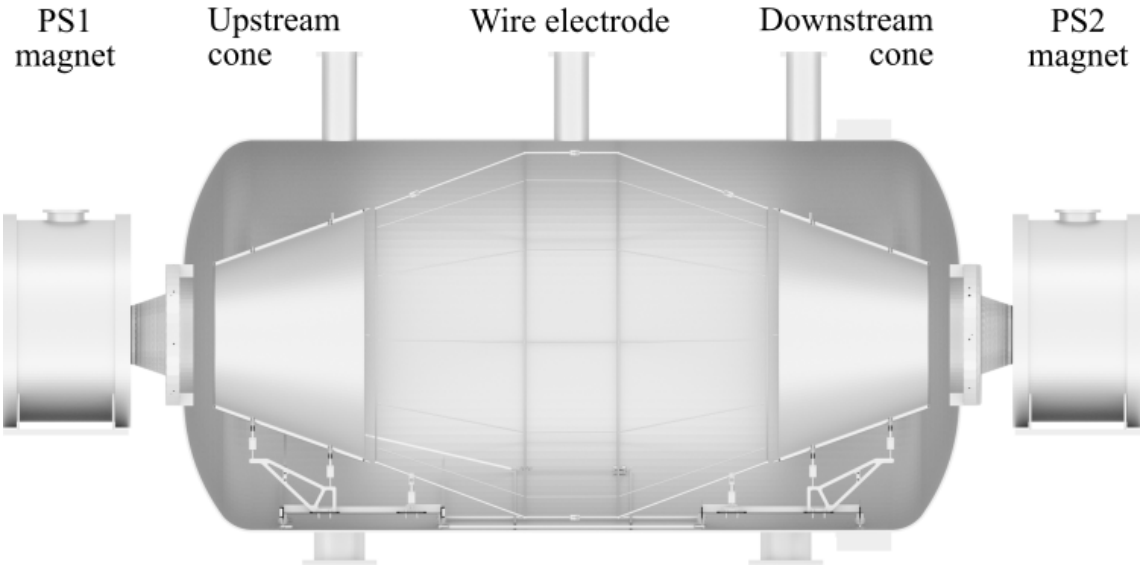

Figure VII.4.: **PS downstream cone electrode.** About 20% of the ions which start in the PS1 superconducting magnet arrive on the downstream cone electrode, while the others go through the wire electrode onto the vessel walls. The neutralisation of ions on the solid electrode creates a current in the voltage supply, which can be measured with an amperemeter as shown in figure VII.5.

VII.2.4. PS downstream cone electrode

When the positive tritium ions enter the potential of the PS, they will be attracted towards the surfaces on negative high voltage. According to section IV.1, 20% of the ions will be neutralise on the downstream cone electrode at nominal PS high voltage. The resulting current in the voltage supply of the cone electrode can be measured with an amperemeter, as depicted in figure VII.5.

The PS current measurement monitors the residual ion flux into the PS during the tritium measurements with about one measurement per second. If an ion current larger than 5 mA was detected for three measurements in a row, the valve between the CPS and PS would be closed automatically in order to protect the spectrometers from the tritium flow. With the ion detection efficiency of about 20% follows a threshold of $2 \cdot 10^8$ ions/s at nominal PS high voltage; this corresponds exactly to the ion flux limit into the PS from radiation protection. In fact, even smaller ion current will cause the closing of the valve if they occur long enough. Figure VII.6 shows the relation between measurement time, trigger threshold and ion current according to the calculations from appendix A.11. In order to prevent false alerts, the LabView program discriminates currents induced by voltage changes at the PS vessel and downstream cone electrode by reading out the PS voltage settings. Also, the V4 closure could be switched off manually, which was used at the beginning of the First Tritium measurements.

For a long-term analysis, the separate measurements from each second can be combined. Each measurement consists of the mean current μ of about $n = 14$ separate measurements. This μ is logged together with the standard deviation σ_μ of the

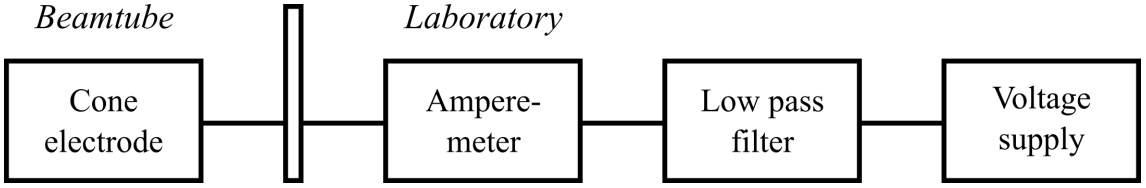

Figure VII.5.: **Current measurement at the PS downstream cone electrode.** The ion neutralisation creates a current between the electrode and the voltage supply, which can be measured with an amperemeter. A low pass filter removes high-frequent voltage noise in order to improve the precision of the current measurement.

measurement and the number of actual measurement values n. The overall mean current of an arbitrary analysis interval can be calculated along with its standard deviation from the statistics equations in appendix A.10.

The PS current measurement was found to be limited by short-term temperature oscillations in the spectrometer hall during First Tritium: these temperature oscillations induced current oscillations on the order of 50 fA (see section IX.1.3.2). The systematic effect can be averaged out after one oscillation period of 2 hours. In that case, a minimum ion flux of $4 \cdot 10^5$ ions/s can be distinguished from a background oscillation at 3σ significance (see section IX.1.3.3). This limit corresponds to a current of 12 fA; it can be reduced by more statistics to 3 fA, which is the minimum systematic uncertainty of the Keithley 6514 picoamperemeter.

The probability of 20% for the positive ions to reach the PS downstream cone electrode at nominal high voltage is the result of simulations from October 2018; previously, KASSIOPEIA simulations had indicated a detection efficiency of more than 99% (see section IV.1). Since the discrepancy between both simulations was not resolved until end of October 2018, the detection efficiency of 20% is used in this thesis as a conservative estimate. A larger detection efficiency of more than 80% is predicted by both simulations in case the PS vessel is grounded and only the downstream cone electrode is at −400 V.

A further improvement of the ion detection efficiency results from the emission of secondary electrons from the stainless steel surface of the cone electrode upon impact of the keV ions (see figure VII.10). The charge multiplication was measured during the STS IIIa commissioning measurements; preliminary results indicate an amplification of the ion current by about one order of magnitude, but further simulations will be required for the analysis.

The amperemeter floats on the potential of the electrode relative to the vessel potential. Due to the voltage limitation of the amperemeter in the voltage supply, not more than ±500 V can be applied to the downstream cone electrode. For the implementation of the current measurement, the existing iseg NHQ 205 M voltage supplies for the inner electrodes of the PS were used. In order to further suppress high-frequent noise on the voltage from the iseg devices, a low pass filter is installed between the voltage supply and the amperemeter. Leakage currents between the core conductor and the shield were reduced by the use of a triax cable between the amperemeter and the vacuum feedthrough at the PS vessel; this allows to apply the

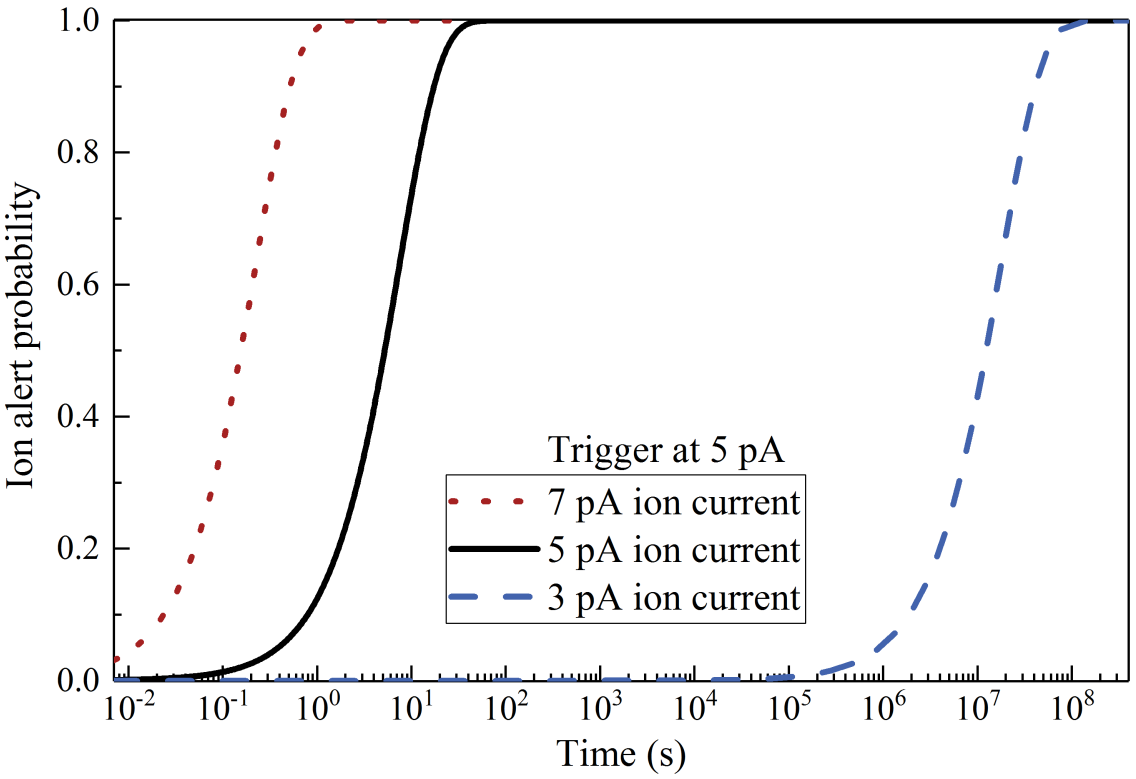

Figure VII.6.: **Probability of an ion alert by the PS current measurement.** At a threshold of 5 pA and an actual ion current of the same size, the alert would be triggered most probably within 1 min. In case of an ion alert, the valve V4 between CPS and PS would be closed automatically.

same potential to the inner shield as to the core conductor, while the outer shield is kept at vessel potential. In order to place it in a minimum of the magnetic field, the amperemeter is located in a distance of about 3 m distance from the center of the flux tube and about 3 m above the floor. Additionally, it is covered by a magnetic shield of about 5 mm thick steel.

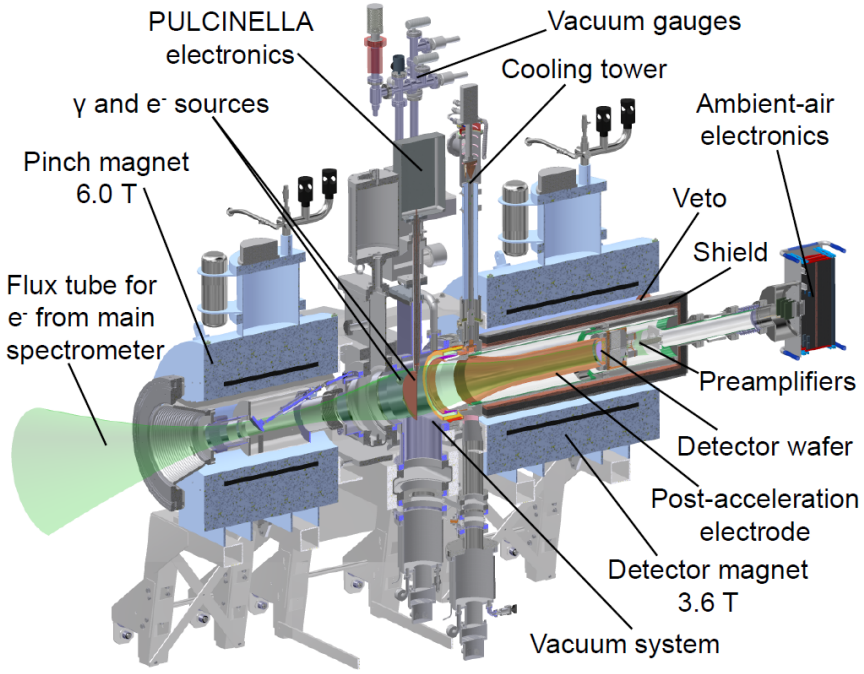

Figure VII.7.: **Detector setup including PULCINELLA.** The disc can be inserted into the flux tube between the MS and the FPD. Figure from [FPD15].

VII.2.5. PULCINELLA

The flux of charged particles from the MS to the FPD can be measured via a current on the PULCINELLA disc (Precision Ultra-Low Current Integrating Normalization Electrometer for Low-Level Analysis) [FPD15, Mar17]. This disc can be inserted mechanically into the flux tube between the pinch magnet and the detector magnet. In this position, the PULCINELLA disc covers the whole transmitted flux tube from the WGTS (for the flux tube transmission see section III.1.2).

PULCINELLA was originally designed to measure the absolute detection efficiency of the FPD. For this purpose, photoelectrons are ejected from the disc with a UV illumination on the detector side and the photocurrent is measured [FPD15]. However, PULCINELLA can also be used to measure the current of charged particles arriving on the disc from the source side. This was used to measure the positive ion flux from ELIOTT during First Light (see section VIII.2.3) and to measure the total beta electron flux during First Tritium (see section IX.1.6).

The current on the PULCINELLA disc is measured with a charge-integrating DDC-114 analog-to-digital converter (ADC) from Texas Instruments [FPD15, Mar17]. An accuracy of about 3% is achieved for pA currents [FPD15]. Around 600 pA, the meter goes into overflow. The ADC is controlled via a field programmable gate array (FPGA) on the meter board [FPD15, Mar17]. This meter board floats on high-voltage [FPD15, Mar17], but also voltages on the order of 10 V have been applied successfully; for example during the First Light campaign, as discussed in section VIII.2.3.

VII.2.6. Statistical analysis

The current measurements from the four previous sections use amperemeters with a precision of a few pA or even less: at the DPS dipole electrodes, the rbd 9103 can measure down to 2 pA (see section VII.2.2). A minimum detectable current of 3 fA can be achieved with the Keithley 6514 at the Faraday cup (section VII.2.3) and the PS downstream cone electrode (section VII.2.4). And even less than 1 fA could be reached in principle with the DDC-114 from Texas Instruments, which is used for the PULCINELLA measurement (section VII.2.5). Data sheets of these three amperemeters can be found in appendix B.2.

But the current measurements were limited by statistical fluctuations, presumably due to thermal noise. These fluctuations had a Gaussian distribution, as demonstrated by figure A.8: the histograms are based on the signal and background measurements from the time series plot in figure VII.8.

Each Gaussian distribution is characterised by its mean current and its peak half width. These parameters were estimated for the analysis with the sample mean and the sample variance [Cow98] as detailed in appendix A.10. Subtracting the mean current of the background measurement from the mean current in presence of an ion flux lead to the ion induced current, which can be converted into an ion flux with eq. VII.4. The statistical uncertainty of the ion induced current was estimated by adding quadratically the uncertainties on the mean currents from the signal and background measurements [Cow98].

The peak width of the Gaussian noise is a property of the setup and the measurement conditions. Obviously, the uncertainty σ_I on a single measurement current I does not depend on the number of measurements n in the sample. The uncertainty σ_μ of the mean μ does however decrease with n according to $\sigma_\mu = \sigma_I/\sqrt{n}$. For this reason, the length of the measurement or analysis interval is a trade-off between the statistical uncertainty and the uncertainty due to systematical effects, which will be discussed next.

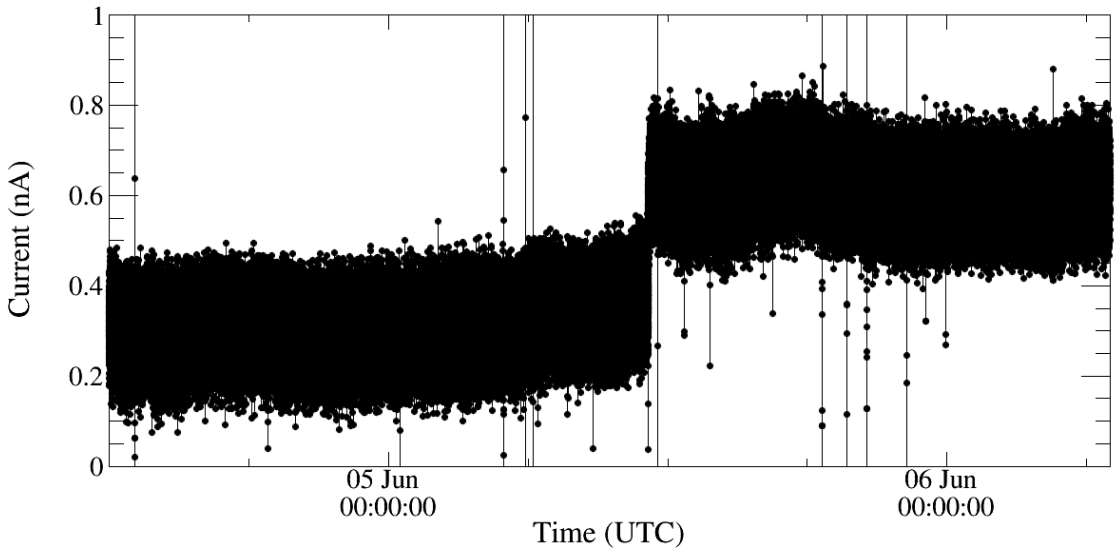

Figure VII.8.: **Time series of the DPS BT1 current** during the start of the First Tritium campaign. The valve V1 between the WGTS and the DPS was opened on June 5 at 11:09 h. Previously, only background current was measured; afterwards, a signal due to an ion flux from the WGTS was present. This time series plot reveals a drift of the background current.

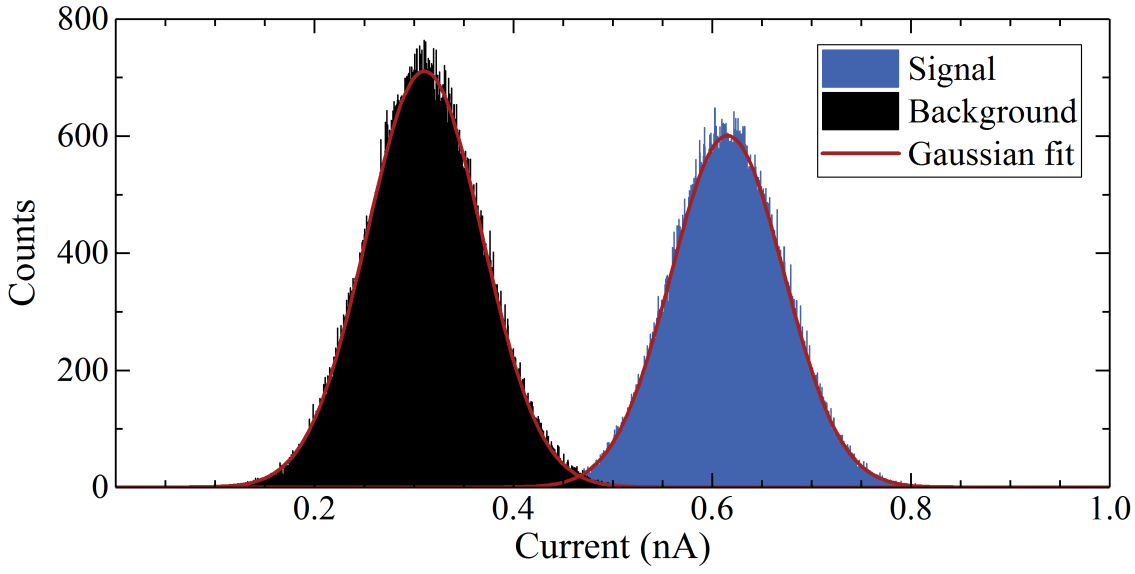

Figure VII.9.: **Histograms of the current from figure VII.8.** The current values have a Gaussian distribution around the mean values, which are clearly different for the measurement of the background and of the ion signal. A bin width of 0.5 pA was chosen, corresponding to the minimum uncertainty of the rbd 9103 picoamperemeter in the measurement range of 2 nA.

VII.2.7. Systematic effects

The statistical analysis from the previous section assumes a Gaussian distribution of the measured current values as in figure A.8. Systematic effects might however lead to changes of the measurement current over time, as indicated by the time series plot of the same measurement in figure VII.8. Also, the trueness of the measurement result might be affected systematically. This section discusses therefore various systematic effects, which might basically affect all of the four current detectors.

Trends and fluctuations All current measurements can be subject to trends or fluctuations, regardless whether an ion signal is present or whether only the background is measured. These time dependent effects become most prominent in a time series display of the measurement current, which was therefore always observed in the analysis of the measurement currents.

Trends of the measurement current like in figure VII.8 might be caused by a general drift or by oscillations. In order to prevent an effect by trends on the measurement, the analysis interval was chosen during the First Tritium analysis as short as possible with regard to the statistical accuracy (see previous section). Optimally, the measurement extended long enough before and after the analysis interval so that the long term stability could be clearly observed.

During the First Tritium measurements, also fluctuations on short time scales occurred. In case of the dipole currents, these spikes were sufficiently rare in order to always choose analysis intervals without spikes (compare section IX.1.1.2). The PS current measurement was however subject to frequent spikes, which mostly exceeded the measurement range of the amperemeter (compare section IX.1.3.2) – for the analysis, these overflow values were reasonably excluded. Spikes within the measurement range could however not be considered, only their effect was damped by the averaging over sufficiently long analysis intervals (see next section).

Current induction on the electrode capacity Each current measurement relies on an electrode inside the beamline, which has a capacitance towards the surrounding beam tube. If the voltage of the electrode is changed, the electrode charges exponentially with a current $I = C \cdot \dot{U}$. Whether this affects the measurements depends on the absolute amplitude of the current, which in turn depends on the capacitance C and the voltage change $\dot{U} = \mathrm{d}U/\mathrm{d}t$. Generally, a stable background current on a certain electrode is reached after a longer time when the change $\mathrm{d}U$ of the current was large.

But even small fluctuations on the supplied electrode voltage can create a significant current due to $I = C \cdot \dot{U} \propto \omega U_0$; the amplitude of this background increases with the frequency ω of the voltage fluctuations and with their amplitude U_0. Fortunately, high frequent noise has generally smaller amplitudes than the voltage ripple around 100 Hz (see the test measurement in section VI.2.4 for the voltage supply of the dipole electrodes, which are iseg devices just like the voltage supply of the PS inner electrodes).

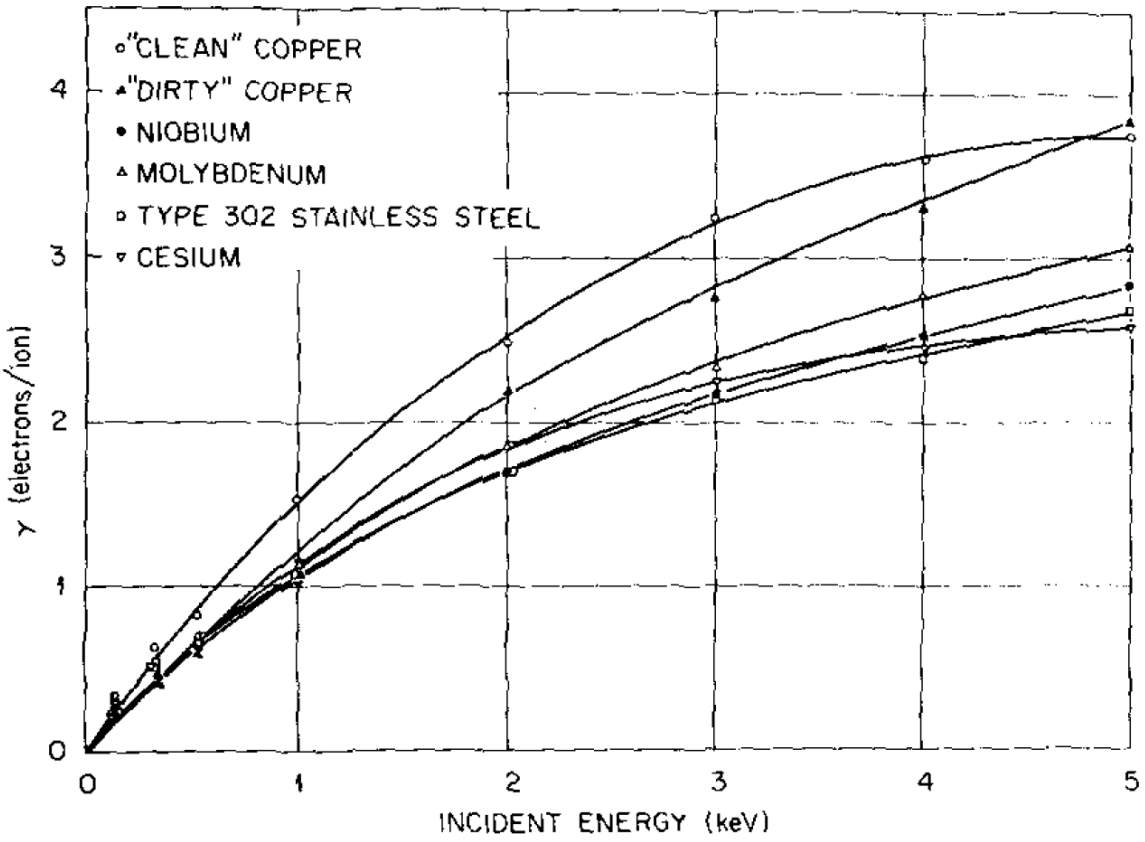

Figure VII.10.: **Secondary electron emission by H^+ ions.** γ denotes the number of secondary electrons per incoming proton. Reproduced from J. A. Ray and C. F. Barnett, *Secondary Electron Emission of Metals Bombarded with 120-eV to 5-keV Protons*, Journal of Applied Physics, https://doi.org/10.1063/1.1660722 [RaB71], with the permission of AIP Publishing.

Trueness While all of the used amperemeters allow rather precise measurements, they are not calibrated with a calibration standard. The trueness of the measurement results can thus not be stated: a fix or a current dependent offset might exist between the measurements and the actual particle fluxes at the electrodes. This becomes relevant for example when comparing the measured ion flux into the PS with the absolute limit of 10^4 ions/s (see section V.3). However, it is assumed that the uncertainty on the trueness is negligible compared to other systematic effects of the measurements.

Secondary electron emission If the charged particles have keV energies, they will eject secondary electrons from the electrode surfaces. This will be the case for all measurements with beta electrons as well as for the accelerated ions in the PS via the current on the cone electrode [RaB71].

The loss of secondary electrons makes the measured current more positive: an electron current will become smaller, while an ion induced current is increases. In both cases, the trueness of the measurement of the impinging particle flux is im-

paired. But with regard to the ion monitoring at the PS, this charge multiplication is actually favourable because it increases the minimum detectable ion flux. Preliminary results of the STS IIIa commissioning phase with deuterium ions indicate a charge multiplication by about one order to magnitude at nominal PS high voltage, in accordance with figure VII.10.

In case of the Faraday cup, these secondary electrons are supposed to be retained by a negative potential at the shield above the board (see section VII.2.3). Similarly, the secondary electrons from the PULCINELLA disc and some of the electrons from the PS downstream cone electrode can be reflected by a negative potential at the PS upstream cone electrode, for example; some of the secondary electrons from the downstream cone electrode can however follows the magnetic field to an anti-Penning electrode between the PS and MS[6].

Electron backscattering If an electron flux impinges the electrode, a certain fraction of electrons might be backscattered and therefore not be detected. This effect was considered for example with GEANT4 simulations in the analysis of the beta electron flux onto PULCINELLA during First Tritium (see section IX.1.6); there, the backscattering was considered together with reflection of the scattered electrons at magnetic mirrors and consequent multiple backscattering.

[6]Internal communication with Ferenc Glück.

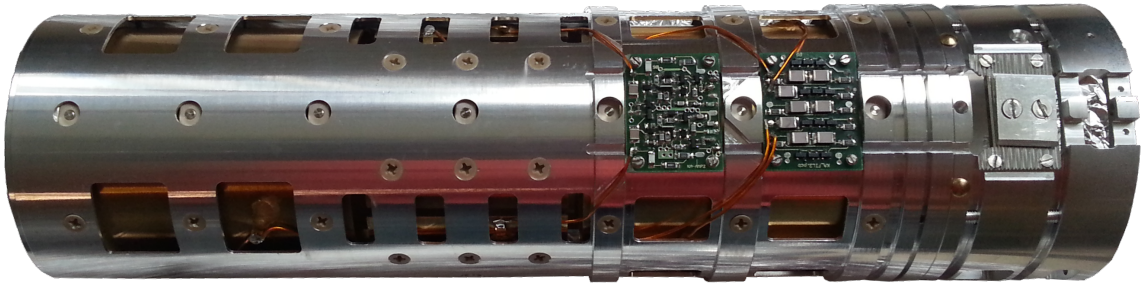

Figure VII.11.: **FT-ICR unit in the DPS BT5.** The first stage of the electronic readout is mounted onto the unit in vacuum.

VII.3. Fourier Transform Ion Cyclotron Resonance

The ion detection via Fourier Transform Ion Cyclotron Resonance (FT-ICR) allows to distinguish different ion species with different charge / mass ratios [Bla06]. A dedicated FT-ICR unit [Ubi09, Ubi11] in the DPS BT5 allows to measure ion fluxes between $(5 \cdot 10^6 \ldots 1 \cdot 10^9)$ ions per second and per species[7].

During the First Light and First Tritium campaigns, the FT-ICR setup was not yet operational. Because of the inadvertent ion blocking in the DPS, which was observed during First Tritium, it is also unknown whether the WGTS ions will reach the FT-ICR unit at the end of the DPS during measurements with 100% tritium. If so, the FT-ICR method could however be used to investigate the source plasma composition during commissioning measurements.

For the measurements, a dedicated FT-ICR unit was installed in the DPS BT5 between the ring electrodes in BT5 and PP5 (see figure VI.3). It will first excite the ions to coherent cyclotron motion with its two excitation electrodes and then measure the mirror charges of the ions on the two pick-up electrodes. During the measurement, the ions are trapped in a Penning trap between the electric potentials of the end caps at each side of the FT-ICR unit.

Inside the Penning trap, the ions oscillate in three dimensions with a defined frequency each (compare figure VII.12 and section III.1.2): longitudinally along the beam tube axis (ω_z), in large magnetron circles (ω_-) and in small cyclotron circles ($\omega_+ = \omega_c - \omega_-$) [Bla06]. A Fourier analysis[8] of the current signal at the pick-up electrodes shows a resonance for each ion species. The ion species can be deduced from the resonance frequency and the relative abundance of the species from the areas below the resonance peaks. Assuming that all ions have the charge $q = 1$ and that the magnetic field B inside the FT-ICR unit is known exactly, an ion with mass

[7] Unless otherwise noted, this section is based on private communication with Stefan Stahl (s.stahl@stahl-electronics.com, Stahl-Electronics, Kellerweg 23, 67582 Mettenheim, Germany), Klaus Blaum (MPIK) and Sven Sturm (MPIK).

[8] Input to the Fourier analysis is either the difference of the electrode signals (dipole moment returns ω_+) or their sum (quadrupole moment returns ω_c). Because inhomogeneous magnetic fields cause uncertainties to the quadrupole method, the dipole method is preferred which returns $\omega_+ = \omega_c - \omega_-$. The small contribution from ω_- can be neglected. Then the q/m ratio follows from $\omega_c = qB/m$ in a given magnetic field B.

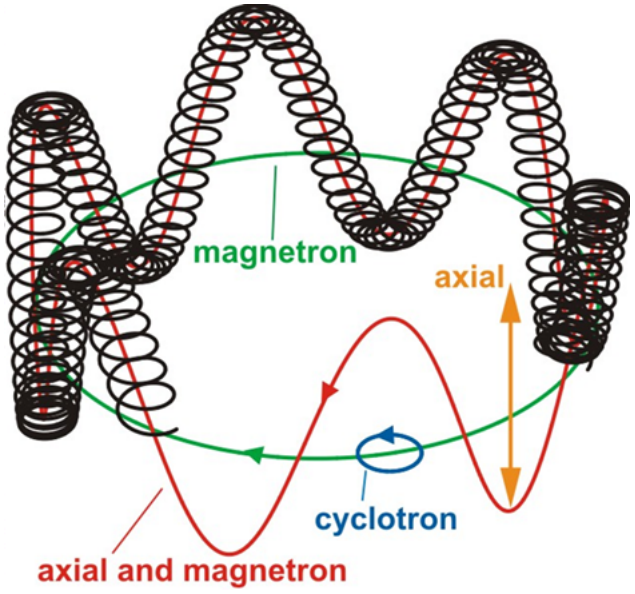

Figure VII.12.: **Oscillation of an ion inside the FT-ICR Penning trap.** The ions are trapped between the potentials of the end caps and oscillate axially along the magnetic fied with frequency ω_z. At the same time, they undergo magnetron drift (ω_-) and cyclotron motion ($\omega_+ = \omega_c - \omega_-$) [Bla06]. Picture from a talk by M. Ubieto-Diaz at the 18. KATRIN collaboration meeting in spring 2010 (BSCW).

m will have a resonance approximately at the cyclotron frequency [Bla06]:

$$\omega_+ \approx \omega_c = \frac{q}{m} \cdot B. \tag{VII.5}$$

A typical FT-ICR measurement takes 3 s and includes 30 measurement cycles of 100 ms. After the ion excitation[9] for about 10 ms, there will be a short time delay in order to prevent picking up any residual signal from the excitation electrodes (see figure VII.13). The large number of measurement cycles served to increase the signal-to-noise ratio; in order to measure the residual ion flux quickly between neutrino mass subruns, the measurement time could be significantly reduced at the cost of not being able to compare the abundance of different ion species.

The minimum detectable flux of the FT-ICR unit is about $\Phi_{\text{ion}} = N/t_b \approx 5 \cdot 10^6$ ions/ per second and per species[10]. A minimum number of about $N = 740$ ions

[9] If the time was shorter, the ions would not get excited sufficiently; longer excitation would increase incoherence due to different magnetic fields which the ions see.

[10] For comparison: the ion flux from the WGTS consists of about 60% T_3^+ ions. Ion species can only be measured if their peak in the Fourier spectrum has at least an area of 1% of the largest peak, because the more abundant species affect the measurement inside the trap. According to table III.1 in section III.2.5, this could concern for example He^+ ions, which make up slightly less than 1% of the total expected ion flux. However, the peak of $^3He^+$ ions could not be distinguished from the peak of T^+ anyway: their mass difference is only $\Delta\omega \approx 100$ Hz, whereas a separation requires $\Delta\omega = 10^{-4}$ in the MHz range where the $\omega_+ \approx \omega_c = qB/m$ of these species will be located.

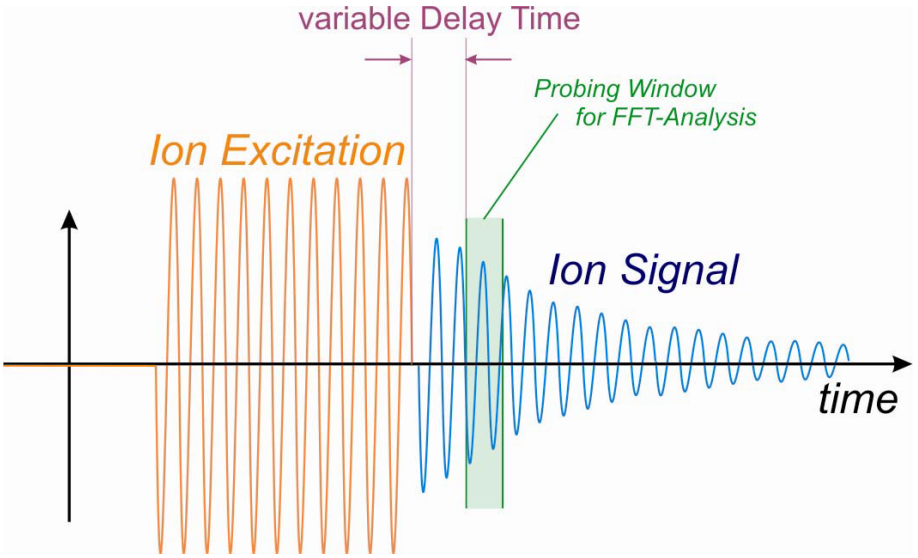

Figure VII.13.: **Timing of the FT-ICR measurements.** Initially, the excitation electrodes induce a current on the pick-up electrodes. For this reason, there is some time delay before measuring with the pick-up electrodes the current from the mirror charges of the coherently moving ions. Because the ions lose coherence, the signal fades. One measurement cycle takes only about 100 ms. Picture from a talk by M. Ubieto-Diaz at the 18. KATRIN collaboration meeting in spring 2010 (BSCW).

will be required inside the FT-ICR trap for the measurement[11]. At the same time, T_3^+ ions with a thermal energy of 300 K will have a bunch time of $t_b = 1.4 \cdot 10^{-4}$ s given a trap length of about 0.1 m. This is a conservative estimate: eventually, the length of the FT-ICR trap will depend on the end cap voltage which is going to be used; and the ions might not become completely thermalised after they leave the 30 K cold WGTS. The minimum number of ions which are required for a measurement should however be calibrated again with another ion detection method.

There is also a maximum flux of $1 \cdot 10^9$ ions per second which can be measured with the FT-ICR unit. This is due to the space charge limit: more than $2 \cdot 10^5$ ions inside the FT-ICR will hinder each other's motion. The resulting strain of the Fourier peaks spoils an accurate determination of the relative abundance of the ion species. It is therefore not possible to measure the complete expected ion flux from the WGTS of about $2 \cdot 10^{11}$ ions/s. The ion space charge could for example be reduced with the dipole electrodes by either drifting out some of the ions or to applying an asymmetric blocking potential. It is possible to investigate the space charge by the relation of the peaks at ω_+ and ω_-.

[11] A minimum number of 1,000 ions was measured for a predecessor of the current FT-ICR unit [Ubi09], which is about a factor 1.35 less sensitive.

Table VII.3.: **Expected and allowed tritium ion flux rates.** The expected ion creation rate and ion flux into the DPS were calculated in section III.2.1 and III.2.5. In section V.3, the total ion flux limit into the PS of 10^4 ions/s was discussed; the limit from radiation protection was derived in section V.1 and and the limit from background by tritium activity or ionisation comes from section V.2. For the calculation of the limits from radiation protection and due to tritium activity, it was assumed that the ions are all T_3^+.

Expected ion creation rate in the WGTS	$2 \cdot 10^{12}$ ions/s
Expected ion flux from the WGTS into the DPS	$2 \cdot 10^{11}$ ions/s
Total ion flux limit into the PS	$1 \cdot 10^4$ ions/s
Ion flux limit into the PS due to radiation protection	$2 \cdot 10^8$ ions/s
Ion flux limit into the PS due to background by tritium activity	8,000 ions/s
Ion flux limit into the MS due to background by ionisation	100 ions/s

Table VII.4.: **Measurement ranges of the ion detection methods.** The minimum and maximum detectable ion fluxes or currents have been discussed for the individual detectors in the previous sections of this chapter. Also stated is the time which is required for the signal and background measurement; no included is however the duration for the preparation of the measurement conditions, for example the argon gas inlet in the PS.

Detection method	Time	Ion flux (ions/s)	Current
Ionisation in PS	10 min	$\sim 10^3 \ldots 5 \cdot 10^8$	
Ionisation in MS (10^{-11} mbar)	1 h	$\sim 10^5 \ldots \sim 10^{13}$	
Current on DPS dipole	10 min	$3 \cdot 10^7 \ldots 1 \cdot 10^{16}$	6 pA ... 2 mA
Current on PS cone electrode	2 h	$4 \cdot 10^5 \ldots 6 \cdot 10^{17}$	4 fA ... 20 mA
Current on PULCINELLA		$2 \cdot 10^5 \ldots 4 \cdot 10^9$	30 fA ... 600 pA
FT-ICR	3 s	$5 \cdot 10^6 \ldots 1 \cdot 10^9$	

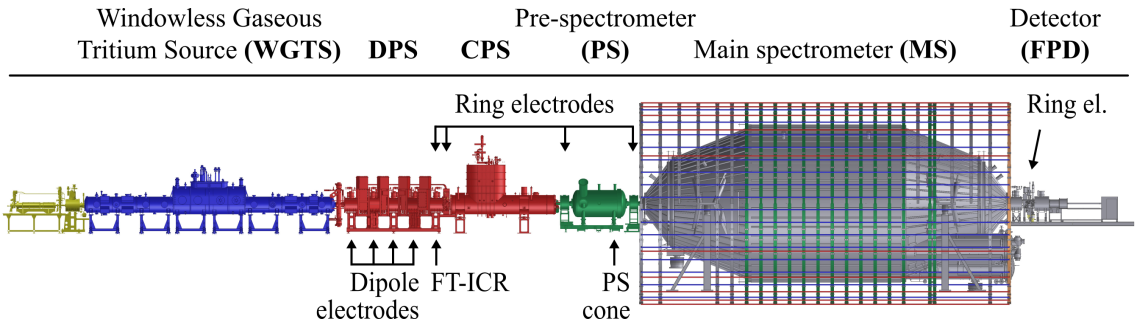

Figure VII.14.: **Position of ion detectors for ion monitoring in the beamline.** Current measurements at the DPS dipole electrodes and the PS downstream cone electrode allow a continuous ion monitoring. The FT-ICR can be used between measurement runs in order to check the residual tritium ion flux downstream from the DPS ring electrodes within the tritium laboratory. Repeated checks of the residual ion flux into the spectrometers should also be carried out with the ionisation method in the PS or MS.

VII.4. Monitoring of the residual ion flux into the PS

A constraint of $1 \cdot 10^4$ ions/s on the residual ion flux into the PS was imposed in section V.3 in order to restrict the MS background by tritium activity to about 1 mcps. Because a flux of about $2 \cdot 10^{11}$ tritium ions/s is expected from the WGTS during the neutrino mass measurements[12] (see section III.2.1), the ion flux has to be reduced by about seven orders of magnitude.

In order to reduce the ion flux from the WGTS, two ring electrodes in the DPS BT5 and PP5 create positive electrostatic blocking potentials (see section VI.1). The voltage on the ring electrodes is monitored constantly, but this might not be enough to ensure that the ions are continuously blocked: secondary electrons might accumulate inside the blocking potentials and neutralise them (see section III.6.3).

The residual ion flux downstream from the DPS ring electrodes therefore needs to be measured directly. This is basically possible with the three different types of ion detectors which have been discussed in the previous section: ionisation in the spectrometers, current measurements and FT-ICR. A summary of their measurement ranges and required measurement times is given in table VII.3. The three detectors complement each other with regard to the continuity of the ion monitoring and the minimum detectable ion flux, as will be discussed in the following and based on First Tritium results in section IX.1.5.

Ionisation measurements The ionisation measurements with the Pre- and Main-spectrometer are the most sensitive ion detection methods inside the KATRIN experiment. According to section VII.1, a pressure-independent ionisation efficiency was found in the PS during the STS IIIa commissioning measurements with deu-

[12] About two third of this flux are T_+^3 ions, less than 10% are negative T^- ions, and the rest are positive ion species. The negative ions will be blocked by the negative potential of the dipole electrodes – if not, there would be the negative potential of the PS.

terium ions. Preliminary results from October 2018 indicate an ionisation efficiency of $2 \cdot 10^{-3}$ counts/ion, which would allow to detect a flux of 10^3 ions/s almost instantaneously; the measurement would be limited by H_2^+ ions which are created by beta electrons from the residual gas of the PS. Nevertheless, this improved sensitivity would allow regular ionisation measurements between neutrino mass runs; the measurement time would be only limited by the ramping of the PS and MS high voltage in order to block beta electrons and transport the secondary electrons from ionisation to the FPD. It is favourable that the PS pressure remains at the level of 10^{-11} mbar as during the neutrino mass measurements, in order to prevent background to the ionisation measurement by beta electron induced ions.

Even during the neutrino mass measurements, the MS background could be monitored in order to detect an increase due to ionisation, for example. Most of the measurement time, the FPD count rate by beta electrons will be on the level of 1 cps, which is small compared to the intrinsic MS background of 400 mcps. An automatic BEANS script could continuously monitor the stability of the MS background. But the use for the ion monitoring is small, because an ion flux of 10^5 ions/s into the MS is required at 10^{-11} mbar residual pressure in order to increase the MS background via ionisation by about 10 mcps. At the same time, the ion flux into the PS needs to be at least four orders of magnitude larger due to the small ion transmission probability through the PS (see section V.3). Such a large ion flux would have already triggered the closing of the valve between the CPS and the PS, as will be discussed next.

Current measurements The ion flux into the PS is continuously monitored by the current measurement at the PS cone electrode (see section VII.2.4). An automatic closing of the valve V4 between the CPS and PS will be triggered within 1 min of the detection of an ion induced current of 5 pA or larger[13]. This current threshold corresponds just to the conservative constraint of $2 \cdot 10^8$ ions/s on the ion flux into the PS which was imposed by radiation protection (see section V.1). The assumed ion detection efficiency of 20% is likewise conservatively, chosen among conflicting simulations as discussed in section IV.1. Another improvement of the detection efficiency is assumed due to charge multiplication via secondary electron emission from the stainless steel electrode upon impact of the keV ions (see section VII.2.7); preliminary results of the STS IIIa commissioning phase suggest a charge multiplication by one order of magnitude.

Longer measurements over 2 hours allow to detect ion fluxes as small as $4 \cdot 10^5$ ions/s at 3σ significance (see section IX.1.3.3). This would allow restrict the background from a continuous ion flux into the PS to 4 mcps; but additional software is required in order to close the valve V4 to the PS automatically based on the analysis of a 2 hour sample. Again, the estimate relies on the conservative assumption of a 20% detection efficiency and does not take into account the charge multiplication by secondary electron emission.

Due to the inadvertent ion blocking in the DPS which was observed during First Tritium, even the current measurements at the DPS dipole electrodes could be used

[13]The trigger probability increases with the measurement time, so that even slightly smaller ion induced currents would lead to a closing of the valve (see figure VII.6).

to monitor the residual ion flux: ions were only observed with the BT1 dipole, but not with those in BT3 and BT4 (see section IX.3)[14]. These two dipole electrodes have an ion detection efficiency of 17% at their nominal voltage settings (see section VII.2.2). With the minimal detectable ion flux is $3 \cdot 10^7$ ions/s at 3σ significance follows that an ion flux of $2 \cdot 10^8$ ions/s could have already been detected. This would be enough to satisfy the constraint on the ion flux into the PS of likewise $2 \cdot 10^8$ ions/s due to radiation protection (see section V.1). However, the systematic drifts of the background current made the monitoring practically impossible (see section IX.1.1.2). Also, Penning ions from tritiated gas were observed to be created in the DPS ring electrodes downstream from the dipole electrodes (see section IX.2.2).

The Faraday cup or the PULCINELLA disc are obviously not suited to monitor the ion flux during the neutrino mass measurements: they need to obstruct part of the flux tube for the measurement and therefore would cast shadows on the FPD.

FT-ICR The FT-ICR can detect an ion flux of at least $5 \cdot 10^6$ ions/s (see section VII.3). Because it is located between the two DPS ring electrodes, the FT-ICR can be used to measure the residual ion flux below the limit of $5 \cdot 10^8$ ions/s from radiation protection. However, the FT-ICR cannot be used continuously during the neutrino mass measurements, because its time-dependent electric fields might influence the neutrino mass measurements. Nevertheless, the short measurement time of 3 s or even less allows repeated checks of the residual ion flux during the neutrino mass runs, for example when the spectrometer settings are changed.

[14]The cable connection to the BT2 dipole was damaged during the measurement campaign.

VII.5. Monitoring of the plasma parameters

Besides the background from tritium ions in the spectrometers, the neutrino measurements can also be affected by systematic effects due to tritium ions in the source (compare section V.4). In case of the background, the critical parameter was the ion flux into the PS: it can be directly observed and monitored continuously as discussed in the previous section. As for the systematic effects however, the critical parameters would be the densities of positive and negative ions all through the WGTS. The only way to deduce them would be test measurements with krypton in the source gas together with simulations for the evaluation of the measured krypton lines (compare section VI.2.3). Apart from krypton mode, the ion densities in the tritium source must be inferred from plasma simulations or the effect of the ions on the electron energy have to measured directly.

Monitoring the end point energy of the tritium beta spectrum would allow to assess the influence of beta electrons with a shifted end point energy due to negative ions: negative ions might create space charges in the WGTS-F (see section V.4.2) and have different final states when they decay (see section V.4.3). This monitoring is a natural outcome of the neutrino mass measurements – it only requires dedicated analysis.

There is no way of monitoring the effect of plasma instabilities during the neutrino mass measurements. In order to assess the smearing of the beta electron energy, test measurements in krypton mode or repeated measurements with the e-gun are required. Based on these results, the dipole electrode voltages can be optimised so as to decrease the positive plasma density as far as possible without effects due to negative ions (see section VI.2.3). During the neutrino mass measurements, the state of the source plasma needs to be inferred from simulations.

An important boundary condition to the plasma simulations in the WGTS is the ion removal rate by the dipole electrodes in the DPS. For example, only 50% of the expected ion flux was measured with the DPS dipole electrodes during First Tritium (see section IX.3); the same measurement can be easily repeated for the conditions of the neutrino mass measurements with $> 95\%$ tritium concentration in the WGTS. However, a constant monitoring of the ion removal rate is currently not possible due to the drift of the background current. Instead, repeated measurements of the ion flux would be possible during breaks between the neutrino mass measurements: blocking all positive ions with a positive potential at the BT1 dipole electrode would allow to measure the background current of the other three dipole electrodes.

Finally, the plasma simulations require the relative concentrations of the ion species as input parameters. These concentrations have been simulated as reported in section III.2, but still need to be verified with FT-ICR measurements[15]. This could be done in dedicated test measurements or with regular checks during the neutrino mass measurements.

[15]The concentration of the ion species are assumed to remain constant between the WGTS-F and the FT-ICR unit at the end of the DPS, because the transformation probability is small due to the small neutral gas density (Estimate by Ferenc Glück).

VIII. The First Light campaign

At First Light, electrons were transmitted for the first time through the whole KATRIN setup: from the rear wall to the detector. The first measurement campaign with the complete KATRIN beamline right after this event allowed also the first ion test measurements[1].

In order to produce the necessary ions for these test measurements, the ELIOTT ion source was mounted to the rear section of KATRIN. The deuterium ions from ELIOTT were injected as a thin pencil beam through the rear wall into the beamline. In the Main spectrometer, the pencil beam was detected via ionisation, which was a proof-of-principle for this detection method. The ion creation at the rear section and ion detection in the MS allowed to test the ion blocking and removal with the ring and dipole electrodes in between.

In contrast to the tritiated ions, which are created inadvertently during the operation of the KATRIN tritium source, the ELIOTT deuterium ions were not radioactive. This allowed extensive measurements with a large ion flux into the spectrometers without any risk of tritium activity and consequent background for the neutrino mass measurements. During the measurements, the ionisation efficiency of positive deuterium ions in the MS could be determined experimentally. Also, the ion transport through the PS was investigated in dependence of the magnetic field and the high voltage of the PS. This provided the first reality check for the KASSIOPEIA simulations of ion detection in the PS during First Tritium and during future neutrino mass measurements[2].

Another first was the observation of inadvertent blocking of thermal ions during First Light. Because the ELIOTT ion source could be set to an offset potential, even the magnitude of the inadvertent blocking potentials could be investigated.

This chapter will first explain the ELIOTT setup at the rear section and its systematic effects (section VIII.1.1). Then, the ion detection in the MS will be discussed along with the experimental determination of the ionisation efficiency (section VIII.2). This scheme of ion creation at the rear section and ion detection in the MS allowed to test the electrostatic ion blocking with the ring electrodes (section VIII.3) and the $E \times B$ drift of the ion pencil beam with the dipole electrodes (section VIII.4). Further, the ion transport through the PS could be investigated (section VIII.5) and the inadvertent ion blocking in the beamline was observed for the first time (see section VIII.6). The final section VIII.7 will summarise the results and show the consequences of the First Light measurements, especially for the further development of the ion monitoring system.

[1] Besides the ion measurements, the alignment of the beamline section was investigated as reported in the PhD thesis of Moritz Hackenjos [Hac17].

[2] See the Master's thesis of Woo-Jeong Baek: *Investigation of background processes of ions and Rydberg atoms in the KATRIN spectrometers*, (2017).

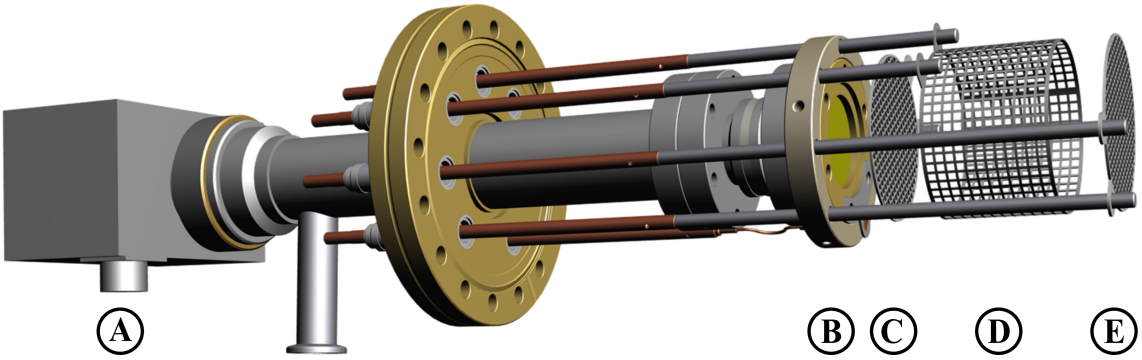

Figure VIII.1.: **Technical drawing of the ELIOTT ion source.** The photons from the UV lamp (A) are guided through a polished aluminium tube onto the gold coated photocathode window (B), from which they eject electrons. These photoelectrons ionise the deuterium gas between the electrodes (C), (D) and (E) as detailed by figure VIII.2.

VIII.1. Creation of deuterium ions with the ELIOTT ion source

During the First Light campaign, the ELIOTT ion source [Luk11] was mounted to the rear section of the KATRIN setup specifically to create ions for the ion test measurements. ELIOTT created non-radioactive ions from deuterium gas, which allowed extensive test measurements over several days with large ion fluxes on the order of 10^9 ions/s. Because ELIOTT was mounted behind the rear wall, only a thin pencil beam was injected into the beamline which could be drifted across the FPD pixels via $E \times B$-drift in the dipole electrodes (see section VIII.4). The electrical insulation of the ELIOTT setup from the rest of the beam tube allowed to provide the ions with an offset energy in order to observe even the thermal ions, which were otherwise blocked inadvertently in the beam tube (see section VIII.6).

The ELIOTT ion source created however also additional systematic effects: mainly, the deuterium pressure in ELIOTT affected the overall ion rate, the ion energy spectrum and even the species of the deuterium ions. Understanding these effects is crucial for the analysis of the ion measurements – the effects will therefore be detailed in the following.

First, this section will explain the basic ion creation mechanism via UV photoelectrons in the electrode setup of ELIOTT (section VIII.1.1). Then the setup of ELIOTT at the rear section and behind the rear wall will be described (section VIII.1.2). Afterwards, the deuterium pressure and its effect on the intensity of the ion flux will be discussed in section VIII.1.3. The pressure also affected the ion energy spectrum, as discussed in section VIII.1.4. Finally, section VIII.1.5 discusses the relative abundance of D_2^+ and D_3^+ ions during the individual measurements, which also depends on the deuterium pressure in ELIOTT.

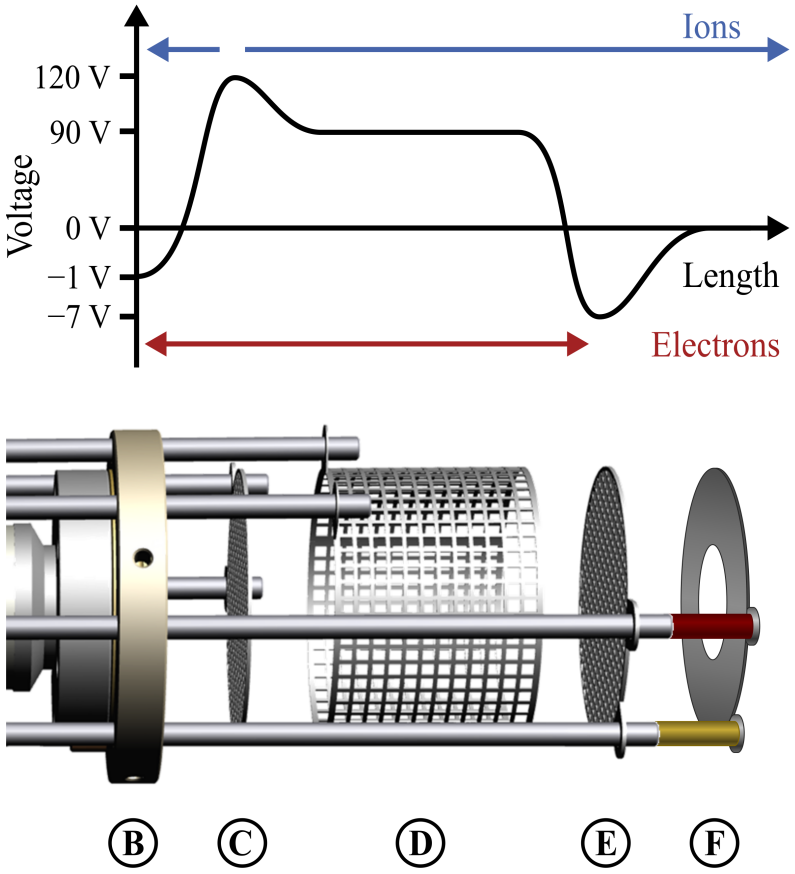

Figure VIII.2.: **Close-up of the ELIOTT electrodes and illustration of the electric potential inside.** UV photons ejected electrons from the photocathode window (B) (compare figure VIII.1). These photoelectrons were accelerated by a small negative voltage of −1 V on the photocathode window towards the large positive voltage of +120 V at the electrode (C). For the longest distance, the electrons traveled through the cage electrode (D) which created a potential of 90 eV. Finally, the electrons were reflected by the electrode (E) with −7 V. The trapped electrons ionised the deuterium gas and the positive ions were accelerated mostly to the front due to the shape of the positive potential. According to figure VIII.3, the rear wall would collimate the ion flux to a thin pencil beam in the center of the beamline. The outmost ions did consequently not reach the KATRIN beamline. This allowed to monitor the ion creation with the ring shaped Faraday cup (F) in front of the electrodes. Because the feedthroughs at the ELIOTT flange were limited (compare figure VIII.1), the Faraday cup ring was mounted to the same rods as the electrode (E). In order to set the Faraday cup to the reference ground potential of the hull, one of the rods was extended with a copper standoff and one with a plastic standoff; the electrode (E) was insulated from the grounded rod with a small plastic ring, too. Outside the vacuum, the current was measured with an amperemeter at the rod that connected to the Faraday cup.

VIII.1.1. Ion creation principle of the ELIOTT ion source

Inside the ELIOTT[3] ion source, photoelectrons ionise the filling gas via inelastic scattering. The ionisation mechanism will be explained in the following; for details on the design considerations and test measurements see [Luk11].

Figure VIII.1 shows the core components of the ELIOTT ion source. The UV lamp (A) emits UV photons which are guided through a polished aluminium tube onto the photocathode window. On the front side of the window, the UV photons eject photoelectrons from the gold coating of the window. Both sides of the window need to be evacuated: the ionisation chamber in order to control the intensity of the ion flux and the light guide tube in order to prevent the creation of ozone, which would among other things absorb the UV light.

Figure VIII.2 shows a close-up of the electrode setup and an illustration of the electric potential. A small negative voltage of -1 V is applied to the photocathode window (B) in order to accelerate the photoelectrons into the ionisation chamber. At the opposite end of the chamber, the electrons are reflected by a slightly more negative potential of -7 V at the electrode (E). The trapped electrodes gain kinetic energy from the $+90$ V at the long cage electrode (D) and produce positive ions by inelastic scattering on the filling gas. Due to the positive potential of the cage electrode, the ions are accelerated out of the ion source. In order to make sure that all ions leave the source to the front side, another electrode (C) between the cage and the photocathode window is set to $+120$ V.

VIII.1.2. The ELIOTT setup at the rear section

For the ion test measurements during First Light, the core components of the ELIOTT ion source from figure VIII.1 were mounted to the rear section of KATRIN as shown in figure VIII.3. The rear wall was not removed from the beam tube for two reasons:

- **Collimation:** The rear wall blocked the majority of the ion flux from ELIOTT. Only a thin pencil beam was transmitted into the beamline by a hole with 5 mm in the center of the rear wall. This hole was initially designed to let pass the electrons beam from the e-gun behind the rear wall.

- **Gas flow reduction:** The small conductance of the rear wall allowed to different pressure regimes in ELIOTT and the rest of the beam tube: the deuterium pressure inside the ELIOTT setup was about 10^{-3} mbar to 10^{-1} mbar, whereas the beam tube was efficiently pumped by its turbomolecular pumps to the level of 10^{-9} mbar. The volume of the rear wall vessel needed additional evacuation by the same pump as the UV light guide tube of ELIOTT.

For practical reasons, the ion source could no be installed in the center of the superconducting magnet but had to be mounted at the rear opening of the magnet hull. This had the advantage that the gas discharge UV lamp could be operated in

[3]ELectron impact IOn source to Test the Transportsection – see Diploma Thesis of Marcel Christian Robert Zoll, *Development of tools and methods for KATRIN DPS2-F test experiments*, 2009

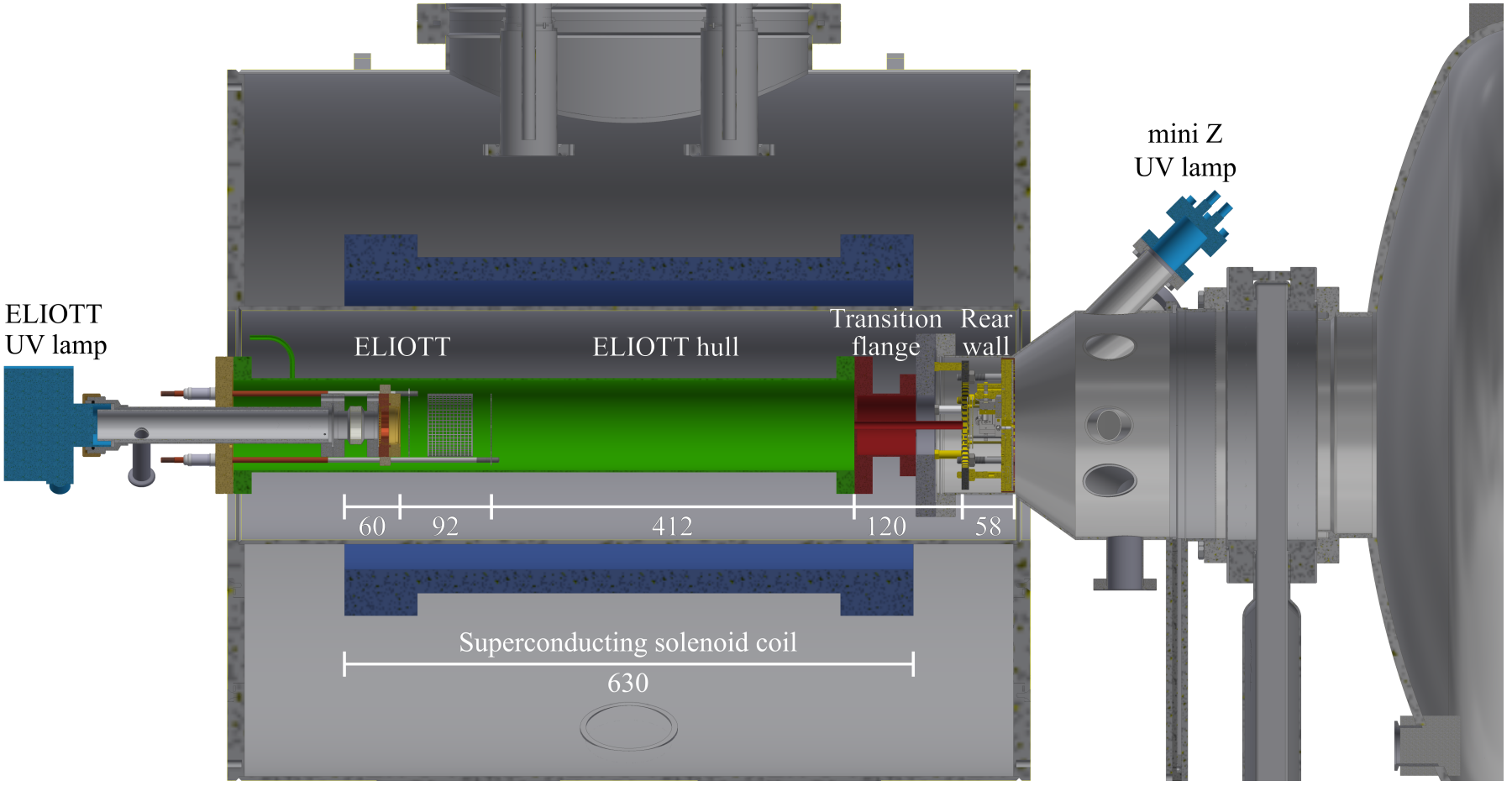

Figure VIII.3.: **Technical drawing of the ELIOTT setup at the rear section.** Dimensions are given in mm. ELIOTT created positive ions from the deuterium gas inside the coil of the rear section superconducting magnet (see figure VIII.2). Most of the ions were thermalised by collisions with the deuterium gas. The gas flowed from the bend inlet pipe at the rear end of the ELIOTT hull through the transition flange and the rear wall into the WGTS. Only a thin ion pencil beam was injected into the beamline due to the collimation at the rear wall, which had only a small hole in the center with 5 mm diameter. For alignment measurements during First Light, electrons were either produced as a pencil beam when ELIOTT was operated without deuterium, or the mini Z UV lamp covered the whole flux tube with photoelectrons from the rear wall. Not shown are the Faraday cup ring 2.5 mm ahead of the tip of the ELIOTT electrodes (compare figure VIII.2) and the prolonged light guide for the ELIOTT UV photons (compare figure VIII.4).

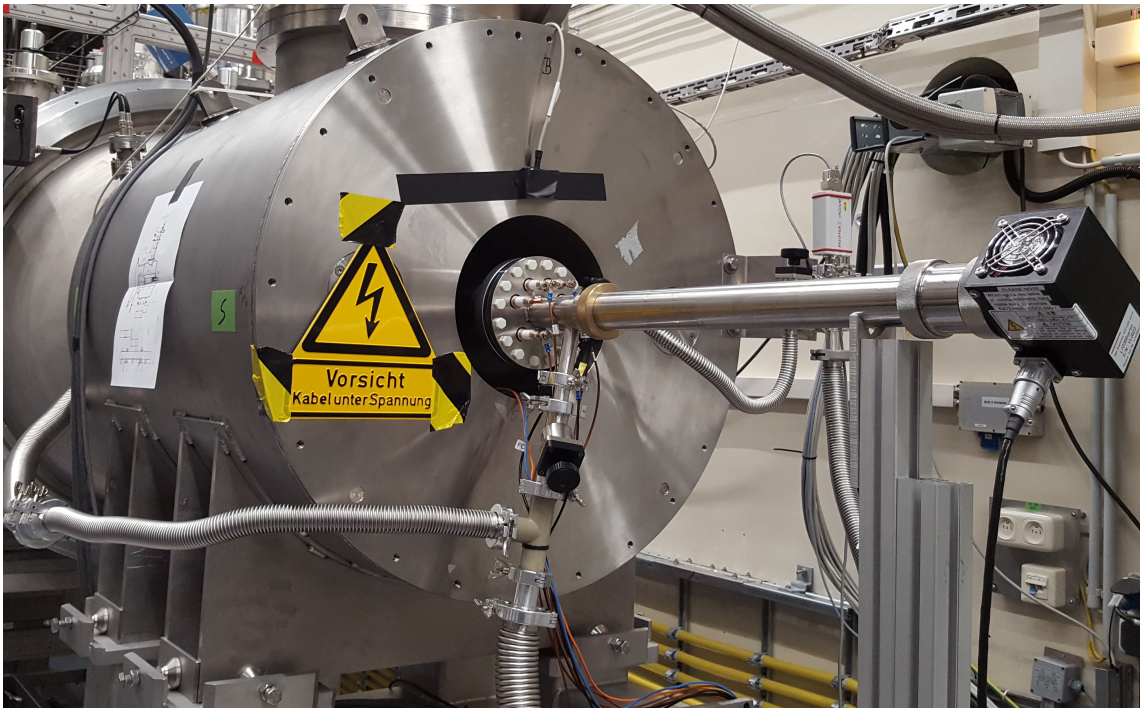

Figure VIII.4.: **ELIOTT ion source inside the superconducting magnet of the rear section.** At the end of the superconducting magnet, the ELIOTT vacuum feedthrough with the rods of the inner electrodes can be seen. Plastic screws were used at the feedthrough in order to electrically insulate the ELIOTT hull. The evacuated light guide was prolonged with another 540 mm long pipe in order to operate the UV lamp outside the magnetic field of the rear section superconducting magnet (right edge of the picture). Behind the light guide, electrical cables and the deuterium gas supply can be seen going into the magnet.

a week magnetic field without significant loss of the UV photons by absorption in a too long light guide; an extension by another 540 mm was sufficient, as shown in figure VIII.4.

The connection between the ELIOTT core components and the rear wall vessel consisted of two stainless steel tubes, which were electrically insulated[4] in order to transport thermal ions (see section VIII.6). Most of the distance between the core components and the rear wall vessel was covered by a 700 mm long CF-100 stainless steel tube which will be referred to as the ELIOTT hull. Floating the hull on a positive potential allowed to accelerate the ions towards the rear wall, which could be floated, too. The distance between hull and rear wall would however been long enough to thermalise the ions in the ground potential defined by rear wall vessel and beam tube. In order to prevent the trapping of positive ions between the hull and rear wall, another insulated transition flange was inserted. The transition

[4]For the insulation, the vacuum tubes were connected with plastic screws and double plastic o-rings.

flange contained a metal pipe with 10 mm diameter which guided the ions to the rear wall[5]. A cascading potential setting allowed to provide the thermalised ions from the ELIOTT ion source with an energy offset at the entrance to the beamline: usually, this was +4 V at the hull, +2.5 V at the transition flange and +2 V at the rear wall.

The operation of ELIOTT without deuterium gas and appropriate electrode settings allowed to produce an electron pencil beam, which was used during the First Light alignment measurements [Hac17]. Alternatively, electrons could also be injected into the whole flux tube at the rear wall with a UV lamp of type mini Z from rbd.

VIII.1.3. Deuterium pressure in ELIOTT

The deuterium gas was injected into ELIOTT via a thin, bend pipe as shown in figure VIII.3. Because the deuterium pressure affected the intensity of the ion flux into the beamline, the pressure in ELIOTT had to be extremely stable. For this purpose, a stable gas flow into ELIOTT was created with a large buffer volume in the deuterium supply. This allowed measurements with a stable ion flux over a long time. Only during measurements with a large pressure inside ELIOTT did the deuterium pressure and ion flux decrease significantly, as will be discussed below.

The strong magnetic field and the space constraints inside the superconducting rear wall magnet prevented a direct measurement of the deuterium pressure inside ELIOTT. Only a pressure gauge in the deuterium supply was used as an indicator. In the following, this pressure will be usually stated in order to identify the measurement conditions. The absolute pressure only needs to be known in order to estimated the ion species in section VIII.1.5. For this purpose, the absolute pressure was estimated with vacuum physics equation in appendix A.12 to be about 40% of the measured pressure in the deuterium supply.

All measurements were carried out with one of the following three pressure settings:

- $3 \cdot 10^{-3}$ **mbar:** This measurement pressure remained stable over the complete measurement day. Using these stable conditions, the blocking efficiency of the ring electrodes (section VIII.3) and some of the transport properties of the PS (section VIII.5) were investigated.

- $5 \cdot 10^{-2}$ **mbar:** This pressure was only used for the investigation of the ionisation efficiency in the MS (section VIII.2.3) in an attempt to maximise the intensity of the ion flux. It was combined with an offset voltage at the ELIOTT hull, transition flange and rear wall in order to transport thermal ions (compare figure VIII.3).

- $1 \cdot 10^{-1}$ **mbar:** Most of the measurements used this pressure in combination with an offset voltage at the ELIOTT hull, transition flange and rear wall, in order to provide thermal ions for the investigation. This concerns the ion

[5]The pipe was adjusted in order to position its opening over the hole in the rear wall and so that the pipe ran as parallel as possible to the magnetic guiding field.

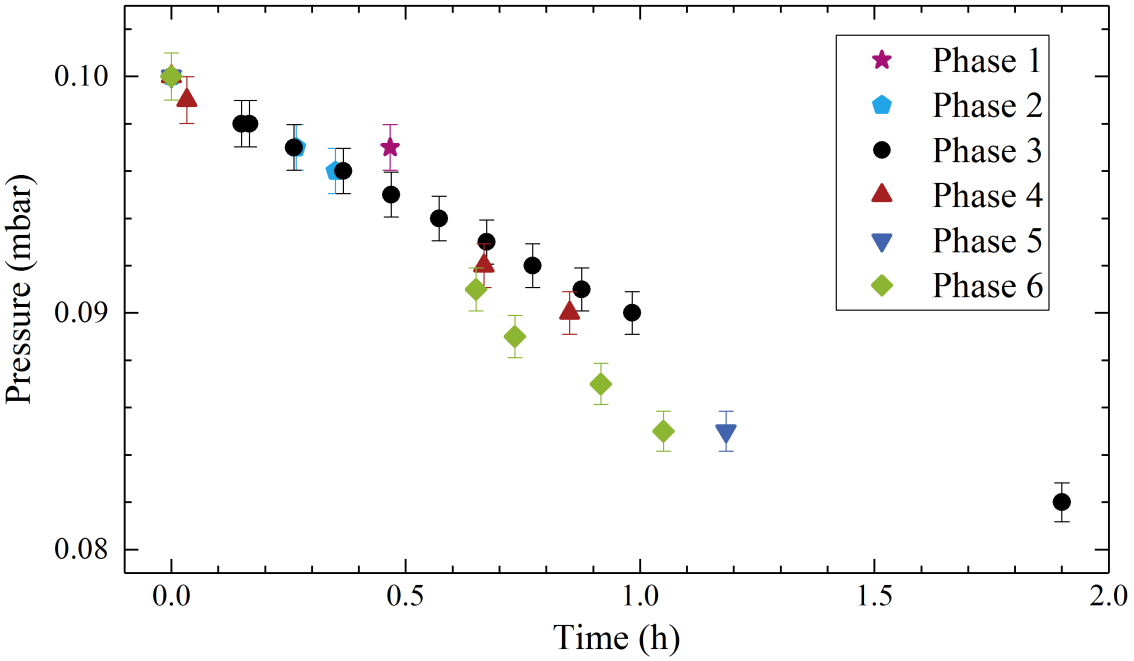

Figure VIII.5.: **Pressure decrease during the measurements with** $1 \cdot 10^{-1}$ **mbar.** Creating such a large measurement pressure required a large gas flow from the deuterium supply through ELIOTT into the WGTS. This gas flow drained the buffer volume in the deuterium supply, which lead to an approximately linear decrease of the pressure and a consequent increase of the ion flux into the MS (compare figure VIII.6). Each time the pressure was manually reset by increasing the gas flow through a valve in the gas supply, the pressure decreased faster because the pressure in the buffer volume decreased significantly, too.

drift with the dipole electrode (section VIII.4), some of the investigation of ion transport through the PS (section VIII.5) and the observation of inadvertent ion blocking (section VIII.6).

A drawback of the measurement at $1 \cdot 10^{-1}$ mbar was that it required a large deuterium flow into ELIOTT. This drained the buffer volume quickly enough to require frequent adjustment of the gas flow. Usually, the pressure decreased by about 10% within one hour, as shown in figure VIII.5. This would however increase the ion rate already by about 50%, as shown in figure VIII.6. The decrease of the ion flux is attributed to more efficient thermalisation of the ions in ELIOTT and their subsequent inadvertent blocking in the beamline, as will be explained section VIII.6.

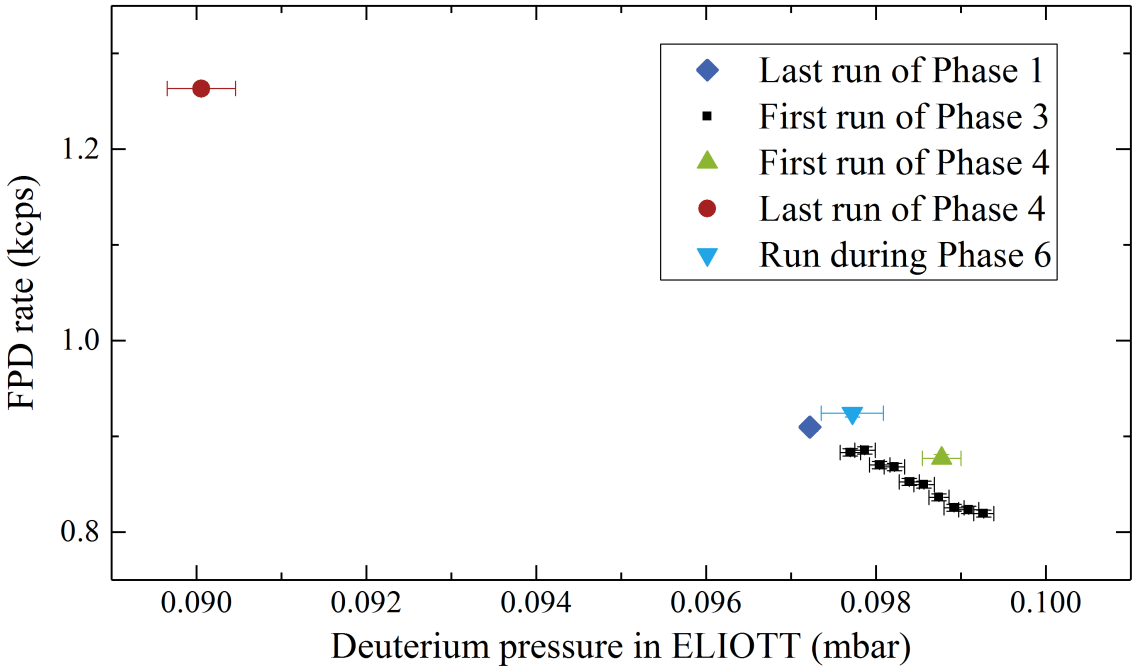

Figure VIII.6.: **Decrease of the ion flux at higher ELIOTT pressures.** At larger pressures, the ions were thermalised more efficiently and a larger fraction of them was blocked inadvertently in the beamline (see section VIII.6).

VIII.1.4. Energy spectra of the ELIOTT ions

The energy spectrum of the ions was scanned in order to investigate whether thermal ions were transported to the MS. For the scan, the voltage of the dipole electrode in DPS BT2 was increased in monopole mode while the ion flux was measured via ionisation rate in the MS (compare section VIII.2.4). Figure VIII.7 shows the measured integrated ion spectra in the upper part and the derived differential spectra in the lower part.

The energy spectrum was measured for all three pressure settings which were discussed in the previous section: at $3 \cdot 10^{-3}$ mbar, $5 \cdot 10^{-2}$ mbar and $1 \cdot 10^{-1}$ mbar deuterium. The scan at $3 \cdot 10^{-3}$ mbar and one of two scans at $1 \cdot 10^{-1}$ mbar were carried out without any offset voltage at ELIOTT; during the measurements at $5 \cdot 10^{-2}$ mbar and the second measurement at $1 \cdot 10^{-1}$ mbar, offset voltages were however applied.

The differential ion energy spectrum shows peaks at three different voltages:

- **Below 3 eV,** a prominent peak appeared when the spectrum was measured at $1 \cdot 10^{-1}$ mbar and an offset voltage of +4 V at the ELIOTT hull, +2.5 V at the transitions flange and +2 V at the rear wall. The peak was not observed in the measurement without offset voltage. This is explained with the inadvertent blocking of thermal ions in the beamline, if they are not provided with an energy offset of a few eV. For a detailed discussion of this effect, see section VIII.6.

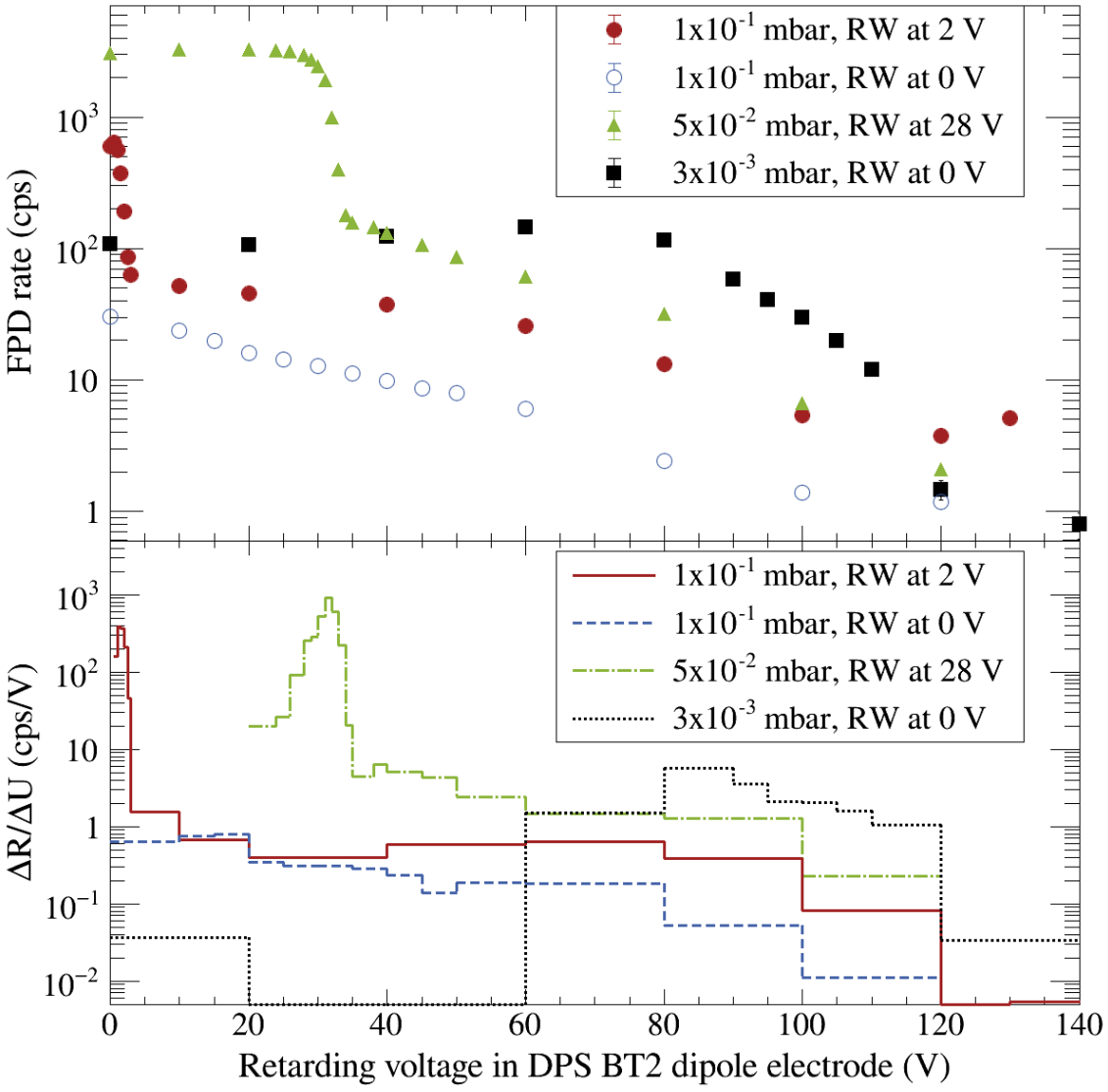

Figure VIII.7.: **Integrated and differential ion energy spectra at different measurement pressures.** The integrated spectra (upper part) were obtained by increasing the voltage of the dipole electrode in DPS BT2 in monopole mode. For the differential spectrum (lower part), the rate decrease between two neighbouring measurement points $R(U_1)$ and $R(U_2)$ was normed with the voltage difference. The histogram shows $\Delta R/\Delta U = (R(U_1) - R(U_2))/(U_2 - U_1)$ between the bin boarders U_1 and U_2. Two peaks below 3 eV and around 30 eV were caused by the transport of thermal ions with different offset voltages at ELIOTT and the rear wall; the peak around 90 eV is due to unscattered ions from the center of the ion source.

- **Around 30 eV**, the measurement with $5 \cdot 10^{-2}$ mbar showed a very large peak, which is also due to thermal ions with a corresponding offset energy. The spectrum was measured when the ionisation efficiency in the MS was investigated (see section VIII.2.3). This was the only occasion that not the usual offset voltages were applied, but instead +32 V to the hull, +30 V to the transition flange and +28 V to the rear wall.

- **Around 90 eV,** all spectra show a peak of unscattered ions from the cylinder electrode in the ion source. According to section III.2.3, the mean free path of an ion with 100 eV will be roughly 0.5 m at $1 \cdot 10^{-3}$ mbar in the center of the WGTS. This corresponds to the conditions inside ELIOTT at a pressure of $3 \cdot 10^{-3}$ mbar in the deuterium supply: the ions from the cylinder electrode have a kinetic energy of 90 eV and will scatter on their 0.5 m long passage to the rear wall with roughly 50% probability. Once they lost energy, the cross section for further energy loss increases strongly and the ions are quickly thermalised. Consequently, only the peak of unscattered ions around the original energy of 90 eV remains. The scattering probability increases also with the deuterium pressure; therefore the peak is smaller at $5 \cdot 10^{-2}$ mbar and almost disappeared at $1 \cdot 10^{-1}$ mbar.

The interpretation of the ion spectra is however limited because an unknown systematic effect influenced the spectral shape obviously: an increase of the integrated spectrum by about a factor of two is observed for the measurements at $3 \cdot 10^{-3}$ mbar and $5 \cdot 10^{-2}$ mbar between 0 eV and the peak position. This is in contradiction to the measurement principle of an integrated spectrum: actually, the rate should decrease monotonically because more and more ions are blocked. The cause of the observed peak remains unclear. One possible explanation is that the blocked ions were stored and created a positive space charge, which would have shifted the ion energy spectrum; this can however not explain, why the ion rate not only remained constant but actually increased. Another possible reason is a drift of the ion beam by a small dipole voltage between the electrodes of the dipole electrodes; a similar increase was observed when the pencil beam was drifted with a negative dipole potential out of the beam tube center, probably because the average ion path through the MS increased.

Nevertheless, the measurements give a good indication of the ion energy spectra. They also demonstrate that thermal ions could be transported when an offset voltage was applied to the ELIOTT hull, the transition flange and the rear wall.

VIII.1.5. Transformation of D_2^+ to D_3^+ ions in ELIOTT

The deuterium ions which were injected by ELIOTT into the KATRIN beamline are assumed to be D_2^+ and D_3^+ ions. Originally, the inelastic electron scattering ionised the neutral D_2 molecules and created D_2^+ ions. These ions could undergo transformation to D_3^+ ions by scattering with neutral gas. Additionally, a small amount of D^+ ions is expected from molecular dissociation after electron impact ionisation.

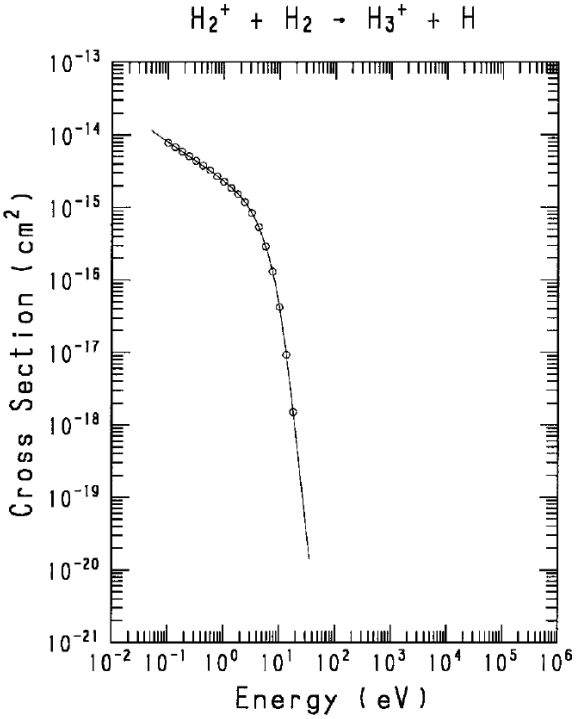

Figure VIII.8.: **Cross section for the transformation of D_2^+ ions to D_3^+ ions.** From [Tab00].

Table VIII.1.: **Mean free paths of D_2^+ ions for the transformation to D_3^+ ions.** The mean free paths $\lambda = 1/(\sigma \cdot \rho)$ were calculated with the cross sections $\sigma(1\text{ eV}) = 2 \cdot 10^{-15}$ cm^2 and $\sigma(20\text{ eV}) = 1 \cdot 10^{-18}$ cm^2 according to figure VIII.8. For the calculation of the deuterium densities ρ from the measurement pressures, a temperature of 300 K was used; it was further considered that the pressure inside ELIOTT was only about 40% of the pressure measured in the gas supply (see appendix refsec.app.ELIOTTpressure).

Pressure in gas supply	λ(1 eV)	λ(20 eV)
$3 \cdot 10^{-3}$ mbar	0.173 m	345 m
$5 \cdot 10^{-2}$ mbar	0.010 m	21 m
$1 \cdot 10^{-1}$ mbar	0.005 m	10 m

In order to estimate the species of the ions during the various measurements, the ion mean free path for the transformation to D_3^+ is shown in table VIII.1 for ions with kinetic energies of 1 eV and 20 eV. According to eq. III.22 from section III.2.3, the mean free path $\lambda = 1/(\sigma \cdot \rho)$ [Per09] depends on the gas density ρ and the cross section σ of the process. The gas densities were calculated from the deuterium pressure for a temperature of 300 K; and the cross sections are shown as a function of the ion energy in figure VIII.8.

Above 10 eV, the cross section decreases sharply. Therefore the mean free path at 20 eV is much larger than the 0.6 m long passage from the ELIOTT electrodes to the rear wall. Consequently, ions with energies of 20 eV or larger are expected to leave ELIOTT as D_2^+ ions. Thermal ions instead will almost always be D_3^+ ions, even if the thermalisation requires some path length.

According to the ion energy spectra from figure VIII.7, most of the ions inside the ion source have either thermal energies or the original energy of 90 eV. In case of the measurements at $3 \cdot 10^{-3}$ mbar, the majority of ions has energies around 90 eV and are therefore D_2^+ ions – this concerns the investigation of ion blocking with the ring electrodes (section VIII.3) and of ion transport through the PS (section VIII.5). At all other measurements with pressures of $5 \cdot 10^{-2}$ mbar and $1 \cdot 10^{-1}$ mbar, the low energetic ions dominated. Especially when an offset voltage was applied, the pencil beam contained almost only thermal ions and therefore D_3^+.

VIII.2. Ion detection via ionisation of residual gas in the MS

The ion pencil beam from the ELIOTT setup was guided magnetically through the beamline into the spectrometers. In the high voltage, the positive ions ionised the residual water and the secondary electrons were detected with the FPD (see section for the detection principle). Because the ions were collimated to a thin pencil beam, they created a beam spot on a few pixels of the FPD.

The ion detection via ionisation in the spectrometers during First Light was the first time that this ion detection method was used – the measurements therefore constituted a proof-of-principle for the method in the first place. The ionisation method was however also the only way to detect ions during the First Light measurements, apart from the Faraday cup ring inside ELIOTT and PULCINELLA during the determination of the ionisation efficiency.

As will be discussed in section VIII.2.2, the rate of secondary electrons from the PS was much higher than the rate of secondary electrons from the MS with the same ELIOTT settings. This was partly due to the larger pressure in the PS, which was not being pumped during the First Light campaign. Nevertheless, prelimnary results of the STS IIIa measurement campaign from October 2018 indicate that the ionisation efficiency in the PS is in fact pressure-independent and lager than predicted. The MS ionisation effieicny, which will be reported in the following, however, agrees well with theory; its pressure dependence could not be investigated during First Light due to technical constraints.

This section will first recall the measurement principle of the ionisation method in section VIII.2.1, which also describes the systematic effects and the analysis procedure during First Light specifically. Then the dependence of the ionisation efficiency on the spectrometer's high voltage will be discussed for the PS and MS in section VIII.2.2; in contrast to the expectations, a much larger secondary electron rate was observed from the PS than from the MS. For this reason and due to measurement time constraints, the ionisation efficiency was only determined for the MS (see section VIII.2.3) and only the MS was used for the detection of ions in further measurements (see section VIII.2.4 for the measurement scheme).

VIII.2.1. Measurement principle, systematic effects and analysis

The ion pencil beam was detected in the Main spectrometer via ionisation of the residual gas: as explained in section IV.1, the negative high voltage in the MS of about -18.6 kV accelerated the positive ions so that they flew non-adiabatically across the flux tube into the spectrometer walls. On their way, the ions ionised in turn the residual gas in the MS as shown in figure VIII.9; the secondary electrons were guided by the magnetic field to the FPD where the electron rate was measured as an indicator for the ion flux.

The inner electrodes of the MS had an asymmetric setting during most of the measurements in order to guide as many secondary electrons as possible to the FPD: the source side steep cone was at -200 V, the source side flat cone at -150 V, the central electrodes and the downstream flat cone were at -100 V and the downstream

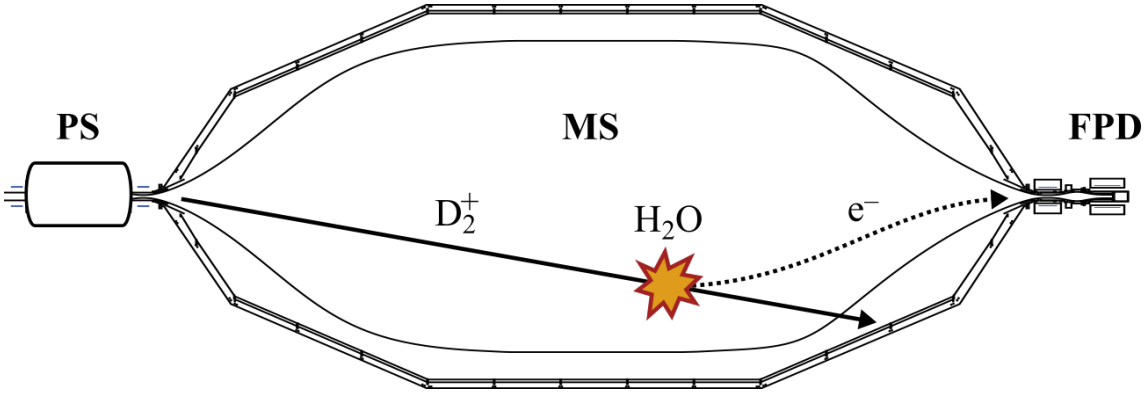

Figure VIII.9.: **Ionisation of residual H_2O in the Main spectrometer.** The D_2^+ and D_3^+ ions of the pencil beam were accelerated by about −18.6 kV and moved non-adiabatically towards the spectrometer walls. On their way across the flux tube, they created secondary electrons. The electrons followed the magnetic field and were detected by the FPD.

steep cone was at −3 V. A symmetric setting was only used during the test of ion blocking with the ring electrodes (section VIII.3): most of the inner electrodes were at −100 V and only the downstream steep cone was set to +97 V for electron transmission to the FPD. The MS vessel was always at −18.5 kV.

The residual gas in the spectrometers was dominated by water, because the setup was not baked for the First Light campaign. During the measurements, the pressure in the MS was on the level of 10^{-9} mbar and varied only by about ±15%. The absolute pressure in the MS volume can however not be determined because the pressure gauge[6] is located in one of the MS pump ports behind a cold baffle.

On the FPD, the secondary electrons from the ionisation process created a spot due to the collimated initial ion beam. This beam spot was usually in the center of the FPD, but could be moved with the DPS dipole electrodes via $E \times B$-drift (see section VIII.4). Around the beam spot, a flare appeared due to the straight motion of the ions through the MS and the consequent creation of secondary electrons all across the flux tube.

In the following sections, the FPD rate will be reported as a measure of the ion flux. This rate included all FPD pixels, because the contributions of the beam spot and the flare could not be separated. The only cut was applied to the energy spectrum of the FPD, which is shown in figure VIII.11: a region of interest of (25.72 . . . 30.72) keV was chosen, because the secondary electrons were created inside the MS potential of about −18.6 kV and were further accelerated in front of the detector by the post acceleration electrode with +10 kV; additionally, a bias voltage of 120 V was applied to the FPD.

[6]The pressure was measured with a Leybold IONIVAC IM 540 ionisation gauge controller with a trueness of ±10%. The calibration factor for nitrogen is 1.66.

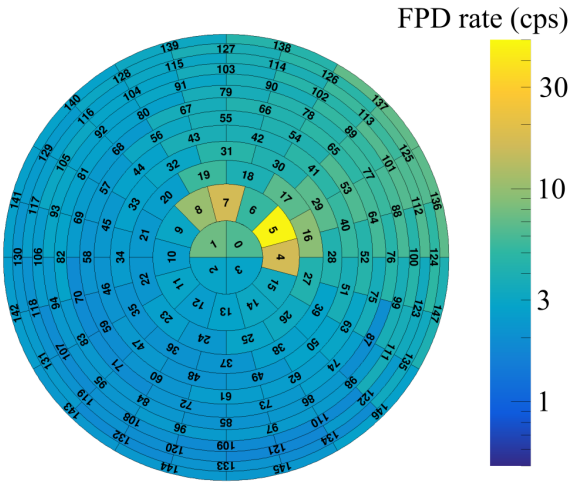

Figure VIII.10.: **Beam spot and flare in the pixelview of the FPD.** The ion pencil beam created a spot of secondary electrons in the center of the FPD; actually, two spots from ions with different kinetic energies can be identified, as detailed in section VIII.4. Starting from the spot and going to the outside, a flare appeared because the ions moved straight through the MS and across the magnetic flux tube (compare figure VIII.9). The flare spread across the complete flux tube probably due to the magnetron drift of magnetically trapped electrons. This FPD pixelview was created from a 10 min measurement of the D_3^+ ions with about 2 eV kinetic energy, right after the measurement of the corresponding spectrum in figure VIII.11.

VIII.2.2. High voltage dependence of the ionisation efficiency

The dependence of the ionisation efficiency on the high voltage of the spectrometers could be investigated during First Light over a broad energy range, because no beta electrons with a spectrum up to 18.6 keV were present, yet.

For this investigation, one of both spectrometers always remained at 0 V while the high voltage of the other was increased stepwise; with the FPD, the relative change of the secondary electron rate was observed. A constant flux of D_2^+ ions into the spectrometers was produced by setting the ELIOTT pressure to about $3 \cdot 10^{-3}$. Because ELIOTT was not floated on an offset voltage, the ion energy was determined by the ELIOTT electrodes: exceptionally, the positive electrodes were set to +90 V (electrode (C) in figure VIII.2) and +50 V (cylinder electrode), so that the ion energy is assumed to have been about 50 eV.

Figure VIII.12 shows that the secondary electron rate increased with the high voltage of the MS and the PS. This had been expected because the high voltage provided ever more kinetic energy to the ELIOTT ions. With the energy of the projectile ions increased however also the cross section for inelastic scattering (see figure IV.3 in section IV.2). The increase appears to be rather linear apart from statistical fluctuations.

In contrast to the expectations however, the secondary electron rate from the PS is much larger than the rate from the MS: actually, the rate from the PS should be

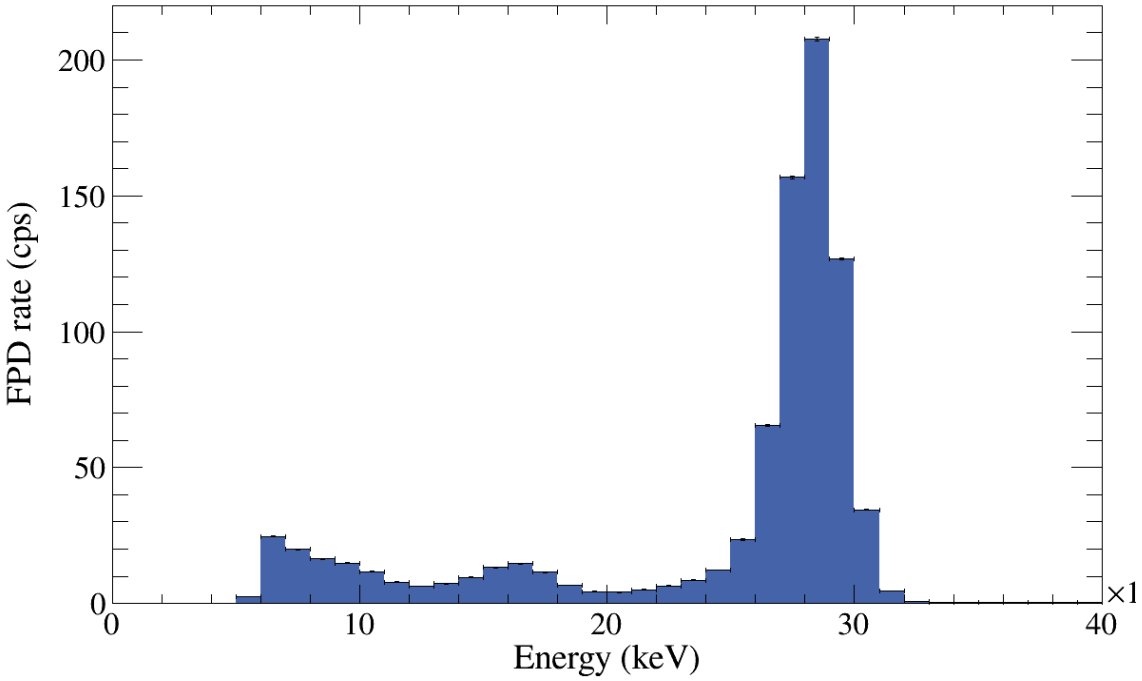

Figure VIII.11.: **Region of interest (ROI) of the FPD energy spectrum.** The ROI was chosen between (25.72 . . . 30.72) keV, because the secondary electrons were created by ionisation in the MS at about −18.6 kV and further accelerated by the post acceleration electrode at the detector with +10 kV. Between 10 keV and 20 keV appears a peak from negative H_2O^- ions which were also created inside the MS but lost part of their energy in the dead layer of the FPD. Below 10 keV, the spectrum becomes cut off due to the post acceleration. This exemplary energy spectrum was created from the same run as figure VIII.10.

about ten times smaller due to the likewise shorter path length of the ions through the PS. The total discrepancy of a factor $1.5 \cdot 10^4$ can be explained in part with the fact that the PS was not pumped during the First Light campaign; according to appendix A.3, the pressure in the PS under these conditions should be 370 times larger than in the MS. Another reason might have been the asymmetric setting of the PS inner electrodes[7]: this was observed to increase the rate of secondary electrons from the PS also by about one magnitude during the preparation for First Tritium. Also, the rate difference might have been due to the larger flare during the PS measurements, about 4 times larger than the beam spot. Eventually, the STS IIIa commissioning measurements with deuterium ions indicated in October 2018 that the ionisation efficiency in the PS is in fact larger than predicted and on top seems to be pressure-independent.

[7]The PS inner electrode setting was −500 V at the upstream cone electrode, −400 V at the wire electrodes and −300 V at the downstream cone electrode.

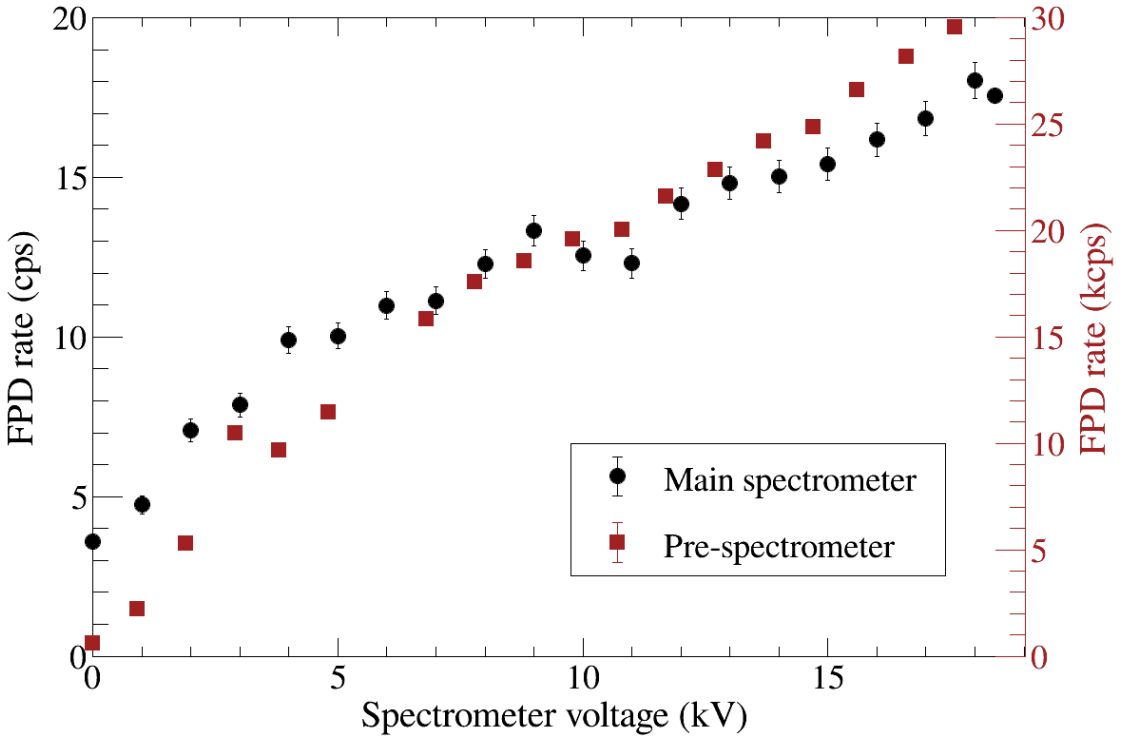

Figure VIII.12.: **Increase of the ionisation efficiency with the high voltage in MS and PS.** With the high voltage increased the energy of the incoming D_2^+ ions and the cross section for the ionisation of residual gas (compare figure IV.3 in section IV.2). The much larger ionisation rate in the PS is mostly explained with the about 370 time larger pressure in the PS, which was not being pumped during First Light; also, preliminary results of the STS IIIa measurements indicate a pressure independent and larger-than-expected ionisation efficiency.

VIII.2.3. Absolute ionisation efficiency

The deuterium ions from the ELIOTT source offered a rare occasion to measure the ionisation efficiency in the spectrometers without risk of tritium activity as a consequence of the ion flux. As will be discussed in the following, the measurement confirmed the result of the KASSIOPEIA simulations for the ionisation efficiency in the MS. The simulations were then transferred to the PS and used for the determination of the upper limit on the ion flux into the PS during First Tritium.

According to section IV.2, the ionisation efficiency is the ratio of the secondary electron rate at the FPD due to ionisation and the total flux of ions into the PS or MS, which causes the ionisation. For the measurement of the total ion flux, the PULCINELLA node between the MS and the FPD was used (see section VII.2.5). Because PULCINELLA could only measure ion fluxes on the order of $6 \cdot 10^6$ ions/s, the ion rate was increased by testing various deuterium pressures and offset voltages in ELIOTT. Eventually, a pressure of $5 \cdot 10^{-2}$ mbar was chosen along with offset voltages of +32 V at the ELIOTT hull, +30 V at the transition flange and +28 V

at the rear wall. This created a pencil beam with mostly D_3^+ ions of about 30 eV energy (see spectrum in figure VIII.1.4).

The rate of secondary electrons from the ionisation processes in the MS was measured to be $R_{\mathrm{FPD}} = 3078 \pm 7$ cps at about -18.6 kV and a pressure of about $3 \cdot 10^{-9}$ mbar residual H_2O; the background of 2 cps was neglected. Right before that, the ion current had been measured with PULCINELLA, which was set to about -20 V in order to prevent the blocking of the ions by the work function of the PULCINELLA disc[8]; after subtracting the background, the net current was converted with the Coulomb number[9] into the total ion flux $\Phi_{\mathrm{ion}} = (2.6 \pm 0.1) \cdot 10^7$ ions/s. Dividing the FPD rate through the total ion flux results in the ionisation efficiency:

$$\mathcal{E} = \frac{R_{\mathrm{FPD}}}{\Phi_{\mathrm{ion}}} = (1.18 \pm 0.05) \cdot 10^{-4} \text{ counts / ion at } 3 \cdot 10^{-9} \text{ mbar and } -18.6 \text{ kV in the MS.} \tag{VIII.1}$$

The stated uncertainties are only statistical, because the systematic uncertainties are hard to quantify:

- **Ion transport through the MS:** Only a fraction of the D_3^+ ions which entered the MS might have been guided magnetically to the PULCINELLA node, but the complete ion flux into the MS affected the ionisation measurement. As will be discussed in section VIII.5.1, the ion transport through the PS was about two times larger when the PS1 and PS2 magnets were at 40% then when they were at 20%. During the measurement of the ionisation efficiency, these two magnets were at 40% and the pinch magnet at the downstream end of the MS was at 20%. Not more than half of the ions which entered the MS might have reached the PULCINELLA disc – a quantitative estimate requires however dedicated KASSIOPEIA simulations, which could also take into account the ion energy of about 30 eV. Qualitatively, the underestimation of the ion flux Φ_{ion} leads to an overestimation of the ionisation efficiency $\mathcal{E}$ by at least a factor 2. A measurement with the ionisation method would therefore underestimate the actual ion flux $\Phi_{\mathrm{ion}} = R_{\mathrm{FPD}}/\mathcal{E}$.

- **Pressure in the MS:** Because the pressure was measured with a pressure gauge behind a cold baffle, the actual pressure in the MS might have been larger by an unknown factor. This, too, would lead to an overestimation of the ionisation efficiency $\mathcal{E}$ and an underestimation of the ion flux $\Phi_{\mathrm{ion}} = R_{\mathrm{FPD}}/\mathcal{E}$ which would be measured with the ionisation method. There is however no way to determine the exact pressure in the volume of the MS; it is possible in the PS, though.

- **Alignment of the pencil beam:** When the ion pencil beam was drifted with the dipole electrodes as shown in section VIII.4, the rate preliminary increased. The assumed reason is that the off-axis ions had another average path length through the MS and therefore another ionisation efficiency. A quantitative assessment of the effect of the radial ion position on the ionisation efficiency

[8] During the measurement with PULCINELLA, the PS and MS were at 0 V.
[9] 1 C=$6.24 \cdot 10^{18}$ charged particles per second.

would require dedicated KASSIOPEIA simulations. The alignment of the ions in the PS2 magnet can however not be determined precisely due to the negative electrostatic drift potential which will also be discussed in section VIII.4.

- **Inner electrode settings:** The setting of the MS inner electrodes during the measurement of the ionisation efficiency was not logged. In case of a symmetric potential, only a fraction of the secondary electrons from ionisation processes in the MS arrive at the FPD. This would lead to an underestimation of the ionisation efficiency $\mathcal{E}$ and an overestimation of the ion flux $\Phi_{\mathrm{ion}} = R_{\mathrm{FPD}}/\mathcal{E}$ which would be measured with the ionisation method.

The measured ionisation efficiency can be compared to the simulation results[10] which were detailed in section IV.2. Under the same conditions of $3 \cdot 10^{-9}$ mbar residual water and -18.6 kV in the MS, the simulations predict an ionisation efficiency of $\mathcal{E} = (7.66 \pm 0.18) \cdot 10^{-5}$ counts/ion. The measurement result is a factor 2 larger than the simulation, as expected due to the ion transport through the magnetic field of the MS. This does however not account for the expected increase of the ionisation efficiency by the underestimated pressure in the MS volume. Also, the simulation was carried out with a symmetric setting of -100 V at all inner electrodes of the MS; if the inner electrode were actually set to a slide potential during the measurement, this would have led to a larger electron rate R_{FPD} and thus to a larger ionisation efficiency $\mathcal{E}$.

VIII.2.4. Measurement scheme of the following sections

For the measurements, which will be presented in the following section, the knowledge of the ionisation efficiency is not necessary. Only the relative change of the FPD rate is required to measure the effect of the ion blocking and removal instruments on the pencil beam, which was created at the rear section and detected via ionisation in the MS.

First, the next section will report that ions could be blocked successfully with the ring electrodes (section VIII.3). After that, the successful ion drift and even removal with the dipole electrodes will be detailed (section VIII.4). In section VIII.5, the ion transport through the PS will be discussed when changing its magnetic field and high voltage.

Ions were however also blocked inadvertently inside the beam tube. As section VIII.6 will report, the application of an offset voltage to the ELIOTT setup eventually equipped thermal ions with enough offset energy to reach the Main spectrometer.

[10] The simulations were carried out by Woo-Jeong Baek for Master's Thesis *Investigation of background processes of ions and Rydberg atoms in the KATRIN spectrometers*, (2017).

VIII.3. Ion blocking with the ring electrodes in DPS and PS

The ion blocking with the ring electrodes was tested successfully with the measurement scheme from section VIII.2.4: deuterium ions were created with ELIOTT and measured via ionisation in the MS. In between, the ring electrode potentials were raised until only the MS background was measured anymore (compare figure VIII.14). The relative decrease of the FPD rate allows to state an ion suppression by about two orders of magnitude for the four ring electrodes in the DPS and in the PS.

For this measurement, the pressure in the ELIOTT deuterium supply was set to $3 \cdot 10^{-3}$ mbar and no offset voltage was applied to ELIOTT. The observed ions were therefore almost exclusively D_2^+ ions (see section VIII.1.5) with an energy around 90 eV as shown by the spectrum in figure VIII.7. The small deuterium pressure provided a stable ion flux over the course of the measurements; however, the magnitude of the unblocked ion flux is larger for the measurements with the DPS than with the PS electrodes. That's because the measurements were carried out on two different days with slightly different settings of the hand valve in the deuterium supply.

Figure VIII.13 shows the decrease of the ion rate as the voltage of the ring electrodes was raised. The rate does not decrease sharply due to the ion energy distribution (see the spectrum in figure VIII.7). In order to completely block the ions with the ring electrode in DPS PP5, a much larger voltage is required than with the other electrodes due to its larger radius: according to section VI.1, the potential in the center of the PP5 ring electrode is only 40% of the applied voltage[11]. At an average ion energy of 90 eV, the ion flux is therefore expected to be half blocked around 225 V – this agrees well with the observation. Likewise, the ring electrode in DPS BT5 should block half of the ions at 107 V (84.2% of the applied voltage in the center) and the ring electrode in the PS1 at 194 V (46.5% in the center). According to figure VIII.13, these voltages were however sufficient to block almost all of the

[11] Master's thesis of Rudolf Sack: *Aufbau einer Ionenquelle und Simulation der Transporteigenschaften der DPS und CPS am KATRIN Experiment*, (2015)

Table VIII.2.: **Observed ion flux reduction with the ring electrodes.** The reduction factor is the ratio of the FPD rate without and with maximal ring electrode voltage. Larger reduction factors could not be observed because the limited unblocked ion flux during this measurement.

Ring electrode	Unblocked rate (cps)	Minimal rate (cps)	Reduction factor
DPS BT5	165.23 ± 2.35	0.93 ± 0.18	177 ± 34
DPS PP5	165.23 ± 2.35	0.89 ± 0.18	185 ± 37
PS1	105.69 ± 1.91	2.45 ± 0.29	43 ± 5
PS2	108.00 ± 1.93	0.83 ± 0.17	131 ± 27

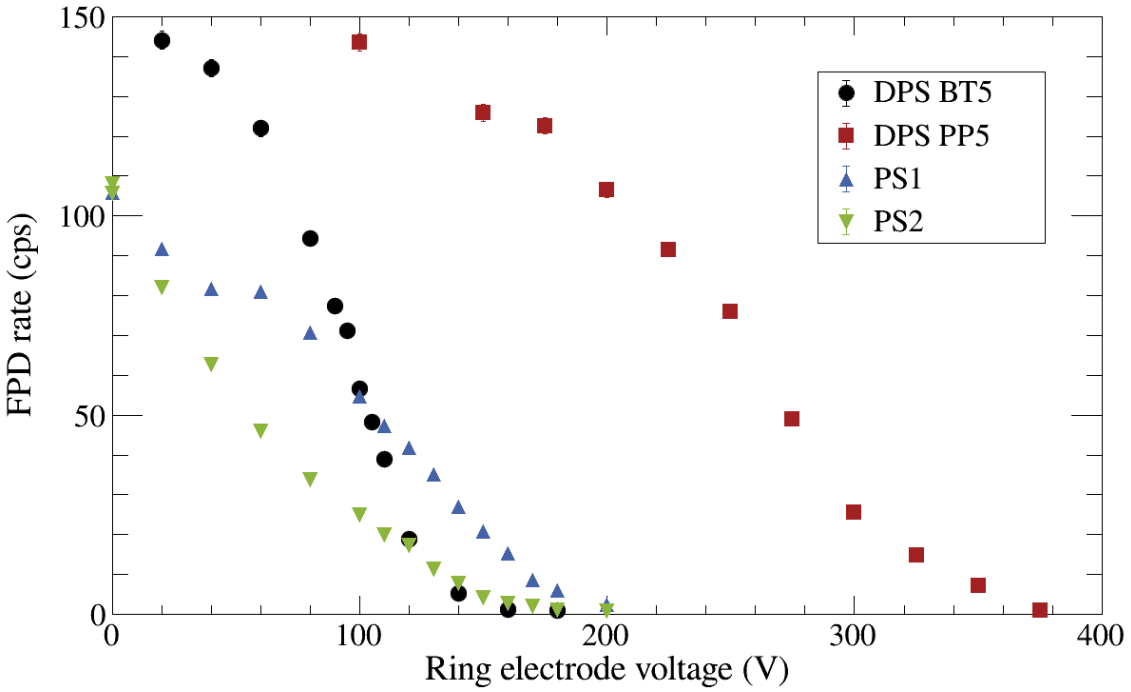

Figure VIII.13.: **Ion blocking with ring electrodes.** For sufficiently large ring electrode voltages, the ion flux into the MS disappears. The width of the rate decrease depends on the energy distribution of the ions around 90 eV and the width of the ring electrodes. Due to different pressure settings at ELIOTT on two different measurement days, the unblocked ion fluxes are also different.

ion flux. It is therefore assumed that the pencil beam was not in the center of these two ring electrodes and experienced a larger blocking potential.

The efficiency of the ion blocking was estimated by the ratio of the FPD rates without and with maximal ring electrode voltage. Table VIII.2 lists the obtained reduction factors: they are mostly on the order of two magnitudes, but only about a factor 40 for th PS1 ring electrode. Larger reduction could not be measured due to the level of the MS background and the unblocked rate, which was limited in order to prevent damage to the FPD.

The observed ion reduction of the DPS ring electrodes by slightly more than two orders of magnitude is not sufficient to reduce the expected ion flux from the WGTS of $2 \cdot 10^{11}$ ions/s (see section III.2.1) below the radiation safety limit of $2 \cdot 10^{8}$ ions/s (see section V.1). Even less can the desired reduction by seven orders of magnitude to the ion flux limit of $1 \cdot 10^{4}$ ions/s be achieved (see section V.3). However, even the First Tritium measurements could not derive stricter reduction factors because the thermal ions did not reach the ring electrodes (see section IX.3) and the total rate of dissociation ions from the WGTS is not known (see section IX.2.3).

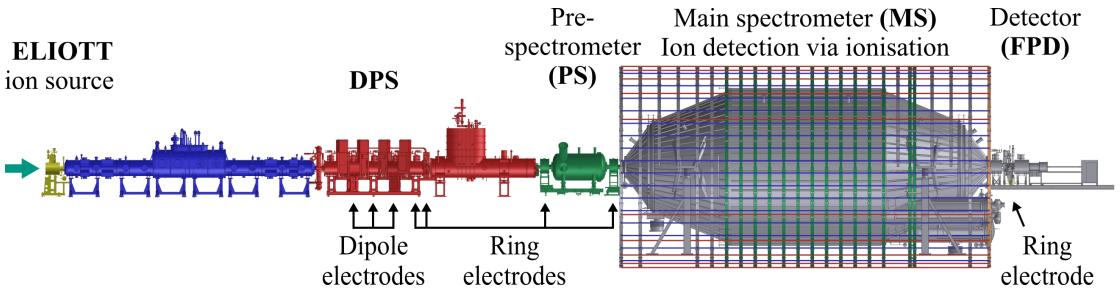

Figure VIII.14.: **Position of the ring and dipole electrodes.** Ions were injected with ELIOTT as a thin pencil beam at the rear section and detected via ionisation in the MS. The fourth dipole electrode in DPS BT1 was only installed after the First Light campaign.

VIII.4. Ion removal with the DPS dipole electrodes

The ion pencil beam from the ELIOTT setup at the rear section created a beam spot on the FPD, which allowed to observe the ion drift with the dipole electrodes: when the dipole voltage was increased, the beam spot drifted across the FPD pixels. This measurement was the proof-of-principle of ion drift and ion removal with the dipole electrode in the DPS BT2, BT3 and BT4, which are shown in figure VIII.14 – the fourth dipole electrode in DPS BT1 was installed only after First Light campaign, as will be explained in section VIII.7.

For this measurement, low energetic ions were preferred because they spent more time inside the dipole electrodes and were consequently stronger affected by the $E \times B$-drift. In order to thermalise the ions most efficiently, the deuterium pressure at ELIOTT was set to $1 \cdot 10^{-1}$ mbar; because the thermal ions were however inadvertently blocked, small offset voltages were applied to the ELIOTT hull (+4 V), the transition flange (+2.5 V) and the rear wall (+2 V). With these settings, the ion pencil beam consisted mostly of D_3^+ ions at about 2 eV energy with a small contribution of D_2^+ ions at about 90 eV (see sections VIII.1.4 and VIII.1.5). The large deuterium pressure decreased however by about 15% during the measurements of about 1 h (compare phase 5 and 6 in figure VIII.5); according to figure VIII.6, this increased the total ion flux by more than 50%. It is therefore not possible to interpret the magnitude of the ion flux during this measurement, only the position of the dominant beam spots on the FPD pixel view.

Figure VIII.15 shows the drift of the beam spot across the FPD due to the drift in the BT2 dipole electrode. The dipole voltage was increased quadratically because the drift distance is expected to increase with the square root of the dipole voltage (see appendix A.6). In figure VIII.15, this square root dependence seems to be fulfilled rather well.

Ultimately, the ion pencil beam could be completely removed with the dipole electrode in BT2 alone: between a dipole voltage of −324 V and −361 V, the beam spot disappears. This observation agrees with the theoretical expectation according to appendix A.6, that the ions should be drifted by (37.63 . . . 40.29) mm for the given dipole voltages; after 40 mm, the pencil beam would be drifted from the center of the dipole electrodes onto the lobes. The efficiency of the ion removal was enhanced

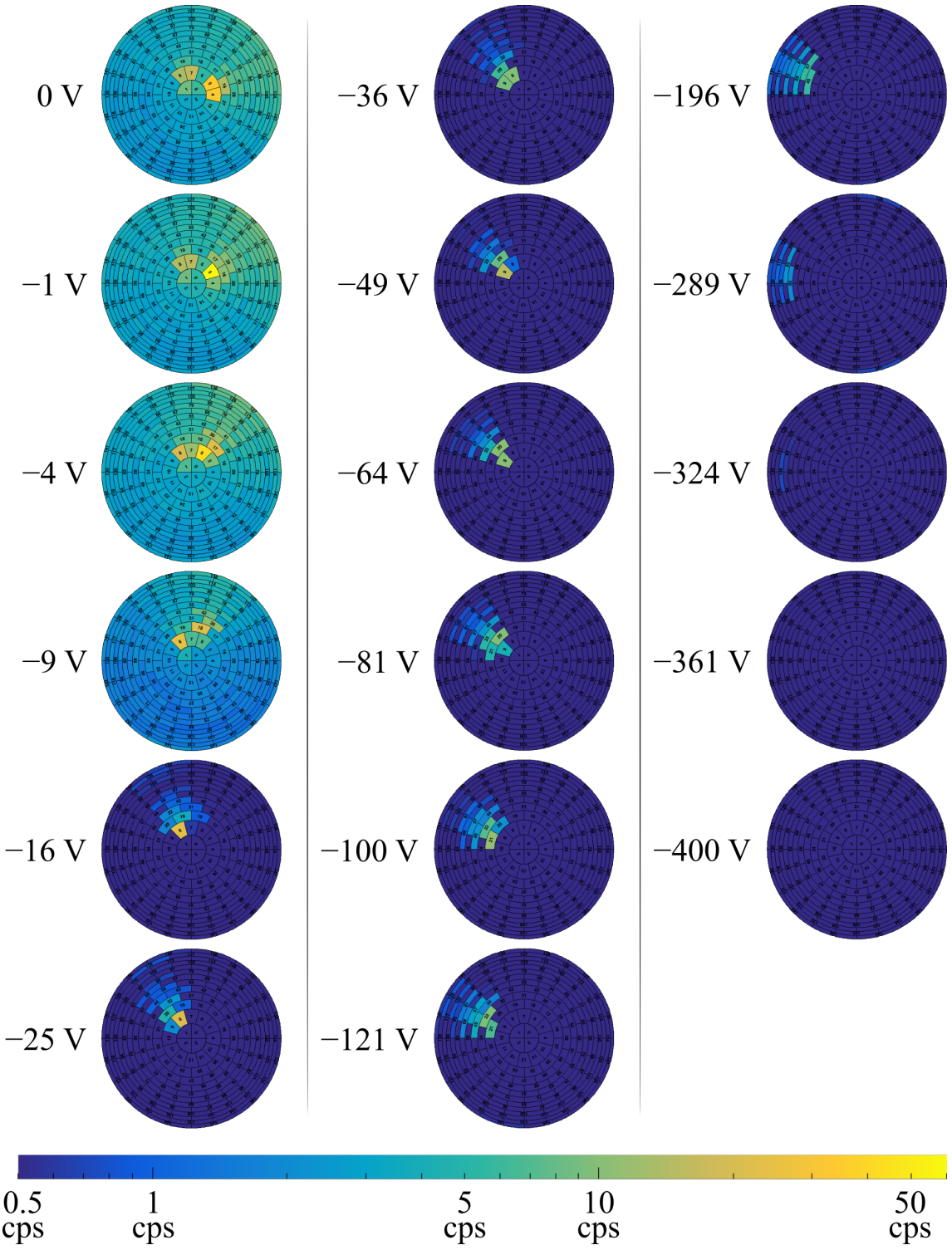

Figure VIII.15.: **Ion drift with the dipole electrode in DPS BT2.** The numbers on the left state the voltage on the upper electrode, whereas the lower electrode was always at 0 V. As expected, the drift distance of the beam spot increased with the square root of the dipole voltage. Between −314 V and −361 V, the pencil beam was removed completely.

by the weak magnetic field of about 1 T in the dipole electrodes, corresponding to 20% nominal magnetic field strength – during the neutrino mass measurements, the magnetic field will be at 70% and the drift distance at the same dipole voltage becomes 3.4 times smaller. Because the ions with the highest kinetic energy should be removed last, the ion energy was assumed to be 120 eV in accordance with the energy spectrum from figure VIII.7.

Also the dipole electrodes in BT3 and BT4 could remove the ion pencil beam completely, as shown in figure VIII.16. The azimuthal angles of the remaining beam spot at −289 V are slightly different, corresponding to the slightly different orientation of the dipole electrodes in the beam tube as a result of the commissioning procedure.

When the negative voltage was applied to the lower electrode, the dipole drift changed direction and moved the beam spot to the right side of the FPD as expected from the $E \times B$-law. Figure VIII.17 shows the corresponding FPD pixel views. But the interpretation of the observations requires to consider the electrostatic potential which was observed during First Light at the position of the PS2 magnet: a negative potential of up 110 eV was observed in the bottom quarter of the flux tube; the center of the potential was rotated clockwise by about 7.5°C relative to the very bottom [Hac17]. This negative potential constantly drifted the ion pencil beam to the right side of the FPD just in front of the MS[12].

Because the thermal ions with about 2 eV offset energy spent more time in the inadvertent dipole potential, they were drifted farther and created the more intense beam spot on the right from the center of the FPD; the less intense hotpot on top of the FPD center was caused by the 90 eV ions which were hardly affected by the inadvertent drift. When the BT2 dipole electrode created another negative potential in the lower half of the flux tube, the drift to the right was increased and the beam spot from thermal ions disappeared already at −9 V. Applying the same voltage to the upper electrode, the beam spot from thermal ions is still in the center of the FPD, because the drift was partly compensated by the negative potential in the PS2 magnet. From −16 V on, the two beam spots were no longer separated; interpreting the intensities of the beam spots is not trivial due to the decrease of the deuterium pressure in ELIOTT and the consequent increase of the total ion flux (see section VIII.1.3).

[12]The magnetic guiding field in the PS1 and PS2 magnets was at 80% to improve the ion transport through the PS.

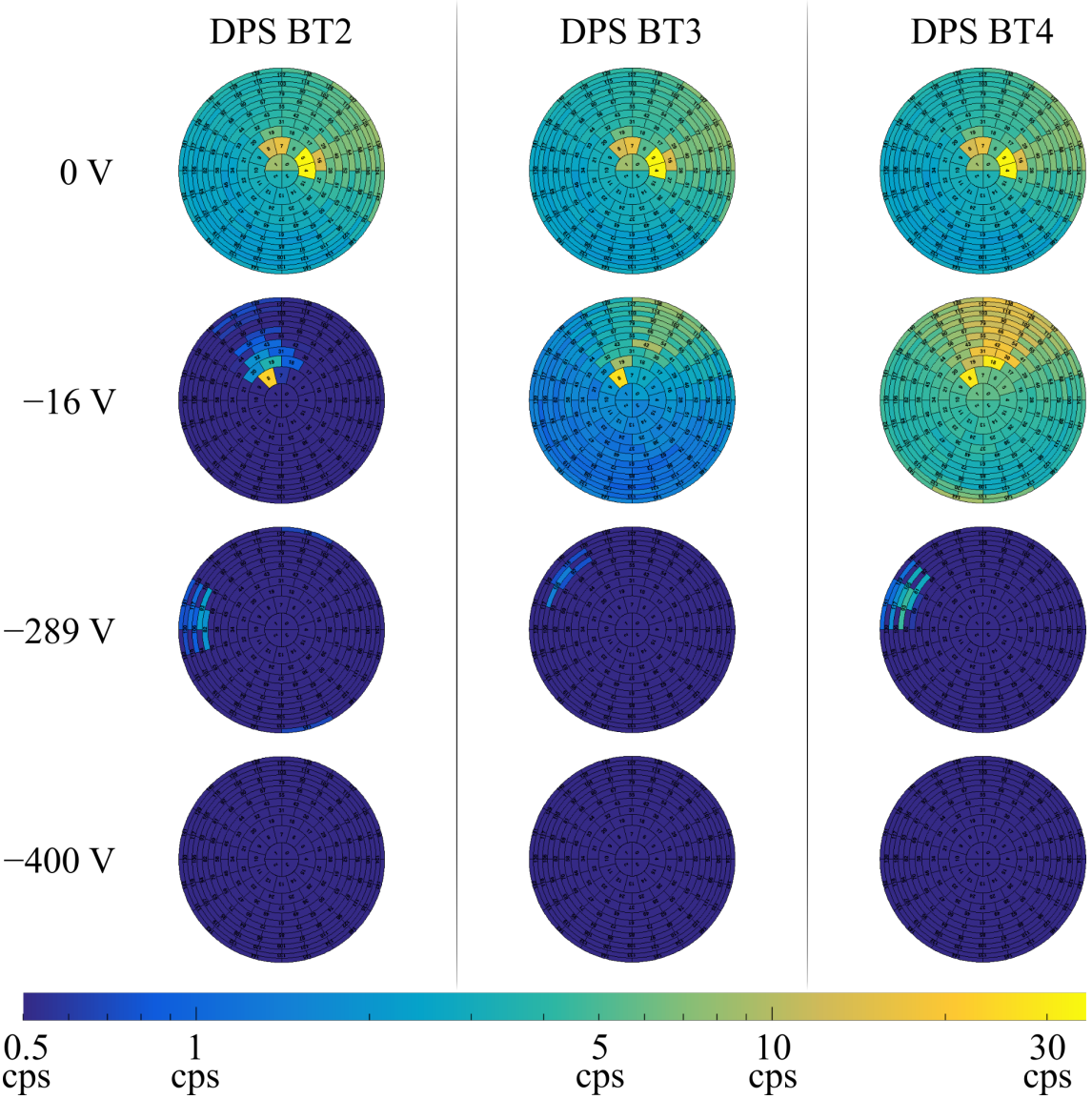

Figure VIII.16.: **Comparison of ion drift in DPS BT2, BT3 and BT4.** The numbers on the left state the voltage on the upper electrode, whereas the lower electrode was always at 0 V. In the top row, the same reference run is displayed for all three dipole electrodes. At −16 V, the flares around the beam spots have different brightness because the deuterium pressure in ELIOTT decreased so that the overall ion flux increased (see section VIII.1.3). The different tilts of the remaining beam spots at −289 V are caused by the orientation of the dipole electrodes in the beam tubes. Eventually, all dipole electrodes remove the ion pencil beam completely.

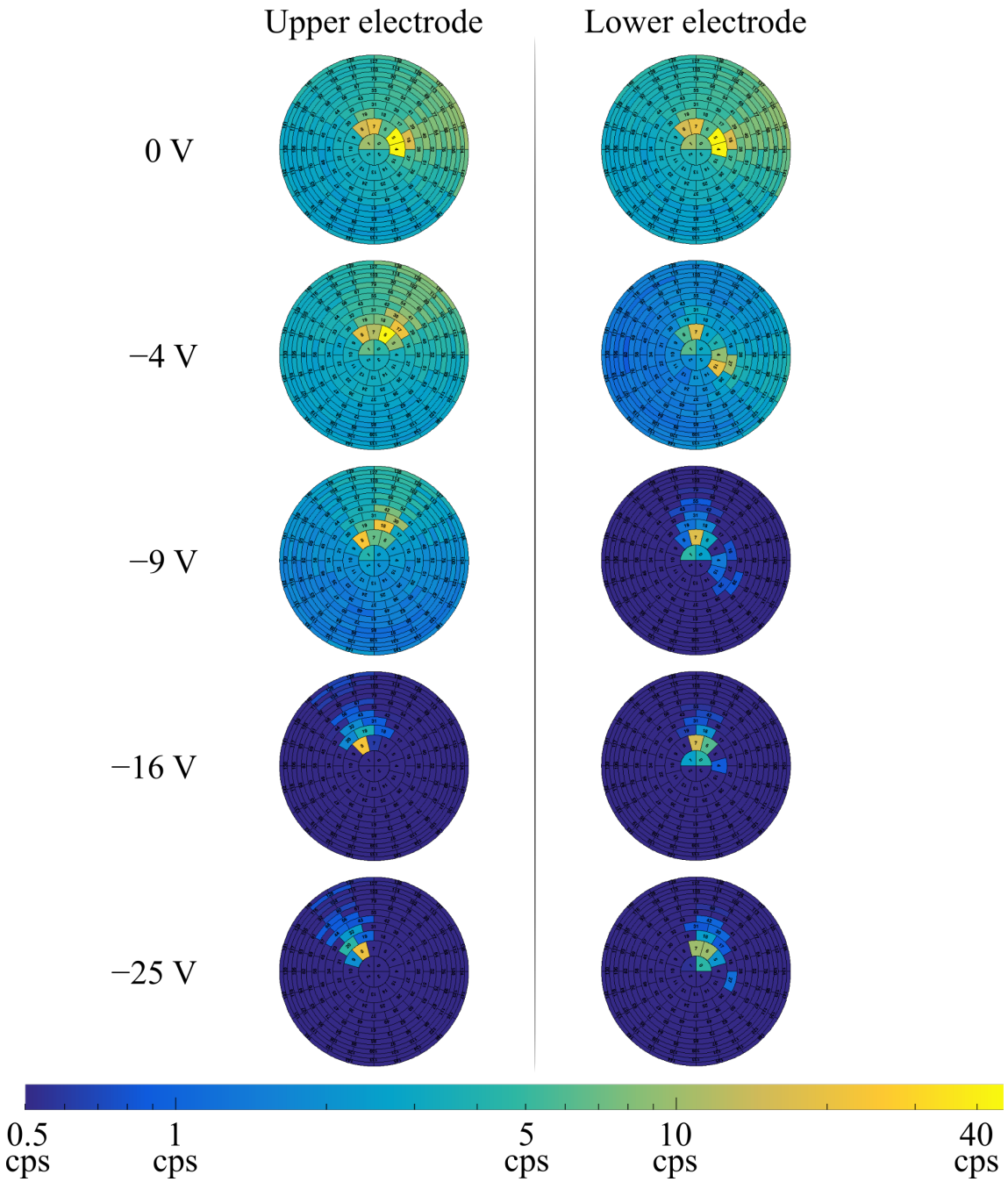

Figure VIII.17.: **Ion drift in opposite directions.** The ions were drifted to the left (right) when the negative voltage was applied to the upper (lower) electrode of the DPS BT2 dipole; this electrode voltage is indicated by the numbers on the left, whereas the lower electrode was always at 0 V. In the top row, the same reference run is displayed: it shows one beam spot from 2 eV ions at the right of the FPD center and one less intense spot by 90 eV ions on top. The two ion energy regimes (compare the spectrum in figure VIII.7) were drifted apart by an inadvertent dipole potential of −110 V on the bottom of the beam tube in the PS2 magnet (see [Hac17]).

VIII.5. Ion transport through the Pre-spectrometer

The First Light measurements allowed to investigate the ion transmission through the PS with a large flux of inactive ions: while the ion flux was measured in the MS, its dependence on the magnetic field strength (section VIII.5.1) and the high voltage in the PS (section VIII.5.2) could be measured.

VIII.5.1. Dependence on the magnetic field strength

Along the magnetic flux tube, the ions are guided adiabatically by the strong magnetic field which is usually on the order of a few Tesla. Inside of the spectrometers however, the magnetic field decreases significantly in order to magnetically collimate the beta electron momenta: the field decreases to the level of about 12 mT in the center of the PS[13] and to (0.3 . . . 1.5) mT in the center of the MS. The beta electrons are still guided adiabatically, but the heavier ions of hydrogen isotopes leave the flux tube non-adiabatically with a certain probability.

Figure VIII.18 shows the ion flux into the MS while only the magnetic field in the PS was ramped up: the ion flux increased rather linearly by almost one magnitude between 20% and 80% nominal magnetic field strength. For this measurement, the ions were created with $3{\cdot}10^{-3}$ mbar ELIOTT pressure; the ions are therefore assumed to be mostly D_2^+ ions with energies between 60 eV and 100 eV (see sections VIII.1.4 and VIII.1.5).

The measurement can be compared to extensive simulations[14] of the ion transport through the PS with KASSIOPEIA. According to these simulations, the transport probability also depends on the initial distance of the ion from the axis of the magnetic field. Right on the axis, the ion transport probability is 0.5 at 20% magnetic field and 0.9 at 80% magnetic field. As the ion moves off-axis, the transport probability decreases: 3.7 cm off axis, at the border of the transported flux tube from the CPS, the transport probability is only a few 10^{-3} at 20% magnetic field and still about 0.2 at 80% magnetic field. The observed increase of the ion flux by about one magnitude is compatible with a position of the pencil beam 1 cm off-axis.

The measurement highlights one of the major systematic uncertainties for the determination of the ionisation efficiency in the MS (see section VIII.2.3): only a fraction of the incoming ions will arrive at the end of the spectrometer due to the weak magnetic field, especially if they are off-axis. The ionisation efficiency was however determined from the FPD rate, caused by all ions which entered the MS, divided by the PULCINELLA current due to ions which arrived at the end of the MS. For comparison: if the pencil beam was in fact 1 cm off-axis, the ion transport probability through the PS at 80% magnetic field was 0.7. In the MS, the transport probability is probably even smaller due to the smaller magnetic field. In order to assess this systematic uncertainty to the experimental determination of the ionisation

[13] 12 mT is the magnetic field in the center of the PS at 70% nominal strength. During First Light, the PS was set to various magnetic field strengths while the rest of the beamline was always at 20% nominal. The field in the center of the PS scales linearly with the applied magnetic field.

[14] The simulations were carried out by Woo-Jeong Baek for her Master's thesis *Investigation of background processes of ions and Rydberg atoms in the KATRIN spectrometers*, (2017).

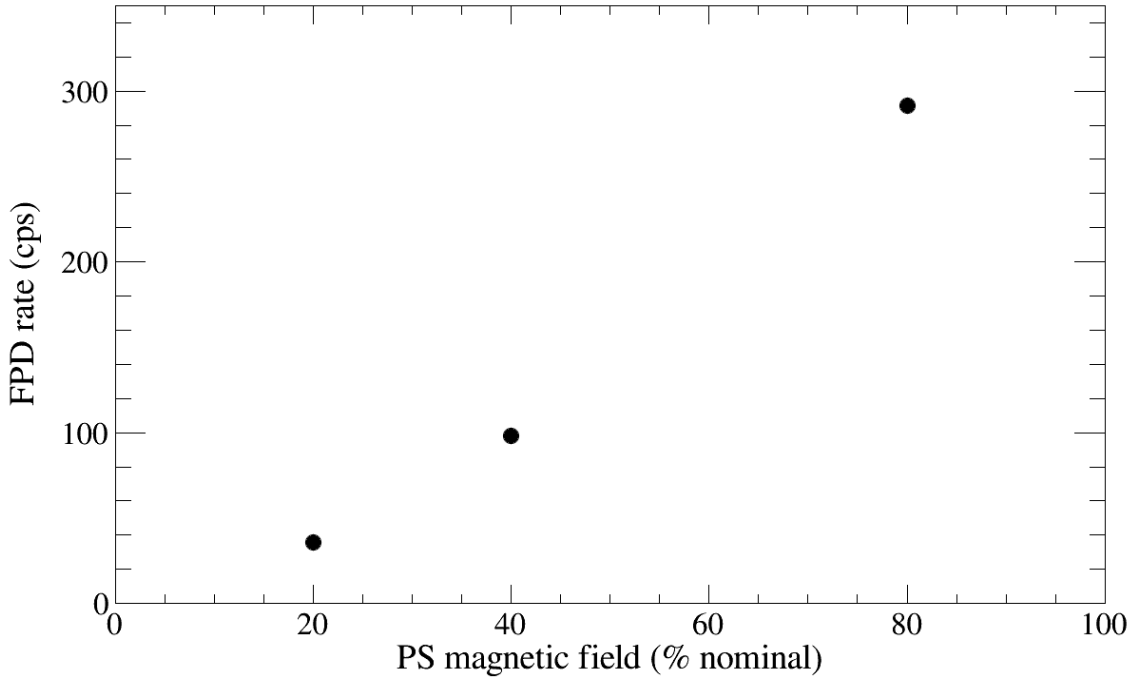

Figure VIII.18.: **Ion flux into the MS depending on the magnetic field in the PS.** The ion transmission probability through the PS increased rather linearly and by about one magnitude between 20% and 80% nominal magnetic field in the PS.

efficiency, dedicated KASSIOPEIA simulations of the ion transport through the MS would be required.

The comparison of measurement and simulation indicates that on-axis ions have the largest transmission probability to the MS with regard to the magnetic field. This is unpleasant, because on-axis ions are also the first to reach the spectrometers in case of a neutralisation of a ring electrode: the blocking potential is minimal in the center of the ring electrode.

VIII.5.2. Dependence on the high voltage

Besides the weak magnetic field, also the high voltage of the PS contributes to the non-adiabatic motion of the ions which eventually makes them leave the magnetic flux tube. As discussed in section IV.1, the negative high voltage accelerates the ions onto the vessel walls and electrodes.

The ion transmission probability through the PS was measured for various high voltage settings up to 1 kV; because the vacuum setup of the spectrometers was not baked for First Light, the pressure was comparatively large and did not allow higher voltages in the PS while the MS was at −18.6 kV for the ion detection via ionisation.

The measurement was carried with two different ion species and magnetic field strengths in the PS:

- With 20% nominal magnetic field in the PS and $3 \cdot 10^{-3}$ mbar ELIOTT pres-

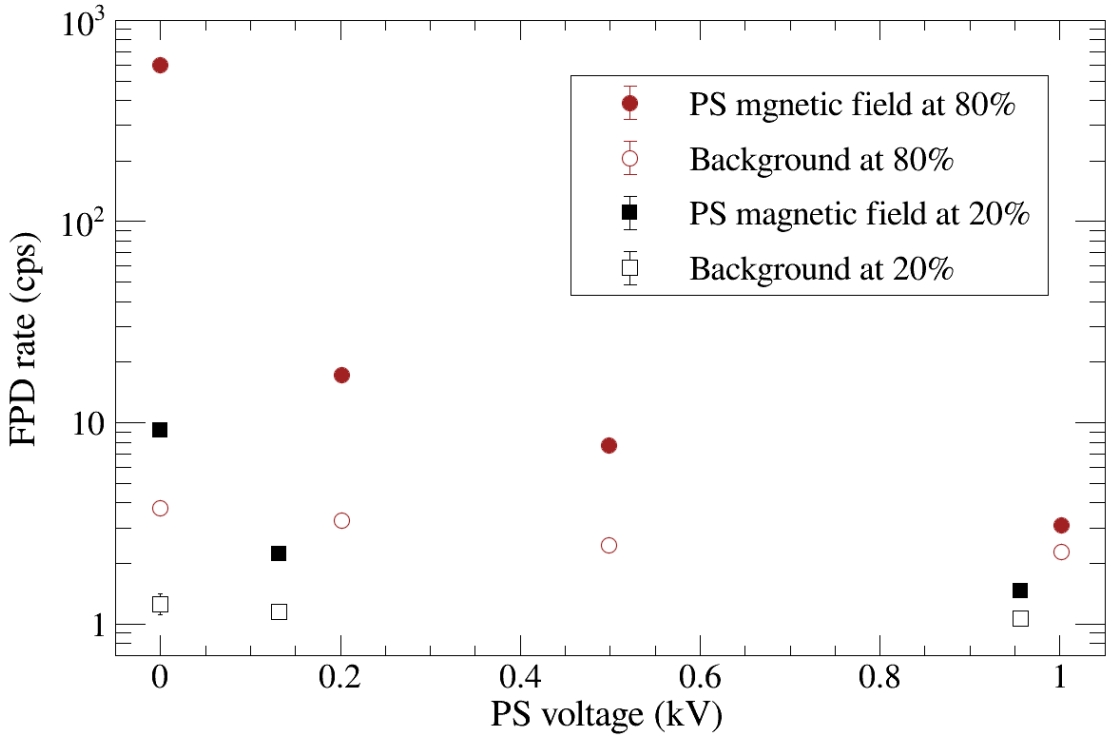

Figure VIII.19.: **Ion flux reduction with the PS high voltage.** The full symbols show the measurements of the ion flux into the MS and the respective empty symbols show the PS background at the corresponding high voltage. An ion flux reduction by a factor 684 ± 115 was achieved with D_3^+ ions of about 2 eV and 80% of the nominal magnetic field in the PS. At smaller magnetic field, the overall ion rate decreased even without high voltage, in accord with figure VIII.18.

sure, which created presumably only D_2^+ ions with energies around 90 eV (see sections VIII.1.4 and VIII.1.5).

- With 80% nominal magnetic field in the PS and $1{\cdot}10^{-1}$ mbar ELIOTT pressure, which created presumably mostly D_3^+ ions (see also section VIII.1.5). Because a voltage offset was applied to ELIOTT for this measurement, most of the ions had energies between 1 eV and 3 eV (see section VIII.1.4).

Figure VIII.19 shows that the ion transport probability decreased non-linearly with the high voltage in the PS. Compared to 1 kV, the original ion flux into the MS without PS high voltage decreased by a factor of 684 ± 115 at 80% magnetic field and by a factor of 20 ± 3 at 20% magnetic field; the analysis accounted for the voltage dependend backgrounds, which are shown as empty boxes in figure VIII.19, and the fluctuation of the ELIOTT deuterium pressure, which was discussed in section VIII.1.3.

As explained in section IV.3, about 1% of a residual tritium ion flux into the PS would always reach the MS due to diffusion of the neutral tritium. The reduction of the residual ion flux into the MS by the PS high voltage should therefore be at

least 10^{-2}, too. As the measurement shows, this suppression factor can be achieved already with a voltage of 1 kV in the PS at 80% nominal magnetic field; however, the nominal PS high voltage during the neutrino mass measurements[15] is −18.3 kV. At 20% nominal magnetic field, the high voltage reduces the transmission probability only by about a factor of 20 because the small magnetic field reduces the ion transmission probability in the first place (see section VIII.5.1).

Simulations with KASSIOPEIA actually predict an ion transmission probability through the PS of less than 10^{-4} for −0.5 kV and even −0.4 kV at the PS downstream cone electrode[16]. The discrepancy between the measurement and the simulation is attributed to the different potential settings of the inner electrodes: in the measurement, the inner electrodes were on the same potential as the PS vessel, while in the simulation only the downstream cone electrode was on negative potential.

The simulations also indicated that the ion transmission probability is maximal in the center of the flux tube, where the ions are accelerated straight through the PS. It is therefore favourable for the assessment of the measurement result that the ion pencil beam was close to the center of the flux tube: in case of the neutralisation of a ring electrode potential, the residual ion flux would increase first in the center of the flux tube and then the ion suppression by about a factor 700 would apply; if an ion flux across the whole flux tube would occur, the transmission probability would be presumably even smaller.

[15] During the neutrino mass measurements, the magnetic field strength of the whole KATRIN setup will be at only 70% of the nominal value.

[16] The simulations were carried out by Woo-Jeong Baek for Master's thesis *Investigation of background processes of ions and Rydberg atoms in the KATRIN spectrometers*, (2017). The ions were started equally distributed within a radius of 0.5 cm around the center of the flux tube.

VIII.6. Inadvertent blocking of thermal ions in the beamline

The ELIOTT setup at the rear wall allowed to provide the deuterium ions with an energy offset. As reported in section VIII.1.4, an offset energy of about 2 eV let appear a peak in the ion energy spectrum at just the offset energy. The observations and possible causes of this inadvertent blocking will be discussed in the following.

Inside ELIOTT, a Faraday cup ring in front of the electrodes allowed to monitor the created ion flux. Figure VIII.20 shows that the ion flux in ELIOTT increased in the pressure range which was used during First Light whereas the ion flux into the MS decreased. This is attributed to the inadvertent blocking of thermal ions in the beam tube and as the pressure increased, ever more ions were thermalised by inelastic scattering. According to section VIII.1.4, the ions had a scattering probability inside ELIOTT of about 50% at $3 \cdot 10^{-3}$ mbar and an even 30 times larger scattering probability at $1 \cdot 10^{-1}$ mbar. The energy loss at each scattering process (see section III.2.3) led to the thermalisation of the ions and to the development of an energy peak around 25 meV at 300 K according to the Maxwell-Boltzmann distribution.

The scans of the ion energy spectrum in section VIII.1.4 showed a peak of thermal ions only when the ions were equipped with a certain offset energy. Figure VIII.21 shows three scans of the thermal ion peak for $1 \cdot 10^{-1}$ mbar and offset voltages of +4 V to the ELIOTT hull, +2.5 V to the transition flange and +2 V to the rear wall. Between 1 eV and 3 eV, a peak appeared in the differential ion energy spectrum. According to the integrated spectrum, the ion flux in the peak region is ten times larger than the flux of ions above 3 eV. Comparing the spectra with and without energy offset in figure VIII.7 shows an overall increased ion rate. This is attributed to the ion transport probability through the PS: the PS magnetic field during the measurement without energy offset was at 20%, and the field during the measurement with energy offset was at 80%.

The appearance of thermal ions when an offset energy was provided, indicates that the ions were inadvertently blocked between the rear wall (where the ions received the offset energy) and the MS (where the ions were measured). Below about 1 eV, no ions can be observed; the magnitude of the ion blocking potentials can however not be determined due to the undue increase of the integrated ion spectrum (see section VIII.1.4).

Blocking potentials on the order of a few 100 meV were expected due to work function differences along the beam tube[17], as explained in section III.6.2. There is however no way to prove that this was in fact the cause. An alternative explanation would be the charging of cables in the DPS flux tube by the ion pencil beam up to about 120 eV; the blocking potential at the position of the pencil beam would

[17] Neutralisation of the positive blocking potentials by electrons as described in section III.6.3 were not expected during First Light: there was no plasma inside the source and all photo- and secondary electrons from ELIOTT were blocked by a negative electrode at the front of the ion source. An assessment of possible neutralisation between the three scans of the thermal ion peak is however not possible due to the drift of the ion flux intensity with the pressure in ELIOTT (see section VIII.1.3).

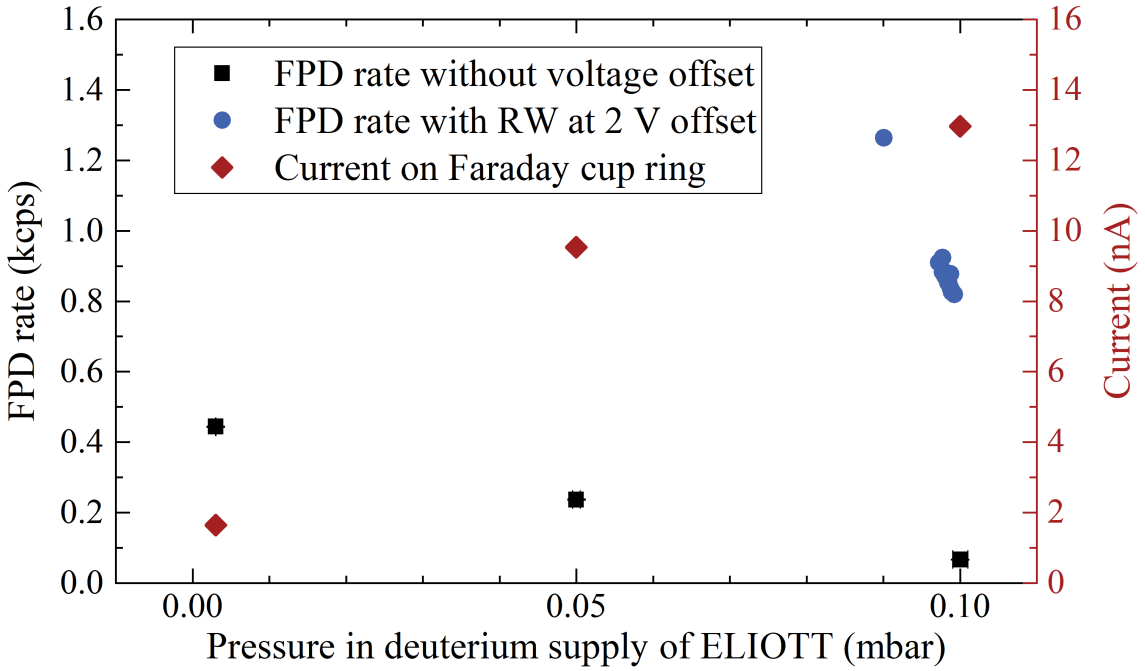

Figure VIII.20.: **Ion flux at various ELIOTT pressures and offset voltages.** Without voltage offset at the ELIOTT hull, the Faraday cup ring (see figure VIII.2) observes a rise of the ion flux with the deuterium pressure, but the ion flux into the MS decreases because the ions are more efficiently thermalised. With offset voltage, the ion flux into the MS decreases even steeper. It is assumed that the actual peak of thermal ions is still blocked, but that a steeper slope closer to the peak was sampled.

depend on the distance from the cable, which explains the observation however only by coincidence. Another argument against charged cables is that inadvertent blocking was also observed during First Tritium (see section IX.3), where the cables in the flux tube had been removed.

Although a peak from thermal ions was observed, it appears that the majority of the thermal ions was still blocked. The FPD rate of 600 cps in figure VIII.21 corresponds to about $7 \cdot 10^7$ ions/s, using the ionisation efficiency from section VIII.2.3; but the current on the Faraday cup ring of about 10 nA in figure VIII.20 corresponds to about $6 \cdot 10^{10}$ ions/s – the difference by three orders of magnitude cannot be explained with the different areas of the Faraday cup ring and the hole in the rear wall alone. Also, figure VIII.20 shows that the FPD rate still decreased with the ELIOTT pressure when an offset voltage was applied: if all thermal ions would have been transported to the MS, the same increase with the ELIOTT pressure would have been expected for the FPD rate as for the current on the Faraday cup. The ion flux into the MS decreased even stronger when the energy offset was applied, which indicates that a steeper slope closer to the peak was sampled. How can the peak of thermal ions lie below 1 eV, although all ions were equipped with another 2 eV at the rear wall? It appears that the ions scattered in front of the rear wall, where the deuterium flow through the rear wall hole could not be pumped off efficiently.

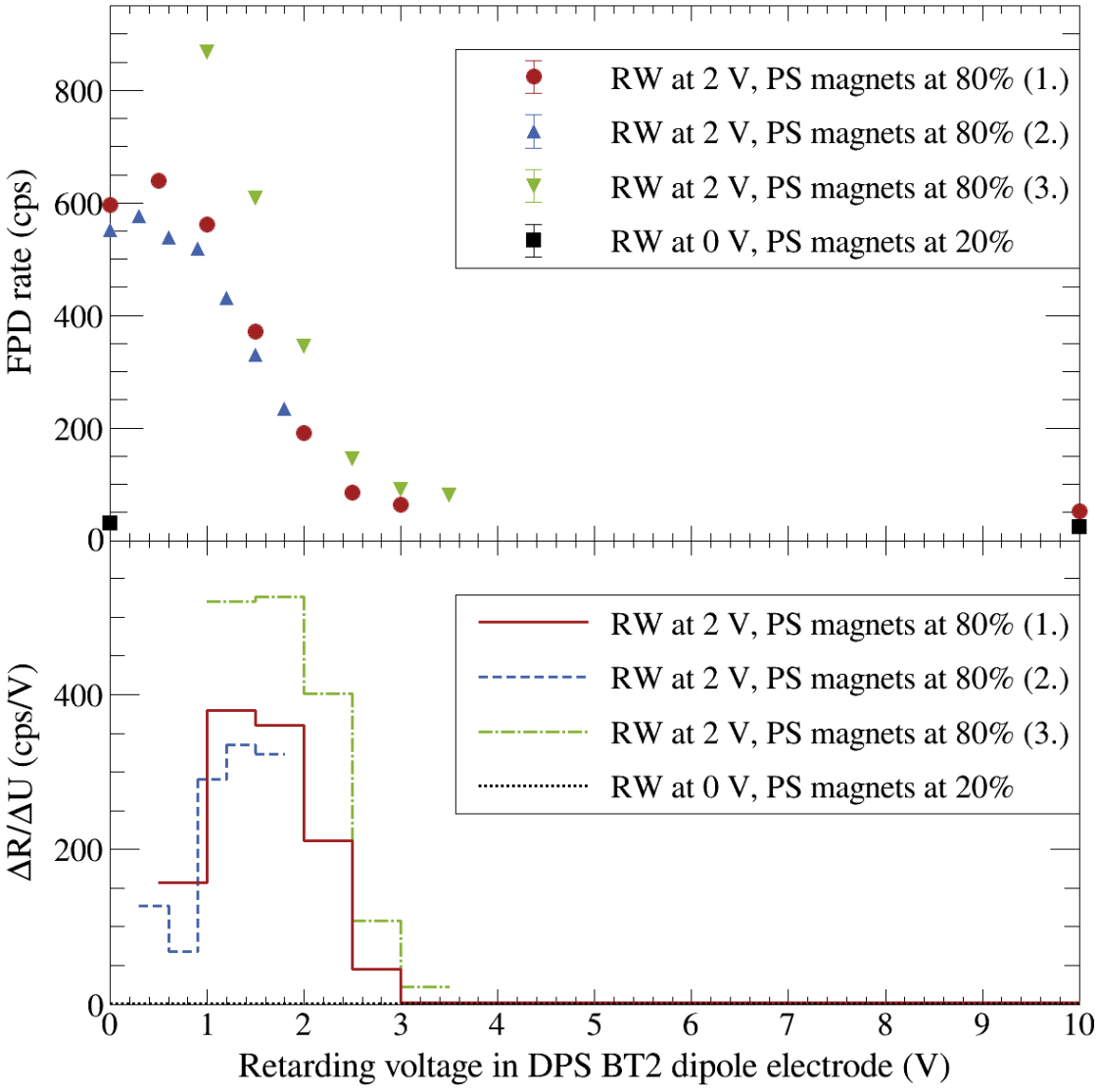

Figure VIII.21.: **Energy spectrum of thermal ions.** The peak of thermal ions appeared only when an offset voltage was applied to the ELIOTT hull (+4 V), the transition flange (+2.5 V) and the rear wall (+2 V). Scanning the peak three times resulted in different peak heights due to the decrease of the deuterium pressure in ELIOTT (see section VIII.1.3). At small energies, the integrated spectrum (upper part of the graph) shows a peak and can therefore not be assessed (compare section VIII.1.4). It appears that the ion spectrum is cut off below 1 eV due to inadvertent blocking potentials in the beamline. For the calculation of the differential spectrum $\Delta R/\Delta U$ in the lower part compare figure VIII.7.

VIII.7. Summary and consequences

The First Light campaign provided the first demonstration of ion blocking and removal in the KATRIN experiment. However, the campaign delivered even more important results which will be summarised in the following. Subsequently, this section will point out consequences of the First Light results with regard to ion safety during future neutrino mass measurements and with regard to the First Tritium campaign, which will be discussed in the following chapter.

Summary Mounting the ELIOTT ion source to the rear section of the KATRIN experiment allowed to create an ion pencil beam through the whole beamline (see section VIII.1). The ions were detected via ionisation in the Main spectrometer, which provided a proof-of-principle for the ion detection via ionisation (see section VIII.2).

The ion pencil beam from ELIOTT allowed the first test of ion blocking and removal with the ring and dipole electrodes: an ion suppression by about two orders of magnitude was demonstrated with each of the four ring electrodes in the DPS and the PS (section VIII.3); and the ion pencil beam could be completely removed with the dipole electrodes via $E \times B$-drift (section VIII.4).

The non-radioactive deuterium ions from ELIOTT also allowed the experimental determination of the ionisation efficiency in the Main spectrometer: at about -18.6 kV and roughly $3 \cdot 10^{-9}$ mbar residual water, the D_3^+ ions created $\mathcal{E} = (1.18 \pm 0.05) \cdot 10^{-4}$ counts / ion (see section VIII.2.3). The measurement contains several systematic effects which cannot been quantified. Still the result is only a factor 2 smaller than the prediction of the KASSIOPEIA simulation. This discrepancy can be explained with the poor ion transport through the weak magnetic field in the center of the spectrometers, which was investigated at the example of the PS in section VIII.5.1. With an additional high voltage of 1 kV at the PS vessel, the flux of D_3^+ ions into the MS was demonstrated to be reduced by a factor 684 ± 115 at 80% nominal magnetic field in the PS (section VIII.5.2). All of these measurements provide important reality checks for the KASSIOPEIA simulations[18] of the ion transport and detection in the PS.

The First Light campaign marked the first observation of inadvertent ion blocking in the beam tube: thermal ions from the ELIOTT ion source only appeared in the ion energy spectrum when an offset voltage of about 2 V was applied to the ELIOTT setup, as explained section VIII.6. Above about 1 eV, the ions were transported to the MS. This is attributed to different work functions of different beam tube materials, which led to effective blocking potentials on the order of a few 100 meV (as detailed in section III.6.2).

Consequences As a consequence of the observed inadvertent ion blocking, a fourth dipole electrode was installed in the beamline: the dipole electrode in DPS BT1 allows to remove the ions right in front of the WGTS-F. Other countermeasures to decrease the plasma density even upstream of the DPS BT1 were rejected, because

[18] For the simulations, see the Master's Thesis of Woo-Jeong Baek: *Investigation of background processes of ions and Rydberg atoms in the KATRIN spectrometers*, (2017).

they would have delayed the commissioning of the KATRIN experiment at least by another half year.

The successful ion monitoring inside ELIOTT with the Faraday cup ring (see the setup in figure VIII.2 and the measurement in figure VIII.20) demonstrated the possibility to measure ions inside the KATRIN setup via their neutralisation current on simple metal electrodes. Because the ions were supposed to be removed in the DPS via neutralisation on the dipole electrodes, the current measurement in the voltage supply of the electrodes was developed and installed (see section VII.2.2). This allowed during the First Tritium measurements to investigate the inadvertent ion blocking between the WGTS and DPS, as well as between the DPS beam tubes (see section IX.3); also, the ion removal can be constantly monitored.

Furthermore, about 20% of the ion flux into the PS will arrive at the PS downstream cone electrode, according to the KASSIOPEIA simulations which had previously been benchmarked. A current measurement with a minimal detectable ion flux of $4 \cdot 10^5$ ions/s within 2 hours of measurement was therefore installed in the voltage supply of the cone electrode; this ion detector allows to constantly monitor the residual ion flux into the PS and in case of an emergency close the valve between CPS and PS automatically (see section VII.2.4 for the setup and section IX.1.3 for its performance during First Tritium). Both current measurements together enabled a continuous monitoring of the tritium ions in KATRIN during the neutrino mass measurements.

All in all, the First Light measurements proved the readiness of the KATRIN setup for the first measurements with tritium ions. These (Very) First Tritium measurements will be discussed in the next chapter.

IX. The (Very) First Tritium campaign

In May and June 2018, the first tritium measurements were performed with the KATRIN experiment. Inevitably, this was also the first time that tritium ions were created inside the beamline. The tritium concentration during these measurements was only about 0.5% as compared to the $> 95\%$ design concentration, and the largest part of the column density was provided by inactive deuterium. These source conditions raised the safety limit on the ion flux into the PS from $1 \cdot 10^4$ ions/s to about 10^6 ions/s for the time being. Nevertheless, extensive tests could be carried out with the ion detectors along the beam tube, most of which could be used for the first time.

The first tritium measurements were divided into two campaigns:

- **Very First Tritium:** The Very First Tritium measurements lasted for two days. On May 18, the ion detectors and ion blocking was investigated in the WGTS, DPS and CPS only. Then, on May 19, the valve between the CPS and the PS was opened for the first time during tritium operation. This allowed to confirm that the ion flux into the PS was on a safe level and to measure the first tritium beta spectrum with KATRIN. For these initial test measurements, the tritium was supplied by sample cylinders which also allowed a variation of the tritium concentration between about 0.3% and 0.6%. Afterwards, the tritium supply was changed to a continuous circulation.

- **First Tritium:** The actual First Tritium campaign took place from June 5 to June 18. During the first two days, the continuous monitoring of the residual ion flux with the PS current measurement and the automatic closing of the valve between CPS and PS was established as safety measure. This allowed continuous measurements with the complete KATRIN beamline over night and on weekends, comprising extensive measurements of the tritium beta spectrum and many more investigations with tritium ions.

This section will present the results of the (Very) First Tritium measurements. First, the performance of the ion detectors will be investigated in section IX.1 and a proof-of-principle will be given for those detectors, which were used for the first time. Then, these detectors will be used in section IX.2 to investigate ions from three different energy regimes: thermalised ions from the major part of the WGTS, ions with energies up to 15 eV due to molecular dissociation and ions from presumed Penning discharges in the positive potentials of some ring electrodes. An important opportunity of the first tritium measurements was the observation of inadvertent blocking of tritium ions from the WGTS in the DPS; this will be discussed in section IX.3 along with hints to a possible neutralisation of the inadvertent blocking

potentials. Even though the majority of the ions was observed to be blocked in the DPS, the confirmation of the safety limit of not more than $1 \cdot 10^4$ ions/s flowing into the PS received a lot of care as reported in section IX.4. Finally, the observed upper limit on the ion flux into the PS and the discovery of Penning ions from the ring electrode potentials require an optimised setting for the ring electrode voltages, which will be discussed in section IX.5. All of these results will be summarised and discussed in section IX.6.

IX.1. Performance of the ion detectors

The (Very) First Tritium measurements provided the first opportunity to both observe tritium ions in the beam tube and test the ion detectors which will be presented below. In order to tell apart the effects of ion creation and transport from effects of the ion detectors, this section will first report the performance of the detectors with minimal assumptions about the ions; this includes proofs-of-principle for the detection methods and extensive investigation of systematic effects. The systematics were investigated based on data from the (Very) First Tritium campaigns because only they provided the necessary long-term stability of the measurement conditions, including magnetic field, high voltage and no mechanical vibrations by construction work at the beamline.

The first four of the following sections will discuss the performance of the ion detector along the beamline from the source towards the spectrometers: first the current measurement on the DPS dipole electrodes (section IX.1.1), then the Faraday cup at the FBM (section IX.1.2), the current measurement on the PS downstream cone electrode (section IX.1.3) and the ionisation of argon in the PS (section IX.1.4). Two specific measurements even allowed to compare the PS current method and the PS ionisation methods directly to each other: the detection of ions from Penning ions and from molecular dissociation which will be discussed in section IX.1.5. Similarly, the current measurements of the PS cone electrode and of Pulcinella could be directly compared with the help of the beta electron flux, as explained in section IX.1.6.

IX.1.1. Current measurement at the DPS dipole electrodes

Four dipole electrodes in the first four beam tube elements of the DPS remove the ion flux from the WGTS via $E \times B$ drift (see section VI.2). When the ions neutralise on the dipole electrodes, they create a current which allows to measure the ion flux from the WGTS (see section VII.2.2). Figure IX.1 recalls the position of the dipole and ring electrodes in the DPS along with their set voltages. These voltages determine the relative probabilities (see appendix A.7) to detect the total ion flux from the WGTS, which is expected to correspond to about 0.5 nA according to section III.2.5.

The current measurement at the DPS dipole electrodes plays an important role in the investigation of ion safety in KATRIN: while they cannot measure the residual ion flux downstream from the dedicated blocking potentials of the ring electrodes, the four dipoles can observe the ion transport along the DPS. As it turns out (see section IX.3), the majority of the ions from the WGTS is blocked inadvertently in

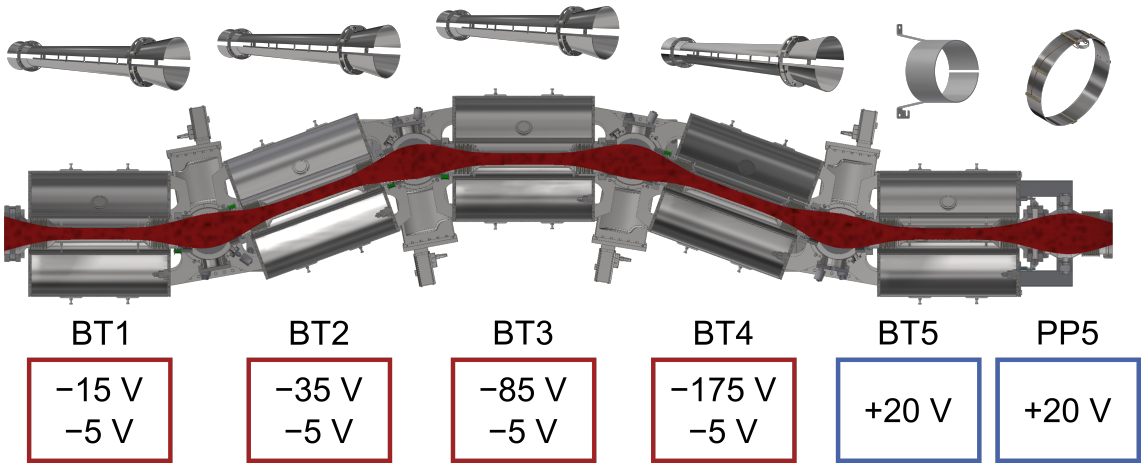

Figure IX.1.: **Voltage settings of the ring and dipole electrodes in the DPS.** The ring electrodes were set to +20 V after the creation of Penning ions in the ring electrode potentials was observed (see section IX.2.2); during the Very First Tritium measurements and at the begin of the First Tritium campaign, the ring electrodes were set to +200 V. In order to remove and measure the ions with the dipole electrodes, the ions had to be neutralised with the lobes which are oriented perpendicular to the magnetic field. In beam tube 1, 2 and 3, the lobes are at the upper, more negative electrode; only in beam tube 4 are the lobes at the lower electrode. The amperemeter for the current measurement is always at the electrode with the lobes (compare figure VI.8).

the DPS. Since the dipole electrodes are the only detectors which can see this major ion flux, they are crucial in order to test the theoretical prediction for the thermal ion fluxes from section III.2.5 (positive ions) and III.2.6 (negative ions).

The first section IX.1.1.1 will give the proof-of-principle for the ion detection with a dipole electrode. Then the observed systematic effects will be discussed in section IX.1.1.2. Finally, the optimal measurement procedure for the DPS dipole currents will be described in section IX.1.1.3 along with the minimal detectable ion flux under these conditions.

IX.1.1.1. Proof-of-principle of ion detection

Ion detection via $E \times B$-drift and subsequent neutralisation was successfully applied during the First Tritium measurements. Figure IX.2 shows a clear correlation between closing or opening the valve V1 between WGTS and DPS as well as the column density of DT gas. This can only be explained with ions: neutral gas is not able to influence the current signal in the observed way, most of the beta electrons are too fast to be drifted significantly by the dipole electrodes and the thermalised secondary electrons are repelled by the negative dipole potential.

While the measurement principle proved to work, the ions were only observed with the dipole electrode in BT1 and at a factor 2 less than expected. This is mostly attributed to partial or complete inadvertent blocking of ions by work function dif-

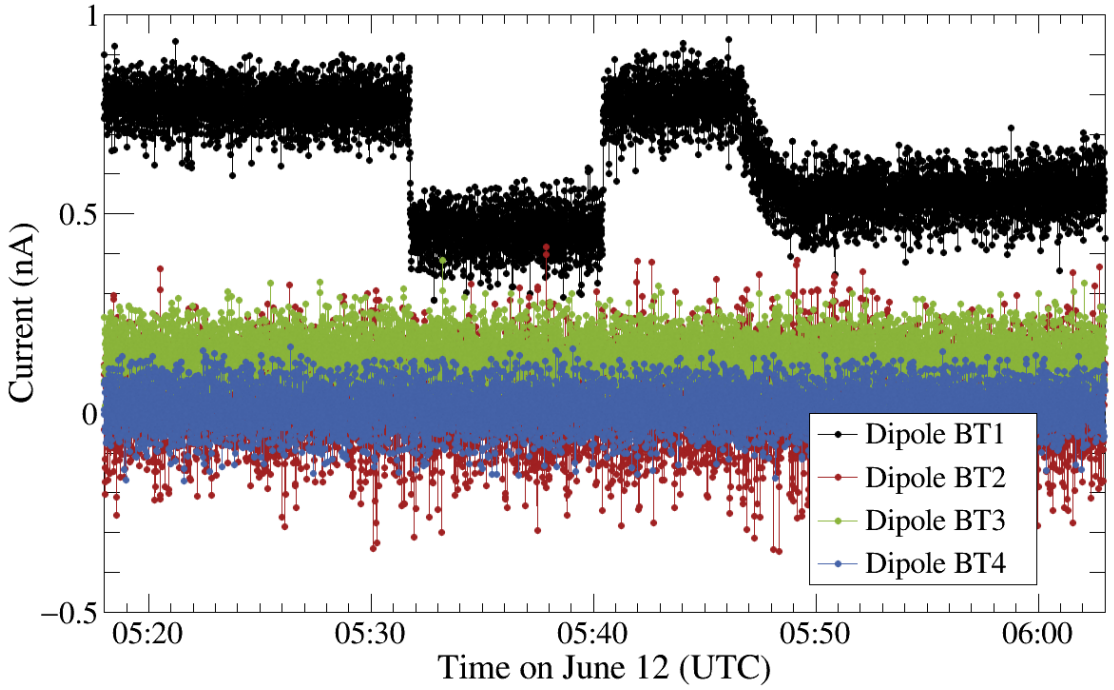

Figure IX.2.: **Current on the DPS dipole electrodes with open and closed V1 and changed column density.** Initially, the valve V1 between the WGTS and the DPS is open. When V1 is closed around 5:32 h and opened again around 5:40 h, the current decreases to background level and returns immediately; and when the column density is decreased around 5:46 h, the current decreases correspondingly. This can only be attributed to ions and proves that the detection via $E \times B$-drift and subsequent neutralisation works as intended in DPS BT1; the other dipole electrodes remain completely unaffected.

ferences along the beamline (see section III.6.2 and IX.3). In case of the dipole electrode in BT2, a dedicated hardware check after the measurement campaign confirmed that the cable connection between electrode and amperemeter was damaged (see figure VI.8), which prevented any ion drift and detection in the first place. The decisive hint to that damage was only obtained by the measurement of the ion energy spectrum (see section IX.2.3.5) on the last day of ion measurements; therefore, no explicit test of ion detection with the BT3 and 4 dipole electrodes could be carried out. For this measurement, the BT1 and BT2 electrodes would have needed to be grounded in order to allow secondary electrons from the WGTS to neutralise all inadvertent blocking potentials (see section III.6.3) up to the respective dipole electrodes.

IX.1.1.2. Systematic effects

In order to assess the uncertainty of the dipole current measurements, the systematic effects have to be understood. They can be divided into the five categories of offset, spikes, interruption of the data acquisition, oscillations and long term drifts. These five categories will be detailed in the following.

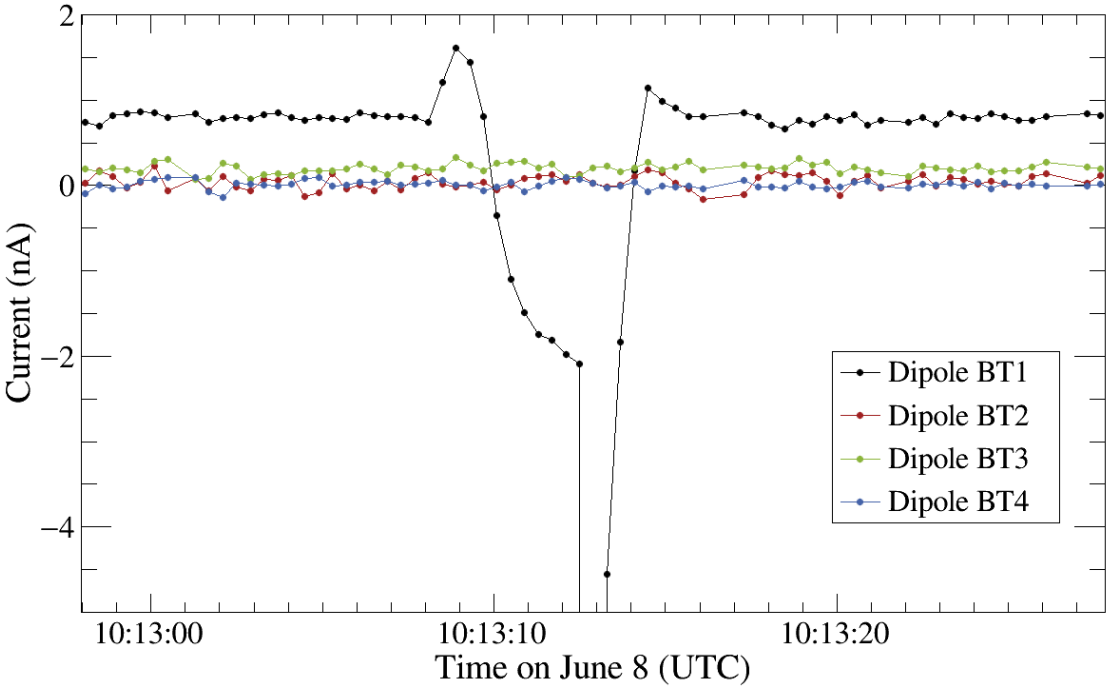

Figure IX.3.: **Spike on the DPS BT1 current during First Tritium.** While the origin of the spikes is unclear, the shape is determined by the autoranging of the amperemeter. As soon as the minimal measurement range of 2 nA was exceeded, the measurement current jumped sharply – outside of the displayed current range lies a single measurement point at −136 nA. The spike affects also the communication speed of the amperemeter and leads to an irregular measurement interval. Deviations from the usual 400 ms measurement intervals can however also be observed before and after the spike; these are attributed to communication delays between the LabView data acquisition and the database.

Offset The measured currents showed an offset, which is not associated to an ion flux in the beamline but rather of electronic origin, probably from within the amperemeters. In order to measure the actual ion flux, the net current has to be calculated by subtracting the offset from the total measured current. Because oscillations and long term drifts (see below) changed the offset current, a dedicated background measurement was required close to each signal measurement.

The magnitude of the offset current which was usually measured with the amperemeter for BT2 (which had a damaged cable connection to the electrode) and BT4 (which floated only on −5 V) was negligible compared to the offset of about 200 pA in BT3. In case of the BT1 dipole – the only one which actually measured an ion flux –, the offset current increased from about 100 pA during Very First Tritium (see figure IX.24) to about (700 . . . 900) pA during the First Tritium measurements (see figure IX.5).

Spikes Sudden, short peaks of the measurement current up to typically a few 100 nA were observed, as for example shown in figure IX.3. These spikes occurred

only a few times per day, as can be estimated from the figures IX.4 and IX.5. The origin of the spikes might be mechanical percussion, because they appeared during the measurements when the magnetic cryostats were running as well as during commissioning works before the measurement campaigns. Their rather seldom occurrence allowed to always choose analysis intervals without spikes – they were not cut from the analysis like in case of the PS current measurement (see section IX.1.3.2).

Irregular measurement intervals Interruptions of the 400 ms measurement frequency were caused by delayed communication between the LabView data acquisition program and the database which stored the measurements. Figure IX.3 shows that the interruptions were frequent, but rather short on the order of 1 s which allowed to neglect them in the data analysis. The actual number of measurement points was used in the analysis of each measurement interval, in order to account for the reduced effective measurement frequency.

Oscillations with 90 min period The measurement current showed oscillations which are assumed to be caused by the effect of the temperature in the laboratory on the amperemeter, just as in case of the PS current measurement. However, the correlation cannot be confirmed because there are no closely logged environmental data for the source and transport section. The magnitude of the oscillations changed up to about 100 pA in the most extreme case in BT1 shown in figure IX.4. Due to their period of about 90 min, the oscillations are the most relevant systematic effect during the dipole current measurements which took about 10 min to 30 min. In order to estimate the effect of the oscillations on the measurement, the background current should be observed for a significant part of the oscillations length, for example 30 min.

Long-term drift Changes of the offset current could be observed over the course of several days and for the period of the working hours in the tritium laboratory, as shown in figure IX.5. The change during the working hours is obviously cause by environmental conditions, while the reason of the long term drifts is unknown. For the dipole current measurements, these slow changes of the offset current can usually be neglected because the background current was carried out in short succession with the signal measurement[1].

IX.1.1.3. Measurement procedure: minimal detectable ion flux

This section will first explain the procedure which was used during the First Tritium for the dipole current measurements. The observations during First Tritium indicate a minimal detectable flux of $3 \cdot 10^7$ ions/s at 3σ significance. Based on these results, the optimal measurement procedure for future campaigns will be suggested.

[1] Figure IX.5 shows an offset change of about 150 pA in about 8 hours on June 11. This was during the inauguration day of the KATRIN experiment, when guided tours were given along the source and transport section. The organisational circumstances might have probably led to a significant temperature decrease in the laboratory.

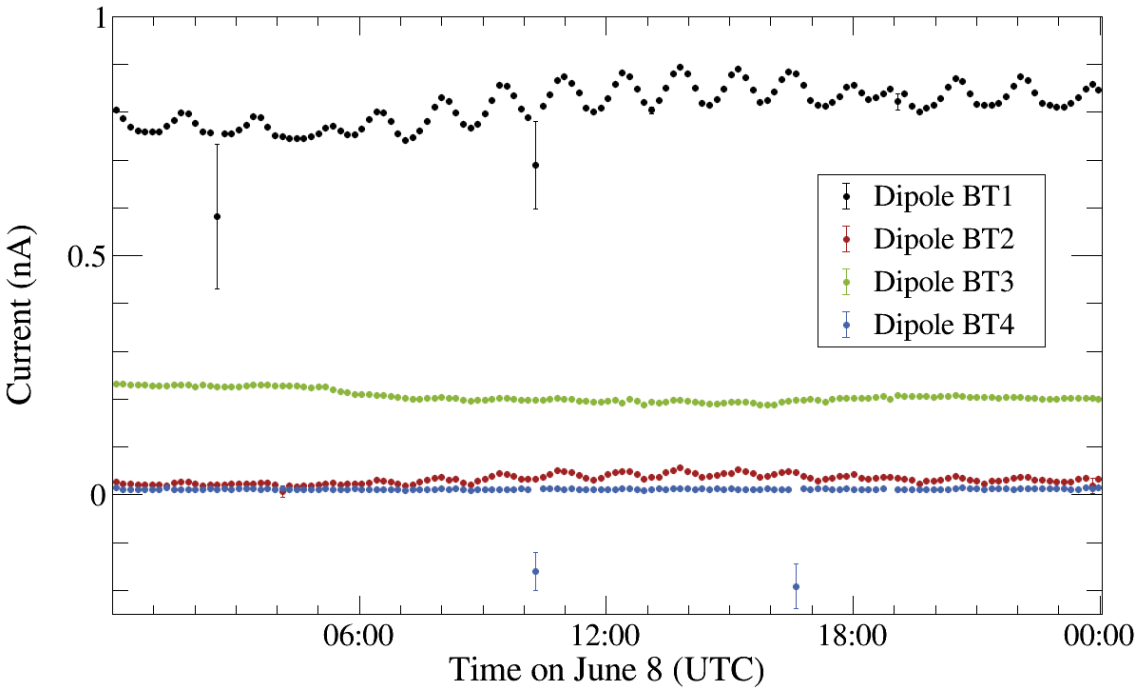

Figure IX.4.: **DPS current over the course of a full measurement day during First Tritium.** During the whole day, the source conditions remained unchanged. The current is averaged over 1500 values, which corresponds to about 10 min at the usual measurement interval of 400 ms. Due to the averaging, several systematic effects become visible: the currents in BT1 and BT3 have substantial offsets of several 100 pA; the offset current of all electrodes except for the BT4 electrode drifted from 5 h (UTC) on, which correspond to the opening hours of the tritium laboratory and finally, the current in BT1 and BT2 oscillated with a period of about 1.5 hours and an amplitude up to 100 eV. Both drift and oscillations might be induced by temperature fluctuations in the tritium laboratory. The spike from figure IX.3 can be seen again at 10:13 h, but there are only few significant spikes; in fact, all evaluations of First Tritium current data could be carried out for analysis intervals without spikes.

Measurement procedure during First Tritium In order to derive an ion flux from the current on the dipole electrodes, the current offset has to be subtracted. For that reason, the usual measurement consisted of two intervals shortly before and after the valve V1 was closed or opened. Because the measurement intervals were usually 1 min to 15 min long and only few minutes apart, systematic effects from long term drifts can be excluded and the effect of oscillations is deemed negligible.

These arguments however do not apply to the measurements where the dependence of the ion flux on the tritium concentration (section IX.2.1.1) and the column density (section IX.2.1.2) was investigated: the measurements stretched over 10 hours and 5 hours respectively with only two and one background measurements respectively. Only the coherent measurement results suggest the influence of systematic effects

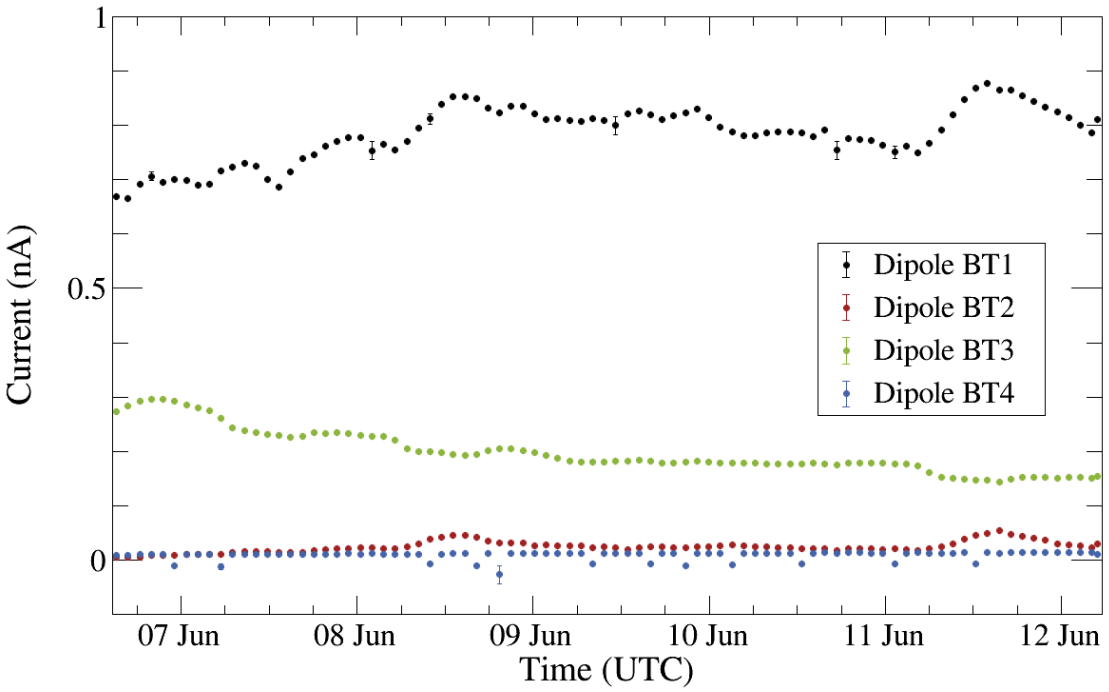

Figure IX.5.: **DPS current over the course of more than five measurement days during First Tritium.** All this time, the column density and tritium concentration remained stable and the valve V1 between the WGTS and the DPS was constantly open. The oscillations from figure IX.4 were removed by averaging over 13,500 current values, which corresponds to the oscillation period of about 90 min for the usual measurement interval of 400 ms. A long-term drift of the current in BT1 up to 200 pA becomes clearly visible. The cause is unclear, but a drift of the ion flux on this magnitude seems unlikely; also, a similar drift occurred for BT3. A temporary shift of the current offset is observed for BT2 and BT3 during the opening hours of the tritium laboratory on workdays June 7, 8 (see figure IX.4) and on the KATRIN inauguration day June 11, but not during the weekend of June 9 and 10; this is attributed to temperature variations. The stable source conditions were interrupted by closing V1 (see figure IX.2).

did not affect the basic conclusions of these measurements.

Minimal detectable ion flux A minimal flux on the order of 10^7 ions/s can be measured with the dipole electrodes, considering only the statistical uncertainty. During the First Tritium measurements, the width of the current distribution was usually observed to be on the order of $\sigma_x = 50$ pA at the dipole electrodes in BT1, BT3 and BT4[2]. According to appendix A.10, the uncertainty of the mean current is $\sigma_\mu = \sigma_x/\sqrt{n}$ after n measurements. At the usual acquisition speed of one

[2] An uncertainty of about 100 pA was observed in BT2; but because the cable connection to the electrode was damaged, the value has to be measured again in presence of magnetic field during upcoming measurement phases.

measurement every 400 ms, a 5 min interval corresponds to $n = 750$ measurement values and reduces the uncertainty on the mean current by about a factor $\sqrt{n} = 30$. This allows to measure a current of 2 pA or $1 \cdot 10^7$ ions/s correspondingly with 1σ significance; a 3σ significance would be reached for the detection of at least $3 \cdot 10^7$ ions/s.

Within a typical measurement duration of 30 min, the dipole current changed up to 100 pA due to current oscillations. Therefore, the influence of systematic effects has to be assessed for each individual measurement. This leads to the optimal measurement procedure as described in the following.

Optimal procedure for future measurements A prompt change of the measurement conditions has proven successful during the First Tritium measurements in order to measure the background in short distance to the signal measurement. Especially closing V1 and measuring only the background is favourable, because it makes sure that no systematic effects from slow neutralisation of inadvertent blocking potentials occur. In the future, ion measurements with the BT2 dipole electrode might also allow to use the BT1 electrode to block the ion flux for even prompter and more frequent measurements than the V1 valve.

In order to exclude systematic effects on the measurement from drifts and oscillations, short intervals of 5 min maximum should be evaluated – longer intervals do not improve the statistical precision much, because the uncertainty on the average current scales only with the square root of time. While the analysis intervals should be made short, the observation intervals of the signal and especially the background should be kept considerably longer during the measurement in order to observe and assess the influence of systematic effects. If spikes or measurement interruptions occur within the envisaged analysis intervals, the measurement should be repeated.

IX.1.2. Faraday cup

During the first measurement day of the Very First Tritium campaign, the valve V4 between the CPS and PS was not open yet. The only detector which could measure the residual ion flux downstream from the DPS ring electrodes was the Faraday cup at the FBM, which had been built just for this purpose (see section VII.2.3). The Faraday cup was unmounted after the Very First Tritium campaign and replaced for the FBM diode board during the First Tritium campaign.

However, the Faraday cup measured only about 2% of the expected beta electron flux and the reason for this discrepancy is unknown. The significance of the Faraday cup results on the flux of secondary electrons and positive ions is therefore hard to assess.

This section will first explain the principles of measurement and analysis, which was inflicted by a rather large current offset and drift. Then the actual detection of a beta electron flux and the possible reason for its small magnitude will be discussed. Finally, the consequences for the detection of positive ions as well as secondary electrons and negative ions will be discussed.

Measurement principle Depending on the voltages of its board and shield, the Faraday cup was designed to detect beta electrons (board at +2 V, shield at −20 V), positive ions (board at −2 V, shield at −20 V) and slow secondary electrons along with negative ions (board at +20 V, shield at +2 V). The voltages of board and shield were controlled with two voltages supplies outside the beam tube; changing between the measurement modes for ions and beta electrons corresponded changing the polarity of the board by switching the banana plugs on the corresponding voltage supply.

For the measurements during the Very First Tritium campaign, the Faraday cup was positioned so that the center of its sensitive surface was at the center of the magnetic flux tube. Then the measurement mode was changed in order to compare the measurement current before and after the change. The irremovable background current from beta electrons was measured by opening or closing the valve V1 between WGTS and DPS.

Current drift and data analysis Just like the DPS dipole electrodes, the current on the Faraday cup showed a considerable offset and drift, no matter whether the board was positioned in- or outside the flux tube. The offset changed between $(-3 \ldots -2)$ pA during the two measurement days, without any apparent correlation or periodicity. Because the measurement signals were on the order of 20 fA, the drift was too large to allow an analysis by averaging the current in certain intervals as done with the DPS dipole and PS cone currents.

Instead, the current was fitted with a straight line in the measurement interval before changing the measurement mode or opening or closing V1 respectively. Then another linear fit was performed in a second measurement interval after the event, but with the slope fixed to the result of the first fit. Finally, the difference between the two offsets returned the net current, which was converted into a charge flux[3].

[3]Method developed by Lutz Schimpf.

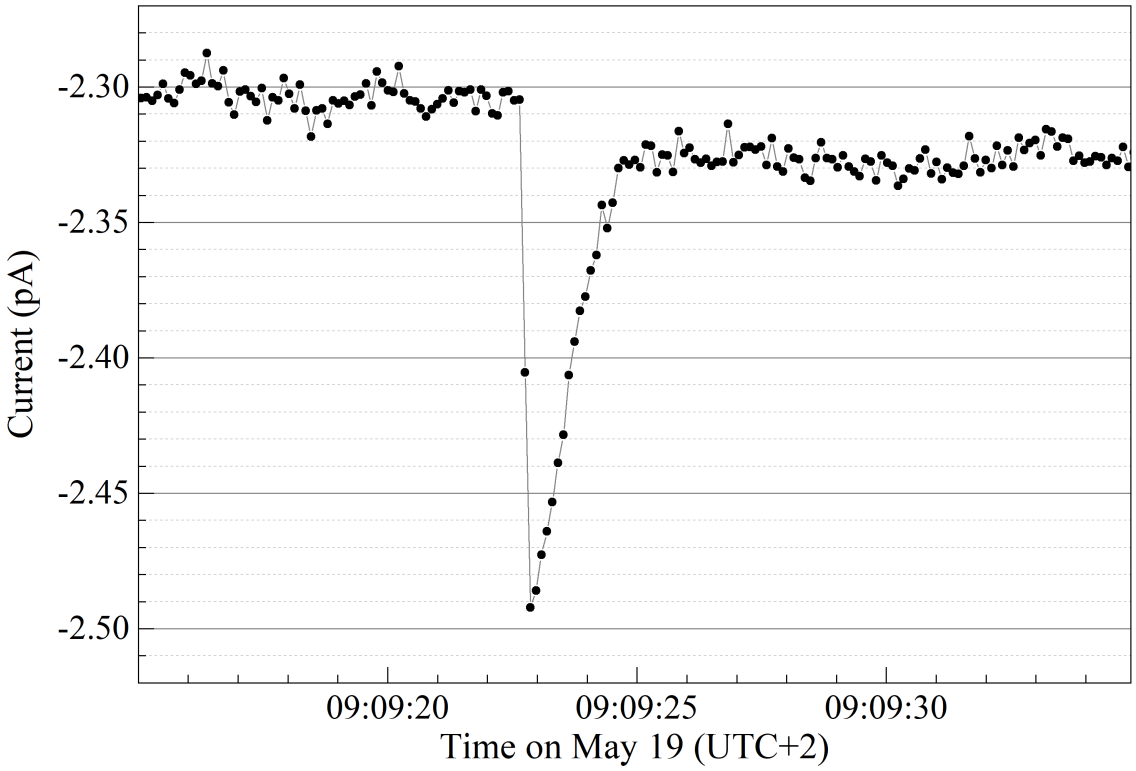

Figure IX.6.: **Beta electron current on the Faraday cup when opening V1.** When the valve V1 between WGTS and DPS was opened, the measurement current on the Faraday cup became more negative. This demonstrates that the Faraday cup did measure beta electrons, but the magnitude of 20 fA was only 2% of the expected current. The spike at opening V1 suggests that maybe the metallic shield above the Faraday cup surface was charged up by the beta electron flux, until only 2% of the spectrum could still reach the Faraday cup surface.

The method implies a certain systematic uncertainty from applying the first slope to the second time interval, yet the slope remained mostly visibly unaffected by the change of the measurement mode or closing or opening V1.

Proof-of-principle and missing beta electron flux The Faraday cup proved to measure a signal which was created by the beta electron flux: when the valve V1 between WGTS and DPS was opened or close, the amplitude of the Faraday cup current changed suddenly and in close correlation to the V1 motion by about 20 fA. The magnitude of this change was found to correlate with the tritium concentration, which changed during the Very First Tritium measurements because of gradual tritium injection from sample cylinders. Nevertheless, the amplitude was only about 2% of what was expected, as will be discussed in section IX.1.6.

The reason for the missing beta electron rate could not be found[4]. All electrical connections between the Faraday cup board and the outside the vacuum had been

[4]The Faraday cup board for the FBM could however not be tested with the ELIOTT ion source due to time constraints.

tested before the setup was pumped down. Also, the electronic setup of the voltage supplies was checked several times by different persons. The FBM setup measured successfully with the diode board during First Tritium, so that issues of the internal cabling seem unlikely – although the FBM board uses a voltage signal while the Faraday cup measures a current. The amperemeter itself had been used at various occasions, including the ELIOTT test setup and ELIOTT measurements during First Light. In both cases, electron and ion fluxes were measured with a Faraday cup of similar design: a simple metal plate perpendicular to the strong magnetic guiding field.

One possible indication why the Faraday cup measured only part of the expected electron flux might be given by figure IX.6: when the valve V1 between the WGTS and DPS was opened on the beginning of the second measurement day of Very First Tritium, the current showed a spike[5] with the magnitude of the expected beta electron induced current of about 200 fA. This could be due to a quick charging of the shield by the beta electrons up to several keV, which would have allowed only a small fraction of the beta electrons to reach the board anymore. Such a charging could however only have occurred if the electric connection of the shield was damaged; the connection was confirmed to exist when the board was mounted to the FBM, but could not be tested due to time constraints when the board was unmounted. A similar spike on the first measurement day could not be observed, because the tritium concentration in the WGTS increased slowly while V1 was constantly open. Ultimately, it remains unclear why the measured beta electron flux at the Faraday cup board was 50 times smaller than expected.

Detection of ions and secondary electrons Because of the strong discrepancy between expected and measured beta electron current, the reliability of the Faraday cup has to be doubted also with regard to measurements of positive ions and secondary electrons. As will be discussed in section IX.4.2, no significant ion flux larger than $2 \cdot 10^4$ positive ions/s was found, in accordance with the results of the ionisation method. Similarly, no secondary electrons or negative ions were observed when the dipole electrodes in the DPS were switched off. Both cases – no observation of ions and no observation of secondary electrons or negative ions – are in accordance with the findings that thermal particles are blocked inadvertently in the DPS (see section IX.3).

[5] Similar spikes occurred when the measurement state was changed electronically, but in this case the cables were left untouched. Only the valve V1 was opened – the pressure change due to neutral gas at the end of the CPS can however be neglected. While it is possible that the tritium gas pressure had increased when V1 was closed and sharply decreased when V1 was open, similar spikes were not observed when V1 was opened at other occasions.

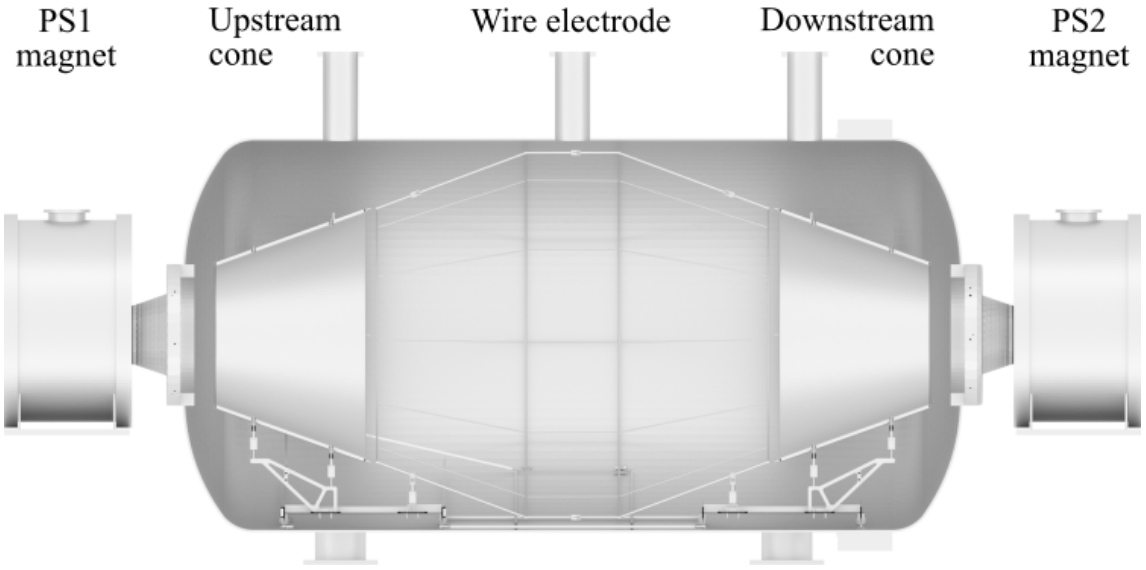

Figure IX.7.: **Detection principle of the PS current measurement.** The positive ions enter the negative potential in the PS as soon as the enter the PS vessel. There, the ions are become accelerated and leave the magnetic flux tube non-adiabatically. About 20% of the ions reach the solid downstream cone electrode and can be detected via their neutralisation current with an amperemeter.

IX.1.3. Current measurement on the PS downstream cone electrode

In the negative potential of the PS, about 20% of the ions are accelerated onto the downstream cone electrode at nominal high voltage settings[6] (see figure IX.7 and section IV.1). The resulting neutralisation current at the cone electrode allows to measure the ion flux into the PS (see section VII.2.4). Due to the emission of secondary electrons upon ion impact, the measured current is amplified (see section VII.2.7); preliminary results of the STS IIIa commissioning measurements from October 2018 after the First Tritium campaign indicate an amplification by about one order of magnitude.

This section will first explain in section IX.1.3.1 the continuous monitoring of the ion flux into the PS during the First Tritium measurements, which would have allowed to automatically close the valve between the CPS and PS in case of a large ion flux. The evaluation of long measurement samples is subject to systematic effects, which will be detailed in section IX.1.3.2. This leads eventually to a minimal detectable ion flux of $4 \cdot 10^5$ ions/s into the PS after 2 hours, as will be discussed in section IX.1.3.2.

Two other measurements via the PS current allowed a proof-of-principle of this ion detection method: a qualitative agreement was found between the PS current method and the ionisation method in the detection of Penning ions (section IX.1.5);

[6]The probability of 20% also applies to the nominal PS high voltage of 16.4 kV during the First Tritium measurements.

besides, the PS current method was also tested with electrons when the PS2 magnet was ramped down and the beta electrons were guided onto the cone electrode (section IX.1.6).

IX.1.3.1. Automatic closing of the valve between CPS and PS

The current measurement at the downstream cone electrode is controlled by a LabView program, which also includes the first analysis step: if the measured current rises above a threshold of 5 pA for three measurements in a row, the program will trigger the closing of the valve V4 between the CPS and PS automatically. However, the relation between trigger threshold, measurement time and actual ion flux is not trivial as shown by figure VII.6 and the calculations in appendix A.11.

The V4 closure was switched off manually at the beginning of First Tritium until the successful demonstration of the PS current detection method with beta electrons (see section IX.1.6). But during most of the campaign from June 7 until the end of the tritium operation on June 18, the monitoring was activated day and night and would have closed the valve V4 in case of a PS current of 5 pA or larger. This threshold corresponds to an ion flux of $2 \cdot 10^8$ ions/s due to the 20% ion detection efficiency of the downstream cone electrode. Such an ion flux would correspond to just the constraint placed by radiation protection, but is still two orders of magnitude larger than the background-motivated ion flux limit of 10^6 ions/s during First Tritium.

IX.1.3.2. Systematic effects

The PS current measurement has to deal with systematic effects from spikes, interruptions of the data acquisition, and oscillations, just like the current measurement on the DPS dipole electrode. In contrast to it, no significant current offset or long-term drift were observed. All five systematic effects will be discussed in the following.

No significant offset observed In contrast to the DPS current measurement, no current offset could be observed at all. When averaging over the period of roughly four days as shown in figure IX.11, the mean current was -0.05 ± 0.62 fA; this is below the limit for meaningful observations of 3 fA which is the detection limit of the amperemeter.

No long-term drift observed The current of the PS cone method is extraordinarily stable, in contrast to the current on the DPS dipole electrodes. No long term drifts were observed, associated to the fact that no current offset was detected. For example, see the period of about four days in figure IX.11.

Spikes Sudden, short spikes on the measurement current were observed, just like in case of the DPS dipole currents but at much higher frequency. Figure IX.8 shows that the majority of the peaks were to negative currents, but the rate of positive peaks up to about 50 pA is still about one per hour. At this rate, the spikes would

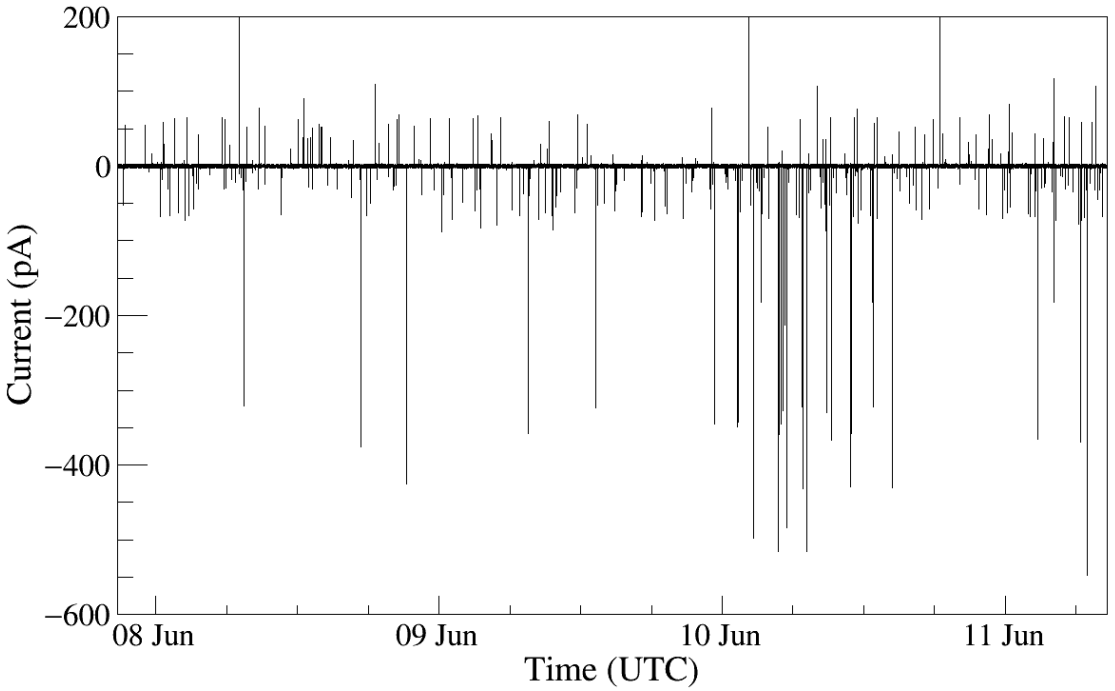

Figure IX.8.: **Spikes on the PS current.** The PS current measurement suffered from large spikes of unknown cause, just like the DPS dipole current but at much higher frequency. Most of these spikes lay outside the measurement range of ±20 pA and were therefore cut from the analysis. In order to prevent a false ion alert including the closing of the valve V4 between CPS and PS, the trigger required three consecutive measurements above the threshold.

not allow to measure the mean current over a long time period like a neutrino mass scan.

In order to remove the spikes from the analysis of long term signals, all values outside the fixed measurement range of the amperemeter of ±20 pA were cut away. Measurement values outside this range are not meaningful anyway; also, the spikes are not attributed to ions arriving on the PS cone electrode, which are supposed to be measured. The ion signal is expected to be a slow increase due to a neutralisation of the ring electrode potentials by secondary electrons. It is however unclear as of today whether the spikes are due to the effect of the magnetic field of the PS on the amperemeter or due to the noise on the high voltage supply of the PS. A minority of the spikes were caused by intentional changes of the PS voltage as shown in figure IX.9.

The spikes also constitute a problem for the automatic trigger of the closing of valve V4 between CPS and PS: in order to prevent an unnecessary interruption of the measurements, the closing of V4 is only triggered when three consecutive measurements lie above the chosen threshold. Investigation of a large sample of spikes showed that they usually comprised only one value outside the measurement range, probably because the communication with the LabView acquisition program was affected by the overflow measurement of the amperemeter.

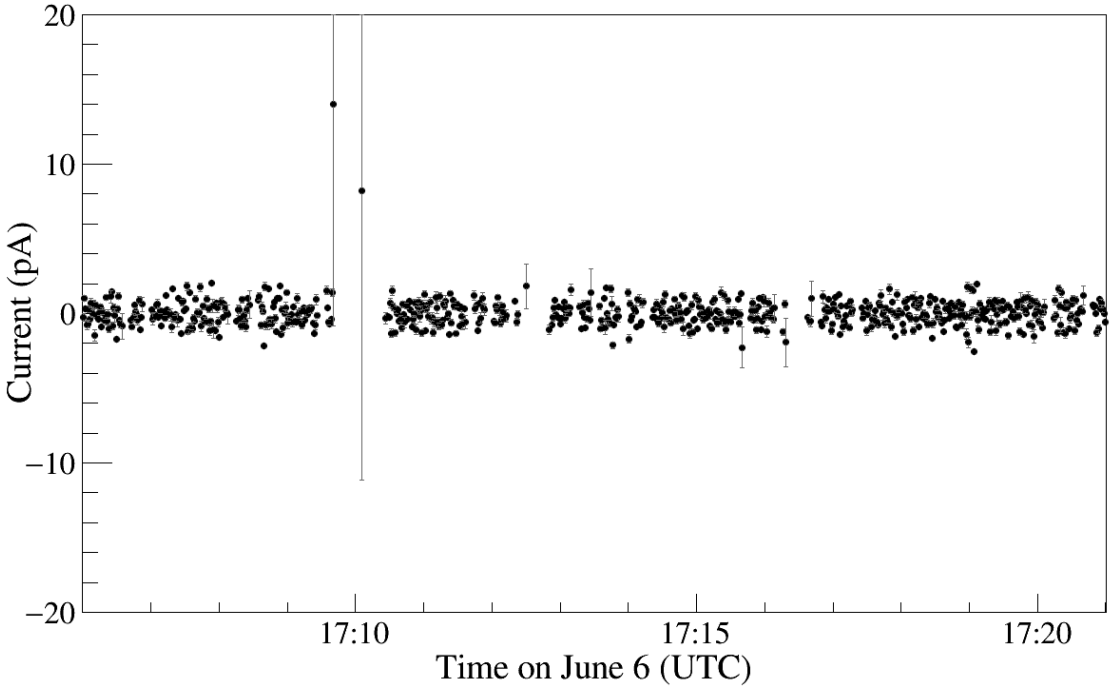

Figure IX.9.: **Interruptions of the PS current measurement.** Current spikes like from the PS voltage change around 17:10 h caused an overflow and interruption of the measurement with the amperemeter. Even more frequently, the communication between the LabView data acquisition program and the data base was slowed down, interrupting the data acquisition likewise. The LabView program usually restarted itself within less than one minute.

Interruption of data acquisition Interruptions of the data acquisition were observed for the PS current measurement, just as for the DPS dipole electrodes. Some of these interruptions can be attributed to a change of the PS voltage settings and the current spike which caused an overflow of the amperemeter measurement and slowed down its communication with the LabView data acquisition program (see figure IX.9); but in the first place, most of these spikes caused a crash of the LabView program, which restarted itself after usually less than one minute. The majority of the interruptions has its cause in the communication between the LabView program the database to where the acquired data was stored.

For the usual analysis of long time intervals, the short interruptions are not relevant because they are seemingly randomly distributed across the measurement interval; also, the actual number of measurements is considered in the analysis anyway, not the length of the measurement interval. For the automatic closing of V4, it has to be kept in mind however that the cycle length of the LabView program can deviate from the 1 second interval and reach longer values up to one minute. It is unclear whether the LabView program would be continuously interrupted during the time of a current overflow.

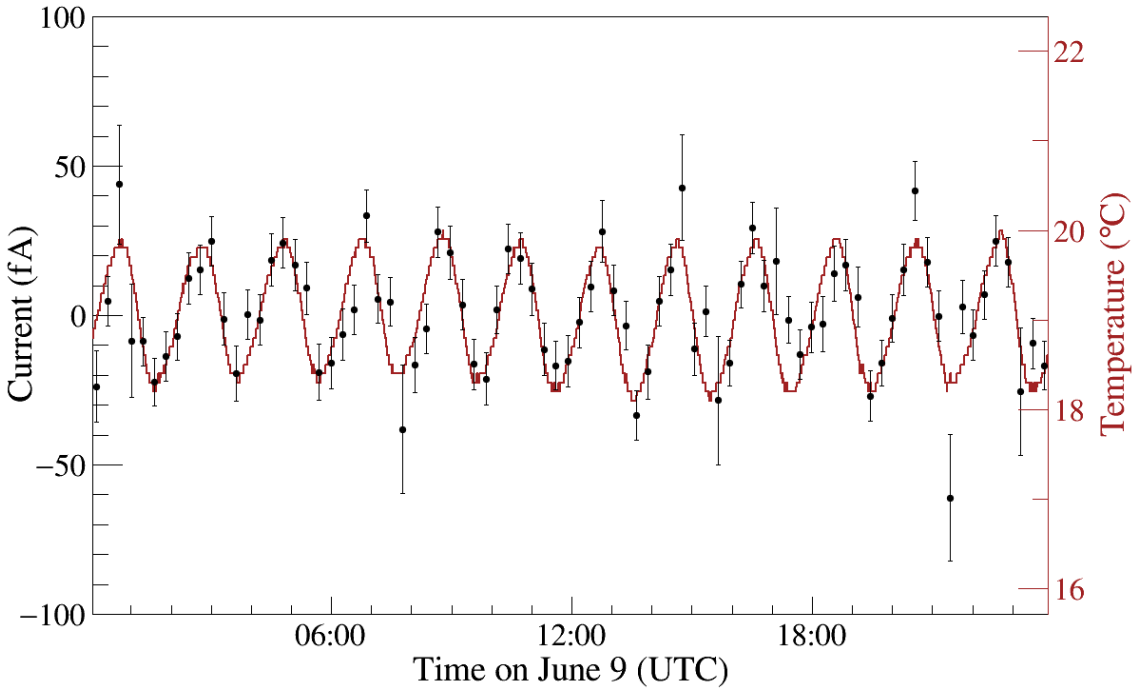

Figure IX.10.: **Oscillation of the PS current and temperature in the spectrometer hall.** Both oscillations with a period of 2 h are clearly correlated. The displayed currents are averaged over 900 values, corresponding to about 15 min.

Oscillations with 2 h period The PS current oscillated with a 2 hour period due to the temperature in the spectrometer hall – figure IX.10 shows a clear correlation. Obviously, the temperature changes in the spectrometer hall affect the temperature-sensitive amperemeter inside its magnetic shielding strong enough to imprint the oscillation on the current measurement[7]. The amplitude of the current oscillation was found to be up to 50 fA, which is considered as the minimal detectable ion flux due to systematic effects.

IX.1.3.3. Minimal detectable ion flux

The automatic closing of the valve V4 would have been triggered during First tritium if the PS current would have risen above a threshold of 5 pA or $2 \cdot 10^8$ ions/s correspondingly (see section VII.2.4). This measurement is limited by the Gaussian noise of the current measurement. Over longer measurement intervals and larger measurement samples, the statistical uncertainty can be reduced down to about 4 fA after 2 hours of measurement. The systematical uncertainty after the same measurement time is 3 fA; it would increase for likewise shorter or longer measurement periods. Both statistical and systematical uncertainties will be detailed in the following.

[7]The humidity in the hall also oscillates and is completely anti-correlated to the temperature. An influence of the humidity on the current measurement is however excluded.

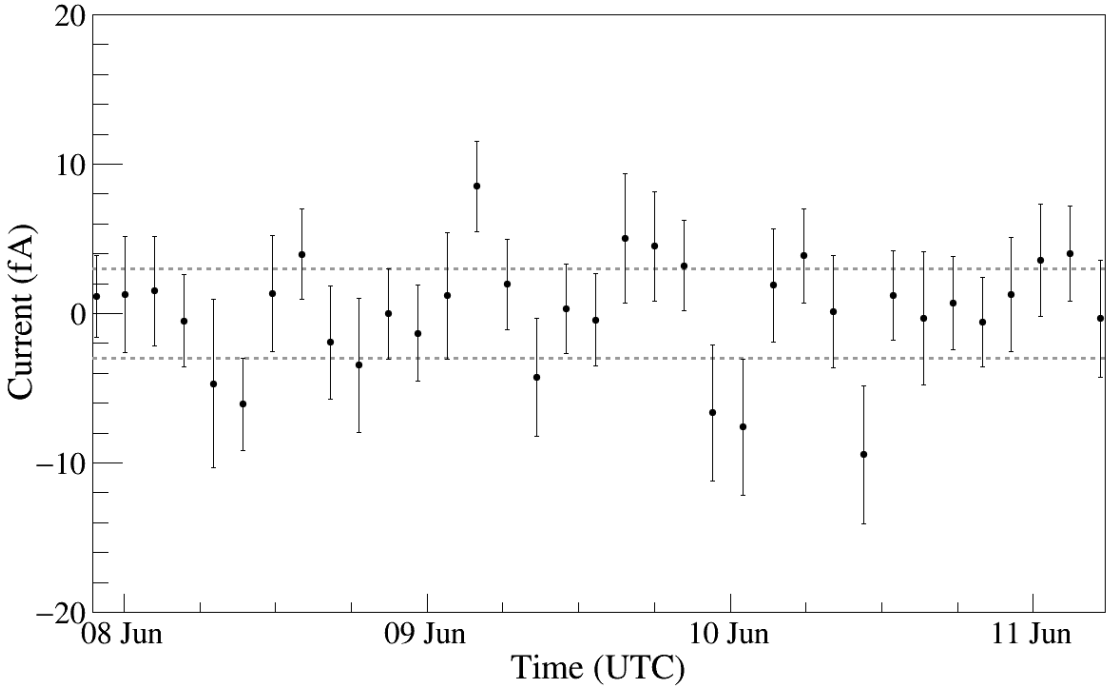

Figure IX.11.: **Long term measurement of the PS current.** The displayed currents are averaged over 7200 values, corresponding to about 2 h. This allowed to remove the oscillations which were shown in figure IX.10. Most of the currents lie below the detection limit of the amperemeter of ±3 fA; almost all agree with this limit within one standard deviation. During the whole measurement, the PS high voltage was not changed, the valve V4 between CPS and PS was open and tritium was circulated in the source. Obviously, there is no continuous ion current larger than 3 fA – for a detailed discussion of the upper limit on the ion flux into the PS see section IX.4.

Systematic limitations Temperature oscillations in the spectrometer hall on the order of ±1° were observed to induce current oscillations on the order of 50 fA with a period of 2 hours (see figure IX.10). As demonstrated in figure IX.11, this systematic effect can be removed by averaging the measurement current over 2 hour intervals. In this case, the current becomes limited by the systematic uncertainty of the amperemeter at 3 fA: All except for two measurement points in figure IX.11 are compatible with the ±3 fA band.

For future PS current measurements, it would still be favourable to reduce the systematic uncertainty from current oscillations by stabilising the temperature in the spectrometer hall to about ±0.1°C. Such stable conditions existed during the measurement of the Penning ions with the PS current method, as will be discussed in section IX.1.5; however, the cause for the stabilisation is unknown and was a rather fortunate circumstance of the test measurement.

Statistical limitations Figure IX.11 shows the mean PS current over more than 4 days of measurement with constant measurement conditions: the magnetic field was

on, the valves V1 and V4 remained open and the tritium concentration and column density was stable. The measured points were averaged over 7,200 values which correspond to roughly 2 hours measurement time. Altogether, the measurement extended over $3 \cdot 10^5$ s, which can be taken as a rough estimate of the number of measurements n_{tot}.

The overall statistical mean current of the roughly four day long measurement is -0.05 ± 0.62 fA; the measurement is thus limited by the 3 fA systematic uncertainty of the amperemeter. Nevertheless, no sign for an ion flux into the PS during this time can be found, as will be detailed in section IX.4.3.

Minimum detectable flux The minimum detectable ion flux can be calculated from the 1σ uncertainty of 0.62 fA over the full number of n_{tot} measurements in figure IX.11. A minimum systematic uncertainty is reached after 2 hours, as discussed above. The number of measurements within this time is apprimately $n_{\mathrm{meas}} = 7{,}200$. Using the statistics equations from appendix A.10, the 1σ uncertainty for a 2 h measurement is larger than the uncertainty over the full measurement time by a factor $\sqrt{n_{\mathrm{tot}}/n_{\mathrm{meas}}} = 6.5$. Thus, the 1σ uncertainty for a 2 hour measurement is 4.0 fA. For the minimum detectable ion flux, a 3σ effect should be required and the ion detection efficiency at the downstream cone electrode of about 20% needs to be taken into account.

Finally, this leads to a minimum detectable ion current of 12 fA, corresponding to a minimum detectable ion flux of $4 \cdot 10^5$ ions/s into the PS. According to section IV.3.4, such an ion flux would create a background of about 4 mcps via tritium activity in the MS. Not considered yet is the emission of secondary electrons from the stainless steel electrode upon ion impact. Preliminary results of the STS IIIa commissioning measurements from October 2018 indicate a current amplification by about one magnitude; the minimum detectable ion flux would be reduced likewise.

IX.1.4. Argon ionisation in the PS

When the positive ions enter the negative potential inside the PS, they are accelerated onto the spectrometer walls and electrode. On their way through the spectrometer, the ions can scatter inelastically on the residual gas, ionise it and create secondary electrons (see section IV.2). These secondary electrons can be detected with the FPD in order to measure the ion flux into the PS (see section VII.1). Of all ion detection methods which were used during First Tritium, the ionisation method allowed to derive the firmest upper limit on the ion flux into the PS (see section IX.4.4).

At the time of the First Tritium campaign, the ionisation efficiency was assumed to scale linearly with the spectrometer pressure (see section VII.1). Consequently, the pressure inside the PS was increased with argon and the ion flux was measured at various pressures in order to distinguish it from pressure-dependent background. It was only after the First Tritium campaign that the STS IIIa commissioning measurements found a pressure-independent and larger-than-expected ionisation efficiency. Because these results were only preliminary as of October 2018, the following evaluation will follow the original assumption of a pressure-dependent ionisation efficiency as obtained from KASSIOPEIA simulations. Since the STS IIIa campaign found an ionisation efficiency of several orders of magnitude above the KASSIOPEIA prediction, the upper limit which will be derived with the ionisation method can be considered as a conservative estimate.

The following section will first discuss how the pressure inside the PS was increased with argon in order to increase the ionisation efficiency of the ions. Then, the systematic effects due to the PS background and potential settings are discussed. Finally, the minimal detectable ion flux of the ionisation method during the First Tritium campaign will be discussed based on the assumption of a pressure-dependent ionisation efficiency.

IX.1.4.1. Systematic effects related to the argon pressure

The pressure in the PS was increased with argon during the ionisation measurements in order to increase the ionisation efficiency of the ions. This led however to a new background from Ar^+ ions, which scaled quadratically with the argon pressure. At the optimal measurement pressure, the minimal detectable ion rate and the Ar^+ rate would be on the same magnitude.

This section will first discuss the ionisation efficiency of ions in the PS, the Ar^+ rate and the optimal pressure before detailing, which argon pressures were actually used for the measurements. Finally, the stability and reproducibility of the argon set pressures will be discussed.

Ionisation efficiency The ionisation efficiency $\mathcal{E}$ must be known in order to calculate the underlying ion flux Φ from a measured FPD rate $R = \Phi \cdot \mathcal{E}$. Previous simulations[8] have established an ionisation efficiency of $\mathcal{E} = 2.6 \cdot 10^{-7}$ counts/ion for scattering of H^+ ions on H_2O residual gas at $p_{\mathrm{PS}} = 1.0 \cdot 10^{-10}$ mbar, -17.9 kV at

[8]Simulations by Woo-Jeong Baek

the vessel and −400 V on the inner electrodes of the PS. When the residual gas is however changed from H_2O to argon, both H^+ ions and Ar^+ ions have an ionisation efficiency of:

$$\mathcal{E} = 1.0 \cdot 10^{-6} \text{ counts/ion} \cdot \frac{p_{\text{PS}}}{10^{-10} \text{ mbar Ar}}. \tag{IX.1}$$

The simulations agree with the First Light measurements up to a factor of 2. However, these measurements were inflicted themselves by systematical uncertainties which are hard to quantify. Also, the ion species which were measured with the ionisation method were not always H^+, but also ^{3}He as suggested by theory of molecular dissociation after tritium decay; the cross section of this process is unknown and might well lead to another uncertainty of a factor 2 or larger.

Ar^+ ions While the argon pressure is assumed to increase the ion detection efficiency in this analysis, it also creates another background by Ar^+ which are created by scattering of beta electrons on the argon gas. Although the beta electrons cannot enter the PS due to the high voltage, they can ionise some of the argon atoms which diffuse from the PS towards the CPS. The ring electrode in the PS1 magnet can prevent some of these ions from entering the PS. However, there is some gas between the ring electrode and the begin of the PS high voltage where the Ar^+ ions can be produced (see figure IX.12).

The magnitude of the Ar^+ flux was estimated in order to consider it in the analysis. Each beta electron has a certain probability $\mathcal{P} = \sigma \cdot \rho \cdot l$ to create an Ar^+ ion. The gas density ρ and the length of the interaction zone between ring electrode and PS high voltage can be estimated; the energy dependence of the scattering cross section σ in combination with the beta electron spectrum require however a more extensive calculation [9]. This leads up to an expected Ar^+ rate of:

$$\Phi_{\text{Ar}^+} = 5 \cdot 10^3 \text{ Ar}^+/\text{s} \cdot \frac{p_{\text{PS}}}{10^{-7} \text{ mbar}}. \tag{IX.2}$$

This calculation does not take into account that the scattering cross section increases significantly when the beta electrons are decelerated by the PS high voltage on a short distance on the order of 1 cm. It will need to be investigated in the future whether the Ar^+ rate which is created on this short distance might be large enough to explain the rate of 3 cps which was observed during the measurements of the upper ion flux limit with the PS ionisation method. If the Ar^+ ions are responsible, there would be two ways of improving the detection efficiency: the magnitude of the Ar^+ background can be limited by measuring at smaller pressures; and the Ar^+ rate can be subtracted from the measurement when its magnitude has been sufficiently investigated by sending rear wall photo electrons at various energies into the argon filled PS.

Optimal pressure for detection of ions from the WGTS During the First Tritium campaign, it was assumed that the ionisation increased with the number of target atoms in the PS. Therefore the argon pressure was raised during the measurement

[9] Calculation carried out by Ferenc Glück.

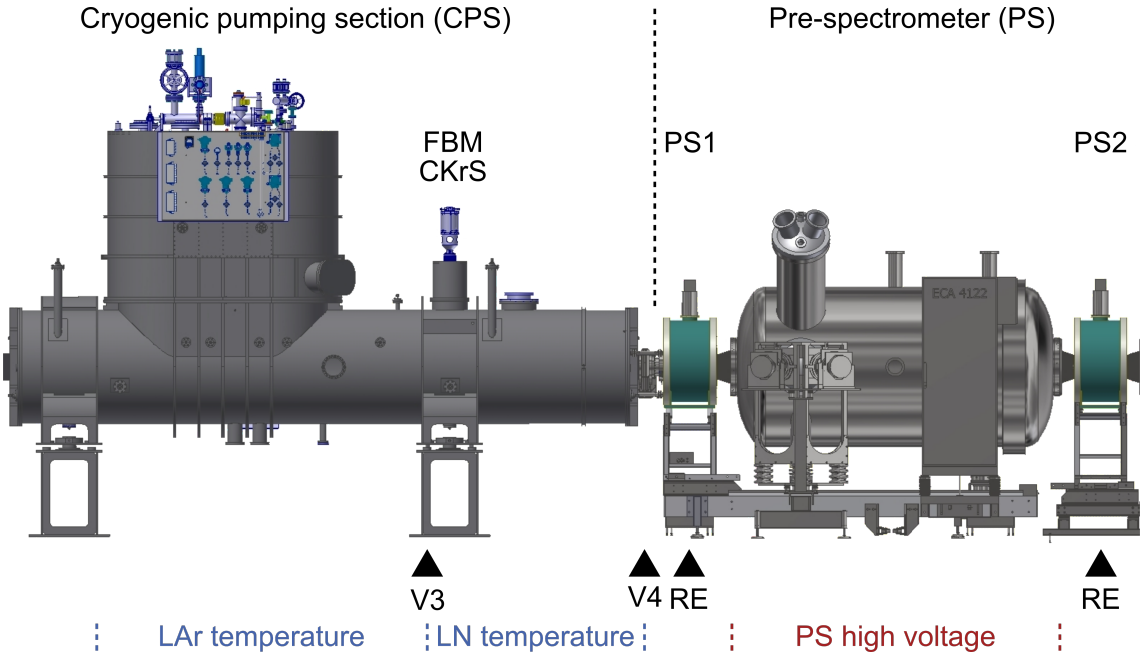

Figure IX.12.: **Setup of the PS ionisation measurement.** During First Tritium, it was assumed that the ionisation efficiency of the hydrogen ions would increase with the pressure inside the PS; it was only afterwards that the STS IIIa measurements indicated a pressure-independent and larger-than-expected ionisation efficiency, according to preliminary results from October 2018. For this reason, the PS was filled with argon up to the order of 10^{-8} mbar. The argon diffused also to the Main spectrometer (outside the picture on the right) and the CPS. Inside the CPS, some of the argon was pumped by turbo molecular pumps near the valve V3, the Forward Beam Monitor (FBM) and Condensed Crypton Source (CKrS); the rest condensed along the argon frost inside the CPS at liquid argon temperatures. Background from Ar^+ was created by the flux of beta electrons, which was mostly reflected at the high voltage of the PS vessel. The beta electrons ionised some of the argon between PS and CPS. Those Ar^+ ions which were created between the PS and the ring electrode (RE) in the PS1 magnet could not be hindered from entering the PS and ionising the argon as well. This Ar^+ background disappeared when the valve V4 was closed in order to measure the intrinsic background of the PS for the given argon pressures.

of Penning ions and dissociation ions in order to detect even small changes of the ion flux.

At large pressures, the rate from argon ions becomes also large. The FPD rate from Ar^+ was assumed to depend quadratically on the argon pressure, because it increased the number of projectile ions and target atoms alike. In order to derive an upper limit on the total ion flux from the WGTS, a smaller background from Ar^+ ions was favourable.

This leads to some optimal argon pressure for the detection of ions from the WGTS. In order to calculate it, the intrinsic PS background has to be estimated very roughly to be $R_{\mathrm{bg}} = 0.1$ cps (see figure IX.27), neglecting its fluctuations and pressure dependence. From that follows a minimal detectable FPD rate of $R_{\mathrm{min}} = \delta R_{\mathrm{bg}} = \sqrt{R_{\mathrm{bg}}/t} = 10$ mcps after $t = 15$ min. Then, the minimal detectable ion flux becomes:

$$\Phi_{\mathrm{min}} = \frac{R_{\mathrm{min}}}{\mathcal{E}} \approx 10 \text{ ions/s} \cdot \frac{10^{-7} \text{ mbar}}{p_{\mathrm{PS}}}. \tag{IX.3}$$

The optimal pressure can be found by equating eq. IX.2 and eq. IX.3:

$$p_{\mathrm{opt}} = 5 \cdot 10^{-9} \text{ mbar argon}. \tag{IX.4}$$

Preliminary results of the STS IIIa measurements indicate instead, that the ionisation efficiency of hydrogen ions in the PS is pressure independent; the same seems to apply to Ar^+ in the PS, so that this background increases linearly with the argon pressure in the PS. For ionisation measurements during future measurement campaigns, the argon pressure should therefore be kept as small as possible.

Pressure conditions during the measurements According to equation IX.2, the detection efficiency was assumed to increase linearly with the argon pressure. In order to detect the smallest possible rates during the investigation of Penning ions and the energy spectrum of dissociation ions, the pressure was set to a few 10^{-8} mbar. Larger pressures were not possible due to a safety interlock of the CPS. In order to derive an upper limit on the ion flux into the PS, the ionisation method was used with various pressures around the optimal pressure of $5 \cdot 10^{-9}$ mbar.

The pressure inside the PS was measured with a MKS 420 cold cathode vacuum gauge. In order to receive the actual argon pressure, the measured pressure has to be multiplied with a calibration factor of 0.81 ± 0.04 [10].

Stability and reproducibility The argon pressure during the measurements was extremely stable: its peak-to-peak fluctuations were usually on the order of a few percent or less. Nevertheless, sudden pressure decreases occurred without apparent reason as shown in figure IX.13. In such cases, the pressure was reset and the measurement was restarted with the stable pressure conditions.

During the measurements for the upper limit of the ion flux, the same argon pressure was required for the measurement of the background with the valve V4 closed and during the signal measurement with V4 open. Of course, when V4 was

[10] The calibration of the pressure gauge was part of the Bachelor's thesis of Philipp Weinreuter, *Calibration of vacuum gauges at the KATRIN spectrometer section*, 2008.

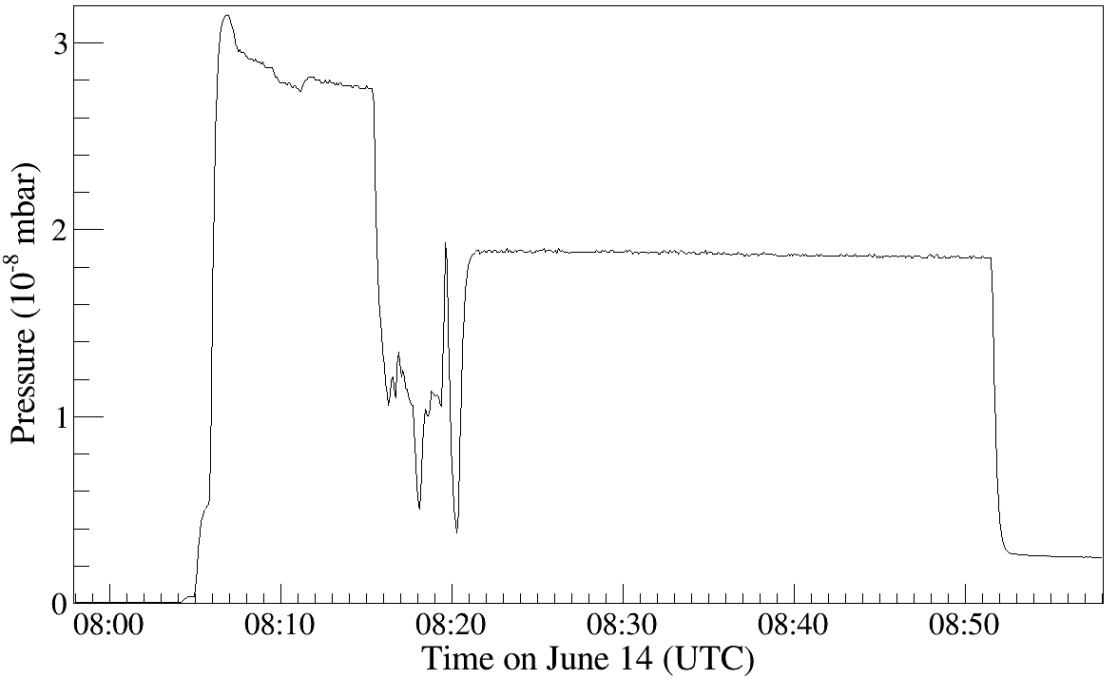

Figure IX.13.: **Break in of the PS argon pressure.** In order to increase the ionisation efficiency of the ions inside the PS, the pressure was increased with argon. At several occasions, the pressure would however break in suddenly without apparent reason and could only be stabilised after several attempts. Once this succeeded, the pressure remained however very stable over the full 15 min of the ionisation measurement until it was eventually changed for the next measurement setting.

open the CPS added to the pumping and reduced the argon pressure. In order to receive exactly the same pressure during both measurements, a fine tuning of the inlet valve would have been necessary. This would have been very time consuming due to technical reasons and therefore not possible during the limited measurement time. For this reason, the background was always measured at slightly larger pressures than the corresponding signal measurement during the investigation of the upper limit on the ion flux. The other measurements with the ionisation method required no resetting of the argon pressure and were therefore not affected by the poor reproducibility.

IX.1.4.2. Systematic effects of the Pre-spectrometer

The ionisation method was afflicted by several systematic effects in the PS. Most notably, a potential well inside the electric potential of the PS was discovered;during the First Tritium campaigns, the potential well was therefore removed with an asymmetric potential setting. Nevertheless, several systematic effects indicate that there might be remaining Penning traps: the pressure dependence of the intrinsic PS background, a hotspot on the right side of the FPD and an occasionally occurring ring on the FPD, which was dubbed donut. All of these effects will be discussed in the following.

Presumed Penning discharge in the PS The PS background was measured at various argon pressures with two different configurations of the inner electrodes: one time with a symmetric setting and one time with an increased voltage on the upper cone electrode. At all investigated pressures, the background increased by at least one order of magnitude to a few 100 mcps.

Dedicated simulations revealed what previous simulations had not found: when the electrons move along the magnetic field lines through the PS, they come across a negative potential well. This well is strongly reduced in the asymmetric setting. If secondary electrons are created inside this well, they are trapped and cannot reach the FPD. These trapped electrons might in turn feed a Penning discharge in the well which can lead to the increased background.

In order to minimise any influence of a PS Penning discharge on the ion measurements, the inner electrodes were set to the so called slide potential setting during all of the ionisation measurements: the upper cone electrode was at −500 V, the wire electrode at −450 V and the downstream cone electrode at −400 V relative to the vessel potential.

The consequences of the potential well for the ionisation method need yet to be quantified. There are no experimental measurements of the ionisation efficiency in the PS with a calibrated ion flux in order to judge whether the slide potential setting leads to the same ionisation efficiency as the simulations. However, the comparison with the (also uncalibrated) PS current measurement shows a very good agreement, as will be discussed in section IX.1.5.

Even with the slide potential, there might be remaining Penning traps inside the PS which could explain the background rate of about 3 cps which limited the ionisation measurements at about 10^{-8} mbar. Future work will have to search for such Penning traps with according simulations in order to propose potential settings that prevent them. Remaining Penning traps could also explain the hotspot on the FPD, which will be detailed next.

Pressure dependence of intrinsic PS background The intrinsic background of the PS was measured with closed valve V4 between the CPS and PS and for various pressures. It was found that the intrinsic background increased with pressure; especially, it jumped around 10^{-9} mbar and 10^{-8} mbar argon pressure. The background increase was observed with both the slide potential and the symmetric potential setting.

Possibly, a remaining Penning discharge is responsible for the increased background. Without a verified model, it is however not possible to interpolate between the background measurements. This adds some systematic uncertainty to the measurement of the upper ion flux limit, because the argon pressure could be set only roughly to the same values with closed and open V4 (see section IX.1.4.1).

Hotspot When the asymmetric potential setting was used, a hotspot appeared on the FPD as shown in figure IX.14. This hotspot scaled with the PS argon pressure and with the magnetic field strength of the CPS. The position of the hotspot shifted slightly between the measurements and also depended on the CPS magnetic field.

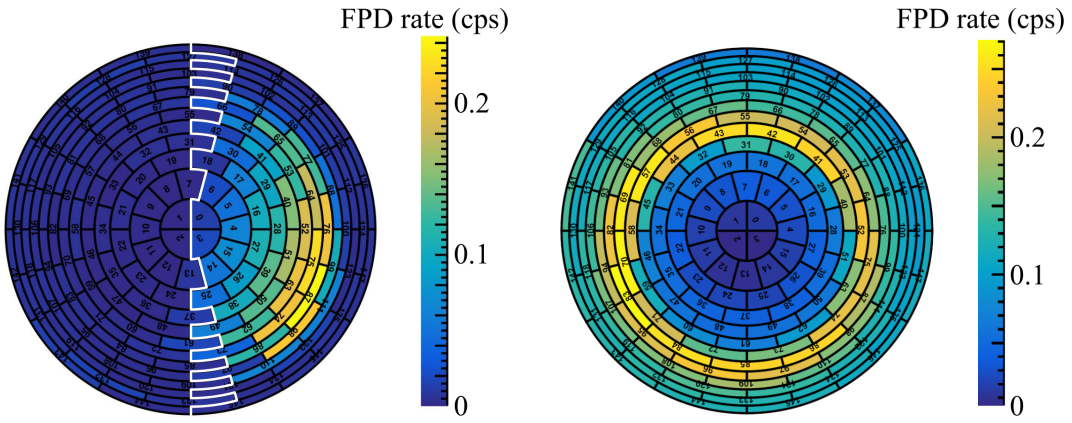

Figure IX.14.: **FPD pixel views of hotspot and donut.** The continuous hotspot (left picture) was considered by analysing only the rate on the left half of the FPD and taking this rate times two. When the donut appeared (right side), the measurement had to be interrupted; the donut eventually vanished by itself after about half an hour. Both systematic effects might have been caused by a Penning trap somewhere in the PS potential.

Given these observations, it seems reasonable that the hotspot was created by a Penning discharge inside the PS which was not detected when the symmetric electrode setting prevented the electrons from arriving at the FPD. The asymmetric position of the hotspot can however not be explained – possibly it is caused by an asymmetry of the wire electrode, which would then not be detectable with simulations.

The hotspot was excluded from the analysis in order to be able to calculate the total ion flux into the PS from the FPD rate; also, a possible non-linear relationship between the ion flux and the hotspot rate should be excluded. Therefore, only the FPD pixels left of the white line in figure IX.14 were considered in the analysis – a slight influence of the hotspot on some of the remaining pixels nevertheless seems to persist. The remaining pixels from the left side of the FPD were taken times two, which led to a slight overestimation of the total ion induced rate because the separation was not completely symmetric.

Donut Occasionally, a sudden increase of the PS background would occur and create a ring shaped pattern on the FPD as shown in figure IX.14. The background rate would peak up to a few hundred or even thousand cps and varied over time. After about 20 min to 30 min, the background would return to normal again without apparent reason.

It seems reasonable that also this phenomenon was caused by a remaining Penning trap in the PS potential. However, there was no way to influence or stop this so called donut. The effect occurred seldomly enough so that it was possible to wait until it was over and then continue the measurements.

IX.1.4.3. Minimal detectable ion flux

The ion dectetion via ionisation during First Tritium relied on an increased argon pressure in order to increase also the ionisation efficiency of the hydrogen ions. Because the background by Ar^+ ions increases likewise, the measurement was performed at usually five different pressure values so that the signal and background could be told apart. This led to an upper limit on the ion flux into the PS on the required level of $1 \cdot 10^4$ ions/s (see section IX.4.4). The same rate has to be taken also as the minimum detectable ion flux, because whether the measurement was actually limited by hydrogen ions or by background instead could not be resolved at this time.

But even without this background, the minimal detectable ion flux could still not be quantified: a measurement of background and signal at the same argon pressure was not possible due to the poor reproducibility of the argon pressure; and the strange pressure dependence of the intrinsic PS background allows no interpolation to the argon pressure of the signal measurement. Also, it is not sure how stable the intrinsic background remained over time.

It was only after the First tritium campaign, that the STS IIIa commissioning campaign indicated a pressure-independent and larger-than-expected ionisation efficiency. According to the preliminary results from October 2018, the absolute value of the ionisation efficiency is much larger than predicted by the KASSIOPEIA simulations; as a consequence, the rate of $1 \cdot 10^4$ ions/s has to be taken as a conservative upper limit. Furthermore, the pressure independent ionisation efficiency implies a linear increase of the Ar^+ rate with the argon pressure. These argon ions presumably dominated the measured rate of $1 \cdot 10^4$ ions/s. The final results of the STS IIIa measurement campaign would be necessary in order to quantify the minimal detectable ion flux at increased argon pressure in the PS; more reasonably, the PS pressure should not be increased during future ionisation measurements anymore.

IX.1.5. Comparison of PS cone current and ionisation method

The two most important detectors for the ion monitoring are the PS ionisation method (see section VII.1 or the previous section) and the PS current method (see sections VII.2.4 or IX.1.3). Because the ionisation method is non-destructive, both methods can be applied simultaneously to the same ion flux. This allows a direct comparison of both methods and the investigation of systematic effects.

The ion flux, which is necessary for the comparison, was created during First Tritium in two different ways: first with Penning ions from the DPS ring electrodes (see sections III.4 and IX.2.2) and also with dissociation ions from the tritium source (see sections III.3 and IX.2.3). Both times, the total flux remained below the First Tritium limit of 10^6 ions/s.

This section will first describe the measurement conditions, followed by the analysis procedure for the ionisation and current measurements. Both methods will then be compared first with Penning ions and then with dissociation ions. Finally, the results of the comparison will be discussed.

Measurement conditions The measurements with Penning ions and dissociation ions were both carried out on the same day. Fortunately, the temperature in the spectrometer hall showed for unknown reasons no oscillations on this day – it was stable to the level of bout ± 0.1°C instead of the usual ± 1°C. For the current measurement, this means that the temperature induced oscillations up to 50 fA amplitude was reduced to about 5 fA (see section IX.1.3).

Analysis procedure For the quantitative comparison of the ionisation and current measurement, both results need to be converted into an ion flux. In contrast to all other analyses of First Tritium data, the preliminary results of the STS IIIa commissioning campaign will be included. This is necessary in order to allow for a meaningful comparison of the First Tritium results with regard to all known systematic effects.

- **Ionisation efficiency:** Before the STS IIIa measurements, the ion to electron conversion in the PS was assumed to be driven by ionisation of residual gas, just like in the MS. A pressure-dependent ionisation efficiency was consequently assumed, too (see eq. IX.1). During the measurements under discussion, the increased argon pressure of $3 \cdot 10^{-8}$ mbar should thus have created an ionisation efficiency of $3 \cdot 10^{-4}$ counts/ion.

  Instead, the STS IIIa measurements determined a pressure-independent ion to electron conversion efficiency of $\epsilon = 2 \cdot 10^{-3}$ counts/ion. Although the underlying conversion mechanism is not yet understood, the conversion factor will be used for the analysis of ionisation measurements in this section.

- **Ion transport probability to the cone electrode:** Roughly 20% of the total ion flux into the PS reaches the downstream cone electrode, according to simulations presented in section IV.1.

- **Secondary electrons emission:** Each impacting ion ejects about 30 secondary electrons, according to calibration measurements during the STS IIIa campaign. The resulting charge amplification allows for the detection of smaller ion fluxes with the same current sensitivity. Previous to the STS IIIa measurements, this systematic effects was deemed negligible.

The ion flux Φ into the PS can be calculated from the measured FPD rate R with the ionisation efficiency $\epsilon = 2 \cdot 10^{-3}$ counts/ion via $\Phi = R/\epsilon$. For the current measurement, an ion flux is obtained by multiplying the result in Ampere with $1 \cdot 10^{18}$: besides the multiplication with the Coulomb number $6.2415 \cdot 10^{18}$ charges per second, the ion transport probability and secondary electrons emission lead to another factor 1/6.

Penning ions A constant ion flux into the PS was created with Penning ions from the DPS ring electrodes (see section IX.2.2). The voltage of both ring electrodes were gradually increased to about +300 V, which had proven to create the largest ion flux into the PS (see figure IX.2.2). Still, the ion flux limit into the PS of 10^6 ions/s during First Tritium was not exceeded.

In the PS, the ions were detected with the ionisation and current methods simultaneously. Each measurement at a certain ring electrode voltage took 15 min in order to reduce the uncertainty of the current measurement to a meaningful level.

Figure IX.15 shows the measured ion fluxes:

- **Above 100 V:** Both ionisation and PS current measurement show the same qualitative behaviour. Also, the quantitative agreement is rather good within roughly a factor 2.

- **20 V:** Two measurements were taken, before and after this 1.5 h long measurement. The results agree rather well, which underlines the stability of the detectors (see for example the current oscillations in section IX.1.3.2); still, the observable disagreement shows that the displayed statistical uncertainties underestimate the actual systematic effects and fluctuations. It is therefore not possible to determine whether Penning ions are still being produced and measured or whether the observed signal is only a background fluctuation.

- **0 V:** These points show the background with closed valve V4 between CPS and PS. With open V4, the FPD rate is significantly larger. This is not attributed to an ion flux from the WGTS or DPS, but rather to beta electron induced Ar^+ ions which are produced between the PS1 ring electrode and the PS.

Dissociation ions The energy spectrum of dissociation ions from the tritium source was observed by gradually decreasing the voltage of the DPS BT5 ring electrode, while all other positive potentials were turned off. This created an ion flux, which was measured simultaneously with the PS ionisation and current measurement.

As figure IX.16 shows, both detection methods observe the same qualitative shape of the ion spectrum. But the statistical uncertainties of the current measurement is large due to the short measurement time of 3 min allows. Therefore, a quantitative analysis is not possible.

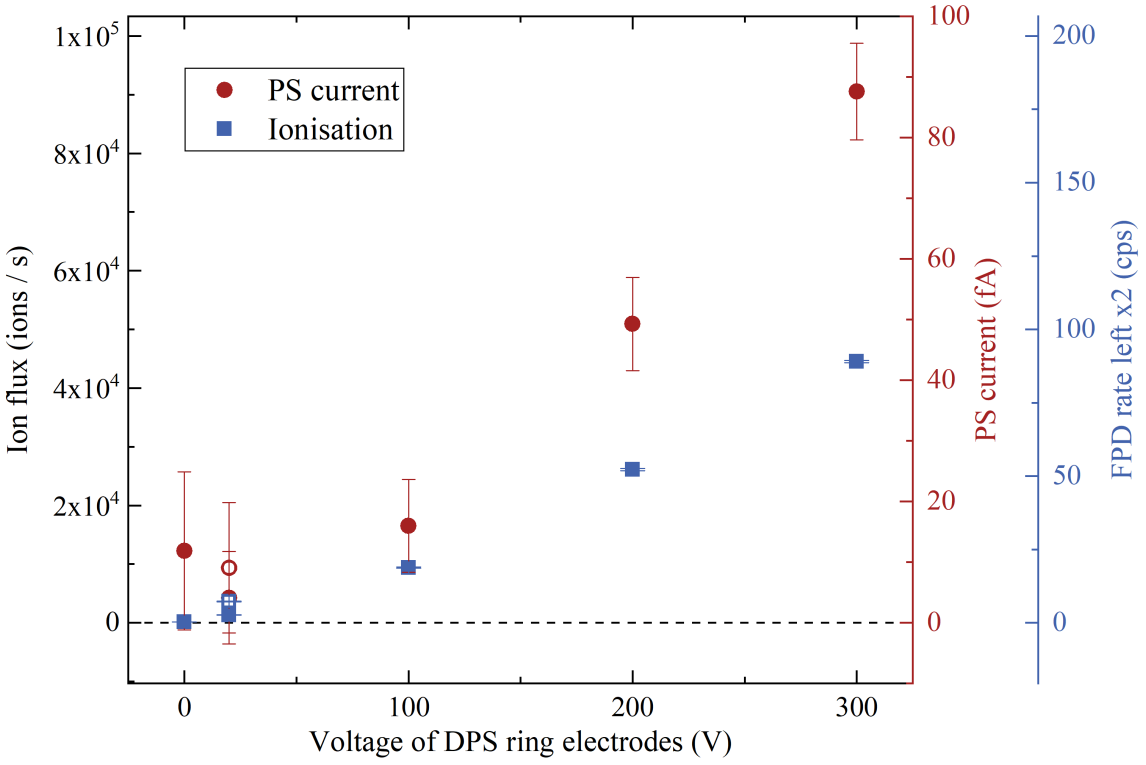

Figure IX.15.: **Penning ions, measured with the PS current and ionisation methods.** Both detectors show the same linear increase with the voltage of the DPS ring electrodes above 100 V due to the increasing Penning ion flux. At 20 V, the ion flux was measured before (empty symbol) and after (full symbol) these three measurements. Each measurement took 15 min, except for a 5 min measurement of the intrinsic background with $(3 \ldots 4) \cdot 10^{-8}$ mbar argon and closed valve V4 between CPS and PS, which is shown at 0 V.
The quantitative analysis includes the preliminary results of the STS IIIa commissioning measurements from October 2018; this is in contrast to all other analyses presented in this thesis, but allows for a meaningful quantitative interpretation of the result. Both measurements agree roughly within a factor 2, which is probably smaller than the systematic uncertainty on the STS IIIa results.

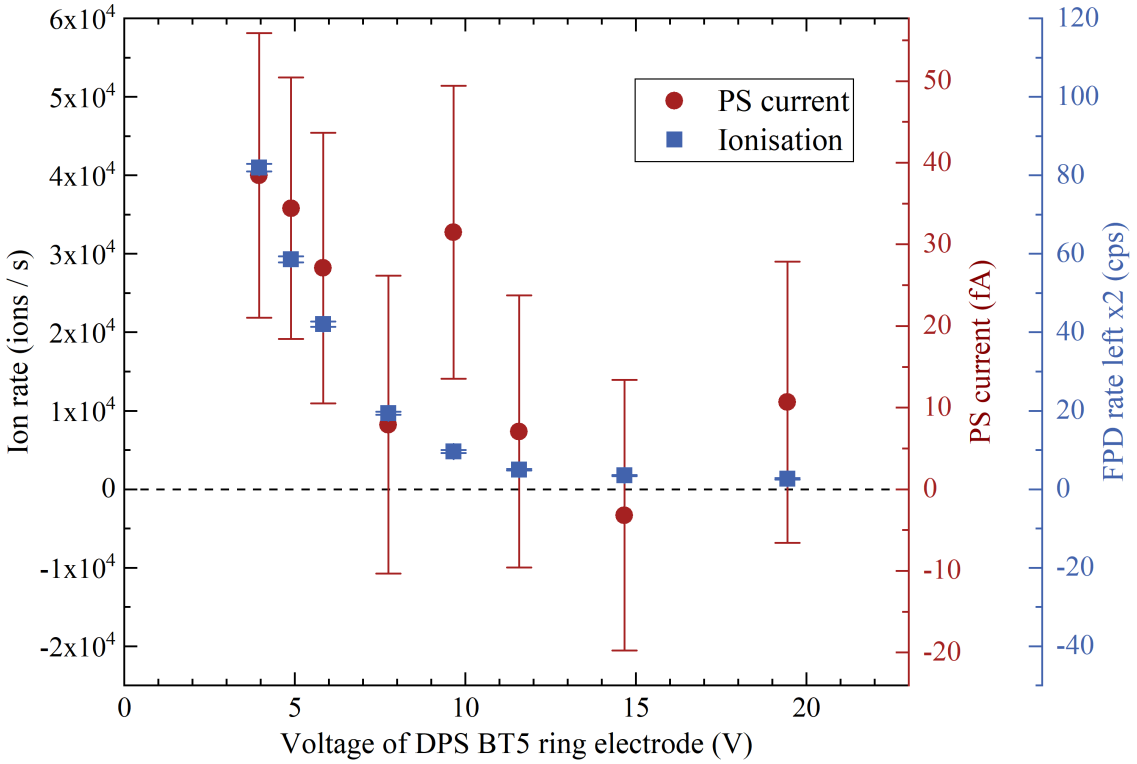

Figure IX.16.: **Dissociation ion spectrum, measured with the PS current and ionisation methods.** Both measurements show the same qualitative behaviour. A quantitative analysis is not possible due to the large statistical uncertainties of the current measurement in these 3 min measurements. Like for figure IX.15, the preliminary results of the STS IIIa measurements have been included in the analysis.

Comparison Both PS ion detection methods via ionisation and current measurement showed the same qualitative result when they measured Penning ions from the DPS or dissociation ions from the tritium source. The quantitative analysis was only meaningful in case of the Penning ion measurement: here, a rather good agreement within a factor 2 was found. The uncertainties on the preliminary results of the STS IIIa measurements are probably larger than a factor 2.

The good agreement is a success of the STS IIIa calibration measurements, which were used for this analysis. This concerns especially the pressure-independent ionisation efficiency, which was one order of magnitude larger than would have been calculated with eq. IX.1; and the secondary electron emission by roughly 30 electrons per ion impact is otherwise not considered at all.

Without the results of the STS IIIa measurements, the discrepancy of the ionisation and current measurement would be about a factor 6. This shows that the systematic effects in at least one of both methods is not yet fully understood. Nevertheless, a conservative limit on the ion flux into the PS can be derived when the results of the STS IIIa measurements is not considered in the analysis.

IX.1.6. Current measurement of the beta electron flux

In the previous section, the ion detection capabilities of the PS downstream cone electrode were demonstrated. But before the Penning ions and dissociation ions had been observed, a proof-of-principle of the PS current measurement was obtained by detecting beta electrons from the WGTS. This established the PS cone current as a reliable ion monitor with the capability to close the valve V4 between CPS and PS automatically and allowed the overnight measurements during the First Tritium campaign.

Another important reason for a current measurement of the beta electron flux is the quick assessment of the total tritium activity in the WGTS. While the activity can be obtained from the FPD measurements by the corresponding parameter in the neutrino mass fit, the current measurement allows an independent measurement at much larger statistics: especially at higher tritium concentrations, the FPD will be able to observe only an interval of about 1 keV below the spectral end point whereas a current measurement can easily measure the whole electron flux.

In order to test the beta electron detection with the PS cone, the PS2 magnet was ramped down to guide the electrons magnetically onto the electrode. Right before that, the electron flux was measured with the even more promising current measurement on PULCINELLA, which requires no special magnetic field settings. The best suited beta electron detector is actually the Faraday cup at the FBM, because its shield retains secondary electrons and minimises systematic effects; however, the measured current was 50 times smaller than expected, which renders this detector inapplicable until its improvement.

Measurement procedure In order to measure the beta electrons via the PS cone current, the PS2 had to be ramped down so that the beta electrons were guided onto the cone electrode. The PS vessel was at 0 V so that the beta electrons were not rejected electrically, yet the upstream cone electrode and the wire electrodes were set to -500 V in order to retain secondary electrons. As for the downstream cone electrode itself, it was set to -50 V because the voltage supply might not have been able to stabilise a smaller voltage.

Before ramping down the PS2 magnet, the beta electron flux was measured with the PULCINELLA disc for 1 min and a flux of $(8.13 \pm 0.14) \cdot 10^7$ electrons per second was observed; the PS was already at the described voltage settings, while PULCINELLA itself was grounded.

Then the PS2 magnet was ramped down and the beta electron current on the PS cone electrode was observed. Figure IX.17 shows two spikes at about 30 A and 0 A current in the PS2 coil, which are attributed to a complex behaviour of the magnetic field lines. During the ramping, field lines end temporarily on the front and back side of the downstream cone electrode and some of the beta electrons are guided onto the cone electrode through the wire electrode; this produces the spike at 30 A. When the PS2 magnet was ramped down, the current was measured during two periods of 10 min and an average electron flux of $(1.52 \pm 0.01) \cdot 10^7$ electrons/s was derived, as stated in table IX.1.

At a later occasion, the beta electron flux was also measured via the PS cone

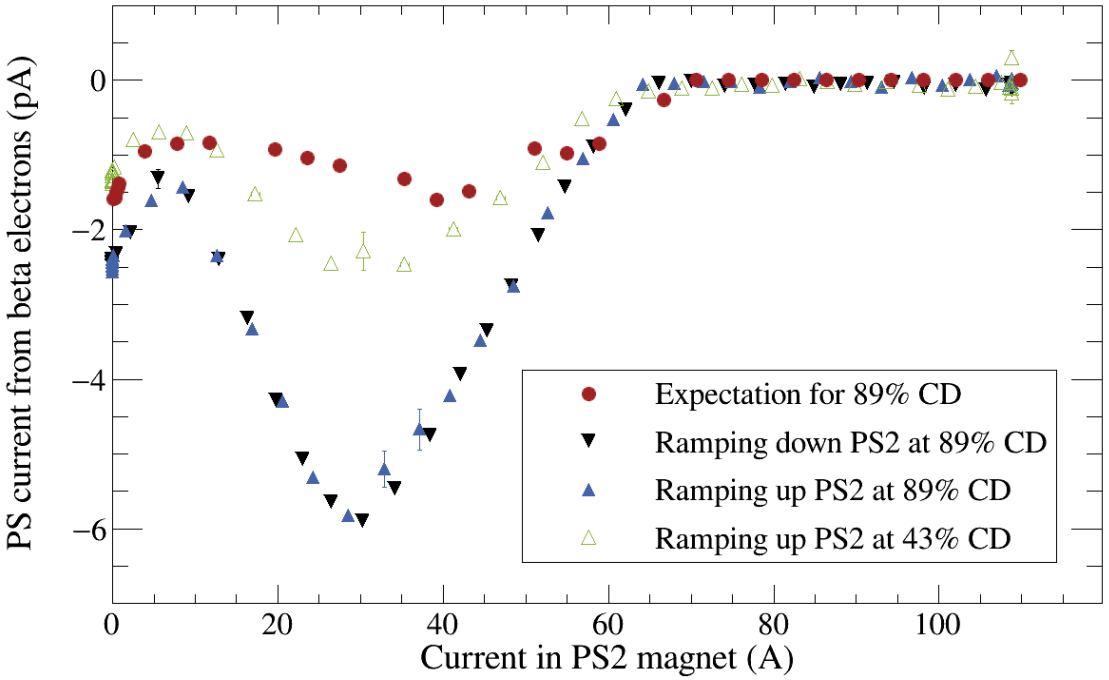

Figure IX.17.: **PS current measurement of beta electrons.** In order to guide the beta electrons onto the downstream cone electrode of the PS, the PS2 magnet was ramped down and up again. Meanwhile the PS current was measured: one time at 89% column density and one time at 43% column density. The measurements agree quite well with each other, but the tracking simulation of the magnetic field lines predict a much smaller rate. This discrepancy might be resolved by simulating the actual tracks of the beta electrons.

current at only 43% column density. No PULCINELLA measurement was carried out this time, and the beta current was observed only while the PS2 magnet was ramped up again as shown in figure IX.17. The current $(7.79 \pm 0.16) \cdot 10^6$ electron/s might slightly overestimate the actual flux: the voltage on the downstream cone electrode had been set to −50 V only half an hour before the magnet was ramped up and there was still a residual current over the capacitance of the cone electrode.

The beta current was measured with the Faraday cup during both measurement days of the Very First Tritium campaign. On the first day, the valve V4 between CPS and PS was still closed and the Faraday cup provided the only measurement of the source activity. All of these measurements yielded currents of (15 . . . 20) fA, which was far below the expectation which will be discussed below. As an example, table IX.1 lists a flux of $(1.23 \pm 2.03) \cdot 10^5$ beta electrons per second which was measured at the V1 opening shown figure IX.6.

Expected currents In order to compare the measurement results to theory, the beta electron fluxes at the location of the detectors were calculated according to section III.1.3. Additionally, the detection efficiencies of the individual detectors have to be taken into account. This leads finally to the expected electron fluxes,

which are listed in table IX.1.

The beta activity in the WGTS followed from equation III.10 by using the column density and tritium concentration at the time of the signal measurement. At the location of the Faraday Cup, the beta flux was reduced by the 50% probability that the electron left the WGTS towards the detector and by the 40% probability that the electron could overcome the magnetic mirror. For the PS current method and PULCINELLA, also the following probabilities were considered: transmission of the fluxtube from the WGTS into the PS (83%), the cut on the beta electrons with less than 500 eV by the PS high voltage (96%) and the effect on this cut by the final states spectral contribution (98%). Not considered are the effects on the beta electron spectrum by scattering inside the WGTS, which would further reduce the expected electron flux. Also not considered for the case of the Faraday cup is the cut on the beta electron spectrum by the negative dipole potential in the DPS.

Not all of the arriving electrons were however detected due to the detection efficiency of the individual detectors. Geometrically, the Faraday cup could only cover 8.9% of the fluxtube with its sensitive surface[11] whereas PULCINELLA is assumed to have been covered by all of the transmitted fluxtube from the WGTS. In case of the PS current method, tracking simulations[12] of the magnetic field lines propose about $(11.8 \pm 0.5)\%$ of the beta electrons to reach the cone electrode – more precise electron tracking simulations will probably lead to a larger factor.

The other important contribution to the detection efficiency comes from electron

[11] The active surface of the Faraday cup is determined by the six openings of the electric shield above the board. Each of the opening measures $(6.5 \cdot 42.0)$ mm^2, which leads to $A_{\mathrm{FC}}^{\mathrm{surf}} = 1{,}638$ mm^2. The beta electrons are created in the WGTS in a $\Phi_{\mathrm{tot}}^{\mathrm{mag}} = 229$ T cm^2 magnetic flux. This leads with the magnetic field at the position of the Faraday cup $B_{\mathrm{FC}} = 1.24$ T to a cross section of $A_{\mathrm{FC}}^{\mathrm{mag}} = \Phi_{\mathrm{tot}}^{\mathrm{mag}} / B_{\mathrm{FC}} \approx 18{,}468$ mm^2.

[12] Simulations carried out by Woo-Jeong Baek.

Table IX.1.: **Current measurements and expectations of the beta electron flux.** The PULCINELLA measurement shows the best agreement with theory. In case of the PS current measurement, the probability of the beta electrons to reach the downstream cone electrode without the field of the PS2 magnet is obviously underestimated by the simulation; charge multiplication by secondary electron emission is excluded due to the -500 V at the wire electrode. The Faraday cup measures only about 2% of the expected electron flux for unknown reasons.

Detector	Measured (e/s)	Expected (e/s)	Measured / exp.
PULCINELLA (89% $\mathcal{N}_0$)	$(8.13 \pm 0.14) \cdot 10^7$	$(8.11 \pm 1.14) \cdot 10^7$	$(100.2 \pm 14.2)\%$
PS cone (89% $\mathcal{N}_0$)	$(1.52 \pm 0.01) \cdot 10^7$	$(9.87 \pm 1.51) \cdot 10^6$	$(153.7 \pm 23.5)\%$
PS cone (43% $\mathcal{N}_0$)	$(7.79 \pm 0.16) \cdot 10^6$	$(4.61 \pm 0.72) \cdot 10^6$	$(169.0 \pm 26.7)\%$
Faraday cup (89% $\mathcal{N}_0$)	$(1.23 \pm 2.03) \cdot 10^5$	$(5.18 \pm 2.34) \cdot 10^6$	$(2.4 \pm 4.1)\%$

backscattering at the metallic surface of all three current detectors, which was simulated[13] with GEANT4. Backscattered electrons can however be reflected by the magnetic mirror effect, too, and might undergo backscattering and magnetic reflection several times before being either absorbed by the surface or escaping through the mirror. Eventually, the expected electron flux is reduced at the Faraday cup[14] to 94% and at the PULCINELLA disc to 99%. In case of the PS cone electrode, all backscattered electrons are assumed to eventually reach the surface due to the extremely strong magnetic mirror while the PS2 magnet was ramped down.

Secondary electrons are assumed to be reflected back onto the detector surface in all three cases. In case of the Faraday cup, its shield was always about 20 V more negative than the cup surface; and when measuring the current with PULCINELLA and the PS cone, the −500 V on the PS upstream cone electrode served as retarding voltage for all secondary electrons.

Comparison and conclusions The PULCINELLA measurement of the beta electron flux shows very good agreement with the theoretical expectation. Unfortunately, the assessment is restricted by the large uncertainty of 14%, which stems mostly from the systematics of the DT concentration measurement by LARA. It is therefore not possible to evaluate whether significant influences have gone unnoticed, which would further decrease the expected electron flux: for example scattering in the WGTS, which decreases the electron energy so that more electrons are rejected by the −500 V in the PS and cannot reach the PULCINELLA surface. But of all three current measurement methods, PULCINELLA has proved to be best suited to measure the source activity in the future. Still, a major drawback of the PULCINELLA measurement is the maximum detectable current of 0.6 nA, which should be increased in the future.

A larger electron current than expected was measured on the PS cone electrode. Both at 89% and 43% column density, the measured current exceeded the expectation by more than two standard deviations. It is assumed that the magnetic field tracking underestimates the number of beta electrons which actually reach the cone electrode. As shown in figure IX.17, these simulations predict qualitatively the observed spikes in the beta electron current for various magnetic field strengths at the PS2, but fail to explain the measurements quantitatively. This discrepancy might be remedied by future electron tracking simulations.

Compared to PULCINELLA, the PS current measurement has also the practical disadvantage that the PS2 magnet needs to be ramped for 2 hours in total in order to measure the beta electron current. Nevertheless, this measurement allowed the first demonstration of the PS current measurement and its use as approved monitoring system during night measurements. Only later were Penning ions in the KATRIN

[13] Simulations by Ellen Förstner and calculations by Ferenc Glück.

[14] The backscattering probability for beta electrons which arrive perpendicular to the silver surface of the Faraday cup is 35.3%. Under nominal conditions (200 A=100% CPS current), the magnetic field at the position of the Faraday cup ($z = -18.271$ m) is $B_{\mathrm{FC}} = 1.24$ T. The maximum field between Faraday cup and WGTS would be $B_{\mathrm{max}} = 5.66$ T under the same conditions. In order to escape through the magnetic mirror, electrons must have a pitch angle θ with $\cos(\theta) < \cos(\theta_{\mathrm{lim}}) = \sqrt{1 - B_{\mathrm{FC}}/B_{\mathrm{max}}} = 0.88$. This assumes that the electrons are backscattered with an isotropic angular distribution.

beamline discovered, which allowed the test measurements from the previous section IX.1.5.

The Faraday cup was found to measure only about 2% of the expected electron flux. This larger discrepancy cannot be explained with uncertainties of the theory, which otherwise has proved to describe the measurements better than by a factor of 2. Instead, the measurement seems to be flawed for unknown reasons (see discussion in section IX.1.2). It would be useful to improve the Faraday cup measurements in order to determine the source activity while the valve V4 between CPS and PS is closed during the start of future measurement campaigns with increased tritium concentrations.

IX.2. Three energy regimes of tritiated ions

Before the First Tritium measurements, it was assumed that all ions inside the KATRIN beamtube would be created by beta decay or subsequent ionisation of gas by the beta electrons. These ions would be mostly created inside the WGTS and leave it only with thermal energies due to frequent scattering with the source gas. Calculations and simulations were carried out in order to quantify the expected ion flux from the WGTS into the DPS.

During the First Tritium measurements, these thermal ions were measured via the current on the DPS dipole electrodes. But other than expected, the ion energy spectrum reached up to energies of 15 eV due to a significant amount of ions which could leave the WGTS unscattered. On top of that, ions were also found to be created by Penning discharges inside the positive potential of the ring electrodes.

This section will first deal with thermal ions and test the predictions concerning their total flux, as well as its dependence on the tritium concentration and column density. Then the observations of Penning ions will be discussed, which are relevant to understand the setting for the measurement of the ion energy spectrum at a few eV energies. This measurement and its confirmation of ions from molecular dissociation with eV energies in the KATRIN beamline will be discussed in the end.

IX.2.1. Positive thermal ions

The current measurements with the dipole electrode in DPS BT1 allow to test the theoretical predictions for the ion flux into the DPS. According to section III.2.5, the positive ion flux should depend linearly on the tritium concentration ϵ_T and quadratically on the column density $\mathcal{N}$. Both expectations could be confirmed with the measurement data, as will be discussed in the following two sections: first for the tritium purity and then for the column density.

IX.2.1.1. Ion flux dependence on the tritium purity ϵ_T

On the second measurement day of the Very First Tritium campaign, the tritium concentration was changed gradually in a special test measurement by the injection of tritiated gas into the inner loop via sample cylinders. From the current of the dipole electrode in DPS BT1, the ion flux was calculated at three different tritium concentrations. The ion flux was found to increase linearly with the tritium concentration, in agreement with expectations, but only at about half the expected magnitude.

Current measurement and conversion to an ion flux rate The tritium concentration was increased in two steps from about 0.3% to about 0.6% over a total of about 10 hours. The ion current was measured during the whole time with the dipole electrode in the DPS BT1, but only evaluated for arbitrarily chosen intervals of 5 min to 10 min. Over the whole measurement day, the valve V1 remained constantly open, allowing rather stable measurement conditions. However, the extraordinary use of sample cylinders to increase the tritium concentration also lead to a decrease of the column density at the end of each measurement phase with a

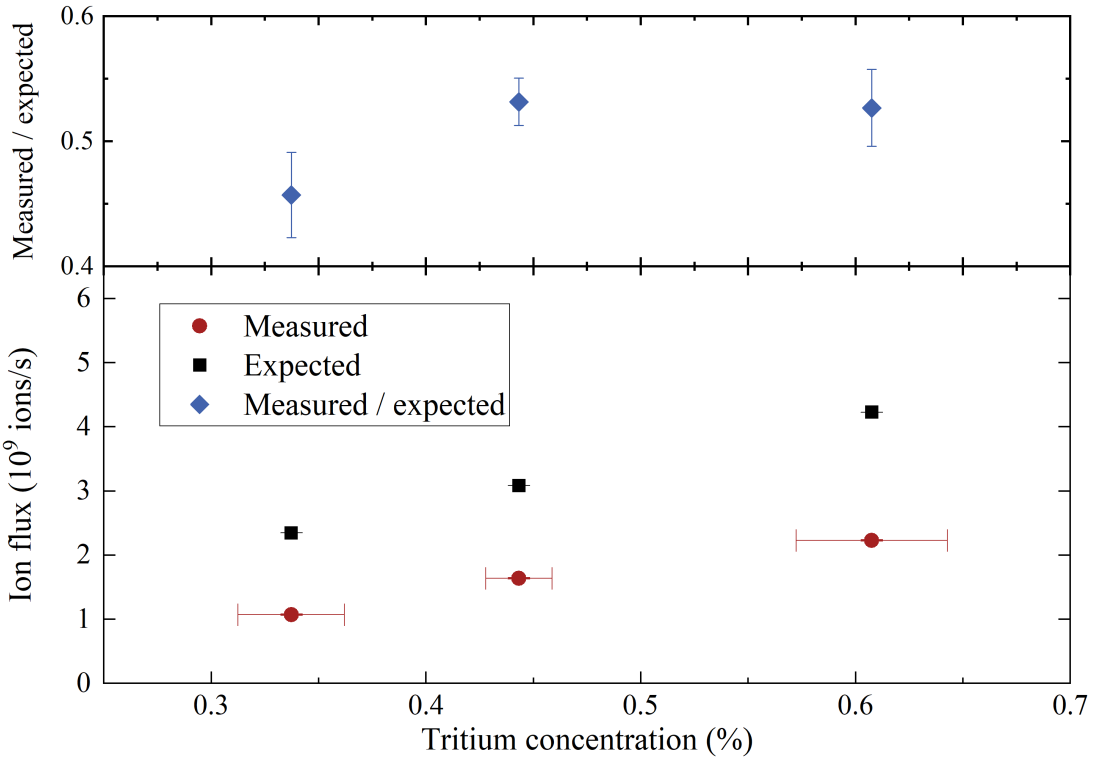

Figure IX.18.: **Ion flux dependence on tritium concentration.** During the Very First Tritium measurements, the tritium was supplied by sample cylinders which caused a small variation of the tritium concentration on the second day of the campaign. The ion flux, which was measured with the DPS BT1 dipole electrode, was only about 50% of the theoretical expectation. This discrepancy is attributed to inadvertent ion blocking between WGTS and DPS (see section IX.3).

certain tritium concentration; the intervals for evaluation of the BT1 current were chosen in order to prevent effect of column density changes.

In order to compare the measured currents between 200 pA and 500 pA to the theory, the corresponding ion fluxes needed to be calculated. To this end, the background current was subtracted from each value and the net current was multiplied with the Coulomb number of $6.2415 \cdot 10^{18}$ ions/Coulomb (see section VII.2.1). The background was taken as the average of the currents which were measured before and after the measurement day, when the valve V1 between WGTS and DPS was closed. Although the values of (78 ± 2) pA and (91 ± 1) pA agree rather well, there might have been oscillations of the background over the measurement day: no account can be taken in this measurement for such oscillations with amplitudes of about 100 pA and 1.5 hour period.

Comparison of measurement and theory The measurement result can be compared to the expected ion fluxes, which were calculated from equation III.33 based on the column density and tritium purity at each measurement point. These expectations are displayed as black squares in the lower part of figure IX.18 and are

generally larger than the measured ion fluxes (red circles). In order to compare measurement and expectation quantitatively, their ratio is shown by the blue diamonds in the upper part of figure IX.18. All three ratios are distributed rather closely around 0.5, which is attributed to inadvertent ion blocking between the WGTS and DPS BT1. The roughly constant ratio is in favour of the theoretical expectation given the measurement data.

IX.2.1.2. Ion flux dependence on the column density $\mathcal{N}$

In a dedicated measurement with various column densities, the ion flux from the WGTS was measured with the dipole electrode in DPS BT1. A good qualitative agreement with theory was found, which predicts a polynomial dependence of the ion flux on the column density $\mathcal{N}$. However, the magnitude of the observed ion flux was two times smaller than expected, presumably due to inadvertent ion blocking as described in section IX.3.

Current measurement and conversion to an ion flux rate The column density was set to 12 different values between $(0.2 \ldots 5.6) \cdot 10^{21}$ m^{-2} over the course of about 5 hours while the current on the dipole electrode in BT1 was measured constantly. With the help of the pressure controlled buffer vessel which controls the gas inlet into the WGTS, it was possible to monitor the actual column density[15]. The dipole current was evaluated during time intervals of 5 min to 10 min towards the end of each measurement phase when the column density was stable to the level of 10^{-5}.

In order to compare the measurement to the theoretically expected the ion flux, the current values were converted into a charge flux with the Coulomb number. Previously, the offset current had to be subtracted however. The measurement at the smallest column density of $0.2 \cdot 10^{21}$ m^{-2} provided a reasonable measurement of this current offset, because the contribution of ions to the current of the dipole measurement should disappear with the column density. For at least ten times larger column densities, this treatment of the linear offset should not affect the signal significantly due to the observed quadratic increase of the measured current with the column density.

The obtained ion fluxes are shown by the red circles in figure IX.19. They exhibit definitely no linear but a rather polynomial behaviour, peaking up to $3 \cdot 10^9$ ions/s at column densities slightly above the KATRIN design value of $\mathcal{N}_0 = 5 \cdot 10^{21}$ m^{-2}. Due to the treatment of the offset current, a zero ion flux is displayed at the minimal column density of $0.2 \cdot 10^{-21}$ m^{-2}.

The overall picture of the result indicates that the measurement was not affected significantly by oscillations of the BT1 dipole current. Current oscillations up to 100 pA have been observed at periods of 1.5 hours (see section IX.1.1.2), which could well have influenced the measured current that lay between 200 pA and 700 pA. No account could however be made for oscillations in this measurement because only one measurement of the background was acquired.

[15]Simulations by Florian Heizmann and calibration by Alexander Marsteller.

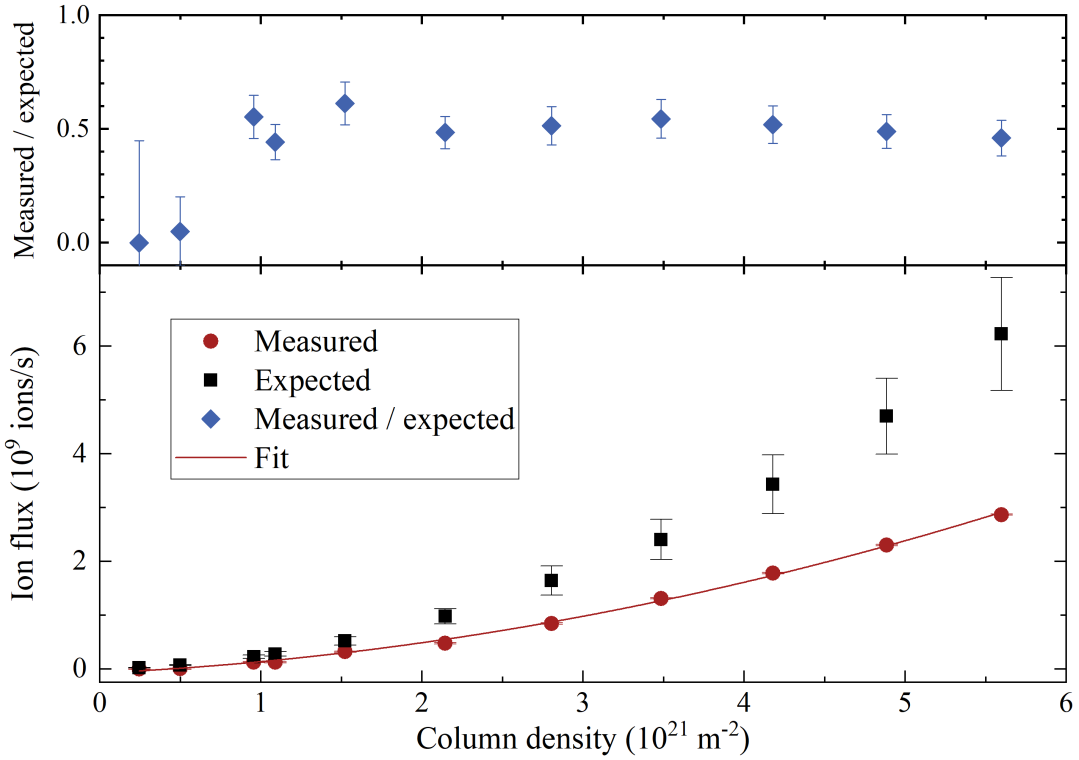

Figure IX.19.: **Ion flux dependence on the column density.** In a dedicated measurement, the column density was varied between almost zero and slightly above the nominal value of $5 \cdot 10^{21}$ m^{-2}. As predicted by theory, the ion flux at the DPS BT1 dipole electrode increased quadratically with the column density. However, the observed ion flux was again only about 50% of the predicted value, which is attributed to inadvertent ion blocking between the WGTS and DPS (see section IX.3). The ratio of measured and expected ion flux becomes zero at the smallest column density because this measurement was assumed as the offset current of the dipole electrode. A second order polynomial fitted well to the measurement, although with slightly different parameters due to the smaller magnitude (see table IX.2).

Comparison of measurement and theory In order to compare the measurement data to the theory, the expected ion flux was calculated for the column density $\mathcal{N}$ of each measurement point. According to equation III.33 from section III.2.5, the relationship between ion flux Φ and column density $\mathcal{N}$ takes the shape of a second order polynomial:

$$\Phi_{\text{ion}}^{\text{tot}}(\mathcal{N}) = a + b \cdot \mathcal{N} + c \cdot \mathcal{N}^2. \tag{IX.5}$$

The coefficients a, b and c are almost completely known from theory. Besides the column density, the only measurement condition which entered the calculation was the tritium concentration ϵ_{T} in the WGTS during any given measurement point. The rather large measurement uncertainties of ϵ_{T} lead to equally large uncertainties on the calculated ion fluxes via Gaussian error propagation.

The calculated ion flux into the DPS is shown by black squares in the lower section of figure IX.19. A good qualitative agreement between measurement and expectation is found: both amplitudes are on the same order of magnitude and show a polynomial growth with increasing column density.

For a quantitative evaluation, the ratio between the measured and expected ion fluxes is shown by the blue diamonds in the top section of figure IX.19. This ratio settles rather stable around 0.5 for most of the column density values which is attributed to the inadvertent blocking of some of the thermal ions in the transport section. Although it is striking that the measured flux seems to be reduced compared to the expectation by just a factor of 2, no theoretical background or influence of the measurement is assumed and the fraction is thought to be coincidental. The only deviation from the ratio of 0.5 is observed at very small column densities where the influence of the offset parameter prevails: because the current offset was determined as the current at the smallest column density, the measured ion flux will inevitably disappear with the column density, just as it is also expected theoretically.

The expected relationship between the ion flux and the column density $\mathcal{N}$ can also be tested by a fit of equation IX.5 to the measurement data. Figure IX.19 shows the fitted curve with a red line, which indicates a rather good agreement between theory and measurement, too. The fit results for the coefficients of the second order

Table IX.2.: **Coefficients of the quadratic fit from figure IX.19 compared to theory**. The fit results in a larger contribution by the linear term b as compared to the quadratic term c than expected. This is attributed to oscillations of the dipole current, which were described in section IX.1.1.2.

Coefficient	Theory	Measurement	Unit
a	0	$(-7.61 \pm 3.11) \cdot 10^{-7}$	1/s
b	$(6.10 \pm 3.26) \cdot 10^{-14}$	$(1.41 \pm 0.30) \cdot 10^{-13}$	m^2/s
c	$(1.83 \pm 0.98) \cdot 10^{-34}$	$(7.02 \pm 0.53) \cdot 10^{-35}$	m^4/s

polynomial are listed in table IX.2 together with the expectations from theory[16]. Obviously, the fit underestimates the quadratic contribution from the column density: the linear term accounts for 75% of the total rate at $1 \cdot 10^{21}$ m^{-2} and makes up even 95% at $6 \cdot 10^{21}$ m^{-2}. This flattening of the measured curve in contrast to the expectation cannot be explained with neutralisation of the inadvertent blocking potentials: the secondary electron density increases with the column density and should allow even more positive ions from the source to enter the DPS unblocked. It seems that oscillations of the dipole current with a period of 1.5 h as described in section IX.1.1.2 distorted the measurement, which took 5 h in total. This systematic effect allows no more detailed interpretation of the measurement.

IX.2.1.3. Conclusion

The current measurement of the dipole electrode in BT1 allowed to confirm the theory of the thermal ion flux in crucial points. Just as expected, the ion flux was found to increase rather linearly with the tritium concentration. Also in agreement with theory, the ion flux dependence on the column density could be described with a second order polynomial. In both cases, the observed magnitude was however only about 50% of the expected rate, which is attributed to the inadvertent blocking of some of the ions between the WGTS and the DPS. Systematic influences on both measurements by oscillations of the background current cannot be excluded, but are not probable either given the good agreement between measurement and expectations.

[16]For these theoretical values and their uncertainties, the average tritium purity during all measurements was calculated and its uncertainty was obtained by quadratic addition.

IX.2.2. Penning discharge ions

Initially, all five ring electrodes along the KATRIN beamtube were set to +200 V in order to safely block all positive ions from the tritium source (see figure IX.20). But when the voltage of some ring electrodes was reduced, the simultaneously observed PS ionisation rate was surprisingly reduced, too. The most reasonable explanation is that ions were created by Penning discharges in the positive ring electrode potentials. However, the observed linear increase of the ion rate with the voltage of the PP5 and PS1 ring electrodes is in contrast to the theoretical expectation from section III.4, which suggests an exponential relationship.

This section will first summarise the measurement results which support the Penning ion hypothesis and then, adopting the hypothesis, show why these Penning discharges are assumed to be not self-sustaining or self-igniting. Finally, the consequences of Penning ions creation in the ring electrodes will be discussed for the KATRIN experiment in general and especially for the choice of the ring electrode voltages.

Effect of ring electrode voltages on the PS ionisation rate In order to investigate the hypothesis of Penning ion creation inside the ring electrodes, the voltage of all ring electrodes was varied while the ionisation rate in the PS was measured with the FPD. Only the left half of the FPD was evaluated and this rate was taken times two, due to the systematic effects which were discussed in section IX.1.4.2. The PS argon pressure inside the PS was set to about $3 \cdot 10^{-8}$ mbar, the PS vessel was at -18.5 kV and the inner electrodes were set to $(-500, -450, -400)$ V (upstream cone electrode, wire electrode, downstream cone electrode).

Most closely, the voltages of the three ring electrodes in BT5, PP5 and the PS1 were investigated: these three can actually block WGTS ions before they reach the PS; and through these flow the beta electrons, which can ignite a Penning discharge according to section III.4. While the voltage of one ring electrodes was changed, the electrodes in BT5 and PP5 were set to at least 10 V in order to safely block tritiated ions from the WGTS; the electrode in PS1 was set to -5 V in order allow an unobstructed measurement with the PS ionisation method[17].

When all three electrodes were set to 10 V, the PS ionisation rate was larger than when at least one of the ring electrodes was at 50 V. This was in contrast to the observation that the rate otherwise increased with increasing ring electrode voltages and pointed to a species of high energetic ions from upstream the DPS ring electrodes. In fact, later measurements confirmed the existence of dissociation ions with an energy spectrum ranging up to 15 eV. For this reason, the measurement points at 10 V will not be considered in the following discussion.

Figure IX.21 shows the results of the measurement:

- **BT5 ring electrode** Even ~ 300 V at the ring electrode in BT5 lead to no increase of the observed ionisation rate. The rate remained stable at about

[17] Penning ions will receive a kinetic energy according to their creation potential. The Penning ions from the DPS electrodes could therefore also have overcome the PS1 electrode if it was set to a positive potential. But because of the negative potential, even ions with smaller energies due to scattering could be observed.

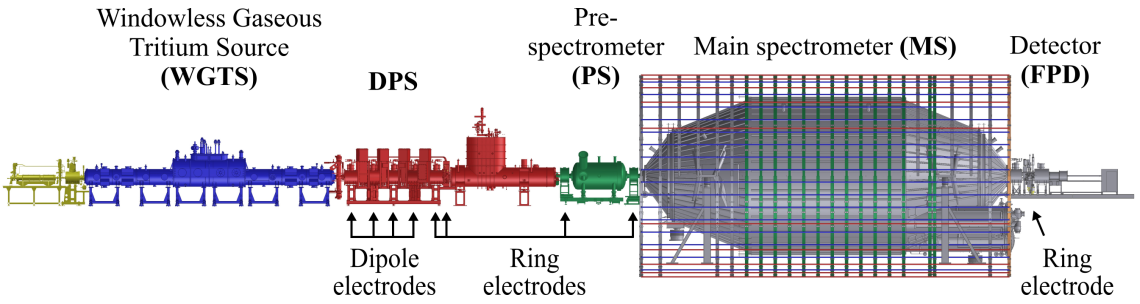

Figure IX.20.: **Position of the ring electrodes in the KATRIN beamtube.** Initially, all ring electrodes were set to +200 V. Due to the discovery of Penning ions from the ring electrodes, the DPS ring electrodes were set to +20 V and the electrodes in the spectrometer to +50 V.

(2.4 ± 0.2) cps, which is even less than when the PP5 or PS1 electrode were at 20 V. Obviously, no Penning discharge occurred in the BT5 electrode.

- **PP5 ring electrode** Between 20 V and 300 V at the BT5 ring electrode, the ionisation rate increased strongly. The linear slope is however in contrast to the exponential increase which was suggested for a Penning discharge in section III.4.2.

- **Both DPS ring electrodes in BT5 and PP5** When the voltage on both DPS electrodes was increased, the ionisation rate increased just as linearly as when only the PP5 electrode voltage was changed, but about 50% steeper. The additional rate cannot be due to the BT5 electrode, because it has shown no Penning discharge at all. Instead, the BT5 electrode is assumed to reflect some of the PP5 Penning ions which are accelerated towards the WGTS. In the WGTS, these ions would lose energy by scattering, but when reflected electrically, they can overcome the PP5 potential[18]. Since the potentials inside the slim ring electrodes are not completely shallow, some of the ions receive not enough energy to overcome the peak potential; therefore, the slope increases by less than a factor two.

- **PS1 ring electrode** The FPD rate increased also linearly with the voltage on the PS1 electrode, which points to a Penning discharge also in this electrode.

Even though the Penning hypothesis cannot explain the observed linear increase of the ion rate with the ring electrode voltage, it allows to explain the different magnitudes of the observed rates with different pressure conditions at the ring electrodes[19]. At the end of the DPS, the pressure cannot be measured experimentally and is only assumed[20] to be on the order of 10^{-10} mbar with large systematic uncertainties. The fact that the Penning ion rate from the PP5 electrode is at least three

[18]The BT5 is slightly large than the PP5 potential at the same set voltage, because the diameter of the BT5 electrode is slightly smaller.

[19]The electrode lengths are similar and the igniting electron flux is identical; the magnetic field strength, which might also affect the Penning ion rate, is of the same magnitude although slightly different between the ring electrodes.

[20]Simulation by Carsten Röttele.

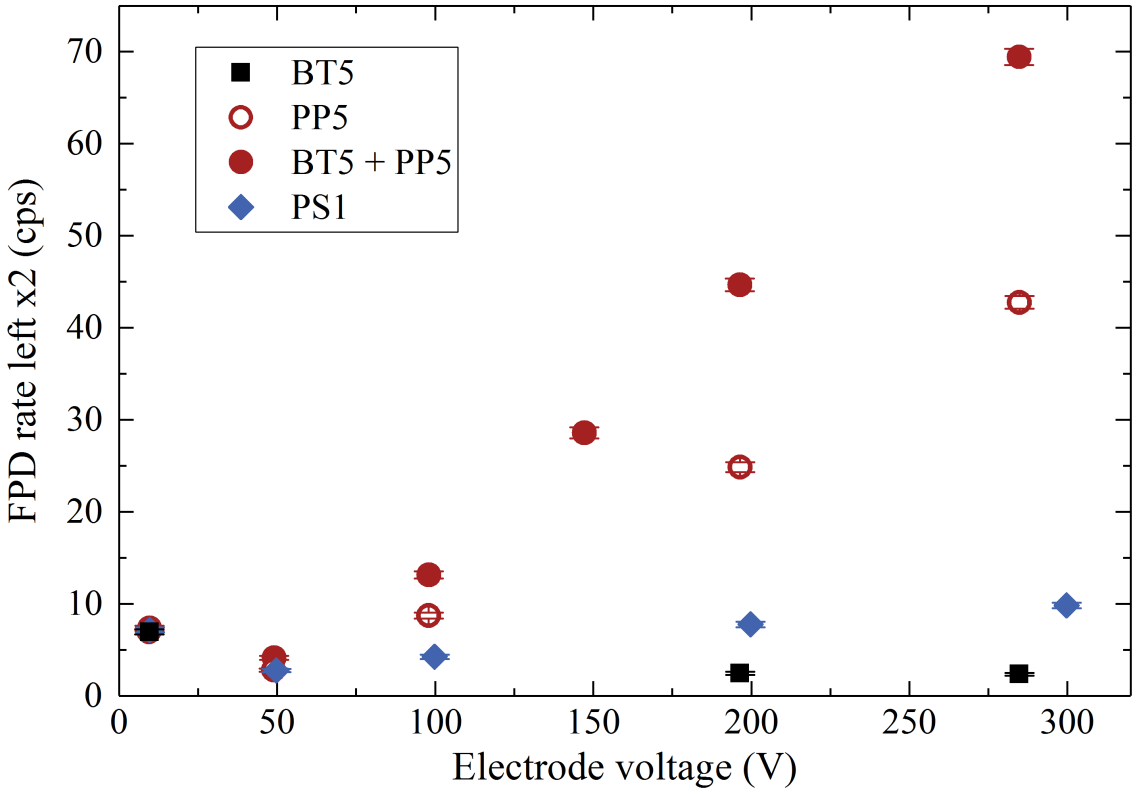

Figure IX.21.: **FPD rate during PS ionisation measurement for various ring electrode voltages.** The increase of the FPD rate at increasing voltages is explained with Penning discharges inside the positive potential of the ring electrodes in PP5 and PS1. No Penning discharge was observed for the ring electrode in BT5. When both DPS electrodes were set to the same voltage, the slope decreased steeper than from the PP5 electrode alone; this is explained with the reflection of Penning ions from the PP5 electrode at the potential of the BT5 electrode with a slightly smaller radius.

orders of magnitude larger than from the BT5 electrode is explained by outgassing from the FT-ICR unit, which is located between the two ring electrodes: while the pressure near the BT5 electrode is reduced by pumping in PP4, there are no actual pumps in PP5, leading to an increased pressure and Penning ion creation. This pressure would however need to be on the order of 10^{-8} mbar, in order to explain why the observed rate was even larger than that of the PS1 electrode.

The PS ionisation rate seemed to be not affected by possible Penning traps in the other two ring electrodes in the spectrometers: when their voltage was reduced from 200 V to 50 V and even to −5 V, no significant change of the FPD rate was observed[21]. Also, no effect on the PS ionisation rate by a potential Penning trap between the PS high voltage and the negative DPS dipole voltages was observed

[21] When changing the voltage from 200 V to 50 V, the FPD rate remained around (3.1 ± 0.3) cps while the DPS electrodes were at 10 V and the PS1 electrode at −5 V. The change from 50 *V* to −5 V in the PS2 electrode and ∼ 0 V in the detector electrode left the rate at (3.1 ± 0.2) cps – here, the DPS electrodes were at 20 V and the PS1 electrode was at 50 V.

when the voltage of the upper dipole electrode in BT4 was reduced[22] from −175 V to −50 V.

Penning discharges in the ring electrodes are not self-sustainable or self-igniting Adopting the hypothesis of Penning ion creation in the PP5 and PS1 ring electrodes, it was investigated if these Penning discharges are self-sustainable and self-igniting. For this test measurement, the ring electrodes in BT5 and PP5 were set to about 300 V and the PS1 electrode was set to −5 V in measure all Penning ions with the PS ionisation method. When the valve V1 between WGTS and DPS was closed, the FPD rate dropped from 89 ± 0.4 cps to 0.26 ± 0.04 cps. Obviously, the Penning discharge did not sustain itself after the igniting beta electron flux was removed. Also when changing the voltages of the DPS ring electrodes down to 20 V and back to 300 V, no reignition of the Penning discharge occurred.

Consequences for the ring electrode voltages Penning ions can harm the KATRIN experiment in two ways:

- In the two DPS electrodes, Penning ions are created from partially tritiated gas. A constant flow of these Penning ions into the PS would correspond to a constant tritium input. In order to prevent this contamination, even though on a small level, the PS1 ring electrode potential should be always two times more positive than the potential of the DPS ring electrodes.
- Penning ions from the PS1 ring electrode cannot be prevented from entering the PS high voltage where they create secondary electrons via ionisation. The secondary electrons do not harm the neutrino mass measurements directly, because they will be rejected by the MS retarding potential. But during test measurements of the residual ion flux into the PS, the Penning ions cannot be distinguished from tritiated ions. Therefore, these Penning ions constrain the upper limit which can be set on the residual flux of tritiated ions into the PS. In consequence, the voltage of the PS1 ring electrode should be set as small as possible during the ion test measurements.

These boundary conditions led to the reduction of the DPS ring electrode voltages to 20 V and of the PS1 electrode to 50 V. Because of a possible small rate of dissociation ions with energies up to 100 eV, the PS1 ring electrode should however be set to +200 V again during future tritium measurements. For a detailed discussion, see section IX.5.

[22] The lower dipole electrode remained at −5 V; the BT3 electrode remained at −85 V on the upper electrode and −5 V on the lower electrode.

IX.2.3. Ions from molecular dissociation

Before the First Tritium measurements, all ions from the WGTS were assumed to be completely thermalised by scattering with the neutral source gas. But the investigation of Penning ions from the previous section revealed an increase of the ion flux around a blocking potential of 10 eV at the ring electrodes. Closer measurements revealed a continuous energy spectrum that increased from 15 eV down to the experimental energy threshold of 4 eV. As explained in section III.3, such ions with eV energies can be created by molecular dissociation of the excited daughter ions from tritium decay and beta electron scattering. The observed ions must have been created in the front part of the WGTS where the gas density was already small enough to let them escape unscattered.

This section will first recall the expected energy ranges and rates of dissociation ions, which were estimated in section III.3.4. Then the measurement conditions are described which were used to investigate the energy spectrum of ions from dissociation: first, the dipole electrode in DPS BT1 was at its nominal negative voltage or grounded; second, this BT1 dipole electrode was at +15 V in monopole mode; and third, the BT2 dipole electrode was set to +15 V in monopole mode instead. Finally, the measurement results will be summarised and their consequences for the ring electrode settings will be discussed.

IX.2.3.1. Expected energy range and rate of dissociation ions

According to the theory from section III.3.4, the dissociation ion rate from the WGTS should be created to roughly the same extent from electron scattering and tritium decay. Above 4 eV, the energy spectrum of the ions from electron scattering has a single dominant peak at about 9 eV and a FWHM of about 5 eV; in case of tritium decay in DT molecules, there will be two peaks with energies between 5 eV and 10 eV and a FWHM of 5 eV and 3.5 eV, respectively. The theory also predicts dissociation ions with energies up to 100 eV at very small rates due to tritium decay.

Ions from the WGTS will however be scattered many times, which leads to a shift of the spectral peak to smaller energies. At the same time, the energy spectrum is distorted from rather a Gaussian distribution towards a Boltzmann spectrum.

The total expected rate of dissociation ions with energies above 4 eV is about $1 \cdot 10^5$ ions/s, considering only unscattered ions from an original region inside the WGTS-F. Scattered ions from upstream the original region might however create considerably more rate. Considering only ions from the DPS BT1 without energy threshold, the total expected ion rate is about $5 \cdot 10^4$ ions/s.

IX.2.3.2. Measurement conditions

In order to measure the integrated ion energy spectrum, the voltage of the ring electrode in BT5 was changed and the rate of ions with energies above the ring electrode potential was measured with the PS ionisation method. The BT5 electrode was not set to less than 4 V in order keep the total ion rate below the threshold of 10^6 ions/s, which had to be observed during the First Tritium measurements. This provided an effective detection threshold of 4 eV.

In the analysis of the ion energy spectrum, it has to be considered that only about a third of the total ion energy can be measured with the ring electrode potential because the ions were emitted isotropically at their creation. Just as any electrostatic filter, the retarding potential of the ring electrode can only measure the longitudinal energy of the charged particle; but in contrast to the MAC-E-filter, there was no angular collimation by a strong decrease of the magnetic field at the location of the ring electrode. The effect from the potential dip in the center of the ring electrode to about 84% of the applied voltage is comparatively small and will be neglected.

During the measurement, the ring electrodes in PP5 and PS1 were set to -5 eV to prevent background from Penning ions which had been previously observed (see section IX.2.2). For some parts of the measurement, the voltages of the dipole electrodes in DPS BT1 and 2 were varied; otherwise the dipole electrodes remained at their nominal negative voltages, but the effect of the dipole drift on the measured rate is assumed to b negligible. The PS vessel was set to -18.5 kV, the inner electrodes were at $(-500, -450, -400)$ V (upstream cone electrode, wire electrode, downstream cone electrode) and the PS pressure was increased with argon to about $3 \cdot 10^{-8}$ mbar.

IX.2.3.3. Dipole electrode in BT1 grounded and at nominal negative voltage

The ion energy spectrum from the entire beamtube could be measured when the dipole electrodes were all at nominal negative voltage or ground, including the dipole electrode in BT1. During most of the measurement, the BT1 dipole electrode was grounded for an attempted measurement of thermal ions with the BT2 dipole electrode. The difference between the two BT1 voltage settings had however no effect on the measurement of the ion energy spectrum, as can be seen from the very good agreement of the black and green measurement points.

Figure IX.22 shows a steeply increasing integrated energy spectrum when approaching the detection threshold of 4 eV from high energies. The monotonically increasing slope indicates no peak of the underlying differential ion energy spectrum. This is in accordance with theoretical expectations: the energy spectrum of the unscattered ions should exhibit peaks between 5 eV and 10 eV, but because only the longitudinal energy of the isotropically emitted ions is observed, these peaks would be shifted to about 3 eV or less.

A comparison of the measurement results with the theoretical expectation from section III.3.4 is difficult, though. According to the preliminary results from the STS IIIa campaign, the ionisation efficiency in the PS is not pressure dependent as assumed in section IX.1.4.1; instead, a constant efficiency of about $\epsilon \approx 10^{-3}$ counts/ion is suggested. Because a total flux of $1 \cdot 10^5$ dissociation ions per second is expected (see table III.7), the resulting rate should be only about 100 cps. However, the rate reached a level of 80 cps already at 4 eV, when the integrated spectrum was still growing increasingly. The constant background from beta electron induced Ar^+ ions seems negligible. Rather, the larger-than-expected rate seems to be actually induced by dissociation ions. One possible reason could be that the original region of dissociation ions inside the WGTS was underestimated; but this could be only resolved with more precise ion scattering simulations in the future.

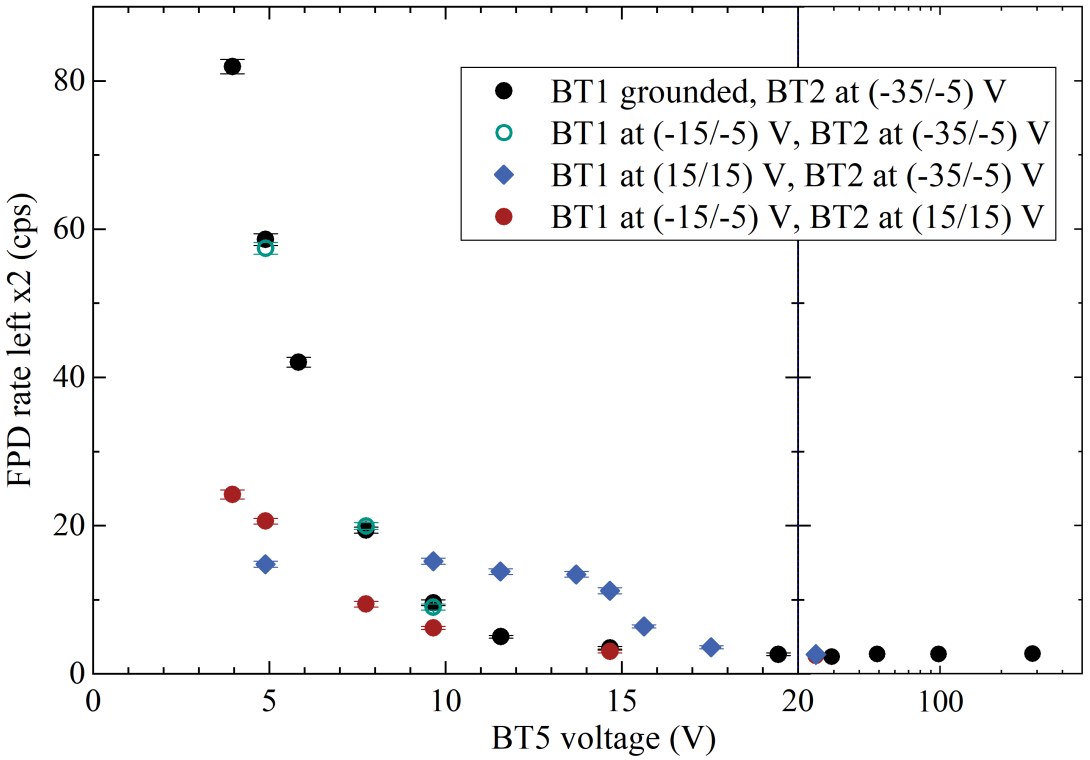

Figure IX.22.: **Energy spectra of ions from molecular dissociation.** The ring electrode in BT5 was used to scan the energy spectrum while the ring electrodes in PP5 and PS1 were set to −5 V. A steep integrated ion spectrum was observed when the dipole electrode in DPS BT1 was either grounded or at a negative potential. When it was set to +15 V in monopole mode, all ions from the WGTS were blocked and the small ion spectrum from BT1 was observed above 15 eV. Setting also the dipole electrode in BT2 to +15 V in monopole mode indicated that it was damaged, because the ions from the WGTS could partially come through.

Above 20 eV, the spectrum becomes flat and no imprint of dissociation ions with energies up to a few 100 eV can be observed (for a close-up see figure C.1). The existence of high energetic ions from tritium decay with energies of a few 100 eV can thus not be confirmed. A dip of the FPD rate at 30 V indicates that the remaining rate of (2.7±0.18) cps might be caused by a small rate of Penning ions from the BT5 ring electrode; but this deviation of a single value could also well be just a statistical fluctuation. Nevertheless, the otherwise stable rate can be used to derive an upper limit on the ion rate between 20 eV and about 300 eV of $(-0{,}04 \pm 0{,}13)$ cps.

IX.2.3.4. Dipole electrode in BT1 at +15 V

In order to measure the full energy spectrum of dissociation ions, the dipole electrode in DPS BT1 was set to about +15 V in monopole mode. This positive potential blocked the large amount of dissociation ions from the WGTS, which prevented measurements below 4 eV previously in order to not violate the safety limit of 10^6 ions/s

into the PS. At the same time, all ions from within the BT1 dipole electrode were accelerated, including the thermal ions which could not have been observed otherwise due to inadvertent ion blocking along the beamline (see section IX.3). The contribution of ions which were created downstream from DPS BT1 were expected to appear as a small spectrum far below 15 eV; because the pressure decreased strongly with each pump port, its contribution to the total rate is assumed to be on the order of 10% (see section III.3.4).

The ion energy spectrum from BT1 is shown by the blue diamonds in figure C.1 and in a close-up in figure IX.23. In the close-up, a dashed blue line indicates the actual voltage at the dipole electrodes, which was 14.67 V. Above this voltage, the integrated ion energy spectrum decreases steeply and below it flattens out. At the offset voltage itself, the rate has not yet reached the plateau of about 14 cps, which must be due to scattering of the thermal ions downstream from DPS BT1. It is hard to tell whether there is an actual, small contribution to the integrated spectrum from ions downstream from the dipole potential; statistical fluctuation are at least responsible for the measurement point at 10 eV, which should not show a higher rate than the measurement point at 5 eV in an integrated spectrum.

The peak of the dissociation ion energy spectrum is expected at about 3 eV. Given the offset voltage of almost 15 V, this peak should show up in the measured spectrum around 18 eV. However, the integrated spectrum shows its steepest increase due to thermal ions just above the offset voltage. There are not enough measurement points around 18 V in order to observe a kink caused by dissociation ions.

Again, the comparison between measurement and theoretical expectation from section III.3.4 is difficult. The analysis will assume an ionisation efficiency of $\epsilon \approx 10^{-3}$ counts/ion, as suggested by the preliminary STS IIIa results. Then the net rate from dissociation of about 12 cps corresponds to $1 \cdot 10^4$ dissociation ions per second. From theoretical side, a slightly larger ion flux of $5 \cdot 10^4$ ions per second was expected (see table III.7). The discrepancy by only a factor of 5 is rather encouraging but needs to be treated cautiously: the column density inside the potential of the BT1 dipole electrode was only extrapolated roughly from simulation results and also the systematic uncertainties of the ionisation efficiency which was used in the conversion are not well known. Also, the ionisation efficiency for this measurement with $3.3 \cdot 10^{-8}$ mbar argon in the PS was never determined correctly and allows no definite interpretation of the measurement result.

IX.2.3.5. Dipole electrode in BT2 at +15 V

Finally, also the dipole electrode in BT2 was set to about +15 V in monopole mode. Again, the dissociation ions from the WGTS were expected to be blocked and so were the ions from DPS BT1. In analogy to the measurement with BT1 at 15 V the observed energy spectrum should have reached a plateau, just at smaller rates due to the smaller gas density in BT2.

Figure IX.22 shows that the energy spectrum reached no plateau and instead exhibited a strong decrease towards smaller ring electrode voltages. Compared to the measurement with all dipole electrodes at either negative voltage or ground, the spectrum has the same shape just at smaller amplitude. And in contrast to

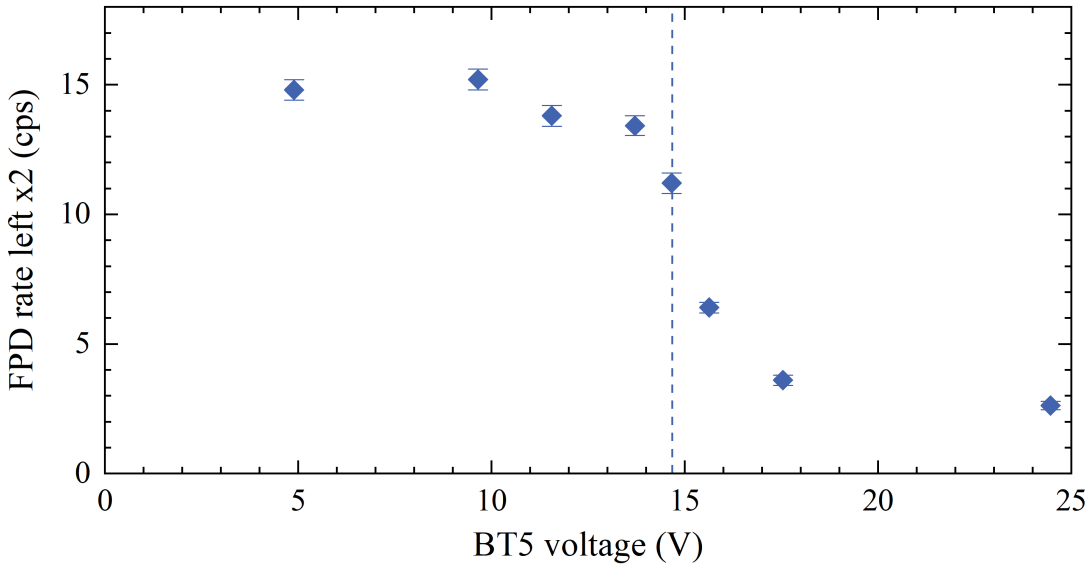

Figure IX.23.: **Close-up of the ion energy spectrum with +14.67 V at the BT1 dipole electrode.** Above the offset voltage (dashed blue line), the integrated ion spectrum decreases steeply although some broadening around the offset voltage can be observed.

the measurement with the BT1 dipole electrode at 15 V, the spectrum exhibits no plateau and reaches even higher FPD rates, which cannot be explained with ion physics; especially scattering should not occur because the ion mean free path grows to 20 m already at the upstream end of the DPS (see figure III.4 in section III.2.3).

The observed spectral shape can only be explained by a malfunction of the voltage supply for the BT2 dipole electrodes. If only part of the voltage which is applied outside the beamtube reaches the electrodes, some fraction of the WGTS spectrum could still be observed. Given the simple layout of the voltage supply, it seems most reasonable that the voltage supply of one of the two electrodes failed completely. In combination with the observation that no thermal ions could be measured with the BT2 dipole electrode at all, the concerned electrode would be most probably the upper electrode with the lobes and current readout.

A specific hardware check after the measurement phase revealed that in fact the voltage supply to the upper electrode of the BT2 dipole was damaged. This explains the the observed ion energy spectrum when the BT2 dipole electrode was intended to be on +15 V in monopole mode. It also shows that no ions could have been measured with the BT2 dipole electrode, which makes it impossible to make a statement about inadvertent blocking of thermal ions between BT1 and BT2 of the DPS from First Tritium data. The damaged voltage supply was however repaired after First Tritium and can be used for further investigations during the upcoming tritium measurements.

IX.2.3.6. Summary and outlook

This section will summarise the measurements at various dipole electrode voltages and compare the results to the theoretical expectations. Then the consequence of

the found dissociation ions for the ring electrode settings will be discussed. Finally, a proposal for future measurements of the dissociation ions will be made.

Measurement summary The ion energy spectrum was measured with the PS ionisation method and the blocking potential of the BT5 ring electrode. A large ion flux was found which can only be explained with dissociation ions which leave the WGTS unscattered. The expected peak of the ion energy spectrum at 3 eV or below could not be observed, however, because the ion flux was assumed to approach the ion flux limit of 10^6 ions/s into the PS already at 4 eV ion energy.

In order to measure the complete ion energy spectrum including thermal ions, the BT1 dipole electrode was set to +15 V in monopole mode. This blocked the large ion flux from the WGTS while at the same time providing the thermal ions from DPS BT1 with an offset voltage to prevent inadvertent blocking. The thermal ion spectrum appeared clearly above the voltage offset, but a peak from the dissociation ion spectrum could not be distinguished.

Also the dipole in BT2 was set to 15 V, which lead to the conclusion that the voltage supply to one of the electrodes was damaged. This was confirmed subsequently in a dedicated hardware check and the damaged was repaired.

Comparison of measured and expected ion rates In general, the calculation of absolute ion flux rates from the measurement is not reliable, because preliminary results from the STS IIIa measurements suggest a rather pressure independent ionisation efficiency of $\epsilon = 10^{-3}$ counts/ion. Nevertheless, the PS argon pressure of $3.3 \cdot 10^{-8}$ mbar might have affected the measurement for example via background mechanisms. This limitation needs to be kept in mind for the following discussion.

The total ion flux from the BT1 dipole at 15 V agreed rather well with the theoretical expectations, although the large uncertainty on the column density inside the BT1 dipole allows no actually firm test of the theory. For the calculation, the dissociation coefficients were however set to 1 because also thermal ions were observed due to the voltage offset by the BT1 dipole; the branching ratios for dissociation after tritium decay and electron scattering could therefore not be tested.

The rate of dissociation ions from the WGTS was larger than expected. Given the good agreement for ions from BT1, the original region of ions which can leave the WGTS unscattered might have been underestimated. Dedicated Monte Carlo simulations will be necessary in order to take account of all facets of ion kinetics in the WGTS (see section III.3.5). Only then can the branching ratios for dissociation of ions from tritium decay be investigated.

Consequences for the ring electrode settings No high energetic tail of the ion energy spectrum could be observed, although the theory of molecular excitation after tritium decay predicts a small flux of ions with kinetic energies of up to 100 eV. Obviously the flux was significantly smaller than $3 \cdot 10^3$ ions/s at 0.5% tritium concentration[23]. However, this leaves the possibility that the flux of high energetic

[23]High energetic ions can be excluded to at least 1 cps, but a tighter limit is not possible because the background might be partially due to Penning ions from the BT5 ring electrode.

ions increases above the limit of 10^4 ions/s at 100% tritium.

Before the upcoming measurements with 100% tritium, the actual flux of high energetic tritium ions should be investigated with another measurement of the ion energy spectrum. Also, the PS1 ring electrode should be set to +200 V in order to block all dissociation ions from the WGTS (see section IX.5 for a detailed discussion).

Proposal for future investigations The investigation of the ion energy spectrum will be much more difficult at 100% tritium: while the amplitude of the spectrum increases by a factor 200 and emphasises its features, the ion flux limit will decrease to 10^4 ions/s. In order to be able to measure the full ion energy spectrum, the dipole electrodes in DPS BT3 or even DPS BT4 can be set to an offset voltage. Conversely, the relative magnitude of the ion spectra in the dipole electrodes can even be used for the most precise measurement of the gas density throughout the DPS.

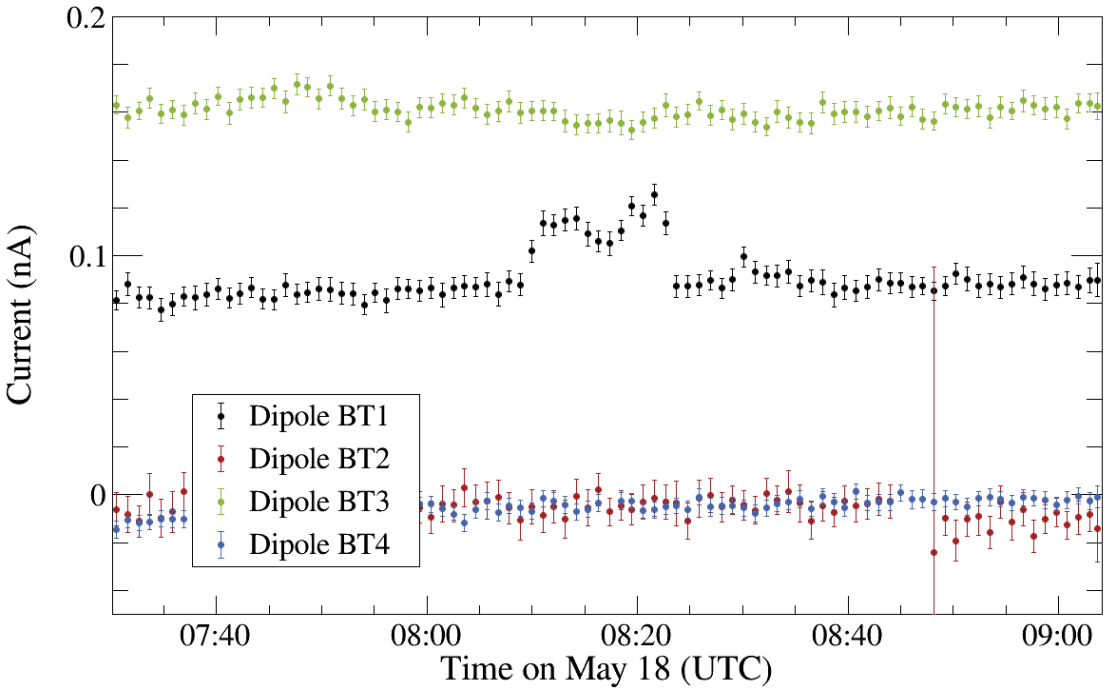

Figure IX.24.: **DPS dipole currents during the very first injection of tritium into the WGTS.** 10% of the expected ion flux are observed in BT1 from 8:10 h on. Actually, ion creation should have started even before that: tritium was injected into the inner loop at 7:48 h and LARA reported a significant tritium concentration around 8:00 h; the Faraday cup might have seen a beta electron flux since 7:51. While this delay of the ion flux might be attributed to the test conditions of the first tritium injection, another observation is unambiguous: The ions vanished promptly when the valve V1 between WGTS and DPS was closed at 08:22 h, but they did not reappear when the valve was opened again at 08:28 h. Half an hour later at 8:59 h, V1 was closed another time but no change of the BT1 current can be seen. Later that day, 20% of the expected current could be observed when the negative voltage of the BT1 dipole was increased to at least $(-80/-50)$ V. On the second day of the Very First Tritium campaign and throughout the First Tritium campaign, the ion flux was always around 50% of the expected level. In this graph, the displayed currents are averaged over 150 measurements, corresponding to about 1 min at the usual 400 ms measurement interval.

IX.3. Inadvertent ion blocking and neutralisation of the blocking potentials

The ion flux from the DPS was observed with the DPS dipole electrodes to be about half of the expected flux throughout the whole First Tritium campaign. Inadvertent positive blocking potentials from work function differences along the beamline are made responsible for this.

All of the observed ions were detected with the dipole electrode in BT1 whereas no ion flux was ever observed with the other dipole electrodes. This is attributed to neutralisation of the inadvertent blocking potentials by secondary electrons, which are abundant in the WGTS upstream from the BT1 dipole electrode but cannot get across the negative potential of the BT1 dipole electrode.

The most striking observations regarding the dynamics of the blocking and neutralisation processes was made during the very first tritium measurements on the first day of the Very First Tritium campaign, which will be summarised in section IX.3.1. Afterwards, the actual effects of inadvertent blocking and neutralisation will be discussed in section IX.3.2 for the cases of both positive ions and secondary electrons. Finally, the consequences of the observed inadvertent ion blocking will be explained in section IX.3.3.

IX.3.1. Ion flux from the WGTS during the Very First Tritium measurements

The ion flux from the WGTS was always found to be roughly half of the expected flux during most of the measurements, except on the first day of the Very First Tritium campaign. On this actually very first measurement day with tritium in the KATRIN experiment, the ion flux reached only up to 20% of the expected value and appeared only sometimes and after some delay.

Figure IX.24 shows the current on the BT1 dipole electrode during the first injection of tritiated gas into the WGTS. When tritium was injected into the KATRIN inner loop for the very first time, an ion flux was observed on the dipole electrode in BT1 but with a delay of about 20 min. It is however not possible to interpret this observation due to the test conditions and the various time delays reported from other detectors: the Faraday cup current seemed to detect beta electron about 2 min after the injection and the LARA measurements detected tritium only after about 10 min.

The observed delay suggests that similar effects might occur after each interruption of the stable measurement conditions by closing V1. However, no such delay was discovered within the measurement resolution of about 1 s at any occasion other than on the very first tritium measurement day. Because when V1 was closed and opened again right after the first measurement of WGTS ions, they did not reappear within 30 min. Longer observation of the ion current was not possible due to the many changes at the source parameters.

While the ions had reached about 10% of the expected flux at their first appearance and completely disappeared afterwards, it was possible to observe about 20% of the expected ion flux later this day. For this measurement, the dipole electrode in BT1

needed to be set to $(-80/-50)$ V and $(-100/-70)$ V (upper / lower electrode), respectively, and the valve V1 was closed and opened for an on/off measurement. From the second measurement day of Very First Tritium and throughout the whole First Tritium campaign, the observed ion flux reached however significantly larger values, all roughly about half of the expected flux.

The gradual increase of the observed ion flux during the Very First Tritium campaign might be due to the neutralisation of work function differences by accumulations of secondary electrons. But then the same increase would have been expected at the beginning of the First Tritium campaign; this was however not observed, although the magnetic field of the source and transport section was ramped down and up again during the 16 days between the two measurement phases. An alternative explanation could be the work functions themselves changed with the new measurement conditions, for example by adsorption of tritium.

IX.3.2. Inadvertent blocking and possible neutralisation effects

This section will discuss the observations which support the theory of inadvertent ion blocking potentials between the WGTS and DPS, as well as hints to the neutralisation of these blocking potentials. Besides the ions, also secondary electrons are assumed to have been blocked inadvertently, as will be discussed at the end.

Inadvertent ion blocking Only about half of the expected ion flux from the WGTS was observed with the current measurement on the DPS dipole electrodes, as reported for example for thermal ions in sections IX.2.1.1 and IX.2.1.2. All of these observations were made only with the dipole electrode in BT1; no current was measured with the other dipole electrodes[24] even when V1 was closed after more than 5 days of continuous measurement conditions with open V1, stable column density and tritium purity as shown by figure IX.25.

The observed inadvertent partial or complete ion blocking is attributed to work function differences along the beamtube according to section III.6.2. Work function differences had already been given as explanation for the inadvertent ion blocking during First Light (see section VIII.6); there, the blocking could be reduced in accord with theory by supplying the ions an energy offset via an electric potential in the ELIOTT ion source. During First tritium, a similar measurement was carried out by applying an offset voltage with the dipole electrode in BT1 (see section IX.2.3.4). In this case, the theoretical estimate for the flux of dissociation plus thermal ions agreed very well with the observation, but at large uncertainties which do not allow to test the theory up to a factor of 1/2.

The rather stable observation of the expected ion flux during most of the measurement campaign suggests that a factor 1/2 might not have been considered in the theory, but no flaw could be discovered so far. Therefore, all of the observed discrepancy is attributed to the inadvertent blocking by work function differences.

[24] As it turned out after the measurements, the connection between the dipole electrode in BT2 and its amperemeter was damaged, so that no ions could be measured for technical reasons. The dipole electrodes in BT3 and BT4 should however been able to detect the signal of an ion flux.

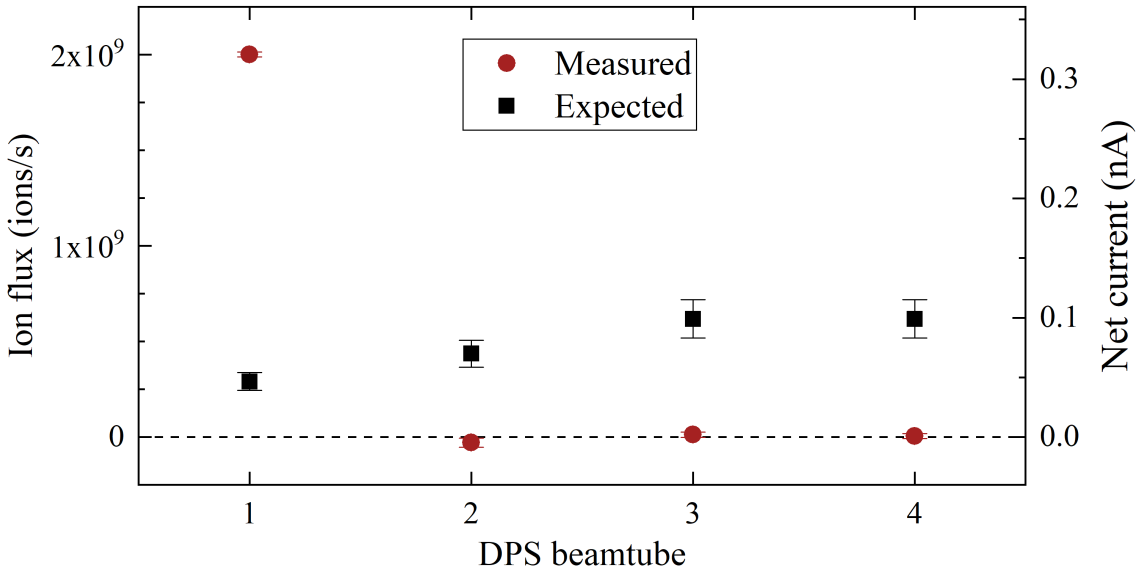

Figure IX.25.: **Ion induced currents at the DPS dipole electrodes.** The ion current was measured when the valve V1 between WGTS and DPS was closed after more than 5 days of stable source conditions (compare figures IX.2 and IX.5). Black squares mark the expected currents according to the voltages of the individual dipole electrodes (see section VII.2.2). However, no ions could ever be measured with the dipole electrodes in DPS BT2, BT3 and BT4; instead, the ion flux in BT1 amounted only to 50% of the total expected flux. Both observations are attributed to inadvertent ion blocking between the WGTS and the DPS.

Neutralisation of positive blocking potentials The slow appearance of ions at the BT1 dipole electrode during the very first tritium measurements can be explained by two different mechanisms: either tritium adsorption on the beamtube walls changed the work functions and removed the inadvertent blocking potentials from work function differences; or slow secondary electrons and negative ions accumulated inside the positive potentials after being trapped by scattering on neutral gas and neutralised them as explained in section III.6.3. The latter is more reasonable in order to explain the efficient neutralisation of all of the positive blocking potentials.

The neutralisation of positive blocking potentials by secondary electrons also allows to explain why ions were measured with the dipole electrode in BT1, but not the other dipole electrodes further downstream: the abundance of secondary electrons from the WGTS was blocked by the negative potential of the first dipole electrode in DPS BT1, as illustrated in figure IX.26. Upstream from BT1, the abundance of secondary electrons could neutralise the blocking potentials easily; downstream from BT1, the significantly smaller gas density decreased the creation rate of secondary electrons and their probability for scattering on residual gas.

In order to test if neutralisation can also occur downstream from DPS BT1, the BT1 dipole electrode was grounded for 7 hours so that both ions and secondary electrons could spread from the WGTS to the DPS BT2. As it turned out after

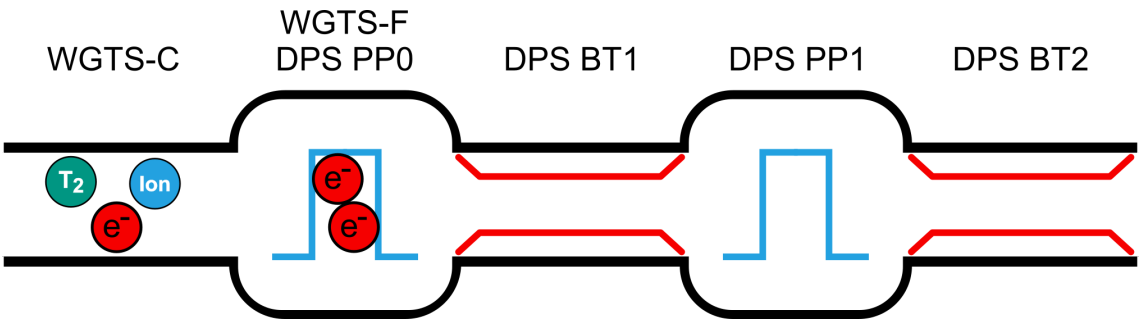

Figure IX.26.: **Neutralisation of inadvertent blocking potentials.** Ions and secondary electrons are created in the center of the WGTS (WGTS-C). Different work functions of different beam tube materials in the WGTS and the DPS create inadvertent blocking potentials. Ions are inadvertently blocked by the positive potentials until secondary electrons accumulate in the potential wells and neutralise them. But the negative voltage of the BT1 dipole electrode blocks the secondary electrons from the WGTS-C: therefore, neutralisation downstream from DPS BT1 was slowed down during First Tritium and ions could only be observed with the BT1 dipole electrode.

the measurements, the voltage supply to the upper electrode of the dipole in BT2 was damaged and did not allow to measure any ions at all. However, no ions were observed on the dipole electrodes in BT3 and BT4 either – this might have been due to the blocking of secondary electrons by the potential of the floating upper electrode and the −5 V on the undamaged lower electrode of the dipole in BT2. Under these conditions, the neutralisation theory can be neither confirmed nor rejected.

Inadvertent blocking of secondary electrons Not only the ions, also the low energetic secondary electrons are blocked between the WGTS and DPS BT1. For this result, the secondary electron flux was measured with a positive dipole voltage in DPS BT1. Within 20 min of the electron flux measurement, also the ion flux was measured for comparison at the same column density and tritium concentration.

The measurement was carried out by first measuring the ion flux with nominal dipole voltage when valve V1 was closed. Then the BT1 dipole voltage was inverted to +15 V on the upper and +5 V on the lower electrode and the electron flux was measured when opening V1 again about 10 min later. Signal and background measurement took between roughly 2 min and 4 min. The signal can be interpreted to be caused by secondary electrons, because the fast beta electrons are hardly affected by the drift and the contribution by negative ions is negligible. During these measurements, the other dipole electrodes were at their nominal negative dipole voltage. From the column density and tritium concentration during the measurement phases, the expected ion and electron fluxes were calculated.

According to the results in table IX.3, about two third of the secondary electrons can reach the dipole electrode in DPS BT1. The measured ion flux was slightly less than half of the expected, in accordance with previous observations. Obviously the secondary electrons are also blocked inadvertently, but to a smaller extent than the

ions: whereas the theoretically expected ratio of ion and electrons flux should be $16/15 = 107\%$, the observed ratio is only about 70%.

IX.3.3. Consequences of inadvertent ion blocking

If in fact only 50% of the created ions can leave the WGTS, the other 50% will accumulate. In the end, all of the accumulated ions will be neutralised by recombination with secondary electrons, but depending on their lifetime they might create a large positive ion density. Most probably, the source plasma will compensate the space charge to some extent by an equivalently large density of secondary electrons. The overall increased plasma density might however lead to plasma instabilities which in turn can affect the neutrino mass measurements. Also, if the positive space charge is not neutralised completely, it can distort the source plasma potential and thereby the observed tritium beta spectrum.

The actual plasma density along the WGTS cannot be measured experimentally but need to be simulated instead with dedicated plasma simulations. What can be investigated experimentally is the effect of the WGTS plasma on the beta electrons, for example with the e-gun. Other consequences of plasma effects were discussed in section V.5 and the limited ways to monitor them were discussed in section VII.5.

It has to be kept in mind that the presented investigations concern only the detector side of the WGTS. Similar inadvertent blocking and neutralisation effects might occur at the rear side, which can also affect the plasma density and the source potential.

Table IX.3.: **Measured and expected fluxes of ions and secondary electrons.** The ions and electrons were measured with negative and positive BT1 dipole voltages, respectively. Both fluxes are much smaller than expected due to inadvertent positive and negative blocking potentials. Only statistical uncertainties are stated, but comparison with figure IX.25 indicates that they clearly underestimate systematic effects. The statistical uncertainties on the expected fluxes are dominated by the tritium concentration; not considered are the systematic uncertainties of the Monte Carlo simulations, on the cross section for electron impact ionisation and on the column density of about 5%.

	Ion flux (ions/s)	Electron flux (el./s)	Ions / electrons
Measured	$(1.62 \pm 0.02) \cdot 10^9$	$(2.37 \pm 0.02) \cdot 10^9$	$(69 \pm 1)\%$
Expected	$(3.69 \pm 0.56) \cdot 10^9$	$(3.50 \pm 0.57) \cdot 10^9$	$(106 \pm 24)\%$
Measured / expected	$(44 \pm 7)\%$	$(68 \pm 11)\%$	

IX.4. Upper limit on the ion flux into the PS

This section will report the safe operation of the KATRIN beamline with regard to tritium ions: an upper limit on the ion flux into the PS at the aspired level of $1 \cdot 10^4$ ions/s could be derived with the ionisation method in the PS. This limit satisfies the background requirements for the neutrino mass operation with $> 95\%$ tritium concentration in the source (see section V.3). Since the tritium concentration during First Tritium was only about 0.5%, a 200 times less restrictive constraint of about 10^6 ions/s into the PS was actually required for the safe operation of the KATRIN beamline during this measurement campaign.

The ion flux through the DPS was below the constraint from radiation protection of $2 \cdot 10^8$ ions/s (see section V.1): this could be measured already with the dipole electrodes[25] in DPS BT3 and BT4. However, the systematic drifts of the dipole current measurement did not allow to monitor this flux continuously (see section IX.1.1.2). Further, tritiated ions were found to be created in the DPS ring electrodes and thus downstream from the dipole electrodes. In order to verify that the actual residual ion flux into the PS is actually on the level of $1 \cdot 10^4$ ions/s, detectors inside the PS or right in front of it are required.

The following section will first state the results of the actual observable, the background in the MS, which was measured before, during and after the tritium campaigns. However, these measurements allow no statement about the MS background to a level of 1 mcps; therefore, the results of the Faraday cup, the PS current method and the PS ionisation method will be discussed subsequently in sections IX.4.2, IX.4.3 and IX.4.4. The strictest limits on the ion flux into the PS can be derived with the PS current and the PS ionisation method, as will be discussed in section IX.4.5; this last section also gives an outlook to measurements of the upper limit during future tritium campaigns.

[25] The minimal detectable ion flux of the dipole electrodes is $3 \cdot 10^7$ ions/s at 3σ significance (see section IX.1.1.3). At the same time, the ion detection efficiency of the dipole electrodes in DPS BT3 and BT4 at their nominal voltage is only 17% (see section VII.2.2).

IX.4.1. MS background over the course of the tritium campaigns

The flux limit of 10^4 ions/s into the PS was derived from a maximum background of 1 mcps which can be tolerated due to tritium activity in the MS during the neutrino mass measurements. Measuring the MS background is therefore the most fundamental observable in order to assess a possible influence of tritium ions on the spectrometers. During (Very) First Tritium however, the 200 times smaller tritium concentration limited the sensitivity of the MS background to the residual ion flux into the PS significantly.

The MS background was measured before, during and after the (Very) First Tritium campaigns. During the measurements with closed valve V4 between CPS and PS, the PS was mostly at 16.4 kV and the MS usually at 18.6 keV – about 40 eV below the end point of the tritium beta spectrum. However, the analysis[26] in the energy range of (14 . . . 32) keV showed no influence of the MS retarding voltage on the background rate.

Over the course of the tritium campaigns, a sizeable although ambiguous increase of the MS background rate was observed:

- Before the start of the Very First Tritium campaign, the MS background was measured for about 20 h over night from May 16 to May 17. A rate of 410.8 ± 2.4 mcps was found.

- The Very First Tritium measurements took place on May 18 and May 19. Valve V4 between CPS and PS was only open during tritium operation on May 19 for about 10 h.

- Between the tritium campaigns, the MS background was measured over the course of 64 hours from May 25 to May 28. The background rate was 428.8 ± 1.4 mcps.

- The First Tritium campaign lasted for 2 weeks from June 5 to June 18. During the first two nights, the valve V4 remained still closed. This was used to measure the MS background in the second night between June 6 to June 7 for about 9 h, with a result rate of 419.4 ± 3.6 mcps. At this measurement, the MS retarding potential was 19 kV.

- After First Tritium, the MS background was found on June 19 and 20 to be 424.9 ± 2.5 mcps. The 21 h long measurement scanned the MS background down to 2 kV below the endpoint of the tritium spectrum.

Apparently, the MS background rose during the measurements with open valve V4 between CPS and PS and decreased between the campaigns. It is strange however, that the background increased by 18 mcps over the Very First Tritium campaign, which included only 10 h of tritium operation with open V4, whereas the First Tritium campaign with almost two weeks of continuous tritium operation led only to an increase by 5.5 mcps. Also, the background after First Tritium was about 4 mcps smaller than after Very First Tritium.

[26] Analysis carried out by Anna Pollithy, TUM.

Judging from the measurement uncertainties, the increase of the background during Very First Tritium is significant by about 7 σ and the increase during First Tritium by about 2 σ. This excludes statistical fluctuations as the cause. Systematic effects of the intrinsic MS background are however more difficult to exclude. At least a slow drift of the background rate does not seem to be responsible because the background was always found to be stable during all measurements, including the 64 hour measurement between the campaigns.

These observations indicate that the tritium campaigns did have an effect on the MS background. But since the increase was not proportional to the exposure time with open valve V4, it does not seem likely that the cause was tritium or any other radioactive substance from the source and transport section.

Even though the background increase was probably not due to tritium, it still constitutes an upper limit on the possible continuous ion flux into the PS during the two measurement campaigns: the 18 mcps over Very First Tritium correspond to about $1.8 \cdot 10^8$ ions/s, and the 5.5 mcps during First Tritium correspond to $5.5 \cdot 10^7$ ions/s. Such a high ion rate can however be excluded at least during most of the First Tritium campaign due to the automatic trigger of the PS current measurement, which was set to $5 \cdot 10^7$ ions/s as explained in section IX.4.3.

IX.4.2. Faraday cup measurements during Very First Tritium

The Faraday cup was used to measure the residual ion flux downstream from the DPS ring electrodes during the Very First Tritium campaign before the valve V4 was opened and the more sensitive PS current and PS ionisation methods could be used. However, no reasonable upper limit on the ion flux can be stated from the Faraday cup measurements due to the statistical uncertainty of the analysis method and the systematic uncertainty of the detector.

The ion flux was measured with the Faraday cup six times on the first day of Very First Tritium and two times at the beginning of the second. All eight measurement results lay within the detection limit of the amperemeter of ± 3 fA, except for one value at 3.10 ± 106.7 fA. The large uncertainty is due to the analysis method, which uses one slope for two fit intervals (see section IX.1.2); all of the uncertainties are in fact on the order of ~ 50 fA.

A large systematic uncertainty arises from the fact that the Faraday cup measured a 50 times smaller electron flux than expected (see section IX.1.6). If this was due to charging of the floating shield by beta electrons as speculated in section IX.1.2, the ion measurement would not have been affected seriously. However, the actual reason remains unknown and the significance of the Faraday cup results on the ion flux is therefore strongly impaired.

IX.4.3. Continuous monitoring with the PS cone electrode

The PS current measurement acquired data during the whole course of the First Tritium campaign. However, the special test conditions during much of the measurement time make it difficult to discuss the current measurements. Especially, the frequent changes of the PS voltage settings blinded the current measurement.

Nevertheless, the PS current measurement allows to derive an upper limit on the ion flux into the PS over the longest continuous time of all detectors. First, the trigger threshold for the automatic measurement interruption can be used to state a limit for 11 days of the two weeks measurement phase; then the actual measurement values can be used to derive a rather firm limit from the accumulated statistics of 3.5 measurement days.

Trigger threshold The PS current measurement will automatically trigger an interruption of the KATRIN measurements if the measured current exceeds a specified threshold (see section IX.1.3.1) for three measurements in a row. During the first two days of the First Tritium campaign, the basic detection capabilities of the cone electrode was tested for example with the beta electron measurement described in section IX.1.6. After this proof-of-principle, the automatic trigger was enabled for the longest part of the First Tritium campaign, from June 7 to its end on Jun 18.

During the whole tritium measurements, no closure of V4 was triggered. Therefore, the trigger threshold of 5 pA allows to state an upper limit on the ion flux into the PS for this time from of about $2 \cdot 10^8$ ions/s. Charge multiplication by secondary electron emission might further decrease this limit by about one order of magnitude, according to preliminary results of the STS IIIa measurements from October 2018. The ion detection efficiency is assumed to be about 20% for the PS high voltage of -16 kV, which used during most of the campaign (see ion detection efficiency in section IV.1).

An ion flux of $2 \cdot 10^8$ ions/s into the PS corresponds just to the constraint from radiation protectoin (see section V.1). With regard to the MS background, however, it would create 1.8 cps (see section IV.3.4). A stricter upper limit on the ion flux into the PS can be placed with a long-term measurement of the PS current.

Long term limit during scans of the beta spectrum The strictest continuous limit on the ion flux into the PS can be derived with the PS current measurement over a long period during the First Tritium campaign like the scans of the tritium beta spectrum. However, not all of the scans were $\gg 2$ hours long, which is required in order to remove systematic effects (see section IX.1.3.2). Also, the various settings of the PS vessel voltage along with other beamline conditions make it difficult to discuss the measurement results. Only the longest scan of the beta spectrum will therefore be discussed as an example.

Figure IX.11 in section IX.1.3.2 shows the PS current during a scan of the beta spectrum over 3.5 days. Each data point was averaged over 2 hours in order to remove the systematic effect from thermally induced oscillations with 2 h period and 50 fA amplitude (see section IX.1.3.2). In the result, the points are firmly distributed around the 3 fA minimum systematic uncertainty of the amperemeter;

the statistical uncertanity is negligible, as indicated by the statistical mean current of -0.05 ± 0.62 fA. The temperature induced current oscillations are therefore not considered to limit the sensitivity of the PS current measurement for measurement times much larger than 2 hours.

The time series plot shows no observable ion flux into the PS over the whole 3.5 measurement days[27]. In order to derive a numerical value for an upper limit, the systematic limitations of the measurement method have to be observed: the detection limit of the amperemeter is 3 fA, and the ion detection efficiency of the downstream cone electrode is about 20%. This leads to a systematics-limited upper limit on the ion flux into the PS of about:

$$\mathrm{UL}^{\mathrm{PScurrent}} = 1 \cdot 10^5 \text{ ions/s}. \tag{IX.6}$$

Such a small ion flux into the PS would actually create about 1 mcps of background and thus complies with the requirements of the KATRIN design report (see section V.2). However, this conservative analysis does not yet take into account the preliminary results of a calibration measurement during the STS IIIa campaign in October 2018: each impacting ion ejects on average roughly 10 more secondary electrons from the electrode surface. The resulting charge amplification would have had allowed to monitor even the aspired limit of $1 \cdot 10^4$ ions/s.

[27] An ion flux is expected to lead a constant or even increasing PS current.

IX.4.4. PS argon ionisation measurement

The strictest upper limit on the residual ion flux into the PS could be determined with the PS ionisation method. All measurements of the signal with open valve V4 between CPS and PS and of the intrinsic background with closed V4 were carried out within about 4 hours in order to prevent effects of a background drift over time. The PS vessel was set to −18.5 kV and a slide potential setting was applied, using −500 V on the upstream cone electrode, −450 V on the wire electrodes and −400 V on the downstream cone electrode.

The ionisation measurement was carried out at various argon pressures in order to distinguish an incoming ion flux from pressure dependent backgrounds. According to section IX.1.4.1, the flux of Ar^+ ions should increase linearly with the argon pressure[28]; the ionisation rate due to the Ar^+ background should therefore scale quadratically with the argon pressure. In contrast, an ion flux from outside the PS was assumed to be independent from the argon pressure – only its ionisation rate should increase linearly.

The lower part of figure IX.27 shows the FPD rates which were measured with the ionisation method. Mostly, the measurements with open V4 lie slightly above the equivalent FPD rate of an ion flux into the PS of $1 \cdot 10^4$ ions/s. Below 10^{-9} mbar, the signal cannot be distinguished from the fluctuating intrinsic background. At $4 \cdot 10^{-11}$ mbar especially, both signal and background are strongly increased – at such a small pressure, an ion flux could however not have created such a large FPD rate and both values are attributed to background fluctuations. The further analysis will therefore only consider the signal measurements above 10^{-9} mbar.

In order to calculate the upper limit on the ion flux into the PS, the intrinsic background of the PS and the background from Ar^+ ions needed to be subtracted. While the argon pressure during measurements with open and closed V4 was usually different, the closest background measurement in terms of pressure was always subtracted from the signal measurements; the background made up about 60% of the total rate at $1 \cdot 10^{-9}$ mbar, about 30% at $2 \cdot 10^{-9}$ mbar and about 10% at the highest pressure of $2 \cdot 10^{-8}$ mbar. Then the net rate was converted into an ion flux with the ionisation efficiency from equation IX.1 based on the argon pressure during the individual measurement. Finally, the expected Ar^+ ion rate was subtracted, too.

The residual ion rates after consideration of all known backgrounds are displayed in the upper part of figure IX.27. An increase of the residual rate with the argon pressure can be observed, even though the pressure dependence of the ionisation method has already been considered via the ionisation efficiency. The reason for this behaviour will be discussed below.

But no matter its cause, the residual rate restricts the upper limit on the ion flux into the PS. Taking the average[29] of the three measurement points leads to a

[28] Preliminary results of the STS IIIa commissioning measurements actually indicate a pressure-independent and larger-than-expected ionisation efficiency. The consequences for the measurement of the upper limit will be discussed below.

[29] The small sample size of $n = 3$ was accounted for by multiplying the uncertainty from Gaussian error propagation with $t(3-1) = 1.32$ according to Student's distribution [GUM95].

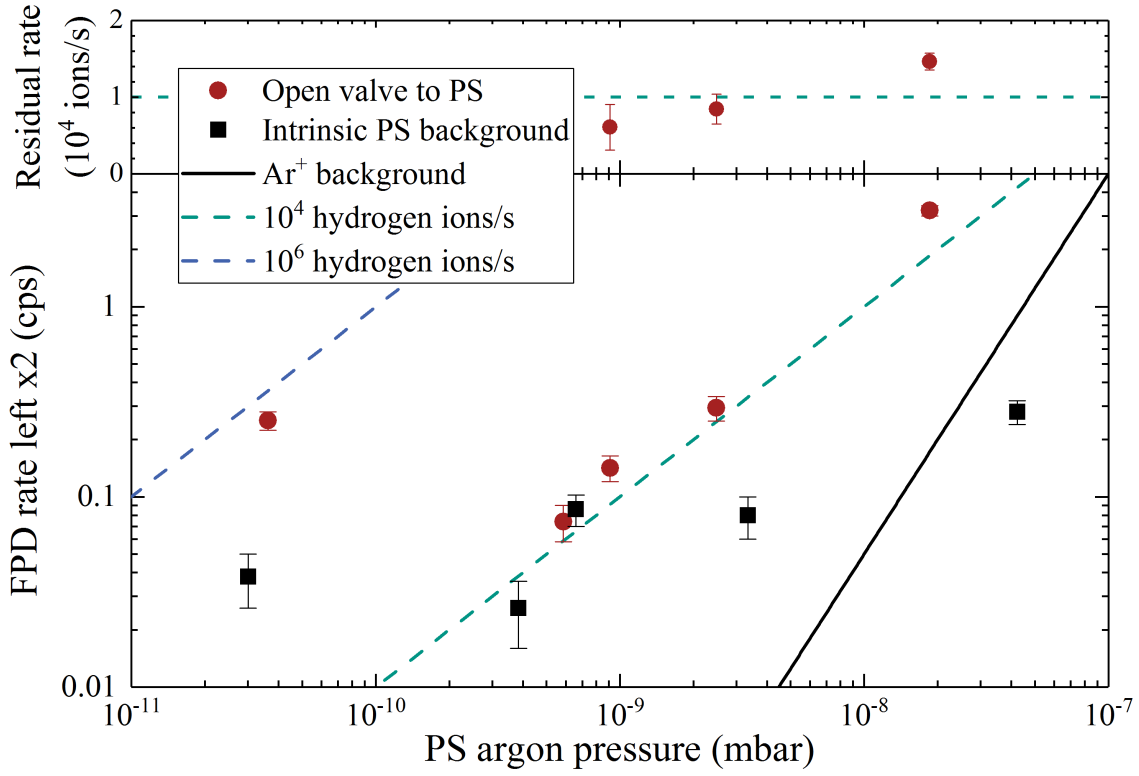

Figure IX.27.: **Measurement of the ion flux into the PS with the ionisation method.** Only the left side of the FPD rate was evaluated and taken times two due to the hotspot, which was described in section IX.1.4.2. The measurement was performed at various argon pressures inside the PS in order to distinguish the Ar^+ ion flux and a flux of ions from outside the PS; during First Tritium, it was assumed that the ion detection efficiency increases linearly with pressure whereas the background from Ar^+ ions would increase quadratically. For this reason, the intrinsic PS background and the assumed Ar^+ ion rate were subtracted from the signal rate. Finally, the residual rate was found to lie around the aspired level of $1 \cdot 10^4$ ions/s into the PS as shown in the upper part.

systematics-limited upper limit slightly below the aspired threshold of $1 \cdot 10^4$ ions/s:

$$\mathrm{UL}^{\mathrm{PSionisation}} = (9.8 \pm 1.6) \cdot 10^3 \text{ ions/s}. \tag{IX.7}$$

The uncertainty on this value comprises only the statistical uncertainties on the signal and background measurements which were propagated according to Gaussian error propagation. Systematic uncertainties are not displayed in figure IX.27: the 5% uncertainty on the PS pressure calibration is much smaller than the presumed uncertainty on the ionisation efficiency, which might be easily on the order of a factor 2 or higher. But even when taking into account all of these systematic uncertainties, the ion flux into the PS is clearly below $1 \cdot 10^5$ ions/s; this ion flux would create only 1 mcps of background and thus already complies with the KATRIN design report, although not within the safety margin of one order of magnitude (see section V.2).

Preliminary results of the STS IIIa commissioning measurements indicate however a pressure-independent and larger-than-expected ionisation efficiency in the PS. Consequently, also the Ar^+ rate is larger than expected and increases linearly with the argon pressure; this explains the pressure dependence of the residual rate[30] in the upper part of figure IX.27. The derived constraint on the ion flux into the PS of $1 \cdot 10^4$ ions/s can be considered as a conservative upper limit. A reevaluation of the measurement would require the final results of the STS IIIa measurements, which were not available until end of October 2018.

[30] An extensive discussion of the residual rate, based on the knowledge before the STS IIIa measurements, can be found in appendix C.

IX.4.5. Conclusion

The ionisation measurements with argon in the PS have put a limit of $(9.8 \pm 1.5) \cdot 10^3$ ions/s on the ion flux into the PS (see section IX.4.4). With this result, is was possible to show that the tritium ion flux into the PS is just below the aspired limit of $1 \cdot 10^4$ ions/s, which has to hold during the neutrino mass measurements. At the same time, this result is clearly below the limit of about 10^6 ions/s for the (Very) First Tritium campaigns. Preliminary results of the STS IIIa measurements indicate, however, that the measurement was dominated by background from Ar^+ ions; consequently, the result can be seen as a conservative limit.

The PS current measurement demonstrated its capability to exclude reliably and continuously ion fluxes down to about $1 \cdot 10^5$ ions/s into the PS during the neutrino mass measurements (see section IX.4.3). Such an ion flux is about one order of magnitude above the conservative constraint of $1 \cdot 10^4$ ions/s, but would create only about the aspired level of 1 mcps background by tritium activity in the MS. For comparison: the MS background was observed to fluctuate by about 5 mcps over the course of the (Very) First Tritium campaigns (see section IX.4.1).

The radiation safety limit of $2 \cdot 10^8$ ions/s into the PS is also monitored by the PS current measurement (see section IX.4.3): if the current surpasses the corresponding current threshold of 5 pA, the valve V4 between CPS and PS will be closed automatically.

Future measurements The aspired upper limit on the tritium ion flux of $1 \cdot 10^4$ ions/s into the PS could just barely be achieved with the PS ionisation method (see section IX.4.4); a residual rate of unknown origin limited the measurement, which was based on the assumption of a pressure-dependent ionisation efficiency. It was only the STS IIIa campaign from September to October 2018, which yielded a pressure-independent and larger-than-expected ionisation efficiency. The residual rate can thus be explained with Ar^+ ions: they created a larger background than expected which increased only linearly with the argon pressure.

Until the end of October 2018, only preliminary results of the STS IIIa measurements were available. The presumable ionisation efficiency of $2 \cdot 10^{-3}$ counts/ion would allow to measure down to 10^3 ions/s almost instantaneously via ionisation in the PS (see section VII.1); the method would be limited by H_2^+ ion creation by beta electrons from the presumable minimum PS pressure of $5 \cdot 10^{-10}$ mbar after the removal of the PS getter pumps, which was decided in October 2018. For the next tritium measurements with a nominal tritium concentration of $> 95\%$ in the source, the final analysis of the STS IIIa measurements is therefore paramount.

IX.5. Optimisation of the ring electrode voltages

The creation of Penning ions in the positive potential of the ring electrodes required an optimisation of the voltage setting of +200 V at all ring electrodes. In order to detect the smallest possible ion fluxes from the WGTS with the PS ionisation method, the ring electrode voltages were however reduced to +20 V in the DPS and +50 V at the spectrometers. The effect of the new ring electrode setting was investigated with an ionisation measurement. Later measurements during the First Tritium campaign led however also to the discovery of ions from molecular dissociation; these can have energies up to slightly below 100 eV and require therefore that the PS1 ring electrode is set to +200 V in the future.

New ring electrode setting due to Penning ions Penning discharges in the DPS PP5 and the PS1 ring electrode were presumably observed during First tritium (see section IX.2.2): when the voltage of the ring electrodes was increased, the simultaneously measured PS ionisation rate followed rather linearly. A minimal ion flux was observed for all ring electrodes between +10 V and +50 V.

The Penning ion flux into the PS had to be reduced in order to detect the smallest possible ion fluxes from the WGTS with the PS ionisation method. Additionally, the Penning discharges in the DPS ring electrodes created ions from partially tritiated residual gas – these tritiated ions had to be prevented from flowing into the PS as well.

Another reason for the prevention of Penning discharges is the increased creation of secondary electrons, all of which become trapped in the positive potential of the ring electrodes. These secondary electrons create a negative space charge which might ultimately neutralise the blocking potentials of the ring electrodes (see section III.6.3). Especially the ring electrodes in the DPS should therefore be set to a minimal voltage.

At the beginning of the First Tritium campaign, all electrodes had been set to +200 V to safely block all ions from the WGTS. In order to minimise the creation rate of Penning ions, a setting of +20 V for all electrodes seemed favourable. The ring electrodes in the spectrometers were however set to +50 V in order to safely block the tritiated ions from the DPS ring electrodes: due to its large radius, the potential in the center of the PS1 electrode dropped to 46.5% of the applied voltage, as compared to 84.2% in the DPS BT5 electrode and about 40% in the PP5 electrode. The ring electrodes in the PS2 magnet and at the detector had not been observed to create Penning ions and were set for clarity to the same voltage as the PS1 electrode.

Ion flux into the PS with old and new ring electrode setting In order to assess the improvement by the new ring electrode setting, the PS ionisation rate was measured at various pressures just as for the determination of the upper limit on the ion flux into the PS in section IX.4.4. The ionisation rate with the old electrode setting (all electrodes at +200 V) was measured along with the intrinsic PS background at closed V4 between CPS and PS; one day later, the rate was repeated for the new electrode setting (DPS electrodes at +20 V and spectrometer electrodes at +50 V).

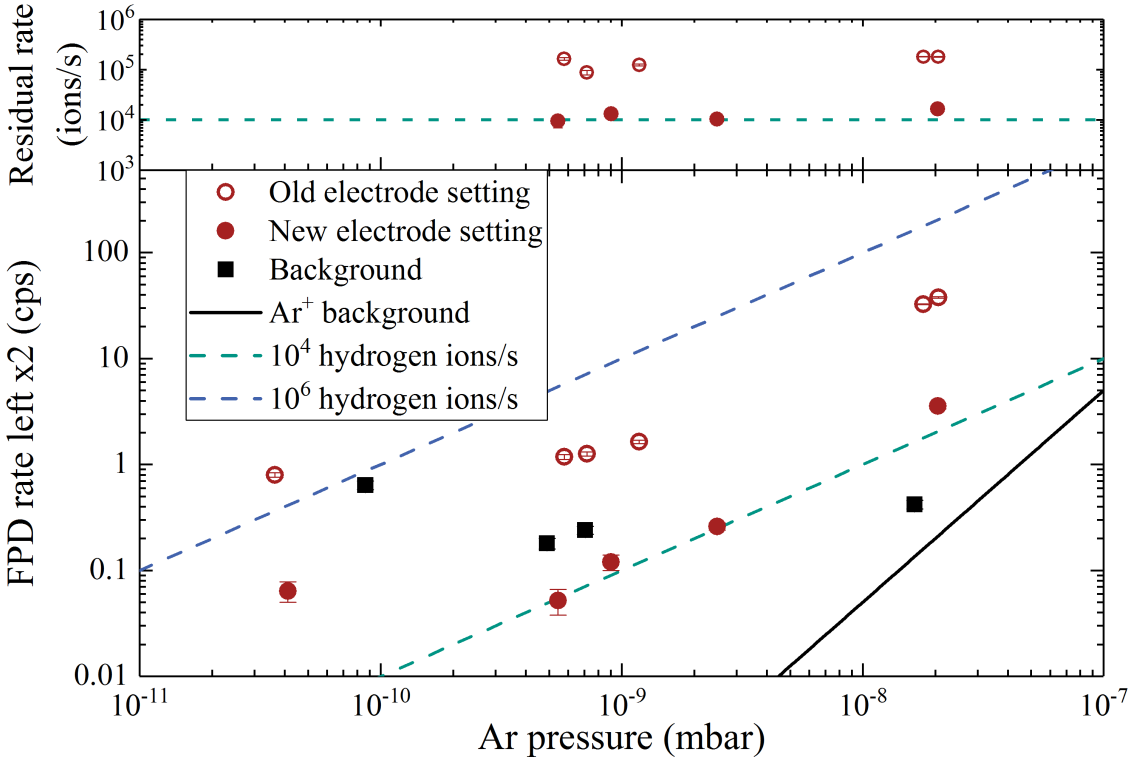

Figure IX.28.: **PS ionisation measurement with two different ring electrode settings.** In the old setting, all ring electrodes were at +200 V. After the discovery of Penning ions, the ring electrodes in the DPS were set to +20 V and those in the spectrometers to +50 V. This reduced the Penning ion flux into the PS by almost one magnitude and allowed to set a limit on the residual ion flux on the order of 10^4 ions/s (see also figure IX.27).

Figure IX.28 shows the result of the ionisation measurement[31]: the reduction of the ring electrode voltages reduced the Penning ion rate into the PS likewise by about one magnitude. With the old ring electrode settings, an upper limit on the ion flux of not less than $(1.46 \pm 0.03) \cdot 10^5$ ions/s could be derived due to the Penning ion flux; with the new ring electrode setting, the upper limit decreases to $(1.2 \pm 0.1) \cdot 10^4$ ions/s into the PS. The preliminary results of the STS IIIa measurement campaign indicate that this upper limit was in turn due to Ar^+ ions; as explained in section IX.4.4, the above analysis based on a pressure-dependent ionisation efficiency constitutes a conservative upper limit.

[31] This conversion was calculated just like in section IX.4.4: from the signal rate at the FPD, the intrinsic background at a close-by argon pressure is subtracted, the net rate is converted into an ion flux and finally the Ar^+ rate is subtracted. The intrinsic background on the first measurement day was however mostly larger than the signal rate with the new electrode setting; due to an obvious drift of the background over night, it could not be subtracted from the measurement with the new electrode setting. The measurement points below 10^{-10} mbar were also excluded because the background was strongly increased, obviously unrelated to an ion flux.

Proposed future ring electrode setting due to ions from molecular dissociation
As discussed in section IX.2.3, the First Tritium measurements also led to the discovery of ions from the WGTS with energies up to 15 eV due to molecular dissociation. These ions had been implicitly observed during the investigation of Penning ions by a large ionisation rate when all electrodes were set to +10 V; consequently, the DPS ring electrodes were set to 20 V.

Extended paper research after the First Tritium campaign indicated however that ions from molecular dissociation could receive energies up to slightly below 100 eV. These ions would not be blocked with the new electrode settings. Even though the expected rate of such ions is small, they should be prevented from reaching the PS during future measurements by a sufficiently large ring electrode voltage.

Therefore, the PS1 electrode should be set to 200 V in order to create a blocking potential of 93 eV in its center. The DPS ring electrodes have to remain at small voltages in order to accelerate no tritiated Penning ions into the PS; also, a Penning discharge would lead to an increased number of trapped electrons and a faster neutralisation.

IX.6. Summary and conclusions

The First Tritium measurements with the KATRIN experiment deomnstrated the safe opertaion with regard to tritiated ions: an upper limit on the ion flux of $1 \cdot 10^4$ ions/s into the PS could be derived with the ionisation method. Complementary, the PS current method was used to monitor the ion flux continuously during the scans of the tritium beta spectrum. Among further results, the energy spectrum of ions from the WGTS was investigated, creation of ions from Penning discharges in the ring electrodes was observed and the ring electrode voltages were adjusted accordingly. Also, the newly-built ion detectors could be tested with ions for the first time and mostly performed very well. In the following, these results will be summarised and conclusions for future tritium measurements with KATRIN will be drawn.

Upper limit on the ion flux into the PS A flux limit of $1 \cdot 10^4$ ions/s into the PS could be derived with the argon ionisation method in the PS (see section IX.4.4), in accord with the background requirements (see section V.3). Preliminary results of the STS IIIa measurements indicated that the measurement was limited by Ar^+ ions due to a pressure-independent and larger-than-expected ionisation efficiency in the PS. In order to mitigate the Ar^+ background during future measurements, the pressure-independent ionisation efficiency in the PS can be applied at minimal PS pressures on the order of 10^{-11} mbar.

Continuous monitoring of the ion flux into the PS During the scans of the beta spectrum with the MS, the ion flux into the PS was monitored continuously via the current on the PS downstream cone electrode. The valve V4 between the CPS and PS would have been closed automatically if a PS current larger than $2 \cdot 10^8$ ions/s had been observed; this however never happened, implying that the radiation safety constraint of $2 \cdot 10^8$ ions/s into the PS was met (see section IX.4.3).

During a 3.5 days long measurement interval, the PS current method allowed to set an upper limit on the ion flux into the PS of $1 \cdot 10^5$ ions/s (see section IX.4.3). A continuous ion flux of this magnitude would lead to a tritium induced background in the MS of 1 mcps, as required by the KATRIN design report. For comparison: fluctuations of the MS background of more than 5 mcps were measured over the course of the (Very) First Tritium campaigns (see section IX.4.1). Thus, the PS current measurement already allows the most sensitive monitoring of the ion flux into the PS during scans of the beta electron spectrum.

Ion energy spectrum Besides the thermal ions from the WGTS (see section IX.2.1), two other ion energy regimes were observed unexpectedly. Ions from molecular dissociation were detected at energies up to 15 eV, but are assumed to even reach energies up to about 100 eV at very small rates (see section IX.2.3). Also, ions were created by Penning discharges in the ring electrodes in DPS PP5 and the PS1 magnet (see section IX.2.2).

Ring electrode voltages The ring electrode voltages were optimised after the discovery of Penning discharges in the ring electrodes and of dissociation ions with energies up to about 100 eV: both DPS ring electrodes were set to +20 V and the three SDS electrodes were set to +50 V (see section IX.5). This setting was chosen in order to minimise the creation of Penning ions while safely blocking the full energy spectrum of dissociation ions. Also, this setting reduces the creation rate of secondary electrons inside the DPS ring electrodes; eventually, these secondary electrons might neutralise the blocking potential of the ring electrodes.

During future measurements, the PS1 ring electrode should be set to +200 V in order to block even the dissociation ions with energies up to about 100 eV which are expected at very small rates from the theory of beta decay (see section IX.5). At this voltage, a non-negligible rate of Penning ions from the PS1 electrode was observed. These Penning ions would not harm the neutrino mass measurements, but restrict the demonstrable upper limit on the ion flux into the PS during future measurements with the ionisation method. For that reason, the PS1 voltage should be reduced to +50 V during the ionisation measurements; it can be safely reset to +200 V afterwards without any negative consequences.

Performance of the ion detectors Most of the ion detectors demonstrated very good ion detection capabilities. The smallest ion flux could be detected via ionisation in the PS: it allowed to set an upper limit on the ion flux into the PS of $1 \cdot 10^4$ ions/s (see section IX.4.4). According to preliminary results of the STS IIIa campaign from October 2018, the method was ultimately limited by Ar^+ ions. This Ar^+ rate could be mitigated during future tritium campaigns by measuring at the minimum PS pressure of about 10^{-11} mbar; in fact, the ionisation efficiency seems to be pressure-independent according to the same preliminary results from STS IIIa.

Also, the two continuous ion monitoring methods on the PS downstream cone electrode and the DPS dipole electrodes proved to work: the PS current measurement was demonstrated with Penning ions and dissociation ions (see section IX.1.5) and has a minimal detectable ion flux of $4 \cdot 10^5$ ions/s at 3σ significance after 2 hours of measurement (see section IX.1.1.3).

The dipole electrode in DPS BT1 measured thermal ions with a minimal detectable flux of $3 \cdot 10^7$ ions/s at 3σ significance (see section IX.1.1.3). No ions could be measured with the dipole electrodes downstream from BT1: this was due to a damaged cable connection between the amperemeter and the dipole electrode in BT2 in the first place, which was repaired after First Tritium; in case of BT3 and BT4, it was attributed to inadvertent ion blocking in the DPS.

The Faraday cup proved to measure beta electrons, but the observed electron rate was 50 times smaller than expected (see section IX.1.2). For that reason, also the Faraday cup results on ions and secondary electrons are considered to be not reliable.

X. Conclusion and Outlook

The KATRIN experiment aims at the model-independent determination of the neutrino mass with a 90% C.L. sensitivity of 200 meV/c^2 by measuring the end point region of the integrated tritium beta spectrum at 18.6 keV (see chapter II). For this purpose, KATRIN employs a high-luminosity gaseous tritium source, in which 10^{11} beta electrons are created each second. The electrons are guided with a strong magnetic field up to 6 T and reach the detector if their energy is sufficient to overcome the high-pass MAC-E filter inside the Main spectrometer.

Tritium ions are inadvertently created in the tritium source as a consequence of beta decay and inelastic scattering of the beta electrons (chapter III). The $2 \cdot 10^{11}$ positive ions/s could follow the magnetic guiding field to the spectrometers (section III.2), where they would be implanted into the vessel walls due to the negative high voltage (section IV.1). Diffusion would lead to tritium reemission from the walls and to the creation of background via decay in the flux tube (section IV.3). On their way across the spectrometer, the ions can further ionise the residual gas and produce background via the secondary electrons (section IV.2). In order to restrict the background from tritium ions to 1 mcps, a constraint on the ion flux into the Pre-spectromer (PS) of $1 \cdot 10^4$ ions/s is imposed (section V.3).

Ion blocking via the electrostatic potentials of five ring electrodes therefore prevents the ions from reaching the spectrometers (section VI.1). However, the blocked ions would be stored between the electrostatic potentials of the ring electrodes and the gas flow from the tritium source and might cause systematic effects: the increased plasma density could undergo instabilities, which might create time-dependent electric fields and smear the energy of the beta electrons (section V.4.1). Also, the positive blocking potentials could be neutralised by trapping of secondary electrons and negative ions from the source (section III.6.3). Both effects are remedied with four dipole electrodes, which remove the stored positive ions via $\vec{E} \times \vec{B}$ drift in a negative dipole potential (section VI.2). The neutralisation of ions on the dipole electrodes creates a current, which can be measured down to 6 pA corresponding to $3 \cdot 10^7$ ions/s at 3σ significance (section VII.2.2).

Two measurement campaigns demonstrated the safe KATRIN operation with regard to tritium ions within the scope of this thesis. The First Light campaign in autumn 2016 marked the first successful test of the ring and dipole electrodes with a pencil beam of deuterium ions from the ELIOTT ion source (chapter VIII). During the (Very) First Tritium measurements with 0.5% tritium in the deuterium source gas, an upper limit on the ion flux into the PS could be derived at the aspired level of $1 \cdot 10^4$ ions/s (section IX.4.4). Further, the observation of ions from Penning discharges in the ring electrodes (section IX.2.2) and the detection of ions with energies up to 15 eV from molecular dissociation (section IX.2.3) led to the optimisation of all five ring electrode potentials (section IX.5).

Inadvertent ion blocking was observed in both measurement campaigns, presumably due to work function differences between the beam tube materials (section III.6.2). During First Light, ions with energies $\lesssim 1$ eV were found to be not transported through the beamline (section VIII.6). During First Tritium, only 50% of the expected ion flux was observed with the first dipole electrode downstream from the source, and no ions at all were observed with the other dipole electrodes (section IX.3). The inadvertently blocked ions will accumulate in the source and increase again the plasma density along with the risk of plasma instabilities and smearing of the beta electron energy (section V.4.1).

The PS downstream cone electrode attracts about 20% of the incoming ions at nominal high voltage settings (section IV.1). Measuring the neutralisation current allows to continuously monitor the ion flux into the PS (section VII.2.4). The valve to the PS will be closed automatically within 1 min if the current surpasses a current of 5 pA. The corresponding flux of $2 \cdot 10^8$ ions/s into the PS matches the constraint on the continuous tritium ion flux into the spectrometers over 3 years of KATRIN operation due to radiation protection (section V.1). After 2 hours of measurement, reduced statistical and systematical uncertainties allow to detect an even 500 times smaller current of 12 fA at 3σ significance (section IX.1.3.3). The corresponding flux of $4 \cdot 10^5$ ions/s into the PS is not as small as the conservative constraint of $1 \cdot 10^4$ ions/s, but would produce only 4 mcps via tritium activity, which is roughly 1% of the total Main spectrometer background (see section IV.3.4).

Ionisation of residual gas by ions in the spectrometers is the most sensitive ion detection method in the beamline (section VII.1). An ion flux of $6 \cdot 10^5$ ions/s into the Main spectrometer is detectable within 15 min at 3σ significance, as determined during the First Light measurements (section VIII.2.3). During the First Tritium measurements, an upper limit on the ion flux into the PS of $1 \cdot 10^4$ ions/s could be derived conservatively with the ionisation method, matching the target bound (section IX.4.4). Preliminary results from STS IIIa measurements with non-tritium ions indicate that the PS ionisation measurement during First Tritium was still limited by background.

The STS IIIa ion measurements in October 2018 observed a larger-than-expected and pressure-independent ionisation efficiency in the PS (section IV.2), which needs to be understood in order to apply the method reliably in the future. Preliminary results for the ionisation efficiency indicate that an ion flux of about 10^3 ions/s into the PS could be measured instantly in the evacuated PS. Further, the preliminary results indicate that the detection efficiency of the PS current measurement might be one order of magnitude larger than assumed in this thesis due to emission of secondary electrons from the electrode surface upon ion impact (section VII.2.4).

Next tritium measurements will take place in spring 2019, reaching nominal tritium concentration of at least 95%. In the beginning, the column density should be raised stepwise to verify the ion blocking at increasing tritium concentrations. At the same time, this procedure would allow to investigate with the dipole currents the possible neutralisation of inadvertent ion blocking potentials at increasing plasma density.

Systematic effects from ions in the tritium source still require particular attention. For example, the dipole electrode voltages need to be optimised with nominal tritium concentration and an admixture of ^{83m}Kr in the source (section VI.2.3). These

optimised dipole voltages and the inadvertent ion blocking will then determine the removal rate of positive ions. The removal rate is required as input parameter for particle-in-cell simulations of the source plasma, which will allow to estimate the systematic effects from possible plasma instabilities (section V.4.1) or negative ion space charges in the tritium source (section V.4.2). While systematic effects due to tritium ions still require further research, ion safety in the KATRIN experiment with regard to background and radiation protection has already been achieved within this thesis.

A. Calculations

A.1. Downstream escape probability of electrons in the spectrometers

The calculation in section IV.3.1 of the background from tritium activity requires the downstream escape probability ϵ_{down} for electrons, which are created inside any of the two spectrometers. These electrons might be beta electrons or secondary electrons from ionisation of residual gas by beta electrons.

Both beta electrons and secondary electrons can be trapped inside the spectrometers due to the magnetic mirror effect, depending on the pitch angle between the electron momentum and the direction of the magnetic field. According to section III.1.2, the maximum pitch angle of an electron in order to be not reflected is:

$$\theta_{\text{max}} = \arcsin \sqrt{\frac{B_{\text{start}}}{B_{\text{max}}}}. \tag{A.1}$$

B_{start} is the magnetic field at the creation of the electron inside the spectrometer. The maximum field B_{max} is for nominal field strengths 6 T in the pinch magnet on the downstream side of the MS and 4.5 T in the PS2 magnet on the upstream side of the MS. Consequently, the maximum pitch angle of the beta electron in order to be not reflected at the downstream side of the MS is smaller than at the upstream side; likewise, the escape probability to the downstream side is smaller.

In the following, it will be assumed that the electrons are created with an isotropic angular distribution. Likewise, when the pitch angle changes due to scattering of the electron, an isotropic distribution is approximately assumed. Then there are three regions of pitch angles θ:

- $\theta > \theta_{\text{max,up}}$: The electron can neither escape through the downstream end nor through the upstream end of the spectrometer.

- $\theta_{\text{max,up}} > \theta > \theta_{\text{max,down}}$: The electron can only escape through the downstream side, which it will eventually do if the the pitch angle is not changed by scattering.

- $\theta_{\text{max,down}} > \theta$: The electron can escape through both the upstream or downstream end of the spectrometer. The probability to escape through either side is 50%.

The larger probability for the electron to escape through the upstream end can be considered via the ratio of the maximum angles. Therefore, the probability to

escape on the downstream side of the spectrometer is:

$$\epsilon_{\text{down}} = 0.5 \cdot \theta_{\text{max,down}}/\theta_{\text{max,up}} \tag{A.2}$$

$$= 0.5 \cdot \sqrt{B_{\text{up}}/B_{\text{down}}} \tag{A.3}$$

$$\approx 0.43. \tag{A.4}$$

In the PS, the probability to leave to the downstream side is 50%: both the PS1 and the PS2 magnet have the same nominal magnetic field strength.

These calculations are in accord with [Mer13] and apply if the electrons are not able to return into the MS, for example by energy loss after inelastic scattering. Otherwise, the electrons can only leave the fluxtube under nominal conditions if they are absorbed by the FPD or by the rear wall. In order to reach the rear wall, the electrons need to overcome the magnetic mirror in the CPS due to its magnetic field of 5.72 T nominal strength. Because this is almost the same strength as the 6 T at the pinch magnet, the electrons from either spectrometer might be actually stored between the CPS and the pinch magnet. The probability to leave the beamline to the downstream side and towards the FPD is then 49%.

A.2. Magnetic self-shielding in the spectrometers

Beta electrons, which are created by tritium decay in the MS outside the magnetic flux tube, cannot reach the FPD and cause background: this argument was used in section IV.3.1 for the calculation of the background from tritium decay in the spectrometers and will be detailed in the following. In a rough approximation, the results are assumed to apply also to the PS.

Charged particles which are created inside the MAC-E-Filter can be trapped by the magnetic mirror effect, which was introduced in section III.1.2. For these particles, the MAC-E-Filter acts like a magnetic bottle, which reflects the particles at the bottlenecks of maximum magnetic field. This is due to the conservation of the magnetic moment $|\vec{m}| = E_\perp/|\vec{B}|$ for adiabatic particles, where $E_\perp$ is the kinetic energy perpendicular to the magnetic guiding field $\vec{B}$.

Due to the magnetic mirror effect, there is an upper limit on the transverse energy $E_\perp$ of those electrons which reach the FPD: their longitudinal kinetic energy must be $E_\parallel > 0$ at any point. Equivalently holds $E_\perp < E_{\text{tot}}$, where $E_{\text{tot}} = E_\perp + E_\parallel$ is the total electron energy upon creation.

The conservation of the magnetic moment under adiabatic conditions implies that the perpendicular energy component will be decreased to the same amount as the magnetic field strength. This ratio becomes maximal for a particle which is created in the center (c) of the MAC-E filter, relative to the bottleneck (n) of the magnetic bottle in the superconducting coils:

$$\frac{E_{\perp,c}}{E_{\perp,n}} = \frac{B_c}{B_n} \sim 10^{-4}. \tag{A.5}$$

The total energy of such a particle depends on the energy from tritium beta decay, which can be up to the endpoint energy energy, plus the local potential inside the

MAC-E filter, which corresponds to the endpoint energy. With $E_{\mathrm{tot}} \lesssim 40$ keV follows:

$$E_{\perp,c} < E_{\mathrm{tot},n} \cdot \frac{B_c}{B_n} \lesssim 4 \text{ eV}. \tag{A.6}$$

The limit on the transverse electron energy limits the distance from the flux tube, in which electrons can be created to contribute to the background. For an electron with $E_\perp \sim 4$ eV in a magnetic field of $B \sim 3$ G as in the analysis plane (a) of the MAC-E filter, the cyclotron radius is:

$$r_a = \sqrt{\frac{2m\ E_\perp}{|q|^2\ B_a^2}} \sim 5 \text{ cm}. \tag{A.7}$$

This penetration depth is two orders smaller than the flux tube radius of several meters. For arbitrary creation positions, a limit on the penetration depth can be derived by combining equations A.6 and A.7:

$$r(B_c) = \sqrt{\frac{2m\ E_{tot}}{|q|^2\ B_n\ B_c}}. \tag{A.8}$$

The flux tube cross section also scales with the magnetic field as $r_\Phi \sim 1/\sqrt{B_c}$, so the penetration depth is always about two orders of magnitude smaller than the flux tube radius. Therefore, the FPD background due to beta electrons from outside the MS flux tube can be neglected.

For secondary electrons, the same argument can be made except for a factor of two: in contrast to the beta electrons, the energy of the secondary electrons at the bottleneck is only about 20 keV from the analysis potential.

The creation of secondary electrons inside the flux tube, however, can also be caused by beta electrons from the gas phase outside the flux tube. According to equation A.7, they can have cyclotron radii on the order of meters in the analysis plane, similar to the flux tube radius. It is unclear whether the simulations for [Mer13] have considered this background from beta decay outside the flux tube.

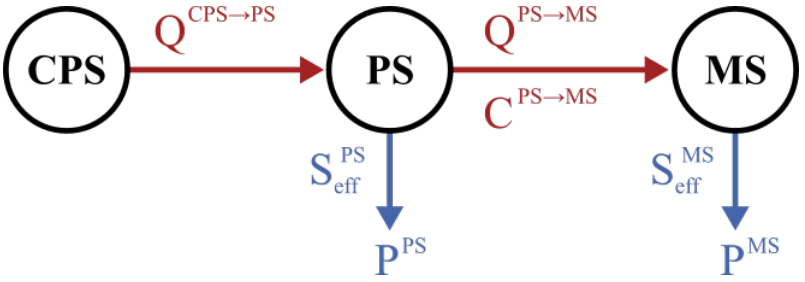

Figure A.1.: **HT flux from the CPS into the spectrometers.** In the PS and MS, the incoming flow rate $Q^{\mathrm{CPS}\to\mathrm{PS}}$ will be pumped with the effective pumping speed S_{eff} at a pump rate P. This leads in equilibrium to a HT flow rate $Q^{\mathrm{PS}\to\mathrm{MS}}$ from the PS into the MS through the conductance $C^{\mathrm{PS}\to\mathrm{MS}}$.

A.3. Diffusion of gaseous tritium in the spectrometers

The consequences of neutral tritium diffusion in the spectrometers for the FPD background was discussed in section IV.3.2. In this section, the underlying relations will be derived from vacuum physics.

Equilibrium conditions The flow rate $Q^{\mathrm{PS}\to\mathrm{MS}}$ between the spectrometers depends on their pressures p and on the conductance $C^{\mathrm{PS}\to\mathrm{MS}}$ between them:

$$Q^{\mathrm{PS}\to\mathrm{MS}} = (p^{\mathrm{PS}} - p^{\mathrm{MS}}) \cdot C^{\mathrm{PS}\to\mathrm{MS}}. \tag{A.9}$$

The flow rate out of the spectrometers due to pumping is the throughput P which depends on the spectrometer pressure p and the effective pumping speed $S_{\mathrm{eff}} = dV/dt$:

$$P^{\mathrm{PS/MS}} = p^{\mathrm{PS/MS}} \cdot S_{\mathrm{eff}}^{\mathrm{PS/MS}}. \tag{A.10}$$

In equilibrium, the flow rates Q of tritium into the PS and MS are just as big as the flow rates out of the spectrometer (see figure A.1): the flow rate Q through a conductance, the pump throughput P, the tritium exchange rate E of the vacuum with the vessel surfaces, and the tritium loss due to the activity A. This leads to the following equations for the PS and MS in equilibrium:

$$Q^{\mathrm{CPS}\to\mathrm{PS}} = P^{\mathrm{PS}} + Q^{\mathrm{PS}\to\mathrm{MS}} + E^{\mathrm{PS}} + A^{\mathrm{PS}}, \tag{A.11}$$

$$Q^{\mathrm{PS}\to\mathrm{MS}} = P^{\mathrm{MS}} + E^{\mathrm{MS}} + A^{\mathrm{MS}}. \tag{A.12}$$

The tritium activity A can be neglected because it is much smaller than the pump throughput P. Also, the tritium exchange between the vacuum and vessel surfaces will be set to zero. If the tritium reemission rate from the PS vessel walls becomes significant, it can be treated like a flow of neutral tritium from the CPS (see further below).

Pressure in the spectrometers for a given flow rate into the PS For the following calculations, it is useful to determine the ratio of the equilibrium pressures in the

PS and MS with the hardware parameters listed in table A.1. Using the equilibrium condition for the MS (eq. A.12) and the definitions of the flow rate (eq. A.9) and of the pump throughput (eq. A.10), one obtains:

$$\begin{aligned} & (p^{\mathrm{PS}} - p^{\mathrm{MS}}) \cdot C^{\mathrm{PS}\to\mathrm{MS}} = p^{\mathrm{MS}} \cdot S_{\mathrm{eff}}^{\mathrm{MS}}, \\ \Leftrightarrow \quad & \frac{p^{\mathrm{MS}}}{p^{\mathrm{PS}}} = \frac{1}{1 + S_{\mathrm{eff}}^{\mathrm{MS}}/C^{\mathrm{PS}\to\mathrm{MS}}} \approx \frac{C^{\mathrm{PS}\to\mathrm{MS}}}{S_{\mathrm{eff}}^{\mathrm{MS}}} \sim 3 \cdot 10^{-3}. \end{aligned} \tag{A.13}$$

Now the tritium partial pressure in the MS can be set in relation to the tritium flow rate from the CPS into the spectrometers. With equations A.9, A.10, A.12, A.13 and table A.1 follows:

$$\begin{aligned} Q^{\mathrm{CPS}\to\mathrm{PS}} &= P^{\mathrm{PS}} + P^{\mathrm{MS}} \\ &= p^{\mathrm{MS}} \cdot \left[\left(\frac{S_{\mathrm{eff}}^{\mathrm{MS}}}{C^{\mathrm{PS}\to\mathrm{MS}}} + 1 \right) \cdot S_{\mathrm{eff}}^{\mathrm{PS}} + S_{\mathrm{eff}}^{\mathrm{MS}} \right] \\ &\approx p^{\mathrm{MS}} \cdot \frac{S_{\mathrm{eff}}^{\mathrm{MS}} \cdot S_{\mathrm{eff}}^{\mathrm{PS}}}{C^{\mathrm{PS}\to\mathrm{MS}}}, \end{aligned} \tag{A.14}$$

$$\Leftrightarrow p^{\mathrm{MS}} = 1 \cdot 10^{-7} \cdot Q^{\mathrm{CPS}\to\mathrm{PS}} \ \mathrm{s/l}, \tag{A.15}$$

$$\Leftrightarrow p^{\mathrm{PS}} = 4 \cdot 10^{-5} \cdot Q^{\mathrm{CPS}\to\mathrm{PS}} \ \mathrm{s/l}. \tag{A.16}$$

Further, it can be calculated how much of a tritium flow $Q^{\mathrm{CPS}\to\mathrm{PS}}$ into the PS will also flow into the MS as $Q^{\mathrm{PS}\to\mathrm{MS}}$:

$$\frac{Q^{\mathrm{PS}\to\mathrm{MS}}}{Q^{\mathrm{CPS}\to\mathrm{PS}}} \approx \frac{P^{\mathrm{MS}}}{P^{\mathrm{PS}}} = \frac{C^{\mathrm{PS}\to\mathrm{MS}}}{S_{\mathrm{eff}}^{\mathrm{PS}}} = 3 \cdot 10^{-2}. \tag{A.17}$$

Tritium amount in the spectrometers for a given flow rate into the PS In the following, it will be assumed that $Q^{\mathrm{CPS}\to\mathrm{PS}}$ completely consists of HT molecules, due to the large number of adsorption and desorption processes in the transport section [Mer13]. Then also the tritium content of the spectrometers will be made up of HT dominantly.

Table A.1.: **Values for some parameters of the PS and MS vacuum setup.** The effective pumping speeds $S_{\mathrm{eff,HT}}$ consider all kinds of pumping of HT.

Vacuum parameter	Notation	Value
PS volume	V^{PS}	$8.5 \cdot 10^3$ l
Effective pumping speed for HT in the PS	$S_{\mathrm{eff,HT}}^{\mathrm{PS}}$	$2 \cdot 10^4$ l/s
Conductance between PS and MS	$C^{\mathrm{PS}\to\mathrm{MS}}$	530 l/s
MS volume	V^{MS}	$1.2 \cdot 10^6$ l
Effective pumping speed for HT in the MS	$S_{\mathrm{eff,HT}}^{\mathrm{MS}}$	$2 \cdot 10^5$ l/s

The tritium induced background rate at the FPD can be calculated from the number of tritium atoms in the MS (see section IV.3.1). This number $N_{\mathrm{T}}^{\mathrm{MS}}$ of tritium atoms is related to the partial HT pressure $p_{\mathrm{HT}}^{\mathrm{MS}}$ by the ideal gas law $pV = Nk_BT$. The MS volume V^{MS} can be found in table A.1 and the vessel temperature of $T = 300$ K corresponds to $k_BT = 4 \cdot 10^{-20}$ mbar·l, where $k_B = 1.4 \cdot 10^{-23}$ J/K is the Boltzmann constant [Flo17].

Using equation A.15 yields eventually:

$$\begin{aligned} N_{\mathrm{T}}^{\mathrm{MS}} &= p_{\mathrm{HT}}^{\mathrm{MS}} \cdot V^{\mathrm{MS}}/(k_BT) \\ &= 3 \cdot 10^{25}\ /\mathrm{mbar} \cdot p_{\mathrm{HT}}^{\mathrm{MS}} && \text{(A.18)} \\ &= 4 \cdot 10^{18}\ \mathrm{s/(mbar{\cdot}l)} \cdot Q_{\mathrm{HT}}^{\mathrm{CPS}\to\mathrm{PS}} && \text{(A.19)} \\ &= 0.2\ \mathrm{s} \cdot \Phi_{\mathrm{HT}}^{\mathrm{CPS}\to\mathrm{PS}}. && \text{(A.20)} \end{aligned}$$

Equivalently, one can derive for the PS:

$$\begin{aligned} N_{\mathrm{T}}^{\mathrm{PS}} &= p_{\mathrm{HT}}^{\mathrm{PS}} \cdot V^{\mathrm{PS}}/(k_BT) \\ &= 2 \cdot 10^{23}\ /\mathrm{mbar} \cdot p_{\mathrm{HT}}^{\mathrm{PS}} && \text{(A.21)} \\ &= 9 \cdot 10^{18}\ \mathrm{s/(mbar{\cdot}l)} \cdot Q^{\mathrm{CPS}\to\mathrm{PS}} && \text{(A.22)} \\ &= 0.4\ \mathrm{s} \cdot \Phi_{\mathrm{HT}}^{\mathrm{CPS}\to\mathrm{PS}}. && \text{(A.23)} \end{aligned}$$

A.4. Expected background after a short tritium ion flux into the PS

The tritium reemission after tritium ion implantation in the PS depends on the diffusion, trapping and desorption processes, which have been introduced qualitatively in section IV.3.3. They govern the tritium reemission in neutral HT molecules form the stainless steel surfaces of the PS, in which the tritium ions would be almost exclusively implanted (see section IV.1).

This section will estimate the time scale of reemission based on Fick's second law of diffusion [Cra79]. In order to apply it to the case of tritium ion implantation in the stainless steel of the PS, the initial tritium concentration will be simulated with SRIM [SRI10]. The dissolving of this initial concentration package is affected by the boundary condition at the surface: if diffusion is the rate limiting step, there will be basically no tritium at the surface; but if the reemission is limited by desorption, then the tritium atoms are approximately reflected by the surface and diffuse deeper into the bulk. From the comparison of both cases, the time evolution of the tritium reemission will be estimated at the end of this section. Unfortunately, the most probably rate limiting step of trapping cannot be considered analytically; therefore, the result can only be interpreted as a minimum waiting time until 1 mcps of background due to tritium decay in the spectrometers is reached again.

Fick's second law of diffusion A general description of diffusion processes is given by Fick's laws of diffusion [Cra79]. According to Fick's second law, the time evolution of a concentration profile $C(x,t)$ depends on the second derivative in space. For the one dimensional case it can be written as:

$$\frac{\mathrm{d}C(x,t)}{\mathrm{d}t} = D \cdot \frac{\mathrm{d}^2C(x,t)}{\mathrm{d}x^2}. \tag{A.24}$$

The diffusion constant D allows to consider the species of the diluted substance, the species of the solvent and their temperature. For tritium in stainless steel, three different literature values have been compared as detailed in appendix A.5. The value chosen for the following discussion is [Aus72]:

$$D(300\ \mathrm{K}) = (1.02^{+0.74}_{-0.56}) \cdot 10^{-12}\ \frac{\mathrm{cm}^2}{\mathrm{s}}, \tag{A.25}$$

For the following discussion, it is useful to find an eigenfunction to Fick's second law for a concentration package which is initially confined between the distances h_1 and h_2 below the surface. Such a solution to the differential equation can be derived

for example with the error function[1] $\mathrm{erf}(x)$:

$$C_{\mathrm{inf}}(x,t) = \frac{C_0}{2} \cdot \left(\mathrm{erf}\left(\frac{x-h_1}{\sqrt{4Dt}} \right) - \mathrm{erf}\left(\frac{x-h_2}{\sqrt{4Dt}} \right) \right). \tag{A.29}$$

A graphical display of this solution was already shown in figure IV.9, and two more graphs with linear superpositions of this solution can be found in figure A.3 and A.4. Its derivative is given by:

$$\frac{\mathrm{d}C_{\mathrm{inf}}(x,t)}{\mathrm{d}x} = \frac{C_0}{\sqrt{4\pi Dt}} \cdot \left(\exp\left(-\frac{(x-h_1)^2}{4Dt} \right) - \exp\left(-\frac{(x-h_2)^2}{4Dt} \right) \right). \tag{A.30}$$

Before this solution can be used for the calculation of desorption rates, it will be necessary to derive values for the depths h_1 and h_2 as well as for the initial concentration C_0. This was done with a SRIM simulation, as detailed in the following.

SRIM simulation of the initial tritium concentration The initial tritium concentration after ion bombardment in the PS was simulated with SRIM [SRI10]. It resulted in a one-dimensional concentration profile $C(x)$, where x is the depth below the stainless steel surface.

For the simulations, the following assumptions were made: all ions are implanted into the PS walls and electrodes, which consist of stainless steel 316 LN. Due to the negative high voltage of the PS, the ions will have energies of 18.3 keV. When the ions impinge the surface, they will be broken into their atomic components with equal energy shares of 6.2 keV. This implies triatomic ions, which is reasonable, since two third of the expected positive ions from the WGTS are T_3^+ ions (see section III.2.1). H^+ ions were used for the simulation of the implantation instead of tritium ions.

Figure A.2 shows the result of the SRIM simulation. The histogram was fitted with the solution to Fick's second law from eq. A.24 as indicated by the red curve, in order to describe the dissolving of the initial concentration package analytically. Although the concentration profile is shaped by the implantation process instead of diffusion, the red curve fits the simulation result rather well.

The fit result for the time t can be interpreted as the duration of the diffusion since an imaginary concentration package was confined between the borders h_1 and h_2 with the homogeneous concentration C_0. The implanted concentration profile corresponds to $t = 10.3$ s. All interpretation of the result before this implantation

[1] The error function $\mathrm{erf}(x)$ is defined as [Cra79]:

$$\mathrm{erf}(x) = \frac{2}{\sqrt{\pi}} \int_0^x e^{-\tau^2} d\tau, \tag{A.26}$$

which has the properties [Cra79]:

$$\mathrm{erf}(0) = 0, \qquad \mathrm{erf}(\infty) = 1, \qquad \mathrm{erf}(-x) = -\mathrm{erf}(x), \tag{A.27}$$

and the derivative [Bro08]:

$$\frac{\mathrm{d}\,\mathrm{erf}(z)}{\mathrm{d}z} = \frac{2}{\sqrt{\pi}} e^{-z^2}. \tag{A.28}$$

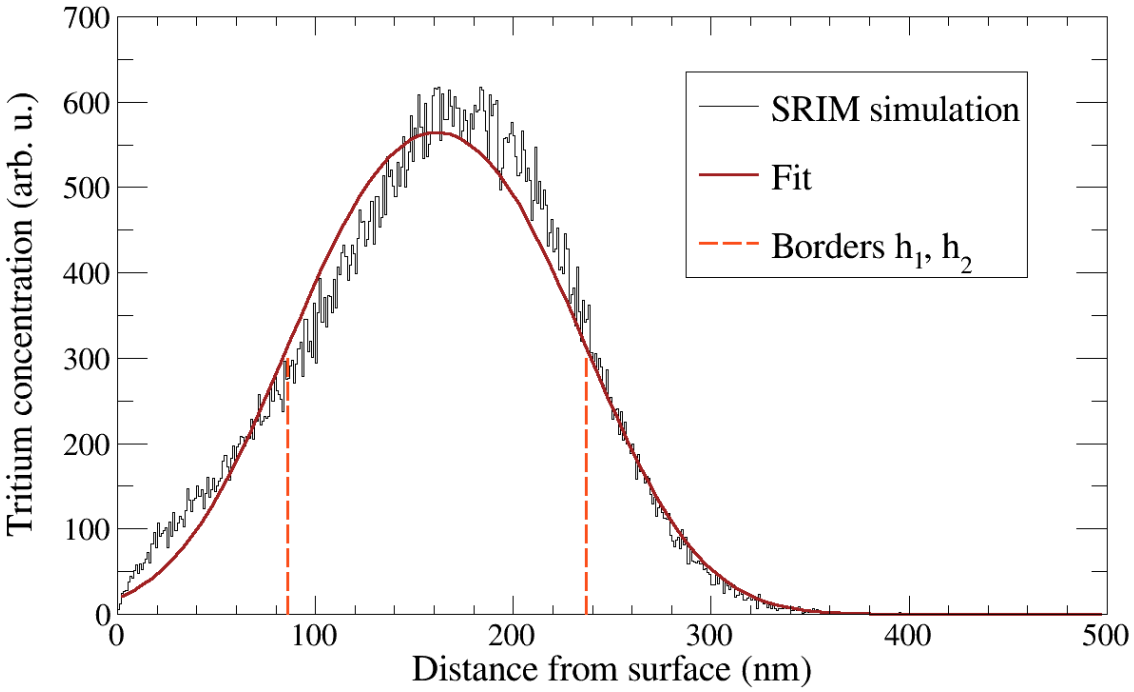

Figure A.2.: **Tritium concentration in stainless steel after implantation of T_3^+ ions with about 18.3 keV.** The result of the SRIM simulation [SRI10] (black histogram) agrees rather well with a fit of the solution to Fick's second law from eq. A.24 (red solid line). Indicated by the yellow dashed lines are the borders h_1 and h_2 of a thought rectangular concentration profile with amplitude C_0, which would have needed 10.3 s to reach this shape via diffusion. It was assumed that the T_3^+ ions break down to 3 T atoms when they impinge on the surface.

time of 10 s is unphysical. On the other hand, if the implantation would take much longer than 10 s, the application of the fit results would no longer be valid because the implanted tritium would have already started to dissolve as shown in figure IV.9. For the case under investigation, this requirement should still hold approximately: an implantation time of about 1 min is assumed because it takes about 20 s for the PS current monitor to trigger the closing of the valve in 95% of the cases (see section VII.2.4); closing the valve then takes about 30 s due to the strong magnetic field.

The depths h_1 and h_2 also result from the fit. They are indicated by the red dotted lines in figure A.2 and have the values:

$$h_1 \approx 86 \text{ nm}, \qquad h_2 \approx 237 \text{ nm}. \tag{A.31}$$

Also the initial concentration C_0 can be estimated from these fit results. It corresponds to the number of implanted tritium atoms divided by the volume into which they were implanted:

$$C_0 = \frac{(1-R)\cdot(n\Phi\tau)_{\text{im}}}{A\cdot(h_2-h_1)} \approx 10^{13}\ \frac{\text{T atoms}}{\text{cm}^3}. \tag{A.32}$$

The factor $R \approx 0.05$ describes the probability that the ions are not implanted but reflected at the stainless steel surface, as discussed in section IV.3.3. For the fluence $(n\Phi t)_{\mathrm{im}}$, the complete expected positive ion flux from the WGTS of $\Phi = 2{\cdot}10^{11}$ ions/s is assumed to flow into the PS for the time $\tau = 60$ s; because most of these ions are T_3^+, there is another factor $n \approx 3$.

The volume of the tritium implantation depends on the width of the initial distribution of $h_2 - h_1$ and on the area A over which the ions are implanted. For the calculation of the reemission rates, the area will cancel out and must therefore not be known exactly. Nevertheless, the area can be estimated very roughly by approximating the inner surface on the downstream side of the PS with a cone, which yields $A \approx 2{\cdot}10^4$ cm^2. For this area, the initial concentration becomes $C_0 \approx 1{\cdot}10^{14}$ tritium atoms/cm^3. This is much smaller than the approximate concentration of bulk atoms in stainless steel[2] of $C_{\mathrm{steel}} \approx 10^{23}$ bulk atoms/cm^3. For this reason, saturation effects are assumed to be negligible.

Diffusion limited case If diffusion will be the rate limiting step of tritium reemission from the stainless steel, then the surface can be considered as quasi-free of tritium due to the comparatively fast desorption. The boundary condition $C(0,t) = 0$ can be realised with a subtractive superposition of the solution for an infinite solid from eq. A.29, as displayed in figure A.3:

$$C_{\mathrm{diff}}(x,t) = C_{\mathrm{inf}}(x,t) - C_{\mathrm{inf}}(-x,t). \tag{A.33}$$

Now, Fick's first law can be used to derive the flux density through the surface at $x = 0$ for any given time t [Cra79][3]:

$$J_{\mathrm{diff}}(t) = -D \cdot \frac{\mathrm{d}C_{\mathrm{diff}}(0,t)}{\mathrm{d}x}. \tag{A.34}$$

This flux density $J(t)$ has the dimension tritium atoms per unit area. It can be converted into the tritium flux $\Phi_{\mathrm{re}} = J \cdot A$ by multiplication with the area A into which the tritium was implanted. This cancels out the value of A, because the initial concentration $C_0 \propto 1/A$:

$$\Phi_{\mathrm{diff}}(t) = A \cdot J_{\mathrm{diff}}(t) \tag{A.35}$$

$$= \sqrt{\frac{D}{\pi t}} \cdot \frac{(1-R)(n\Phi\tau)_{\mathrm{im}}}{h_2 - h_1} \cdot \left(\exp\left(-\frac{h_1^2}{4Dt}\right) - \exp\left(-\frac{h_2^2}{4Dt}\right)\right). \tag{A.36}$$

The relation between the tritium flux Φ and the background R_{T} from tritium activity in the spectrometers was derived in sections IV.3.1 and IV.3.2. In order to calculate how long it takes to reach a certain background level, the above equations

[2]The density of 316LN stainless steel was taken from a data sheet *Acidur 4429* of *Deutsche Edelstahlwerke GmbH* to be $\rho_{316} = 8{,}0$ g/cm^3 and the atomic weight of iron was assumed to be $m_{\mathrm{Fe}}^{\mathrm{atom}} \approx 56$ u.

[3]Mind however that the fit introduces an offset time $t = 10.3$ s at which the implantation took place.

need to be inverted with regard to the time t using an approximation[4]. Then follows:

$$t(\Phi_{\text{diff}}) \approx \left(\frac{(h_1 + h_2) \cdot (1 - R) \cdot (n\Phi\tau)_{\text{im}}}{4\sqrt{\pi D} \cdot \Phi_{\text{diff}}} \right)^{2/3}. \tag{A.37}$$

Desorption limited case If the tritium reemission is desorption limited, the comparatively slow desorption rate will lead to the reflection of the tritium atoms at the boundary. The corresponding boundary condition of $\mathrm{d}C(0,t)/\mathrm{d}x = 0$ can be realised by an additive superposition of the solution to Fick's second law for the infinite solid from eq. A.29:

$$C_{\text{des}}(x,t) = C_{\text{inf}}(x,t) + C_{\text{inf}}(-x,t). \tag{A.38}$$

The dominant desorption process is assumed to be Langmuir-Hinshelwood desorption according to section IV.3.3. In this process, the tritium recombines with another chemisorbed atom at the surface or from just below the surface [Wil81], which liberates enough energy for the molecule to leave the surface. The flux density of desorption is given by [Wil81]:

$$J_{\text{des}}(t) = k \cdot C_{\text{H}} \cdot C_{\text{T}}(0,t). \tag{A.39}$$

In analogy to the diffusion constant, the recombination rate constant k carries all information about the diluted substance, the solvent and their temperature. There is however a large uncertainty by two orders of magnitude on its value for hydrogen desorption from stainless steel [Wil81]:

$$k(300\ \text{K}) \approx 4 \cdot 10^{-27\pm2}\ \text{cm}^4/(\text{atoms}\cdot\text{s}). \tag{A.40}$$

It is assumed that all tritium atoms will leave the stainless steel bond in HT molecules, because the hydrogen density is larger than the tritium concentration in the scenario under investigation. The hydrogen density C_{H} can be calculated from the flux density of hydrogen outgassing in the MS, which is known from [KAV16] to be $J_{\text{H}_2} = 2.5 \cdot 10^7$ tritium atoms/(cm^2·s):

$$C_{\text{H}} = \sqrt{J_{\text{H}_2}/k}. \tag{A.41}$$

Just like for the diffusion limited case, the flux density $J(t)$ can be converted into a tritium flux Φ via:

$$\Phi_{\text{des}}(t) = A \cdot J_{\text{des}}(t) \tag{A.42}$$

$$= \sqrt{kJ_{\text{H}_2}} \cdot \frac{(1 - R)(n\Phi\tau)_{\text{im}}}{h_2 - h_1} \cdot \left(\operatorname{erf}\left(-\frac{h_1}{\sqrt{4Dt}} \right) - \operatorname{erf}\left(-\frac{h_2}{\sqrt{4Dt}} \right) \right). \tag{A.43}$$

Again the result is inverted, this time using an approximation for the error function[5]. This allows to calculate the time t until a certain reemission flux Φ_{des} is

[4] The approximation $\exp(x) \approx 1 + x$ is valid for $|x| \ll 1$ or correspondingly $t \gg h^2/4D \approx 100$ s at 300 K.

[5] Inserting the approximation $\exp(x) \approx 1 + x$ for $x \ll 1$ into the definition of the error function in eq. A.26 yields:

$$\operatorname{erf}(x) \approx \frac{2}{\sqrt{\pi}} \left(x - \frac{1}{3}x^3 \right), \qquad x \ll 1, \tag{A.44}$$

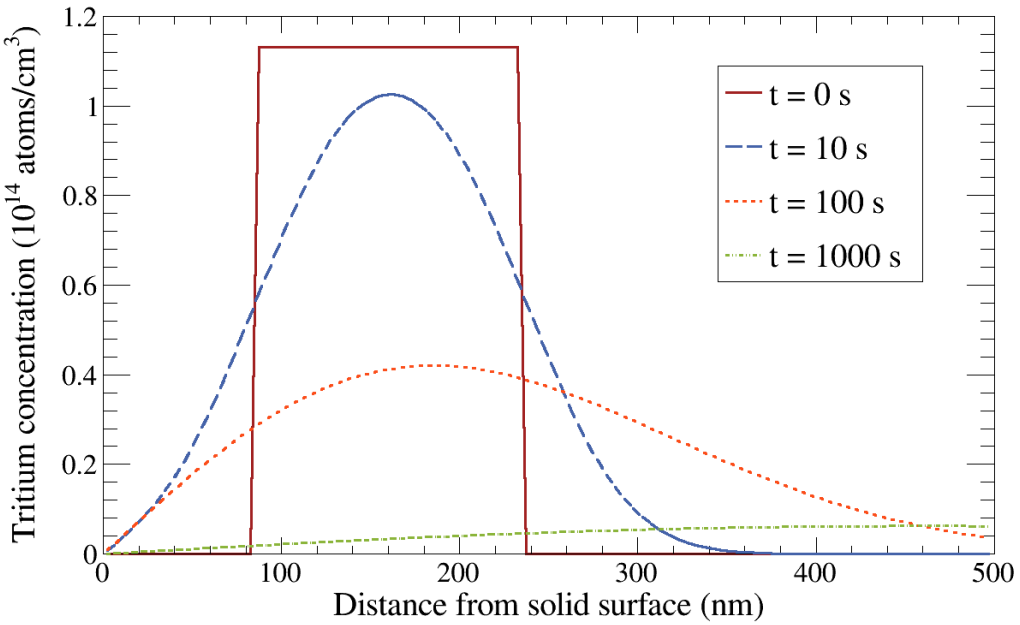

Figure A.3.: **Diffusion limited case of a dissolving tritium concentration in stainless steel.** Due to the comparatively fast desorption, the surface has basically a tritium concentration of zero. The concentration profile at $t = 10$ s corresponds to the state of the tritium concentration right after implantation.

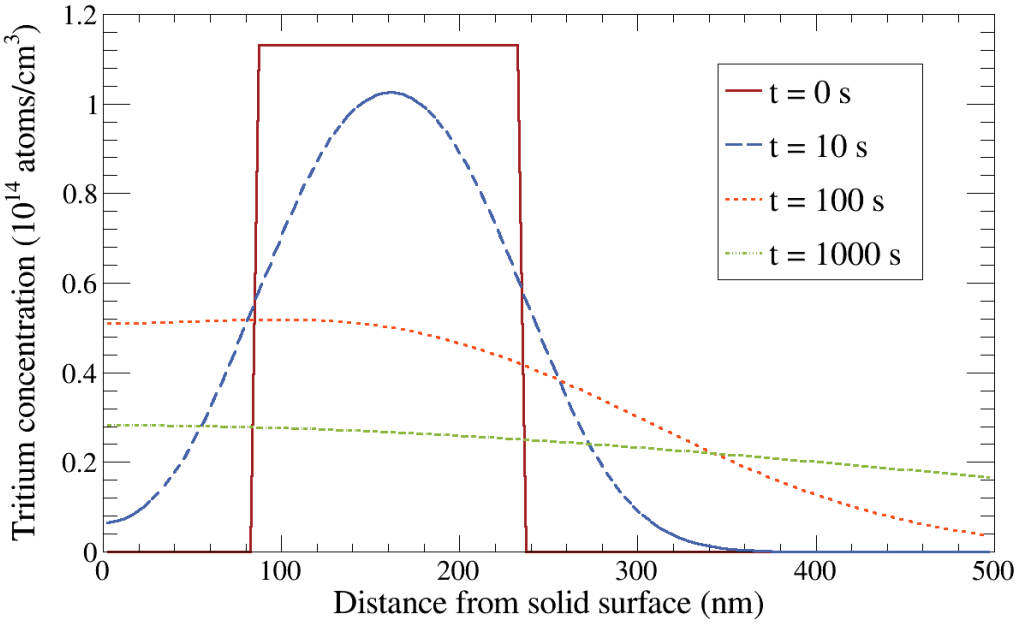

Figure A.4.: **Desorption limited case of a dissolving tritium concentration in stainless steel.** Due to the comparatively slow desorption, the diffusing tritium atoms are reflected at the surface.

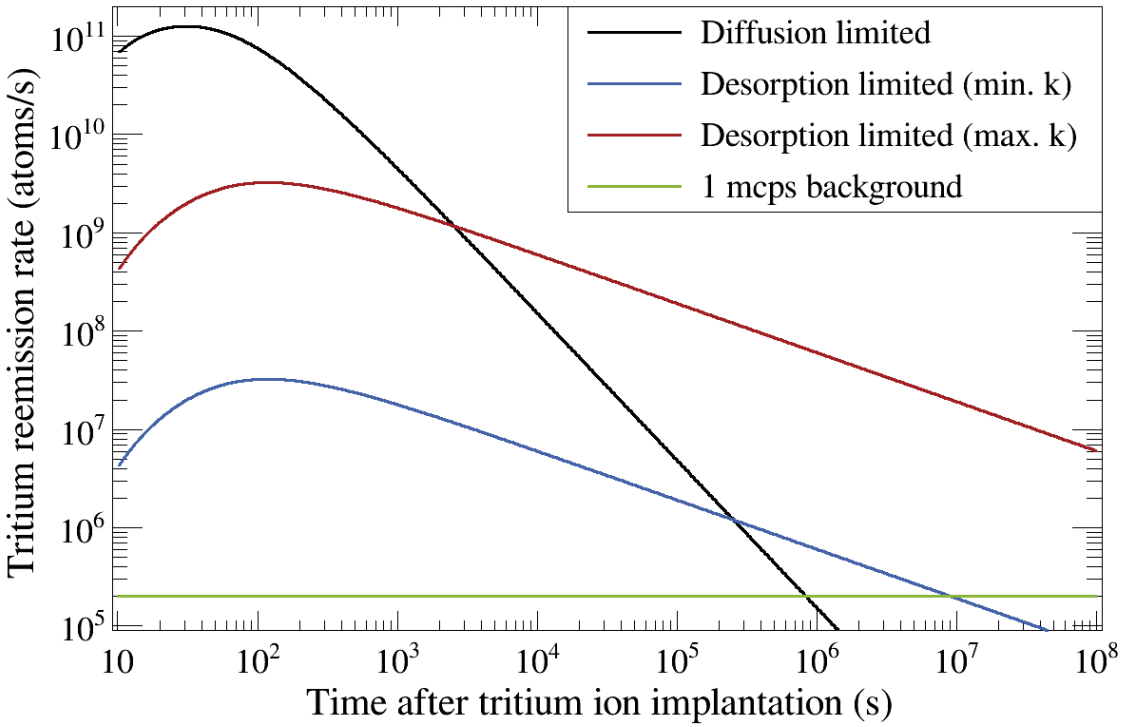

Figure A.5.: **Tritium reemission after 60 s unblocked tritium ion flux into the PS.**

reached:

$$t(\Phi_{\mathrm{des}}) \approx k J_{\mathrm{H_2}} \cdot \left(\frac{(1-R)\cdot(n\Phi\tau)_{\mathrm{im}}}{\sqrt{\pi D}\cdot\Phi_{\mathrm{des}}} \right)^2 . \tag{A.45}$$

Subsiding background after tritium implantation in the PS Figure A.5 shows the tritium reemission rate from eq. A.36 and eq. A.43 for the purely diffusion and purely desorption limited case. In order to account for the uncertainty on the recombination rate constant k of ± 2 orders of magnitude, one line has been drawn each for the assumed maximum and minimum value. Clearly, the amplitude increases by two orders of magnitude as predicted by the dependence $\Phi \propto \sqrt{k}$ in eq. A.43; also, the time to reach the same reemission rate increases according to $t \propto k$ like in eq. A.45. Generally, the linear approximations for the reemission rates appear valid for the predicted threshold $t \gg h^2/4D \approx 100$ s at 300 K.

During the first hour after the tritium implantation, the desorption rate is clearly smaller then the diffusion rate. Desorption is therefore the rate limiting step and the tritium concentration in the solid will therefore behave like shown in figure A.4.

Diffusion becomes rate limiting around the time when the two curves intersect. This is a rather rough approximation, because the desorption limited case will leave a slightly larger tritium concentration below the surface; however, much of it has diffused deep into the bulk up to this time (compare figures A.3 and A.4).

The time to reach a reemission rate which produces only 1 mcps background via tritium decay will therefore lie somewhere between the times for the desorption and the diffusion limited case. If the recombination rate constant k is close to its minimal

presumed value, this time can be narrowed down to between 2 weeks and 4 months after the tritium implantation. However, if the actual value of k should be larger, it would easily require several years until the background decreases to 1 mcps again.

The calculation is rough though, because the actual rate limiting step around 300 K might be trapping at radiation damage sites (see section IV.3.3 and figure IV.10). Trapping could however not be considered analytically and would require numeric simulations. It might very well be that the rate limitation by trapping stresses the time scale of tritium reemission even further. In order to consider trapping, the differential equation of Fick's second law is extended by a trapping term as suggested in [Wil82] and [Ber14].

Other physics issues which have not been considered in full detail are the wide range of possible surface conditions like surface roughness, oxide or water layers; these conditions surely affect the tritium reemission but might not necessarily have been captured by the reemission rate constant k. Further small uncertainties arise from the number of tritium atoms per ion (which could be verified with FT-ICR measurements), diffusion in the solid parallel to the surface, the reflection probability at the surface during the ion bombardment. The reemission rate which causes 1 mcps background has been calculated using the probability factors ϵ, which also contain systematic uncertainties (see section IV.3.1).

If a moderate amount of tritium should have been implanted in the PS and caused background via radioactivity, a possible remedy would be to bake the PS. At 500 K, the diffusion speed is much larger: the tritium atoms would diffuse away from the surface and the reemission rate would be limited by diffusion earlier. No trapping would also occur at this temperature at radiation damage sites with 0.1 eV or 0.3 V trapping potential, as reported by [Wil81]; in contrast, the lattice defects might even be healed by the bake-out.

A.5. Diffusion constant of tritium in stainless steel

The previous section estimated the tritium reemission rate after tritium ion implantation in the PS. For the quantitative calculation, the desorption coefficient of tritium in stainless steel has to be known explicitly. This section will therefore review various results for the diffusion coefficient of hydrogen isotopes in stainless steel 316 (SS-316) along with the very different corresponding measurement conditions. Figure A.6 also shows the results.

1. Tritium for 25°C $< T <$ 222°C by Austin and Elleman [Aus72]:

$$D_{\text{Austin}} = 1.8^{+1.1}_{-0.7} \cdot 10^{-2} \cdot \exp\left(\frac{-0.61 \pm 0.01 \text{ eV}}{kT}\right) \frac{\text{cm}^2}{\text{s}}. \tag{A.46}$$

   The cylindrical steel specimen were recoil injected with ^{3}H using reactor neutrons and transmutation in a surface blanket enriched with ^{6}LiF. Maximum tritium concentration at the surface ranged between $(0.5...7) \cdot 10^{-9}$ ^{3}H by weight. After diffusion annealing, tritium concentration profiles were determined by successive removal of sections of 0.1...20 µm via electropolishing in a chemical solution. The distilled tritium amount was measured with liquid scintillation counting.

   The surfaces were prepared by strain annealing the specimen at 1000°C and 10^{-5} Torr for 1 h and a subsequent air quench. Tritium diffusion in SS-304 was also investigated in this experiment, resulting in the same diffusion coefficient. Tritium release rates from the surface proportional to $\sqrt{Dt}$ yielded apparent diffusion coefficients two to three orders below the bulk diffusion coefficients.

2. Tritium for 603 K $< T <$ 853 K by Sugisaki et. al [Sug85]:

$$D_{\text{Sugisaki}} = 4.2 \cdot 10^{-2} \cdot \exp\left(\frac{-64 \text{ kJ}}{RT}\right) \frac{\text{cm}^2}{\text{s}}. \tag{A.47}$$

   The measurement was performed with a gas absorption method on disc-type specimen of 10 mm diameter and 1 mm thickness, that were exposed to 80 Torr tritium gas at 800°C. After rapidly quenching the specimen to room temperature, the amount of tritium in each specimen was determined amongst others with liquid scintillation counting. The surfaces were prepared by mechanical polishing and bake-out at 1000°C and $2 \cdot 10^{-5}$ Torr for 1 h. Specimen subsequently exposed to air at room temperature showed a delayed diffusion, which was attributed to the effect of a surface oxide layer.

3. Hydrogen for 502 K $< T <$ 863 K by Grant et al. [Gra88]:

$$D_{\text{Grant}} = (7.3 \pm 0.9) \cdot 10^{-3} \cdot \exp\left(\frac{-(6.30 \pm 0.11) \cdot 10^3 \text{ K}}{T}\right) \frac{\text{cm}^2}{\text{s}}. \tag{A.48}$$

   With a pressure modulation technique, the gaseous permeation through foils of 0.05 mm and 0.1 mm thickness was measured. The surfaces were chemically

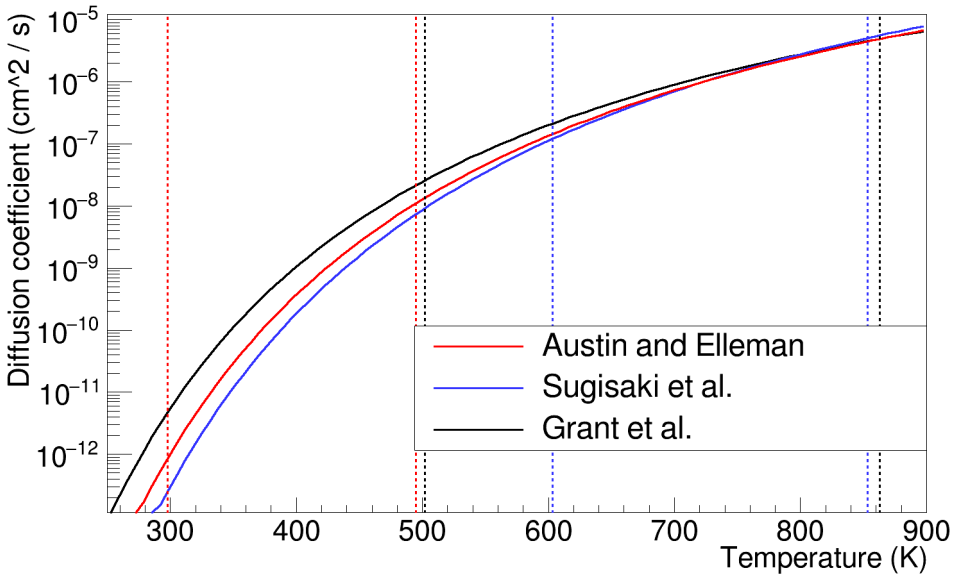

Figure A.6.: **Diffusion constant for hydrogen isotopes in stainless steel 316.** Indicated as dashed lines of the corresponding colour are the ranges inside of which the diffusion coefficients were measured. Beyond these limits, the results were extrapolated. For the modelling of tritium diffusion in the spectrometers, the result from Austin and Elleman will be used, because it was determined with tritium and inside the relevant range of 300 K to 500 K. At 300 K, the three results from [Aus72, Sug85, Gra88] deviate by about half a magnitude.

cleaned followed by in-situ irradiation of both surfaces with a 4 kV hydrogen beam ($5 \cdot 10^{-2}$ A/m^{-2}) for 100 h. However, the same diffusion coefficient was obtained with specimen which were baked after this cleaning in air at 0.1 kPa for 12 h at 973 K in order to produce a stable oxide layer.

4. A fourth value from [Wil81] was not reviewed yet.

For the calculations in appendix A.4, the first result was used because this measurement was performed with actual tritium and within the relevant temperature range for the KATRIN spectrometers:

$$D_{\text{Austin}}(300\ \text{K}) = (1.02^{+0.74}_{-0.56}) \cdot 10^{-12}\ \frac{\text{cm}^2}{\text{s}}, \tag{A.49}$$

$$D_{\text{Austin}}(500\ \text{K}) = (1.28^{+0.84}_{-0.58}) \cdot 10^{-8}\ \frac{\text{cm}^2}{\text{s}}. \tag{A.50}$$

A.6. Drift distance in the dipole electrodes

In the following, the drift distance of a charged particle inside the dipole electrodes will be calculated. This requires some preparatory calculations first, because the drift distance is the product of the drift velocity and the time of stay of the charged particle in the dipole electrode.

Drift velocity v_{DE} Inside an electric field $\vec{E}$ perpendicular to a magnetic field $\vec{B}$, a charged particle will undergo an $\vec{E}\times\vec{B}$-drift. According to eq. III.3 in section III.1.2, the drift velocity is:

$$|\vec{v}_{\mathrm{DE}}| = \left|\frac{\vec{E}\times\vec{B}}{B^2}\right| = \frac{E}{B}. \tag{A.51}$$

In order to calculate the drift velocity inside the DPS dipole electrodes, the absolute values E and B of the electric and magnetic field are required. The magnetic field is rather homogeneous along the dipole electrode; during the neutrino mass measurements, the magnetic field will be at 70% of its nominal strength, which corresponds to 3.5 T. The electric field is inhomogeneous as shown in figure VI.5. Its strength depends on the voltages U_{up} and U_{low} of the upper and lower electrode and on the distance h_{DE} between the two electrodes. Approximating the dipole electrodes as parallel planes leads to:

$$E \approx \frac{e|U_{\mathrm{up}} - U_{\mathrm{low}}|}{h_{\mathrm{DE}}}. \tag{A.52}$$

With that, one can write the drift velocity as:

$$v_{\mathrm{DE}} = \frac{e|U_{\mathrm{up}} - U_{\mathrm{low}}|}{B \cdot h_{\mathrm{DE}}}. \tag{A.53}$$

In the center is $h_{\mathrm{DE}} = 89$ mm, but at the maximum radius is the remaining gap between the electrodes only $h_{\mathrm{DE}} = 20$ mm (compare figure VI.4). Using voltages of $U_{\mathrm{up}} = -5\ V$ and $U_{\mathrm{low}} = -15$ V like for the dipole electrode in BT1 leads to a drift velocity of $v_{\mathrm{DE}} = 32$ m/s when the charged particle is close to the center of the dipole electrode.

Time of stay t_{DE} inside the dipole electrode The time of stay of the charged particle inside the dipole electrode depends on its longitudinal velocity and the length of the dipole electrode. While the length of the dipole electrode is known to be $l_{\mathrm{DE}} = 844$ mm, the longitudinal velocity has to be calculated: for non-relativistic particles[6], the kinetic energy is $E_{\mathrm{kin}} = \frac{1}{2}mv_l^2$. The kinetic energy itself consists of the initial energy E_0 of the particle before it entered the dipole electrode and the energy which it gains when it enters the dipole potential, which is on average $e\langle U\rangle = e|U_{\mathrm{up}} + U_{\mathrm{low}}|/2$. Putting all of this together leads to the time of stay t_{DE} inside the dipole electrode:

$$t_{\mathrm{DE}} = \frac{l_{\mathrm{DE}}}{v_l} \approx \frac{\sqrt{m}\cdot l_{\mathrm{DE}}}{\sqrt{|eU_{\mathrm{up}} + eU_{\mathrm{low}}| + 2E_0}}. \tag{A.54}$$

[6]Non-relativistic calculation is always correct for ions in the DPS dipole electrodes; secondary electrons will gain on the order of 1% of the speed of light.

Drift distance s_{DE} The drift distance s_{DE} is the product of the drift velocity v_{DE} of the particle and its time of stay inside the dipole electrode t_{DE}:

$$s_{\mathrm{DE}} = v_{\mathrm{DE}} \cdot t_{\mathrm{DE}} \approx \frac{\sqrt{m}}{B} \cdot \frac{l_{\mathrm{DE}}}{h_{\mathrm{DE}}} \cdot \frac{|eU_{\mathrm{up}} - eU_{\mathrm{low}}|}{\sqrt{|eU_{\mathrm{up}} + eU_{\mathrm{low}}| + 2E_0}}. \tag{A.55}$$

The particle species enters only via its mass m. For a T_3^+ ion, the mass is $m \approx 9\ \mathrm{GeV/c^2}$. In the center of the dipole electrode in BT1 (-15 V and -5 V), this ion will be drifted during neutrino mass measurements (3.5 T) by about $s_{\mathrm{DE}} = 1.9$ mm. Close to the boarder of the dipole electrode, the drift distance is however $s_{\mathrm{DE}} = 8.5$ mm.

For comparison: the radius of the dipole electrode is 44.5 mm and the straight distance from the center to the lobes is 40 mm. The width of the lobes is about 6 mm. These estimates can be used to determine the ion detection probability of the current measurement at the dipole electrodes; this will be done in the following section.

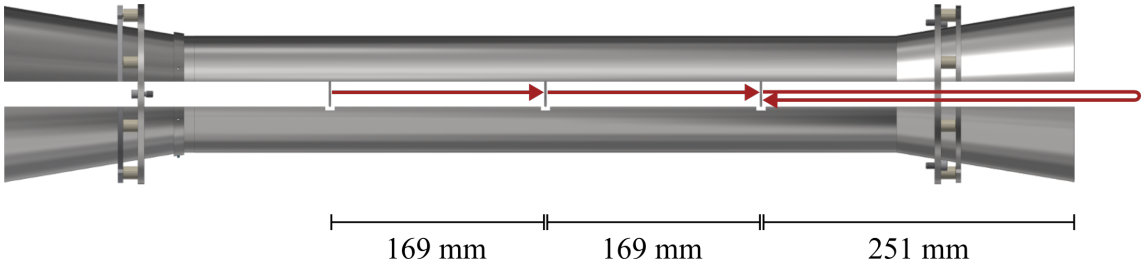

Figure A.7.: **Ion detection probability.** The distance between to lobes is 169 mm. If the ion is trapped in the electrode, it will experience the dipole field over a distance of 502 mm before it can hit another lobe.

A.7. Ion detection probability of the dipole electrodes

Ions are removed with the dipole electrodes via $E \times B$-drift: eventually all ions are neutralised on some conducting surface. But this does not necessarily need to be the dedicated lobes which have been welded onto the dipole halves: those lobes are intended to be hit by the ions due to their longitudinal motion through the dipole electrode. However, if the ion is drifted too far across the flux tube before reaching another lobe, it can slip outside the dipole. This mechanism will be considered in the following in order to calculate the ion detection efficiency of the dipole electrodes.

For these calculations, several rough but conservative assumptions will be made. The drift velocity of the ions is calculated with the electric field in the 20 mm gap between the upper and lower electrode, because this is about the field which the ions experience before they reach the lobes. Further, it is assumed that ions cannot be detected once they get outside the dipole electrodes, because they neutralise on cables or the mounts of the dipole electrodes. Outside the dipole, the ion is assumed to be drifted perpetually although the shape of the electric field changes; likewise, distortions of the electric field close to the lobes are neglected. Finally, the curvature of the electric field inside the dipole is neglected and the drift of the ions is assumed to be strictly horizontal. An exact determination of the detection efficiency would require simulations, for example with KASSIOPEIA.

Ion detection probability In the previous section, the drift distance of the ions has been calculated as a function of the dipole voltages (see eq. A.55). Now, the ion detection probability can be obtained by comparing the drift distance to the 6 mm width of the lobes: if the drift distance is larger than the lobe width, a certain fraction of ions can slip outside without being detected. These are stated as the ion detection probabilities in table A.2. The calculation assumes T_3^+ ions with no initial kinetic energy.

Ion detection with each dipole individually Each ion has three chances to hit a lobe while moving through the dipole electrode (see figure A.7): two times in the center, where the lobes are $l = 169$ mm apart, and a third time after 502 mm, assuming that it is reflected and returns to the dipole. This leads to two different ion detection probabilities for the 169 mm and 502 mm distances. These probabilities

Table A.2.: **Ion detection probabilities.** The first three rows state the nominal voltage settings of the dipole electrodes. From the resulting drift distances, the ion detection probabilities can be calculated in comparison with the lobe width of 6 mm: first for the distances of 169 mm and 502 mm between two lobes (see figure A.7), then for the whole dipole electrode. If all four dipoles are at nominal voltage at the same time, their ion detection probability needs to be multiplied with the ion removal probability.

Dipole electrode	BT1	BT2	BT3	BT4
Upper electrode	−15 V	−35 V	−85 V	−175 V
Lower electrode	−5 V	−5 V	−5 V	−5 V
Each dipole individually				
Drift distance on $l = 169$ mm	1.71 mm	3.62 mm	6.44 mm	9.67 mm
Detection probability	100%	100%	93%	62%
Drift distance on $l = 502$ mm	5.17 mm	10.76 mm	19.12 mm	28.74 mm
Detection probability	100%	56%	31%	21%
Total detection probability	100%	74%	56%	37%
All four dipoles together				
Drift distance on $l = 846$ mm	8.53 mm	18.09 mm	32.15 mm	48.31 mm
Removal probability	8%	17%	30%	45%
Total detection probability	8%	12%	17%	17%

are averaged and weighted with the respective distance in order to obtain the total ion detection probability of each dipole electrode.

This calculation assumes for the sake of simplicity that the ions are removed after multiple transitions of a single dipole electrode. This is the case if ions are trapped, for example after scattering with neutral gas inside the negative potential of the dipole. More importantly, the assumption is valid for the evaluation of the First Tritium measurements, because inadvertent blocking potentials in the DPS prevented the ions from reaching the other dipole electrodes (see section IX.3). In this case, the ion detection probability was in fact 100%.

Ion detection with all four dipoles at the same time During future measurements with larger tritium activity, the ions from the WGTS are presumed to reach all four dipole electrodes. The relation between the total ion flux from the WGTS and the measured ion currents on the dipole electrodes depends on the ion detection probability and the ion removal probability of each dipole. This ion removal probability is taken as the relative drift distance of an ion inside the respective dipole, as compared to the combined drift distance of all four dipoles. Multiplying the probabilities for ion removal and detection leads to the total ion detection probability during operation of all four dipole electrodes.

Table A.2 shows that the dipole in BT4 has a large ion removal probability[7]; but because of the poor ion detection probability, the expected ion current is the same as on the dipole in BT3 and only a factor 2 larger than the on the dipole in BT1. Although the complete ion flux is removed, only a total of 54% of the ions can be detected.

[7]This assumes that ions can reach the lobes, although they are at the lower and more positive electrode in BT4.

A.8. Background due to dipole electrode potentials

The positive ions which will be blocked by the ring electrodes need to be removed with dipole electrodes in the DPS in order to prevent systematic effects on the neutrino mass measurements. But the negative dipole potentials can in turn create an energy dependent background (see section VI.2.2): it changes with the retarding potential of the MS.

The spectrum of beta electrons, which are created inside the negative potential, can be thought of as a second beta spectrum which is superimposed to the beta spectrum from the WGTS. This second spectrum is weaker due to the much smaller tritium density, but its end point energy E_0 is shifted to larger retarding potentials. Because the tritium spectrum increases as $(E_0 - E)^3$ with smaller electron energies E, the distortion of the measured tritium spectrum grows quickly.

The integrated rate R of the tritium beta spectrum close to its end point $E_0 \approx$ 18,572 eV can be approximated with [Ott08]:

$$R(\epsilon) \approx a \cdot \epsilon^3 + b, \tag{A.56}$$

where $\epsilon = E_0 - E$ is the reduced energy of the beta electrons, which have a total kinetic energy E. The constant b describes the background, which will be neglected in the following considerations; but the amplitude a has to be estimated in order to calculate the absolute value of the background. Obviously, the amplitude depends on the total integrated rate R_{tot}, which is measured at an electron energy $E = 0$ or $\epsilon = E_0$. In a very rough estimate, the approximation from eq. A.56 will be extended to the complete integrated tritium beta spectrum[8] so that the amplitude becomes $a = R_{\mathrm{tot}}/E_0^3$. With this, the integrated beta electron rate becomes:

$$R(\epsilon) = R_{\mathrm{tot}} \cdot \left(\frac{\epsilon}{E_0}\right)^3. \tag{A.57}$$

If now the electrons are created in a negative offset potential, the end point energy of the spectrum will be shifted as $E_0 \to E_0 + \Delta E$. With that, the integrated rate becomes[9]:

$$\begin{aligned} R(\epsilon + \Delta E) &= R_{\mathrm{tot}} \cdot \left(\frac{\epsilon + \Delta E}{E_0}\right)^3 \\ &= \underbrace{R_{\mathrm{tot}} \cdot \left(\frac{\epsilon}{E_0}\right)^3}_{S} + \underbrace{\frac{R_{\mathrm{tot}}}{E_0^3} \cdot \left[3\,\epsilon^2\,\Delta E + 3\,\epsilon\,(\Delta E)^2 + (\Delta E)^3\right]}_{B}. \end{aligned} \tag{A.58}$$

[8] Obviously, not the complete tritium beta spectrum follows this approximation because the differential spectrum does not increase monotonically, but the estimate still yields usable results. While the estimate corresponds to $a \approx 188 \cdot 10^{-3}$ Hz/eV^3, the design report uses $a \approx 1.1 \cdot 10^{-3}$ Hz/eV^3 [CDR04]. Because a is below the third root (see below), the used approximation leads to a roughly 6 time stricter voltage limit than the value from the design report.

[9] The shift of the end point does not affect the E_0 in the normalisation, which is actually the width of the energy spectrum.

The first term corresponds to the unshifted signal $S = R(\epsilon)$ from the DPS electrons, whereas the following terms constitute the background B due to the shifted spectrum. This allows to write the background as:

$$B = \frac{R_{\mathrm{tot}}}{E_0^3} \cdot \left[(\epsilon + \Delta E)^3 - \epsilon^3\right]. \tag{A.59}$$

In order to derive a limit on the dipole voltage, the above equation has to be resolved for the energy shift $\Delta E = e\Delta U$, which corresponds to the offset voltage ΔU of the dipole electrode:

$$e\Delta U = \Delta E = \left[\left(B \cdot \frac{E_0^3}{R_{\mathrm{tot}}} + \epsilon^3\right)^{1/3} - \epsilon\right] \cdot f. \tag{A.60}$$

The factor $f = 1.6$ accounts for the dipole potential of the electrodes[10]; so far, the calculation had treated the dipole electrodes only in monopole mode.

In order to calculate the allowed energy shift, the total beta electron rate R_{tot} has to be known for each DPS beam tube. At nominal column density $\mathcal{N}$, a flux of $2 \cdot 10^{10}$ beta electrons per second into the MS is expected (see section III.1.3). Inside the WGTS-F beam tube 2, the relative column density will be about $1.5 \cdot 10^{-4}\, \mathcal{N}/\mathcal{N}$, according to [Kuk16]. Consequently, a total rate of $R_{\mathrm{tot}} = 1.5 \cdot 10^7$ cps is expected from beam tube 2 of the WGTS-F. In each consecutive beam tube of the DPS, the pressure and likewise the electron rate are assumed[11] to decrease by about a factor 5.

Table A.3 shows the limits for the dipole voltages ΔU in the first four beam tubes of the DPS at various retarding potentials ϵ in the MS. For the background, an arbitrary but conservative limit of $B = 10$ mcps was chosen. The set voltages of the dipole electrodes are derived from the limits at the maximum MS retarding potential of 30 eV; this yields of course the largest backgrounds because the beta spectrum was approximated with a monotonously increasing ϵ^3 law. Dedicated simulations will be necessary in order to investigate the effect of the offset voltage on the beta spectrum around the end point and the neutrino mass imprint. Only then, the actual effect on the neutrino mass measurements can be assessed.

[10] Simulation by Ferenc Glück.
[11] Internal communication with Joachim Wolf.

Table A.3.: **Voltage limits for dipole electrodes in the DPS beam tubes.** The limits were derived for a background of $B = 10$ cmps.

MS retarding potential (eV)	30	5	0	−5	dipole set voltage
DPS beam tube 1 (V)	10.3	36.5	44.4	52.4	10
DPS beam tube 2 (V)	33.8	67.9	75.9	83.9	35
DPS beam tube 3 (V)	83.9	121.8	129.8	137.8	85
DPS beam tube 4 (V)	174.7	213.9	221.9	229.9	175

A.9. Stability requirements for the voltage supply of ring and dipole electrodes

A time-dependent electric field is not conservative and can change the energy of a traversing charged particle. By this effect, fluctuating potentials at the ring and dipole electrodes could change the beta electron energy (see section VI.2.2).

In order to prevent a smearing of the beta spectrum, the ring and dipole electrodes need a stable voltage supply (see sections VI.2.2 and VI.2.4). The stability requirements will be derived in the following for the dipole electrodes, but can easily be transferred to the ring electrodes by changing the electrode length accordingly.

Theory The change of a charged particle's energy by a time-dependent electric field can be described by the Lagrange mechanism. According to [Lan60], the general form of the Lagrangian for a single particle which moves with the velocity $\dot{q}$ through an external field V is:

$$L = \frac{1}{2}m\dot{q}^2 - V(q,t). \tag{A.61}$$

If the Lagrangian depends explicitly on time, the energy E of the particle will be changed:

$$\frac{\mathrm{d}E}{\mathrm{d}t} = \frac{\mathrm{d}}{\mathrm{d}t}\left(\dot{q}\frac{\partial L}{\partial \dot{q}} - L\right) = \frac{\partial L}{\partial t} = -\frac{\partial V(q,t)}{\partial t}. \tag{A.62}$$

The potential energy V generally depends on the velocity $\vec{v}$:

$$V = q \cdot (\phi - \vec{v} \times \vec{A}), \tag{A.63}$$

but because the particles move parallel to the magnetic field, $\vec{v} \parallel \vec{B} = \vec{\nabla} \times \vec{A}$, the term with the magnetic vector potential $\vec{A}$ becomes zero. Now the potential energy depends only on the electric potential ϕ and the particle charge q [Bit04]. Without loss of generality, its time variation can be assumed to be harmonic with angular frequency ω [Bit04]:

$$\phi(t) = \phi_0 \exp(-i\omega t). \tag{A.64}$$

In order to obtain the energy change ΔE for fluctuations with arbitrary frequencies ω, eq. A.62 needs to be integrated (only the real part of $\phi(t)$ is considered):

$$\Delta E = -e(\phi(t_2) - \phi(t_1)) < 2e\phi_0 \sin(\omega \Delta t), \tag{A.65}$$

where the charged particle stays inside the time-dependent field from t_1 to t_2 over the time interval $\Delta t = t_2 - t_1$.

Interpretation Eq. A.65 can be interpreted as follows: when the electron enters the negative electric potential, it is decelerated according to the potential's amplitude ϕ_0. While the electron stays inside the potential, the amplitude of the potential changes $\phi_0 \rightarrow \phi_0'$, but the energy of the electron remains the same. When the electron leaves the potential again, it will be accelerated according to the new amplitude ϕ_0'l.

The size of the energy shift ΔE also depends on the time of stay Δt of the electron inside the potential and on the speed of the potential variation, which is described

with the angular frequency ω. If the electron's time of stay inside the potential is shorter than the period of the potential's variation, the energy change is described by eq. A.65. However, if the electron stays inside the potential for at least one period of the potential's variation, the full energy change might be in the worst case $\Delta E = 2e\phi_0$.

Calculation of the stability requirements For the neutrino mass measurements, fluctuations of the beta electron energy by $\Delta E = 5$ meV are chosen to be acceptable. This maximum energy shift occurs if the electron experiences the fluctuation from peak-to-peak, where $U_{\mathrm{pp}} = 2\phi_0$. Translating the energy limit into a limit on a peak-to-peak voltage ripple leads to $\Delta U_{\mathrm{pp}} = 5$ mVpp.

The relevant beta electrons with $E = 18.6$ keV stay inside the $\Delta s = 844$ mm long dipole electrodes for a time $\Delta t = 1.0 \cdot 10^{-8}$ if their momentum is completely parallel to the magnetic field. However, the pitch angle of the detected beta electrons can be up to $\theta_{\mathrm{max}} = 50.8°$; then their time of stay increases to $\Delta t = 1.6 \cdot 10^{-8}$.

For electrons with the maximum pitch angle follows from $\omega \Delta t = \pi/2$ (see eq. A.65) a threshold frequency of about $f = 15$ MHz. The angular frequency $\omega = 2\pi \cdot f$ was replaced by f for the case of non-harmonic fluctuations.

With these considerations, eq. A.65 can be written explicitly for the two cases that the fluctuation is faster or slower than the corresponding time of stay of the electron in the potential:

$$f > 15 \text{ MHz} : U_{\mathrm{pp}} < 5 \text{ mVpp}, \tag{A.66}$$

$$f < 15 \text{ MHz} : U_{\mathrm{pp}} < \frac{5 \text{ mVpp}}{\sin(2\pi f \Delta t)}. \tag{A.67}$$

In these expressions, the maximum potential variation $2\phi_0$ was replaced with the peak-to-peak voltage ripple U_{pp} on the dipole electrodes.

A.10. Statistical analysis of current measurements

This section describes the statistical analysis which was used throughout this thesis, mainly for the analysis of the current measurements (see section VII.2). First, the basic concepts of the mean current, its standard deviation and the standard deviation of the measurement current will be introduced. Then these terms are illustrated for a Gaussian distribution; as will be discussed afterwards, the measured ion current is actually expected to follow a Gaussian distribution. These results allow to describe the evaluation of a small current signal in a long term measurement. All of these considerations are based on [Cow98] unless otherwise noted.

Mean current and standard deviations Any current measurement will be subject to statistical fluctuations due to thermal noise. The results of the current measurements will therefore be stated in terms of the mean current and its standard deviation. In order to calculate the standard deviation of the mean, the standard deviation of the current population has to be calculated.

The mean current μ_x can be estimated[12] with the arithmetic mean of the measured current values $\{x_i | i = 1, \dots n\}$:

$$\hat{\mu}_x = \frac{1}{n} \sum_{i=1}^{n} x_i. \tag{A.68}$$

The statistical uncertainty of $\hat{\mu}_x$ can be estimated with the standard deviation of the mean $\hat{\sigma}_{\hat{\mu}}$, which in turn relates to the number n of measurements in the data set and the estimated sample standard deviation $\hat{\sigma}_x$:

$$\hat{\sigma}_{\hat{\mu}} = \frac{\hat{\sigma}_x}{\sqrt{n}}. \tag{A.69}$$

The sample standard deviation $\hat{\sigma}_x$ can be estimated from the measurement data:

$$\hat{\sigma}_x = \sqrt{\frac{1}{n-1} \sum_{i=1}^{n} (x_i - \hat{\mu}_x)^2}. \tag{A.70}$$

The sample standard deviation $\hat{\sigma}_x$ is a property of the measurement setup and as such remains constant under stable measurement conditions. With eq. A.69, the sample standard deviation allows to predict the number of measurements which are necessary to reach a certain standard deviation of the mean current, or in other words a certain measurement uncertainty. It is therefore useful to estimate the uncertainty of $\hat{\sigma}_x$ with $\hat{\sigma}_{\hat{\sigma}x}$, the standard error of the sample standard deviation. For large numbers of measurement values n, one can use [Ahn03]:

$$\hat{\sigma}_{\hat{\sigma}x} = \frac{\hat{\sigma}_x}{\sqrt{2\,(n-1)}}. \tag{A.71}$$

As an alternative to the analytic calculation, the mean and its standard deviation can be determined by fitting a constant to the measured data. This can be done for example with a linear fit with zero slope or with a polynomial fit of zeroth order.

[12] Estimators are denoted with a hat.

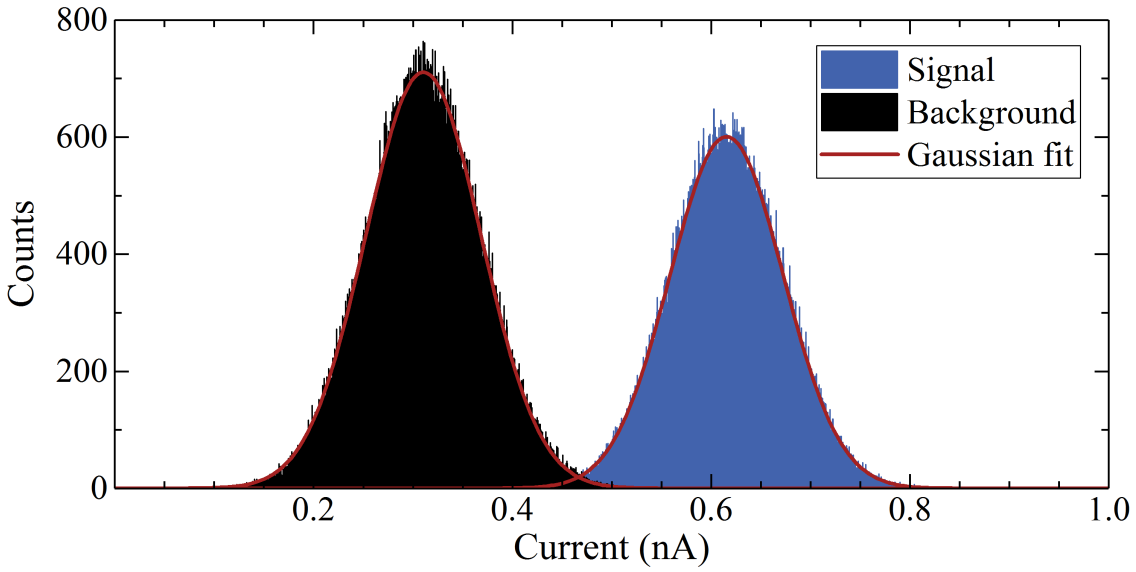

Figure A.8.: **Histogram of the measurement currents from figure VII.8.** Both populations have a Gaussian distribution, but the mean value is clearly shifted in presence of an ion signal. A bin width of 0.5 pA was chosen, corresponding to the minimum uncertainty of the rbd 9103 picoamperemeter in the measurement range of 2 nA.

Illustration with a Gaussian distribution To illustrate the mean current μ_x, its standard deviation σ_μ and the population variance σ_x^2, the current signal from figure VII.8 can be displayed as histogram like in figure A.8. As expected for thermally induced noise, the population or probability density $\rho_{\mathrm{bg}}(x)$ of the current values x_i follows a Gaussian distribution:

$$\rho_{\mathrm{bg}}(x) = \mathrm{Gauss}\left(x \mid \mu_{x,\mathrm{bg}}, \sigma_{x,\mathrm{bg}}^2\right) = \frac{1}{\sqrt{2\pi\sigma_{x,\mathrm{bg}}^2}} \exp\left(-\frac{(x-\mu_{x,\mathrm{bg}})^2}{2\sigma_{x,\mathrm{bg}}^2}\right). \tag{A.72}$$

The peak of the Gauss shape is at the mean value μ_x and the FWHM of this symmetric distribution is two times the square root of the population variance σ_x^2. As usually with Gaussian distributed random variables, 68% of the measured currents x_{meas} will lie in this interval:

$$P(\mu_x - \sigma_x \leq x_{\mathrm{meas}} \leq \mu_x + \sigma_x) = 68\%. \tag{A.73}$$

The population depends on the true value of μ_x, while equation A.68 only states its estimator $\hat{\mu}_x$. But as any other random variable, this estimator is subject to statistical fluctuations. However, due to the large number of measurements, the distribution of the experimental values of $\hat{\mu}_x$ is again Gaussian. Then, there is a 68% chance that the determined estimator $\hat{\mu}_x$ lies in an interval of width $2\hat{\sigma}_x$ around the true value μ_x:

$$P(\mu_x - \hat{\sigma}_x \leq \hat{\mu}_x \leq \mu_x + \hat{\sigma}_x) = 68\%. \tag{A.74}$$

Due to these relations, the mean current and its standard deviation can also be determined from a Gaussian fit to a histogram of the current data, as can the population variance. The main drawback of this method compared to analytic expressions

in eq. A.68 to A.70 is the additional uncertainty from the binning, which is hard to quantify. As a rule of thumb, the bin width should be chosen on the order of the measurement uncertainty of the amperemeter.

Probability density in presence of an ion signal When ions are neutralised on the detectors, the measured current x_{meas} consists of a contribution from the background x_{bg} and of a contribution from the ion signal x_{s}:

$$x_{\mathrm{meas}} = x_{\mathrm{bg}} + x_{\mathrm{s}}. \tag{A.75}$$

Since the signal consists of charges which arrive rather independently on the detector surface, their probability density is expected to be a Poisson distribution. Because the current measurements can only detect a large number of charged particles ($> 10^4$), the Poisson distribution can be treated in good approximation as a Gaussian; actually, the computational effort even requires it. The only parameter of this Gauss distribution is the number of charges ν:

$$\rho_{\mathrm{s}}(x) = \mathrm{Poisson}\left(x \mid \nu\right) = \mathrm{Gauss}\left(x \mid \nu, \nu\right). \tag{A.76}$$

In the above equation, ν is equal to both the expectation value μ and the variance σ^2. Because the units of μ and σ should match, this is obviously only possible when ν is dimensionless. For an application on the measured values, which are currents with unit Ampere, the dimensionless number of particles ν can be converted using the Coulomb number $\mathrm{C} = 6.2415 \cdot 10^{18}$ elementary charges per Coulomb [FeP09] and the measurement time t_{meas}:

$$\mu_{x,\mathrm{s}} = \frac{\nu}{\mathrm{C} \cdot t_{\mathrm{meas}}}, \tag{A.77}$$

$$\sigma_{x,\mathrm{s}} = \frac{\sqrt{\nu}}{\mathrm{C} \cdot t_{\mathrm{meas}}}. \tag{A.78}$$

Inserting these equations into eq. A.76 returns the Gaussian probability density for the signal current:

$$\rho_{\mathrm{s}}(x) = \mathrm{Gauss}\left(x \mid \mu_{x,\mathrm{s}}, \sigma^2_{x,\mathrm{s}}\right) = \frac{\mathrm{C} \cdot t_{\mathrm{meas}}}{\sqrt{2\pi\nu}} \cdot \exp\left(-\frac{(x \cdot \mathrm{C} \cdot t_{\mathrm{meas}} - \nu)^2}{2\nu}\right). \tag{A.79}$$

The measured current is the sum of the background current and of the signal current as stated in eq. A.75. Therefore, the probability density $\rho_{\mathrm{meas}}(x)$ of the measured current will be the convoluted probability densities of the background current from eq. A.72 and of the signal current from eq. A.79. Since both constituent densities are Gaussians, the resulting probability density of the measured current is also a Gaussian with the sum of their expectation values and variances:

$$\begin{aligned}
\rho_{\mathrm{meas}}(x) &= \rho_{\mathrm{bg}}(x) * \rho_{\mathrm{s}}(x) && \text{(A.80)}\\
&= \mathrm{Gauss}\left(x \mid \mu_{x,\mathrm{bg}},\ \sigma^2_{x,\mathrm{bg}}\right) * \mathrm{Gauss}\left(x \mid \mu_{x,\mathrm{s}},\ \sigma^2_{x,\mathrm{s}}\right) && \text{(A.81)}\\
&= \mathrm{Gauss}\left(x \mid \mu_{x,\mathrm{bg}} + \mu_{x,\mathrm{s}},\ \sigma^2_{x,\mathrm{bg}} + \sigma^2_{x,\mathrm{s}}\right) && \text{(A.82)}\\
&= \mathrm{Gauss}\left(x \mid \mu_{x,\mathrm{meas}},\ \sigma^2_{x,\mathrm{meas}}\right). && \text{(A.83)}
\end{aligned}$$

Evaluation of a small current signal in a long term measurement In the analysis of a current signal, three questions are of primary interest:

- How large is the current signal? The answer is given by the estimate of the signal mean current $\hat{\mu}_{x,\mathrm{s}}$.
- To which uncertainty is the signal known? This is quantified by the estimated standard deviation $\hat{\sigma}^2_{\mu,\mathrm{s}}$ of the mean signal current.
- How significant is the finding – can it actually be distinguished from background? As an indicator, the p-value can be calculated.

The mean value $\hat{\mu}_{x,\mathrm{meas}}$ of the measured current can be calculated according to equation A.68. If the mean value $\hat{\mu}_{x,\mathrm{bg}}$ of the background current was previously determined with a background measurement, the mean signal current follows as:

$$\hat{\mu}_{x,\mathrm{s}} = \hat{\mu}_{x,\mathrm{meas}} - \hat{\mu}_{x,\mathrm{bg}}. \tag{A.84}$$

If the standard deviations of the mean current were determined for the measurement of interest and for the background according to eq. A.69, the standard deviation of the signal mean current will be:

$$\hat{\sigma}^2_{\hat{\mu},\mathrm{s}} = \hat{\sigma}^2_{\hat{\mu},\mathrm{meas}} + \hat{\sigma}^2_{\hat{\mu},\mathrm{bg}}. \tag{A.85}$$

Since at least a couple of ten thousand ions are necessary for a detection, the standard deviation of small signals will be negligible (compare eq. A.77 and A.78). The standard deviation of the signal mean for small signals can thus be estimated with $\hat{\sigma}_{\hat{\mu},\mathrm{s}} \approx \sqrt{2} \cdot \hat{\sigma}_{\hat{\mu},\mathrm{bg}}$.

Small signals will be hard to distinguish from a background fluctuation. The power of a test to separate both hypotheses can be quantified with the p-value:

$$p = \int_{\mu_{x,\mathrm{s}}}^{\infty} \mathrm{Gauss}\left(x \mid \hat{\mu}_{x,\mathrm{bg}},\ \hat{\sigma}^2_{x,\mathrm{bg}}\right) \mathrm{d}\, x \tag{A.86}$$

$$= 1 - \mathrm{CDF}\left(\hat{\mu}_{x,\mathrm{s}} \mid \hat{\mu}_{x,\mathrm{bg}},\ \hat{\sigma}^2_{x,\mathrm{bg}}\right). \tag{A.87}$$

CDF is the cumulative distribution function of the Gaussian probability density. Mind that the p-value for any possible signal can already stated before the measurement, because it otherwise depends only on background parameters.

A.11. Probability for automatic closing of the valve V4 between CPS and PS due to ions

The ion flux into the PS is constantly monitored via the PS cone current (see section VII.2.4) – if an ion flux above a certain threshold is detected for three measurements in a row, the valve V4 between the CPS and the PS will be closed automatically. Due to the statistical fluctuations of the measurement current, the probability for a closing of the valve depends not only on the trigger threshold and the actual ion flux, but also on the measurement time. These relations will be investigated in the following with statistical means in order to minimise the risk of an unnecessary interruption of the neutrino mass measurements.

The measured current consists of the mean current $\mu_{x,\mathrm{bg}}$ and a fluctuating noise which can be described by the standard deviation $\sigma_{x,\mathrm{bg}}$. The closing of the valve between CPS and PS will be triggered as soon as a current x_{meas} above the current threshold x_{trig} is measured:

$$x_{\mathrm{meas}} > x_{\mathrm{trig}} = \hat{\mu}_{x,\mathrm{bg}} + a \cdot \hat{\sigma}_{x,\mathrm{bg}}, \tag{A.88}$$

where $a > 0$. The mean current and the standard deviation of the current can be estimated before the monitoring phase from background measurements, but their validity should be checked regularly, preferably with the data taken during each maintenance interval between the neutrino mass runs.

Obviously, the choice of the trigger thresholds influences the probability of a false alert in a trade-off with safety demands:

- The lower the threshold, the larger the probability of a false alert (false positive).
- The higher the threshold, the larger the probability that an actual ion emergency is not discovered (false negative).

The probability $P(1,1)$ to make a single current measurement above the trigger threshold x_{trig} becomes:

$$P(1,1) = \int_{x_{\mathrm{trig}}}^{\infty} \mathrm{d}\,x \;\; \mathrm{Gauss}\left(x \mid \hat{\mu}_{x,\mathrm{s}} + \hat{\mu}_{x,\mathrm{bg}},\; \hat{\sigma}^2_{x,\mathrm{bg}}\right) \tag{A.89}$$

$$= 1 - \mathrm{CDF}\left(x_{\mathrm{trig}} \mid \hat{\mu}_{x,\mathrm{s}} + \hat{\mu}_{x,\mathrm{bg}},\; \hat{\sigma}^2_{x,\mathrm{bg}}\right), \tag{A.90}$$

with the parameters:

- The trigger threshold x_{trig} is set to 5 pA, which corresponds to about $3 \cdot 10^7$ ions/s.
- The mean current $\hat{\mu}_{x,\mathrm{s}} + \hat{\mu}_{x,\mathrm{bg}}$ is the sum of the signal and background currents, according to appendix A.10. During First Tritium, the PS background current was found to be negligible.
- The variance $\sigma^2_{x,\mathrm{bg}}$ of the background current population is known from the First Tritium measurements to be $(750\ \mathrm{fA})^2$. Due to the large number of measured ions, the variance of the signal can be neglected (see appendix A.10).

In order to prevent a false alert by the numerous spikes on the PS current measurement during First Tritium, the valve between CPS and PS would have only been closed if a current above the trigger threshold was measured three times in a row[13]. The probability to trigger such an emergency is thus:

$$P(3,1) = (P(1,1))^3. \tag{A.91}$$

This relationship can be verified with the binomial distribution for a number of occurences k given a total number of measurements n and a probability p for the occurence:

$$B(k|p,n) = \binom{n}{k}\ p^k\ (1-p)^{(n-k)}. \tag{A.92}$$

The same distribution allows to take into account that the measurement is repeated about every second. After a number of measurements n, an ion alert is given if $k > 1$. The probability for this occurence is given by $P(3,1)$. In order to simplify the consideration of multiple occurences during the measurment interval, first the probability $\neg P(3,n)$ for no occurence will be calculated:

$$\neg P(3,n) = B(0|P(3,1),n) = (1 - P(3,1))^n. \tag{A.93}$$

Consequently, the probability for an ion alert after n measurements is:

$$P(3,n) = 1 - (\neg P(3,n)). \tag{A.94}$$

Putting all of these results together yields the explicite form of the ion alert probability in dependence of the number of measurements n and the trigger threshold x_{trig}:

$$P(3,n) = 1 - \{1 - [1 - \text{CDF}\left(x_{\text{trig}} \mid \hat{\mu}_{x,\text{s}} + \hat{\mu}_{x,\text{bg}},\ \hat{\sigma}^2_{x,\text{bg}}\right)]^3\}^n. \tag{A.95}$$

The result is visualised in figure VII.6, assuming a detection frequency of one per second. The probability for a false alert during the neutrino mass measurements could be obtained with the standard deviation of the background $\sigma^2_{x,\text{bg}} = 750$ fA, the trigger threshold of $x_{\text{trig}} = 5$ pA and negligible mean current from signal and background. After a net measurement time of 3 years for the neutrino mass, about $n = 10^8$ measurements would have been made. However, the resulting value is extremely small.

[13]The measurement frequency was about one per second.

Figure A.9.: **Simplified model of the ELIOTT vacuum setup at the rear section.** The conductance C and the gas flow Q determine the pressures in the three volumes.

A.12. Absolute pressure in ELIOTT during First Light

The absolute pressure inside the ELIOTT ion source at the rear section during First Light does not need to be known for most of the analysis in chapter VIII; instead, the pressure which was measured at the buffer volume in the deuterium gas supply can be used. Only the determination of the mean free path of ions inside ELIOTT requires to know the absolute pressure: it is about 40% of the pressure in the deuterium supply, as will be shown in the following.

For the derivation of the absolute pressure, it is useful to separate the ELIOTT vacuum setup into three volumes as shown in figure A.9:

- the buffer vessel in the deuterium supply, in which the pressure could be measured,
- the ELIOTT hull, where the deuterium gas was ionised,
- and the beam tube on the other side of the rear wall, where the deuterium was pumped off with turbomolecular pumps.

During the measurements, the pressures in these three volumes were in equilibrium. These equilibrium pressures resulted from a constant gas flow Q through all three volumes and the conductance C in between them, according to[14]:

$$Q = \Delta p \cdot C. \tag{A.96}$$

Further considerations require the conductance C between the volumes[15]. Between the buffer volume and ELIOTT, the conductance C^{SE} was roughly assumed to be dominated by the bend gas inlet pipe at the ELIOTT hull; the pipe had a diameter of $d = 0.4$ cm and a length of $l = 2$ cm. Between ELIOTT and the WGTS, the conductance C^{EW} is dominated by the pipe on the transition flange with $d = 1$ cm and $l = 20$ cm. For long round pipes with these dimensions, the conductances are[16]:

$$C_{\mathrm{pipe,mol}} = \frac{\bar{c} \cdot \Pi \cdot d^3}{12 \cdot l}, \qquad C^{\mathrm{SE}} = 1.5 \cdot 10^{-3}\ \mathrm{l/s}, \qquad C^{\mathrm{EW}} = 2.3 \cdot 10^{-3}\ \mathrm{l/s}. \tag{A.97}$$

Because the pressure was always $\leq 1 \cdot 10^{-1}$ mbar and the pipe diameters were on the order of 1 cm, a molecular gas flow can be assumed[17]. Since the gas was a hydrogen

[14] Chapter 1.2.8 in Pfeiffer: *The Vacuum Technology Book Volume II*, 2013
[15] The conductance of the ELIOTT hull is negligible, because it measures about 10 cm in diameter at 70 cm length.
[16] Chapter 1.2.8 in Pfeiffer: *The Vacuum Technology Book Volume II*, 2013
[17] Chapter 1.2.6 in Pfeiffer: *The Vacuum Technology Book Volume II*, 2013

isotope, the average thermal particle velocity $\bar{c}_{H_2} = 175.4$ cm/s of hydrogen at 20°C can be used[18].

The two conductances together yield the total conductance of the setup from the buffer volume to the WGTS[19]:

$$C^{\text{tot}} = \left(\frac{1}{C^{\text{SE}}} + \frac{1}{C^{\text{EW}}} \right) = 9.0 \cdot 10^{-4} \text{ l/s}. \tag{A.98}$$

Now the conductances can be used to describe the pressures in the buffer volume and in ELIOTT. Because the pressure in the WGTS was always kept at about 10^{-9} mbar, it can be approximated as zero. With that follows:

$$Q^{\text{tot}} = p_{\text{S}} \cdot C^{\text{tot}}, \qquad Q^{\text{EW}} = p_{\text{E}} \cdot C^{\text{EW}}. \tag{A.99}$$

Because the gas flow is conserved, it is $Q^{\text{tot}} = Q^{\text{EW}}$ and therefore:

$$p_{\text{E}} = \frac{Q^{\text{EW}}}{C^{\text{EW}}} = p_{\text{S}} \cdot \frac{C^{\text{tot}}}{C^{\text{EW}}} \approx 0.4 \cdot p_{\text{S}}. \tag{A.100}$$

In summary, the pressure p_{E} in ELIOTT is about 40% of the pressure p_{S} in the deuterium supply. This can be used to compare the measurements at the rear section to previous test measurements. A maximum ion flux had previously been created with $2.6 \cdot 10^{-2}$ mbar D_2 in ELIOTT. This corresponds to a pressure of $6.5 \cdot 10^{-2}$ mbar in the deuterium supply of the rear section setup. In fact, the Faraday cup ring in ELIOTT observed the maximum pressure at $1 \cdot 10^{-1}$ mbar; but figure A.9 suggests that the ion flux was still going exponentially to an equilibrium value. Either the calculation overestimates the pressure in ELIOTT or the much stronger magnetic field of the rear section super conductor is responsible for the deviation. In the end, the quality of the calculation cannot be assessed by this comparison.

[18]Chapter 1.2.4 in Pfeiffer: *The Vacuum Technology Book Volume II*, 2013
[19]Chapter 1.2.8 in Pfeiffer: *The Vacuum Technology Book Volume II*, 2013

B. Hardware

This appendix collects information on the ion related hardware in KATRIN. First, the data sheet of the voltage supply at all ring and dipole electrodes is reprinted; then follow the data sheets of all three different types of amperemeters which were used for ion related current measurements in KATRIN. The final section contains the operating instructions for the Faraday cup, which was employed at the FBM in the First Tritium campaign.

B.1. Data sheet of the voltage supply for ring and dipole electrodes

The stability requirements for the voltage supply of the ring and dipole electrodes was discussed in section VI.2.4. In order to achieve them, several voltage sources from iseg were used. Their exact model specification is DPr 05 106 24 5_SHV-THQ-EPU, and their properties are summarised by the following data sheet.

DPS with option EPU - Precision High Voltage Module

Technical Data **DPR *vv iii* 24 5_EPU** *vv iii*	**05 106**	**10 106**	**15 805**	**20 605**	**30 405**	**40 305**	**50 205**	**60 155**
V_{OUTnom}	500 V	1 kV	1.5 kV	2 kV	3 kV	4 kV	5 kV	6
I_{OUTnom}	10 mA	10 mA	8 mA	6 mA	4 mA	3 mA	2 mA	1.5 mA
Polarity switchable with TTL-signal **at V_{OUT} = 0 !**	green LED-ON: negative (related to GND, PIN 6 and metal box) red LED-ON: positive (related to GND, PIN 6 and metal box)							
V_{IN}	24 V-DC ± 5% / < 0,8 A (V_{OUT}= 0 ; I_{OUT}= 0: < 50 mA)							
Ripple and noise	typ. < $3mV_{P-P}$ max. $7mV_{P-P}$							
Stability	$\Delta V_{OUT} / \Delta V_{IN}$ < $1 * 10^{-5} * V_{OUTnom}$ load to no load: ΔV_{OUT} < $5 * 10^{-5} * V_{OUTnom}$							
Temperature coeff.	< $5 * 10^{-5}/_{K}$							
Temperature range	Operating: -20°C to +40°C				Storage: -20°C to +85°C			
Control and Remote control with	direct coupled analogue I/O with $V_{SET/MON}$ = 0 to 5 V							
Hardware limit	Current and voltage limit, setting with potentiometer LIMIT I resp. V							
HV output **Attention !**	- Lemo HV-cable 9 kV, shielded (LEMO 106330), length = 600 mm - **optional** built-in SHV-connector (**-ESH**) - short-circuit and overload protection							

Only one short circuit or arc per second allowed!
The integral output current must be externally limited to the nominal output current of the module otherwise.

9-pin male D-Sub connector

PIN	Name	Description
1	0 V	Power 0 V (connected to PIN 6, GND and metal box)
2	IMON	Monitor voltage corresponding I_{OUT} I_{OUT}= 0 to I_{OUTnom} ± 1% ⇒ V_{2-6} = 0 to V_{MON} (R_{OUT} = 10 kΩ)
3	ON	HV-ON/OFF (TTL level): open or High-level ⇒ HV-off Low-level ⇒ HV-on with ramp speed ≈ V_{OUTnom}/4s
4	POL	Polarity switch (TTL level): open or High-level ⇒ positive, Low-level ⇒ negative
5	+ VIN	+ V_{IN}
6	GND	Signal 0 V (connected to PIN 1, GND and metal box)
7	VMON	Monitor voltage corresponding V_{OUT} V_{OUT}= 0 to V_{OUTnom} ± 1% ⇒ V_{7-6} = 0 to V_{MON} (R_{OUT} = 10 kΩ)
8	VSET	Setting voltage: V_{8-6} = 0 to V_{SET} (R_{IN} = 1 MΩ) ⇒ V_{OUT} = 0 to V_{OUTnom} ± 1%
9	REF	V_{9-6} = 5 V (1 mA) Internal reference voltage for an external pot.(Sliding contact on VSET)

iseg Spezialelektronik GmbH
Bautzner Landstr. 23
D - 01454 Radeberg / Rossendorf
Email: sales@iseg-hv.de
http://www.iseg-hv.com
Tel ++ 49 (0)351 / 26 996 - 0
Fax ++ 49 (0)351 / 26 996 - 21

B.2. Data sheets of the amperemeters for ion detection

Section VII.2 presented four different ion detectors which measure the neutralisation current of ions on an electrode inside the beamline. These four detector use three different types of amperemeters:

- **rbd 9103:** Four of these amperemeters are used to measure the current at the four DPS dipole electrodes (see section VII.2.2). The corresponding data sheet can be found on the following two pages.
- **Keithley 6514:** One such electrometer is permanently installed at the PS in order to measure the current at the PS downstream cone electrode (see section VII.2.4). A second device was used in order to measure the current on the Faraday cup inside ELIOTT during First Light (see section VIII.1), and later on the Faraday cup at the FBM during First Tritium (see section VII.2.3). Excerpts from the manual with regard to the current measurement properties can be found on the third and fourth of the following pages.
- **DDC-114:** This current measuring ADC from Texas Instruments is the core of the PULCINELLA readout electronics (see section VII.2.5). An excerpt is presented on the fifth and sixth of the following pages.

rbd instruments
advancing materials science

usb graphing picoammeter

9103

description

The 9103 is a versatile, general-purpose picoammeter designed to accurately measure DC current from the nA to mA range. The easy-to-read user interface is designed to provide optimal control and quick access to all functions. Features such as an ASCII programming language and data recording/graphing are standard.

applications

- Electron & ion beam current measurements
- Mass spectrometer current measurements
- Photodiode current & leakage measurements
- Beam and particle monitoring
- Spectrometer measurements
- Data logging current comparisons

benefits

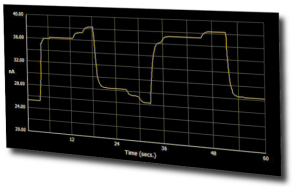

USB Interface: Windows® software included

Data Recording: Sample data can be recorded and saved

Data Graphing: Real-time graphing with polarity options

Programmable: ASCII command interface

Sync: Multiple 9103's can be synchronized using RBD's Actuel software to create a multichannel current data logger

Bias (Optional): Increases accuracy of electron or ion beam current measurements by reducing secondary electron emission

specifications

Resolution & Accuracy per Range

Range	*Resolution*	*Accuracy / Offset* *(18° – 28°C, 0 - 70% RH)**
2 nA	100 fA	0.5 ± % +500 fA
20 nA	1 pA	0.5 ± % +3 pA
200 nA	10 pA	0.4 ± % +20 pA
2 µA	100 pA	0.4 ± % +200 pA
20 µA	1 nA	0.4 ± % +2 nA
200 µA	10 nA	0.4 ± % +20 nA
2 mA	100 nA	0.4 ± % +200 nA

*Temperature Coefficient: 0°–18°C & 28°–50°C. For each °C, add 0 1 × (% rdg + offset) to accuracy spec.

usb graphing picoammeter

9103

specifications

General:

USB Interface	160 mW power consumption
2 nA Min. DAC Resolution	0.1 pA
2 mA Min. DAC Resolution	100 nA
Range	2 nA to 2 mA with 100 fA resolution
Input Protection	± 2.000 V per range
Recorder Output Voltage	2 nA to 2 mA with 100 fA resolution
Voltage Burden	If the current is in the range of measurement of the instrument, the voltage drop should be less than ± 26 µV + (3.2 * I), where I is the current flowing into the instrument, 3.2 is the resistance of the fuse, and ± 26 µV is the offset voltage spec. of the op-amp. The current measurement circuit uses an op-amp to convert current to voltage; the op-amp inputs are referenced to the ground circuit of the current source. If the current goes outside the range of measurement of the instrument, the voltage is clamped to ± 1V by a low-leakage diode clamp circuit using two diodes in parallel w/ one diode connected anode to ground, cathode to the current measurement node, and the second diode connected cathode to ground, anode to the current measurement node.
Warm-up	1 hour to rated accuracy
Environment	Operating 0° C to 50 ° C
Mechanical Dimensions	55H x 170W x 165L (mm) 2.11H x 6.68W x 6.30L (inches)
Net. Weight	0.816 kg / 1.5 lbs
Connections	Input: Isolated BNC (two or three-lug TRIAX inputs available on request). Analog Output: Banana jacks
Bias Options	No Bias; Internal (± 90 V DC); External (BNC)
Safety	Conforms to USB Power Specification - for use by qualified personnel who are trained in the use of test and measurement instrumentation
Accessories Included	Instructions manual, low noise BNC cable, USB power cable, USB driver, installation instructions, Actuel software

rbd instruments

2437 NE Twin Knolls Drive • Suite 2 • Bend, Oregon • 97701
Phone: 541.330.0723 • Fax: 541.330.0991
email: sales@rbdinstruments.com • web: www.rbdinstruments.com

VOLTS RANGE	5½ DIGIT RESOLUTION	ACCURACY (1 Year)[1] 18°–28°C ±(%rdg+counts)	TEMPERATURE COEFFICIENT 0°–18°C & 28°–50°C ±(%rdg+counts)/°C
2 V	10 µV	0.025 + 4	0.003 + 2
20 V	100 µV	0.025 + 3	0.002 + 1
200 V	1mV	0.06 + 3	0.002 + 1

Note:
[1] When properly zeroed, 5½-digit. Rate: Slow (100ms integration time).

NMRR: 60dB on 2V, 20V, >55dB on 200V, at 50Hz or 60Hz ±0.1%.

CMRR: >120dB at DC, 50Hz or 60Hz.

INPUT IMPEDANCE: >200TΩ in parallel with 20pF, < 2pF guarded (10MΩ with zero check on).

SMALL SIGNAL BANDWIDTH AT PREAMP OUTPUT: Typically 100kHz (–3dB).

AMPS RANGE	5½ DIGIT RESOLUTION	ACCURACY (1 Year)[1] 18°–28°C ±(%rdg+counts)	TEMPERATURE COEFFICIENT 0°–18°C & 28°–50°C ±(%rdg+counts)/°C
20 pA	100 aA[2]	1 + 30	0.1 + 5
200 pA	1 fA[2]	1 + 5	0.1 + 1
2 nA	10 fA	0.2 + 30	0.1 + 2
20 nA	100 fA	0.2 + 5	0.03 + 1
200 nA	1 pA	0.2 + 5	0.03 + 1
2 µA	10 pA	0.1 + 10	0.005 + 2
20 µA	100 pA	0.1 + 5	0.005 + 1
200 µA	1 nA	0.1 + 5	0.005 + 1
2 mA	10 nA	0.1 + 10	0.008 + 2
20 mA	100 nA	0.1 + 5	0.008 + 1

Notes:
[1] When properly zeroed, 5½-digit. Rate: Slow (100ms integration time).
[2] aA =10^{-18}A, fA=10^{-15}A.

INPUT BIAS CURRENT: <3fA at T_{CAL} (user adjustable). Temperature coefficient = 0.5fA/°C .

INPUT BIAS CURRENT NOISE: <750aA p-p (capped input), 0.1Hz to 10Hz bandwidth, damping on. Digital filter = 40 readings.

INPUT VOLTAGE BURDEN at T_{CAL} ±1°C (user adjustable)**:**

<20µV on 20pA, 2nA, 20nA, 2µA, 20µA ranges.
<100µV on 200pA, 200nA, 200µA ranges.
<2mV on 2mA range.
<4mV on 20mA range.

TEMPERATURE COEFFICIENT OF INPUT VOLTAGE BURDEN: <10µV/°C on pA, nA, µA ranges.

PREAMP SETTLING TIME (to 10% of final value): 2.5s typical on pA ranges, damping off, 3s typical on pA ranges damping on, 15ms on nA ranges, 5ms on µA and mA ranges.

NMRR: >95dB on pA, 60dB on nA, µA, and mA ranges at 50Hz or 60Hz ±0.1%. Digital Filter = 40.

GENERAL

DISPLAY: 6½-digit vacuum fluorescent.

OVERRANGE INDICATION: Display reads "OVRFLOW".

RANGING: Automatic or manual.

CONVERSION TIME: Selectable 0.01 PLC to 10 PLC.

PROGRAMS: Provide front panel access to IEEE address, choice of engineering units or scientific notation, and digital calibration.

MAXIMUM INPUT: 250V peak, DC to 60Hz sine wave; 10s per minute maximum on mA ranges.

MAXIMUM COMMON MODE VOLTAGE (DC to 60Hz sine wave): Electrometer, 500V peak;

ISOLATION (Meter COMMON to chassis): Typically $10^{10}\Omega$ in parallel with 500pF.

INPUT CONNECTOR: Three lug triaxial on rear panel.

2V ANALOG OUTPUT: 2V for full range input. Inverting in Amps and Coulombs mode. Output impedance 10kΩ.

PREAMP OUTPUT: Provides a guard output for Volts measurements. Can be used as an inverting output or with external feedback in Amps and Coulombs modes.

DIGITAL INTERFACE:
Handler Interface: Start of test, end of test, 3 category bits.
Digital I/O: 1 Trigger input, 4 outputs with 500mA sink capability.
Connector: 9 Pin D subminiature, male pins.

EMC: Conforms with European Union Directive 89/336/EEC EN55011, EN50082-1, EN61000-3-2, EN61000-3-3, FCC part 15 class B.

SAFETY: Conforms with European Union Directive 73/23/EEC EN61010-1.

GUARD: Switchable voltage and ohm guard available.

TRIGGER LINE: Available, see manual for usage.

READING STORAGE: 2500 readings.

READING RATE:

To internal buffer	1200 readings/second[1]
To IEEE-488 bus	500 readings/second[1,3]
To front panel	17 readings/second at 60Hz;[2]
	15 readings/second at 50Hz[2]

Notes:
[1] 0.01 PLC, digital filters off, front panel off, auto zero off.
[2] 1.00 PLC, digital filters off.
[3] Binary transfer mode.

DIGITAL FILTER: Median and averaging (selectable from 2 to 100 readings).

DAMPING: User selectable on Amps function.

ENVIRONMENT:
Operating: 0°–50°C; relative humidity 70% non-condensing, up to 35°C.
Storage: –25° to +65°C.

WARM-UP: 1 hour to rated accuracy (see manual for recommended procedure).

POWER: 90–125V or 210–250V, 50–60Hz, 60VA.

PHYSICAL:
Case Dimensions: 90mm high × 214mm wide × 369mm deep (3½ in. × 8⅜ in. × 14⁹⁄₁₆ in.).
Working Dimensions: From front of case to rear including power cord and IEEE-488 connector: 15.5 inches.
Net Weight: <4.6 kg (<10.1 lbs).
Shipping Weight: <9.5 kg (<21 lbs).

SBAS255C − JUNE 2004 − REVISED APRIL 2009

Quad Current Input, 20-Bit Analog-To-Digital Converter

FEATURES

- SINGLE-CHIP SOLUTION TO DIRECTLY MEASURE FOUR LOW-LEVEL CURRENTS
- HIGH PRECISION, TRUE INTEGRATING FUNCTION
- INTEGRAL LINEARITY: ±0.01% of Reading ±0.5ppm of FSR
- VERY LOW NOISE: 5.2ppm of FSR
- LOW POWER: 13.5mW/channel
- ADJUSTABLE DATA RATE: Up to 3.125kSPS
- PROGRAMMABLE FULL SCALE
- DAISY-CHAINABLE SERIAL INTERFACE

APPLICATIONS

- CT SCANNER DAS
- PHOTODIODE SENSORS
- INFRARED PYROMETERS
- LIQUID/GAS CHROMATOGRAPHY

Protected by US Patent #5841310

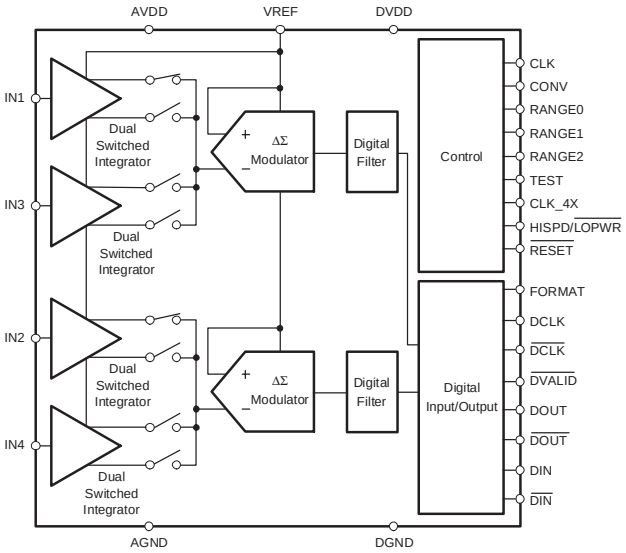

DESCRIPTION

The DDC114 is a 20-bit, quad channel, current-input analog-to-digital (A/D) converter. It combines both current-to-voltage and A/D conversion so that four low-level current output devices, such as photodiodes, can be directly connected to its inputs and digitized.

For each of the four inputs, the DDC114 provides a dual-switched integrator front-end. This design allows for continuous current integration: while one integrator is being digitized by the onboard A/D converter, the other is integrating the input current. Adjustable full-scale ranges from 12pC to 350pC and adjustable integration times from 50µs to 1s allow currents from fAs to µAs to be measured with outstanding precision. Low-level linearity is ±0.5ppm of the full-scale range and noise is 5.2ppm of the full-scale range.

Two modes of operation are provided. In Low-Power mode, total power dissipation is only 13.5mW per channel with a maximum data rate of 2.5kSPS. High-Speed mode supports data rates up to 3.125kSPS with a corresponding dissipation of 18mW per channel.

The DDC114 has a serial interface designed for daisy-chaining in multi-device systems. Simply connect the output of one device to the input of the next to create the chain. Common clocking feeds all the devices in the chain so that the digital overhead in a multi-DDC114 system is minimal.

The DDC114 is a single-supply device using a +5V analog supply and supporting a +2.7V to +5.25V digital supply. Operating over the industrial temperature range of −40°C to +85°C, the DDC114 is offered in a QFN-48 package.

ELECTRICAL CHARACTERISTICS

At T_A = +25°C, AVDD = +5V, DVDD = 3V, VREF = +4.096V, Range 5 (250pC), and continuous mode operation, unless otherwise noted.
Low-Power Mode: T_{INT} = 400µs and CLK = 4MHz; High-Speed Mode: T_{INT} = 320µs and CLK = 4.8MHz.

PARAMETER	TEST CONDITIONS	Low-Power Mode			High-Speed Mode			UNITS
		MIN	TYP	MAX	MIN	TYP	MAX	
ANALOG INPUT RANGE								
Range 0		10.2	12	13.8	*(1)	*	*	pC
Range 1		47.5	50	52.5	*	*	*	pC
Range 2		95	100	105	*	*	*	pC
Range 3		142.5	150	157.5	*	*	*	pC
Range 4		190	200	210	*	*	*	pC
Range 5		237.5	250	262.5	*	*	*	pC
Range 6		285	300	315	*	*	*	pC
Range 7		332.5	350	367.5	*	*	*	pC
Negative Full-Scale Range		−0.4% of Positive Full-Scale Range				*		pC
Input Current(2)			750			*		µA
DYNAMIC CHARACTERISTICS								
Data Rate				2.5			3.125	kSPS
Integration Time, T_{INT}	Continuous Mode	400		1,000,000	320		*	µS
	Non-continuous Mode, Range 1 to 7	50			*			µS
System Clock Input (CLK)								
CLK_4X = 0				4			4.8	MHz
CLK_4X = 1				16			19.2	MHz
Data Clock (DCLK)				16			*	MHz
ACCURACY								
Noise, Low-Level Input(3)	C_{SENSOR}(4) = 50pF, Range 5 (250pC)		5.2	6.5		5.5	7	ppm of FSR(5), rms
Integral Linearity Error(6)		±0.01% Reading ± 0.5ppm FSR, typ				*		
		±0.025% Reading ± 1.0ppm FSR, max				*		
Resolution	FORMAT = 1	20			*			Bits
	FORMAT = 0	16			*			Bits
Input Bias Current			0.1	10		*	*	pA
Range Error Match(7)	All Ranges		0.1	0.5		*	*	% of FSR
Range Sensitivity to VREF	V_{REF} = 4.096 ± 0.1V		1:1			*		
Offset Error			±400	±1000		*	*	ppm of FSR
Offset Error Match(7)			±100			*		ppm of FSR
DC Bias Voltage(9)	Low-Level Input (< 1% FSR)		±0.05	±2		*	*	mV
Power-Supply Rejection Ratio	at dc		±25	±200		*	*	ppm of FSR/V
Internal Test Signal			11			*		pC
Internal Test Accuracy			±10			*		%
PERFORMANCE OVER TEMPERATURE								
Offset Drift			±0.5	±3(8)		*	*	ppm of FSR/°C
Offset Drift Stability			±0.2	±1(8)		*	*	ppm of FSR/ minute
DC Bias Voltage Drift(9)			3			*		µV/°C
Input Bias Current Drift	T_A = +25°C to +45°C		0.01	1(8)		*	*	pA/°C
Range Drift(10)			25			*		ppm/°C
REFERENCE								
Voltage		4.000	4.096	4.200	*	*	*	V
Input Current(11)	Average Value		75			95		µA

(1) * indicates that specification is the same as Low-Power Mode.
(2) Exceeding maximum input current specification may damage device.
(3) Input is less than 1% of full scale.
(4) C_{SENSOR} is the capacitance seen at the DDC114 inputs from wiring, photodiode, etc.
(5) FSR is Full-Scale Range.
(6) A best-fit line is used in measuring nonlinearity.
(7) Matching between side A and side B of the same input.
(8) Ensured by design, not production tested.
(9) Voltage produced by the DDC114 at its input which is applied to the sensor.
(10) Range drift does not include external reference drift.
(11) Input reference current decreases with increasing T_{INT} (see the *Voltage Reference* section, page 11).

B.3. Operating instructions for the Faraday cup

In order to change between the measurement modes of the Faraday cup, the voltage of the Faraday cup and its shield have to change in magnitude and polarity. The voltage magnitude can be changed with a knob on the voltage supplies; changing the polarity is however only possible by unplugging the cables and plugging them into the output jacks of the inverse sign.

Overview over the electronics setup Figure B.1 shows the electronics cabling of the Faraday cup setup in beta electron mode. Voltage supply channel 1 provides the voltage for the shield (red banana plug) and the grounded strip (black banana plug and always grounded). Channel 2 provides the offset voltage for Faraday cup via the chassis and common potential of the Keithley 6514 amperemeter.

The ground potential is by definition the beam tube potential. Due to the triax cable[1], the chassis (CHS) of the Keithley 6514 is on ground potential. From there, the ground potential is provided to the voltage supplies via banana cables. For example, the voltage supply channel 2 provides the offset voltage for the Faraday cup[2] The voltage offset from supply channel 2 is applied with banana cables to the common potential (CMN) of the Keithley 6514.

The currents measured by the Keithley 6514 are read out by a LabVIEW-program on a local computer. Computer and Keithley 6514 are connected via an adapter cable from USB (computer) to RS-232 (Keithley 6514).

Changing between ion mode and beta electron mode According to table B.1, the modes for detection of ions and beta electrons only vary by the polarity of the Faraday cup voltage. In order to apply -2 V for ion detection, all three cables on voltage supply channel 2 in figure B.1 must be switched to the opposite sign: then the voltage supply outputs a negative voltage relative to ground, which is defined by the beam tube through the chassis (CHS) of the Keithley 6514.

The magnitude of the voltage supply channel 1 can remain at 2 V when switching from ions to beta electrons. However, in order to minimise any potential electronic hazard, the voltage should be set to 0 V before unplugging the cables and reset to 2 V when all cables are plugged again. Voltage supply channel 2 remains at 20 V and its polarity untouched.

Secondary electron mode In order to measure secondary electrons, the polarity of the shield voltage must be inverted as compared to beta electron mode and the magnitude at both voltage supply channels must be changed. According to table B.1, the magnitude of voltage supply channel 1 has to be reduced to 2 V, while channel 2 must be set to 20 V.

[1] A triax cable is a coaxial cable with two shields: an outer and an inner shield. In this setup, the outer shield is on beam tube potential and the inner one floats on common potential just as the signal.

[2] For measurements with the small Faraday cup, the Keithley 6514 must be connected to a second triax cable coming from the beam tube.

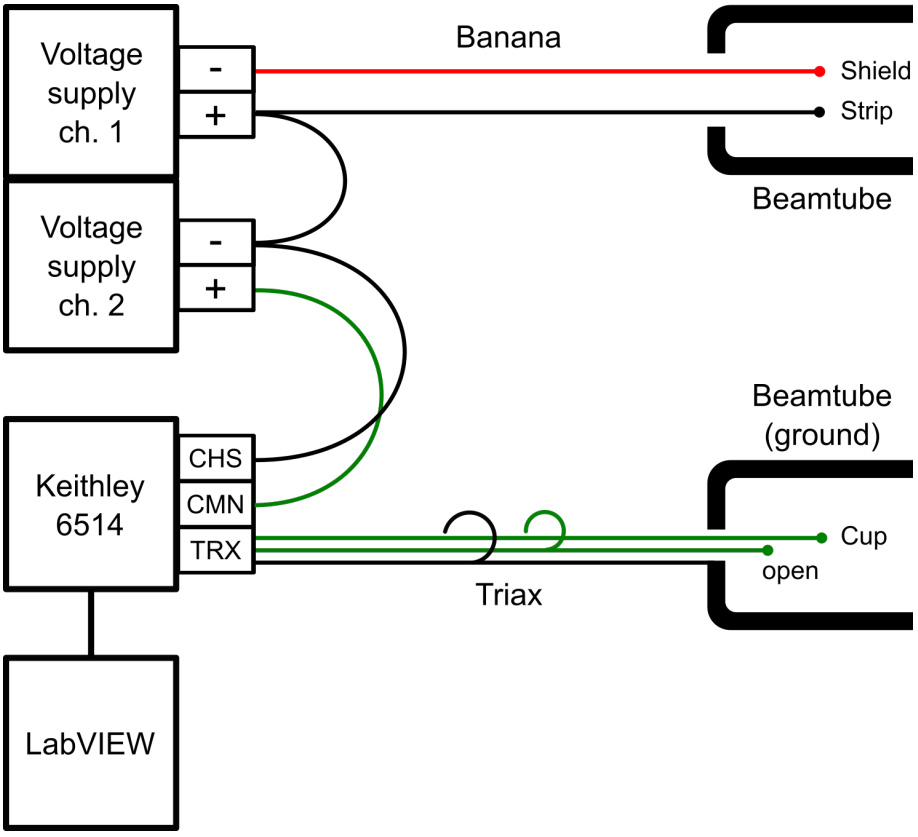

Figure B.1.: **Electronics setup of the Faraday cup** in beta electron mode. A triax cable connects the Faraday cup inside the beam tube with the triax jack of the Keithley 6514 amperemeter. All other cables have banana plugs, including those to the Keithley's chassis (CHS) and common potential (CMN).

Table B.1.: **Measurement modes of the Faraday Cup.** Positive potentials at the board reject positive ions, negative potentials reject negative ions and secondary electrons. The potential of the shield is always more negative than the board in order to retain secondary electrons.

Investigated particles	Shield	Board
Beta electrons	−20 V	+2 V
Positive ions	−20 V	−2 V
Secondary electrons and negative ions	+2 V	−20 V

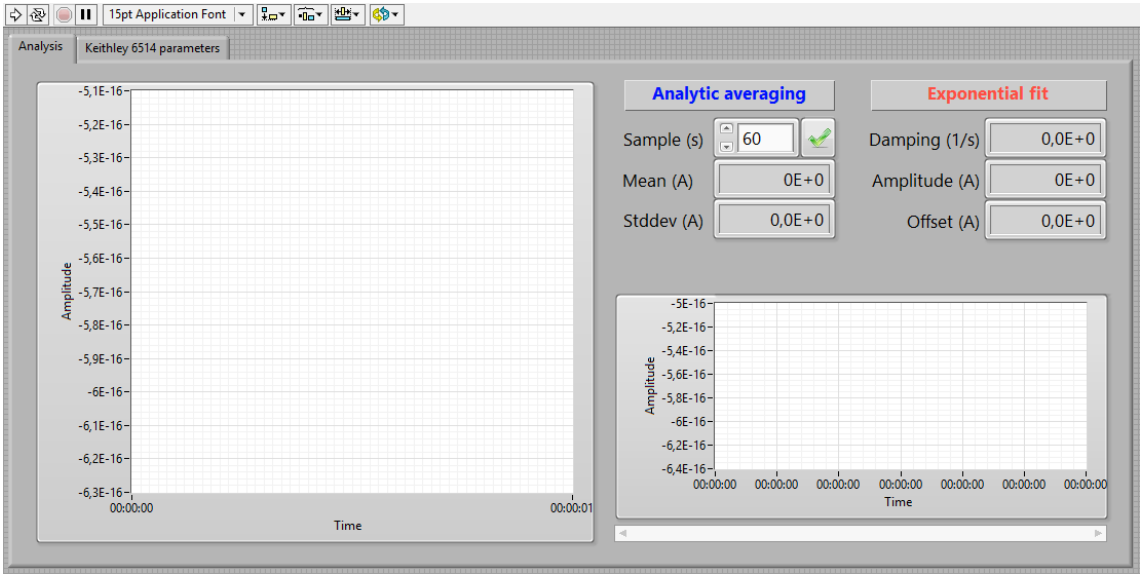

Figure B.2.: **Front end of the LabVIEW program** for the current readout.

Operating the LabVIEW program The current on the Faraday Cup will be measured by the Keithley 6514 and read out by a LabVIEW program on a nearby computer. This program most importantly writes the measurement current to the local hard drive of the computer at a measurement speed of about nine values per second. On top of that, the program interface (shown in figure B.2) allows to monitor live the measured current and to quickly evaluate whether the ion flux is blocked or not.

Two graphs allow to monitor the time development of the current signal and judge the statistical noise visually: the large graph on the left side displays all data that is the basis for the analytic averaging and exponential fit (see below) and the narrow graph on the right displays all data which was acquired since the execution of the program. The time labels of the left graph are given in relative seconds within the chosen time window, while the right graph is plotted versus the local time of the laptop.

From the same set of data, which is displayed in the large, left graph, the analytic average and an exponential fit are calculated with each new acquired value (every 110 ms). The boundary conditions for the exponential fit can be entered in six control boxes on the very right side of the program (not shown in figure B.2).

The time period on which this live analysis is applied, can be chosen with the numeric control box *Sample (s)*. Editing this box will affect the graph and the exponential fit immediately – the analytic average and its standard deviation are however calculated from the former entry until the green check mark right from the control box is pressed.

All features discussed so far are collected on the *Analysis* tab of the LabVIEW program's front end. The second tab, termed *Keithley 6514 parameters*, contains advanced settings that should only be changed by experts.

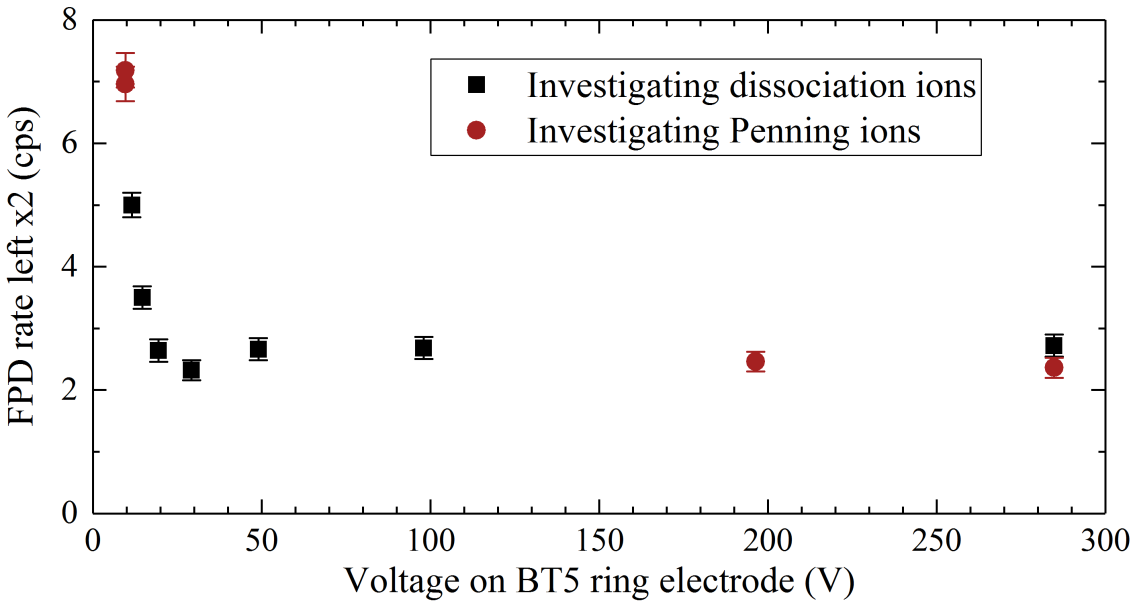

Figure C.1.: **Effect of the BT5 ring electrode voltage on the residual background.** The residual rate never decreased below the level of (2 . . . 3) cps during the investigation of Penning ions and ions from molecular dissociation with the PS ionisation method. Above 20 V, the integrated rate becomes rather stable and no significant rate of dissociation ions can be observed.

C. Residual rate during First Tritium PS ionisation measurements

As discussed in section IX.4.4, a residual rate restricted the measurement of the upper limit on the ion flux into the PS with the ionisation method during First Tritium. The STS IIIa campaign solved this problem by finding a pressure-independent and larger-than-expected ionisation efficiency. This indicates that the complete measurement was actually dominated by Ar^+ ions with a linear pressure-dependence. However, the cause of the pressure-independent ionisation efficiency is unknown so far; as a reference for further considerations, the original discussion of the residual rate has been archived in the following.

A measurement of the residual rate at various column densities showed a rather linear pressure dependence (see table C.1). It had to be assumed that this rate would also increase with the tritium concentration: in contrast to First Tritium, future campaigns will have an up to 200 times larger tritium concentration of about 100%. Assuming that the residual rate consists of tritium ions from the source, the

ion safety limit of 10^4 ions/s would probably not be observed any more. It was therefore necessary to reduce the residual rate and identify its cause in the first place.

In the discussion of the possible reasons for the residual rate of the PS ionisation measurement, the following observations were taken into account:

- The residual rate increased with the argon pressure, as discussed above and shown in figure IX.27. This suggests that the cause of the rate lies inside the argon gas. However, no such linear increase was observed in a less precise measurement with the PS ionisation method shown in figure IX.28.

- The residual rate increased proportionally to the column density, as summarised in table C.1. This indicates that the cause is either a flux of ions from the WGTS or that it is driven by the beta electron flux between the WGTS and the PS high voltage.

- The residual rate never decreased below the level of $(2 \ldots 3)$ cps during the ionisation measurements with about $3 \cdot 10^{-8}$ mbar argon in the PS. During the measurements displayed in figure C.1, the PS1 electrode was at -5 V and the other two electrodes in the spectrometers were at $+50$ V; the PP5 ring electrode was at $+10$ V during the investigation of Penning ions and at -5 V during the investigation of dissociation ions.

Based on these observations, the following causes of the residual rate were discussed:

- **Penning ions from the PS1 ring electrode (section IX.2.2)** The linear increase of the residual rate with the argon pressure and with the column density agree both with the expected behaviour of the Penning ion rates. When the PS1 electrode was at $+50$ V during the investigation of the Penning ion

Table C.1.: **Increase of the residual rate with the column density.** Like for the rates in figure IX.27, the intrinsic PS background was subtracted, the net FPD rate was converted into an ion flux with the ionisation efficiency and finally the Ar^+ ions were subtracted, too. The increase is linear with a slope slightly larger than 1, considering the different argon pressures. The uncertainties on the column density are on the order of 10^{-5}.

	Pressure (mbar)	Column density (m^{-2})	Residual rate (ions/s)
22% $\mathcal{N}_0$	$(2.50 \pm 0.06) \cdot 10^{-8}$	$1.1 \cdot 10^{21}$	$(3.0 \pm 0.3) \cdot 10^3$
89% $\mathcal{N}_0$	$(1.87 \pm 0.00) \cdot 10^{-8}$	$4.5 \cdot 10^{21}$	$(1.4 \pm 0.1) \cdot 10^4$
Increase by:	0.7 ± 0.0	4.1 ± 0.0	4.7 ± 0.6

rates, just the usual level of the residual rate of 3 cps was observed[1]. However, the observation of the same 3 cps when the PS1 electrode was set to −5 V during the investigation of Penning ions and dissociation ions contradicts the PS1 electrode as cause of the residual rate. Penning ions from the DPS electrodes cannot be the cause since they were blocked by the PS1 potential during the determination of the upper limit on the ion flux into the PS.

- **Ar^+ ions (section IX.1.4.1)** The linear increase of the residual rate with the argon pressure and with the column density agrees also with the expectation for the Ar^+ ions. Even that the residual rate remained unaffected when the PS1 potential was set to −5 V does not disfavour this theory. However, the predicted rate of Ar^+ was between 16 and 130 times smaller than the residual rate in figure IX.27 and the observed slope was not as steep as expected. Nevertheless, the Ar^+ ion rate is a valid candidate; it should be investigated in future test measurements by shooting photoelectrons from the rearwall with variable energy and flux rate into the argon filled PS.

- **High energetic ions from molecular dissociation (section IX.2.3)** A flux of high energetic dissociation ions into the PS would be a problem, however there is little which supports this theory. The ion flux from the WGTS should not depend on the argon pressure and would require to interpret the observed linear pressure increase as a statistical fluctuation. But in contrast to the expected quadratic increase of the ion rate with the column density, the residual rate rose rather linearly. And finally the flux of dissociation ions should have decreased when the voltage of the BT5 ring electrode was increased; it seems rather unlikely that the decrease of the dissociation ion rate was exactly compensated by a small Penning ion rate from the BT5 electrode although a small bump of the rate around 50 V might hint to that.

- **Penning discharge inside the PS (section IX.1.4.2)** The intrinsic PS background was found to be pressure dependent; and several particular systematic effects of the PS background can only be explained with Penning discharges inside the PS, which would depend on the ambient argon pressure. However, the beta electron flux is not able to enter the high voltage of the PS and cannot fuel the Penning discharge directly. A discharge inside the PS would however explain why it remained unaffected by various settings of the ring electrode voltage.

In summary, the observations favour none of the possible causes for the residual rate during the PS ionisation measurements. Among all of them, a PS1 Penning discharge or Ar^+ ions seem to be the most probable candidates, although there are also arguments against both of them.

[1]The PS argon pressures during both measurements were comparable

References

[Aba12] K. N. Abazajian et al., *Light sterile neutrinos: a white paper*, arXiv preprint arXiv:1204.5379 (2012).

[Adh17] R. Adhikari et al., *A white paper on keV sterile neutrino dark matter*, Journal of cosmology and astroparticle physics 2017.01 (2017): 025.

[Agh18] N. Aghanim et al., *Planck 2018 results. VI. Cosmological parameters*, arXiv preprint arXiv:1807.06209 (2018).

[Ago17] M. Agostini et al., *Background-free search for neutrinoless double-β decay of ^{76}Ge with GERDA*, Nature 544.7648 (2017): 47.

[Ago18] M. Agostini et al., *Improved Limit on Neutrinoless Double-β Decay of Ge 76 from GERDA Phase II*, Physical review letters 120.13 (2018): 132503.

[Ahn03] S. Ahn and J. A. Fessler, *Standard errors of mean, variance, and standard deviation estimators*, EECS Department, The University of Michigan (2003): 1-2.

[Alp15] B. Alpert et al., *Holmes*, The European Physical Journal C 75.3 (2015): 112.

[Als78] C. J. Altstetter et. al., *Depth profiling of deuterium implanted into stainless steel at room temperature*, Nuclear Instruments and Methods 149.1-3 (1978): 59-63.

[Ams07] C. Amsler, *Kern-und Teilchenphysik, vdf Hochschulverl*, AG an der ETH Zürich, Zürich (2007).

[Ase11] V. N. Aseev et al., *Upper limit on the electron antineutrino mass from the Troitsk experiment*, Physical Review D 84.11 (2011): 112003.

[Asn15] D. M. Asner et al., *Single-electron detection and spectroscopy via relativistic cyclotron radiation*, Physical review letters 114.16 (2015): 162501.

[Aus72] J. H. Austin and T. S. Elleman, *Tritium diffusion in 304-and 316-stainless steels in the temperature range 25 to 222° C*, Journal of Nuclear Materials 43.2 (1972): 119-125.

[Bab12] M. Babutzka et al., *Monitoring of the operating parameters of the KATRIN Windowless Gaseous Tritium Source*, New Journal of Physics 14.10 (2012): 103046.

[Bab14] M. Babutzka, *Design and development for the Rearsection of the KATRIN experiment*, Ph.D. thesis, Karlsruhe Institute of Technology (KIT), Karlsruhe Germany, (2014).

[Bah96] J. N. Bahcall, *Solar neutrinos: Where we are, where we are going*, Nuclear Physics B-Proceedings Supplements 48.1-3 (1996): 309-316.

[Beh75] R. Behrisch et. al., *Implantation profiles of low-energy helium in niobium and the blistering mechanism*, Applied Physics Letters 27.4 (1975): 199-201.

[Ber14] R. F. Berg, *Hydrogen traps in the outgassing model of a stainless steel vacuum chamber*, Journal of Vacuum Science & Technology A: Vacuum, Surfaces, and Films 32.3 (2014): 031604.

[Bit04] J. A. Bittencourt, *Fundamentals of Plasma Physics*, Springer Science + Business Media (2004).

[Bla06] K. Blaum, *High-accuracy mass spectrometry with stored ions*, Physics Reports 425.1 (2006): 1-78

[Ble78] R. S. Blewer et al., *Trapping and replacement of 1-14 keV hydrogen and deuterium in 316 stainless steel*, Journal of Nuclear Materials 76 (1978): 305-312.

[Bod15] L. I. Bodine, D. S. Parno and R. G. H. Robertson, *Assessment of molecular effects on neutrino mass measurements from tritium* β *decay*, Physical Review C 91.3 (2015): 035505.

[Bot74] C. Bottcher, *Dissociative ionization of the hydrogen molecule*, Journal of Physics B: Atomic and Molecular Physics 7.11 (1974): L352.

[BPG04] J. N. Bahcall and C. Pena-Garay, *Solar models and solar neutrino oscillations*, New Journal of Physics 6.1 (2004): 63.

[Bro08] I. N. Bronstein et. al., *Taschenbuch der Mathematik, 7. vollständig überarbeitete und ergänzte Auflage*, Verlag Harri Deutsch, 2008

[CDR04] J. Angrik et al. (KATRIN Collaboration), KATRIN Design Report 2004, Wissenschaftliche Berichte FZKA 7090, http://bibliothek.fzk.de/zb/berichte/FZKA7090.pdf

[Cou17] F. Couchot et al., *Cosmological constraints on the neutrino mass including systematic uncertainties*, Astronomy & Astrophysics 606 (2017): A104.

[Cow98] G. Cowan, *Statistical data analysis*, Oxford University Press, 1998.

[Cra79] J. Crank, *The mathematics of diffusion*, Oxford University Press, 1979.

[Day12] F. P. An et al., *Observation of electron-antineutrino disappearance at Daya Bay*, Physical Review Letters 108.17 (2012): 171803.

[Din00] M. Dingfelder et al., *Inelastic-collision cross sections of liquid water for interactions of energetic protons*, Radiation physics and chemistry 59.3 (2000): 255-275.

[Dun63] G. H. Dunn and L. J. Kieffer, *Dissociative ionization of H 2: A study of angular distributions and energy distributions of resultant fast protons*, Physical Review 132.5 (1963): 2109.

[Ell17] E. Ellinger et al., *Monitoring the KATRIN source properties within the beamline*, Journal of Physics: Conference Series. Vol. 888. No. 1. IOP Publishing, 2017.

[Erh18] M. Erhard et al., *Technical design and commissioning of the KATRIN large-volume air coil system*, Journal of Instrumentation 13.02 (2018): P02003.

[Esf17] A. A. Esfahani et al., *Determining the neutrino mass with cyclotron radiation emission spectroscopy – Project 8*, Journal of Physics G: Nuclear and Particle Physics 44.5 (2017): 054004.

[FeP09] N. Feltin and F. Piquemal, *Determination of the elementary charge and the quantum metrological triangle experiment*, The European Physical Journal Special Topics 172.1 (2009): 267-296.

[Fis14] S. Fischer, *Commissioning of the KATRIN Raman system and durability studies of optical coatings in glove box and tritium atmospheres*, Ph.D. thesis, Karlsruhe Institute of Technology (KIT), Karlsruhe Germany, (2014).

[Flo17] N. E. Flowers-Jacobs et al., *The NIST Johnson Noise Thermometry System for the Determination of the Boltzmann Constant*, Res. Natl. Inst. Stand. Technol. submitted (2017).

[FPD15] J. F. Amsbaugh et al., *Focal-plane detector system for the KATRIN experiment*, Nuclear Instruments and Methods in Physics Research Section A: Accelerators, Spectrometers, Detectors and Associated Equipment 778 (2015): 40-60.

[Fra10] F. M. Fränkle, *Background investigations of the KATRIN pre-spectrometer*, Ph.D. thesis, Karlsruhe Institute of Technology (KIT), Karlsruhe Germany, (2010).

[Fre16] F. Frémont, *Electron capture and single ionization in H++ Ar collisions: classical calculations*, Journal of Physics B: Atomic, Molecular and Optical Physics 49.6 (2016): 065206.

[FRS18] F. Friedel et al., *Time-dependent simulation of the flow reduction of D2 and T2 in the KATRIN experiment*, Vacuum 159 (2019): 161-172.

[Fuk98] Y. Fukuda et al., *Evidence for oscillation of atmospheric neutrinos*, Physical Review Letters 81.8 (1998): 1562.

[Gal12] P. Gallagher, *Introduction to plasma physics, lectures 1-2*, lecture slides, (2012), available at: https://www.tcd.ie/Physics/people/Peter.Gallagher/lectures/PlasmaPhysics/Lecture1n2_basic_properties.pdf.

[Gan16] A. Gando et al., *Search for Majorana Neutrinos Near the Inverted Mass Hierarchy Region with KamLAND-Zen*, Physical review letters 117.10 (2016): 109903.

[Gas17] L. Gastaldo et al., *The electron capture in 163Ho experiment–ECHo*, The European Physical Journal Special Topics 226.8 (2017): 1623-1694.

[Gil18] W. Gil, *First Operation of the Complete KATRIN Superconducting Magnet Chain*, IEEE Transactions on Applied Superconductivity 28.4 (2018): 1-5. © 2018 IEEE.

[Gra88] D. M. Grant et al., *Hydrogen in 316 steel – diffusion, permeation and surface reaction*, Journal of Nuclear Materials 152.2-3 (1988): 139-145.

[Gro15] S. Groh, *Modeling of the response function and measurement of transmission properties of the KATRIN experiment*, Ph.D. thesis, Karlsruhe Institute of Technology (KIT), Karlsruhe Germany, (2015).

[GUM95] ISO, IEC and BIPM OIML, *Guide to the Expression of Uncertainty in Measurement*, Geneva, Switzerland (1995).

[Hac17] M. Hackenjos, *KATRIN "First Light" – Commissioning and Modelling of the Beamline*, Ph.D. thesis, Karlsruhe Institute of Technology (KIT), Karlsruhe Germany, (2017)

[Hak06] H. Haken and H. C. Wolf, *Molekülphysik und Quantenchemie: Einführung in die experimentellen und theoretischen Grundlagen*, Springer-Verlag (2006)

[Har15] F. Harms, *Characterization and Minimization of Background Processes in the KATRIN Main Spectrometer*, Ph.D. thesis, Karlsruhe Institute of Technology (KIT), Karlsruhe Germany, (2015).

[Hil11] B. Hillen, *Untersuchung von Methoden zur Unterdrückung des Spektrometeruntergrunds beim KATRIN experiment* (in German), Ph.D. thesis, Westfälische Wilhelms-Universität Münster, Münster Germany, (2011).

[Hoe12] M. Hötzel, *Simulation and analysis of source-related effects for KATRIN*, Ph.D. thesis, Karlsruhe Institute of Technology (KIT), Karlsruhe Germany, (2012).

[Joh76] R. Johnsen et al., *Three-body association reactions of H^+ and H_3^+ ions in hydrogen from 135 to 300 K*, The Journal of Chemical Physics 65.4 (1976): 1539-1541.

[Jon99] S. Jonsell, A. Saenz and P. Froelich, *Neutrino-mass determination from tritium β decay: Corrections to and prospects of experimental verification of the final-state spectrum*, Physical Review C 60.3 (1999): 034601.

[KAV16] M. Arenz et al. (KATRIN Collaboration), *Commissioning of the vacuum system of the KATRIN Main Spectrometer*, Journal of Instrumentation 11.04 (2016): P04011.

[KBB05] C. Kraus et al., *Final results from phase II of the Mainz neutrino mass searchin tritium β decay*, The European Physical Journal C-Particles and Fields 40.4 (2005): 447-468.

[KFL18] M. Arenz et al. (KATRIN Collaboration), *First transmission of electrons and ions through the KATRIN beamline*, Journal of Instrumentation 13.04 (2018): P04020.

[Kle14] M. Kleesiek, *A Data-Analysis and Sensitivity-Optimization Framework for the KATRIN Experiment*, Ph.D. thesis, Karlsruhe Institute of Technology (KIT), Karlsruhe Germany, (2014).

[Kle18] M. Kleesiek et al., *β-Decay Spectrum, Response Function and Statistical Model for Neutrino Mass Measurements with the KATRIN Experiment*, arXiv preprint arXiv:1806.00369 (2018).

[Kuc18] L. Kuckert et al., *Modelling of gas dynamical properties of the KATRIN tritium source and implications for the neutrino mass measurement.*, Vacuum (2018), arXiv:1805.05313.

[Kuk16] L. Kuckert, *The Windowless Gaseous Tritium Source of the KATRIN Experiment - Characterisation of Gas Dynamical and Plasma Properties*, PhD thesis (2016)

[Lan60] L. D. Landau and E. M. Lifshitz, *Classical mechanics*, ed: Pergamon Press, Oxford (1960).

[Lar62] L. N. Large and W. S. Whitlock, *Secondary electron emission from clean metal surfaces bombarded by fast hydrogen ions*, Proceedings of the Physical Society 79.1 (1962): 148.

[Lob03] V. M. Lobashev, *The search for the neutrino mass by direct method in the tritium beta-decay and perspectives of study it in the project KATRIN*, Nuclear Physics A 719 (2003): C153-C160.

[Lob85] V. M. Lobashev and P. E. Spivak, *A method for measuring the electron antineutrino rest mass*, Nuclear Instruments and Methods in Physics Research Section A: Accelerators, Spectrometers, Detectors and Associated Equipment 240.2 (1985): 305-310.

[Luc00] L. L. Lucas and M. P. Unterweger, *Comprehensive review and critical evaluation of the half-life of Tritium*, Journal of research of the National Institute of Standards and Technology 105.4 (2000): 541.

[Luk11] S. Lukic et al., *Ion source for tests of ion behavior in the Karlsruhe tritium neutrino experiment beam line*, Review of Scientific Instruments 82.1 (2011): 013303.

[Mar17] E. Martin, *Electron Detection Systems for KATRIN Detector and Spectrometer Section*, Ph.D. thesis, University of Washington, Seattle USA, (2017).

[Mer13] S. Mertens et al., *Background due to stored electrons following nuclear decays in the KATRIN spectrometers and its impact on the neutrino mass sensitivity*, Astroparticle Physics 41 (2013): 52-62

[Mol16] M. Ady and R. Kersevan, *MOLFLOW+*, molecular flow TPMC simulation code, Tech. rep., CERN (2016). http://molflow.web.cern.ch/

[Nob15] The Nobel Prize in Physics 2015, *NobelPrize.org*, Nobel Media AB 2018, Mon. 22 Oct 2018. https://www.nobelprize.org/prizes/physics/2015/summary/

[Nuf17] I. Esteban et al., *Updated fit to three neutrino mixing: exploring the accelerator-reactor complementarity*, Journal of High Energy Physics 2017.1 (2017): 87.

[Oen76] O. S. Oen and M. T. Robinson, *Computer studies of the scattering of low energy hydrogen ions from polycrystalline solids*, Journal of Nuclear Materials 63 (1976): 210-214.

[Ols70] R. E. Olson et al., *Ion-Ion Recombination Total Cross Sections – Atomic Species*, The Journal of Chemical Physics 53.9 (1970): 3391-3397.

[Ott08] E. W. Otten and C. Weinheimer, *Neutrino mass limit from tritium* β *decay*, Reports on Progress in Physics 71.8 (2008): 086201.

[Pag10] G. Pagliaroli, F. Rossi-Torres and F. Vissani, *Neutrino mass bound in the standard scenario for supernova electronic antineutrino emission*, Astroparticle Physics 33.5 (2010): 287-291.

[Pau30] W. Pauli, *letter to a local meeting on radioactivity at Tübingen*, Germany (dated Dec. 4, 1930), original German version reprinted in: R. Kronig and V. Weisskopf (eds.), Wolfgang Pauli, Collected Scientific Papers, Vol. 2, Interscience, New York (1964) 1316; for an English translation see, e.g., Physics Today, 09/1978.

[PDG18] M. Tanabashi et al., *APS: Review of Particle Physics*, Phys. Rev. D 98 (2018): 030001.

[Per09] D. H. Perkins, *Particle astrophysics*, No. 10. Oxford University Press, 2009.

[Pic92] A. Picard et al., *A solenoid retarding spectrometer with high resolution and transmission for keV electrons*, Nuclear Instruments and Methods in Physics Research Section B: Beam Interactions with Materials and Atoms 63.3 (1992): 345-358.

[Pop11] V. N. Popok, *Energetic cluster ion beams: Modification of surfaces and shallow layers*, Materials Science and Engineering: R: Reports 72.7 (2011): 137-157.

[Pov09] B. Povh et al., *Teilchen und Kerne: eine Einführung in die physikalischen Konzepte*, Springer-Verlag, 2009.

[Pra11] M. Prall, *Background reduction of the KATRIN spectrometers: transmission function of the pre-spectrometer and systematic test of the main-spectrometer wire electrode*, Ph.D. thesis, Westfälische Wilhelms-Universität Münster, Münster Germany, (2011).

[PSB15] F. Priester, M. Sturm and B. Bornschein, *Commissioning and detailed results of KATRIN inner loop tritium processing system at Tritium Laboratory Karlsruhe*, Vacuum 116 (2015): 42-47.

[PTO13] S. Betts et al., *Development of a relic neutrino detection experiment at PTOLEMY: princeton tritium observatory for light, early-universe, massive-neutrino yield*, arXiv preprint arXiv:1307.4738 (2013).

[RaB71] J. A. Ray and C. F. Barnett, *Secondary Electron Emission of Metals Bombarded with 120-eV to 5-keV Protons*, Journal of Applied Physics 42.8 (1971): 3260-3261. https://doi.org/10.1063/1.1660722

[Roe17] C. Röttele, *Results of the first Cool-down of the KATRIN Cryogenic Pumping Section*, Journal of Physics: Conference Series. Vol. 888. No. 1. IOP Publishing, 2017.

[Roe19] C. Röttele, *Tritium suppression factor of the KATRIN-Experiment*, Ph.D. thesis, Karlsruhe Institute of Technology (KIT), Karlsruhe Germany, forthcoming work.

[Rud01] M. E. Rudd et al., *Cross sections for ionization of water vapor by 7–4000-keV protons*, Physical Review A 31.1 (1985): 492.

[Rud02] M. E. Rudd et al., *Electron production in proton collisions: total cross sections*, Reviews of modern physics 57.4 (1985): 965.

[Rup16] S. Rupp, *Development of a highly sensitive hollow waveguide based Raman system for the compositional analysis of the KATRIN tritium source gas*, Ph.D. thesis, Karlsruhe Institute of Technology (KIT), Karlsruhe Germany, (2016).

[Sch13] M. Schlösser, *Accurate calibration of the Raman system for the Karlsruhe Neutrino Experiment*, Ph.D. thesis, Karlsruhe Institute of Technology (KIT), Karlsruhe Germany, (2013).

[Sch16] K. Schönung, *Development of a Rear Wall for the KATRIN Rear Section and investigation of tritium compatibility of Rear Section components*, Ph.D. thesis, Karlsruhe Institute of Technology (KIT), Karlsruhe Germany, (2016).

[Shi93] D. Shiner et al., *H_2, D_2, and HD ionization potentials by accurate calibration of several iodine lines*, Physical Review A 47.5 (1993): 4042.

[Smi03] A. Y. Smirnov, *The MSW effect and solar neutrinos*, arXiv preprint hep-ph/0305106 (2003).

[Sne57] A. H. Snell, F. Pleasonton and H. E. Leming, *Molecular dissociation following radioactive decay: tritium hydride*, Journal of Inorganic and Nuclear Chemistry 5.2 (1957): 112-117.

[SNO09] N. Jelley, A. B. McDonald and R. G. H. Robertson, *The sudbury neutrino observatory*, Annual Review of Nuclear and Particle Science 59 (2009): 431-465.

[SRI10] J. F. Ziegler et. al., *SRIM–The stopping and range of ions in matter (2010)*, Nuclear Instruments and Methods in Physics Research Section B: Beam Interactions with Materials and Atoms 268.11 (2010): 1818-1823.

[Str96] H. C. Straub et al., *Absolute partial cross sections for electron-impact ionization of H_2, N_2, and O_2 from threshold to 1000 eV*, Physical Review A 54.3 (1996): 2146.

[Sug85] M. Sugisaki et al., *Surface reaction and bulk diffusion of tritium in SUS-316 stainless steel*, Journal of nuclear materials 133 (1985): 280-283.

[Tab00] T. Tabata and T. Shirai, *Analytic cross sections for collisions of H^+, H_2^+, H_3^+, H, H_2, and H^- with hydrogen molecules*, Atomic Data and Nuclear Data Tables 76.1 (2000): 1-25.

[Tho80] E. W. Thomas, *Retention and re-emission of 0.125-1 keV deuterium in stainless steel*, Journal of Applied Physics 51.2 (1980): 1176-1183.

[Tok85] N. Tokoro et al., *Energy and angular distributions of ejected electrons for hydrogen-cluster-ion (Hn+, Dn+, n= 1-3) impacts on helium in the intermediate energy region*, Journal of Physics B: Atomic and Molecular Physics 18.9 (1985): 1771.

[Ubi09] M. Ubieto-Diaz et al., *A broad-band FT-ICR Penning trap system for KATRIN*, International Journal of Mass Spectrometry 288.1 (2009): 1-5.

[Ubi11] M. Ubieto-Diaz, *Off-line commissioning of a non-destructive FT-ICR detection system for monitoring the ion concentration in the KATRIN beamline*, Ph.D. thesis, Ruperto-Carola University of Heidelberg, Heidelberg Germany, (2011).

[Val09] K. Valerius, *Spectrometer-related background processes and their suppression in the KATRIN experiment*, Ph.D. thesis, Westfälische Wilhelms-Universität Münster, Münster Germany, (2009).

[Val10] K. Valerius, *The wire electrode system for the KATRIN main spectrometer*, Progress in Particle and Nuclear Physics 64.2 (2010): 291-293.

[Wex59] S. Wexler, *Dissociation of TH and T_2 by β-decay*, Journal of Inorganic and Nuclear Chemistry 10.1-2 (1959): 8-16.

[Wil81] K. L. Wilson, *Hydrogen recycling properties of stainless steels*, Journal of Nuclear Materials 103 (1981): 453-463.

[Wil82] K. L. Wilson and M. I. Baskes, *Deuterium re-emission from 304LN stainless steel*, Journal of Nuclear Materials 111 (1982): 622-627.

[Zac15] M. Zacher, *High-field electrodes design and an angular-selective photoelectron source for the KATRIN spectrometers*, Ph.D. thesis, Westfälische Wilhelms-Universität Münster, Münster Germany, (2015).

[Zan88] A. Zangwill, *Physics at surfaces*, Cambridge university press, 1988.

[Zub06] K. Zuber, *Neutrinoless double beta decay experiments*, arXiv preprint nucl-ex/0610007 (2006).

Thank you...

- Prof. Guido Drexlin and Prof. Günter Quast for the opportunity of writing this thesis and for the education which you provided to this end since my undergraduate years.
- Kathrin Valerius for the supervision of my thesis, many a good conversation and especially for the organisational back-up of the ion safety report.
- Ferenc Glück for your pivotal groundwork to many aspects of this thesis and for the great teamwork! I will surely miss our collaborative contemplation.
- Floran Heizmann, Laura Kuckert, Karol Debowski and Jonas Kellerer for the companionship in room 207. Special thanks to Florian for the shared learning phase which is still ahead of us. And special thanks also to Laura for all the conversations about plasma and any other business in the office and on the bike.
- Woo-Jeong Baek for your crucial KASSIOPEIA simulations of ions in the spectrometers.
- Kerstin Schönung and Klaus Schlösser for the essential collaboration on the ELIOTT ion source during the preparation of the First Light measurement, as well as on the rear wall irradiation before and after First Light.
- for the help during and beside the measurement phases: Alexander Jansen, Magnus Schlösser, Florian Fränkle, Carsten Röttele, Joachim Wolf, Thomas Thümmler, Moritz Hackenjos, Ana Paula Vizcaya Hernandez, Rudolph Sack, Lutz Schimpf, Fabian Friedel, Caroline Rodenbeck, Johannes Heizmann, Alexander Marsteller, Markus Steidl, Katharina Fischer, Emma Malcherek...
- Sascha Wüstling and Armen Beglarian from the IPE for your support in advice and action.
- Siegfried Horn, Monika Kaiser, Jörg Bohn, Holger Frenzel and the whole workshop team from building 601.
- Thomas Höhn, Jürgen Grimm, Arne Felden and the whole group for Measurement Techniques and Automation Systems from building 601.
- Rolf Rinderspacher, Steffen Lichter, Holger Krause, Michaela Meloni and the whole group for Mechanical Engineering from building 601.
- Stephanie Hickford, Enrico Ellinger and Norman Haußmann for the friendly collaboration on the Faraday cup board for the Forward Beam Monitor.

- Sanshiro Enomoto, Florian Heizmann, Jan Behrens and Stephanie Hickford for the programming support, especially with BEANS.
- Christoph Heidecker, Thomas Huber, Nicolas Kurz, Bennet Krasch, Matthias Schnepf, Paul Schütze and Nicolai Walter for many years in lecture halls and mountain cabins.
- to my father Dietrich, my mother Margit, and all of my family for their support and the education, which brought me this far.
- Marie for her practical support, love and understanding throughout this thesis.